UNIVERSITY OF CALIFORNIA SAN DIEGO

Kinematics, Multiplicity, Rotational Dynamics, and Population Properties of Ultracool Dwarfs Inferred from High-Resolution Near-Infrared Spectroscopy

A dissertation submitted in partial satisfaction of the
requirements for the degree
Doctor of Philosophy

in

Physics

by

Chih-Chun Hsu (許智鈞)

Committee in charge:

Adam J. Burgasser, Chair
Jelena Bradic
Raphael Flauger
George M. Fuller
Christopher R. Gelino
Quinn M. Konopacky

2022

The dissertation of Chih-Chun Hsu (許智鈞) is approved, and it is acceptable in quality and form for publication on microfilm and electronically.

University of California San Diego

2022

DEDICATION

To my father, Kae-Chau Sheu (許凱超),

mother, Ya-Mien Chen (陳雅綿),

grandma, Chiu-Lan Hsu-Lin (許林秋蘭),

and brother, He-Ling Hsu (許鶴齡),

TABLE OF CONTENTS

LIST OF FIGURES

LIST OF TABLES

ACKNOWLEDGEMENTS

I would like to thank my family in Taiwan, my father, Kae-Chau Sheu (許凱超), mother, Ya-Mien Chen (陳雅綿), grandma, Chiu-Lan Hsu-Lin (許林秋蘭), and brother, He-Ling Hsu (許鶴齡), for their continuous support over the course of my life. They have been always allowing me to pursue what I really enjoy and love, so that I had the opportunity to pursue my doctoral degree in Physics at the University of California San Diego and the Center for Astrophysics and Space Sciences (CASS).

I would like to thank my thesis advisor, Professor Adam Burgasser, for his guidance since Fall 2016 when I joined the Cool Star Lab at UC San Diego. Adam has provided all-around Ph.D. training, support, and various opportunities for me, including abundant observing experience, proposal writing, undergraduate student mentorship, outreach activities, teaching experience, as well as informal discussions about personal improvements and learning, making me an independent researcher. There were numerous moments when I did not believe in myself, but Adam has faith in me. One incident coined in my heart is the concept of the growth mindset in a workshop led by Adam during my first year. I was a more fixed mindset person, and I am so glad that over time I have moved toward the growth mindset side. I am truly fortunate to have Adam to be my thesis advisor, and I also believe that Adam will be my lifelong mentor after I conclude my Ph. D. Adam really cares about his students and has been empathetic, understanding as well as adapting to my personal situation when I was severely injured and sick.

I would like to thank my committee members, Professor Quinn Konopacky, Dr. Christopher Gelino, Professor Raphael Flauger, Professor George Fuller, and Professor Jelena Bradic. Quinn has provided me with several research opportunities related to exoplanets and high-resolution spectroscopy and helped me learn more about the exoplanet research field. I have been enjoying the combo cool star and hot exoplanet group meeting and paper discussions with Quinn. Chris Gelino has provided the access to archival

data from the Keck Observatory Archive (KOA). Raphael and George have provided valuable theoretical discussions, and I also enjoyed your lectures, which have improved my understanding in physics and my way of studying a physics problem. Jelena has provided suggestions about computation and statistical foundations.

I would like to thank my research group, Dr. Christopher Theissen, Christian Aganze, and Roman Gerasimov. Chris Theissen has been my unofficial Ph. D. mentor since the first year when I joined the Cool Star Lab. His generous help in programming, advice, as well as suggestions on writing papers and proposals. I am truly grateful for what Chris has offered me, and I will miss the coffee trip after I leave with Chris. Christian and Roman are my friends and colleagues who provided insights into programming and computation skills as well as research discussions. Christian is the first person that I met as the Cool Star Lab member since I joined UCSD. One of the reasons that I was convinced that Adam will be an excellent advisor for me was through chatting with Christian about Adam and the lab before officially joining the lab. Christian also helped me learn and introduced numerous computational tools and skills at the beginning of my Ph. D. studies. Roman also introduced numerous computational skills and tools to me, and I also enjoyed playing tennis with him. Together with Adam, we also had informal group activities on campus, beaches, and sports for our off-research social activities.

I would like to thank Gregory Doppmann, Percy Gomez, Carlos Alvarez, and other Keck Observatory staff and support astronomers at the W. M. Keck Observatory for their help in more than 30 nights of NIRSPEC and NIRES observations. Using the W. M. Keck Observatory for my dissertation work has been my dream before starting my Ph. D., and I am glad that I had obtained abundant observing experience. These successful observing runs would not happen without your timely and detailed support and suggestions.

I would like to acknowledge the funding supported by the National Aeronau-

tics and Space Administration under Grant No. NNX15AI75G and National Science Foundation under award No. AST-1517177.

Chapter 2, in full, is a reprint of the material as it appears in the Astrophysical Journal Supplement Series 2021, Volume 257, Number 45. Hsu, Chih-Chun; Burgasser, Adam J.; Theissen, Christopher A.; Gelino, Christopher R.; Birky, Jessica L.; Diamant, Sharon J. M.; Bardalez Gagliuffi, Daniella C.; Aganze, Christian; Blake, Cullen H., Faherty, Jacqueline K. The thesis author was the primary investigator and author of this paper.

Chapter 3, in full is currently being prepared for submission for publication of the material. Hsu, Chih-Chun; Burgasser, Adam J.; Theissen, Christopher A.; Birky, Jessica L.; Aganze, C.; Gerasimov, R.; Covey K. R.; Blake, Cullen H.; Moreno-Hilario, E. The thesis author was the primary investigator and author of this paper.

VITA

2014	B. S. in Physics, National Tsing Hua University, Hsinchu, Taiwan
2016–2021	Graduate Teaching Assistant, Department of Physics, University of California San Diego
2020	Ph. D. candidate in Physics, University of California San Diego
2022	Graduate Student Researcher, Center for Astrophysics and Space Sciences, University of California San Diego
2022	Ph. D. in Physics, University of California San Diego

PUBLICATIONS

Hsu, C.; Burgasser, A. J.; Theissen, C. A.; Gelino, C. R.; Birky, J. L.; Diamant, S. J. M.; Bardalez Gagliuffi, D. C.; Aganze; C., Blake, C. H., Jacqueline K. Faherty,"The Brown Dwarf Kinematics Project (BDKP). VI. Radial and Rotational Velocities of late-M and L Dwarfs from Keck/NIRSPEC High-Resolution Spectroscopy", in prep.

Hsu, C.; Burgasser, A. J.; Theissen, C. A.; Birky, J. L.; Aganze, C.; Gerasimov, R.; Blake, C. H.; Covey, K. R.; Moreno-Hilario, E.,"*Ultracool Dwarf Radial and Rotational Velocity Survey with SDSS/APOGEE High-Resolution Spectrometer*", in prep.

Hsu, C.; Burgasser, A. J.; Bardalez Gagliuffi, D. C.; Sahlmann, Johannes; Theissen, C. A., "2MASS J21265916+7617440: A Long Period Brown Dwarf Binary System", in prep.

Hsu, C.; Burgasser, A. J.; Theissen, C. A.; Gelino, C. R.; Birky, J. L.; Diamant, S. J. M.; Bardalez Gagliuffi, D. C.; Aganze; C., Blake, C. H., Jacqueline K. Faherty,"The Brown Dwarf Kinematics Project (BDKP). V. Radial and Rotational Velocities of T Dwarfs From Keck/NIRSPEC High-Resolution Spectroscopy", ApJS 257, 45, December 2021.

Kiwy, Frank; Faherty, Jacqueline K.; Meisner, Aaron; Schneider, Adam C.; Kirkpatrick, J. Davy; Kuchner, Marc J.; Burgasser, Adam J.; Casewell, Sarah; Kiman, Rocio; Calamari, Emily; Aganze, Christian; **Hsu, Chih-Chun**; Sainio, Arttu; Thakur, Vinod; The Backyard Worlds: Planet 9 Collaboration, "Discovery of 34 low-mass comoving systems using NOIRLab Source Catalog DR2", accepted in ApJ, April 2022, arXiv:2204.09739

Aganze, Christian; Burgasser, Adam J ; Malkan, Mathew; Theissen, Christopher A; Tejada Arevalo, Roberto A; **Hsu, Chih-Chun**; Bardalez Gagliuffi, Daniella C; E Ryan, Russell, Jr; Holwerda, Benne, "Beyond the Local Volume II: Population Scaleheights and Ages of Ultracool Dwarfs in Deep HST/WFC3 Parallel Fields", accepted in ApJ, April 2022, arxiv:2204.07621

Softich, Emma; Schneider, Adam C.; Patience, Jennifer; Burgasser, Adam J.; Shkolnik, Evgenya; Faherty, Jacqueline K.; Caselden, Dan; Meisner, Aaron M.; Kirkpatrick, J. Davy; Kuchner, Marc J.; Gagne, Jonathan; Bardalez-Gagliuffi, Daniella; Cushing, Michael C.; Casewell, Sarah L.; Aganze, Christian; **Hsu, Chih-Chun**; Andersen, Nikolaj Stevnbak; Kiwy, Frank; Thevenot, Melina; The Backyard Worlds: Planet 9 Collaboration, "CWISE J014611.20-050850.0AB: The Widest Known Brown Dwarf Binary in the Field", ApJL, 922, L12, February 2022

Faherty, Jacqueline K; Gagne, Jonathan; Popinchalk, Mark; Vos, Johanna M.; Burgasser, Adam J.; Schumann, Jorg; Schneider, Adam C.; Kirkpatrick, J. Davy; Meisner, Aaron M.; Kuchner, Marc J.; Bardalez Gagliuffi, Daniella C.; Marocco, Federico; Caselden, Dan; Gonzales, Eileen C.; Rothermich, Austin; Casewell, Sarah L.; Debes, John H.; Aganze, Christian; Ayala, Andrew; **Hsu, Chih-Chun**; Cooper, William J.; Smart, R. L.; Gerasimov, Roman; Theissen, Christopher A.; The Backyard Worlds: Planet 9 Collaboration, "A Wide Planetary Mass Companion Discovered Through the Citizen Science Project Backyard Worlds: Planet 9", ApJ, 923, 48, December 2021

Aganze, Christian; Burgasser, Adam J ; Malkan, Mathew; Theissen, Christopher A; Tejada Arevalo, Roberto A; **Hsu, Chih-Chun**; Bardalez Gagliuffi, Daniella C; E Ryan, Russell, Jr; Holwerda, Benne, "Beyond the Local Volume I: Surface Densities of Ultracool Dwarfs in Deep HST/WFC3 Parallel Fields", ApJ, 924, 144, January 2022

Schneider, Adam C.; Meisner, Aaron M.; Gagne, Jonathan; Faherty, Jacqueline K.; Marocco, Federico; Burgasser, Adam J.; Kirkpatrick, J. Davy; Kuchner, Marc J.; Gramaize, Leopold; Rothermich, Austin; Brooks, Hunter; Vrba, Frederick J.; Bardalez Gagliuffi, Daniella; Caselden, Dan; Cushing, Michael C.; Gelino, Christopher R.; Line, Michael R.; Casewell, Sarah L.; Debes, John H.; Aganze, Christian Ayala, Andrew; Gerasimov, Roman; Gonzales, Eileen C.; **Hsu, Chih-Chun**; Kiman, Rocio; Popinchalk, Mark; Theissen, Christopher; Backyard Worlds: The Planet 9 Collaboration, "Ross 19B: An Extremely Cold Companion Discovered via the Backyard Worlds: Planet 9 Citizen Science Project", ApJ, 921, 150, November 2021

Theissen, C. A.; Konopacky , Q. M.; Lu, J. R.; Kim D.; Zhang, S. Y.; **Hsu, C.**; Chu, L.; Wei, L., "The 3-D Kinematics of the Orion Nebula Cluster: NIRSPEC-AO Radial Velocities of the Core Population", ApJ, 926, 141, February 2022

Meisner, Aaron M.; Schneider, Adam C.; Burgasser, Adam J.; Marocco, Federico; Line, Michael R.; Faherty, Jacqueline K.; Kirkpatrick, J. Davy; Caselden, Dan; Kuchner, Marc J.; Gelino, Christopher R.; Gagne, Jonathan; Theissen, Christopher; Gerasimov, Roman; Aganze, Christian; **Hsu, Chih-Chun**; Wisniewski, John P.; Casewell, Sarah L.; Bardalez Gagliuffi, Daniella C.; Logsdon, Sarah E.; Eisenhardt, Peter R. M., "New Candidate Extreme T Subdwarfs from the Backyard Worlds: Planet 9 Citizen Science Project", ApJ, 915, 120, July 2021

J. Davy Kirkpatrick; Christopher R. Gelino; Jacqueline K. Faherty; Aaron M. Meisner; Dan Caselden; Adam C. Schneider; Federico Marocco; Alfred J. Cayago; R. L. Smart; Peter R. Eisenhardt; Marc J. Kuchner; Edward L. Wright; Michael C. Cushing; Katelyn N. Allers; Daniella C. Bardalez Gagliuffi; Adam J. Burgasser; Jonathan Gagne; Sarah E. Logsdon; Emily C. Martin; James G. Ingalls; Patrick J. Lowrance; Ellianna S. Abrahams; Christian Aganze; Roman Gerasimov; Eileen C. Gonzales; **Chih-Chun Hsu**; Nikita Kamraj; Rocio Kiman; Jon Rees; Christopher Theissen; Kareem Ammar; Nikolaj Stevnbak Andersen; Paul Beaulieu; Guillaume Colin; Charles A. Elachi; Samuel J. Goodman; Leopold Gramaize; Leslie K. Hamlet; Justin Hong; Alexander Jonkeren; Mohammed Khalil; David W. Martin; William Pendrill; Benjamin Pumphrey; Austin Rothermich; Arttu Sainio; Andres Stenner; Christopher Tanner; Melina Thevenot; Nikita V. Voloshin; Jim Walla; Zbigniew Wedracki; "The Field Substellar Mass Function Based on the Full-sky 20-pc Census of 525 L, T, and Y Dwarfs", ApJS, 253, 7, March 2021

Sahlmann, Johannes; Dupuy, Trent J.; Burgasser, Adam J.; Filippazzo, Joseph C.; Martín, Eduardo L.; Bardalez Gagliuffi, Daniella C.; **Hsu, Chih-Chun**; Lazorenko, Petro F.; Liu, Michael C., "Individual Dynamical Masses of DENIS J063001.4−184014AB Reveal A Likely Young Brown Dwarf Triple", MNRAS, 500, 5453, January 2021

Meisner, Aaron M.; Faherty, Jacqueline K.; Kirkpatrick, J. Davy; Schneider, Adam C.; Caselden, Dan; Gagné, Jonathan; Kuchner, Marc J.; Burgasser, Adam J.; Casewell, Sarah L.; Debes, John H.; Artigau, Étienne; Bardalez Gagliuffi, Daniella C.; Logsdon, Sarah E.; Kiman, Rocio; Allers, Katelyn; **Hsu, Chih-Chun**; Wisniewski, John P.; Allen, Michaela B.; Beaulieu, Paul; Colin, Guillaume Durantini Luca, Hugo A.; Goodman, Sam; Gramaize, Léopold; Hamlet, Leslie K.; Hinckley, Ken; Kiwy, Frank; Martin, David W.; Pendrill, William; Rothermich, Austin; Sainio, Arttu; Schümann, Jörg; Andersen, Nikolaj Stevnbak; Tanner, Christopher; Thakur, Vinod; Thévenot, Melina; Walla, Jim; Wędracki, Zbigniew; Aganze, Christian; Gerasimov, Roman; Theissen, Christopher; The Backyard Worlds: Planet 9 Collaboration, "Spitzer Follow-up of Extremely Cold Brown Dwarfs Discovered by the Backyard Worlds: Planet 9 Citizen Science Project", ApJ, 889, 123, August 2020

Schneider, Adam C.; Burgasser, Adam J.; Gerasimov, Roman; Marocco, Federico; Gagné, Jonathan; Goodman, Sam; Beaulieu, Paul; Pendrill, William; Rothermich, Austin; Sainio, Arttu; Kuchner, Marc J.; Caselden, Dan; Meisner, Aaron M.; Faherty, Jacqueline K.; Mamajek, Eric E.; **Hsu, Chih-Chun**; Greco, Jennifer J.; Cushing, Michael C.; Kirkpatrick, J. Davy; Bardalez-Gagliuffi, Daniella Logsdon, Sarah E.; Allers, Katelyn; Debes, John H.; Backyard Worlds: Planet 9 Collaboration, "WISEA J041451.67-585456.7 and WISEA J181006.18-101000.5: The First Extreme T-type Subdwarfs?", ApJ, 989, 77, July 2020

Paudel, R. R., Gizis, J. E., Burgasser, A. J., **Hsu, C.**, "2MASS J10274572+0629104: the very short period young M6 dwarf binary system identified in K2 data", MNRAS, 486, 4144, July 2019

Low, Ryan; Burgasser, Adam J.; Reylé, Céline; Gerasimov, Roman; **Hsu, Chih-Chun**; Theissen, Christopher A, “Spectroscopic Confirmation of an M6 Dwarf Companion to the Nearby Star BD-08 2582", RNAAS, 5, 26, February 2021

ABSTRACT OF THE DISSERTATION

Kinematics, Multiplicity, Rotational Dynamics, and Population Properties of Ultracool Dwarfs Inferred from High-Resolution Near-Infrared Spectroscopy

by

Chih-Chun Hsu (許智鈞)

Doctor of Philosophy in Physics

University of California, San Diego, 2022

Adam J. Burgasser, Chair

Ultracool dwarfs (UCDs) are the lowest-mass stars and brown dwarfs, with mass < 0.1 $M_\odot$ effective temperatures $\leq 3,000$ K. Since they are abundant and long-lived, they can be tracers of the Milky Way formation and evolution history. In the past two decades, tens of thousands of UCDs have been discovered with all-sky surveys including the Two Micron All Sky Survey (2MASS), Wide-field Infrared Survey Explorer (*WISE*), and more recently the *Gaia* satellite. It is now possible to statistically and critically assess these objects as a population, by examining local UCD kinematics and angular momentum evolution, probing their formation history and evolution, and testing brown dwarf evolu-

tionary models. However, only a few hundred precise (3 km s^{-1}) radial (RV) and rotation velocities ($v \sin i$) are presently available due to these sources' faintness. I have developed a Markov Chain Monte Carlo forward-modeling technique to extract precise RVs and $v \sin i$s in the UCD regime and applied it to new and existing high-resolution near-infrared spectroscopic data obtained with the Near-Infrared Spectrometer (NIRSPEC) on the Keck II Telescope and the Apache Point Observatory Galactic Evolution Experiment (APOGEE) from the Sloan Digital Sky Survey (SDSS). These spectrographs cover the near-infrared waveband, which allow me to increase the number of precise RV and $v \sin i$ measurements for low-temperature UCDs, even for relatively low signal-to-noise ratios. I have modeled 219 unique UCDs with measurements taken over 773 epochs. Such a statistically large sample enables assessments of local UCD kinematics and angular momentum evolution, and identifications of substellar binaries. From my analysis, I have resolved a decade-long mystery of local L dwarfs having old kinematics, inconsistent with population simulations incorporating brown dwarf evolutionary models; this can be explained by a high rate of contamination of thick disk L dwarfs in the local sample. I also identified a kinematic break around L4–L6 subtypes, which aligns with the terminus of the stellar Main Sequence. I have identified and confirmed 21 UCD binaries using the RV method, including the first two T dwarf binary systems and one of the shortest period UCD binaries identified to date. UCDs statistically rotate faster from late-M to T types, indicating that their angular momentum is not efficiently lost through magnetized winds as it is for normal stars, consistent with previous studies. For a subset of M and L dwarfs with APOGEE data and measured variability periods, I found that the projected radii generally decline as a function of age, and that the inclination distribution of the $\sim$10 Myr Upper Scorpius cluster and field objects are both consistent with random orientation distribution. I provide a comprehensive sample of RVs, $v \sin i$s, effective temperatures ($T_{\rm eff}$) and surface gravities ($\log g$) for 349 late-M, L, and T dwarfs based on observations

made in this work.

Chapter 1

Introduction

1.1 Ultracool Dwarfs

Ultracool dwarfs (UCDs) are low-mass ($M < 0.1$ $M_\odot$) stellar and substellar objects with effective temperatures $T_{\rm eff} \leq 3{,}000$ K and spectral types M7 or later, encompassing late-M, L, T, and Y dwarf spectral classes (Kirkpatrick et al. 1999; Kirkpatrick 2005; Burgasser et al. 2006b; Cushing et al. 2011). Figure 1.1 (McLean et al. 2003; Kirkpatrick et al. 1995) shows a spectral sequence of UCDs, ranging from M6–T8 in the near-infrared waveband. Distinct from F-, G-, and K-type stars which show mostly hydrogen and other atomic absorption features, UCDs have photospheric temperatures low enough to host abundant molecular species and associated absorption features. The prominent molecular features of late-M and L dwarfs in the near-infrared are H_2O, CO, FeH, and alkali lines such as K I and Na I, and clouds of condensates such as iron or corundum (Al_2O_3) in L dwarfs Allard et al. (2001). As the spectral sequence transitions to the T dwarf regime, CH_4 emerges as the prominent absorption feature of T dwarfs, converted from CO at the L/T transition. Collision-induced absorption (CIA) H_2 also appears in late-L and T dwarf spectra, widely suppressing K-band flux (Linsky 1969;

Burgasser et al. 2002). Figure 1.2 illustrates the theoretical thermal evolution of UCDs based on models from Burrows et al. (1997), Chabrier et al. (2000), and Baraffe et al. (2003). The thermal evolution of stellar UCDs (i.e. lowest-mass stars) reflects their slower contraction over $\sim$1 Gyr followed by the ignition of core nuclear H fusion reactions in the Main Sequence. The minimum core temperature for H fusion is 3×10^6 K in the Burrows et al. (1997) models. Substellar UCDs, never reach thermal equilibrium, but maintain hydrostatic equilibrium between electron degeneracy pressure and gravity (Kumar 1962, 1963; Hayashi & Nakano 1963). As such, substellar UCDs constantly cool over time. Late-M (3,000 K $\gtrsim T_{\rm eff} \gtrsim$ 2,500 K) and L dwarfs (2,500 K $\gtrsim T_{\rm eff} \gtrsim$ 1,400 K) are a mixed population of low-mass stars and brown dwarfs, while T dwarfs (1,400 K $\gtrsim T_{\rm eff} \gtrsim$ 600 K) and Y dwarfs ($T_{\rm eff} \lesssim$ 600 K) are all substellar.

UCDs are abundant in the Galaxy (20–50% of all stars; Bochanski et al. 2007a; Kirkpatrick et al. 2019, 2021; Reylé et al. 2021) and have lifetimes several orders of magnitude longer than the current age of the Universe (Laughlin et al. 1997). UCDs thus provide a means of investigating the low-mass star formation and chemical enrichment history of the Milky Way and its substructures (Bochanski et al. 2007a; Burgasser 2009). In addition, the long-term cooling brown dwarfs makes them useful tracers of age in various populations. Indeed, brown dwarfs have been used to age-date young clusters (Stauffer et al. 1998; Martín et al. 2018) and binaries (Song et al. 2002), and could potentially be used to age-date other Galactic populations such as globular clusters and the Galactic halo (Burgasser 2009; Caiazzo et al. 2017; Gerasimov et al. 2022).

Over the past two decades, thousands of UCDs have been discovered with large-area sky surveys such as the Deep Near Infrared Survey of the Southern Sky (DENIS; Epchtein et al. 1997), the Two Micron All Sky Survey (2MASS; Skrutskie et al. 2006), the Sloan Digital Sky Survey (SDSS; York et al. 2000), the UKIRT Infrared Deep Sky Survey (UKIDSS; Lawrence et al. 2007), *Wide-field Infrared Survey Explorer* (*WISE*; Cutri & et

al. 2012), the Panoramic Survey Telescope and Rapid Response System (Pan-STARRS; Chambers et al. 2016), Canada-France-Hawaii Telescope Legacy Survey (CFHTLS; Gwyn 2012), the VISTA Hemisphere Survey (VHS; McMahon et al. 2013), and *Gaia* (Gaia Collaboration et al. 2018a, 2021), among others. These surveys have provided photometry and astrometry measurements, including proper motions and parallaxes, useful for studying the statistical properties of UCDs (Faherty et al. 2009). As will be shown in the following sections, the addition of high-resolution spectroscopy facilitates studies of kinematics and age (Section 1.2), multiplicity (Section 1.3), and rotation (Section 1.4).

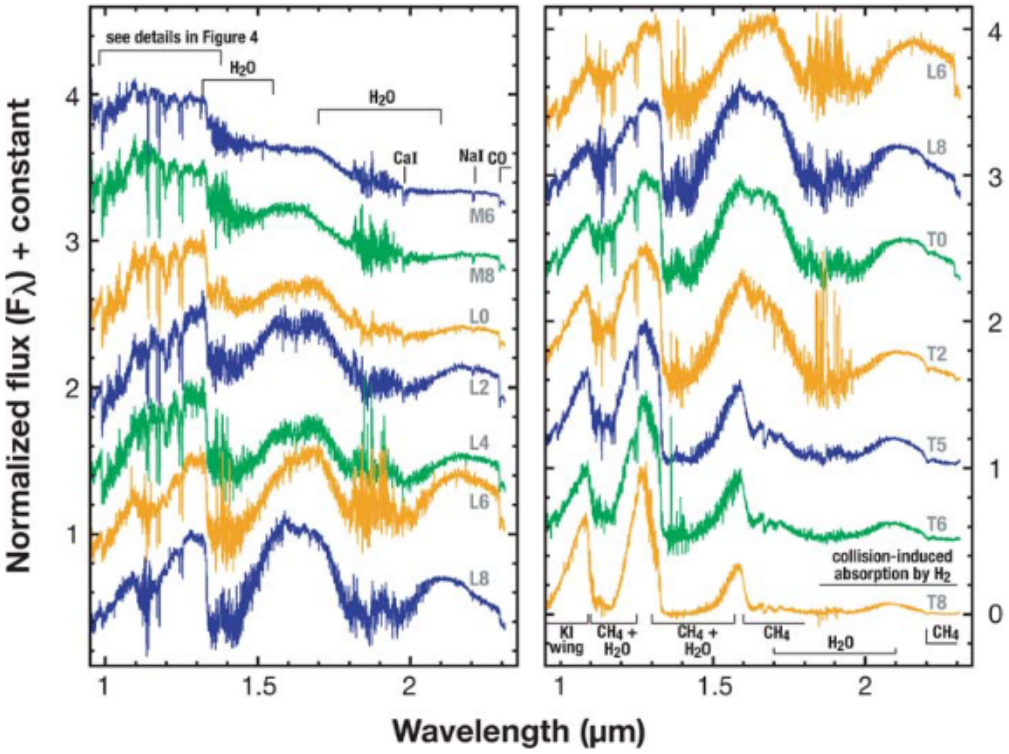

Figure 1.1: Near-infrared spectral sequence of UCDs, ranging from M6 (top left) to T8 (bottom right), over a wavelength range of 0.95–2.3 μm. Prominent atomic and molecular absorption features are labeled. (Figure 3 from Kirkpatrick 2005, data originally from McLean et al. 2003).

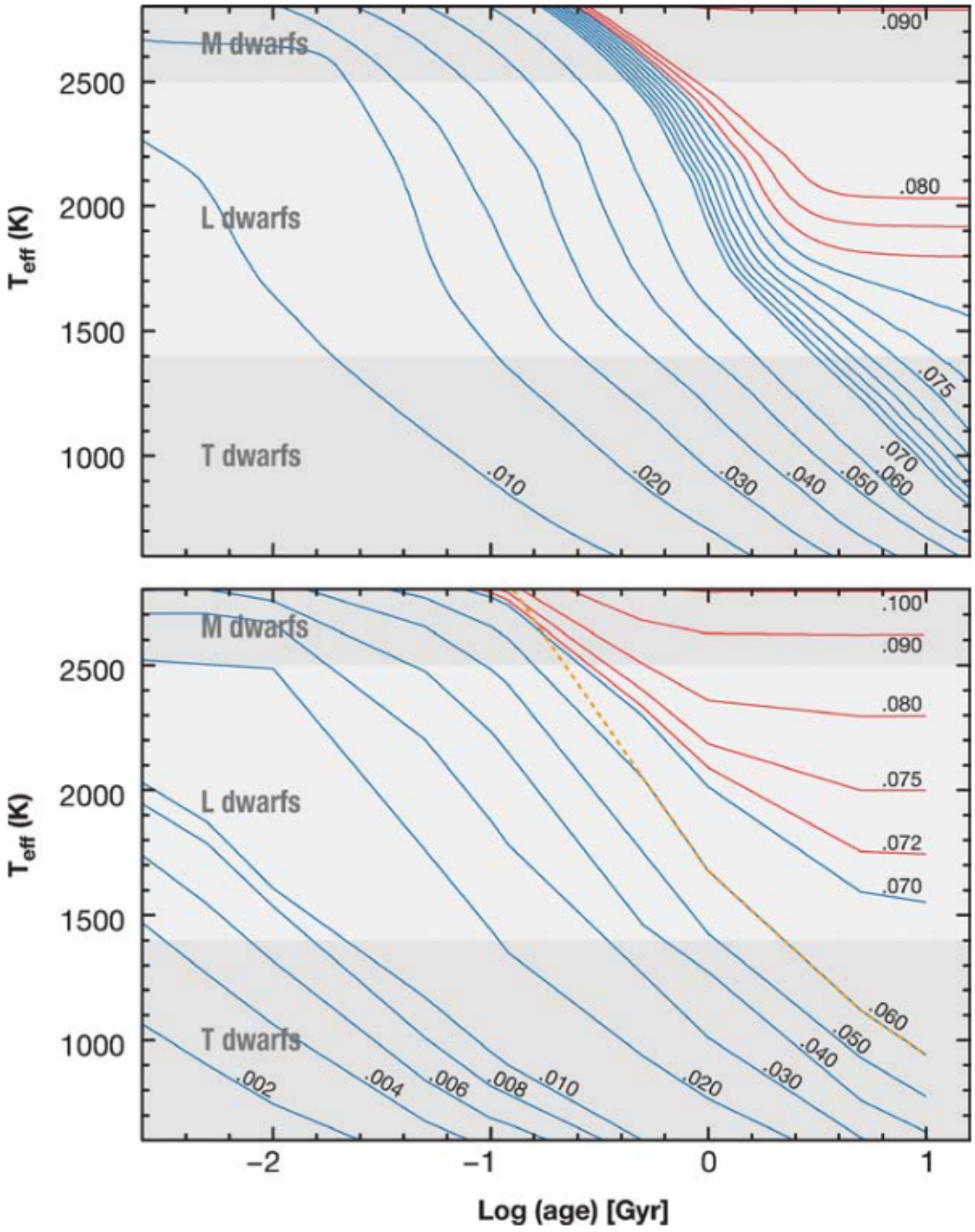

Figure 1.2: Theoretical thermal evolution tracks of ultracool dwarfs. Stars and brown dwarfs are labeled in red and blue lines, representing constant masses in $M_{\odot}$. The approximate temperature ranges of late-M, L, and T dwarfs are labeled in different grey bands. *Top*: Models from Burrows et al. (1997). *Bottom*: Models from Chabrier et al. (2000) for $T_{\rm eff}$ >1,500 K and Baraffe et al. (2003) for $T_{\rm eff}$ <1,500 K. The orange line in the bottom panel shows the 50% depletion of primordial lithium computed by Chabrier et al. (2000). (Figure 10 from Kirkpatrick 2005).

1.2 Kinematics, Age, and Evolution

Stellar kinematics can provide an independent method of measuring the age of Galactic populations. Coarse ages can be inferred through different Galactic populations for thin disk, thick disk, and halo populations (Bensby et al. 2003; Pinfield et al. 2014). For an ensemble of stars, empirical age-velocity dispersion relations can be used to measure their statistical age caused by disk heating mechanisms. Stars form in clusters within the Galactic disk. After their birth, they undergo diffuse dynamical scattering with giant molecular clouds, the Galactic spiral arms, and bar structure, resulting in larger velocity dispersion over time (Wielen 1977; Aumer & Binney 2009). The study of UCD populations must account for the distinct thermal and dynamical evolution of stars and brown dwarfs. UCD population analyses make use of simulations incorporating stellar and substellar evolution to map physical properties (age, mass, composition) to present-day observables (Reid et al. 1999; Burgasser 2004; Kirkpatrick et al. 2019). A consistent prediction of these simulations is that L-type UCDs, a mix of stars and rapidly-cooling brown dwarfs (typical L-type dwarf cooling timescale $\tau \approx 0.5$–1 Gyr; Burrows et al. 1997; Baraffe et al. 2003), should be on average younger than late M-type UCDs, which are predominantly long-lived stars (Reid et al. 1999; Burgasser 2004; Allen et al. 2005; Ryan et al. 2017). Observations of statistical ages through kinematics have mostly contradicted this prediction. In one of the first 3D kinematic studies of UCDs, combining RVs and tangential velocities, Zapatero Osorio et al. (2007) found that local L and T dwarfs had a lower velocity dispersion than local late-M dwarfs, although the sample included only 21 L and T dwarfs. A 2D proper motion survey of 277 UCDs by Faherty et al. (2009) found local 20 pc L dwarfs to be marginally older than late-M and T dwarfs, while their whole sample of 841 UCDs gave consistent ages. Schmidt et al. (2010) identified both young and old L dwarf populations in a 3D kinematic survey of

over 300 sources using low-resolution spectroscopy. The diagnostic power of these early studies was limited by incomplete samples and relatively low-precision measurements ($\sigma_{\rm RV} \gtrsim$ 5–10 km s^{-1}).

Subsequent volume-limited 3D kinematic surveys of late-M and L dwarfs using high-resolution spectra and improved astrometry have consistently found the local L dwarf population to be significantly more dispersed, and hence older, than the late-M dwarfs, in disagreement with simulation predictions (Reiners & Basri 2009a; Seifahrt et al. 2010; Blake et al. 2010; Burgasser et al. 2015a). The most recent study prior to this thesis by Burgasser et al. (2015a) attempted to explain this discrepancy as an evolution of the mass function over time, with a greater abundance of brown dwarfs at earlier ages. While this ansatz was able to correctly predict the relative ages of late-M and L dwarfs, the absolute ages and corresponding mass function were inconsistent with observations. Whether this persistent disagreement between simulated and observed ages of L dwarfs arises from a more complex star and brown dwarf formation history, a problem with brown dwarf evolutionary models, or incompleteness or bias in the local UCD sample, remains uncertain.

The kinematics of local T dwarfs can provide clarity on this issue. These low-temperature, evolved brown dwarfs have cooling ages of several Gyr, and are predicted to be kinematically older than L dwarfs (Burgasser 2004). T dwarfs are also intrinsically fainter than late-M and L dwarfs, limiting the number of sources with suitable high-precision RV measurements. While there are more than 500 T dwarfs currently known, there are fewer than 15 T dwarfs with precise RV ($\sigma_{\rm RV} \leq 3$ km s^{-1}) and rotational velocity ($\sigma_{v \sin i} \leq 5$ km s^{-1}) measurements reported in the literature (Zapatero Osorio et al. 2006, 2007; Prato et al. 2015; Gagné et al. 2017, 2018a; Vos et al. 2017, 2018). This sample is insufficient to accurately measure kinematic dispersions and ages, or test population simulations. This lack of data motivated my study to expand the local T dwarf

high-resolution spectroscopic sample using Keck/NIRSPEC data.

1.3 Multiplicity

Multiplicity is the direct outcome of star formation. Identifying and characterizing multiple systems through observations provide measurements of orbital parameters including separations, periods, and eccentricity in different environments and ages, which can be used to refine the Initial Mass Function (IMF) and constrain binary formation theories, as well as long-term dynamical evolution and stability of such systems (Duchêne & Kraus 2013). The multiplicity frequency (MF) generally decreases from higher mass (MF $\geq 80\%$ for stellar mass $M \gtrsim 16$ $M_\odot$; Chini et al. 2012) to the ultracool dwarfs ($22^{+6}_{-4}\%$, Allen 2007; $\approx 20\%$, Burgasser 2007). The distribution of binary mass ratios ($q = M_{\rm secondary}/M_{\rm primary}$), often characterized by a power-law distribution ($f(q) = q^\gamma$), broadens with mass, meaning that higher-mass stars prefer to form unequal mass binaries ($\gamma = -0.5 \pm 0.2$ for $1.5\ M_\odot \lesssim M \lesssim 5$ $M_\odot$; Duchêne & Kraus 2013), while UCD binaries are likely to form in equal masses ($\gamma = 4.2 \pm 1.0$; Burgasser et al. 2007). The separation distribution is larger for high-mass stars than lower-mass stars, and its frequency $f(P)$ can be characterized by a power law with period P, $f(P) \propto P^{-1}$ (Öpik 1924), a trend that continues down to early M dwarf primaries (Dhital et al. 2010). In the UCD regime, the typical binary separation is 4–7 AU while limited by instrumental resolutions (Burgasser et al. 2007; Dupuy & Liu 2017). The eccentricity distribution favors higher eccentricities for solar-type stars (all binaries $e > 0.1$; Raghavan et al. 2010) and lower eccentricities for UCDs (most binaries with $e < 0.2$; Dupuy & Liu 2017). The difference may be explained by longer-lived dissipative gas disks for UCDs (Dupuy & Liu 2017). Similar to the multiplicity frequency trend over mass, high-order multiple systems (hierarchical systems) are more likely to be present in higher-mass stars than UCDs (Dhital et al. 2010;

Duchêne & Kraus 2013), although higher-order multiple systems of UCDs are more difficult to identify due to their faintness. To statistically constrain multiplicity properties, careful and complete surveys must be conducted, a challenge for intrinsically faint UCDs.

Most of the UCD binaries discovered to date are resolved binaries (Bardalez Gagliuffi et al. 2019a; Figure 1.3), largely found through high-resolution imaging with the *Hubble Space Telescope* and ground-based, large aperture, adaptive optics instruments (e.g. Konopacky et al. 2010; Dupuy & Liu 2017; Brandt et al. 2019). Imaging observations are useful in providing dynamical masses but have a resolution limit $\sim$1 AU (Dupuy & Liu 2017; Bardalez Gagliuffi et al. 2019a). Closer systems need to be identified through other techniques, such as overluminosity, spectral binaries, astrometric variability, and radial velocity variability. Overluminosity on color-magnitude diagrams is an efficient means of identifying unresolved binaries but requiring accurate parallaxes, favoring equal-mass binaries, and can be contaminated by other effects such as metallicity, age, reddening, and background contamination, so follow-up spectroscopic, astrometric, or adaptive optics observations are needed to confirm (Smart et al. 2019). Spectral binaries are identified by the peculiar blended-light spectra of binaries with different components, which can be inferred through binary template fitting with low-resolution spectra (Burgasser et al. 2008, 2010; Bardalez Gagliuffi et al. 2014). Again, contamination by metallicity and other effects requires follow-up imaging, astrometric and/or high-resolution spectroscopic observations to verify such systems. Astrometric variables arise from the orbital motion of the center of light of a system relative to the center of mass, favoring unequal brightness systems at close separations (Sahlmann et al. 2015, 2020, 2021). These systems necessitates very precise astrometry and are blind to equal-brightness/equal-mass systems. Radial velocity (RV) variables are detected from the Doppler shift of the spectra of the primary (single-line binary; SB1) or both components (double-line binary; SB2) and can detect both high- and low-mass companions

(RV variability is the technique used for the detection of the first exoplanet 51 Pegasi b; Mayor & Queloz 1995). This method for UCDs typically requires high-resolution near-infrared spectrometers on large aperture telescopes due to UCDs' intrinsic faintness (Blake et al. 2010; Burgasser et al. 2015b, 2016). However, this method is limited to close binaries while wide binaries can be discovered through imaging with consistent proper motions and astrometry (RV can be still used to verify the comoving nature of wide binaries).

To precisely characterize the orbits of unresolved, close UCD binaries requires high-resolution spectroscopy. The other methods cannot provide precise mass measurements for short period binaries such as 2MASSW J1510478−281817AB system (Figure 1.4). Due to the need for near-infrared high-resolution spectroscopy on large aperture telescopes, only 7 UCD binaries prior to this work have been discovered or verified through the RV method. Relevant systems include the M8.5 + T5 binary 2MASS J03202839−0446358 (Blake et al. 2010), the resolved M9 + T5 binary WISE J072003.20−084651.2 (Burgasser et al. 2015b; Dupuy et al. 2019), and the young M9 + M9 eclipsing binary 2MASSW J1510478−281817 (Triaud et al. 2020; Figure 1.4). It is noted that 2MASS J03202839−0446358 and WISE J072003.20−084651.2 were both identified as spectral binaries. Blake et al. (2010) estimate an RV binary fraction of $2.5^{+8.6}_{-1.6}$ for UCDs (Table 1.1), compared to 3–4% for M dwarfs (Clark et al. 2012) and 24±4% for higher-mass stars (Moe et al. 2019).

1.4 Rotation

Stellar rotation is another quantity that connects to star formation and evolution (and age), as well as the generation of magnetic fields and stellar activity. There are two primary methods of measuring stellar rotation, including variability rotation periods from

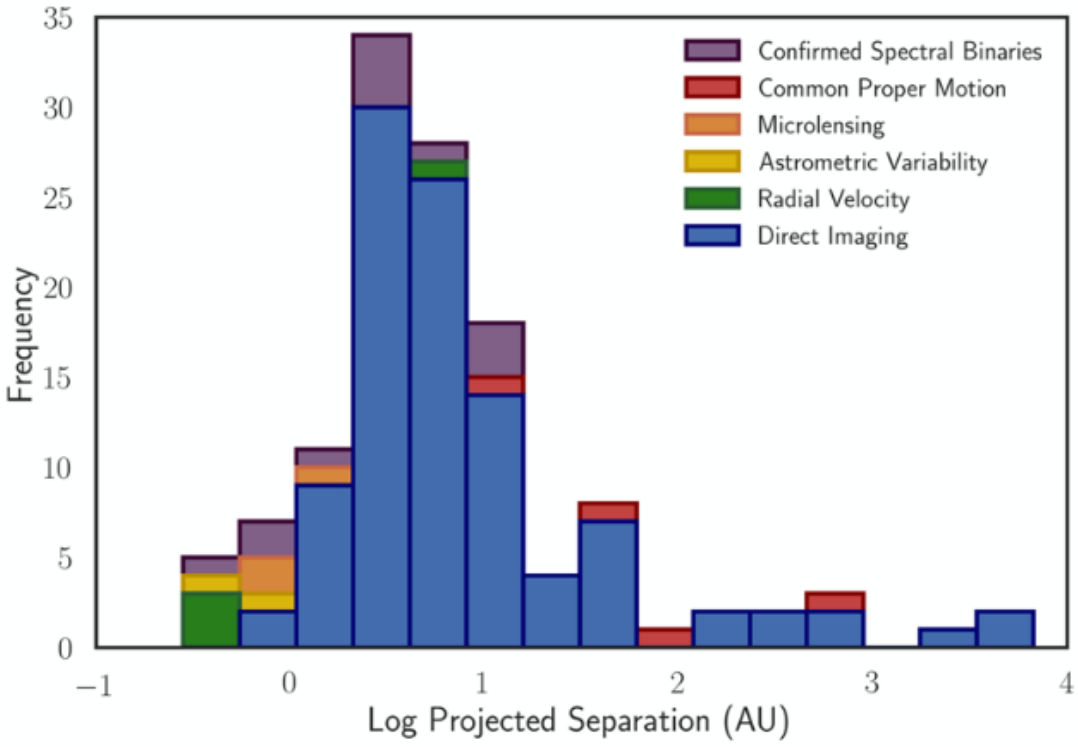

Figure 1.3: Binary detection frequency and projected separation distribution of ultracool binaries discovered up to 2014. The detection techniques are labeled in different colors as shown in the legend. The peak at 2.5 AU corresponds to the imaging resolution limit of the *Hubble Space Telescope* and ground-based adaptive optics instruments. The "Common Proper Motion" binaries are identified and confirmed with *Gaia* proper motion, which are a subset of the "Direct Imaging" binaries. (Figure 1 from Bardalez Gagliuffi et al. 2019a).

light curves and Doppler line broadening from high-resolution spectroscopy. Rotation periods for UCDs have been measured with *Spitzer* (Werner et al. 2004), the *Kepler* and *K2* Mission (Koch et al. 2010; Howell et al. 2014), the *Transiting Exoplanet Survey Satellite* (*TESS*; Ricker et al. 2015), and ground-based facilities such as MEarth (Nutzman & Charbonneau 2008), and SPECULOOS (Sebastian et al. 2021) among others. This method is limited to objects that are varying and periodic. Late-M dwarfs have no clear correlation with period and amplitude and show both short and long periods from 0.1 to >100 days (Irwin et al. 2011; Newton et al. 2016). Metchev et al. (2015) found that photometric variability is common among L dwarfs (80^{+20}_{-27}%) and becomes lower for

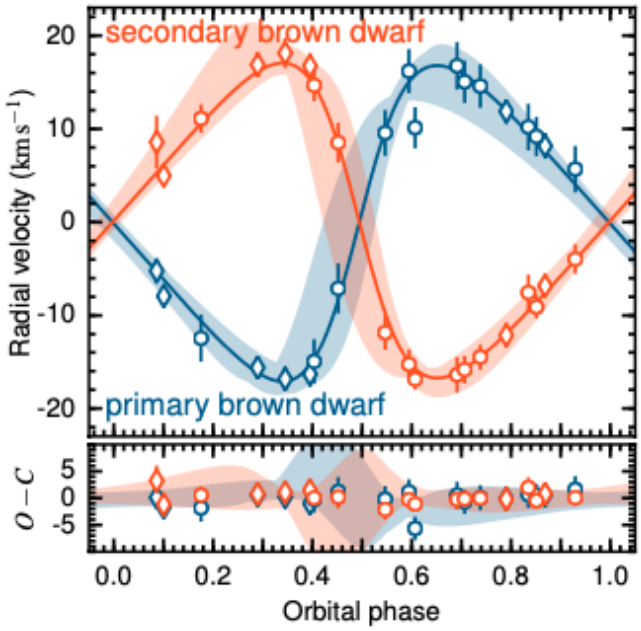

Figure 1.4: Phase-folded RV time series of M9 + M9 eclipsing binary 2MASS J1510478−281817. *Top*: The primary (blue) and secondary (orange) RV measurements (VLT/UVES: circles; Keck/NIRSPEC: diamonds) and the corresponding RV orbital fits (same colors with 2-σ uncertainties in shaded regions). *Bottom*: Residuals (data−model) and the corresponding uncertainties for both components with the same colors. (Figure 5b from Triaud et al. 2020).

T dwarfs (36^{+26}_{-17}%). Vos et al. (2022) found young brown dwarfs are more likely to exhibit variability between L2–T4 dwarfs than the field dwarfs. These studies assume observed variability arises from stable starspots or clouds, and that these features align with bulk rotational dynamics. Projected rotational velocity ($v \sin i$) is measured from high-resolution spectroscopy through the Doppler broadening of spectral lines (Gray 1992; Collins & Truax 1995), which does not rely on variability but is limited sources with strong features. Mohanty & Basri (2003) showed that the $v \sin i$s increase from mid-M to L dwarfs. Zapatero Osorio et al. (2006), which is the largest T dwarf $v \sin i$ survey prior to this work, illustrated the trend continue to increase to T dwarfs. Both of the studies used high-resolution spectroscopy. Although the $v \sin i$ method has a lower limit set by the spectral resolution limit, $v \sin i$s of L and T dwarfs measured in the

Table 1.1: Confirmed UCD RV Binaries

short name	full name	SpT	Type	Ref
J0320−0446	2MASS J03202839−0446358	M8.5+T5	SB1[b]	(2)
J0535−0546	2MASS J05352184−0546085	M6.5+M6.5	SB2[a]	(1)
J0630−1840	DENIS J063001.4−184014	M9+L2	SB1[c]	(7)
J0720−0846	WISE J072003.20−084651.2	M9.5+T5	SB1[b]	(3)
J0805+4812	SDSS J080531.84+481233.0	L3.5+T4.5	SB1[b]	(4)
J1059−2113	2MASS J10595138−2113082	L0+T3.5	SB1[b]	(6)
J1106+2754	2MASS J11061197+2754225	T0+T4.5	SB1[b]	(8)
J1510+2818	2MASS J15104761−2818234	M9+M9	SB2[a]	(5)
J2126+7617	2MASS J21265916+7617440	L7+T3.5	SB1[b]	(8)

Reference: (1) Stassun et al. (2006), (2) Burgasser et al. (2008), (3) Burgasser et al. (2015b), (4) Burgasser et al. (2016), (5) Triaud et al. (2020), (6) Sahlmann et al. (2020), (7) Sahlmann et al. (2021), (8) Hsu et al. (2021)
Note: (a) eclipsing binary, (b) spectral binary, (c) astrometric binary.

literature typically are well above the resolution limit and well below the break up speed ($\sqrt{GM/R}$ = 155 – 365 km s^{-1}, assuming mass M = 0.013 – 0.072 $M_\odot$ and radius R = 1 $R_{\rm Jupiter}$).

Rotation connected to stellar age over time through the loss of angular momentum through magnetized winds. Normal F-, G-, and K-type stars have a well-characterized connection between age, rotational spin-down, and declined activity encompassed by the Skumanich Law ($\tau^{-0.5}$, where τ is the stellar age; Skumanich 1972), which has been extensively used to age-date the stars through rotation (so-called "gyrochronology"). At their earliest ages, stars first spin up due to contraction and converge into a narrow range of rapid rotation rates until reaching the zero-age Main Sequence (ZAMS) around 600 Myr. As these stars have convective envelopes, they draw dynamos that generate magnetic fields which strength with faster rotation speeds. Differential rotation of solar-type stars twists the magnetic fields and generates stellar flares and winds, leading to the ejection of material that also carries away angular momentum (Barnes 2003, 2007; Irwin et al. 2011). The resulting spin-down reduces magnetic field strength, connecting

age, rotation, and activity. The spin-down trend continues into fully convective M dwarfs although the spin-down timescale become longer for M dwarfs than solar-type stars (West et al. 2008; Irwin et al. 2011). Mohanty & Basri (2003) have shown that M9–L6 dwarfs can be fast rotators with weak magnetic emission (indicated from Hα emission observations), which can be explained by their cool and neutral atmospheres becoming decoupled from magnetic fields, and thus breaking the rotation-magnetic activity relation. This has been validated in rotational periods in different cluster ages (Baraffe et al. 2003; Angus et al. 2019), and projected rotational velocity measured with high-resolution spectroscopy (Mohanty & Basri 2003; Irwin et al. 2011; Crossfield 2014). Figure 1.5 illustrates a compilation of period, variability, and $v \sin i$ from Crossfield (2014). Note that periods tend to get shorter and $v \sin i$ tends to increase toward later spectral type, which can be explained with reduced angular momentum loss for cooler UCDs.

Rotation also provides insight into the geometry of a star, including radius and viewing orientations. The combination of rotational period, $v \sin i$, and radius allows stellar inclination to be measured (Vos et al. 2017, 2022). Sources with edge-on inclinations (90 deg) can be prioritized for the search for exoplanet systems (Triaud et al. 2010; Triaud 2018), while pole-on inclinations (0 deg) can be used for studies of magnetic field axis alignments with stellar rotational orientations (Smith et al. 1974; Acuna & Ness 1976). For bright UCDs such as the Luhman 16AB (Luhman 2013; Burgasser et al. 2013), the Doppler imaging technique can be used to infer global cloud properties by measuring variations in the line shape over time (Donati et al. 2006; Crossfield et al. 2014). Zeeman line broadening or splitting in spectra, which originates from the quantum mechanical spin-orbit coupling of electron orbitals with a magnetic field and splits energy level (Zeeman 1897), can be measured through magnetically sensitive lines such as FeH at $\sim$1 μm in high signal-to-noise ratio high-resolution spectra (Reiners & Basri 2007, 2009b).

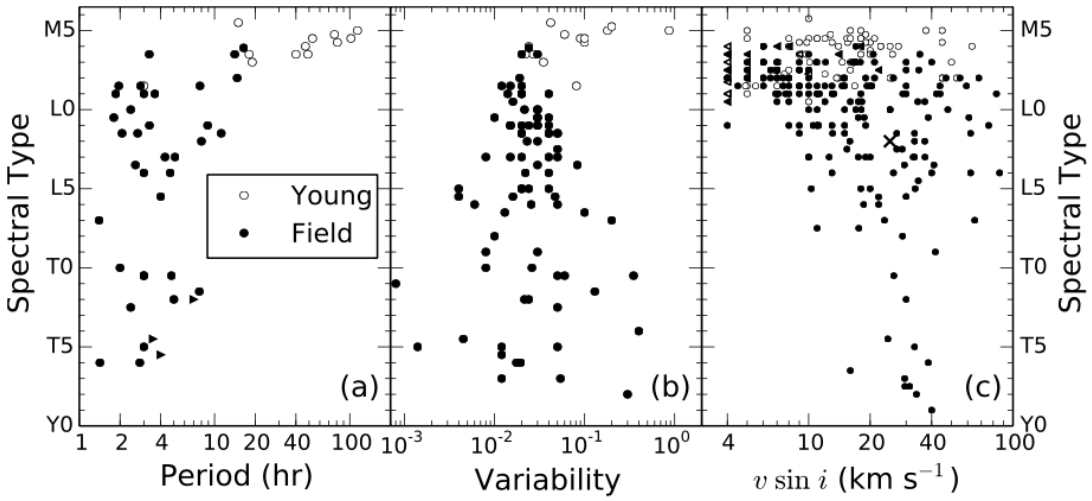

Figure 1.5: Compilation of literature measurements versus spectral type for (a) periods, (b) variability (photometric variability semi-amplitude in any filters), and (c) projected rotational velocity ($v \sin i$). Young (sources associated with known young clusters or young moving groups reported in literature) and field objects are labeled in open and solid dots, respectively. The triangles in (a) and (c) indicate the upper limit on periods and lower limits to $v \sin i$, respectively. The cross symbol indicates the young giant exoplanet Beta Pic b (Snellen et al. 2014). (Figure 1 from Crossfield 2014).

1.5 High-resolution Spectroscopy

High-resolution spectroscopy provides several opportunities for studying UCDs in detail, including precise measurements of RVs, $v \sin i$s, stellar abundances, and detailed spectral line-profile modeling. Radial velocities are essential for full 3D precise kinematics, which can then be used to determine their Galactic populations (Bensby et al. 2003) and membership in nearby young clusters and moving groups (Gagné et al. 2018c). Kinematic distribution also probes the ages of stellar populations through empirical age-velocity dispersion relations (Wielen 1977; Aumer & Binney 2009) (Section 1.2). Multi-epoch precise radial velocities allow me to identify single-line or double-line low-mass binaries (e.g. Blake et al. 2010; Burgasser et al. 2016; Triaud et al. 2020), crucial in constraining binary parameters including orbital periods, separation, and eccentricity (Section 1.3). Projected rotational velocities ($v \sin i$) for UCDs of known ages map angu-

lar momentum evolution as a function of age and magnetic activity (Zapatero Osorio et al. 2006; Irwin et al. 2011), while individual rotational velocities probe spin/orbit alignment (Rossiter–McLaughlin effect) for exoplanet systems, and can be used to prioritize transit searches (Triaud et al. 2010; Triaud 2018, Section 1.4). High-resolution spectroscopy is also necessary to determine precise abundances, including those of species such as C, O, Na, Mg, Al, Si, K, Ca, Ti, V, Cr, Mn, Fe, and N (Souto et al. 2022) and isotopes (e.g. ^{12}CO and ^{13}CO; Tsuji 2016; Souto et al. 2017; Crossfield et al. 2019). Finally, high-resolution spectroscopy enables detailed line modeling, influenced by Zeeman splitting (magnetic field strength), limb darkening (atmospheric structure), Doppler variations (magnetic spots and clouds), and pressure broadening (surface gravity; e.g. Reiners & Basri 2006; Shulyak et al. 2010; Crossfield 2014).

Despite these opportunities, the currently published high-resolution spectroscopic sample of UCDs is limited to a few hundred sources, due to their intrinsic faintness and the necessity of observing at near-infrared wavelengths (Blake et al. 2010; Burgasser et al. 2015a). Fortunately, there is a wealth of near-infrared high-resolution spectra that have been taken over the past two decades, particularly with the Near-Infrared Spectrometer (NIRSPEC; McLean et al. 1998, 2000) on the Keck II Telescope and the Apache Point Observatory Galactic Evolution Experiment (APOGEE; Majewski et al. 2017) survey from the Sloan Digital Sky Survey (SDSS).

NIRSPEC is a high-resolution near-infrared spectrometer ($\lambda/\Delta\lambda$ $\sim$25,000 pre-upgrade, McLean et al. 1998, 2000; $\lambda/\Delta\lambda$ $\sim$35,000 post-upgrade, Martin et al. 2018), covering the entire J, H, and K-bands. With the large 10 m aperture at Keck, NIRSPEC is ideal for expanding the high-resolution spectroscopic sample of UCDs, with limiting brightness of $J \approx 15.5$ mag and $K \approx 14.5$ mag. Previous high-resolution studies with NIRSPEC include the RV and $v \sin i$ survey of local L and T dwarfs by Zapatero Osorio et al. (2006, 2007), the RV survey of 59 late-M and L dwarfs with $\sim$600 measurements by

Blake et al. (2010), the RV and $v \sin i$ survey of 23 late-M dwarfs by Tanner et al. (2012), the RV survey of 25 late-M/L/T dwarfs (Prato et al. 2015), and various individual UCD RV binaries (Burgasser & McElwain 2006; Burgasser et al. 2015b, 2016; Konopacky et al. 2010). Figure 1.6 shows the NIRSPEC spectrum of WISE J072003.20−084651.2 from Burgasser et al. (2015b), which the 2.285 to 2.318 μm region covering the CO (v=2–0) bandhead. This spectral order has abundant telluric absorption features that provide a simultaneous absolute reference frame of wavelength scale down to precisions of $\sim$50 m s^{-1} (Tanner et al. 2012). Full usage of the existing NIRSPEC spectral data has not been achieved, as 400 unique UCDs and >5,000 science files of published and unpublished data are available on the Keck Observatory Archive[1] (KOA). Even considering only data with S/N > 5, there are >250 unique UCDs with >2,700 science files. Precise RVs and $v \sin i$s can be measured with an accurate modeling technique (see Section 2.2), which can drastically improve the modeling precision for sources measured with other methods (e.g. the cross-correlation method; Zapatero Osorio et al. 2007; Prato et al. 2015).

APOGEE provides high resolution ($\lambda/\Delta\lambda$ $\sim$22,500, Majewski et al. 2017; Wilson et al. 2019) near-infrared spectra covering the entire H-band, ideal for expanding the high-resolution spectroscopic sample of UCDs. APOGEE has observed more than 730,000 stars in multiple epochs (Abdurro'uf et al. 2022), enabling the discovery of thousands of binary candidates, including $\sim$4,000 single-lined binaries for giants (Price-Whelan et al. 2018), >7,000 double-lined binaries for A stars to mid-M dwarfs (effective temperatures from 8,000 K down to 3,000 K; Kounkel et al. 2021), and 44 double-lined binaries for early- to mid-M dwarfs (Skinner et al. 2018). However, the APOGEE pipeline does not provide robust RVs and $v \sin i$s for late-M dwarfs, as the APOGEE Stellar Parameter and Chemical Abundances Pipeline (ASPCAP) pipeline (García Pérez et al. 2016) and a recent radial velocity pipeline `Doppler` (Nidever 2021) has difficulty in precise determinations

[1] https://koa.ipac.caltech.edu/

of these parameters for low-temperature atmospheres. This limitation motivated specific efforts to improve APOGEE measurements of UCDs through the APOGEE M dwarf Ancillary Program (Deshpande et al. 2013; Holtzman et al. 2015). Deshpande et al. (2013) presented RVs and $v \sin i$ measurements of 253 M dwarfs related to this program, using cross-correlation and forward-modeling methods with BT-Settl models (Allard et al. 2012), achieving typical RV and $v \sin i$ uncertainties of 0.18 km s^{-1} and 1.0 km s^{-1}, respectively. Figure 1.7 shows an example spectrum and the best-fit BT-Settl model ($T_{\rm eff}$ = 3000 K, $\log g$ = 5.0 dex, and [Fe/H] = 0.3) from Deshpande et al. (2013). While the best-fit model provides reasonable match to the data, there are some spectral regions that do not fit well, especially in redder wavelength regions (Figure 1.7 middle and bottom panels). As I will show, I can improve fidelity and accuracy on the same data with up-to-date models.

1.6 Organization of Thesis

In this thesis, I present multi-epoch RV and $v \sin i$ measurements of 37 T dwarfs with Keck/NIRSPEC in Chapter 2, 182 M4–L2 dwarfs with SDSS APOGEE in Chapter 3. Appendix lists diagnostics of minimum $v \sin i$ determination and population simulations in Chapter 2 and binary candidates identified in Chapter 3. The conclusions of the work and future directions are summarized in Chapter 4.

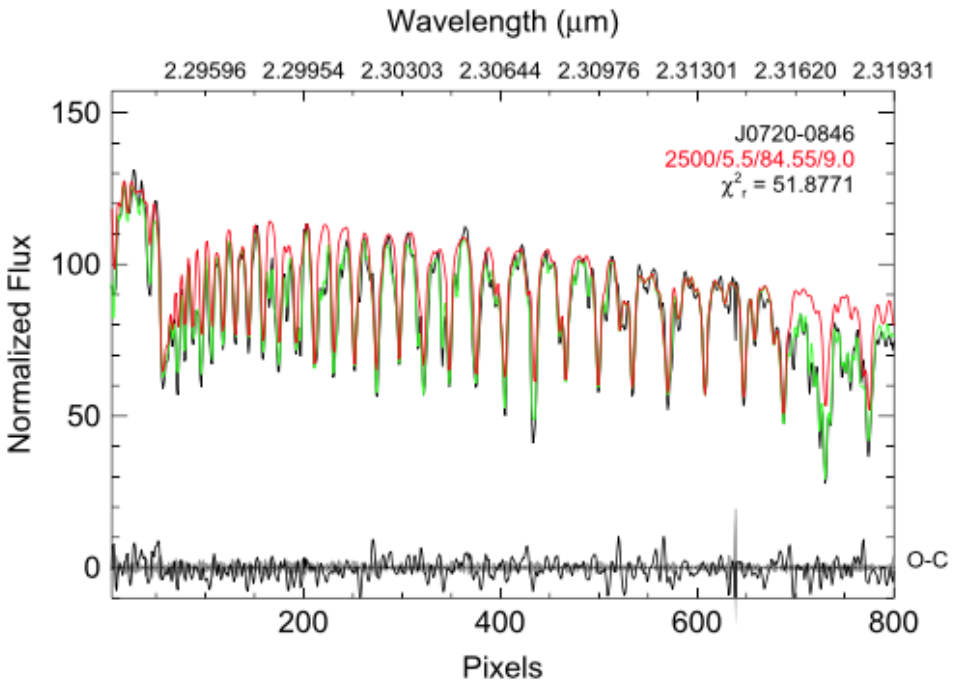

Figure 1.6: NIRSPEC high-resolution spectrum of M9 + T5 Binary WISE J072003.20−084651.2. The data are shown in black, and model with and without the telluric correction are shown in green and red, respectively. The uncertainty is shown in the shaded grey region and the residual (data−model) is shown in black at the bottom of the figure. This spectral order focuses on the CO bandhead ∼2.3 μm and telluric CH_4 absorption for simultaneous wavelength calibration. (Figure 8 from Burgasser et al. 2015b).

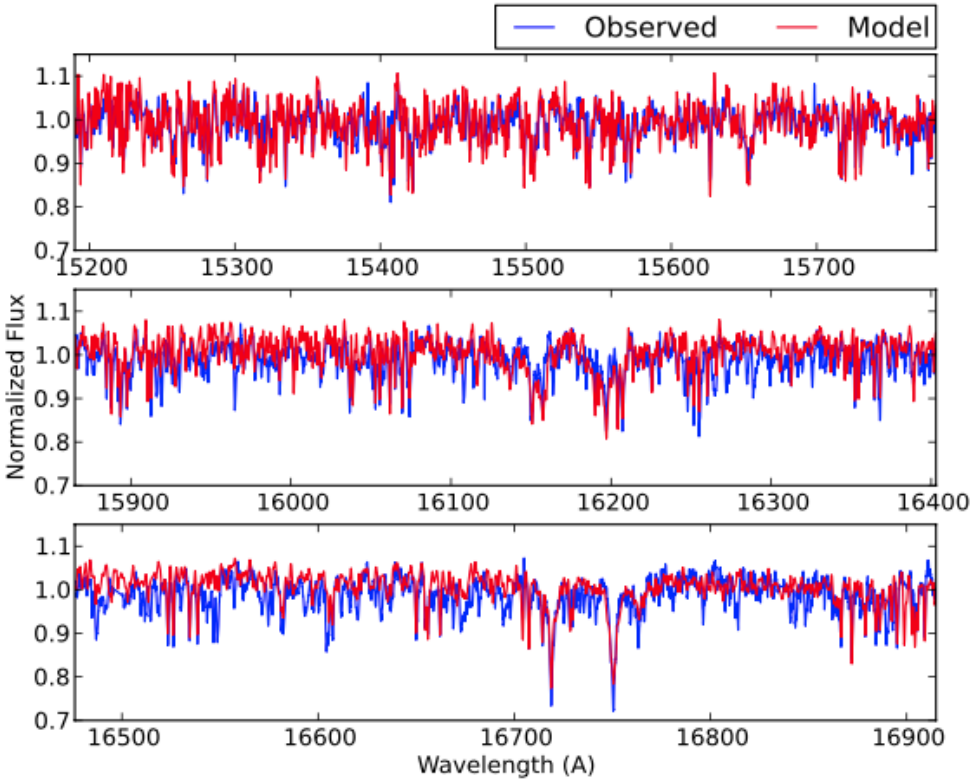

Figure 1.7: APOGEE high-resolution spectrum compared to the best-fit model. The data and BT-Settl model ($T_{\rm eff}$ = 3000 K, $\log g$ = 5.0 dex, and [Fe/H] = 0.3) are shown in blue and red, respectively. (Figure 10 from Deshpande et al. 2013).

Chapter 2

Keck/NIRSPEC

2.1 NIRSPEC T Dwarf Observations

My T dwarf sample was compiled from sources observed with the Keck Near-Infrared Spectrometer (NIRSPEC; McLean et al. 1998, 2000). NIRSPEC is a high-resolution, near-infrared, cross-dispersed spectrograph, mounted on the Keck II telescope, spanning 0.95 to 5.5 μm with a spectral resolution of $\sim$25,000 (pre-upgrade) and $\sim$35,000 (post-upgrade) for a slit width of $0\farcs432$. Table 2.1 lists the 37 T dwarfs in my sample, with photometry from the Two Micron All Sky Survey (2MASS; Skrutskie et al. 2006) and the UKIRT Infrared Deep Sky Survey (UKIDSS; Lawrence et al. 2013); astrometry from 2MASS, the *Wide-field Infrared Survey Explorer* (*WISE*; Cutri & et al. 2012), the Panoramic Survey Telescope and Rapid Response System (Pan-STARRS; Chambers & et al. 2017) and *Gaia* (Gaia Collaboration et al. 2018b, 2021); and classifications from the literature. My sample encompasses observations taken between 2000 and 2021, including publicly available archival data obtained from the Keck Observatory Archive (KOA)[1]. All public data were downloaded directly from KOA, with the exception of

[1] https://koa.ipac.caltech.edu

data from 2001 June 15 (Zapatero Osorio et al. 2006, 2007) and 2005 July 19 (Prato et al. 2015) which were provided by the PIs of these programs. Fourteen sources were observed after the NIRSPEC upgrade (Martin et al. 2018). Table 2.2 lists the details for each observation, segregated by epoch. Most observations were accompanied by observation of an early type star (typically A0) for telluric absorption correction. In total, I analyzed 290 near-infrared spectra in order $N3$ (1.143–1.375 μm) and 101 near-infrared spectra in order $N7$ (1.839–2.630 μm).

2.1.1 NIRSPEC Data Reduction

NSDRP Pipeline and Modifications

All of the NIRSPEC data were reduced using a modified version of the NIRSPEC Data Reduction Pipeline (NSDRP; Tran et al. 2016). My modifications were as follows:

1. I loosened the criteria for determining the edges of each dispersion order. NSDRP determines these edges from flat field frames, but the threshold value for edge detection was too strict and cut off some science spectra in certain orders. Note that NSDRP only processes orders that are completely within the image. Orders that are cut off at the top or bottom of the detector are ignored.

2. NSDRP determines the wavelength calibration using only sky emission lines, so I added arc lamp and etalon lamp exposures as additional inputs for wavelength calibration. Arc lamp line identifications were drawn primarily from the National Institute of Standards and Technology (NIST; Kramida et al. 2019), the Atomic Line List (Van Hoof 2018), and Outred (1978). Etalon lamp lines are not tied to an absolute wavelength scale but provide a way to refine the relative wavelength calibration across an order.

3. When spatially rectifying the tilted orders, NSDRP uses the top and bottom of the edges of the flat field dispersions. This is suitable for data with low S/N, such as my science spectra. For data with high S/N, such as my telluric star spectra, I found that this rectification can be offset by 1–2 pixels across the spectral order. For these data, I used the trace of the bright object spectrum, determined by a Gaussian profile fit along each column.

4. I added a 3-σ clipping algorithm to find the optimal spectral tilt (spatial y-direction) from the emission line traces.

5. I added new coefficients for the grating equation, determined empirically, for $N3$ (J-band) and $N7$ (K-band) data obtained with the upgraded NIRSPEC instrument.

These modifications have been integrated into an updated version of the NSDRP.[2]

In addition, I implemented an algorithm to correct for fringing features in the flat field images. Interference from reflections between the echelle gratings and internal optics in NIRSPEC produce fringing patterns, easily visible in high signal-to-noise (S/N) data and flat field images. The interference patterns reduce both my ability to model the spectra and achieve high radial velocity precision. I therefore added a defringing algorithm for the raw flat field files using the wavelet analysis described in Rojo & Harrington (2006) and the *wavelets*[3] package described in Torrence & Compo (1998). Briefly, each pixel in the flat field data is substituted for the median-average value of the nearest 10 pixels in the vertical direction, making the horizontal fringe patterns more prominent. A continuum profile is determined from the binned data using a low-order cubic spline. Subtracting this continuum, I fit the difference using a wavelet analysis. The modeled fringe pattern for the flat images was then subtracted from the original flat field frame. This algorithm was only applied to flat field images, so fringing remains in

[2]https://github.com/ctheissen/NIRSPEC-Data-Reduction-Pipeline
[3]https://github.com/aaren/wavelets

the science frames. As my data were typically low S/N, I did not attempt to correct the science frames for fringing, and defer this to a future study.

Telluric Wavelength Calibration

The wavelength calibration from NSDRP is a second-order polynomial fit to the sky, arc, and etalon lamp emission lines in the science and calibration data. I found this default calibration to be insufficient for precise RV measurement. I therefore adopted the wavelength calibration method described in Burgasser et al. (2016), cross-correlating the associated telluric standard star spectrum with a telluric absorption model (Moehler et al. 2014) over discrete wavebands of width 15 Å. This fit was performed after first modeling out the continuum of the A0 V with a second-order polynomial and a Voigt absorption profile for orders containing H I absorption lines[4]. I used a fit to the residual shift to update the wavelength solution, both represented as fourth-order polynomial functions. This process was iterated until the wavelength solution residuals reached a minimum. The calibrated wavelength solution of each telluric standard star spectrum was applied to the corresponding science spectrum with a wavelength offset determined in the forward-modeling (Section 2.2). The typical standard deviation of velocity residuals in the calibrated telluric spectra ranges from 0.1 to 0.6 km s^{-1}, with a median residual of 0.3 km s^{-1}. My baseline *N*3 order 58 has a median residual of 0.2 km s^{-1}, while my baseline *N*7 order 33 has a median residual of 0.4 km s^{-1}. I also determined wavelength calibrations for orders 32, 34, 37, and 38 (*N*7); and 57, 63, 64, 65, and 66 (*N*3). Orders 35 and 36 (*N*7), and 59, 60, 61, 62 (*N*3) do not have sufficient telluric absorption features to apply this method, while orders 55 and 56 have excessively strong telluric absorption and do not provide sufficient signal for my targets.

[4]Order 59 in *J*-band and order 35 in *K*-band are fit with a Voigt profile, multiplied by a second-order polynomial function, using *scipy*'s `special.wofz` function. The Voigt profile parameters are optimized by a least squares fit.

Table 2.1: NIRSPEC T Dwarf Sample

Source Name	Coordinates (J2000)	SpT	2MASS J (mag)	$J-K$ (mag)	μ_α (mas yr^{-1})	μ_δ (mas yr^{-1})	d (pc)	Published RV (km s^{-1})	Published $v \sin i$ (km s^{-1})	References[a]
J0000+2554	00 00 13.54 +25 54 18.0	T4.5	15.06 ± 0.04	0.22 ± 0.13	-19 ± 2	127 ± 1	14.12 ± 0.38	···	···	(18, 14, 13)
J0034+0523	00 34 51.58 +05 23 05.1	T6.5	15.140 ± 0.004	-0.933 ± 0.03	674 ± 1	178 ± 2	8.42 ± 0.19	···	···	(8, 10, 35)
J0136+0933[b]	01 36 56.56 +09 33 47.3	T2.5	13.46 ± 0.03	0.68 ± 0.04	1238 ± 1	-16 ± 0	6.12 ± 0.02	11.5 ± 0.4	50.9 ± 0.8	(1, 14, 33, 39)
J0150+3827	01 50 09.97 +38 27 25.9	T0	16.11 ± 0.08	1.63 ± 0.1	881 ± 1	-120 ± 1	22.42 ± 1.61	···	···	(17, 35)
J0213+3648	02 13 19.86 +36 48 38.0	T3	15.3 ± 0.5	0.5 ± 0.5	65 ± 65	0 ± 0	14.28 ± 0.04	···	···	(12, 32)
J0243−2453	02 43 13.72 −24 53 29.8	T6	15.38 ± 0.05	0.17 ± 0.18	-288 ± 4	-208 ± 3	10.68 ± 0.41	···	···	(5, 14, 31)
J0415−0935	04 15 19.54 −09 35 06.7	T8	15.7 ± 0.1	0.3 ± 0.2	2214 ± 1	536 ± 1	5.71 ± 0.06	49.6 ± 1.2	33.5 ± 2.0	(5, 13, 43)
J0559−1404	05 59 19.19 −14 04 49.2	T4.5	13.8 ± 0.02	0.23 ± 0.06	571 ± 1	-338 ± 1	10.5 ± 0.08	-9.0 ± 3.0	20.1 ± 4.8	(5, 20, 33, 41)
J0627−1114	06 27 20.08 −11 14 24.1	T6	15.49 ± 0.05	0.06 ± 0.19	-13 ± 1	-338 ± 1	13.37 ± 0.64	···	···	(17, 34)
J0629+2418	06 29 05.12 +24 18 08.7	T2sb[e]	15.89 ± 0.09	0.72 ± 0.18	-35 ± 4	-368 ± 4	26.67 ± 2.35	···	···	(23, 35)
J0755+2212	07 55 47.95 +22 12 16.9	T5	15.73 ± 0.06	0.0 ± 0.2	-21 ± 1	-256 ± 1	14.84 ± 0.7	···	···	(5, 35)
J0819−0335	08 19 58.21 −03 35 26.6	T4	14.99 ± 0.04	0.41 ± 0.11	-199 ± 3	-166 ± 2	14.01 ± 0.43	···	···	(17, 29, 35)
J0909+6525	09 09 00.86 +65 25 27.6	T1.5+T2.5[e]	16.03 ± 0.09	0.86 ± 0.17	-223 ± 1	-120 ± 1	15.65 ± 0.96	···	···	(10, 9, 35)
J0937+2931	09 37 34.88 +29 31 41.0	T6	14.65 ± 0.04	-0.62 ± 0.13	973 ± 6	-1298 ± 5	6.12 ± 0.07	-5.0 ± 3.0	60 ± 10.0	(5, 14, 31, 41)
J1106+2754	11 06 11.92 +27 54 21.6	T0+T4.5[f]	14.82 ± 0.04	1.02 ± 0.07	-271 ± 1	-452 ± 1	20.3 ± 0.5	···	···	(21, 9, 33)
J1217−0311	12 17 11.10 −03 11 13.2	T7.5	15.86 ± 0.06	-0.03 ± 0.07	-1054 ± 2	76 ± 2	11.01 ± 0.27	5.0 ± 1.6	31.4 ± 2.1	(3, 25, 14, 31, 43)
J1225−2739	12 25 54.32 −27 39 46.7	T5.5+T8[f]	15.26 ± 0.05	0.19 ± 0.16	385 ± 3	-628 ± 2	13.32 ± 0.44	···	···	(3, 13, 14, 31)
J1254−0122	12 54 53.90 −01 22 47.3	T2e	14.89 ± 0.04	1.05 ± 0.06	-492 ± 4	111 ± 3	13.48 ± 0.42	4.0 ± 3.0	27.3 ± 2.5	(19, 6, 32, 41)
J1324+6358[c]	13 24 33.86 +63 58 30.7	T2p	15.6 ± 0.07	1.54 ± 0.09	-364 ± 2	-72 ± 2	10.03 ± 0.56	-23.7 ± 0.4	11.5 ± 1.0	(21, 17, 35, 40)
J1331−0116	13 31 48.95 −01 16 50.1	T0	15.46 ± 0.04	1.39 ± 0.08	-422 ± 6	-1039 ± 5	20.0 ± 2.0	···	···	(15, 26, 37)
J1346−0031	13 46 46.35 −00 31 50.1	T6.5	16.0 ± 0.1	0.23 ± 0.29	-503 ± 3	-114 ± 2	14.64 ± 0.49	-23.1 ± 1.5	< 15	(3, 9, 14, 31, 43)
J1457−2122	14 57 14.96 −21 21 47.8	T8	15.32 ± 0.05	0.08 ± 0.16	1034 ± 2	-1726 ± 1	5.91 ± 0.06	28.9 ± 2.4	28.6 ± 2.4	(4, 38, 31, 43)
J1503+2525	15 03 19.61 +25 25 19.8	T5.5	13.94 ± 0.02	-0.03 ± 0.06	87 ± 1	558 ± 1	6.42 ± 0.03	-40.5 ± 2.1	32.8 ± 2.0	(7, 33, 43)
J1506+7027	15 06 52.44 +70 27 25.1	T6	13.7 ± 0.03	-0.09 ± 0.07	-1194 ± 1	1042 ± 1	5.16 ± 0.02	···	···	(16, 17, 33)
J1520+3546	15 20 39.75 +35 46 21.0	T0	15.54 ± 0.06	1.54 ± 0.08	315 ± 2	-378 ± 2	13.59 ± 1.05	···	···	(10, 14, 35)
J1553+1532	15 53 02.28 +15 32 36.9	T6.5+T7.5[f]	15.83 ± 0.07	0.32 ± 0.2	-386 ± 1	166 ± 1	13.32 ± 0.16	-32.9 ± 3.0	29.4 ± 2.3	(5, 13, 43)
J1624+0029	16 24 14.37 +00 29 15.8	T6	15.49 ± 0.05	-0.02 ± 0.07	-373 ± 2	-9 ± 2	11.0 ± 0.15	-30.7 ± 3.0	38.5 ± 2.0	(27, 5, 14, 31, 43)
J1629+0335	16 29 18.41 +03 35 37.1	T2	15.29 ± 0.04	1.11 ± 0.07	234 ± 2	-144 ± 2	12.99 ± 0.67	···	···	(11, 24, 28, 29)
J1809−0448	18 09 52.56 −04 48 08.1	T1	15.14 ± 0.05	1.18 ± 0.08	-54 ± 2	-402 ± 5	20.33 ± 1.2	···	···	(2, 35)
J1928+2356	19 28 41.55 +23 56 01.6	T6	14.34 ± 0.06	0.25 ± 0.08	-248 ± 1	239 ± 1	6.46 ± 0.08	···	···	(24, 35)
J1952+7240[d]	19 52 46.66 +72 40 00.8	T4	15.09 ± 0.05	0.44 ± 0.09	-294 ± 1	-355 ± 2	12.1 ± 0.3	···	···	(17, 28)
J2030+0749	20 30 42.33 +07 49 35.8	T1.5	14.22 ± 0.03	0.91 ± 0.05	664 ± 1	-112 ± 1	9.73 ± 0.08	···	···	(24, 33)
J2126+7617	21 26 59.14 +76 17 43.3	T0p[f]	14.34 ± 0.03	1.18 ± 0.05	756 ± 1	822 ± 1	16.35 ± 0.16	···	···	(16, 17, 33)
HN Peg B	21 44 31.33 +14 46 18.9	T2.5	15.86 ± 0.03	0.46 ± 0.03	231 ± 0	-113 ± 0	18.13 ± 0.01	···	···	(22, 33)
J2236+5105	22 36 16.86 +51 05 48.7	T5	14.58 ± 0.04	0.13 ± 0.1	729 ± 2	324 ± 2	9.97 ± 0.36	···	···	(2, 35)
J2254+3123	22 54 18.92 +31 23 49.8	T5	15.26 ± 0.05	0.36 ± 0.15	60 ± 3	187 ± 2	13.89 ± 0.58	14.0 ± 3.0	15 ± 5.0	(5, 28, 36, 41)
J2356−1553	23 56 54.77 −15 53 11.1	T6	15.82 ± 0.06	0.05 ± 0.19	-423 ± 4	-616 ± 4	13.44 ± 1.05	19.0 ± 3.0	15 ± 5.0	(5, 31, 41)

Table 2.1 (*continued*)

Table 2.1 (*continued*)

Source Name	Coordinates (J2000)	SpT	2MASS J (mag)	$J-K$ (mag)	μ_α (mas yr^{-1})	μ_δ (mas yr^{-1})	d (pc)	Published RV (km s^{-1})	Published $v \sin i$ (km s^{-1})	References[a]

[a] References are in the order of discovery, classification, astrometry, previously published RV and $v \sin i$ measurements.
[b] Previously identified as a member of the Carina-Near moving group.
[c] Previously identified as a member of the AB Doradus moving group.
[d] Distance is estimated using M_J/spectral type relation in Dupuy & Liu (2012).
[e] Suspected binary based on blended light spectrum; the component types are estimated to be L7+T5.5 for J0629+2418 (Mace et al. 2013) and T1.5+T2.5 for J0909+6525 (Burgasser et al. 2010).
[f] Confirmed binary as reported in Burgasser et al. (2003c, 2006c, 2010); Kirkpatrick et al. (2010); Dupuy & Liu (2012); and this paper
References – Source discovery/classification: (1) Artigau et al. (2006), (2) Best et al. (2013), (3) Burgasser et al. (1999), (4) Burgasser et al. (2000a), (5) Burgasser et al. (2002), (6) Burgasser et al. (2003a), (7) Burgasser et al. (2003b), (8) Burgasser et al. (2004), (9) Burgasser et al. (2010), (10) Chiu et al. (2006), (11) Deacon et al. (2011), (12) Deacon et al. (2017), (13) Dupuy & Liu (2012), (14) Faherty et al. (2009), (15) Hawley et al. (2002), (16) Kirkpatrick et al. (2010), (17) Kirkpatrick et al. (2011), (18) Knapp et al. (2004), (19) Leggett et al. (2000), (20) Liu et al. (2006), (21) Looper et al. (2007), (22) Luhman et al. (2007), (23) Mace et al. (2013), (24) Mace (2014), (25) Metchev et al. (2008), (26) Schneider et al. (2014), (27) Strauss et al. (1999), Source astrometry: (28) Best et al. (2018), (29) Best et al. (2020), (30) Dupuy & Liu (2017), (31) Faherty et al. (2012), (32) Gaia Collaboration et al. (2018b), (33) Gaia Collaboration et al. (2021), (34) Kirkpatrick et al. (2019), (35) Kirkpatrick et al. (2021), (36) Manjavacas et al. (2013), (37) Smart et al. (2018), (38) Weinberger et al. (2016), Source previously published RV and $v \sin i$: (39) Gagné et al. (2017), (40) Gagné et al. (2018a), (41) Prato et al. (2015), (42) Zapatero Osorio et al. (2006), (43) Zapatero Osorio et al. (2007)

Table 2.2: NIRSPEC T Dwarf Observing Log

Source	Program PI	UT Date	UT Time[a] (hh:mm:ss)	Integration[b] (s)	Airmass[a]	Filter[d]	Slit	Echelle Angle[a] (deg)	Cross-disperser Angle[a] (deg)	Barycentric Correction (km s^{-1})
J0000+2554[c]	Burgasser	2019-10-17	08:39:13	2 × 1500	1.01	*N*3	0.″432×12	62.97	34.09	−6.329
J0034+0523[c]	Burgasser	2020-09-03	08:39:31	2 × 1400	1.62	*N*3	0.″432×12	62.98	34.09	14.315
J0136+0933	McLean	2008-12-04	04:38:53	4 × 600	1.21	*N*3	0.″432×12	63.00	34.08	−21.792
···	Burgasser	2013-10-16	11:42:53	2 × 900	1.08	*N*7	0.″432×12	62.97	35.47	0.857
···	Burgasser	2016-02-03	05:04:31	2 × 750	1.15	*N*7	0.″432×12	63.03	35.46	−29.081
J0150+3827[c]	Burgasser	2020-08-05	13:56:36	2 × 1500	1.10	*N*7	0.″432×12	62.98	35.73	26.588
J0213+3648[c]	Burgasser	2020-09-03	10:08:18	1 × 750	1.54	*N*3	0.″432×12	62.98	34.09	24.419
J0243−2453[c]	Burgasser	2021-01-01	05:27:08	2 × 1800	1.45	*N*3	0.″432×12	62.95	34.06	−22.462
J0415−0935	Martín	2005-10-26	12:55:37	2 × 600	1.16	*N*3	0.″432×12	63.00	34.08	11.18
···	Wainscoat	2006-01-18	09:01:02	2 × 600	1.39	*N*3	0.″432×12	63.00	34.08	−22.389
J0559−1404	Engineering	2000-10-10	13:53:03	4 × 600	1.27	*N*3	0.″576×12	63.00	34.08	22.527
···	McLean	2001-10-09	15:06:35	2 × 600	1.20	*N*3	0.″432×12	63.00	34.08	22.564
···	Rayner	2001-11-02	13:17:34	10 × 300	1.21	*N*3	0.″432×12	63.00	34.08	17.938
···	McLean	2001-12-29	07:49:17	2 × 600	1.41	*N*3	0.″432×12	63.00	34.08	−3.097
···	Martín	2002-11-25	13:06:34	3 × 600	1.25	*N*3	0.″576×12	63.00	34.08	10.44
···	Wainscoat	2004-12-05	13:03:11	2 × 300	1.34	*N*3	0.″432×12	63.00	34.08	6.31
···	Martín	2005-10-26	13:37:56	3 × 480	1.21	*N*3	0.″432×12	63.00	34.08	19.706
···	Martín	2005-10-27	12:35:45	3 × 480	1.29	*N*3	0.″432×12	63.00	34.08	19.593
···	Martín	2005-10-28	12:49:07	3 × 480	1.26	*N*3	0.″432×12	63.00	34.08	19.326
···	McLean	2006-01-11	07:48:54	26 × 300	1.27	*N*3	0.″432×12	63.00	34.08	−8.445
···	McLean	2008-03-19	05:55:54	7 × 600	1.30	*N*3	0.″432×12	63.00	34.08	−23.852
···	Burgasser	2015-12-29	11:17:25	2 × 1500	1.30	*N*7	0.″432×12	63.02	35.48	−3.265
··· [c]	Burgasser	2021-01-01	07:58:37	2 × 1200	1.33	*N*3	0.″432×12	62.95	34.06	−4.434
J0627−1114[c]	Burgasser	2021-01-01	09:08:11	2 × 1800	1.21	*N*3	0.″432×12	62.95	34.06	−1.101
J0629+2418	Burgasser	2012-11-28	12:50:54	2 × 1500	1.00	*N*7	0.″432×12	63.02	35.55	14.826
J0755+2212[c]	Burgasser	2021-01-01	10:16:22	1 × 1800	1.05	*N*3	0.″432×12	62.95	34.06	8.315
J0819−0335[c]	Burgasser	2021-01-01	11:36:35	2 × 1800	1.09	*N*3	0.″432×12	62.95	34.06	12.859
J0909+6525	Burgasser	2010-12-26	12:12:07	4 × 1200	1.45	*N*7	0.″432×12	63.00	35.55	7.764
J0937+2931	McLean	2002-04-23	05:15:35	4 × 300	1.03	*N*3	0.″432×12	63.00	34.08	−27.634
···	McLean	2003-03-24	08:12:11	6 × 600	1.02	*N*3	0.″432×12	63.00	34.08	−20.594
···	Prato	2003-05-12	05:30:39	13 × 300	1.03	*N*3	0.″432×12	63.00	34.08	−28.564
···	McLean	2006-01-10	13:10:31	24 × 300	1.02	*N*3	0.″432×12	63.00	34.08	13.261
···	McLean	2006-05-19	07:15:48	8 × 300	1.35	*N*3	0.″432×12	63.00	34.08	−28.282
J1106+2754	McLean	2008-03-19	08:19:51	12 × 600	1.06	*N*3	0.″432×12	63.00	34.08	−10.193
···	Burgasser	2010-12-26	15:07:25	3 × 1000	1.01	*N*3	0.″432×12	62.95	34.08	25.007
···	Burgasser	2012-04-02	11:07:11	3 × 1500	1.20	*N*7	0.″432×12	63.00	35.52	−16.475
···	Burgasser	2012-11-27	13:42:12	3 × 1200	1.43	*N*7	0.″432×12	63.01	35.52	28.583

Table 2.2 (*continued*)

Table 2.2 (*continued*)

Source	Program PI	UT Date	UT Time[a] (hh:mm:ss)	Integration[b] (s)	Airmass[a]	Filter[d]	Slit	Echelle Angle[a] (deg)	Cross-disperser Angle[a] (deg)	Barycentric Correction (km s^{-1})
···	Burgasser	2013-02-05	14:15:17	3 × 1500	1.07	*N*7	0.″432×12	63.03	35.46	9.608
···	Burgasser	2015-01-01	15:00:50	2 × 1500	1.01	*N*7	0.″432×12	63.03	35.46	23.434
···	Burgasser	2016-01-18	14:03:05	2 × 1500	1.01	*N*7	0.″432×12	63.02	35.48	17.818
···	Burgasser	2016-02-16	09:47:02	3 × 1400	1.13	*N*7	0.″432×12	63.03	35.48	5.18
···	Burgasser	2016-04-22	08:43:42	3 × 1500	1.06	*N*7	0.″432×12	62.98	35.48	−22.888
···	Burgasser	2016-05-22	07:56:10	3 × 1500	1.22	*N*7	0.″432×12	62.97	35.48	−27.661
···	Burgasser	2017-03-22	13:00:58	2 × 900	1.02	*N*7	0.″432×12	63.02	35.52	9.678
···	Burgasser	2017-05-06	07:14:02	2 × 1200	1.01	*N*7	0.″432×12	63.02	35.52	−25.802
···	Burgasser	2018-01-01	14:47:39	2 × 1500	1.01	*N*7	0.″432×12	63.01	35.48	23.406
···	Burgasser	2018-06-03	06:19:27	2 × 1500	1.05	*N*7	0.″432×12	63.01	35.38	−27.541
··· [c]	Burgasser	2021-01-01	12:57:30	2 × 1500	1.11	*N*3	0.″432×12	62.95	34.06	23.544
··· [c]	Burgasser	2021-01-01	14:20:08	2 × 1500	1.01	*N*7	0.″432×12	62.95	34.06	23.394
J1217−0311	Martín	2001-06-15	06:08:18	2 × 900	1.11	*N*3	0.″576×12	63.00	34.08	−28.873
···	Wainscoat	2006-01-18	14:07:41	2 × 600	1.10	*N*3	0.″432×12	63.00	34.08	27.977
···	Wainscoat	2006-01-19	12:40:31	3 × 1200	1.27	*N*3	0.″432×12	63.00	34.08	27.929
J1225−2739	McLean	2002-04-23	08:37:15	6 × 300	1.48	*N*3	0.″432×12	63.00	34.08	−6.921
J1254−0122	McLean	2001-12-31	15:13:36	3 × 300	1.15	*N*3	0.″432×12	63.00	34.08	30.294
···	Basri	2002-05-17	06:55:33	9 × 300	1.09	*N*3	0.″432×12	63.00	34.08	−19.715
···	Prato	2003-05-14	05:50:51	14 × 300	1.24	*N*3	0.″432×12	63.00	34.08	−18.322
···	Wainscoat	2006-01-19	13:55:21	9 × 600	1.15	*N*3	0.″432×12	63.00	34.08	29.206
···	McLean	2007-05-31	06:51:50	8 × 600	1.15	*N*3	0.″432×12	63.00	34.08	−24.187
···	Burgasser	2011-06-10	05:46:19	2 × 900	1.07	*N*7	0.″432×12	63.00	35.53	−26.549
J1324+6358	Burgasser	2016-05-22	09:03:28	2 × 3000	1.44	*N*7	0.″432×12	62.97	35.48	−13.606
J1331−0116	Burgasser	2011-03-18	12:20:39	4 × 1200	1.07	*N*7	0.″432×12	63.00	35.47	12.621
···	Burgasser	2011-07-06	06:32:30	2 × 1500	1.17	*N*7	0.″432×12	63.00	35.53	−28.921
···	McLean	2013-05-24	08:27:28	4 × 600	1.08	*N*3	0.″432×12	63.00	34.08	11.046
J1346−0031	Martín	2001-06-15	07:10:43	3 × 900	1.08	*N*3	0.″576×12	63.00	34.08	−24.832
···	Wainscoat	2006-01-18	14:55:32	3 × 600	1.14	*N*3	0.″432×12	63.00	34.08	29.934
J1457−2122	Martín	2001-06-15	08:58:36	2 × 900	1.41	*N*3	0.″576×12	63.00	34.08	−17.283
···	Wainscoat	2006-01-18	15:37:10	2 × 600	1.53	*N*3	0.″432×12	63.00	34.08	28.542
···	McLean	2008-03-19	11:22:16	8 × 600	1.61	*N*3	0.″432×12	63.00	34.08	23.02
J1503+2525	Wainscoat	2006-01-19	15:54:04	2 × 300	1.08	*N*3	0.″432×12	63.00	34.08	23.037
···	McLean	2008-03-19	13:48:14	8 × 600	1.01	*N*3	0.″432×12	63.00	34.08	13.207
J1506+7027[c]	Burgasser	2020-09-03	05:17:38	2 × 1200	1.77	*N*3	0.″432×12	62.98	34.09	2.035
J1520+3546	Burgasser	2012-04-02	14:19:49	2 × 1200	1.09	*N*7	0.″432×12	63.00	35.52	6.498
J1553+1523	Martín	2001-06-15	09:38:29	2 × 900	1.03	*N*3	0.″576×12	63.00	34.08	−12.915
J1624+0029	Martín	2001-06-15	10:22:21	2 × 900	1.11	*N*3	0.″576×12	63.00	34.08	−9.423
···	Basri	2002-05-17	12:23:06	8 × 300	1.12	*N*3	0.″432×12	63.00	34.08	3.83

Table 2.2 (*continued*)

Table 2.2 (*continued*)

Source	Program PI	UT Date	UT Time[a] (hh:mm:ss)	Integration[b] (s)	Airmass[a]	Filter[d]	Slit	Echelle Angle[a] (deg)	Cross-disperser Angle[a] (deg)	Barycentric Correction (km s^{-1})
···	McLean	2005-06-04	08:08:51	1 × 600	1.18	*N*3	0.″432×12	63.00	34.08	−4.155
J1629+0335	Burgasser	2011-08-11	06:55:17	2 × 1500	1.11	*N*7	0.″432×12	63.00	35.47	−25.693
···	Burgasser	2011-09-07	05:15:20	2 × 1200	1.12	*N*7	0.″432×12	63.00	35.46	−26.499
J1809−0448[c]	Burgasser	2020-08-25	06:37:23	2 × 1500	1.10	*N*7	0.″432×12	62.98	35.75	−24.312
J1928+2356[c]	Burgasser	2019-09-12	08:00:26	1 × 1500	1.04	*N*7	0.″432×12	63.00	35.76	−16.283
···	Burgasser	2019-10-17	06:31:42	2 × 1200	1.2	*N*3	0.″432×12	62.97	34.09	−21.221
J1952+7240[c]	Burgasser	2019-10-17	07:31:51	2 × 1500	1.91	*N*3	0.″432×12	62.97	34.09	1.957
J2030+0749[c]	Burgasser	2020-07-10	09:55:16	2 × 900	1.13	*N*7	0.″432×12	63.00	35.73	10.869
J2126+7617	Burgasser	2011-06-10	14:59:25	2 × 750	1.81	*N*7	0.″432×12	63.00	35.53	3.919
···	Burgasser	2011-07-06	13:51:48	2 × 1200	1.83	*N*7	0.″432×12	63.00	35.53	7.054
···	Burgasser	2011-08-11	11:38:20	2 × 1500	1.84	*N*7	0.″432×12	63.00	35.47	9.141
···	Burgasser	2011-09-07	10:49:22	2 × 1200	1.92	*N*7	0.″432×12	63.00	35.46	8.549
···	Burgasser	2013-09-17	10:46:37	2 × 1500	2.00	*N*7	0.″432×12	62.97	35.51	7.816
···	Burgasser	2013-10-16	10:34:47	2 × 1500	2.38	*N*7	0.″432×12	62.97	35.47	4.528
···	Burgasser	2014-09-02	09:25:11	2 × 1200	1.81	*N*7	0.″288×12	63.02	35.49	8.839
··· [c]	Burgasser	2020-08-25	08:52:17	2 × 1500	1.82	*N*7	0.″432×12	62.98	35.75	9.12
··· [c]	Burgasser	2020-09-03	06:46:14	2 × 1200	1.93	*N*3	0.″432×12	62.98	34.09	8.838
HN Peg B	Skemer	2017-06-09	11:21:04	20 × 13200	1.59	*N*7	0.″432×12	63.01	36.60	25.737
···	Skemer	2017-10-08	05:36:07	10 × 9000	1.07	*N*7	0.″432×24	62.93	36.55	−17.657
J2236+5105[c]	Burgasser	2020-09-03	07:44:53	2 × 1200	1.34	*N*3	0.″432×12	62.98	34.09	8.472
J2254+3123	Prato	2003-08-10	09:20:13	10 × 300	1.32	*N*3	0.″432×12	63.00	34.08	16.077
···	McLean	2005-07-19	12:17:11	4 × 600	1.06	*N*3	0.″432×12	63.00	34.08	21.277
···	McLean	2004-11-21	05:38:26	1 × 300	1.03	*N*5	0.″288×24	62.61	36.90	−21.596
···	McLean	2007-06-26	14:15:19	4 × 600	1.04	*K*	0.″432×24	63.00	35.65	23.945
J2356−1553	McLean	2003-07-20	12:50:03	4 × 600	1.36	*N*3	0.″432×12	63.00	34.08	23.527
···	McLean	2005-07-19	13:52:18	3 × 600	1.25	*N*3	0.″432×12	63.00	34.08	23.519
···	McLean	2005-12-10	05:21:03	6 × 600	1.23	*N*3	0.″432×12	63.00	34.08	−29.26

[a] Values are taken from the configuration of the first file within the same night.
[b] The number of files times the individual integration time.
[c] Observed with the upgraded NIRSPEC.
[d] Filters: *N*3 (NIRSPEC-3), *N*5 (NIRSPEC-5), *N*7 (NIRSPEC-7), and *K* (NIRSPEC K)

2.2 Forward-Modeling Method

As part of my thesis work, I have implemented a Markov Chain Monte Carlo forward-modeling framework written in Python called *Spectral Modeling Analysis and RV Tool* "`SMART`", which can extract precise radial and rotational velocities as well as effective temperatures and surface gravities. My thesis work is focused on the analysis of Keck/NIRSPEC and SDSS/APOGEE. However, the `SMART` is capable of modeling several instruments, including Keck/NIRSPEC, SDSS/APOGEE, Keck/HIRES (the HIgh-Resolution Echelle Spectrometer; Vogt et al. 1994), Gemini South/IGRINS (Immersion GRating INfrared Spectrometer; Mace et al. 2018), Lick/APF (Automated Planet Finder; Vogt et al. 2014), Keck/OSIRIS (OH-Suppressing Infrared Imaging Spectrograph; Larkin et al. 2006), and Keck/NIRES (Near-Infrared Echellette Spectrometer Wilson et al. 2004). In this section, I described the modeling routines for Keck/NIRSPEC and SDSS/APOGEE.

Overview

The typical approach to spectral reduction is to correct for instrumental and telluric atmospheric effects to infer the target's emitted spectrum. Here, I model these effects explicitly using a forward-modeling approach, following Blake et al. (2010) and Burgasser et al. (2016) (see also Tanner et al. 2012; Allers et al. 2016; Vos et al. 2017; Cale et al. 2019). The stellar parameters (effective temperature, surface gravity, rotational velocity, and radial velocity), and calibration factors (continuum and wavelength corrections, instrumental line-spread function, and strength of telluric absorption) are determined using a Markov Chain Monte Carlo (MCMC) algorithm (Goodman & Weare 2010) using the package *emcee* (Foreman-Mackey et al. 2013). My forward-modeling method is optimal in those spectral orders with both strong telluric absorption features for

accurate wavelength calibration, and sufficient structure in the stellar spectrum to distinguish it from the telluric absorption. I found order 33 in the K-band ($N7$; 22690–23410 Å) and order 58 in the J-band ($N3$; 12990–13290 Å) to be the ideal orders for the T dwarfs, similar to prior studies (Blake et al. 2010; Konopacky et al. 2010; Burgasser et al. 2012; Tanner et al. 2012). My forward-modeling routine *Spectral Modeling Analysis and RV Tool* (SMART; Hsu et al. 2021) is open source and available online.[5]

To summarize, there are three main steps in my MCMC forward-modeling scheme:

1. An MCMC fit of the telluric spectrum is performed to determine the parameters for the instrumental line-spread function (LSF) and the strength of telluric absorption, which are used to initialize the MCMC of the science spectrum.

2. An initial MCMC fit of the science spectrum is conducted to estimate the stellar parameters for effective temperature ($T_{\rm eff}$), surface gravity ($\log g$), rotational velocity ($v \sin i$), and radial velocity (RV), as well as calibration and nuisance parameters.

3. The residuals between the best-fit model spectrum and data are used to generate a mask array to identify discrepant pixels, and a final MCMC fit of the masked science spectrum is run to obtain the best estimates of the fit parameters.

Telluric Star Modeling

Each telluric standard star was forward-modeled to obtain initial estimates of the LSF and strength of telluric absorption. The data (D) are modeled as:

$$D[p] = C[p(\lambda)] \times \left[T \left[p^*(\lambda) \right]^{\alpha} \otimes \kappa_G(\Delta v_{\rm inst}(p)) \right] + C_{\rm flux}. \tag{2.1}$$

[5] https://github.com/chihchunhsu/smart

Here, p is the pixel coordinate, $p^*(\lambda) = p(\lambda) + C_\lambda$ is the mapping of wavelength to pixel with a small constant offset, $C[p]$ is a second-order polynomial representing the continuum correction, $\kappa_G(\Delta v_{\rm inst})$ is the intrumental LSF, assumed to be Gaussian of velocity width $\Delta v_{\rm inst}$ ($\otimes$ represents convolution), $T\left[p\right]$ is a model for telluric absorption from Moehler et al. (2014), α is a constant that scales with the airmass and precipitable water vapor, and $C_{\rm flux}$ is an additive offset for the overall flux. The default precipitable water vapor (pwv) for the Moehler et al. (2014) models used was 0.5 mm. For some data, a telluric model with pwv = 1.5 mm produced a better fit and these were used instead. I fit the parameters, $\Delta v_{\rm inst}$, $C_{\rm flux}$, C_λ, and α assuming uniform priors (Table 2.3), while the continuum was determined after each iteration through a least-squares fit of the ratio of the data and model to a second-order polynomial (i.e., the continuum fit was done outside of the MCMC). The likelihood function was computed by assuming the noise follows a normal distribution:

$$\ln \mathscr{L} = -0.5 \times \left[\sum \chi^2 + \sum \ln(2\pi\sigma^2)\right], \tag{2.2}$$

where $\chi = \frac{Data[p]-D[p]}{\sigma[p]}$, and $Data$ and σ are the observed spectrum and noise. I used 50 walkers of 400 steps each and a burn-in of 300 steps, with these parameters chosen[6] to optimize convergence. The convergence of each fit was checked visually and quantified using both the Gelman-Rubin scale reduction factor (Gelman & Rubin 1992) and integrated autocorrelation time statistics (Goodman & Weare 2010). For each fit, I inferred the best-fit parameter values and their uncertainties by computing the 50$^{\rm th}$, 16$^{\rm th}$, and 84$^{\rm th}$ percentiles of the marginalized posterior distributions from the residual MCMC chains.

[6]See Section 2.2 for discussions on convergence.

T Dwarf Modeling

The T dwarf spectra were forward-modeled as:

$$D[p] = C[p] \times \left[\left(M\left[p^* \left(\lambda \left[1 + \frac{RV^*}{c} \right] \right), T_{\rm eff}, \log g \right] \right. \right. \\ \left. \left. \otimes \kappa_R(v \sin i) \right) \times T\left[p^*(\lambda) \right]^{\alpha} \right] \otimes \kappa_G(\Delta v_{\rm inst}) + C_{\rm flux} \,, \tag{2.3}$$

where the additional terms compared to equation (2.1) include the solar-metallicity stellar atmosphere model[7] $M[p]$ drawn from the BT-Settl (Allard et al. 2012) and Sonora (Marley et al. 2018) model grids, parameterized by effective temperature ($T_{\rm eff}$) and surface gravity ($\log g$); $RV^* = RV + v_{\rm bary}$ is the radial velocity of the source plus barycentric motion of the Earth at the observed epoch; c is the speed of light; κ_R is the rotational broadening profile defined in Gray (1992) assuming a constant limb-darkening coefficient of $\varepsilon = 0.6$ (Claret 2000); and $v \sin i$ is the projected rotational velocity. Atmosphere model log fluxes were linearly interpolated between grid points to approximate a continuous distribution of $T_{\rm eff}$ and $\log g$ values. The likelihood function is:

$$\ln \mathscr{L} = -0.5 \times \left[\sum \chi^2 / C_{\rm noise}^2 + \sum \ln(2\pi (C_{\rm noise} \sigma)^2) \right] , \tag{2.4}$$

where $C_{\rm noise}$ is a constant scaling factor for the noise (σ) to take into account underestimates or overestimates of observational noise in computing χ^2; as well as systematic errors between the model and the spectrum, such as missing line features. I performed an initial MCMC fit for the parameters $T_{\rm eff}$, $\log g$, RV^*, $v \sin i$, α, C_λ, $C_{\rm flux}$[8], and $C_{\rm noise}$, modeling the continuum in the same manner as the telluric standard. The nuisance pa-

[7] See Section 2.2.1 for discussions of model selection

[8] The values are determined based on the percentage of median flux $C_{\rm flux} = C_{\rm flux^*} \times F$, where F is the median flux.

rameter C_λ takes into account the small shift in instrument alignment between the telluric and science integrations. RVs inferred between subsequent nods are more consistent when this nuisance parameter in included in the forward model. Stellar model parameter prior ranges were chosen to encompass the typical properties of T dwarfs, with $T_{\rm eff}$ = 600 to 1300 K, $\log g = 3.5$ to 5.5 dex (in units of cm s^{-2}), $v \sin i = 0$ to 100 km s^{-1}, and $RV^* = -200$ to $+200$ km s^{-1}. The MCMC bounds of $T_{\rm eff}$ are set for the whole range of the available model sets (BT-Settl = 500 to 3500 K and Sonora = 200 to 2400 K) (Table 2.3). The initial MCMC used 50 walkers of 600 steps each and burn-in of 300 steps, and convergence was verified by inspection of parameter chains and a requirement of the Gelman-Rubin scale reduction factor (Gelman & Rubin 1992) of less than 1.32. Typically convergence occurred after the first 100–200 steps.

The Gelman-Rubin scale reduction factor and autocorrelation time suggested by Goodman & Weare (2010) were used to test convergence for a representative set of telluric and science spectra, and to set the number of walkers and steps for all fits. I tested the MCMC runs with 50 chains of 600 to 8,000 steps each. The χ^2 values were similar, and the best-fit parameters were fully consistent within the uncertainties, but longer chains reduced the scale reduction factor from 1.2 to 1.01. The longest autocorrelation time was 120 steps, estimated from the runs with 8000 steps. Among these select sets of fits, I found that longer chains did not significantly improve the fits, which only have lower Gelman-Rubin scale reduction factor and converged autocorrelation times, but not change to the parameter values or uncertainties. Due to my limited computational resources, I chose to run only 600 steps, where the convergence was checked visually and confirmed by the requirement that the Gelman-Rubin scale reduction factors were all less than 1.32 (50$^{\rm th}$, 16$^{\rm th}$, and 84$^{\rm th}$ percentiles of R = 1.05, 1.03, and 1.13).

Residuals between the best-fit model and data from this first pass were used to

generate a pixel mask rejecting 2.5σ outliers[9], typically cosmic rays and bad pixels in the detector. A second MCMC was then run on the masked data using the same MCMC fit parameters and initializing model parameters from the first MCMC fit plus a random offset drawn from uniform parameter ranges spanning $\Delta T_{\rm eff} = \pm 20$ K, $\Delta \log g = \pm 0.1$ dex, $\Delta v \sin i = \pm 1$ km s^{-1}, and $\Delta RV = \pm 1$ km s^{-1}. The masking step considerably improved the RV and $v \sin i$ uncertainties and the overall spectral fit. The derived RVs were corrected to the heliocentric frame using the *astropy* function `radial_velocity_correction` to compute $v_{\rm bary}$.

Each individual spectrum was forward-modeled, and measurements both within an epoch and across epochs (for multi-epoch data) were averaged using uncertainty weighting, with weight $W \propto 1/(\sigma^2_{\rm lower} + \sigma^2_{\rm upper})$, where $\sigma_{\rm lower}$, $\sigma_{\rm upper}$ are the uncertainties associated with the 16$^{\rm th}$ and 84$^{\rm th}$ percentiles of each marginalized parameter distribution. In a few cases where the S/N of an individual spectrum is lower than 10, all spectra in an epoch were coadded before forward-modeling. Table 2.4 lists the RV, $v \sin i$, $T_{\rm eff}$ and $\log g$ values inferred for each source and epoch, along with previously published values from the literature.

2.2.1 Evaluating the Fits

Fit Quality and Parameter Correlations

Figures 2.1–2.4 illustrate representative fits to science data in orders 33 (T2.5 J0136+0933) and 58 (T4.5 J0559−1404).

For the order 33 fit, residuals between the data and the best-fit BT-Settl model are on par with the scaled noise (χ^2_r = 1.3,[10] for $C_{\rm noise}$ = 0.7), and all of the marginalized

[9] Typically, ∼3% of the pixels are masked.

[10] χ^2_r is the reduced chi-square statistic computed as $\chi^2_r = \frac{1}{N_{\rm DOF}} \sum Mask[p] \left(\frac{Data[p] - D[p]}{C_{\rm noise} \sigma[p]} \right)^2$, where $Mask[p]$ is the pixel mask ($Mask$ = 1 for good data, $Mask$ = 0 for bad data) and $N_{\rm DOF}$ is the number of degrees of freedom computed as $N_{\rm DOF}$ = [number of unmasked data pixels]/3 − [number of fit parame-

Table 2.3: Modeling Parameter Ranges

Description	Symbol (unit)	Priors[a]	Bounds
	Telluric Standard Star		
Line Spread Func.	$\Delta v_{\rm inst}$ (km s^{-1})	(3.0, 6.0)	(2.0, 10.0)
Flux Offset	$C_{\rm flux}$	$(-1.0, +1.0)$	$(-500, +500)$
Wavelength Offset	C_λ (Å)	$(-0.02, +0.02)$	$(-0.04, +0.04)$[b]
Telluric Scaling	α	(0.3, 3.0)	(0.3, 10.0)
	T Dwarf		
Effective Temp.	$T_{\rm eff}$ (K)	(600, 1300)	B[c](500, 3500)
...	...	...	S[d](200, 2400)
Surface Gravity	$\log g$ (cm s^{-2})	(3.5, 5.5)	(3.5, 5.5)
Rotational Velocity	$v \sin i$ (km s^{-1})	(0, 100)	(0, 100)
Radial Velocity	RV (km s^{-1})	$(-200, +200)$	$(-200, +200)$
Flux Offset	$C_{\rm flux^*}$	$(-0.01, +0.01)$	$(-0.05, +0.05)$[e]
Wavelength Offset	C_λ (Å)	$(-0.6, +0.6)$	$(-0.6, +0.6)$[b]
Telluric Scaling	α	(0.9, 1.1)	(0.1, 10.0)
Noise Factor	$C_{\rm noise}$	(0.99, 1.01)	(0.1, 5.0)

[a] Uniform priors

[b] The Telluric Standard Star wavelength offset bounds range is much smaller than the T Dwarf offset bounds range as the data for the former are used to formally derive the wavelength solution while the data for the latter incur pixel shifts due to instrumental flexure between pointings. See Section 2.2 for more details.

[c] BT-Settl model

[d] Sonora model

[e] The values are determined based on the percentage of median flux $C_{\rm flux} = C_{\rm flux^*} \times F$, where F is the median flux.

distributions show normal distributions, modulo parameter limits (e.g., $\log g$). This fit exemplifies parameter correlations found in some (but not all) of the order 33 fits. First, I find a negative correlation between $v \sin i$ ($\Delta v \sin i = 3$ km s^{-1}) and $\log g$ ($\Delta \log g = 0.2$ dex) that I attribute to a degeneracy between rotational and pressure broadening. A larger $\log g$ results in greater pressure broadening, which is compensated for by a smaller $v \sin i$, and vice-versa. Disentangling this correlation in the line spread shape would require higher resolution and higher signal-to-noise data than is available with the current dataset. Second, I find a positive correlation between $T_{\rm eff}$ ($\Delta T_{\rm eff} = 50$ K) and $\log g$ ($\Delta \log g = 0.2$ dex) that I attribute to temperature and pressure effects in the primary carbon reduction reaction, $CO + 3H_2 \Leftrightarrow CH_4 + H_2O$. This reaction is driven toward the right (weaker CO and stronger CH_4) at low temperatures and high pressures. Disentangling the $T_{\rm eff}$-$\log g$ correlation could be achieved with an accurate measure of the surface flux, and hence the luminosity and radius of each source, which is beyond the scope of this work. Finally, I find a positive correlation between RV ($\Delta RV = 0.4$ km s^{-1}) and C_λ ($\Delta C_\lambda = 0.03$ Å) which is inherent to the simultaneous fitting of the Doppler shift of the source and instrumental shift of the wavelength calibration. As noted above, the C_λ term is necessary to enforce agreement of RVs measured within a single epoch, which far exceed the slight increase to my marginalized RV uncertainties.

For the order 58 fit, residuals between the data and the best-fit Sonora model are again consistent with uncertainty ($\chi^2_r = 1.7$ for $C_{\rm noise} = 1.2$), and marginalized distributions for most parameters reflect normal distributions with the exception of $\log g$ (parameter limit) and $v \sin i$, the latter of which shows a sharp lower cutoff at 17 km s^{-1}. I find only a slight positive correlation between RV ($\Delta RV = 0.2$ km s^{-1}) and C_λ ($\Delta C_\lambda = 0.01$ Å).

ters]. The factor of 1/3 takes into account the pixel-to-pixel correlations caused by the finite slit width, typically 3 pixels (0.″432). I consider fits with $\chi^2_r < 2.5$ to be consistent within uncertainties.

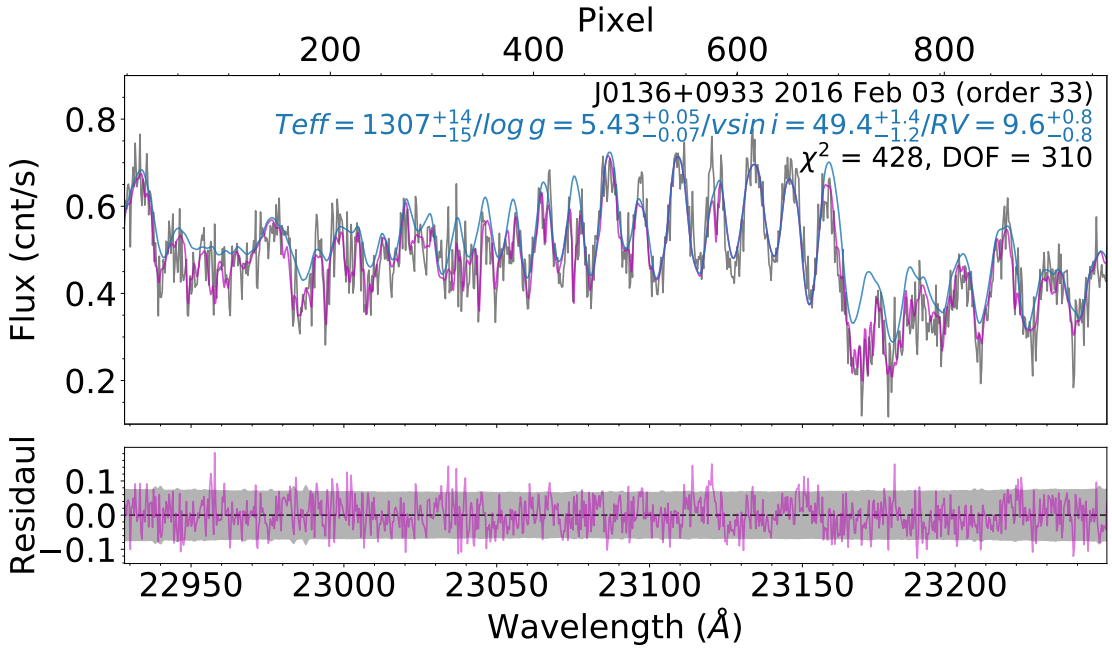

Figure 2.1: BT-Settl model fit of the order 33 spectrum of the T2.5 J0136+0933, observed on 2016 February 3 (UT). The horizontal axis displays both pixel position (top axis) and wavelength (bottom axis). Upper panel: the grey line is the observed spectra; the magenta and blue lines are the stellar model with and without telluric absorption, respectively. Lower panel: difference of the data minus model (magenta) with $\pm 1\sigma$ data uncertainty shaded in grey. The best-fit parameters are listed at the upper right corner of the top panel, with effective temperature ($T_{\rm eff}$) in K, surface gravity ($\log g$) in cm s^{-2}, rotational velocity ($v \sin i$) in km s^{-1}, and radial velocity (RV) in km s^{-1}.

Substellar Atmosphere Model Selection

Both BT-Settl and Sonora model sets were used for all forward-modeling analyses, and I determined the best choice between these sets for each source and order through a combination of visual inspection, χ^2, F-test, and Bayesian information criterion[11] (BIC). In general, the Sonora models provide significantly better fits to order 58 (J-band) spectra of mid- and late-T dwarfs, while the BT-Settl models provide marginally better fits for order 33 (K-band) spectra of early-T dwarfs. I attribute the significant improvement in

[11] BIC = $\chi^2_{\rm min}$ + k $\log_{10} N$, where χ^2 is the chi-square statistic for the best-fitting model, k is the number of parameters, and N is the number of data points (Schwarz 1978). Statistical significance for ruling out the null hypothesis (in this case, that the model sets provide equivalent fits) is assessed following Kass & Raftery (1995), in which the ΔBIC ranges of 0–2, 2–6, 6–10, and > 10 are categorized as insignificant, positive, strong, and very strong evidence against the null hypothesis, respectively.

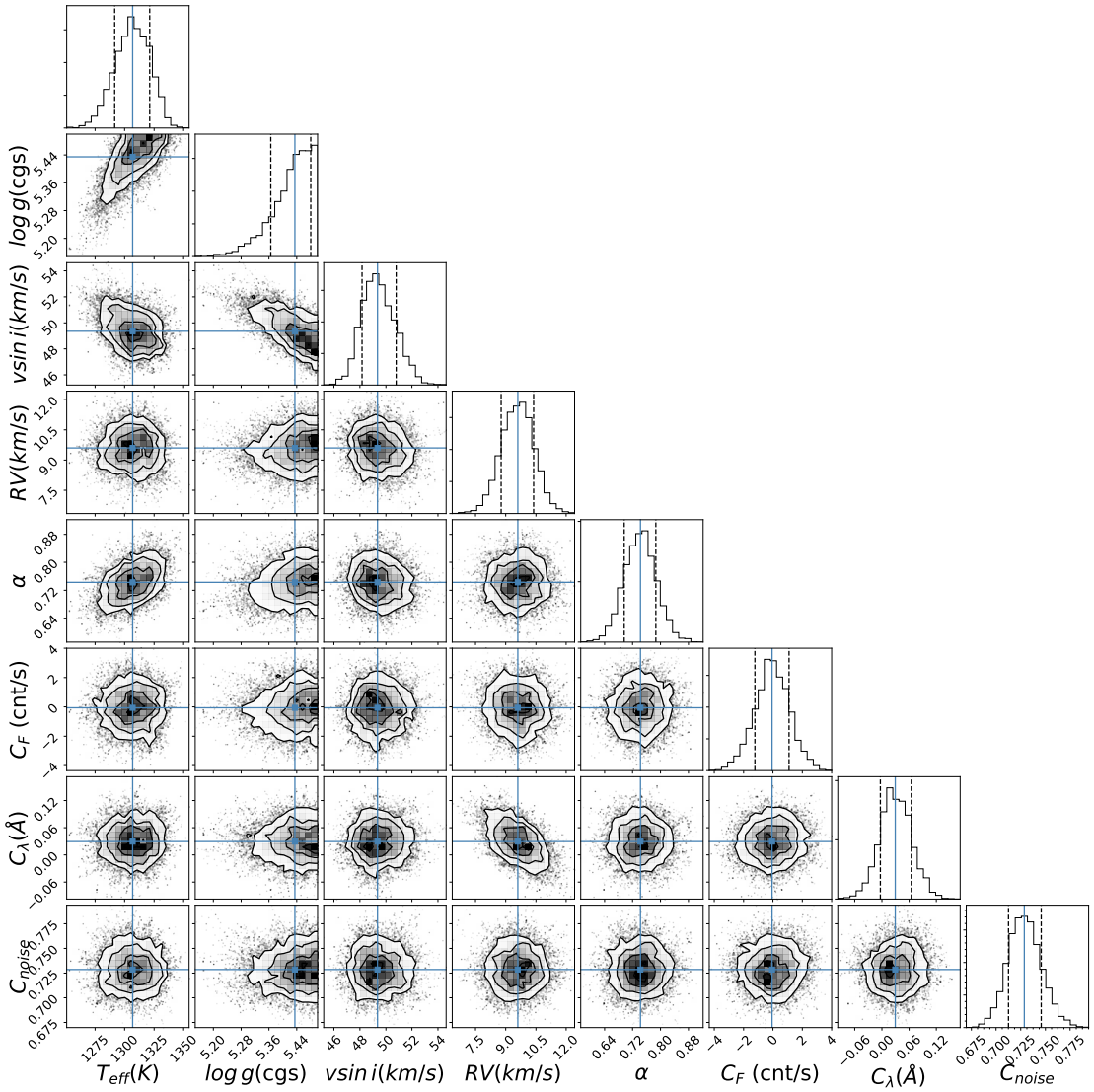

Figure 2.2: The posterior probability distribution of fits to the order 33 spectrum of the T2.5 J0136+0933 observed on 2016 February 3 (UT). The parameters shown are effective temperatures ($T_{\rm eff}$) in K, surface gravity ($\log g$) in cm s^{-2}, projected rotational velocity ($v \sin i$) in km s^{-1}, radial velocity (RV) in km s^{-1}, telluric scale factor (α), nuisance flux parameter (C_F) in count/s, nuisance wavelength parameter (C_λ) in Å, and noise scale factor ($C_{\rm noise}$). The black dash lines are the 16$^{\rm th}$ and 84$^{\rm th}$ percentiles in the marginalized distributions (diagonal plots), and the blue lines denote the median values in both marginalized distributions and interior parameter correlation plots.

Sonora model fits to the J-band data to the updated CH_4 opacities in these models, a particularly important factor for the coldest brown dwarfs. The slightly better fits for the BT-Settl models at K-band may be due to the inclusion of cloud opacity in these models,

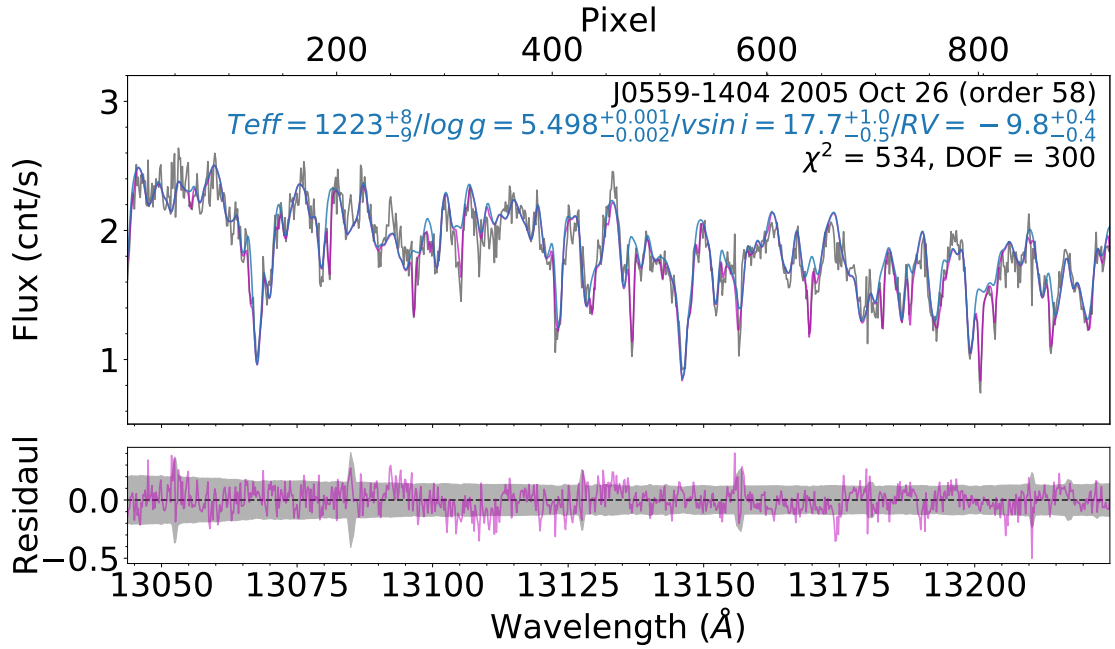

Figure 2.3: Sonora model fit of the order 58 spectrum of the T4.5 J0559−1404, observed on 2005 October 26 (UT). Notation is identical to Figure 2.1.

which are absent in the Sonora grid, although such opacity should have relatively modest influence in the 2 μm region.

The choice of model does influence the physical parameters inferred for each source. Comparing the best-fit parameters between the two models across all sources, orders, and epochs, I found that measured RV and $v\sin i$ values are relatively robust to model choice, with median model discrepancies (Sonora minus BT-Settl) of ΔRV = 0.6 ± 1.5 km s^{-1} and $\Delta v\sin i = -2 \pm 4$ km s^{-1}. The RV offset between the models is dominated by order 58 fits of mid- and late- T dwarfs, for which ΔRV = 1.2 km s^{-1}. Order 33 fits of early-T dwarfs have ΔRV = 0.4 km s^{-1}. The $v\sin i$ offsets are again dominated by order 58 fits, where the velocity kernel must be broadened for the BT-Settl models to compensate for missing CH_4 opacities. The median $\Delta v\sin i$ for order 58 is -2.9 km s^{-1} while the median $\Delta v\sin i$ for order 33 is 0.0 km s^{-1}. The most discrepant $v\sin i$ measurements are among the order 58 fits for mid-T dwarfs, where the Sonora

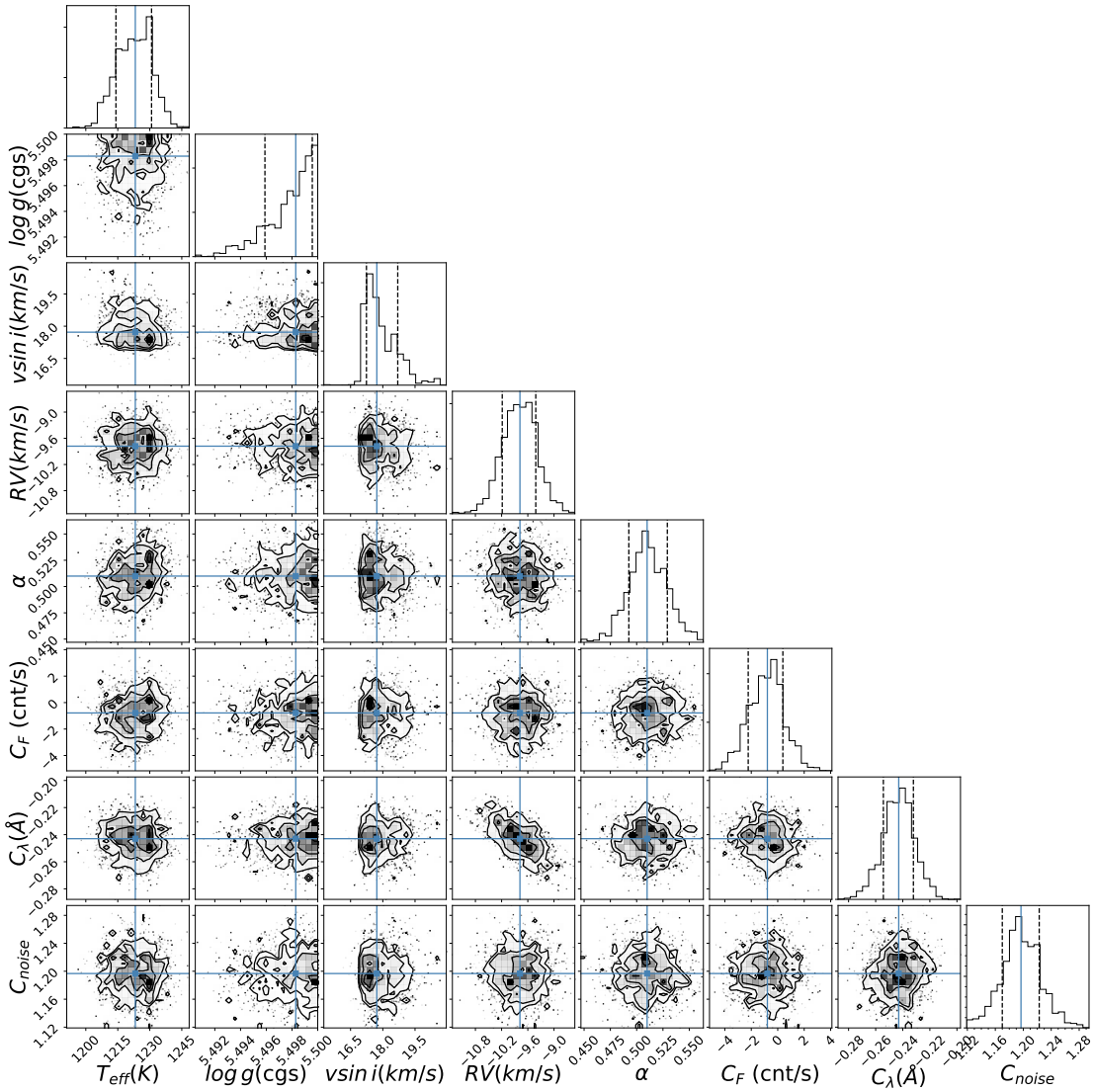

Figure 2.4: The posterior probability distribution of fits to the order 58 spectrum of the T4.5 J0559−1404, observed on 2005 October 26 (UT). Notation is identical to Figure 2.2.

models are far more robust.

The atmosphere parameters $T_{\rm eff}$ and $\log g$ show considerably more variance between the models (Figure 2.5). $T_{\rm eff}$s inferred from the Sonora model fits are consistently hotter than those inferred from the BT-Settl model fits for early- to mid-T dwarfs in both orders 33 and 58, with a median offset of 240 $\pm$ 110 K. For late-T dwarfs, the Sonora model fits are cooler. More striking is the difference in $\log g$ values inferred for

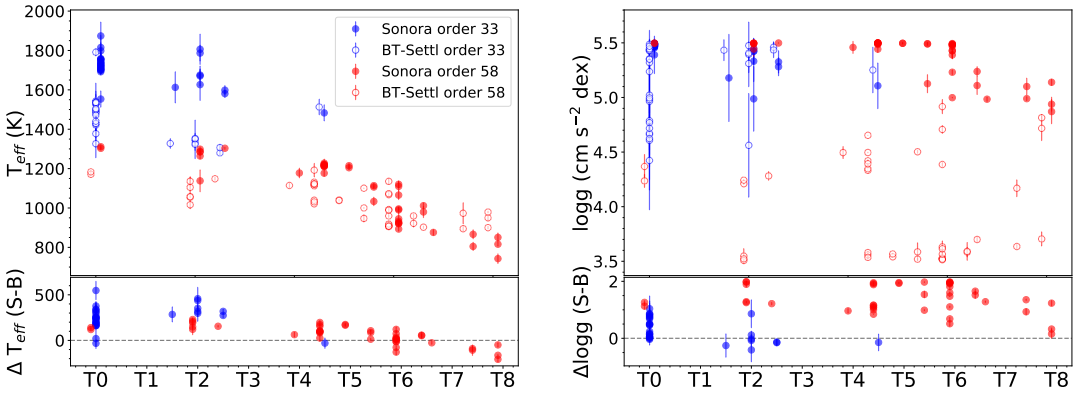

Figure 2.5: Comparison of inferred $T_{\rm eff}$ (left) and $\log g$ (right) parameters between the BT-Settl (open circles) and Sonora (filled circles) models as a function of spectral type, in orders 33 (blue) and 58 (red). Differences (Sonora−BT-Settl) are shown in the lower panels. The Sonora models are slightly offset in subtypes for better visual comparisons.

order 58 (J-band) data, for which BT-Settl models typically converge to $\log g \approx 3.5$ dex, the minimum of the model parameter range. In contrast, $\log g$ values inferred from fits to order 33 (K-band) data are generally consistent between the models, with a median difference of only 0.14 ± 0.40 dex, although both models often converge to the maximum model parameter value of 5.5 dex.

Examination of Fits Across Different Orders

For the sources with measurements in both bands, I examined the consistency of $T_{\rm eff}$ and $\log g$ measurements between orders for six sources with measurements with both J- and K-band spectra. These sources are J0136+0933, J0559−1404, J1106+2754, J1254−0122 (orders 33 and 58), J1928+2356 (orders 37 and 58), and J2126+7617 (orders 33 and 57). $T_{\rm eff}$ values inferred from K-band data are consistently higher than those inferred from J-band data (average $\Delta T_{\rm eff}$ = 187 K, range −182 K to 341 K; excluding J2126+7617 yields an average $\Delta T_{\rm eff}$ = 260 K, range 140 K to 341 K). $\log g$ values differed by up to 1.20 dex between orders but with no clear trend (average $\log g$ = 0.27 dex, range

−0.39 dex to 1.20 dex). For J1928+2356 and J2126+7617, the average differences in $T_{\rm eff}$ and $\log g$ between orders are more than 150 K and 0.08 dex, respectively. RV and $v \sin i$ values are generally consistent across the orders, except for sources with low S/N data (J1254−0122 on 2011 Jun 10 and J1928+2356 on 2019 Sep 12[12]) and binaries (J1106+2754 and J2126+7617).

The best-fit parameters for sources observed in multiple orders were determined generally by spectral type: $N7$ for early T dwarfs and $N3$ for mid- and late-T dwarfs. For J1254−0122, I used the order with the higher S/N data.

Minimum $v \sin i$

The finite resolution of NIRSPEC data places a fundamental limit on my ability to measure rotational broadening for the slowest rotators, which scales with the width of the instrumental LSF. Blake et al. (2010) found a minimum detectable $v \sin i$ of 9 km s^{-1} for their NIRSPEC sample of M8–L6 dwarfs. My T dwarf spectra contain a higher density of molecular features, with overlapping CO and CH_4 absorption bands, and lower S/N. I empirically determined the minimum detectable $v \sin i$ limits for order 33 and 58 data by analyzing simulated NIRSPEC data derived from the model grids, using the same forward-modeling method as the science data. I evaluated a representative set of models with $T_{\rm eff}$ = 900, 1200, 1500 K; $\log g$ = 5.0 dex; RV = 0 km s^{-1}; pwv = 1.5 mm; airmass = 1.0; instrumental LSF = 4.8 km s^{-1} (my typical value); $v \sin i$ = 1–15 km s^{-1} in steps of 1 km s^{-1}, and 15–25 km s^{-1} in steps of 5 km s^{-1}; and S/N = 1–10 in steps of 1, and 10–25 in steps of 5. Gaussian noise was applied using pre-upgrade NIRSPEC values for detector gain, read noise, and dark current, and I assumed an integration time of 1500 s. I defined a robust measurement to be the difference between the true $v \sin i$ and measured $v \sin i$ of less than 1 km s^{-1}. With this benchmark, I determined the minimum robust $v \sin i$ to be

[12]RV values are consistent, but $v \sin i$ values are not.

9 km s^{-1} for S/N $\geq$ 5 for both orders 33 and 58, equivalent to the minimum $v \sin i$ for late-M and L dwarfs determined by Blake et al. (2010). Discrepancies generally increase from high to low S/N[13]. For S/N $<$ 5 data, $v \sin i$ fits become much less robust and a more conservative $v \sin i$ lower limit of 15 km s^{-1} is adopted. Hence, the slowest rotators in my sample, J0000+2554 ($v \sin i = 4 \pm 2$ km s^{-1}, S/N = 5), J0627−1114 ($v \sin i = 5.4^{+2.5}_{-2.0}$ km s^{-1}, S/N = 6), J0819−0335 ($v \sin i = 8.5^{+1.4}_{-2.4}$ km s^{-1}, S/N = 9), and J2236+5105 ($v \sin i = 6.6 \pm 0.9$ km s^{-1}, S/N = 22) are assigned limits of $<$ 9 km s^{-1}; while J2030+0749 ($v \sin i = 14.0^{+0.9}_{-1.0}$, S/N = 4), is assigned a limit of $<$15 km s^{-1}.

[13] See the diagnostic plots in Appendix A

2.3 Modeled Parameters

2.3.1 Radial Velocities

My RV measurements range over -43 to +56 km s^{-1} with a median value of 1.2 km s^{-1} and a median uncertainty of 0.6 km s^{-1}. These measurements are consistent with a population drawn from the local disk, as verified in further detail below. These measurements are also largely consistent with 14 sources previously reported in the literature (Figure 2.6; Table 2.4), but with a median factor of 5.5 improvement in uncertainty. The only significant ($> 3\sigma$) RV outlier is J1346$-$0031, for which my measurement of $-17.5^{+0.6}_{-0.5}$ km s^{-1} is 5.1 km s^{-1} higher than that reported in Zapatero Osorio et al. (2007). For this source (and others), I found my RVs to be consistent between nod pairs in individual epochs and across 2 epochs, albeit with a relatively large C_λ correction of 4 km s^{-1}, which may explain the difference with the previously reported value. I found no correlation between RV discrepancies and spectral type. The spatial kinematics of my sources are described further in Section 2.5.

2.3.2 Projected Rotational Velocities

My $v \sin i$ measurements range over 4[14] to 90 km s^{-1}, with a median value of 27 km s^{-1} and a median uncertainty of 0.9 km s^{-1}. These velocities correspond to maximum rotational periods of 1.5 hr to 28 hr for spheres of radius $R = 1\ R_{\rm Jup}$ observed at an inclination of 90° (equator-on), and indicate a population of rapid rotators as previously inferred from other studies (Zapatero Osorio et al. 2006; Prato et al. 2015; Radigan et al. 2012; Metchev et al. 2015; Vos et al. 2017; Tannock et al. 2021). My $v \sin i$ measurements are generally consistent with those previously reported in the literature

[14] In Section 2.2.1, I determined the minimum $v \sin i$ to be 9 km s^{-1}, with four sources of my sample under such limit.

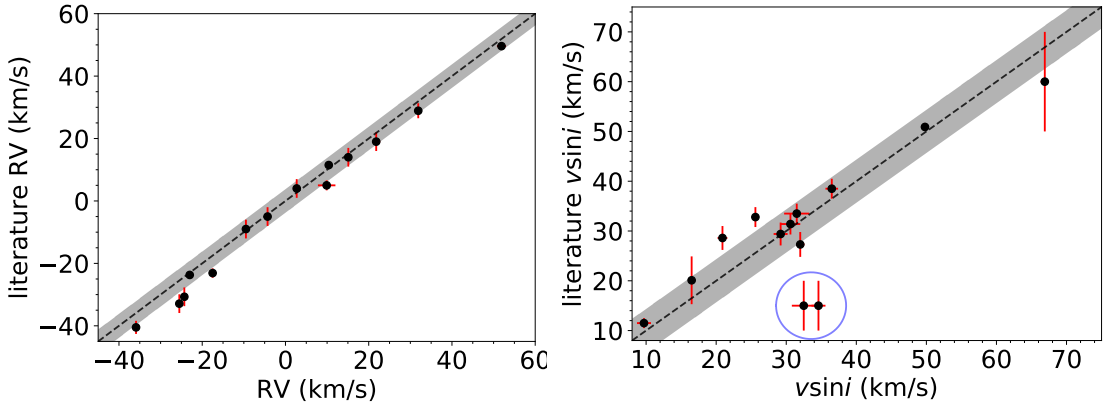

Figure 2.6: Comparison of RV (left) and $v \sin i$ (right) measurements from my NIRSPEC data to previously reported values for the same sources in the literature (see Table 2.4). The black dashed line delineates perfect agreement. The shaded region indicates the $\pm 1\sigma$ scatter (3.8 km s^{-1} for RV and 4.3 km s^{-1} for $v \sin i$) between observed and previously reported values. Two outliers in the $v \sin i$ plot, noted by a blue circle, are excluded in computation of the $v \sin i$ scatter and are discussed in Section 3.3.2.

(Figure 2.6), with a median factor of 2.7 improvement in uncertainties. Again, I found internal agreement between nod pairs and across multiple epochs for $v \sin i$ measurements of these sources. The largest discrepancies were values reported in Prato et al. (2015) for J2254+3123 and J2356−1553. That study visually compared their spectra with spectral templates convolved with a rotational broadening profile for different $v \sin i$ values. Forward-model fits to these spectra with $v \sin i$ values fixed to the Prato et al. (2015) measurements result in significantly worse fits, with p-values[15] of $<$0.001 and 0.003, respectively.

Figure 2.7 compares the distribution of my T dwarf $v \sin i$ measurements along with values reported in the literature (Crossfield 2014, and references therein; Tannock et al. 2021) between M4 and T9 dwarfs. The median $v \sin i$ for T dwarfs in my sample is greater than those of both mid/late M dwarfs (12 km s^{-1}) and L dwarfs (20 km s^{-1}), continuing a previously identified trend of increasing rotation rate with decreasing mass

[15]Throughout this paper, I adopt the convention that a p-value ≤ 0.1 is marginally significant, a p-value ≤ 0.05 is significant, and a p-value ≤ 0.01 is highly significant (Nuzzo 2014).

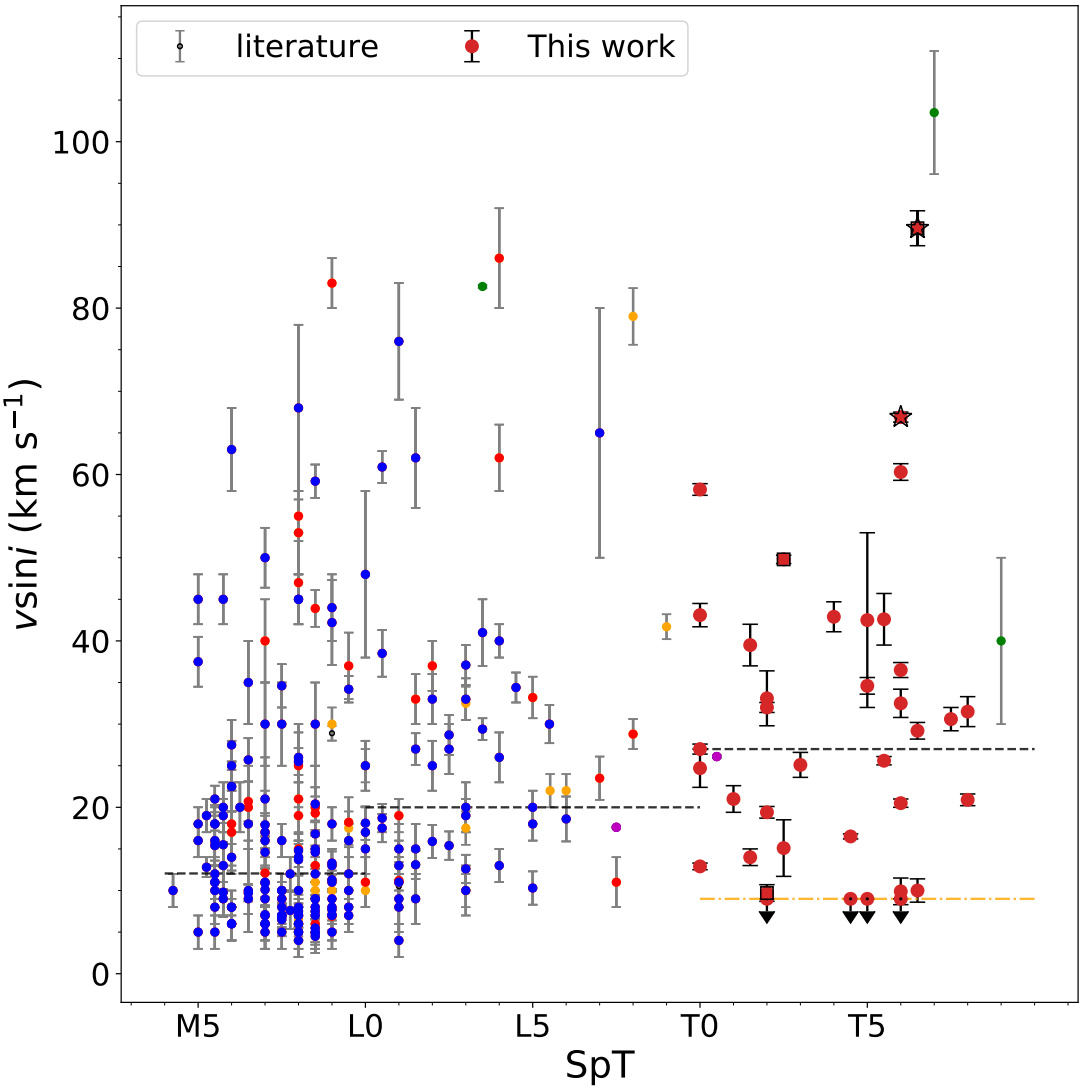

Figure 2.7: $v \sin i$ measurements as a function of spectral type for a compilation of M4–T9 dwarfs from this work (large symbols) and the literature (small symbols). All symbols are color-coded by instrument resolutions (green for $R < 10,000$, orange for $10,000 \leq R < 20,000$, red for $20,000 \leq R < 30,000$, blue for $30,000 \leq R < 50,000$, magenta for $R \geq 50,000$). My T dwarf measurements are further segregated into normal sources (circles), young cluster members (squares), and spectrally peculiar (stars). The horizontal grey dashed lines indicate the median rotational velocities for late-M, L, and T dwarfs, respectively, in this sample. The horizontal orange dashed line indicates the NIRSPEC minimum $v \sin i$ floor.

and later spectral type (Mohanty & Basri 2003; Reiners & Basri 2010; Irwin et al. 2011). Such a correlation is expected for both the smaller radii of lower mass stars and brown dwarfs, and the reduced angular momentum loss from weakened magnetic winds among lower-temperature dwarfs (Mohanty & Basri 2003; Reiners & Basri 2008). It should be noted that many of the M and L dwarfs shown in this panel were observed with higher-resolution spectrometers than NIRSPEC, and therefore have a lower $v \sin i$ floor. However, the observed trend persists even when a minimum cutoff of $v \sin i = 9$ km s^{-1} is applied. Among the T dwarfs, there is no significant correlation between $v \sin i$ and spectral type ($R = 0.10$, p-value = 0.56).

2.3.3 Effective Temperatures and Surface Gravities

I evaluated my $T_{\rm eff}$ and $\log g$ values by examining spectral type correlations with RV and $v \sin i$, and comparing to literature measurements. Table 2.4 lists the best-fit $T_{\rm eff}$ and $\log g$ for each source (744 K to 1700 K and 4.2 dex to 5.5 dex, respectively)[16]. These are based on order 33 or 58 fits, averaged over all spectra with a specific order. Note that the uncertainties reported here for $T_{\rm eff}$ and $\log g$ are just the Monte Carlo uncertainty, and do not reflect systematic error that may be present due to the narrow spectral bands I chose to model. As expected, $T_{\rm eff}$ is strongly correlated with spectral type, decreasing to later types (Figure 2.8; R=-0.94, p-value $< 10^{-3}$), although the scatter about a linear trend can be as high as $\pm$300 K (standard deviation = 77 K). Differences in $T_{\rm eff}$ among equivalently-classified sources can be related to other physical properties (e.g., metallicity, $\log g$), but may also reflect systematic offsets between orders and between models, as discussed in Section 2.2.1. I also find that my $\log g$ measurements based on Sonora model fits to order 58 data are strongly correlated with spectral type (R=-0.62, p-value < 0.01).

[16]The observations of J1520+3546 on 2012 Apr 2 and J2126+7617 on 2020 Sep 3 have $T_{\rm eff} \sim$1700 K, which are determined with a wider $T_{\rm eff}$ prior range to ensure the values are robust. The MCMC bounds are well above these temperatures. See Section 2.2 for more details.

Up to spectral type T5, $\log g$ is consistently around 5.5 dex, and then drops to lower values for later spectral types. This could reflect a systematic error or a real physical shift to lower average masses for cooler brown dwarfs.

Next, I evaluated correlations among $T_{\rm eff}$, $\log g$, RV, and $v \sin i$. I find my inferred $T_{\rm eff}$ and $\log g$ values to be positively correlated (Figure 2.9) for Sonora model fits because of the temperature and pressure dependence of the CO$\rightarrow$CH$_4$ reduction reaction as described above (see Figure 2.2). Such a trend is not found in BT-Settl model fits, however, for which the lowest $\log g$ values correspond to L+T binaries (J0629+2418 and J2126+7617) and the blue L dwarf J1331$-$0116 (see Section 2.4.4). Excluding these three sources, the $\log g$ values are greater than 5.2 cm s^{-2} dex for all fits, close to the $\log g$ ceiling of the models. There are clear positive trends between $T_{\rm eff}$ and $\log g$ paralleled to isoage lines (Figure 2.9). I found no significant correlations between $\log g$ and $v \sin i$, $\log g$ and RV, $T_{\rm eff}$ and $v \sin i$, or $T_{\rm eff}$ and RV.

Several T dwarfs in my sample have $T_{\rm eff}$ and $\log g$ values inferred from other analysis, including high-resolution spectra, medium-/low-resolution spectra, and spectral energy distribution (SED) measurements. Figure 2.10 shows my measurements of $T_{\rm eff}$ and $\log g$ compared to the literature measurements.[17] Comparing against high-resolution spectra, my $T_{\rm eff}$ values are on average 22$\pm$280 K lower and $\log g$ values on average are 0.6$\pm$0.4 dex higher than literature values, indicating overall consistency but with large scatter. Large discrepancies in $T_{\rm eff}$ values inferred from high-resolution spectra have been previously reported in the literature. Gagné et al. (2017) and Vos et al. (2017) analyzed NIRSPEC data for J0136+0933, both using forward-modeling techniques with the same model set, and report $T_{\rm eff}$ and $\log g$ values that differ by 192 K and 1.14 dex cm s^{-2},

[17]The literature $T_{\rm eff}$ and $\log g$ are drawn from Stephens et al. (2009, medium-/low-resolution spectroscopy); Del Burgo et al. (2009, high-resolution spectroscopy); Liu et al. (2011, medium-resolution spectroscopy); Sorahana & Yamamura (2012, low- and medium-resolution spectroscopy); Filippazzo et al. (2015, SEDs); Line et al. (2017, low-resolution spectroscopy); Vos et al. (2017, high-resolution spectroscopy); Gagné et al. (2017, high-resolution spectroscopy); Gagné et al. (2018a, high-resolution spectroscopy); and Miles et al. (2020, low-resolution spectroscopy).

respectively. Del Burgo et al. (2009) found a comparable degree of scatter in $T_{\rm eff} \approx 200$ K and $\log g \approx 0.7$ dex in fits of PHOENIX AMES-COND cloudless models (Allard et al. 2001) across multiple orders of T dwarf NIRSPEC spectra. Outdated methane opacities in the PHOENIX AMES-COND may be responsible for this scatter, as discussed in Section 2.2.1. Comparing against low- and medium-resolution spectra, I find smaller differences and scatter, with our $T_{\rm eff}$ values on average 63 ± 150 K higher and $\log g$ values on average 0.4 ± 0.4 dex higher than literature values. Similarly, our $T_{\rm eff}$ values are on average 68 ± 145 K higher and $\log g$ values on average 0.3 ± 0.4 dex higher than SED measurements from Filippazzo et al. (2015). Again, such discrepancies are common in the literature, and reflect ongoing challenges in accurately modeling brown dwarf spectra. In accord with my analysis, Logsdon et al. (2018) found that $\log g$ values inferred from medium-resolution spectra of late-T dwarfs were highly dependent on the spectral band used, with the best-fit values of 3.0–3.5 dex in the Y-band ($\sim0.95-1.12$ μm) and 5.0–5.5 dex in the H-band ($\sim1.5-1.68$ μm) using the BT-Settl models. Different atmosphere models also yielded significantly different $\log g$ values, as discussed in Section 2.2.1 (see Table 3 in Logsdon et al. 2018).

Given the differences in $T_{\rm eff}$ and $\log g$ values inferred between orders and in comparison with prior results, I urge caution in interpreting these quantities as they may not be accurate. Nevertheless, I have found that they are weakly correlated or uncorrelated with RV and $v \sin i$ and will not significantly influence the subsequent kinematic analysis.

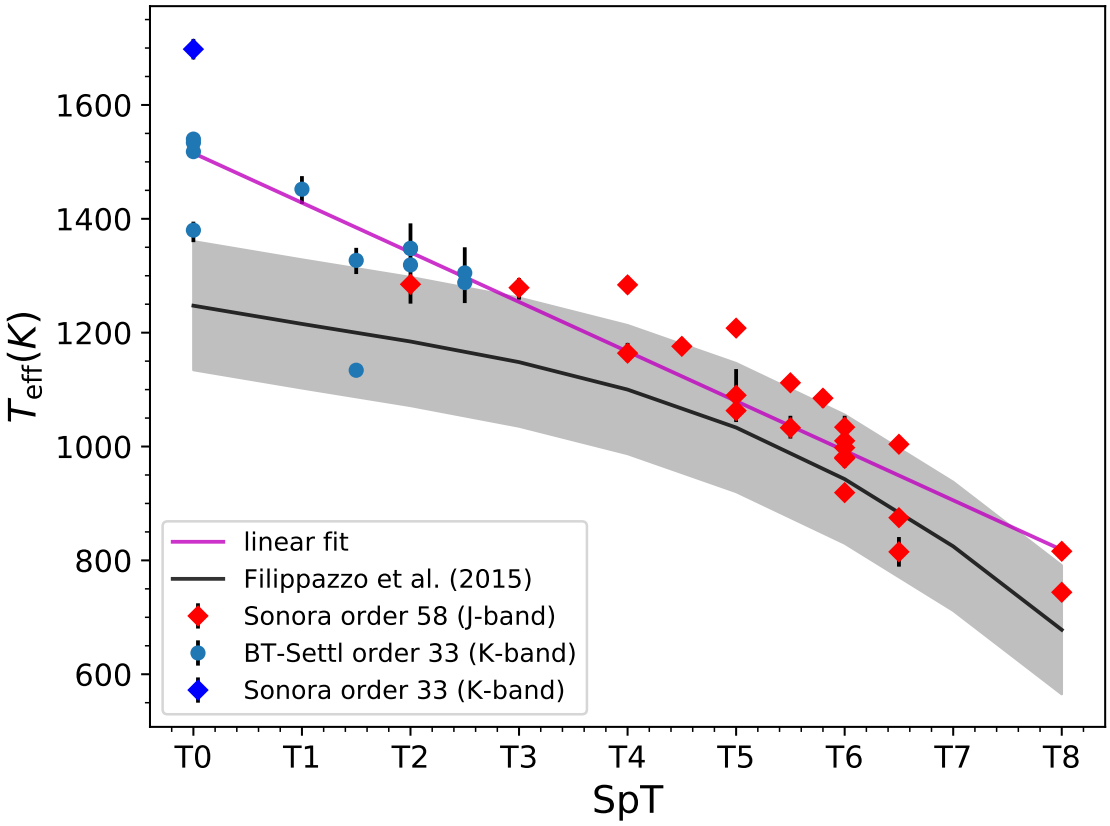

Figure 2.8: Measured $T_{\rm eff}$ values as a function of spectral type based on fits to orders 33 (blue) and 58 (red) data, compared to the $T_{\rm eff}$/spectral type relation of Filippazzo et al. (2015) (black line with $\pm 1\sigma$ uncertainty shaded in grey). The BT-Settl and Sonora model fits are marked as circles and diamonds, respectively. A linear fit to all of the measurements is indicated by the magenta line.

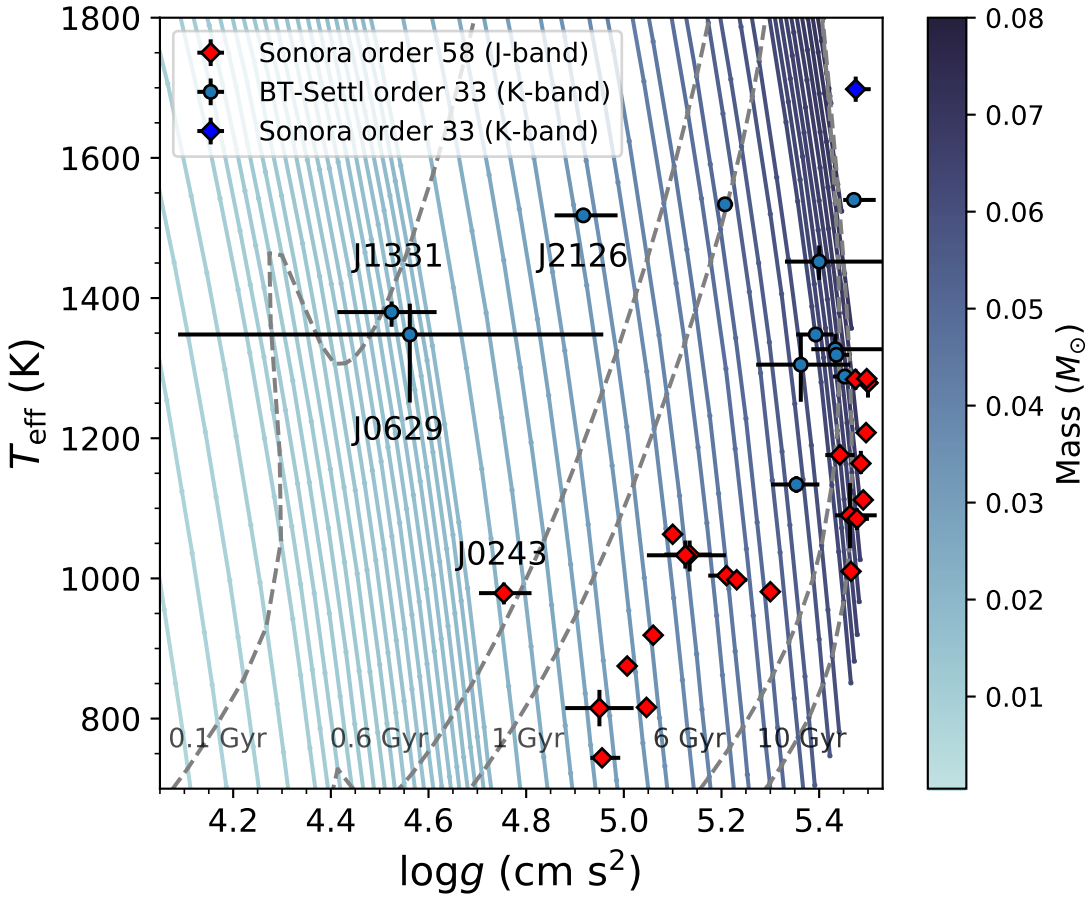

Figure 2.9: Comparison of measured $T_{\rm eff}$ and $\log g$ values based on fits to orders 33 (blue) and 58 (red) data. The BT-Settl and Sonora model fits are marked as circles and diamonds, respectively. The Marley et al. (2018) evolutionary models are plotted, with lines of constant mass indicated by solid color-coded lines and lines of constant age (0.1, 0.6, 1, 6, and 10 Gyr) indicated by labeled dashed grey lines. There are clear positive trends between $T_{\rm eff}$ and $\log g$ for both BT-Settl and Sonora model fits that run parallel to isoage lines. Note that earlier T dwarfs are mostly observed in K-band (orders 33), while later T dwarfs are mostly observed in J-band (order 58).

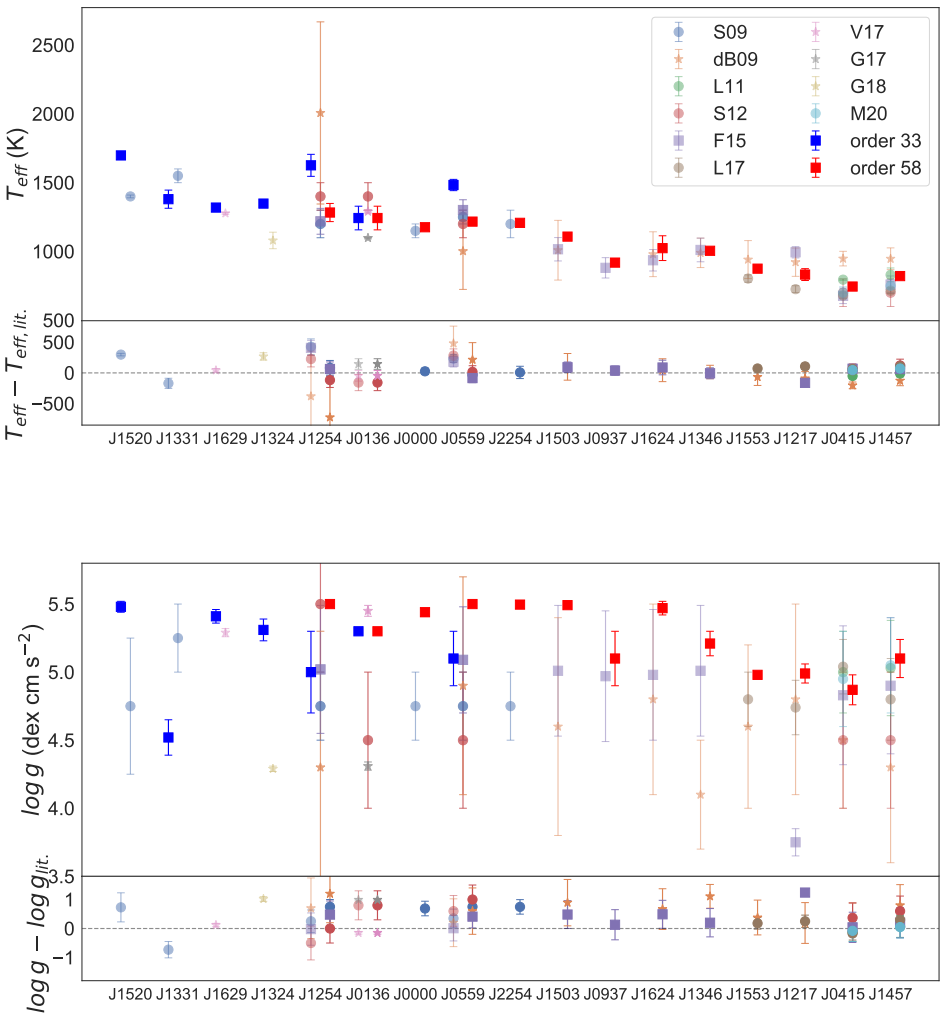

Figure 2.10: Comparison of $T_{\rm eff}$ measurements (top) and $\log g$ measurements (bottom) from my analysis with measurements from the literature. For each figure, the top panels show the measurements, with literature values slightly offset horizontally for clarity; the lower panels show the difference between measurement and literature values for each source. Measurements for orders 33 and 58 fits are labeled as blue and red squares, respectively. Literature references (from top to bottom in the legend) are: (S09): Stephens et al. (2009) (light blue), (dB09): Del Burgo et al. (2009) (orange), (L11): Liu et al. (2011) (green), (S12): Sorahana & Yamamura (2012) (red), (F15): Filippazzo et al. (2015) (purple), (L17): Line et al. (2017) (brown), (V17): Vos et al. (2017) (pink), (G17): Gagné et al. (2017) (grey), (G18): Gagné et al. (2018a) (olive), and (M20): Miles et al. (2020) (cyan). The stars, circles, and squares denote literature measurements based on high-resolution spectroscopy, medium-/low-resolution spectroscopy, and spectral energy distribution, respectively.

Table 2.4: Spectral Model Fit Parameters

Source	SpT	UT Date	O[a]	S/N	RV (km s^{-1})	$v \sin i$ (km s^{-1})	$\langle \mathrm{RV} \rangle^a$ (km s^{-1})	$\mathrm{RV}^c_{\mathrm{LIT}}$ (km s^{-1})	$\langle v \sin i \rangle^b$ (km s^{-1})	$v \sin i^c_{\mathrm{LIT}}$ (km s^{-1})	T_{eff} (K)	$\langle T_{\mathrm{eff}} \rangle^a$ (K)	$\log g$ (cm s^{-2})	$\langle \log g \rangle^b$ (cm s^{-2})	M[d]	Ref.[e]
J0000+2554	T4.5	2019 Oct 17	58	5	$6.4^{+0.4}_{-0.5}$	$4.4^{+2.0}_{-2.5}$	$6.4^{+0.4}_{-0.5}$	···	$< 9^{k}$	···	1176^{+13}_{-15}	1176^{+13}_{-15}	$5.44^{+0.03}_{-0.03}$	$5.442^{+0.03}_{-0.03}$	S	
J0034+0523	T6.5	2020 Sep 3	58	14	$16.6^{+1.4}_{-1.6}$	$89.6^{+2.1}_{-2.1}$	$16.6^{+1.4}_{-1.6}$	···	$89.6^{+2.1}_{-2.1}$	···	815^{+26}_{-26}	815^{+26}_{-26}	$4.95^{+0.07}_{-0.07}$	$4.95^{+0.07}_{-0.07}$	S	
J0136+0933[h]	T2.5	2008 Dec 4	58	78	$10.4^{+0.3}_{-0.4}$	$49.9^{+0.9}_{-1.2}$	$10.4^{+0.3}_{-0.3}$	11.5 ± 0.4	$49.8^{+0.5}_{-0.5}$	50.9 ± 0.8	1148^{+6}_{-7}	1288^{+8}_{-8}	$4.28^{+0.04}_{-0.04}$	$5.45^{+0.02}_{-0.04}$	B	(4)
···	···	2013 Oct 16	33	10	$11.6^{+0.8}_{-0.8}$	$48.1^{+1.3}_{-1.3}$	···	···	···	···	1291^{+7}_{-8}	···	$5.46^{+0.03}_{-0.05}$	···	B	
···	···	2016 Feb 3	33	7	$9.6^{+0.8}_{-0.8}$	$49.4^{+1.4}_{-1.2}$	···	···	···	···	1303^{+6}_{-7}	···	$5.43^{+0.05}_{-0.07}$	···	B	
J0150+3827	T0	2020 Aug 5	33	4	$56.2^{+0.9}_{-0.9}$	$24.7^{+2.3}_{-2.3}$	$56.2^{+0.9}_{-0.9}$	···	$24.7^{+2.3}_{-2.3}$	···	1540^{+7}_{-7}	1540^{+7}_{-7}	$5.47^{+0.02}_{-0.04}$	$5.47^{+0.02}_{-0.04}$	B	
J0213+3648	T3	2020 Sep 3	58	4	$-3.8^{+1.0}_{-0.9}$	$25.1^{+1.1}_{-1.5}$	$-3.8^{+1.0}_{-0.9}$	···	$25.1^{+1.1}_{-1.5}$	···	1279^{+21}_{-17}	1279^{+21}_{-17}	$5.5^{+0.01}_{-0.02}$	$5.5^{+0.01}_{-0.02}$	S	
J0243−2453	T6	2021 Jan 1	58	5	$-0.6^{+0.6}_{-0.7}$	$9.9^{+1.6}_{-1.6}$	$-0.6^{+0.6}_{-0.7}$	···	$9.9^{+1.6}_{-1.6}$	···	979^{+16}_{-15}	979^{+16}_{-15}	$4.75^{+0.05}_{-0.06}$	$4.754^{+0.051}_{-0.057}$	S	
J0415−0935	T8	2005 Oct 26	58	5	$50.4^{+2.1}_{-2.5}$	$34.3^{+3.4}_{-2.9}$	$51.9^{+1.1}_{-1.1}$	49.6 ± 1.2	$31.5^{+1.8}_{-1.7}$	33.5 ± 2.0	744^{+12}_{-12}	744^{+12}_{-12}	$4.87^{+0.08}_{-0.11}$	$4.96^{+0.02}_{-0.04}$	S	(2); (1)
J0559−1404[i]	T4.5	2000 Oct 10[g]	58	···	···	···	$-9.5^{+0.1}_{-0.1}$	-9 ± 3	$16.5^{+0.3}_{-0.2}$	20.1 ± 4.8	···	1218^{+2}_{-2}	···	$5.493^{+0.001}_{-0.001}$	···	(3); (1)
···	···	2001 Oct 9	58	42	$-9.7^{+0.5}_{-0.5}$	$16.5^{+1.1}_{-1.3}$	···	···	···	···	1211^{+4}_{-4}	···	$5.5^{+0.002}_{-0.004}$	···	S	
···	···	2001 Nov 2	58	59	$-10.3^{+0.3}_{-0.3}$	$15.4^{+0.8}_{-0.4}$	···	···	···	···	1218^{+5}_{-6}	···	$5.5^{+0.001}_{-0.002}$	···	S	
···	···	2001 Dec 29	58[f]	28	···	···	···	···	···	···	···	···	···	···	···	
···	···	2004 Dec 5	58	10	$-6.2^{+1.3}_{-1.2}$	$21.6^{+1.5}_{-1.6}$	···	···	···	···	1221^{+10}_{-11}	···	$5.49^{+0.01}_{-0.01}$	···	S	
···	···	2005 Oct 26	58	35	$-9.6^{+0.3}_{-0.3}$	$18.7^{+0.7}_{-1.3}$	···	···	···	···	1215^{+6}_{-6}	···	$5.5^{+0.001}_{-0.002}$	···	S	
···	···	2005 Oct 27	58	29	$-8.9^{+0.3}_{-0.3}$	$19.8^{+0.7}_{-0.4}$	···	···	···	···	1211^{+6}_{-6}	···	$5.5^{+0.001}_{-0.003}$	···	S	
···	···	2005 Oct 28	58	27	$-9.9^{+0.3}_{-0.3}$	$15.6^{+0.9}_{-0.6}$	···	···	···	···	1220^{+6}_{-6}	···	$5.5^{+0.001}_{-0.002}$	···	S	
···	···	2006 Jan 11	58	23	$-8.0^{+0.8}_{-0.7}$	$15.8^{+0.9}_{-0.8}$	···	···	···	···	1222^{+9}_{-11}	···	$5.5^{+0.002}_{-0.004}$	···	S	
···	···	2008 Mar 19	58	28	$-9.8^{+0.5}_{-0.6}$	$16.4^{+2.0}_{-1.8}$	···	···	···	···	1227^{+13}_{-20}	···	$5.48^{+0.01}_{-0.02}$	···	S	
···	···	2015 Dec 29	33	3	$-8.6^{+1.2}_{-1.1}$	$16.8^{+1.8}_{-1.6}$	···	···	···	···	1503^{+23}_{-24}	···	$5.11^{+0.17}_{-0.21}$	···	S	
···	···	2021 Jan 1	58	6	$-9.3^{+0.2}_{-0.2}$	$13.0^{+0.5}_{-0.7}$	···	···	···	···	1231^{+5}_{-5}	···	$5.48^{+0.0}_{-0.0}$	···	S	
J0627−1114	T6	2021 Jan 1	58	6	$1.2^{+0.8}_{-1.1}$	$5.4^{+2.5}_{-2.9}$	$1.2^{+0.8}_{-1.1}$	···	$< 9^{k}$	···	1034^{+24}_{-20}	1034^{+24}_{-20}	$5.13^{+0.05}_{-0.04}$	$5.135^{+0.052}_{-0.045}$	S	
J0629+2418	L7+T5.5	2012 Nov 28	33	1	$0.5^{+2.3}_{-2.1}$	$33.1^{+3.2}_{-3.3}$	$0.5^{+2.3}_{-2.1}$	···	$33.1^{+3.2}_{-3.3}$	···	1348^{+97}_{-44}	1348^{+97}_{-44}	$4.6^{+0.5}_{-0.4}$	$4.6^{+0.5}_{-0.4}$	B	
J0755+2212	T5	2021 Jan 1	58	5	$22.3^{+2.7}_{-1.7}$	$43.0^{+10.0}_{-9.0}$	$22.3^{+2.7}_{-1.7}$	···	$43.0^{+10.0}_{-9.0}$	···	1090^{+47}_{-46}	1090^{+47}_{-46}	$5.46^{+0.03}_{-0.05}$	$5.463^{+0.03}_{-0.055}$	S	
J0819−0335	T4	2021 Jan 1	58	9	$14.4^{+0.8}_{-0.9}$	$8.5^{+1.4}_{-2.4}$	$14.4^{+0.8}_{-0.9}$	···	$< 9^{k}$	···	1284^{+15}_{-15}	1284^{+15}_{-15}	$5.47^{+0.02}_{-0.03}$	$5.474^{+0.018}_{-0.026}$	S	
J0909+6525	T1.5+T2.5	2010 Dec 26	33	2	$37.8^{+1.6}_{-1.6}$	$39.5^{+2.5}_{-2.4}$	$37.8^{+1.6}_{-1.6}$	···	$39.5^{+2.5}_{-2.4}$	···	1327^{+24}_{-22}	1327^{+24}_{-22}	$5.43^{+0.05}_{-0.1}$	$5.43^{+0.05}_{-0.10}$	B	
J0937+2931	T6p	2002 Apr 23	58	20	$-4.4^{+0.9}_{-1.0}$	$64.9^{+1.4}_{-1.4}$	$-4.3^{+0.4}_{-0.4}$	-5 ± 3	$66.9^{+0.5}_{-0.6}$	60 ± 10	932^{+8}_{-10}	919^{+3}_{-4}	$5.48^{+0.01}_{-0.02}$	$5.06^{+0.001}_{-0.003}$	S	(3)
···	···	2003 Mar 24	58	25	$-5.6^{+1.0}_{-0.9}$	$64.9^{+1.7}_{-1.9}$	···	···	···	···	893^{+10}_{-10}	···	$5.47^{+0.02}_{-0.03}$	···	S	
···	···	2003 May 12	58	34	$-3.8^{+0.9}_{-0.7}$	$76.6^{+0.7}_{-1.6}$	···	···	···	···	920^{+7}_{-8}	···	$5.0^{+0.001}_{-0.003}$	···	S	
···	···	2006 Jan 10	58	15	$-3.2^{+1.5}_{-1.4}$	$63.0^{+1.8}_{-1.9}$	···	···	···	···	923^{+15}_{-14}	···	$5.49^{+0.01}_{-0.02}$	···	S	
···	···	2006 May 19	58	25	$-4.4^{+0.6}_{-0.7}$	$63.3^{+1.1}_{-0.9}$	···	···	···	···	923^{+8}_{-7}	···	$5.49^{+0.004}_{-0.01}$	···	S	
J1106+2754[h]	T0+T4.5	2008 Mar 19	58	20	$-3.1^{+0.3}_{-0.7}$	$26.3^{+1.1}_{-1.8}$	$2.5^{+0.2}_{-0.2}$	···	$12.9^{+0.4}_{-0.4}$	···	1171^{+6}_{-8}	1534^{+1}_{-1}	$4.24^{+0.06}_{-0.05}$	$5.207^{+0.008}_{-0.016}$	B	
···	···	2010 Dec 26	58	15	$-3.7^{+1.6}_{-0.6}$	$24.3^{+2.2}_{-2.2}$	···	···	···	···	1183^{+6}_{-6}	···	$4.37^{+0.12}_{-0.07}$	···	B	
···	···	2012 Apr 2	33	8	$3.5^{+0.8}_{-0.7}$	$12.7^{+1.7}_{-1.6}$	···	···	···	···	1564^{+3}_{-6}	···	$5.49^{+0.01}_{-0.02}$	···	B	
···	···	2012 Nov 27	33	3	$1.6^{+0.8}_{-1.0}$	$13.3^{+1.3}_{-1.2}$	···	···	···	···	1490^{+18}_{-21}	···	$5.35^{+0.09}_{-0.11}$	···	B	
···	···	2013 Feb 5	33	7	$1.0^{+0.8}_{-0.8}$	$10.4^{+1.2}_{-1.3}$	···	···	···	···	1522^{+3}_{-4}	···	$5.0^{+0.3}_{-0.2}$	···	B	
···	···	2015 Jan 1	33	1	$5.9^{+1.4}_{-1.4}$	$19.3^{+2.4}_{-2.6}$	···	···	···	···	1480^{+33}_{-35}	···	$5.43^{+0.06}_{-0.11}$	···	B	
···	···	2016 Jan 18	33	4	$11.1^{+0.9}_{-0.7}$	$11.6^{+2.1}_{-1.8}$	···	···	···	···	1539^{+4}_{-5}	···	$5.44^{+0.05}_{-0.09}$	···	B	
···	···	2016 Feb 16	33	8	$4.8^{+0.5}_{-0.4}$	$12.0^{+0.9}_{-0.7}$	···	···	···	···	1532^{+1}_{-2}	···	$5.43^{+0.05}_{-0.06}$	···	B	
···	···	2016 Apr 22	33	10	$5.1^{+0.5}_{-0.6}$	$14.8^{+1.0}_{-1.0}$	···	···	···	···	1537^{+2}_{-3}	···	$5.45^{+0.04}_{-0.07}$	···	B	
···	···	2016 May 22	33	9	$2.9^{+0.6}_{-0.6}$	$14.7^{+1.0}_{-1.0}$	···	···	···	···	1540^{+3}_{-3}	···	$5.32^{+0.09}_{-0.1}$	···	B	
···	···	2017 Mar 22	33	4	$-1.9^{+0.8}_{-0.7}$	$9.9^{+1.6}_{-1.3}$	···	···	···	···	1536^{+4}_{-3}	···	$5.47^{+0.02}_{-0.04}$	···	B	

Table 2.4 (*continued*)

Table 2.4 (*continued*)

Source	SpT	UT Date	O[a]	S/N	RV (km s^{-1})	$v \sin i$ (km s^{-1})	$\langle \mathrm{RV} \rangle^a$ (km s^{-1})	$\mathrm{RV}^c_{\mathrm{LIT}}$ (km s^{-1})	$\langle v \sin i \rangle^b$ (km s^{-1})	$v \sin i^c_{\mathrm{LIT}}$ (km s^{-1})	T_{eff} (K)	$\langle T_{\mathrm{eff}} \rangle^a$ (K)	$\log g$ (cm s^{-2})	$\langle \log g \rangle^b$ (cm s^{-2})	M[d]	Ref.[e]
···	···	2017 May 6	33	5	$-1.1^{+0.8}_{-0.8}$	$13.7^{+1.2}_{-1.3}$	···	···	···	···	1529^{+3}_{-3}	···	$5.35^{+0.1}_{-0.12}$	···	B	
···	···	2018 Jan 1	33	2	$-21.0^{+2.4}_{-3.0}$	$7.8^{+3.0}_{-3.8}$	···	···	···	···	1585^{+28}_{-51}	···	$5.0^{+0.4}_{-0.4}$	···	B	
···	···	2018 Jun 3	33	8	$-2.6^{+0.9}_{-0.9}$	$6.7^{+2.3}_{-3.1}$	···	···	···	···	1523^{+5}_{-6}	···	$5.24^{+0.17}_{-0.38}$	···	B	
···	···	2021 Jan 1	33	6	$-3.8^{+1.6}_{-1.2}$	$11.9^{+2.0}_{-2.2}$	···	···	···	···	1524^{+10}_{-12}	···	$5.37^{+0.09}_{-0.15}$	···	B	
···	···	2021 Jan 1	58	8	$-2.5^{+1.3}_{-0.9}$	$20.7^{+2.0}_{-1.7}$	···	···	···	···	1171^{+12}_{-17}	···	$4.37^{+0.17}_{-0.12}$	···	B	
J1217−0311	T7.5	2001 Jun 15[g]	58	7	···	···	$9.9^{+2.3}_{-1.9}$	5.0 ± 1.6	$30.6^{+1.3}_{-1.4}$	31.4 ± 2.1	···	830^{+14}_{-14}	···	$4.993^{+0.008}_{-0.018}$	···	(2); (1)
···	···	2006 Jan 18	58	4	$10.0^{+2.6}_{-2.1}$	$30.7^{+1.6}_{-1.8}$	···	···	···	···	804^{+18}_{-20}	···	$4.99^{+0.01}_{-0.02}$	···	S	
···	···	2006 Jan 19	58	4	$9.4^{+5.0}_{-4.0}$	$30.3^{+2.1}_{-2.4}$	···	···	···	···	866^{+23}_{-21}	···	$5.1^{+0.08}_{-0.07}$	···	S	
J1225−2739	T5.5+T8	2002 Apr 23	58	6	$18.5^{+1.5}_{-1.2}$	$42.6^{+3.1}_{-2.7}$	$18.5^{+1.5}_{-1.2}$	···	$42.6^{+3.1}_{-2.7}$	···	1033^{+19}_{-21}	1033^{+19}_{-21}	$5.13^{+0.08}_{-0.08}$	$5.13^{+0.08}_{-0.08}$	S	
J1254−0122[i]	T2	2001 Dec 31[g]	58	3	$40.8^{+4.3}_{-3.7}$	$41.1^{+4.7}_{-4.1}$	$2.7^{+0.4}_{-0.5}$	4 ± 3	$32.0^{+0.6}_{-0.6}$	27.3 ± 2.5	1137^{+51}_{-55}	1285^{+5}_{-6}	$5.44^{+0.04}_{-0.07}$	$5.497^{+0.001}_{-0.002}$	S	(3); (1)
···	···	2002 May 17	58	17	$0.8^{+0.9}_{-1.0}$	$33.4^{+1.3}_{-1.2}$	···	···	···	···	1264^{+13}_{-11}	···	$5.49^{+0.004}_{-0.01}$	···	S	
···	···	2003 May 14	58	16	$3.3^{+0.9}_{-1.0}$	$31.7^{+1.6}_{-1.4}$	···	···	···	···	1298^{+9}_{-11}	···	$5.5^{+0.003}_{-0.01}$	···	S	
···	···	2006 Jan 19	58	17	$4.1^{+1.2}_{-1.0}$	$31.5^{+1.2}_{-1.2}$	···	···	···	···	1284^{+11}_{-13}	···	$5.5^{+0.003}_{-0.01}$	···	S	
···	···	2007 May 31	58	27	$1.8^{+0.6}_{-0.9}$	$33.3^{+1.2}_{-1.7}$	···	···	···	···	1286^{+9}_{-9}	···	$5.5^{+0.001}_{-0.003}$	···	S	
···	···	2011 Jun 10	33	2	$1.4^{+2.1}_{-2.0}$	$21.9^{+2.6}_{-2.4}$	···	···	···	···	1626^{+80}_{-69}	···	$4.99^{+0.28}_{-0.3}$	···	S	
J1324+6358	T2	2016 May 22	33	6	$-23.0^{+0.5}_{-0.4}$	$9.7^{+1.0}_{-0.9}$	$-23.0^{+0.5}_{-0.4}$	-23.7 ± 0.4	$9.7^{+1.0}_{-0.9}$	11.5 ± 1.0	1348^{+9}_{-9}	1348^{+9}_{-9}	$5.31^{+0.08}_{-0.06}$	$5.39^{+0.04}_{-0.04}$	B	(5)
J1331−0116	T0p	2011 Mar 18	33	8	$-2.8^{+0.5}_{-0.5}$	$27.7^{+0.7}_{-0.8}$	$-3.3^{+0.4}_{-0.4}$	···	$27.0^{+0.6}_{-0.6}$	···	1421^{+27}_{-24}	1380^{+21}_{-15}	$4.61^{+0.13}_{-0.1}$	$4.52^{+0.11}_{-0.09}$	B	
···	···	2011 Jul 6	33	4	$-4.7^{+0.8}_{-0.9}$	$25.0^{+1.3}_{-1.3}$	···	···	···	···	1328^{+36}_{-20}	···	$4.4^{+0.3}_{-0.3}$	···	B	
J1346−0031	T6.5	2001 Jun 15	58	10	$-17.5^{+0.6}_{-0.6}$	$10.1^{+1.4}_{-1.6}$	$-17.5^{+0.6}_{-0.5}$	-23.1 ± 1.5	$10.0^{+1.2}_{-1.4}$	<15	1011^{+14}_{-13}	1004^{+12}_{-11}	$5.24^{+0.04}_{-0.03}$	$5.21^{+0.04}_{-0.03}$	S	(2); (1)
···	···	2006 Jan 18	58	4	$-17.5^{+1.4}_{-1.3}$	$9.8^{+2.3}_{-2.6}$	···	···	···	···	979^{+26}_{-28}	···	$5.11^{+0.07}_{-0.08}$	···	S	
GL 570D	T8	2001 Jun 15	58	14	$31.6^{+0.3}_{-0.4}$	$20.5^{+1.1}_{-0.9}$	$31.9^{+0.3}_{-0.3}$	28.9 ± 2.4	$20.9^{+0.7}_{-0.6}$	28.6 ± 2.4	814^{+6}_{-6}	816^{+5}_{-5}	$5.14^{+0.03}_{-0.03}$	$5.046^{+0.014}_{-0.018}$	S	(2); (1)
···	···	2006 Jan 18	58	6	$33.8^{+1.5}_{-1.7}$	$25.5^{+2.5}_{-2.6}$	···	···	···	···	826^{+13}_{-12}	···	$4.94^{+0.04}_{-0.06}$	···	S	
J1503+2525	T5.5	2006 Jan 19	58	20	$-34.9^{+0.6}_{-0.6}$	$25.3^{+0.8}_{-1.0}$	$-35.9^{+0.4}_{-0.3}$	-40.5 ± 2.1	$25.6^{+0.4}_{-0.5}$	32.8 ± 2.0	1118^{+6}_{-7}	1112^{+4}_{-4}	$5.49^{+0.01}_{-0.01}$	$5.49^{+0.004}_{-0.008}$	S	(2); (1)
···	···	2008 Mar 19	58	57	$-37.1^{+0.6}_{-0.4}$	$24.9^{+0.6}_{-0.7}$	···	···	···	···	1106^{+7}_{-6}	···	$5.49^{+0.01}_{-0.01}$	···	S	
J1506+7027	T6	2020 Sep 3	58	35	$2.5^{+0.4}_{-0.5}$	$60.3^{+0.9}_{-1.0}$	$2.5^{+0.4}_{-0.5}$	···	$60.3^{+0.9}_{-1.0}$	···	981^{+5}_{-5}	981^{+5}_{-5}	$5.3^{+0.01}_{-0.01}$	$5.3^{+0.011}_{-0.012}$	S	
J1520+3546	T0	2012 Apr 2	33	7	$3.4^{+1.4}_{-1.5}$	$45.9^{+2.0}_{-1.8}$	$4.1^{+1.0}_{-1.0}$	···	$43.1^{+1.4}_{-1.3}$	···	1698^{+18}_{-18}	1698^{+18}_{-18}	$5.48^{+0.02}_{-0.04}$	$5.475^{+0.014}_{-0.031}$	S	
J1553+1523	T6.5+T7.5	2001 Jun 15	58	10	$-24.4^{+0.8}_{-0.8}$	$31.8^{+1.5}_{-1.0}$	$-25.5^{+0.6}_{-0.5}$	-32.9 ± 3.0	$29.2^{+1.0}_{-0.8}$	29.4 ± 2.3	875^{+9}_{-8}	875^{+9}_{-8}	$4.98^{+0.01}_{-0.02}$	$5.007^{+0.011}_{-0.018}$	S	(2); (1)
J1624+0029	T6	2001 Jun 15	58	13	$-25.0^{+0.7}_{-0.8}$	$34.1^{+1.3}_{-1.2}$	$-24.3^{+0.5}_{-0.5}$	-30.7 ± 3.0	$36.5^{+0.9}_{-0.9}$	38.5 ± 2.0	987^{+8}_{-9}	1010^{+6}_{-7}	$5.39^{+0.03}_{-0.03}$	$5.465^{+0.007}_{-0.015}$	S	(2); (1)
···	···	2002 May 17	58	18	$-22.1^{+1.4}_{-1.0}$	$45.4^{+2.1}_{-2.0}$	···	···	···	···	1120^{+16}_{-17}	···	$5.49^{+0.01}_{-0.02}$	···	S	
···	···	2005 Jun 4	58	5	$-24.1^{+1.8}_{-1.8}$	$36.4^{+3.0}_{-3.1}$	···	···	···	···	944^{+28}_{-29}	···	$5.43^{+0.05}_{-0.07}$	···	S	
J1629+0335	T2	2011 Aug 11	33	3	$6.4^{+1.6}_{-1.5}$	$19.7^{+2.5}_{-2.2}$	$7.6^{+0.6}_{-0.6}$	···	$19.4^{+0.7}_{-0.7}$	···	1289^{+17}_{-16}	1319^{+7}_{-7}	$5.41^{+0.07}_{-0.09}$	$5.435^{+0.014}_{-0.026}$	B	
···	···	2011 Sep 7	33	4	$7.7^{+1.2}_{-1.2}$	$20.1^{+1.3}_{-1.5}$	···	···	···	···	1329^{+9}_{-9}	···	$5.47^{+0.02}_{-0.04}$	···	B	
J1809−0448	T1	2020 Aug 25	33	6	$-43.4^{+1.3}_{-1.3}$	$21.0^{+1.3}_{-1.6}$	$-43.4^{+1.3}_{-1.3}$	···	$21.0^{+1.3}_{-1.6}$	···	1452^{+26}_{-23}	1452^{+26}_{-23}	$5.4^{+0.07}_{-0.14}$	$5.4^{+0.07}_{-0.14}$	B	
J1928+2356[i]	T6	2019 Sep 12	37	5	$-27.1^{+1.0}_{-1.1}$	$25.6^{+1.5}_{-1.4}$	$-26.3^{+0.2}_{-0.3}$	···	$20.5^{+0.5}_{-0.5}$	···	1172^{+25}_{-25}	998^{+4}_{-2}	$5.48^{+0.02}_{-0.03}$	$5.23^{+0.02}_{-0.02}$	S	
···	···	2019 Oct 17	58	14	$-25.9^{+0.5}_{-0.5}$	$19.9^{+0.8}_{-0.8}$	···	···	···	···	998^{+4}_{-2}	···	$5.23^{+0.02}_{-0.02}$	···	S	
J1952+7240	T4	2019 Oct 17	58	5	$-11.8^{+2.0}_{-1.0}$	$40.2^{+3.0}_{-2.7}$	$-12.0^{+1.3}_{-0.7}$	···	$42.9^{+1.8}_{-1.8}$	···	1164^{+15}_{-18}	1164^{+15}_{-18}	$5.46^{+0.03}_{-0.06}$	$5.485^{+0.008}_{-0.017}$	S	
J2030+0749	T1.5	2020 Jul 10	33	4	$-21.2^{+0.6}_{-0.7}$	$14.0^{+0.9}_{-1.0}$	$-21.2^{+0.6}_{-0.7}$	···	<15[k]	···	1134^{+12}_{-12}	1134^{+12}_{-12}	$5.35^{+0.05}_{-0.05}$	$5.35^{+0.05}_{-0.05}$	B	
J2126+7617	T0p	2011 Jun 10	33	6	$-17.7^{+1.0}_{-1.1}$	$58.8^{+1.9}_{-1.8}$	$-18.4^{+0.4}_{-0.4}$	···	$58.2^{+0.7}_{-0.7}$	···	1462^{+20}_{-29}	1518^{+5}_{-9}	$4.66^{+0.14}_{-0.3}$	$4.92^{+0.06}_{-0.07}$	B	
···	···	2011 Jul 6	33	10	$-18.8^{+1.1}_{-1.2}$	$59.5^{+2.1}_{-1.8}$	···	···	···	···	1504^{+16}_{-21}	···	$4.77^{+0.25}_{-0.15}$	···	B	
···	···	2011 Aug 11	33	2	$-24.3^{+5.3}_{-4.1}$	$51.1^{+10.3}_{-7.8}$	···	···	···	···	1532^{+61}_{-101}	···	$4.7^{+0.7}_{-0.7}$	···	B	
···	···	2011 Sep 7	33	8	$-18.7^{+1.6}_{-1.2}$	$56.1^{+2.7}_{-2.5}$	···	···	···	···	1553^{+8}_{-23}	···	$5.0^{+0.3}_{-0.3}$	···	B	
···	···	2013 Sep 17	33	5	$-20.3^{+2.1}_{-2.0}$	$58.4^{+3.2}_{-2.9}$	···	···	···	···	1475^{+25}_{-34}	···	$5.0^{+0.2}_{-0.2}$	···	B	
···	···	2013 Oct 16	33	4	$-20.7^{+1.7}_{-1.8}$	$59.7^{+2.8}_{-2.9}$	···	···	···	···	1448^{+41}_{-49}	···	$4.6^{+0.4}_{-0.4}$	···	B	

Table 2.4 (*continued*)

Table 2.4 (*continued*)

Source	SpT	UT Date	O[a]	S/N	RV (km s^{-1})	$v \sin i$ (km s^{-1})	$\langle \mathrm{RV} \rangle^a$ (km s^{-1})	$\mathrm{RV}^c_{\mathrm{LIT}}$ (km s^{-1})	$\langle v \sin i \rangle^b$ (km s^{-1})	$v \sin i^c_{\mathrm{LIT}}$ (km s^{-1})	T_{eff} (K)	$\langle T_{\mathrm{eff}} \rangle^a$ (K)	$\log g$ (cm s^{-2})	$\langle \log g \rangle^b$ (cm s^{-2})	M[d]	Ref.[e]
⋯	⋯	2014 Sep 02	33	6	$-19.5^{+1.6}_{-1.7}$	$57.5^{+2.7}_{-2.5}$	⋯	⋯	⋯	⋯	1540^{+11}_{-17}	⋯	$4.7^{+0.3}_{-0.3}$	⋯	B	
⋯	⋯	2020 Aug 25	33	4	$-14.9^{+1.7}_{-1.5}$	$54.9^{+2.1}_{-2.1}$	⋯	⋯	⋯	⋯	1507^{+104}_{-156}	⋯	$5.2^{+0.19}_{-0.2}$	⋯	B	
⋯	⋯	2020 Sep 3	57[j]	14	$-14.1^{+0.9}_{-0.9}$	$60.4^{+1.0}_{-1.0}$	⋯	⋯	⋯	⋯	1700^{+2}_{-2}	⋯	$5.0^{+0.01}_{-0.01}$	⋯	B	
HN Peg B	T2.5	2017 Jun 09	33	5	$-19.5^{+1.3}_{-1.3}$	$15.1^{+3.0}_{-3.4}$	$-19.5^{+1.3}_{-1.3}$	⋯	$15.1^{+3.0}_{-3.4}$	⋯	1305^{+53}_{-45}	1305^{+53}_{-45}	$5.36^{+0.09}_{-0.1}$	$5.36^{+0.09}_{-0.10}$	B	
J2236+5105	T5	2020 Sep 3	58	22	$-1.2^{+0.3}_{-0.3}$	$6.6^{+0.9}_{-0.9}$	$-1.2^{+0.3}_{-0.3}$	⋯	< 9[k]	⋯	1063^{+8}_{-8}	1063^{+8}_{-8}	$5.1^{+0.01}_{-0.01}$	$5.1^{+0.011}_{-0.01}$	S	
J2254+3123	T5	2003 Aug 10	58	17	$14.3^{+0.5}_{-0.7}$	$32.5^{+1.2}_{-1.2}$	$15.1^{+0.5}_{-0.6}$	14 ± 3	$34.6^{+0.9}_{-1.0}$	15 ± 5	1214^{+12}_{-11}	1208^{+7}_{-7}	$5.5^{+0.003}_{-0.01}$	$5.496^{+0.002}_{-0.005}$	S	(3)
⋯	⋯	2005 Jul 19	58	16	$16.8^{+1.0}_{-0.9}$	$37.4^{+1.3}_{-1.5}$	⋯	14 ± 3	⋯	15 ± 5	1204^{+9}_{-11}	⋯	$5.5^{+0.003}_{-0.01}$	⋯	S	
J2356−1553	T6	2005 Jul 19	58	6	$23.6^{+1.3}_{-1.5}$	$30.6^{+2.2}_{-2.1}$	$21.8^{+0.9}_{-1.0}$	19 ± 3	$32.5^{+1.7}_{-1.6}$	15 ± 5	1065^{+22}_{-22}	1085^{+16}_{-15}	$5.48^{+0.01}_{-0.03}$	$5.477^{+0.013}_{-0.025}$	S	(3)
⋯	⋯	2005 Dec 10	58	6	$20.3^{+1.3}_{-1.4}$	$35.4^{+2.7}_{-2.6}$	⋯	19 ± 3	⋯	15 ± 5	1109^{+24}_{-23}	⋯	$5.43^{+0.05}_{-0.07}$	⋯	S	

References – (1) Zapatero Osorio et al. (2006), (2) Zapatero Osorio et al. (2007), (3) Prato et al. (2015), (4) Gagné et al. (2017), (5) Gagné et al. (2018a)

[a] Spectral order of data.

[b] Weighted average over all epochs.

[c] Previously reported values in the literature.

[d] Models used: S = Sonora 2018 (Marley et al. 2018); B = BT-Settl (Allard et al. 2012).

[e] References for prior RV and $v \sin i$ measurements

[f] No telluric observations available for this epoch.

[g] Measurements are considered unreliable due to low S/N.

[h] Adopted T_{eff} and $\log g$ are determined using order 33 measurements only; see Section 2.3.3.

[i] Adopted T_{eff} and $\log g$ are determined using order 58 measurements only; see Section 2.3.3.

[j] The spectra of order 57 are modeled in this case, as order 58 spectra are almost featureless due to large large $v \sin i$.

[k] The $v \sin i$ detection floor for NIRSPEC is 9 km s^{-1} for S/N ≥ 5, and 15 km s^{-1} for S/N < 5 data; see Section 2.2.1.

Note – Measurements from individual spectra over individual or multiple epochs are combined using inverse uncertainty weighting (weight = $1/(\sigma^2_{\mathrm{upper}} + \sigma^2_{\mathrm{lower}})$); upper and lower uncertainties are also combined using inverse uncertainty weighting. In cases where individual spectra have S/N < 10, spectral data are combined first, the modeled.

2.4 Analysis

2.4.1 Galactic *UVW* Space Motions and Kinematic Populations

I combined astrometry and my measured RVs to compute Galactic *UVW* space motions for my sample following the prescription of Johnson & Soderblom (1987). *UVW* velocities are defined here in a right-handed rectangular coordinate system centered on the Sun, with U in the direction toward the Galactic center, V in the direction of Galactic rotation, and W in the direction toward the Galactic North pole (opposite the Galactic angular velocity vector). Uncertainties were propagated from the input quantities using the Monte Carlo method assuming Gaussian noise. I adopted a correction from the heliocentric frame to the local standard of rest (LSR) of $(U_\odot, V_\odot, W_\odot) = (11.1, 12.24, 7.25)$ km s^{-1} from Schönrich et al. (2010). The T dwarf J1952+7240 does not have a parallax measurement, so I estimated its distance and uncertainty using the absolute magnitude/spectral type relations in Dupuy & Liu (2012). Results are tabulated in Table 2.5.

Figure 2.11 compares the distribution of *UVW* velocities to the 2σ velocity dispersion volumes of local thin and thick disk populations from Bensby et al. (2003). The average U and W velocities of the T dwarfs are consistent with zero, while a marginally significant net negative average V velocity ($\langle V \rangle = -3.6 \pm 2.7$ km s^{-1}) can be attributed to asymmetric drift (Strömberg 1924). I do not find any significant correlation between *UV*, *UW*, or *VW* velocities.

Following Bensby et al. (2003), I computed relative probabilities of membership in the thick disk versus the thin disk ($P(\mathrm{TD})/P(\mathrm{D})$) and halo versus the thin disk ($P(\mathrm{H})/P(\mathrm{D})$) using the threshold criteria defined in Burgasser et al. (2015a): thin disk membership is assigned for $P(\mathrm{TD})/P(\mathrm{D}) < 0.1$, thick disk membership is assigned for $P(\mathrm{TD})/P(\mathrm{D}) > 10$, and intermediate population membership is assigned for $0.1 < P(\mathrm{TD})/P(\mathrm{D}) < 10$. All but one of my sources are thin disk members, with

J1331−0116 being identified as an intermediate thin disk/thick disk member and an unusually blue L dwarf (see Section 2.4.4). None of the sources in my sample have a significant probability of halo membership.

2.4.2 Galactic Orbits

Additional insight into my sample's kinematic properties can be inferred by computing their Galactic orbits and orbital parameters. I used the package *galpy* (Bovy 2015) to compute the orbits, which is an ordinary differential equation solver that satisfies conservation of energy and angular momentum. I assumed an axisymmetric Galactic potential in a galactocentric cylindrical coordinate system (R, ϕ, Z) using the parameters of Miyamoto & Nagai (1975), a Solar azimuthal velocity v_ϕ = 220 km s^{-1} (Bovy & Tremaine 2012), and a Solar coordinate of ($R_\odot$, $Z_\odot$) = (8.43, 0.027) kpc at $\phi_\odot$ = 0 (Chen et al. 2001; Reid et al. 2014). Orbits were sampled over the period −5 to +5 Gyr. Uncertainties in the present-day position and velocity of each source were propagated using Monte Carlo sampling assuming Gaussian noise, resulting in 1,000 orbits per source from which I computed minimum and maximum Galactic cylindrical radius ($R_{\rm max}, R_{\rm min}$), maximum absolute Galactic vertical height ($|Z|$), median orbital eccentricity ($e \equiv \langle R_{\rm max} - R_{\rm min}\rangle / \langle R_{\rm max} + R_{\rm min}\rangle$), and median orbital inclination ($\tan i \equiv |Z/\sqrt{X^2+Y^2}|$), with uncertainties determined from the distribution of simulated orbits.

The majority of my sample possess circular and planar orbits ($e \leq 0.20$, $i \leq 2^\circ$) as expected for a thin disk population. The intermediate thin/thick disk star J1331−0116 has the largest inclination and eccentricity in the sample ($i = 2.5^\circ \pm 0.8^\circ$, $e = 0.29 \pm 0.06$, $R_{\rm min} = 4.6 \pm 0.6$ kpc). The median orbital parameters for the sample, $R_{\rm min} = 7.5$ kpc, $R_{\rm max} = 9.2$ kpc, $e = 0.12$, and $i = 0.69^\circ$, are consistent with the orbital parameters of local late-M and L dwarfs reported in Burgasser et al. (2015a).[18]

[18]These values are $R_{\rm min}$ = 8.0 kpc, $R_{\rm max}$ = 9.5 kpc, and e = 0.11 for late-M dwarfs, and $R_{\rm min}$ = 7.8 kpc,

2.4.3 Cluster Membership

UCDs, including T dwarfs, have been found to be members of nearby association and clusters, which provide independent age determinations and can potentially break the age-mass-$L_{\rm bol}$ degeneracy. Cluster membership probability can be determined by the alignment in 6D configuration space (heliocentric *XYZ* spatial and *UVW* velocity coordinates) with other association members. *XYZ* spatial coordinates are defined in the same direction as *UVW*. I used the BANYAN Σ web tool[19] (Gagné et al. 2018c) to compare the astrometry and radial velocities of my sources to 27 young clusters within 150 pc of the Sun. I confirmed that J0136+0933 (Gagné et al. 2017) and J1324+6358 (Gagné et al. 2018a) are probable members (99%) of the ∼200 Myr Carina-Near and 130 Myr AB Doradus moving groups, respectively (Zuckerman et al. 2006; Gagné et al. 2018b). I also confirmed that J0819−0335 is a candidate kinematic member of the β Pictoris moving group (age τ = 24±3 Myr, Bell et al. 2015), with a 95% probability of membership and a 5% probability of being a field dwarf (Zhang et al. 2021b). J1553+1532 is also confirmed as a kinematic member of Carina-Near moving group, with a 98% probability of membership (2% field object; Zhang et al. 2021b). I discuss these two sources in further detail below. I are able to rule out three young moving group candidates reported in Zhang et al. (2021b), identified on the basis of spatial coordinates, proper motion, and the BANYAN Σ tool. These are J0627−1114 (99% field object), J1624+0029 (27% Carina-Near; 73% field object), and J2236+5105 (99% field object). My ability to excluded these candidates highlights the importance of precise RV measurements in assessing cluster membership.

$R_{\rm max}$ = 10 kpc, and e = 0.16 for late L dwarfs, with $i \leq 2^\circ$ for both populations.

[19] http://www.exoplanetes.umontreal.ca/banyan/

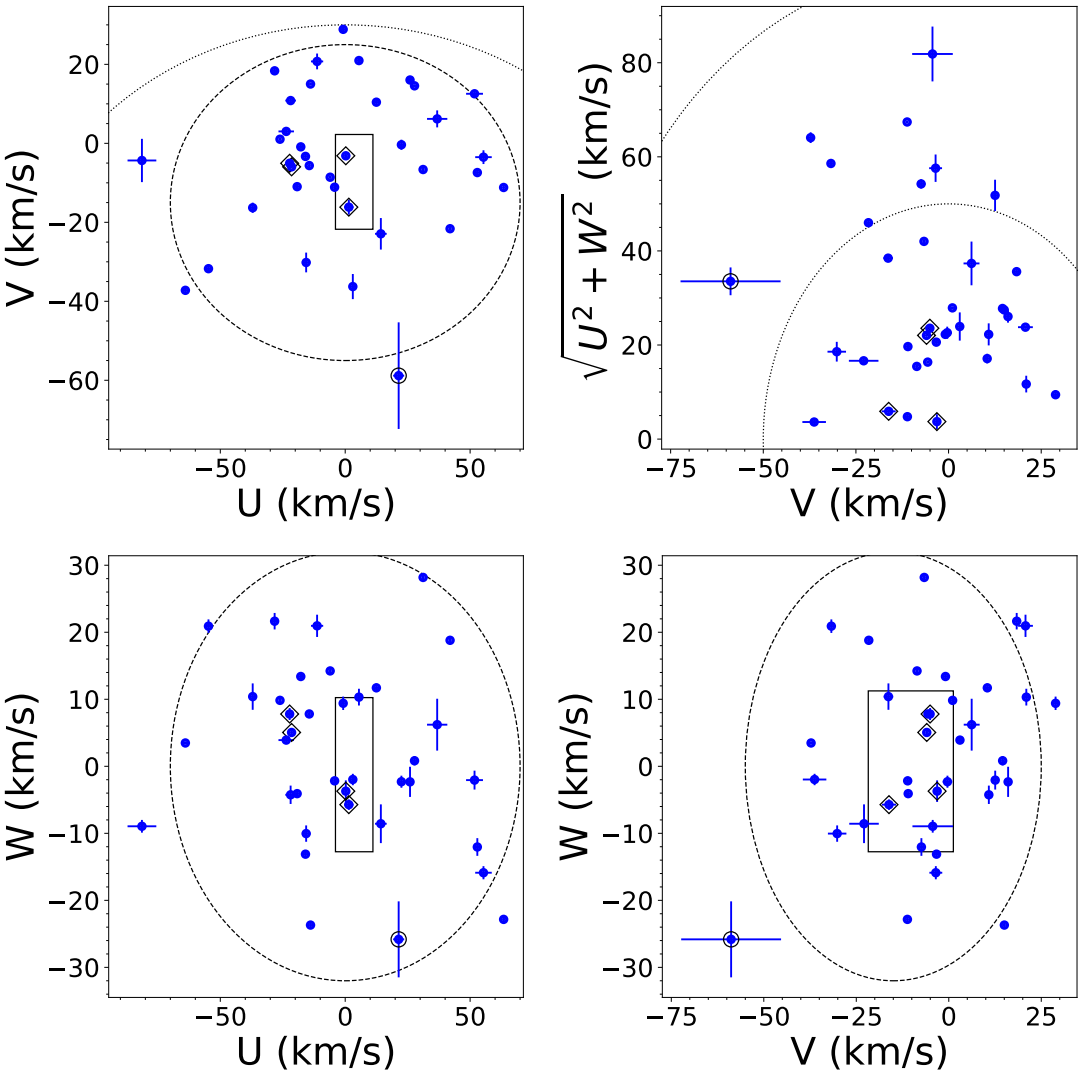

Figure 2.11: *UVW* space motions of the T dwarf sample in the Local Standard of Rest (Schönrich et al. 2010). The *UV*, *UW*, and *VW* velocities are shown along with the 2σ uncertainty spheres for the thin disk (dashed lines) and thick disk (dotted lines) populations from Bensby et al. (2003). The "good box" from Zuckerman & Song (2004) that segregates members of young moving groups is also labeled. The upper-right corner is a Toomre plot, with total velocities $v_{\rm tot} = \sqrt{U^2+V^2+W^2}$ indicated in steps of 50 km s^{-1} in dotted circles. Young sources and intermediate thin/thick disk sources ($0.1 < P({\rm TD})/P({\rm D}) < 10$) are highlighted with open diamonds and open circles, respectively.

Table 2.5: Radial Velocities and Heliocentric Space Motions

Source Name	SpT	Adpoted RV (km s^{-1})	U (km s^{-1})	V (km s^{-1})	W (km s^{-1})	P[TD]/P[D][a]	Population[a]
J0000+2554	T4.5	$6.4^{+0.4}_{-0.5}$	7.1±0.2	21.6±0.4	10.5±0.4	0.01	D
J0034+0523	T6.5	$16.6^{+1.4}_{-1.6}$	−19.0±0.7	11.5±0.8	−4.6±1.4	0.01	D
J0136+0933	T2.5	$10.4^{+0.3}_{-0.3}$	−21.5±0.2	−6.0±0.1	5.1±0.2	0.01	D
J0150+3827	T0	$56.2^{+0.9}_{-0.9}$	−94.6±5.0	−15.5±4.6	−5.2±0.8	0.09	D
J0213+3648	T3	$-3.8^{+1.0}_{-0.9}$	10.7±3.2	7.2±3.6	10.1±4.1	0.01	D
J0243−2453	T6	$-0.6^{+0.6}_{-0.7}$	27.8±0.7	14.6±0.3	0.8±0.7	0.01	D
J0415−0935	T8	$51.9^{+1.1}_{-1.1}$	−54.9±0.8	−31.8±0.4	21.2±0.8	0.05	D
J0559−1404	T4.5	$-9.5^{+0.1}_{-0.1}$	31.1±0.1	−6.4±0.2	28.0±0.1	0.02	D
J0627−1114	T6	$1.2^{+0.9}_{-1.1}$	23.8±1.0	−1.7±1.0	−3.0±0.5	0.01	D
J0629+2418	L7+T5.5[b]	$0.5^{+2.3}_{-2.1}$	13.9±2.3	−27.1±3.5	−17.8±2.3	0.01	D
J0755+2212	T5	$22.3^{+2.7}_{-1.7}$	−5.9±2.3	−10.8±1.1	9.0±1.1	0.01	D
J0819−0335	T4	$14.4^{+0.8}_{-0.9}$	0.3±0.6	−3.5±0.7	−4.5±0.6	0.01	D
J0909+6525	T1.5+T2.5[b]	$37.8^{+1.6}_{-1.6}$	−28.1±1.4	19.6±0.8	21.0±1.2	0.02	D
J0937+2931	T6	$-4.3^{+0.4}_{-0.4}$	42.0±0.4	−21.6±0.4	18.8±0.4	0.02	D
J1106+2754	T0+T4.5[b]	$2.5^{+0.2}_{-0.2}$	3.2±0.2	−37.0±1.2	−2.0±0.3	0.01	D
J1217−0311	T7.5	$9.9^{+2.3}_{-1.9}$	−37.0±1.2	−16.3±1.3	10.4±2.0	0.01	D
J1225−2739	T5.5+T8[b]	$18.5^{+1.5}_{-1.2}$	52.9±1.3	−7.4±1.1	−12.0±1.3	0.01	D
J1254−0122	T2e	$2.7^{+0.4}_{-0.5}$	−17.8±1.0	−0.9±0.5	13.4±0.5	0.01	D
J1324+6358	T2p	$-23.0^{+0.5}_{-0.4}$	5.5±0.7	−12.5±0.8	−6.8±0.5	0.01	D
J1331−0116	T0	$-3.3^{+0.4}_{-0.4}$	25.4±1.6	−83.8±9.7	−36.3±4.1	0.27	D/TD
J1346−0031	T6.5	$-17.5^{+0.6}_{-0.5}$	−19.2±0.8	−11.0±1.0	−4.1±0.5	0.01	D
J1457−2122	T8	$31.9^{+0.3}_{-0.3}$	63.4±0.4	−11.2±0.2	−22.8±0.5	0.04	D
J1503+2525	T5.5	$-35.9^{+0.4}_{-0.3}$	−13.8±0.2	14.9±0.1	−23.7±0.4	0.02	D
J1506+7027	T6	$2.5^{+0.4}_{-0.5}$	−26.0±0.2	1.0±0.4	9.8±0.3	0.01	D
J1520+3546	T0	$4.1^{+1.0}_{-1.0}$	42.4±2.4	13.3±0.5	0.8±1.1	0.01	D
J1553+1532	T6.5+T7.5[b]	$-25.5^{+0.6}_{-0.5}$	−21.6±0.4	−4.6±0.2	7.1±0.5	0.01	D
J1624+0029	T6	$-24.3^{+0.5}_{-0.5}$	−14.4±0.4	−5.6±0.2	7.8±0.3	0.01	D
J1629+0335	T2	$7.6^{+0.6}_{-0.6}$	26.0±0.7	16.9±0.2	−2.8±0.8	0.01	D
J1809−0448	T1	$-43.4^{+1.3}_{-1.3}$	−12.0±1.5	−38.0±2.0	−11.8±0.9	0.02	D
J1928+2356	T6	$-26.3^{+0.2}_{-0.3}$	−5.3±0.2	−9.1±0.3	16.0±0.1	0.01	D
J1952+7240	T4	$-12.0^{+1.3}_{-0.7}$	39.2±0.7	5.4±1.2	9.7±0.5	0.01	D
J2030+0749	T1.5	$-21.2^{+0.6}_{-0.7}$	−16.2±0.4	−3.3±0.5	−13.5±0.3	0.01	D
J2126+7617	L7+T3.5[b]	$-18.4^{+0.4}_{-0.4}$	−62.6±0.8	−36.7±0.5	3.5±0.1	0.05	D
HN Peg B	T2.5	$-19.5^{+1.3}_{-1.3}$	−4.2±0.4	−11.1±1.1	−2.2±0.6	0.01	D
J2236+5105	T5	$-1.2^{+0.3}_{-0.3}$	−25.2±1.3	2.6±0.4	3.6±0.2	0.01	D
J2254+3123	T5	$15.1^{+0.5}_{-0.6}$	0.1±0.4	28.7±0.6	8.9±0.5	0.01	D
J2356−1553	T6	$21.8^{+0.9}_{-1.0}$	55.4±3.3	−3.5±1.7	−15.9±1.0	0.02	D

[a] Galactic thin disk (D), thick disk (TD), intermediate populations (D/TD) are assigned according to probability ratios $P(\mathrm{TD})/P(\mathrm{D}) < 0.1$, $P(\mathrm{TD})/P(\mathrm{D}) > 10$, and $0.1 < P(\mathrm{TD})/P(\mathrm{D}) < 10$, respectively, following Bensby et al. (2003).
[b] Known or candidate binary.

2.4.4 Individual Sources of Interest

2MASS J00345157+0523050 is a peculiar T6.5/T7 (Chiu et al. 2006; Burgasser et al. 2004). It has the largest $v \sin i$ in my sample ($v \sin i = 90 \pm 2$ km s^{-1}), making it one

of the fastest rotating brown dwarfs found to date [20]. Assuming a radius of 1 $R_{\rm Jup}$ and edge-on rotation, this corresponds to a *maximum* rotational period of 1.4 hr. Assuming a mass of 0.05 $M_\odot$ (which corresponds to a 900 K brown dwarf at 5 Gyr; Baraffe et al. 2003), the observed velocity corresponds to 30% of the break-up rotational velocity ($v_{\rm break} = \sqrt{GM/R} \sim 300$ km s^{-1}). The source exhibits a very blue near-infrared color $J-K = -0.93 \pm 0.03$ (Lawrence et al. 2013) and other spectral peculiarities that have been attributed to enhanced H_2 collision-induced absorption (CIA) in the high-pressure atmosphere of a relatively massive (high surface gravity) and/or low-metallicity (low opacity) brown dwarf (Linsky 1969; Burgasser et al. 2004). The absence of the K I doublet absorption at 1.25 μm, which is generally present in the spectra of T6–T7 dwarfs (Martin et al. 2017), may be an indicator of low metallicity effects or shallowing of the line features due to the object's fast rotation. Either trait would imply that J0034+0523 is a relatively old brown dwarf with a high mass and compact radius which has not undergone significant angular momentum loss. I note that my forward-modeling fit utilizes solar-metallicity atmosphere models, and the potential subsolar metalicity of this peculiar T dwarf may influence the derived parameters, including $v \sin i$.

2MASS J02431371−2453298 (Burgasser et al. 1999) stands out in Figure 2.9 as the only non-binary or unusually blue L dwarf with a gravity-based model age significantly less than 1 Gyr. This T6 dwarf had previously been identified as a candidate member of the ∼400 Myr Ursa Majoris moving group based on its distance and proper motion (Bannister & Jameson 2007; Jameson et al. 2008b), and prior low-resolution spectral analyses have also indicated evidence of low surface gravity (Burgasser et al. 2006a). This source thus exhibits both kinematic and spectral indicators of relative youth, and is a potential benchmark for spectral age indicators for mid- and late-type T

[20] Other unusually fast rotators plotted in Figure 2.7 include 2MASS J04070752+1546457 (82.6 ± 0.2 km s^{-1}), LP 349-25B (83 ± 3 km s^{-1}), HD 130948BC (86 ± 6 km s^{-1}), and 2MASS J03480772−6022270 (104 ± 7 km s^{-1}); see Konopacky et al. (2012); Tannock et al. (2021).

dwarfs. However, it should be noted that two other mid- to late-type T dwarfs identified by (Bannister & Jameson 2007) as potential members of the ∼650 Myr Hyades moving group, the T7 J1217−0311 and the T6 J1624+0029, are not identified as low surface gravity objects in this analysis.

2MASS J05591914−1404488 (Burgasser et al. 2000b) is a relatively bright and seemingly overluminous T4.5 (M_J = 13.7), but has not yet been confirmed as a binary system (Burgasser et al. 2003a; Golimowski et al. 2004; Liu et al. 2006; Stephens et al. 2009; Burgasser et al. 2010; Dupuy & Liu 2017; Manjavacas et al. 2019). It is one of five sources in my sample that has multi-epoch observations, with 10 observations spanning 2001 Oct 9 to 2021 Jan 1. These measurements show significant evidence of RV variation, differing from a constant velocity model by χ^2 = 26, (Degrees of freedom DOF = 9, p-value $\leq$ 0.005; Figure 2.12). This is in contrast to the conclusions of Zapatero Osorio et al. (2007) and Prato et al. (2015) who report constant—but differing—RVs based on subsets of the same data. Indeed, the standard deviation of my re-analyzed measurements ($\sigma_{\rm RV}$ = 1.2 km s^{-1}) is smaller than the difference between the previously published RVs ($RV_{\rm Zap} - RV_{\rm Pra}$ = −5.0 km s^{-1}). The sparse sampling of the data prevents a robust assessment of potential orbital motion, and follow-up RV measurements are warranted to validate this RV variation and assess the multiplicity of this potentially unresolved source.

2MASS J08195820−0335266 (Kirkpatrick et al. 2011) is a T4 dwarf with spatial and kinematic evidence of membership in the 24 Myr-old β Pictoris moving group (see Section 2.4.3), consistent with Zhang et al. (2021b) on the basis of 5D kinematics. At this age, and assuming $T_{\rm eff}$ = 1100 K based on Filippazzo et al. (2015), evolutionary models predict a mass of only 7 Jupiter masses, well below the deuterium burning mass limit (Baraffe et al. 2003). However, spectral evidence of youth for this source is not clear. Its near-infrared low-resolution spectrum is fully consistent with the T4 standard

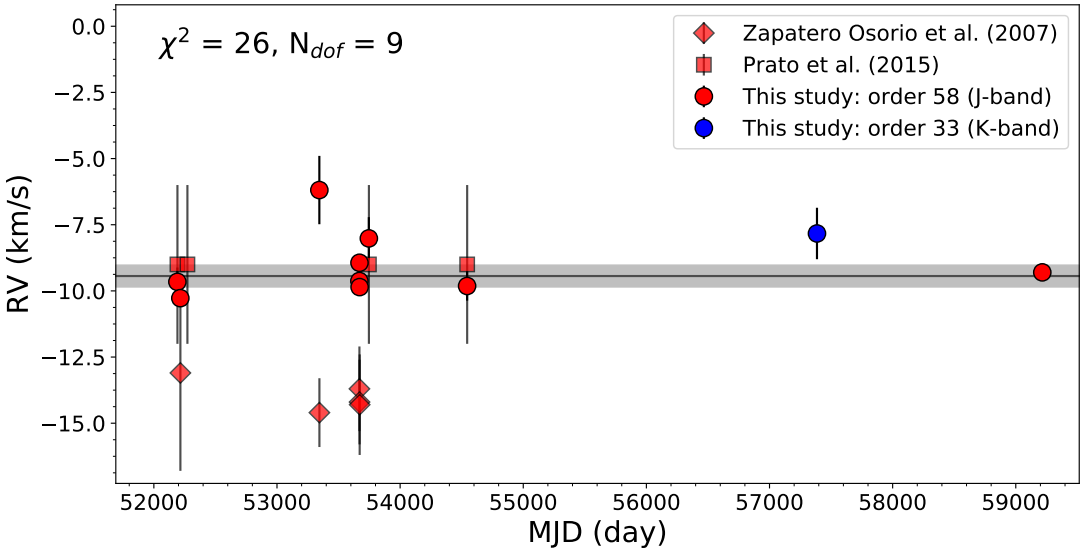

Figure 2.12: RV time series for all of the NIRSPEC measurement epochs for 2MASS J0559−1404. Measurements made in order 33 and 58 are shown as blue and red circles, respectively. The weighted average of my measurements and uncertainty are indicated by the horizontal line and grey shading. Prior measurements reported by Zapatero Osorio et al. (2007) and Prato et al. (2015) based on NIRSPEC data are indicated by red diamonds and red squares, respectively.

2MASSI J2254188+312349 (Figure 2.13; Burgasser et al. 2004). Pineda et al. (2016) reported the red optical (0.7–1.0 μm) spectrum of this source, recommending it as the T4 optical standard with features that naturally transition between T2 and T5 optical standards (Burgasser et al. 2003a). They found no evidence of Hα emission to a limit of $\log_{10} L_{\mathrm{H}\alpha}/L_{\mathrm{bol}} < -5.7$. The lack of activity is consistent with its small $v \sin i$, for which I are only able to determine an upper limit of $v \sin i < 9$ km s^{-1}. Heinze et al. (2015) report the possible detection of variability ($> 3.6\%$ in amplitude) at red optical wavelengths (0.7–0.95 μm), which is common for both young brown dwarfs and objects spanning the L dwarf/T dwarf transition (Radigan et al. 2012; Metchev et al. 2015). Taken together, I suspect that this source is a field brown dwarf with a chance kinematic alignment with the β Pictoris moving group.

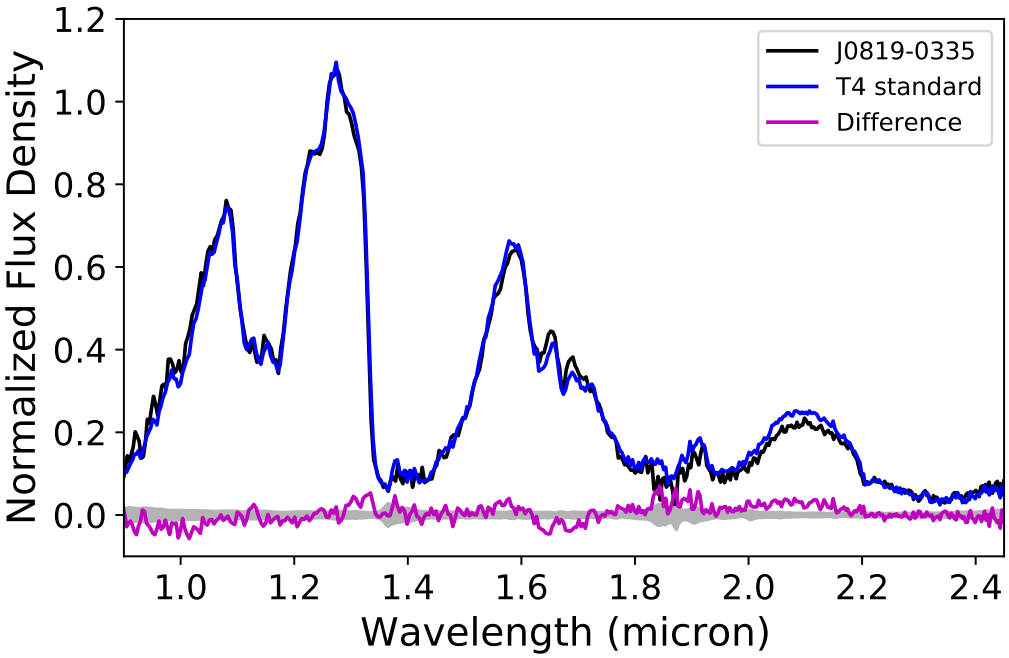

Figure 2.13: Low-resolution near-infrared spectrum of the T dwarf 2MASS J0819−0335 (black lines; uncertainty in grey shading centered at zero flux) from Burgasser et al. (2004) compared to (blue lines) the T4 near-infrared spectral standard 2MASSI J2254188+312349 (data from Kirkpatrick et al. 2011). The spectra are normalized to align in the 0.90–1.25 μm region, and the magenta lines show the difference spectra (template minus J0819−0335).

2MASSI J0937347+293142 (Burgasser et al. 2002) is a peculiar T6 dwarf with the second largest rotational velocity in my sample, $v \sin i = 66.9^{+0.5}_{-0.6}$ km s^{-1}. Assuming a radius of 1 R_{Jup}, this rotational speed corresponds to a maximum rotation period of 2 hours. Like J0034+0523, J0937+2931 has an unusually blue near-infrared color $J-K = -1.10 \pm 0.06$ (Leggett et al. 2010). This and other spectral peculiarities, including the weak or absent K I lines at 1.25 μm, have been cited as evidence of high surface gravity and/or subsolar metallicity for this source (Burgasser et al. 2002, 2006a; McLean et al. 2007; Prato et al. 2015; Martin et al. 2017; Zhang et al. 2019). The rapid rotation of J0937+2931 may also be partly responsible for the weakened atomic features. Again, these physical traits imply an old age, indicating that J0937+2931 is a massive and compact brown dwarf that has not had appreciable angular momentum loss in its late evolution.

2MASS J11061197+2754225 (Looper et al. 2007) is a previously reported candidate binary system with hypothesized T0.0+T4.5 components based on analysis of its low-resolution near-infrared spectrum (Looper et al. 2007; Burgasser et al. 2010; Bardalez Gagliuffi et al. 2014). It is also highly overluminous (Manjavacas et al. 2013), but has not been resolved by direct imaging (Looper et al. 2008). My measurements show highly significant RV variations over 15 epochs spanning 2008 Mar 19 to 2021 Jan 1, deviating from a constant velocity model by $\chi^2 = 318$ (DOF = 15, p-value $<$ 0.001; Figure 2.14). I performed a preliminary orbit fit on 11 epochs of these data ($\chi^2 = 155$, p-value < 0.001), rejecting order 33 data from 2016 Jan 18 and 2018 Jan 1 due to the slit width $0\farcs432$ being wider than the seeing on these nights; and order 58 data on 2008 Mar 19 and 2010 Dec 26 which are likely contaminated by light from the secondary, which is brighter than the primary in the J-band (see Burgasser et al. 2010). I used the package *RadVel* (Fulton et al. 2018), and converged on a set of solutions with primary semi-amplitude $K_1 = 6.30 \pm 0.05$ km s^{-1}, period $P = 3.92^{+0.07}_{-0.09}$ yr, eccentricity

$e = 0.33^{+0.04}_{-0.02}$, and center of mass radial velocity $V_{COM} = 2.0 \pm 0.1$ km s^{-1}. This system is examined in further detail in a companion paper (Burgasser et al., in prep).

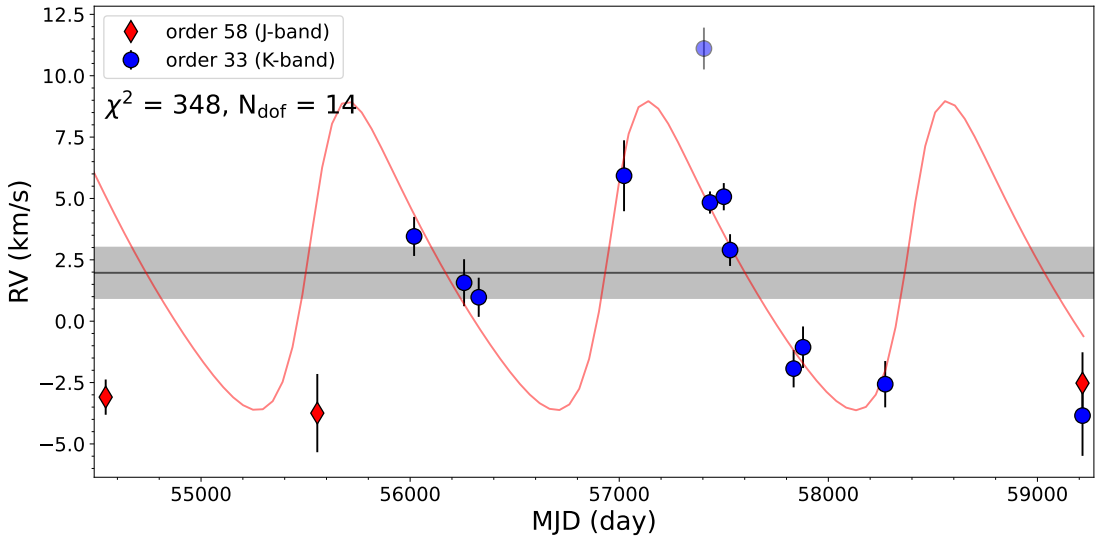

Figure 2.14: RV time series for all of the NIRSPEC measurement epochs of 2MASS J1106+2754. Measurements of orders 33 (K-band) and 58 (J-band) are labeled as blue circles and red diamonds, respectively. The horizontal line is the weighted average of my measurements, with the uncertainty shaded in grey. Also shown in a best-fit RV orbital curve with a semi-amplitude of K_1 = 6.30 km s^{-1} and a period of $P = 3.92$ yr, based on eleven epochs in order 33 with a removal of a bad observation on 2016 Jan 18 (light blue) and 2018 Jan 1 (outside of the range presented here). The data in order 58 were not fit because the secondary component is brighter at J-band. See Section 2.4.4 for details.

SDSS J133148.92−011651.4 (Hawley et al. 2002) is the only source in my sample identified as an intermediate member in the Galactic thin and thick disk populations. Like J0937+2931, this source has an unusually blue near-infrared color for an early-T dwarf ($J-K = 1.279 \pm 0.008$; Lawrence et al. 2007) and a peculiar spectrum that has challenged classification. Optical spectral classifications have ranged from L1 pec (Marocco et al. 2013) to L6 (Hawley et al. 2002) while near-infrared spectral classifications have ranged from L6 (Bardalez Gagliuffi et al. 2014) to T0 (Schneider et al. 2014). There are also conflicting determinations of this source being either metal-poor (Marocco et al. 2013) or lacking in subdwarf spectral features (Kirkpatrick et al. 2016), and model fits indicate

unusually thin clouds for a late L dwarf (Stephens et al. 2009). Figure 2.15 shows the low-resolution near-infrared spectrum of this source from Bardalez Gagliuffi et al. (2014) compared to L6 and T0 spectral standards, and the near-infrared spectrum of the L subdwarf 2MASS J11181292−0856106 (Kirkpatrick et al. 2010). The L subdwarf is the best match of the three, meaning that J1331−0116 is likely an old, slightly metal-poor L dwarf whose spectrum is shaped by enhanced H_2 CIA and possibly atmospheric condensates. Given its distinct classification from the rest of the T sample, I exclude this source from the T dwarf kinematic analysis presented below.

2MASS J15530228+1532369AB (Burgasser et al. 2002) is a resolved T6.5+T7.5 binary with a separation of $0\farcs349 \pm 0\farcs005$, $\Delta M_{\rm bol} = 0.31 \pm 0.12$, and mass ratio $q = 0.90 \pm 0.02$. Here, I find spatial and kinematic evidence of membership in the ∼200 Myr-old Carina-Near moving group (see Section 2.4.3), consistent with Zhang et al. (2021b) on the basis of 5D kinematics. At this age, and assuming component $T_{\rm eff}$s = 750 K and 890 K based on Filippazzo et al. (2015), evolutionary models predict masses of $10^{+0.8}_{-1.6}$ and $11.3^{+0.4}_{-0.5}$ Jupiter masses, below the deuterium burning mass limit (Baraffe et al. 2003). The kinematically young late-type T binary could join an exclusive club of AB Doradus T3.5 GU Psc b (Naud et al. 2014), AB Doradus T5.5 SDSS J111010.01+011613.1 (Gagné et al. 2015a), and candidate AB Doradus L+T binary WISE J135501.90−825838.9 (Bardalez Gagliuffi et al. 2018), and TW Hydrae L7 binary 2MASS J11193254−1137466 (Best et al. 2017). However, spectral evidence of youth for this source is lacking. Its near-infrared low-resolution spectrum is fully consistent with the T7 standard 2MASS J07271824+1710012 (Figure 2.16; Burgasser et al. 2010) and inconsistent with the 20 Myr T dwarf 51 Eri b[21] ($T_{\rm eff}$=760±20 K; data from VLT/SPHERE and Gemini Planet Imager; Macintosh et al. 2015; Samland et al. 2017). Line et al. (2017) measured a $\log g$

[21]The spectral features might not be the same between 20 Myr and 200 Myr T7 dwarf, as L dwarfs have different spectral features between intermediate and very-low gravity in Allers & Liu (2013). T7 dwarfs at the ages of 20 Myr and 200 Myr correspond to $\log g$=3.5–4.0 dex and 4.2–4.5 dex, respectively, using Baraffe et al. (2003) models.

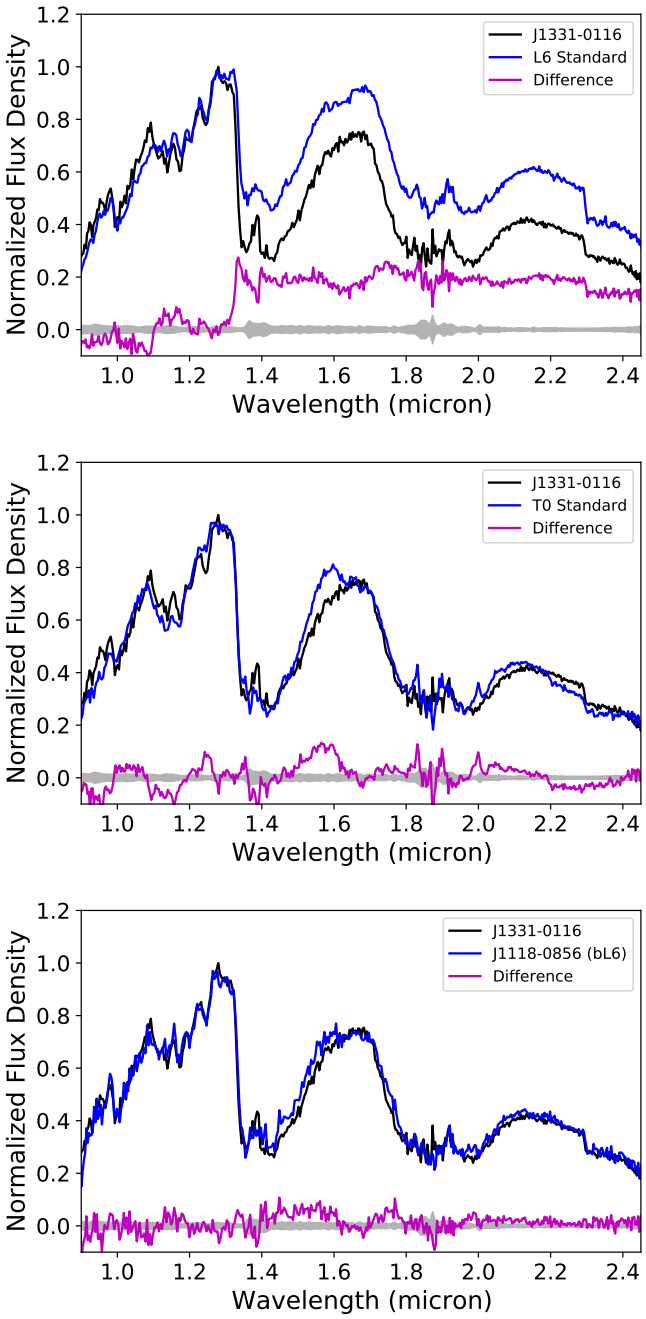

Figure 2.15: Low-resolution near-infrared spectrum of the peculiar L dwarf J1331−0116 (black lines; uncertainty in grey shading centered at zero flux) from Bardalez Gagliuffi et al. (2014) compared to (blue lines) the L6 near-infrared spectral standard 2MASSI J1010148−040649 (top; data from Reid et al. 2006), the T0 spectral standard SDSS J120747.17+024424.8 (middle; data from Looper et al. 2007), and the unusually blue L6 dwarf 2MASS J11181292−0856106 (bottom; data from Kirkpatrick et al. 2010). All spectra are normalized to align in the 0.90–1.25 μm region, and the magenta lines show the difference spectra (template minus J1331−0116).

of $4.8^{+0.1}_{-0.2}$ dex for J1553+1532 after correcting for binarity, but with subsolar metallicity ($[M/\mathrm{H}] = -0.19^{+0.04}_{-0.06}$ dex and supersolar $\log \mathrm{C/O} = -0.11^{+0.09}_{-0.09}$). This source does not exhibit significant variability in JHK_S or J_S (Koen et al. 2004; Wilson et al. 2014). Taken together, I suspect that this source is also a field brown dwarf with a chance kinematic alignment with the Carina-Near moving group.

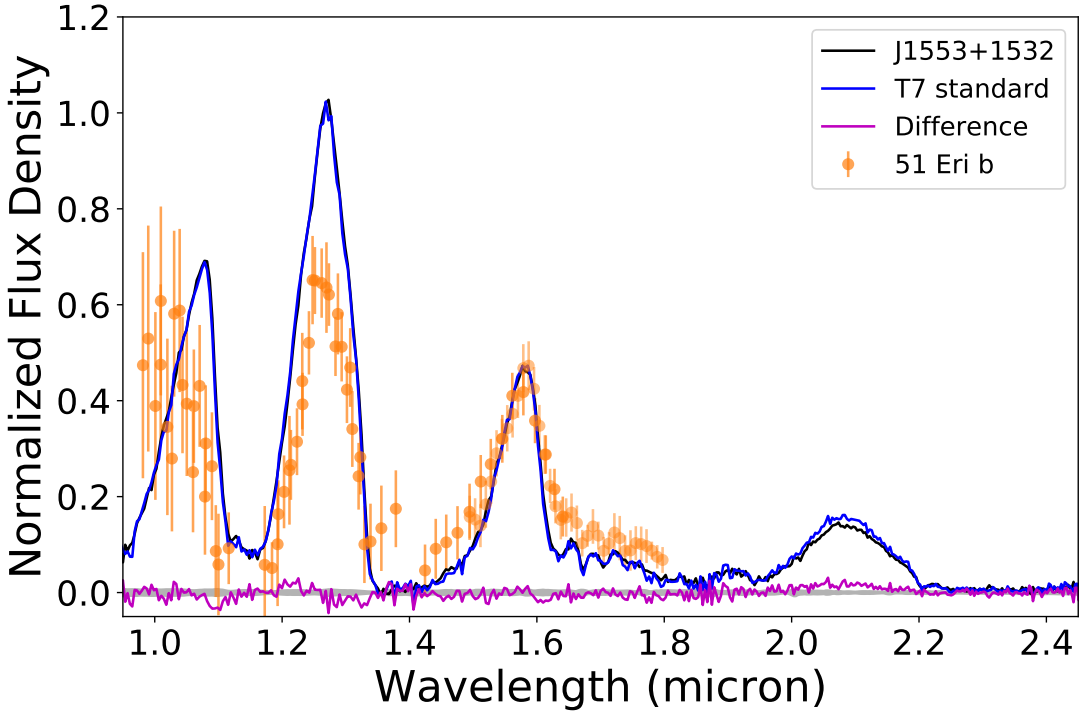

Figure 2.16: Low-resolution near-infrared spectrum of the T dwarf 2MASS J1553+1532 (black line; uncertainty in grey shading centered at zero flux) from Burgasser et al. (2010) compared to the T7 near-infrared spectral standard 2MASS J07271824+1710012 (blue line; data from Burgasser et al. 2006a). The spectra are normalized to align in the 0.90–1.25 μm region, and the magenta line shows the difference spectrum (template minus J1553+1532). Also shown is the 51 Eri b spectrum from Samland et al. (2017), normalized to H band peak.

2MASS J21265916+7617440 is a T0p dwarf proposed to be an L7+T3.5 blended-light binary based on medium-resolution spectroscopy (Kirkpatrick et al. 2010). High-resolution imaging by Bardalez Gagliuffi et al. (2015) failed to resolve the system and constrained its angular separation to $<$106 mas or $<$1.3 au. My measurements

show significant RV variations over 10 epochs spanning 2011 Jun 10 to 2020 Sep 3, deviating from a constant velocity model by χ^2=39 (DOF = 9, p-value < 0.001; Figure 2.17). Following the analysis of J1106+2754, I performed a preliminary orbit fit to the RV data using *RadVel*, and converged on a set of solutions with primary semi-amplitude $K_1 = 3.0^{+0.7}_{-0.6}$ km s^{-1}, period $P = 12.0^{+1.5}_{-1.2}$ yr, and center of mass radial velocity $V_{COM} = -17.5 \pm 0.4$ km s^{-1}. This system is examined in detail in a companion paper (Hsu et al., in prep).

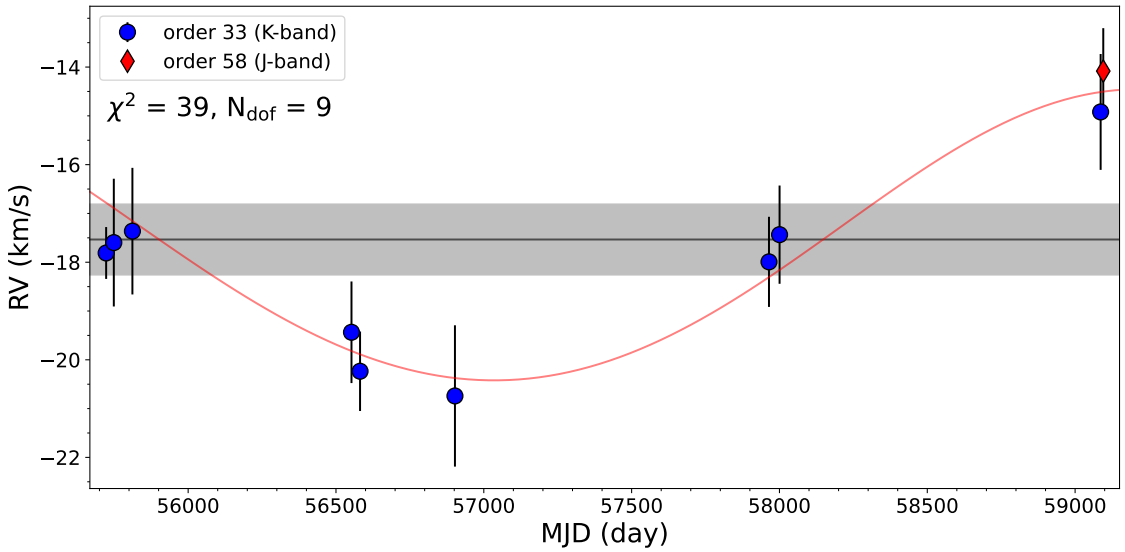

Figure 2.17: RV time series for all of the NIRSPEC measurement epochs of 2MASS J2126+7617. Measurements of orders 33 (K-band) and 57 (J-band) are labeled as blue circles and red diamonds, respectively. The horizontal line is the weighted average of my measurements, with the uncertainty shaded in grey. Also shown is a best-fit RV orbital curve with a semi-amplitude K_1 = 3.0 km s^{-1} and period $P = 12.0$ yr.

HN Peg B (Luhman et al. 2007) is a T2.5 dwarf that is a wide companion (782 au) to the young ($\sim$300 Myr) G0V star HN Peg. It is an important benchmark for testing brown dwarf evolutionary models near the L dwarf/T dwarf transition (Leggett et al. 2008). My best-fit models of HN Peg B for data from 2017 Jun 9 yield RV = -19.5 ± 1.3 km s^{-1}, consistent with the primary star's RV = -17.18 ± 0.17 km s^{-1} (Gaia Collaboration et al. 2018b). HN Peg B is also a photometrically variable source (Metchev

et al. 2015; Zhou et al. 2018; Vos et al. 2019). My $v \sin i = 15 \pm 3$ km s^{-1} combined with the period measurement from Zhou et al. (2018) of 15.4 ± 0.5 hr yields a rotation axis inclination angle of $63^\circ \pm 7^\circ$ assuming a model radius of $0.108^{+0.014}_{-0.006}$ $R_\odot$ using the theoretical evolutionary models of Burrows et al. (1997) and Baraffe et al. (2003) (Luhman et al. 2007). This is consistent with the current hypothesis that the frequency and amplitude of variability are higher for brown dwarfs observed at intermediate-to-high viewing angles ($i > 60^\circ$; Heinze et al. 2013; Metchev et al. 2015; Vos et al. 2017).

2.5 Ultracool Dwarf Kinematics in the Local Neighborhood

2.5.1 Velocity Dispersions and the Kinematic Age of T Dwarfs

The velocity dispersion,

$$\sigma_{\rm tot}^2 = \sigma_U^2 + \sigma_V^2 + \sigma_W^2 \tag{2.5}$$

of a stellar population evolves as the population ages, as gravitational interactions with Galactic structures perturb orbits, increasing Galactic scale heights and relative velocities over time (Wielen 1977). Velocity dispersions thus provide a means of measuring the ages of stellar populations, including UCDs, which depend on the mass function, star formation history, and thermal evolution of brown dwarfs (Burgasser 2004).

I measured a total velocity dispersion for my T dwarfs to be $\sigma_{\rm tot} = 39.0 \pm 1.0$ km s^{-1}. To convert this into an age, I evaluated two age-dispersion relations. The first is the exponential decay law from Wielen (1977) based on the $|W|$-weighted total velocity dispersion:

$$\bar{\sigma}_{\rm tot}(\tau)^3 = \sigma_{\rm tot,0}^3 + 1.5\,\gamma_{\nu,p}\,T_\gamma\,(e^{\tau/T_\gamma} - 1), \tag{2.6}$$

where τ is the statistical age in Gyr, $\sigma_{\rm tot,0} = 10$ km s^{-1}, $\gamma_{\nu,p} = 1.1 \times 10^4$ (km s^{-1})^3 Gyr^{-1}, $T_\gamma = 5$ Gyr, and $\bar{\sigma}_{\rm tot}$ is the $|W|$-weighted total velocity dispersion in km s^{-1}:

$$\begin{aligned}\bar{\sigma}_{\rm tot}^2 = &\frac{\Sigma_i |W_i| (U_i - \bar{U})^2}{\Sigma_i |W_i|} + \frac{\Sigma_i |W_i| (V_i - \bar{V})^2}{\Sigma_i |W_i|} \\ &+ 0.5 \frac{\Sigma_i |W_i| (W_i - \bar{W})^2}{\Sigma_i |W_i|},\end{aligned} \tag{2.7}$$

I also examined the age-dispersion law from Aumer & Binney (2009):

$$\sigma_{\rm tot} = \nu_{1,0}\Big(\frac{\tau+\tau_1}{10\,{\rm Gyr}+\tau_1}\Big)^{\beta}, \tag{2.8}$$

where $\nu_{1,0} \in (55.179, 57.975)$ km s^{-1}, $\tau_1 \in (0.148, 0.261)$ Gyr, and $\beta \in (0.349, 0.385)$ are model parameters drawn from Table 2 of Aumer & Binney (2009). It is noted that Bird (2019) measured a very similar $\beta = 0.389 \pm 0.018$ using *Gaia* and APOGEE red clump stars.

Kinematic ages were inferred by inverting these relations to solve for τ. The age uncertainty was estimated statistically through Monte-Carlo sampling, assuming that *UVW* velocity uncertainties follow normal distributions. To account for the small sample bias, I applied a Jackknife test by iteratively removing one source from my sample and recomputing dispersions and kinematic ages for each of the resulting subsamples. The resulting *UVW* dispersions are summarized in Table 2.6.

Using the Aumer & Binney (2009) relation (averaged over all model parameters), I inferred a kinematic age of 3.5 ± 0.3 Gyr for my full sample of 36 T dwarfs (excluding J1331−0116). The Wielen relation yields a smaller but statistically consistent age of 3.0 ± 0.1 Gyr. To mitigate possible velocity biases, I also examined kinematic ages for the sample excluding the resolved and candidate binaries J0629+2418, J0909+6525, J1106+2754, J1225−2739, J1553+1532, and J2126+7617 (Burgasser et al. 2006c; Dupuy & Liu 2012; Manjavacas et al. 2013; Bardalez Gagliuffi et al. 2014); and separately the young T dwarfs J0136+0933, J0819−0335, J1324+6538, J1553+1532, and HN Peg b (Gagné et al. 2017, 2018a; Leggett et al. 2008; Zhang et al. 2021b), and found equivalent ages as the full sample (Table 2.6). I also found consistent kinematic ages between early-T (T0–T4; 3.3 ± 0.6 Gyr) and late-T (T5–T8; 3.6 ± 0.4 Gyr) subgroups. The age of local T dwarfs from the Aumer & Binney (2009) relation is consistent with the age of

local M dwarfs, but is younger than local L dwarfs (Reid et al. 2002; Reiners & Basri 2009a; Blake et al. 2010; Seifahrt et al. 2010; Burgasser et al. 2015a), as discussed in further detail below.

Figure 2.18 shows *UVW* velocity probability plots, or probit plots, following Lutz & Upgren (1980) and based on the percent point function defined in Filliben (1975); see also Reid et al. (2002) and Bochanski et al. (2007a). Probit plots are linear if the velocities are drawn from a single normal distribution, with the slope equal to the distribution width (σ). Both U and V velocities show two populations, with an inner "shallow" population in the $\pm 1\sigma$ region and a steeper "wide" population. To quantify the difference in kinematic ages, I performed a piece-wise linear fit to each component and used the slopes to compute ages with the Aumer & Binney (2009) relations and Monte Carlo uncertainties (Bochanski et al. 2007a; Burgasser et al. 2015a). The ages for the inner and outer components are 3.2 ± 0.5 Gyr and 4.0 ± 0.3 Gyr, respectively, and hence marginally consistent.

Table 2.6: Velocity Dispersions and Group Kinematic Ages

Sample	N	$\langle U \rangle$ (km s^{-1})	$\langle V \rangle$ (km s^{-1})	$\langle W \rangle$ (km s^{-1})	σ_U (km s^{-1})	σ_V (km s^{-1})	σ_W (km s^{-1})	σ_{tot} (km s^{-1})	Age (Gyr)	Note
All Sources	36	-1.6 ± 5.5	-3.6 ± 2.7	2.1 ± 2.0	33.1 ± 0.8	16.5 ± 0.5	12.3 ± 0.3	39.0 ± 1.0	3.5 ± 0.3	Unweighted
					35.5 ± 0.9	16.4 ± 0.5	11.6 ± 0.3	40.8 ± 0.8	3.0 ± 0.1	$\|W\|$ Weighted
Shallow[a]	24	-2.7 ± 3.5	-2.6 ± 1.7	2.3 ± 1.4	31.9 ± 2.2	15.8 ± 1.0	12.7 ± 1.0	37.8 ± 1.9	3.2 ± 0.5	Unweighted
Wide[a]	12	0.9 ± 15.0	-5.0 ± 7.4	2.3 ± 5.5	34.7 ± 1.0	17.2 ± 0.7	12.9 ± 0.7	40.8 ± 0.9	4.0 ± 0.3	Unweighted
Not Young T Dwarfs	31	-0.2 ± 6.3	-2.6 ± 3.1	2.6 ± 2.3	35.1 ± 1.0	17.4 ± 0.5	13.1 ± 0.3	41.3 ± 1.1	4.1 ± 0.4	Unweighted
					36.3 ± 1.1	16.8 ± 0.5	12.0 ± 0.3	41.8 ± 1.0	3.1 ± 0.2	$\|W\|$ Weighted
Not Binary T Dwarfs	30	-0.3 ± 5.9	-1.0 ± 2.7	2.4 ± 2.3	32.1 ± 1.1	14.6 ± 0.4	12.6 ± 0.3	37.4 ± 1.2	3.1 ± 0.3	Unweighted
					35.3 ± 1.2	15.9 ± 0.6	11.9 ± 0.3	40.5 ± 1.0	2.9 ± 0.2	$\|W\|$ Weighted
Not Binary or Young T Dwarfs	26	0.6 ± 6.7	0.2 ± 3.0	3.0 ± 2.6	34.2 ± 1.2	15.1 ± 0.5	13.3 ± 0.4	39.7 ± 1.3	3.7 ± 0.4	Unweighted
					36.1 ± 1.3	16.2 ± 0.6	12.1 ± 0.4	41.4 ± 1.2	3.1 ± 0.2	$\|W\|$ Weighted
T0–T4 dwarfs	18	-3.7 ± 7.6	-5.2 ± 4.1	2.3 ± 2.6	32.1 ± 1.9	17.5 ± 0.7	11.0 ± 0.6	38.2 ± 2.1	3.3 ± 0.6	Unweighted
					31.1 ± 2.3	15.8 ± 0.9	10.2 ± 0.5	36.4 ± 2.0	2.3 ± 0.3	$\|W\|$ Weighted
T5–T8 dwarfs	18	0.7 ± 7.9	-1.6 ± 3.5	2.2 ± 3.2	33.7 ± 1.1	14.9 ± 0.6	13.5 ± 0.5	39.2 ± 1.4	3.6 ± 0.4	Unweighted
					39.2 ± 1.4	17.0 ± 0.8	12.2 ± 0.4	44.5 ± 1.3	3.6 ± 0.2	$\|W\|$ Weighted

Note – Ages for unweighted velocities are computed from equation (2.8) using the parameters in Aumer & Binney (2009). Ages for $|W|$-weighted velocities are computed from equation (2.6) using the parameters in Wielen (1977).

[a] Piece-wise linear fits to unweighted velocities, with separate fits for sources within $\pm 1\sigma$ (shallow) and outside of $\pm 1\sigma$ (wide); see Section 2.5.1.

2.5.2 Velocity Dispersions and the Kinematic Ages of Late-M and L Dwarfs

To place the T dwarf velocity dispersions and kinematic ages in context, I compiled all late-M and L dwarfs within 20 pc with published RV measurements that have uncertainties of ≤ 3 km s^{-1}, based on medium and high-resolution spectroscopic measurements (Table 2.7). There are 65 late-M dwarfs (M7–M9) and 71 L dwarfs (L0–L9) that match these criteria (J1331−0116 is included here; see Section 2.4.4 for more details). Figure 2.19 shows the spectral type distribution of the full late-M, L, and T dwarf RV sample, overplotted with a simulated local population and local 20 pc UCDs found to date (see Section 2.5.4 for further discussion). I combined RV measurements with *Gaia* DR2 and eDR3 parallaxes and proper motions where available to improve the *UVW* precisions over prior studies, following the same analysis as that done for the T dwarfs.

Results are summarized in Table 2.8 and Figure 2.20. I note that two late-M dwarfs in this sample (M7 2MASS J02530084+1652532 and M9 2MASS J03341218−4953322) are kinematically associated with the thick disk population, the L5.5 2MASSI J1721039+334415 is associated with the intermediate thick disk/halo population, and 17 sources (6 late-M dwarfs and 11 L dwarfs) are associated with intermediate thin/thick disk population, which includes J1331−0116, which I classify as a blue L6. Evaluating the distribution of *UVW* velocities, I find that the L dwarfs in this sample exhibit significant correlations between *UV* ($R = 0.33$, p-value < 0.01), *UW* ($R = -0.32$, p-value < 0.01) and *VW* velocities ($R = -0.27$, p-value = 0.02). For the late-M dwarfs, I find a significant correlation between *UV* velocities ($R = 0.32$, p-value < 0.01), but not between *UW* or *VW* velocities. The *UV* velocity correlation for the L dwarfs is weaker than that previously reported in Burgasser et al. (2015a, $R = 0.43 \pm 0.03$), but nevertheless significant. If I remove the thick disk, intermediate thick disk/halo, and intermediate thin/thick disk population

members from my sample, the *UV* velocity correlation becomes less significant for the late-M dwarf sample ($R = 0.25$, p-value = 0.06) and insignificant for the L dwarfs in all three velocity pairs. This result indicates that the *UVW* velocity correlations are driven by the older kinematic populations. As noted above, the T dwarfs, which are all thin disk sources, show no significant correlations in *UV*, *UW*, or *VW* velocity pairs. The average *U* and *W* velocities of the late-M and L dwarfs are each consistent with zero, while the negative average *V* velocity (greater for the L dwarfs) can again be attributed to asymmetric drift. I note that the average *U* velocity offset for the L dwarfs reported in Burgasser et al. (2015a) is not seen here and is likely an artifact of small sample statistics in that study.

The corresponding kinematic ages for all of the late-M and L dwarfs in my sample using the Wielen (1977) and Aumer & Binney (2009) relations are given in Table 2.9. In my sample, I find highly significant correlations between $v_{\rm tot}^2$ and $|W|$ for the late-M dwarfs ($N = 65$, $R = 0.42$, p-value < 0.001) and L dwarfs ($N = 71$, $R = 0.61$, p-value $< 10^{-4}$), and significant correlation for T dwarfs ($N = 37$, $R = 0.33$, p-value = 0.05). However, if the thin/thick disk sources are removed, the significances of these correlations are reduced: marginally significant for late-M dwarfs ($N = 57$, $R = 0.22$ and p-value = 0.09) , significant for L dwarfs ($N = 59$, $R = 0.27$ and p-value < 0.05), and insignificant for T dwarfs ($N = 36$, $R = 0.25$ and p-value = 0.13). These results suggest that the $v_{\rm tot}^2$, $|W|$ correlation is dominated by a few sources from a distinct population, so that Wielen's age-dispersion relation may not be as accurate for this sample as the Aumer and Binney relations. The ages from the latter relations are 4.9 ± 0.3 Gyr and 7.1 ± 0.4 Gyr, respectively, for the full late-M and L dwarf samples (Figure 2.21, upper left panel). These values confirm the significant (4.4σ) discrepancy between late-M and L dwarf kinematic ages found in previous studies. If I remove the thick disk sources, the kinematic ages are reduced to 4.1 ± 0.3 Gyr for the late-M dwarfs and 5.8 ± 0.3 Gyr for

the L dwarfs. These ages are still significantly (4.0σ) discrepant, while the late-M and T dwarfs in my sample have statistically equivalent ages.

Figure 2.22 displays the log probability of thin disk to thick disk membership for late-M, L and T dwarfs, again following Bensby et al. (2003). These distributions show that there is a marginally higher proportion of intermediate thin/thick disk and thick disk sources relative to thin disk sources among the L dwarfs ($8^{+5}_{-2}\%$). as compared to the late-M dwarfs ($3^{+3}_{-1}\%$) and T dwarfs ($3^{+6}_{-2}\%$), with ratio statistics computed using binomial statistics following Burgasser et al. (2003c). The intermediate thin/thick disk sources in particular skew the kinematic dispersions and ages toward higher values. To truly assess the kinematic age of the thin disk population without discarding too many old thin disk sources, I refined my selection requirement to $P[\mathrm{TD}]/P[\mathrm{D}] \leq 1.0$, since $P[\mathrm{TD}]/P[\mathrm{D}] = 1.0$ denotes a 50% probability as a thin or thick disk source. This thin disk sample has similar kinematic ages of 4.1 ± 0.3 Gyr and 4.2 ± 0.3 Gyr for the late-M and L dwarfs, respectively, which are slightly older but consistent with the T dwarfs. These values imply equivalent ages across the entire late-MLT sequence.

Refining the sample to high-probability thin disk sources appears to resolve the long-standing discrepancy between late-M and L dwarf kinematics (Faherty et al. 2009; Seifahrt et al. 2010; Burgasser et al. 2015a). In Section 2.5.4, I will show the observed thin disk ages of late-MLT dwarfs are also consistent with my population simulations. What remains unclear is why the local L dwarf sample has a higher fraction of thick disk sources compared to late-M and T dwarfs. I will evaluate the properties of the thick disk L dwarfs, several of which are classified as unusually blue L dwarfs, in Section 2.6.2.

For completeness, I evaluated the more recent age-velocity dispersion relation of Yu & Liu (2018), based on the kinematics and ages of >3500 sub-giant and giant branch stars. The ages were estimated from empirical trends in [C/M] and [N/M] abundances (Ho et al. 2017). Yu & Liu (2018) fit power-law relations to the velocity dispersions

in Galactic cylindrical coordinates, age $= C\sigma_i^{\beta}$, where i = R, ϕ, and Z direction, and $C = 1$ Gyr (km s^{-1})$^{-\beta}$ is a unit conversion factor. Using the z-coordinate relation from this study with $\beta_z = 0.56 \pm 0.14$, and propagating uncertainties with Monte Carlo sampling, I compute ages for late-M dwarfs (all/thin disk = $4.9^{+2.4}_{-1.6}$ Gyr/$4.8^{+2.3}_{-1.5}$ Gyr), L dwarfs (all/thin disk = $5.1^{+2.5}_{-1.7}$ Gyr/$4.6^{+2.1}_{-1.4}$ Gyr), and T dwarfs ($4.1^{+1.7}_{-1.2}$ Gyr) that are consistent with each other, albeit with higher statistical uncertainties. The R and ϕ relations of Yu & Liu (2018) yield significantly younger ages (2.6–3.4 Gyr) which may be attributed to the very different spatial distributions of the sub-giant/giant sample as compared to the local ultracool dwarf sample.

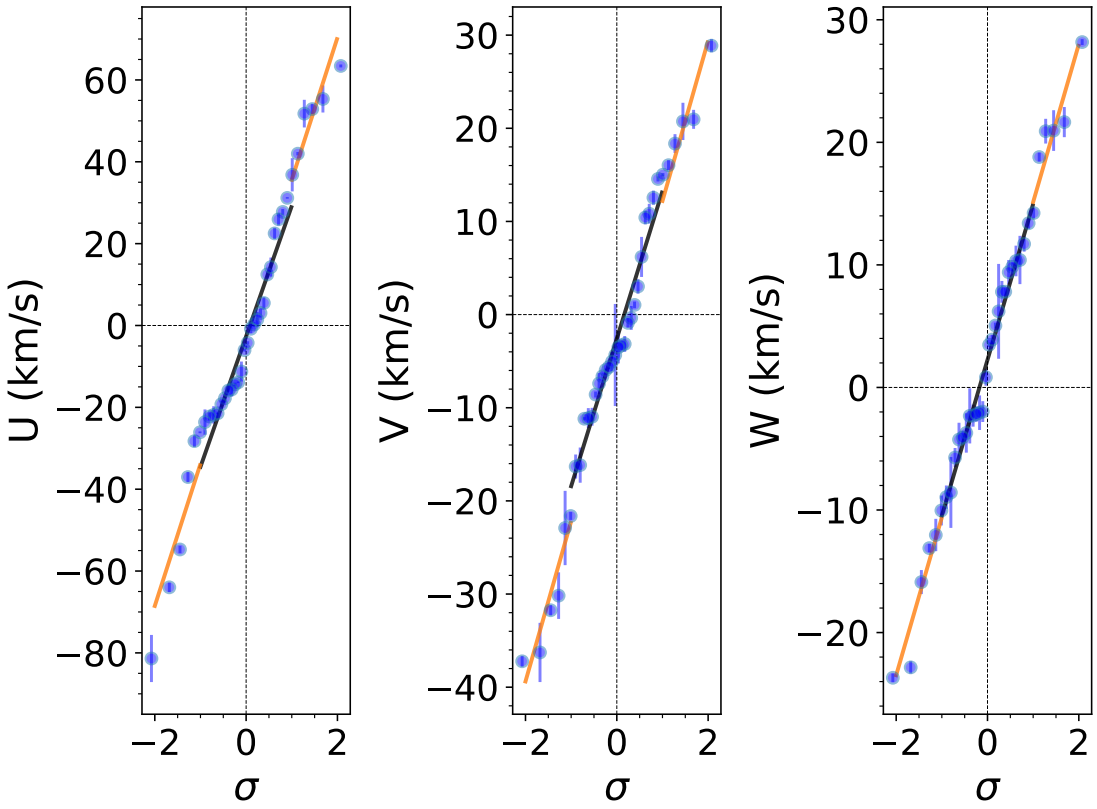

Figure 2.18: Space velocity probability plots (probit plots) of the T dwarf sample. Individual velocities are indicated by blue circles, while a piece-wise linear fit broken at $\pm 1\sigma$ for each velocity component (black and orange dashed lines, respectively) are shown. Note that the unusually blue L dwarf J1331−0116 is not included here.

Table 2.7: Late-M and L Dwarf Sample at the Local 20 pc

Source Name	Coordinates (J2000)	SpT	2MASS J (mag)	$J-K_s$ (mag)	μ_α (mas yr^{-1})	μ_δ (mas yr^{-1})	d (pc)	Published RV (km s^{-1})	References[a]
J0004−4044	00 04 34.86 −40 44 06.4	L5+L5	13.11 ± 0.02	1.71 ± 0.04	671.1 ± 0.4	−1498.2 ± 0.5	12.18 ± 0.06	32.8 ± 0.2	(17); (53); (53); (61)
J0004−2058	00 04 41.46 −20 58 29.8	M9	12.4 ± 0.02	1.01 ± 0.03	758.2 ± 0.3	85.2 ± 0.2	15.08 ± 0.04	−33 ± 2	(18); (53); (53); (47)
J0015+3516	00 15 44.77 +35 16 02.6	L1	13.88 ± 0.03	1.62 ± 0.04	55.2 ± 0.5	−257.1 ± 0.3	17.06 ± 0.11	−37.4 ± 0.2	(33); (53); (53); (61)
J0019+5213	00 19 45.83 +52 13 17.5	M9	12.79 ± 0.02	1.17 ± 0.03	310.7 ± 0.2	−279.1 ± 0.2	19.96 ± 0.07	−29 ± 3	(16); (53); (53); (60)
J0024−0158	00 24 24.63 −01 58 19.9	L0.5	11.99 ± 0.04	1.45 ± 0.04	−77.2 ± 0.5	141.1 ± 0.3	12.51 ± 0.03	11.6 ± 1.6	(33); (53); (53); (39)
J0024−2708B	00 24 44.22 −27 08 25.0	M8.5	9.25 ± 0.03	1.01 ± 0.05	−107 ± 6	691 ± 8	7.72 ± 0.15	−35 ± 3	(2); (48); (42); (60)
J0027+2219	00 27 55.98 +22 19 32.8	M8e	10.61 ± 0.02	1.05 ± 0.03	406 ± 5	−170 ± 2	15.3 ± 0.9	−11.9 ± 1.3	(10); (41); (46); (20)
J0036+1821	00 36 16.11 +18 21 10.2	L3.5	12.47 ± 0.03	1.41 ± 0.03	901.6 ± 0.4	124.0 ± 0.2	8.74 ± 0.02	20.9 ± 0.14	(3); (53); (53); (71)
J0045+1634[b]	00 45 21.41 +16 34 44.7	L0β	13.06 ± 0.02	1.69 ± 0.03	358.9 ± 0.4	−48.1 ± 0.2	15.38 ± 0.05	3.3 ± 0.2	(39); (53); (53); (61)
J0047+6803[c]	00 47 00.38 +68 03 54.3	L7	15.6 ± 0.07	2.55 ± 0.07	380.7 ± 1.1	−204.2 ± 1.4	12.3 ± 0.3	−19.4 ± 1.2	(29); (50); (52); (71)
J0102−3737	01 02 51.05 −37 37 43.7	M9	11.13 ± 0.02	1.06 ± 0.03	1470.1 ± 0.3	251.19 ± 0.14	11.38 ± 0.02	−5 ± 2	(32); (53); (53); (47)
J0107+0041	01 07 52.42 +00 41 56.4	L8	15.82 ± 0.06	2.11 ± 0.07	623 ± 10	91.0 ± 1.0	15.6 ± 1.1	8.2 ± 0.5	(31); (16); (44); (71)
J0109−5100	01 09 01.52 −51 00 49.4	M8.5e	12.23 ± 0.02	1.14 ± 0.03	219.19 ± 0.14	77.7 ± 0.2	15.91 ± 0.03	−1.3 ± 0.2	(13); (53); (53); (59)
J0109+2949	01 09 21.87 +29 49 26.4	M9.5	12.91 ± 0.02	1.23 ± 0.03	1011.3 ± 0.5	368.2 ± 0.3	15.93 ± 0.06	38.9 ± 0.8	(17); (53); (53); (56)
J0109−0343	01 09 51.20 −03 43 26.3	M9e	11.69 ± 0.02	1.27 ± 0.03	372.0 ± 0.6	8.7 ± 0.3	10.59 ± 0.04	−6.3 ± 1.8	(10); (53); (53); (64)
J0140+2701	01 40 02.64 +27 01 50.0	M8.5	12.49 ± 0.02	1.06 ± 0.03	60.3 ± 0.3	−255.3 ± 0.3	18.99 ± 0.06	8.2 ± 0.4	(25); (53); (53); (56)
J0144−0716	01 44 35.40 −07 16 14.3	L6.5	14.19 ± 0.03	1.92 ± 0.03	384.0 ± 1.1	−196.9 ± 0.7	12.7 ± 0.1	−2.6 ± 0.1	(31); (53); (53); (61)
J0205−1159	02 05 29.40 −11 59 29.6	L7+L7	14.59 ± 0.03	1.59 ± 0.04	427.0 ± 0.4	52.0 ± 0.5	19.8 ± 0.6	7 ± 2	(15); (16); (44); (69)
J0213+4444	02 13 28.79 +44 44 45.2	L1.5	13.49 ± 0.03	1.28 ± 0.03	−52.1 ± 0.6	−145.8 ± 0.4	19.35 ± 0.14	−23.47 ± 0.11	(16); (53); (53); (61)
J0215−3040	02 15 08.04 −30 40 01.3	M8	11.62 ± 0.03	1.08 ± 0.03	768.6 ± 0.3	−360.3 ± 0.3	14.06 ± 0.03	0.005 ± 0.009	(16); (53); (53); (68)
J0217+3526[d]	02 17 10.01 +35 26 32.5	M7	9.98 ± 0.02	0.97 ± 0.03	548.4 ± 0.2	−260.3 ± 0.2	10.339 ± 0.012	11 ± 3	(30); (53); (53); (70)
J0255−4700	02 55 03.69 −47 00 51.3	L9	13.25 ± 0.03	1.69 ± 0.04	1011.2 ± 0.4	−554.8 ± 0.5	4.87 ± 0.006	18 ± 3	(31); (53); (53); (58)
J0253+1652	02 53 02.41 +16 52 34.9	M7	8.39 ± 0.03	0.81 ± 0.05	3429.5 ± 0.3	−3806.2 ± 0.3	3.831 ± 0.004	68.30 ± 0.05	(73); (53); (53); (66)
J0306−3647	03 06 11.59 −36 47 52.8	M9	11.69 ± 0.02	1.06 ± 0.03	−172.48 ± 0.12	−669.3 ± 0.2	13.26 ± 0.02	11.4 ± 0.2	(33); (53); (53); (61)
J0314+1603	03 14 03.44 +16 03 05.4	M9.5	12.53 ± 0.02	1.29 ± 0.03	−242.4 ± 0.3	−55.1 ± 0.3	13.62 ± 0.05	−6.8 ± 0.2	(33); (53); (53); (59)
J0320+1854	03 20 59.71 +18 54 22.7	M8	11.76 ± 0.02	1.12 ± 0.03	353.0 ± 0.3	−257.2 ± 0.2	14.65 ± 0.03	45.5 ± 0.6	(24); (53); (53); (66)
J0331−3042	03 31 30.25 −30 42 38.8	M7.5	11.36 ± 0.02	1.1 ± 0.03	51.76 ± 0.14	−403.3 ± 0.2	12.51 ± 0.02	19 ± 2	(9); (53); (53); (47)
J0334−4953	03 34 12.59 −49 53 30.4	M9	11.38 ± 0.03	0.98 ± 0.03	2360.51 ± 0.15	482.2 ± 0.2	8.878 ± 0.007	70.2 ± 1.0	(18); (53); (53); (58)
J0339−3525[e]	03 39 35.25 −35 25 43.6	M9β	10.73 ± 0.02	1.18 ± 0.03	308.9 ± 0.2	268.2 ± 0.2	6.42 ± 0.004	7.4 ± 0.7	(5); (53); (53); (39)
J0351−0052	03 51 00.02 −00 52 44.9	M8	11.3 ± 0.02	1.07 ± 0.03	11.1 ± 0.3	−470.2 ± 0.2	14.7 ± 0.04	−11 ± 2	(25); (53); (53); (47)
J0355+1133[c]	03 55 23.37 +11 33 43.7	L3-L6γ	14.05 ± 0.02	2.52 ± 0.03	219.8 ± 1.6	−631.3 ± 0.8	9.12 ± 0.06	11.9 ± 0.2	(37); (53); (53); (61)
J0417−0800	04 17 37.49 −08 00 00.5	M7.5	12.18 ± 0.03	1.09 ± 0.04	454.6 ± 0.2	48.96 ± 0.15	18.09 ± 0.05	40.6 ± 1.4	(25); (53); (53); (64)
J0423−0414	04 23 48.58 −04 14 03.2	L6.5+T2	14.47 ± 0.03	1.54 ± 0.04	−347 ± 2	70.2 ± 1.1	14.7 ± 0.3	30.5 ± 0.6	(26); (53); (53); (71)
J0429−3123A	04 29 18.46 −31 23 56.7	M7.5	10.87 ± 0.02	1.1 ± 0.03	67.0 ± 0.3	100.5 ± 0.4	16.84 ± 0.06	40 ± 3	(16); (53); (53); (60)
J0435−1606	04 35 16.14 −16 06 57.2	M8e	10.41 ± 0.03	1.05 ± 0.03	161.3 ± 0.4	317.8 ± 0.3	10.58 ± 0.03	48.5 ± 1.4	(5); (53); (53); (64)
J0440−0530[d]	04 40 23.27 −05 30 08.1	M7.5e	10.66 ± 0.02	1.11 ± 0.03	333.1 ± 0.2	128.15 ± 0.13	9.76 ± 0.01	29.9 ± 0.2	(5); (53); (53); (65)
J0500+0330	05 00 21.01 +03 30 50.0	L4p	13.67 ± 0.02	1.61 ± 0.03	10.2 ± 0.6	−351.7 ± 0.4	13.12 ± 0.06	15.9 ± 0.2	(37); (53); (53); (61)

Table 2.7 (*continued*)

Table 2.7 (*continued*)

Source Name	Coordinates (J2000)	SpT	2MASS J (mag)	$J-K_s$ (mag)	μ_α (mas yr^{-1})	μ_δ (mas yr^{-1})	d (pc)	Published RV (km s^{-1})	References[a]
J0501−0010[e]	05 01 24.08 −00 10 45.5	L4γ	14.98 ± 0.04	2.02 ± 0.05	189.3 ± 1.5	−145.3 ± 1.2	13.1 ± 0.8	21.8 ± 0.7	(37); (53); (44); (39)
J0517−3349	05 17 37.69 −33 49 03.0	M8	12.0 ± 0.02	1.17 ± 0.03	446.5 ± 0.2	−332.6 ± 0.2	16.87 ± 0.03	−39 ± 2	(25); (53); (53); (47)
J0523−1403	05 23 38.22 −14 03 02.0	L2.5	13.08 ± 0.02	1.45 ± 0.04	107.3 ± 0.3	160.9 ± 0.3	12.76 ± 0.03	12.21 ± 0.09	(16); (53); (53); (61)
J0539−0059	05 39 52.00 −00 59 01.4	L5	13.85 ± 0.03	1.32 ± 0.04	162.4 ± 0.8	321.1 ± 0.8	12.73 ± 0.09	13.9 ± 0.2	(31); (53); (53); (61)
J0602+3911[e]	06 02 30.46 +39 10 58.5	L1β	12.3 ± 0.02	1.44 ± 0.03	156.9 ± 0.3	−506.3 ± 0.3	11.68 ± 0.02	7.94 ± 0.05	(11); (53); (53); (61)
J0641−4322	06 41 18.42 −43 22 32.4	L2.5	13.75 ± 0.03	1.3 ± 0.04	211.8 ± 0.4	632.0 ± 0.4	19.5 ± 0.07	74 ± 2	(33); (53); (53); (47)
J0652−2534	06 52 19.76 −25 34 50.4	M9	12.76 ± 0.02	1.24 ± 0.03	−235.5 ± 0.2	88.2 ± 0.3	16.01 ± 0.04	12 ± 2	(33); (53); (53); (47)
J0652+4710	06 52 30.71 +47 10 34.9	L3.5+L6.5	13.51 ± 0.02	1.82 ± 0.03	−118.8 ± 0.7	131.9 ± 0.8	9.12 ± 0.04	−7.03 ± 0.07	(20); (53); (53); (61)
J0700+3157	07 00 36.71 +31 57 25.5	L3+L6.5	12.92 ± 0.02	1.61 ± 0.03	92.1 ± 0.6	−552.3 ± 0.5	11.33 ± 0.04	−42.42 ± 0.09	(26); (53); (53); (61)
J0714+3702[e]	07 14 03.94 +37 02 46.0	M7.5β	11.98 ± 0.02	1.14 ± 0.03	−89.0 ± 0.3	−183.1 ± 0.3	15.61 ± 0.07	40.03 ± 0.11	(16); (53); (53); (57)
J0720−0846	07 20 03.25 −08 46 49.9	M9.5+T5	10.63 ± 0.02	1.16 ± 0.03	−58 ± 6	−126 ± 6	6.0 ± 1.0	83.8 ± 0.3	(34); (51); (34); (23)
J0741+1738	07 41 06.78 +17 38 44.8	M7	12.01 ± 0.02	1.07 ± 0.03	−201.7 ± 0.3	−499.1 ± 0.2	18.69 ± 0.08	41.8 ± 1.2	(25); (53); (53); (64)
J0746+2000	07 46 42.49 +20 00 32.6	L0.5	11.76 ± 0.02	1.29 ± 0.03	−370 ± 4	−42.0 ± 1.0	11.6 ± 0.6	52.37 ± 0.06	(3); (41); (44); (61)
J0751−2530	07 51 16.30 −25 30 43.0	L1	13.16 ± 0.02	1.17 ± 0.03	−879.0 ± 0.2	146.0 ± 0.2	17.68 ± 0.05	32 ± 2	(33); (53); (53); (47)
J0825+2115	08 25 19.61 +21 15 51.5	L7.5	15.1 ± 0.03	2.07 ± 0.04	−508.5 ± 1.8	−303.7 ± 1.3	10.84 ± 0.14	20 ± 2	(3); (53); (53); (57)
J0828−1309	08 28 34.17 −13 09 19.8	L2	12.8 ± 0.03	1.5 ± 0.04	−581.6 ± 0.2	27.5 ± 0.2	11.69 ± 0.02	25.85 ± 0.08	(8); (53); (53); (61)
J0830+0947	08 30 32.57 +09 47 15.4	M7.5	11.89 ± 0.02	1.13 ± 0.03	−489.6 ± 0.2	−458.87 ± 0.14	16.69 ± 0.04	41 ± 2	(12); (53); (53); (47)
J0835−0819	08 35 42.53 −08 19 23.3	L6.5	13.17 ± 0.02	2.03 ± 0.03	−535.7 ± 0.4	302.7 ± 0.4	7.214 ± 0.014	29.89 ± 0.06	(31); (53); (53); (61)
J0847−1532	08 47 28.74 −15 32 37.3	L1.5	13.51 ± 0.03	1.45 ± 0.03	132.7 ± 0.5	−199.7 ± 0.6	17.567 ± 0.098	2.0 ± 0.1	(31); (53); (53); (61)
J0853−0329	08 53 36.16 −03 29 32.2	M9e	11.21 ± 0.03	1.27 ± 0.04	−516.9 ± 0.2	−199.41 ± 0.13	8.673 ± 0.009	7 ± 2	(14); (53); (53); (47)
J0921−2104	09 21 14.10 −21 04 44.4	L1	12.78 ± 0.02	1.09 ± 0.03	245.9 ± 0.3	−911.6 ± 0.3	12.61 ± 0.04	80.53 ± 0.11	(31); (53); (53); (61)
J0949+0806	09 49 22.23 +08 06 45.1	M8.5	12.31 ± 0.02	1.1 ± 0.04	39.5 ± 0.3	−894.9 ± 0.3	16.53 ± 0.05	16 ± 2	(33); (53); (53); (47)
J1004−3335	10 04 39.32 −33 35 19.1	L5	14.48 ± 0.04	1.56 ± 0.04	345.8 ± 0.9	−354.3 ± 0.9	18.8 ± 0.2	−8 ± 2	(27); (53); (53); (47)
J1022+5825[e]	10 22 48.22 +58 25 45.3	L1β	13.5 ± 0.03	1.34 ± 0.04	−810.8 ± 0.3	−737.0 ± 0.3	18.4 ± 0.11	19.29 ± 0.11	(33); (53); (53); (61)
J1029+1626	10 29 21.70 +16 26 51.8	L2.5	14.29 ± 0.03	1.67 ± 0.03	355.2 ± 1.0	−364.4 ± 0.9	19.1 ± 0.3	−28.2 ± 1.4	(3); (53); (53); (62)
J1045−0149	10 45 23.98 −01 49 57.7	L2	13.08 ± 0.01	1.3 ± 0.01	−507.7 ± 0.4	−10.2 ± 0.3	17.05 ± 0.07	6.3 ± 0.1	(27); (53); (53); (61)
J1048−3956	10 48 14.57 −39 56 06.8	M9	9.54 ± 0.02	1.09 ± 0.03	−1179.2 ± 0.2	−988.1 ± 0.2	4.045 ± 0.002	−11 ± 2	(12); (53); (53); (47)
J1048+0111	10 48 42.81 +01 11 58.2	L1	12.92 ± 0.02	1.3 ± 0.03	−440.0 ± 0.4	−231.5 ± 0.3	15.05 ± 0.05	24.25 ± 0.06	(31); (53); (53); (61)
J1055+0808	10 55 47.34 +08 08 42.9	M9	12.55 ± 0.03	1.18 ± 0.03	−329.8 ± 0.2	−138.2 ± 0.2	18.75 ± 0.05	5 ± 2	(21); (53); (53); (47)
J1058−1548	10 58 47.83 −15 48 17.2	L2.5	14.16 ± 0.04	1.62 ± 0.05	−258.1 ± 0.8	31.1 ± 0.7	18.3 ± 0.2	19 ± 2	(31); (53); (53); (55)
J1108+6830[e]	11 08 30.77 +68 30 16.7	L1γ	13.12 ± 0.02	1.54 ± 0.03	−237.6 ± 0.3	−198.1 ± 0.4	16.3 ± 0.05	−9.84 ± 0.11	(37); (53); (53); (61)
J1121−1313	11 21 49.17 −13 13 08.7	M8.5	11.93 ± 0.02	1.19 ± 0.03	−472.2 ± 0.3	−46.3 ± 0.2	14.39 ± 0.04	33.8 ± 0.3	(33); (53); (53); (20)
J1124+3808	11 24 04.88 +38 08 05.4	M8.5	12.71 ± 0.02	1.14 ± 0.03	125.5 ± 0.2	−9.0 ± 0.3	18.47 ± 0.07	−14 ± 3	(9); (53); (53); (60)
J1126−5003	11 26 39.80 −50 03 54.8	L5	14.0 ± 0.03	1.17 ± 0.04	−1589.2 ± 0.5	451.0 ± 0.4	16.23 ± 0.09	49.3 ± 1.1	(31); (53); (53); (71)
J1141−2232	11 41 44.04 −22 32 15.01	M8	12.63 ± 0.02	1.06 ± 0.03	−166.2 ± 0.3	404.7 ± 0.2	19.01 ± 0.07	8 ± 3	(9); (53); (53); (60)
J1155−3727	11 55 39.53 −37 27 35.5	L2.5	12.81 ± 0.02	1.35 ± 0.03	43.1 ± 0.2	−790.9 ± 0.2	11.82 ± 0.03	45.51 ± 0.11	(33); (53); (53); (61)
J1155−2224	11 55 42.85 −22 24 58.7	M7.5	10.93 ± 0.02	1.05 ± 0.03	−374.0 ± 0.2	−187.49 ± 0.13	10.92 ± 0.02	−13 ± 3	(32); (53); (53); (60)
J1203+0016	12 03 58.13 +00 15 50.1	L5	14.01 ± 0.03	1.53 ± 0.04	−1217.6 ± 1.3	−282.6 ± 0.5	14.87 ± 0.12	−0.2 ± 0.2	(33); (53); (53); (61)

Table 2.7 (*continued*)

Table 2.7 (*continued*)

Source Name	Coordinates (J2000)	SpT	2MASS J (mag)	$J-K_s$ (mag)	μ_α (mas yr^{-1})	μ_δ (mas yr^{-1})	d (pc)	Published RV (km s^{-1})	References[a]
J1221+0257	12 21 27.71 +02 57 19.7	L0.5	13.07 ± 0.01	1.16 ± 0.01	−145.4 ± 0.5	−43.5 ± 0.3	18.54 ± 0.09	−8.79 ± 0.14	(31); (53); (53); (61)
J1224−1238	12 24 52.18 −12 38 35.7	M9	12.57 ± 0.02	1.22 ± 0.03	−304.6 ± 0.4	−189.0 ± 0.3	17.21 ± 0.06	−2.9 ± 0.6	(7); (53); (53); (39)
J1300+1912	13 00 42.50 +19 12 34.6	L1.5	12.72 ± 0.02	1.09 ± 0.03	−810.5 ± 0.3	−1248.5 ± 0.2	13.95 ± 0.04	−17.6 ± 0.12	(33); (53); (53); (61)
J1305−2541	13 05 40.17 −25 41 05.8	L2+L3.5	13.41 ± 0.03	1.67 ± 0.03	−313.5 ± 1.2	−20.0 ± 0.8	18.6 ± 0.2	6.4 ± 0.4	(28); (53); (53); (61)
J1309−2330	13 09 21.85 −23 30 35.7	M8	11.79 ± 0.02	1.12 ± 0.03	16.5 ± 0.3	−382.8 ± 0.3	15.0 ± 0.04	15 ± 2	(7); (53); (53); (47)
J1315−2649	13 15 30.86 −26 49 51.8	L3.5+T7	15.2 ± 0.05	1.73 ± 0.07	−688.6 ± 1.9	−288.1 ± 1.4	18.6 ± 0.4	−8 ± 3	(23); (53); (53); (47)
J1332−0441	13 32 24.48 −04 41 12.6	M7.5	12.37 ± 0.03	1.09 ± 0.03	87 ± 87	50 ± 50	19 ± 2	−12 ± 2	(16); (16); (47); (47)
J1356+4343	13 56 41.46 +43 42 59.1	M8	11.71 ± 0.02	1.06 ± 0.03	−452.5 ± 0.7	38.5 ± 0.7	20.0 ± 0.2	−22 ± 3	(36); (53); (53); (60)
J1403+3007	14 03 22.29 +30 07 54.6	M8.5	12.68 ± 0.02	1.08 ± 0.03	−802.5 ± 0.3	39.0 ± 0.3	19.81 ± 0.08	−39.2 ± 0.4	(21); (53); (53); (56)
J1425−3650[c]	14 25 27.98 −36 50 23.2	L4γ	13.75 ± 0.03	1.94 ± 0.04	−283.9 ± 0.6	−469.3 ± 0.5	11.83 ± 0.05	5.4 ± 0.2	(37); (53); (53); (61)
J1428+3310	14 28 43.22 +33 10 39.2	M9	11.99 ± 0.02	1.25 ± 0.03	−346.76 ± 0.10	−710.1 ± 0.2	10.99 ± 0.02	−39.1 ± 0.4	(14); (53); (53); (39)
J1438+6408	14 38 08.26 +64 08 36.3	L0	12.99 ± 0.02	1.34 ± 0.03	643.8 ± 0.4	−206.3 ± 0.3	17.04 ± 0.04	−45 ± 3	(33); (53); (53); (60)
J1439+1929	14 39 28.36 +19 29 14.9	L1	12.76 ± 0.02	1.21 ± 0.03	−1236 ± 57	402 ± 19	14.4 ± 0.1	−26.74 ± 0.09	(31); (16); (44); (61)
J1450+2354	14 50 16.00 +23 54 41.8	L4	13.8 ± 0.5	1.54 ± 0.71	144.7 ± 0.8	32.4 ± 0.7	17.9 ± 0.3	5 ± 3	(6); (18); (44); (20)
J1454+1606B	14 54 29.41 +16 06 08.6	M8.5	···	···	315.8 ± 1.0	−187.8 ± 1.2	9.7 ± 0.2	−10.5 ± 0.2	(1); (53); (26); (20)
J1456−2809[c]	14 56 38.26 −28 09 48.6	M7e	9.97 ± 0.03	1.04 ± 0.04	−491.1 ± 0.2	−843.3 ± 0.2	7.058 ± 0.005	1.0 ± 1.5	(35); (53); (53); (64)
J1501+2250	15 01 08.18 +22 50 02.1	M9	11.87 ± 0.02	1.16 ± 0.03	−43.8 ± 0.3	−64.0 ± 0.3	10.7 ± 0.02	6 ± 2	(24); (53); (53); (47)
J1504−2355	15 04 16.17 −23 55 56.5	M7.5	12.01 ± 0.03	0.98 ± 0.04	−331.3 ± 0.3	−87.6 ± 0.3	19.68 ± 0.07	−29 ± 2	(7); (53); (53); (47)
J1506+1321	15 06 54.32 +13 21 06.0	L3	13.37 ± 0.02	1.62 ± 0.03	−1071.0 ± 0.4	−11.9 ± 0.4	11.68 ± 0.04	−0.68 ± 0.11	(31); (53); (53); (61)
J1507−1627	15 07 47.67 −16 27 40.1	L5	12.83 ± 0.03	1.52 ± 0.04	−151.6 ± 0.6	−895.7 ± 0.6	7.39 ± 0.02	−39.85 ± 0.05	(3); (53); (53); (61)
J1510−0241	15 10 16.83 −02 41 08.0	M9	12.61 ± 0.02	1.27 ± 0.03	−399.1 ± 0.7	32.1 ± 0.5	18.04 ± 0.11	−41 ± 2	(24); (53); (53); (47)
J1515+4847	15 15 00.83 +48 47 41.6	L6	14.11 ± 0.03	1.61 ± 0.04	−950.0 ± 21.0	1471.0 ± 21.0	9.75 ± 0.06	−29.97 ± 0.11	(16); (43); (52); (61)
J1521+5053	15 21 01.05 +50 53 22.7	M7.5	12.01 ± 0.02	1.09 ± 0.03	53.9 ± 0.2	−172.6 ± 0.2	16.13 ± 0.03	1 ± 3	(16); (53); (53); (60)
J1524+2925	15 24 24.75 +29 25 31.5	M7.5	11.21 ± 0.02	1.05 ± 0.03	−56.8 ± 0.1	−629.04 ± 0.11	13.072 ± 0.015	−15.9 ± 0.5	(24); (53); (53); (56)
J1534−1418	15 34 56.93 −14 18 49.2	M7	11.38 ± 0.02	1.08 ± 0.03	−918.5 ± 0.3	−330.2 ± 0.2	10.91 ± 0.02	−71 ± 2	(33); (53); (53); (47)
J1539−0520	15 39 41.92 −05 20 42.7	L4	13.92 ± 0.03	1.35 ± 0.04	590.2 ± 0.7	104.6 ± 0.7	17.0 ± 0.12	27.3 ± 0.2	(33); (53); (53); (61)
J1555−0956	15 55 15.77 −09 56 06.0	L1.5	12.56 ± 0.02	1.11 ± 0.03	931.6 ± 0.4	−785.1 ± 0.2	13.58 ± 0.03	14.8 ± 0.1	(33); (53); (53); (61)
J1607−0442	16 07 31.23 −04 42 09.6	M9	11.9 ± 0.02	1.18 ± 0.03	−14.7 ± 0.4	−422.7 ± 0.2	15.24 ± 0.05	11 ± 2	(17); (53); (53); (47)
J1615+0546	16 15 42.45 +05 46 40.0	M9	12.88 ± 0.02	1.14 ± 0.03	141.6 ± 0.3	−103.22 ± 0.15	17.83 ± 0.06	7 ± 2	(16); (53); (53); (47)
J1615+3559	16 15 44.15 +35 58 59.5	L3	14.54 ± 0.03	1.6 ± 0.04	−29.8 ± 0.6	−528.7 ± 0.8	19.98 ± 0.15	−20.2 ± 0.9	(3); (53); (53); (57)
J1632+1904	16 32 29.11 +19 04 40.7	L8	15.87 ± 0.07	1.87 ± 0.08	293.0 ± 1.0	−54.0 ± 1.0	15.2 ± 0.5	−6 ± 2	(31); (18); (44); (58)
J1645−1320	16 45 22.09 −13 19 52.2	L1	12.45 ± 0.03	1.31 ± 0.04	−362.1 ± 0.3	−808.25 ± 0.15	11.26 ± 0.02	26.58 ± 0.06	(31); (53); (53); (61)
J1655−0823	16 55 35.25 −08 23 40.7	M7	9.78 ± 0.03	0.96 ± 0.04	−813.4 ± 0.2	−870.61 ± 0.11	6.501 ± 0.005	15.39 ± 0.11	(1); (53); (53); (63)
J1658+7026	16 58 03.80 +70 27 01.7	L1	13.29 ± 0.02	1.37 ± 0.03	−139.5 ± 0.3	−315.4 ± 0.4	18.48 ± 0.07	−25.6 ± 0.12	(16); (53); (53); (61)
J1705−0516	17 05 48.35 −05 16 46.3	L1	13.31 ± 0.03	1.28 ± 0.04	116.7 ± 0.6	−120.2 ± 0.4	18.98 ± 0.13	12.19 ± 0.11	(31); (53); (53); (61)
J1707+6439	17 07 18.30 +64 39 33.1	M8.5	12.54 ± 0.02	1.16 ± 0.03	227.3 ± 0.2	−94.6 ± 0.3	18.06 ± 0.04	−10.1 ± 0.06	(38); (53); (53); (66)
J1707−0558	17 07 23.43 −05 58 24.9	M9+L3	12.05 ± 0.02	1.34 ± 0.03	100 ± 55	45 ± 24	16.5 ± 1.0	3 ± 2	(17); (16); (47); (47)
J1721+3344	17 21 03.60 +33 44 16.9	M9	13.63 ± 0.02	1.14 ± 0.03	−1855.6 ± 0.4	591.6 ± 0.4	16.31 ± 0.05	−102.8 ± 0.2	(33); (53); (53); (71)

Table 2.7 (*continued*)

Table 2.7 (*continued*)

Source Name	Coordinates (J2000)	SpT	2MASS J (mag)	$J-K_s$ (mag)	μ_α (mas yr^{-1})	μ_δ (mas yr^{-1})	d (pc)	Published RV (km s^{-1})	References[a]
J1731+2721[c]	17 31 29.74 +27 21 23.2	L0	12.09 ± 0.03	1.18 ± 0.03	−90.2 ± 0.2	−252.9 ± 0.2	11.94 ± 0.02	−29.76 ± 0.11	(17); (53); (53); (61)
J1745−1640	17 45 34.66 −16 40 53.9	L1.5	13.65 ± 0.03	1.24 ± 0.04	106.9 ± 0.5	−100.3 ± 0.4	19.6 ± 0.11	26 ± 2	(33); (53); (53); (47)
J1750−0016	17 50 24.81 −00 16 15.0	L5	13.29 ± 0.02	1.45 ± 0.03	−397.2 ± 0.5	197.9 ± 0.4	9.24 ± 0.02	19 ± 3	(40); (53); (53); (47)
J1757+7042	17 57 15.40 +70 42 01.1	M7.5	11.45 ± 0.02	1.06 ± 0.03	6.1 ± 0.4	331.5 ± 0.6	19.02 ± 0.09	−12.3 ± 0.6	(25); (53); (53); (66)
J1807+5015	18 07 15.93 +50 15 31.6	L1	12.93 ± 0.02	1.33 ± 0.03	24.5 ± 0.2	−136.9 ± 0.3	14.63 ± 0.03	−0.4 ± 0.5	(31); (53); (53); (61)
J1821+1413[f]	18 21 28.15 +14 14 00.8	L5	13.43 ± 0.02	1.78 ± 0.03	227.3 ± 0.5	−246.4 ± 0.6	9.36 ± 0.02	9.8 ± 0.2	(31); (53); (53); (61)
J1835+3259	18 35 37.88 +32 59 53.3	M8.5	10.27 ± 0.02	1.1 ± 0.03	−72.8 ± 0.2	−754.84 ± 0.15	5.687 ± 0.003	8 ± 2	(25); (53); (53); (64)
J1843+4040	18 43 22.12 +40 40 21.3	M7.5e	11.31 ± 0.02	1.01 ± 0.03	−120.5 ± 0.2	591.6 ± 0.2	14.4 ± 0.02	−19 ± 2	(10); (53); (53); (64)
J1845−6357B	18 45 05.25 −63 57 47.4	M8.5+T6	9.54 ± 0.02	1.04 ± 0.03	2584.3 ± 0.13	589.0 ± 0.2	4.001 ± 0.002	−18 ± 2	(34); (53); (53); (47)
J1906+4011	19 06 48.07 +40 11 08.5	L1	13.08 ± 0.02	1.31 ± 0.03	438.3 ± 0.2	−180.0 ± 0.3	16.79 ± 0.04	−22.8 ± 0.3	(22); (53); (53); (71)
J1916+0508	19 16 57.61 +05 09 01.5	M8	9.91 ± 0.03	1.14 ± 0.03	−598.2 ± 0.2	−1365.3 ± 0.2	5.918 ± 0.005	35.0 ± 1.5	(1); (53); (53); (58)
J2057−0252[e]	20 57 54.09 −02 52 30.2	L2β	13.12 ± 0.02	1.4 ± 0.03	−2.9 ± 0.4	−102.2 ± 0.2	15.51 ± 0.06	−24.7 ± 0.4	(31); (53); (53); (61)
J2104−1037	21 04 14.96 −10 37 37.3	L2	13.84 ± 0.03	1.47 ± 0.04	594.6 ± 0.7	−295.7 ± 0.4	17.19 ± 0.12	−21.09 ± 0.12	(31); (53); (53); (61)
J2139+0220[c]	21 39 26.76 +02 20 22.7	L8.5+T3.5	14.71 ± 0.0	1.13 ± 0.04	486 ± 2	125 ± 3	9.9 ± 0.2	−25.1 ± 0.3	(19); (45); (45); (71)
J2148+4003	21 48 16.29 +40 03 59.3	L7	14.15 ± 0.03	2.38 ± 0.04	773.3 ± 0.7	458.0 ± 0.9	8.11 ± 0.03	−14.5 ± 0.7	(31); (53); (53); (39)
J2224−0158	22 24 43.85 −01 58 53.2	L4.5	14.07 ± 0.03	2.05 ± 0.04	471.0 ± 0.8	−874.9 ± 0.8	11.55 ± 0.09	−36.48 ± 0.01	(3); (53); (53); (39)
J2234+2359	22 34 14.01 +23 59 55.8	M9.5	13.15 ± 0.02	1.31 ± 0.03	851.7 ± 0.4	−57.8 ± 0.3	18.48 ± 0.07	17.2 ± 0.6	(4); (53); (53); (56)
J2244+2043[c]	22 44 31.67 +20 43 43.3	L6–L8γ	16.48 ± 0.14	2.46 ± 0.16	230.3 ± 0.9	−234.8 ± 1.0	17.0 ± 0.3	−16.0 ± 0.9	(39); (50); (50); (72)
J2306−0502	23 06 29.36 −05 02 29.0	M8	11.35 ± 0.02	1.06 ± 0.03	930.9 ± 0.2	−479.4 ± 0.2	12.43 ± 0.02	−54 ± 2	(16); (53); (53); (47)
J2322−3133[e]	23 22 46.82 −31 33 23.4	L2β	13.58 ± 0.03	1.25 ± 0.04	−203.2 ± 0.5	−540.5 ± 0.6	19.9 ± 0.2	33.9 ± 1.1	(33); (53); (53); (39)
J2331−2749	23 31 21.74 −27 49 49.6	M7	11.65 ± 0.02	1.0 ± 0.03	90.4 ± 0.3	745.2 ± 0.3	13.66 ± 0.03	−3.0 ± 1.5	(25); (53); (53); (64)
J2346+1129	23 46 46.02 +11 29 09.4	M8	12.8 ± 0.02	1.19 ± 0.03	−386.2 ± 0.4	−83.6 ± 0.2	19.67 ± 0.07	0 ± 2	(16); (53); (53); (47)

Table 2.7 (*continued*)

Table 2.7 (*continued*)

Source Name	Coordinates (J2000)	SpT	2MASS J (mag)	$J - K_s$ (mag)	μ_α (mas yr^{-1})	μ_δ (mas yr^{-1})	d (pc)	Published RV (km s^{-1})	References[a]

[a] References are in the order of spectral classification, astrometry, and RV measurement.
[b] Identified as a member of the Argus moving group using BANYAN Σ
[c] Identified as a member of the AB Doradus moving group using BANYAN Σ
[d] Identified as a member of the Carina-Near moving group using BANYAN Σ
[e] Suspected young source from Faherty et al. (2016)
[f] Weird red L dwarf; also reported as L4pec in Faherty et al. (2016)

References – Classification: (1) Kirkpatrick et al. (1991), (2) Leinert et al. (2000), (3) Reid et al. (2000), (4) Gizis et al. (2000), (5) McCaughrean et al. (2002), (6) Goto et al. (2002), (7) Gizis (2002), (8) Scholz & Meusinger (2002), (9) Cruz et al. (2003), (10) Reid et al. (2003) (11) Salim et al. (2003), (12) Henry et al. (2004), (13) Lodieu et al. (2005), (14) Reid & Gizis (2005),(15) Reid et al. (2006), (16) Schmidt et al. (2007), (17) Reid et al. (2008), (18) Faherty et al. (2009), (19) Burgasser et al. (2010), (20) Konopacky et al. (2010), (21) West et al. (2011), (22) Gizis et al. (2011), (23) Burgasser et al. (2011), (24) Kirkpatrick et al. (2011), (25) Deshpande et al. (2012), (26) Dupuy & Liu (2012), (27) Marocco et al. (2013), (28) Koen (2013), (29) Thompson et al. (2013), (30) Newton et al. (2014), (31) Schneider et al. (2014), (32) Dieterich et al. (2014), (33) Bardalez Gagliuffi et al. (2014), (34) Burgasser et al. (2015b), (35) Davison et al. (2015), (36) West et al. (2015), (37) Gagné et al. (2015b), (38) Metodieva et al. (2015), (39) Faherty et al. (2016), (40) Koen et al. (2017), (73) Burgasser et al. (2008); Astrometry: (41) Monet et al. (2003), (42) Costa et al. (2005), (43) Jameson et al. (2008a), (44) Faherty et al. (2012), (45) Smart et al. (2013), (46) Dittmann et al. (2014), (47) Burgasser et al. (2015a), (48) Weinberger et al. (2016), (49) Schneider et al. (2016), (50) Liu et al. (2016), (51) Kirkpatrick et al. (2016), (52) Dahn et al. (2017), (53) Gaia Collaboration et al. (2018b), (54) Gagné et al. (2018a); Radial Velocity: (55) Basri et al. (2000), (56) Reid et al. (2002), (57) Bailer-Jones (2004), (58) Zapatero Osorio et al. (2007), (59) Blake et al. (2007), (60) Reiners & Basri (2009a), (61) Blake et al. (2010), (62) Seifahrt et al. (2010), (63) Morin et al. (2010), (64) Deshpande et al. (2012), (65) Shkolnik et al. (2012), (66) Tanner et al. (2012), (67) Deshpande et al. (2013) (68) Barnes et al. (2014), (69) Prato et al. (2015), (70) Terrien et al. (2015), (71) Vos et al. (2017), (72) Vos et al. (2018)

Table 2.8: Radial Velocities and Heliocentric Space Motions of Late-M and L Dwarfs Within 20 pc of the Sun

Source Name	SpT	Published RV (km s^{-1})	U (km s^{-1})	V (km s^{-1})	W (km s^{-1})	P[TD]/P[D][a]	Population[a]
J0004−4044	L5+L5	32.84 ± 0.17	21.68 ± 0.05	−85.7 ± 0.4	−11.90 ± 0.17	3.42	D/TD
J0004−2058	M9	−33 ± 2	−42.5 ± 0.2	−13.2 ± 0.4	30 ± 2	0.04	D
J0015+3516	L1	−37.35 ± 0.16	28.01 ± 0.07	−27.23 ± 0.14	5.31 ± 0.14	0.01	D
J0019+5213	M9	−29 ± 3	4.2 ± 1.4	−30 ± 3	−16.9 ± 0.6	0.02	D
J0024−0158	L0.5	11.65 ± 1.6	9.4 ± 0.2	25.8 ± 0.7	0.8 ± 1.4	0.01	D
J0024−2708B	M8.5	−35 ± 3	−0.1 ± 0.4	31.2 ± 0.5	43 ± 3	0.24	D/TD
J0027+2219	M8e	−11.9 ± 1.3	−5 ± 3	−17 ± 3	3 ± 3	0.01	D
J0036+1821	L3.5	20.90 ± 0.14	−29.83 ± 0.08	9.08 ± 0.09	−5.9 ± 0.1	0.01	D
J0045+1634	L0β	3.29 ± 0.17	−10.8 ± 0.1	−1.89 ± 0.12	1.82 ± 0.12	0.01	D
J0047+6803	L7	−19.4 ± 1.3	21.5 ± 0.7	−4.1 ± 1.1	5.48 ± 0.11	0.01	D
J0102−3737	M9	−5 ± 2	−62.27 ± 0.16	−20.6 ± 0.4	13 ± 2	0.03	D
J0107+0041	L8	8.2 ± 0.5	−32 ± 3	−6.2 ± 1.7	6.1 ± 0.7	0.01	D
J0109−5100	M8.5e	−1.3 ± 0.2	−5.85 ± 0.05	7.54 ± 0.07	7.22 ± 0.18	0.01	D
J0109+2949	M9.5	38.9 ± 0.8	−78.6 ± 0.5	7.7 ± 0.6	14.6 ± 0.5	0.05	D
J0109−0343	M9e	−6.3 ± 1.8	−2.6 ± 0.5	0.04 ± 0.5	14.5 ± 1.65	0.01	D
J0140+2701	M8.5	8.2 ± 0.4	7.6 ± 0.2	1.0 ± 0.2	−14.8 ± 0.2	0.01	D
J0144−0716	L6.5	−2.6 ± 0.1	0.9 ± 0.1	−11.5 ± 0.2	10.2 ± 0.1	0.01	D
J0205−1159	L7+L7	7 ± 2	−23 ± 4	−9 ± 5	13 ± 3	0.01	D
J0213+4444	L1.5	−23.47 ± 0.11	30.89 ± 0.09	−5.3 ± 0.08	−0.06 ± 0.12	0.01	D
J0215−3040	M8	0.005 ± 0.009	−7.87 ± 0.04	−38.29 ± 0.11	24.28 ± 0.04	0.04	D
J0217+3526	M7	11 ± 3	−14 ± 2	−6 ± 2	0.5 ± 1.1	0.01	D
J0253+1652	M7	68.30 ± 0.05	−58.11 ± 0.04	−58.93 ± 0.09	−51.64 ± 0.03	14.17	TD
J0255−4700	L9	18 ± 3	6.2 ± 0.2	−19.2 ± 1.4	6.2 ± 2.4	0.01	D
J0306−3647	M8.5	11.44 ± 0.19	47.63 ± 0.07	−10.95 ± 0.09	−4.81 ± 0.16	0.01	D
J0314+1603	M9.5	−6.8 ± 0.2	25.9 ± 0.2	18.77 ± 0.06	0.76 ± 0.14	0.01	D
J0320+1854	M8	45.5 ± 0.6	−34.96 ± 0.5	−6.94 ± 0.15	−15.12 ± 0.31	0.01	D
J0331−3042	M7.5	19 ± 2	21.3 ± 0.8	−12.6 ± 0.9	−7.7 ± 1.6	0.01	D
J0334−4953	M9	71 ± 3	−60.60 ± 0.12	−88.1 ± 0.6	5.6 ± 0.8	10.77	TD
J0339−3525	M9β	7.4 ± 0.7	−2.4 ± 0.2	6.9 ± 0.4	6.8 ± 0.6	0.01	D
J0351−0052	M8	−11 ± 2	35.4 ± 1.5	−11.2 ± 0.3	0.0 ± 1.3	0.01	D
J0355+1133	L3–L6γ	11.9 ± 0.2	5.79 ± 0.19	−14.25 ± 0.19	−8.47 ± 0.14	0.01	D
J0417−0800	M7.5	40.6 ± 1.4	−34.0 ± 1.0	−21.5 ± 0.4	11.1 ± 0.9	0.01	D
J0423−0414	L6.5+T2	30.5 ± 0.6	−8.1 ± 0.5	23.3 ± 0.5	−25.2 ± 0.5	0.03	D
J0429−3123A	M7.5	40 ± 3	−15.2 ± 1.4	−9.8 ± 1.7	−14.8 ± 2.0	0.01	D
J0435−1606	M8e	48.5 ± 1.4	−34.5 ± 0.9	−3.5 ± 0.6	−11.3 ± 0.9	0.01	D
J0440−0530	M7.5e	29.9 ± 0.2	−19.6 ± 0.16	−2.64 ± 0.06	5.55 ± 0.11	0.01	D

Table 2.8 (*continued*)

Table 2.8 (*continued*)

Source Name	SpT	Published RV (km s^{-1})	U (km s^{-1})	V (km s^{-1})	W (km s^{-1})	P[TD]/P[D][a]	Population[a]
J0500+0330	L4p	15.94 ± 0.16	6.30 ± 0.15	-8.9 ± 0.1	-9.00 ± 0.08	0.01	D
J0501−0010	L4γ	21.8 ± 0.7	-5.3 ± 0.7	-8.03 ± 1.13	3.7 ± 0.8	0.01	D
J0517−3349	M8	-39 ± 2	48.7 ± 0.9	8.0 ± 1.4	52.8 ± 1.1	0.9	D/TD
J0523−1403	L2.5	12.21 ± 0.09	-4.94 ± 0.07	8.28 ± 0.05	10.86 ± 0.05	0.01	D
J0539−0059	L5	13.91 ± 0.15	-10.82 ± 0.15	15.6 ± 0.1	20.45 ± 0.14	0.01	D
J0602+3911	L1β	7.94 ± 0.05	-1.11 ± 0.05	-15.20 ± 0.06	2.51 ± 0.02	0.01	D
J0641−4322	L2.5	74 ± 2	-60.3 ± 0.6	-51.6 ± 1.8	17.5 ± 0.7	0.2	D/TD
J0652−2534	M9	12 ± 2	-5.4 ± 1.1	12.2 ± 1.6	-8.2 ± 0.4	0.01	D
J0652+4710	L3.5+L6.5	-7.03 ± 0.07	17.96 ± 0.07	18.14 ± 0.04	2.10 ± 0.04	0.01	D
J0700+3157	L3+L6.5	-42.42 ± 0.09	52.30 ± 0.09	-13.74 ± 0.12	-10.94 ± 0.05	0.02	D
J0714+3702	M7.5β	40.03 ± 0.11	-30.1 ± 0.1	1.18 ± 0.06	10.94 ± 0.07	0.01	D
J0720−0846	M9.5+T5	83.8 ± 0.3	-47.6 ± 0.4	-47.7 ± 0.4	7.5 ± 0.6	0.07	D
J0741+1738	M7	41.8 ± 1.2	-23.1 ± 1.1	-37.7 ± 0.5	-11.7 ± 0.4	0.02	D
J0746+2000	L0.5	52.37 ± 0.06	-43.3 ± 0.5	-1.8 ± 0.5	7.7 ± 1.1	0.01	D
J0751−2530	L1	32 ± 2	-46.9 ± 0.9	5.9 ± 1.8	-49.26 ± 0.16	0.44	D/TD
J0825+2115	L7.5	21 ± 2	-16.8 ± 1.6	-5.6 ± 0.7	-8.6 ± 1.1	0.01	D
J0828−1309	L2	25.85 ± 0.08	-22.18 ± 0.06	-3.6 ± 0.07	-11.49 ± 0.06	0.01	D
J0830+0947	M7.5	41 ± 2	-28.1 ± 1.5	-35 ± 1.0	-19.9 ± 0.9	0.03	D
J0835−0819	L6.5	29.89 ± 0.06	-22.66 ± 0.05	-1.78 ± 0.05	7.52 ± 0.03	0.01	D
J0847−1532	L1.5	2.0 ± 0.1	27.54 ± 0.11	0.7 ± 0.1	7.14 ± 0.05	0.01	D
J0853−0329	M9e	7 ± 2	-2.3 ± 1.1	2.7 ± 1.4	-10.0 ± 0.9	0.01	D
J0921−2104	L1	80.53 ± 0.11	31.37 ± 0.13	-83.91 ± 0.12	11.14 ± 0.08	2.99	D/TD
J0949+0806	M8.5	16 ± 2	34.9 ± 1.0	-54.5 ± 1.1	-5.5 ± 1.4	0.08	D
J1004−3335	L5	-8 ± 2	55.0 ± 0.5	16.2 ± 1.9	-0.6 ± 0.6	0.02	D
J1022+5825	L1β	19.29 ± 0.11	-58.8 ± 0.4	-55.8 ± 0.4	7.14 ± 0.12	0.19	D/TD
J1029+1626	L2.5	-28.2 ± 1.4	61.9 ± 0.8	0.8 ± 0.6	-7.1 ± 1.2	0.02	D
J1045−0149	L2	6.3 ± 0.1	-24.54 ± 0.14	-3.12 ± 0.08	-7.51 ± 0.11	0.01	D
J1048−3956	M9	-11 ± 2	-0.1 ± 0.3	13.0 ± 1.9	-22.2 ± 0.6	0.01	D
J1048+0111	L1	24.25 ± 0.06	-13.12 ± 0.07	-23.14 ± 0.08	4.53 ± 0.09	0.01	D
J1055+0808	M9	5 ± 2	-9.7 ± 0.5	-8.8 ± 1.0	-5.4 ± 1.7	0.01	D
J1058−1548	L2.5	19 ± 2	-10.2 ± 0.2	-7.7 ± 1.6	11.6 ± 1.3	0.01	D
J1108+6830	L1γ	-9.84 ± 0.11	0.84 ± 0.08	-10.88 ± 0.08	1.90 ± 0.08	0.01	D
J1121−1313	M8.5	33.9 ± 0.3	-14.65 ± 0.07	-25.4 ± 0.2	17.93 ± 0.19	0.01	D
J1124+3808	M8.5	-14 ± 3	26.0 ± 1.1	15.16 ± 0.07	-2 ± 3	0.01	D
J1126−5003	L5	49.3 ± 1.1	-92.2 ± 0.7	-76.6 ± 1.1	9.3 ± 0.2	9.53	D/TD
J1141−2232	M8	8 ± 3	-17.1 ± 0.5	17 ± 2	35.6 ± 1.8	0.06	D
J1155−3727	L2.5	45.51 ± 0.11	43.98 ± 0.06	-38.3 ± 0.1	-13.0 ± 0.1	0.04	D
J1155−2224	M7.5	-13 ± 3	-4.5 ± 0.7	9 ± 2	-12 ± 2	0.01	D
J1203+0016	L5	-0.22 ± 0.16	-54.2 ± 0.6	-41.5 ± 0.5	-17.7 ± 0.3	0.07	D

Table 2.8 (*continued*)

Table 2.8 (*continued*)

Source Name	SpT	Published RV (km s^{-1})	U (km s^{-1})	V (km s^{-1})	W (km s^{-1})	P[TD]/P[D][a]	Population[a]
J1221+0257	L0.5	-8.79 ± 0.14	0.96 ± 0.07	6.67 ± 0.08	-3.75 ± 0.13	0.01	D
J1224−1238	M9	-2.9 ± 0.6	-4.26 ± 0.16	-8.1 ± 0.4	-7.4 ± 0.5	0.01	D
J1300+1912	L1.5	-17.60 ± 0.12	10.31 ± 0.03	-84.1 ± 0.3	-19.65 ± 0.12	3.55	D/TD
J1305−2541	L2+L3.5	6.4 ± 0.4	-8.0 ± 0.4	-8.4 ± 0.3	11.2 ± 0.2	0.01	D
J1309−2330	M8	15 ± 2	28.0 ± 1.0	-11.2 ± 1.2	-4.4 ± 1.3	0.01	D
J1315−2649	L3.5+T7	-8 ± 3	-34.9 ± 1.8	-31 ± 2	-12.3 ± 1.8	0.02	D
J1331−0116	T0/L6blue	-3.3 ± 0.4	21.4 ± 2.2	-58.8 ± 13.5	-25.8 ± 5.7	0.27	D/TD
J1332−0441	M7.5	-12 ± 2	10 ± 7	24 ± 7	-2 ± 5	0.01	D
J1356+4343	M8	-22 ± 3	-23.0 ± 0.4	-20.4 ± 1.1	-3.7 ± 3	0.01	D
J1403+3007	M8.5	-39.2 ± 0.4	-52.9 ± 0.2	-41.1 ± 0.2	-9.8 ± 0.4	0.05	D
J1425−3650	L4γ	5.4 ± 0.3	5.78 ± 0.19	-14.70 ± 0.17	-7.63 ± 0.12	0.01	D
J1428+3310	M9e	-39.1 ± 0.4	17.45 ± 0.08	-37.08 ± 0.13	-20.2 ± 0.4	0.03	D
J1438+6408	L0	-45 ± 3	64 ± 0.5	11.5 ± 1.9	-39 ± 2	0.22	D/TD
J1439+1929	L1	-26.74 ± 0.09	-71 ± 4	-28 ± 4	21.7 ± 1.7	0.08	D
J1450+2354	L4	5 ± 3	18.3 ± 1.0	23.5 ± 0.7	6 ± 2	0.01	D
J1454+1606B	M8.5	-10.5 ± 0.2	17.1 ± 0.2	14.92 ± 0.11	-8.8 ± 0.2	0.01	D
J1456−2809	M7e	1.0 ± 1.5	5.7 ± 1.2	-17.0 ± 0.6	-6.3 ± 0.7	0.01	D
J1501+2250	M9	6 ± 2	14.6 ± 0.8	10.1 ± 0.5	13.1 ± 1.7	0.01	D
J1504−2355	M7.5	-29.0 ± 2.0	-28.35 ± 1.61	-4.49 ± 0.65	1.97 ± 0.99	0.01	D
J1506+1321	L3	-0.68 ± 0.11	-21.87 ± 0.13	-27.94 ± 0.14	35.87 ± 0.13	0.07	D
J1507−1627	L5	-39.85 ± 0.05	-14.52 ± 0.04	-4.71 ± 0.07	-33.47 ± 0.05	0.03	D
J1510−0241	M9	-41 ± 2	-37.7 ± 1.4	-6.86 ± 0.16	-3.3 ± 1.4	0.01	D
J1515+4847	L6	-29.97 ± 0.11	-72.2 ± 1.1	-1.3 ± 0.8	-10.6 ± 0.6	0.03	D
J1521+5053	M7.5	1 ± 3	24.6 ± 0.2	9.6 ± 1.8	9 ± 2	0.01	D
J1524+2925	M7.5	-15.9 ± 0.5	33.41 ± 0.19	-21.0 ± 0.2	-6.2 ± 0.4	0.01	D
J1534−1418	M7	-71 ± 2	-65.5 ± 1.7	-23.4 ± 0.3	-13.9 ± 1.1	0.04	D
J1539−0520	L4	27.3 ± 0.2	50.8 ± 0.2	50.4 ± 0.3	0.2 ± 0.2	0.14	D/TD
J1555−0956	L1.5	14.8 ± 0.1	65.30 ± 0.14	13.37 ± 0.02	-51.33 ± 0.18	1.34	D/TD
J1607−0442	M9	11 ± 2	32.7 ± 1.7	-10.4 ± 0.2	-1.5 ± 1.1	0.01	D
J1615+0546	M9	7 ± 2	25.3 ± 1.5	15.4 ± 0.5	-0.3 ± 1.2	0.01	D
J1615+3559	L3	-20.2 ± 0.9	46.2 ± 0.5	-26.1 ± 0.6	-7.6 ± 0.7	0.02	D
J1632+1904	L8	-6 ± 2	16.0 ± 1.4	20.4 ± 1.1	-13.0 ± 1.5	0.01	D
J1645−1320	L1	26.58 ± 0.06	43.5 ± 0.06	-31.25 ± 0.08	7.18 ± 0.03	0.02	D
J1655−0823	M7	15.39 ± 0.11	30.0 ± 0.1	-20.99 ± 0.03	18.36 ± 0.04	0.01	D
J1658+7026	L1	-25.6 ± 0.12	40.2 ± 0.1	-14.5 ± 0.1	8.7 ± 0.1	0.01	D
J1705−0516	L1	12.19 ± 0.11	28.04 ± 0.11	13.09 ± 0.06	-2.16 ± 0.11	0.01	D
J1707+6439	M8.5	-10.10 ± 0.06	22.41 ± 0.03	15.19 ± 0.06	-12.99 ± 0.05	0.01	D
J1707−0558	M9+L3	3 ± 2	14 ± 3	20 ± 4	4 ± 4	0.01	D
J1721+3344	L5	-102.8 ± 0.2	-88.9 ± 0.2	-122.5 ± 0.3	78.6 ± 0.4	>100	TD/H

Table 2.8 (*continued*)

Table 2.8 (*continued*)

Source Name	SpT	Published RV (km s^{-1})	U (km s^{-1})	V (km s^{-1})	W (km s^{-1})	P[TD]/P[D][a]	Population[a]
J1731+2721	L0	-29.76 ± 0.11	6.28 ± 0.06	-17.78 ± 0.08	-6.62 ± 0.05	0.01	D
J1745−1640	L1.5	26 ± 2	38.5 ± 2.0	14.4 ± 0.4	-3.1 ± 0.2	0.01	D
J1750−0016	L5	19 ± 3	24 ± 3	17.7 ± 1.3	30.6 ± 0.7	0.04	D
J1757+7042	M7.5	-12.3 ± 0.6	-16.28 ± 0.17	-3.2 ± 0.5	-0.4 ± 0.3	0.01	D
J1807+5015	L1	-0.4 ± 0.5	20.18 ± 0.09	11.6 ± 0.4	4.0 ± 0.2	0.01	D
J1821+1413	L5	9.78 ± 0.16	24.16 ± 0.12	16.67 ± 0.11	-4.00 ± 0.05	0.01	D
J1835+3259	M8.5	8 ± 2	33.0 ± 0.9	11.5 ± 1.7	4.3 ± 0.6	0.01	D
J1843+4040	M7.5e	-19 ± 2	-30.4 ± 0.7	0.6 ± 1.8	21.7 ± 0.6	0.01	D
J1845−6357B	M8.5+T6	-18 ± 2	-8.0 ± 1.6	49.0 ± 0.9	-26.5 ± 0.8	0.18	D/TD
J1906+4011	L1	-22.8 ± 0.3	6.0 ± 0.1	0.6 ± 0.3	-34.93 ± 0.11	0.03	D
J1916+0508	M8	35.0 ± 1.5	64.6 ± 1.1	3.0 ± 1.0	2.15 ± 0.09	0.02	D
J2057−0252	L2β	-24.7 ± 0.4	-0.4 ± 0.3	-9.1 ± 0.3	16.2 ± 0.2	0.01	D
J2104−1037	L2	-21.09 ± 0.12	-26.02 ± 0.19	-18.04 ± 0.16	-25.6 ± 0.3	0.02	D
J2139+0220	L8.5+T3.5	-25.1 ± 0.3	-19.8 ± 0.4	-2.6 ± 0.2	9.6 ± 0.3	0.01	D
J2148+4003	L7	-14.5 ± 0.7	-23.23 ± 0.13	-2.5 ± 0.7	4.21 ± 0.13	0.01	D
J2224−0158	L4.5	-36.48 ± 0.01	0.84 ± 0.04	-52.0 ± 0.4	-0.5 ± 0.3	0.04	D
J2234+2359	M9.5	17.2 ± 0.7	-47.5 ± 0.2	7.7 ± 0.6	-42.1 ± 0.4	0.17	D/TD
J2244+2043	L6–L8γ	-16.0 ± 0.9	4.77 ± 0.13	-15.1 ± 0.8	-5.9 ± 0.6	0.01	D
J2306−0502	M8	-54 ± 2	-33.3 ± 0.4	-55.5 ± 1.0	19.9 ± 1.7	0.16	D/TD
J2322−3133	L2β	33.9 ± 1.1	57.5 ± 0.5	-25.3 ± 0.5	-16.0 ± 1.1	0.03	D
J2331−2749	M7	-3.0 ± 1.5	-14.2 ± 0.4	53.8 ± 0.2	9.0 ± 1.4	0.11	D/TD
J2346+1129	M8	0 ± 2	46.3 ± 0.2	22.3 ± 1.3	11.4 ± 1.5	0.02	D

[a] Galactic thin disk (D), thick disk (TD), intermediate thin/thick disk populations (D/TD), and intermediate thick
[a] disk/halo populations (D/H) assigned in the same manner as Table 2.5.

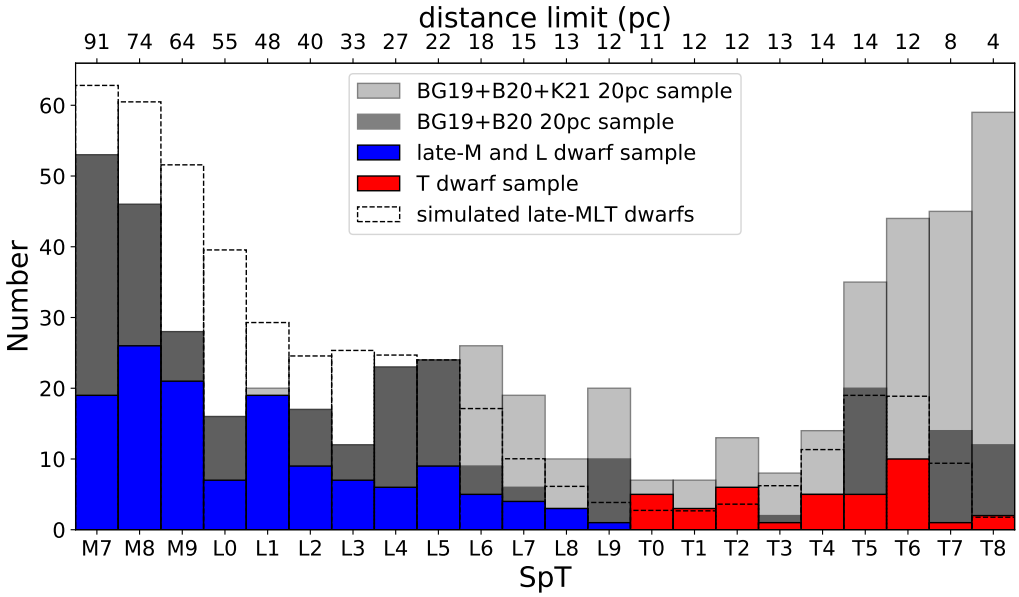

Figure 2.19: Spectral type distribution of my 20 pc late-M and L dwarf kinematic sample with RV uncertainty of ≤ 3 km s^{-1} (blue histogram), and my NIRSPEC T dwarf sample (red histogram). Also shown are the combined volume-limited samples of M7−L5 dwarfs from Bardalez Gagliuffi et al. (BG19; 2019b) and L0−T8 dwarfs from (B20; Best et al. 2020) (dark grey), a 20 pc full sample from BG19, B20, and Kirkpatrick et al. (K21; 2021) (light grey), and a simulated population (dashed histogram; Section 2.5.4) normalized to agree with the observed sample at spectral type L5. Distance limits assuming an apparent magnitude limit of $J, K < 15.5$ are shown along the top x-axis.

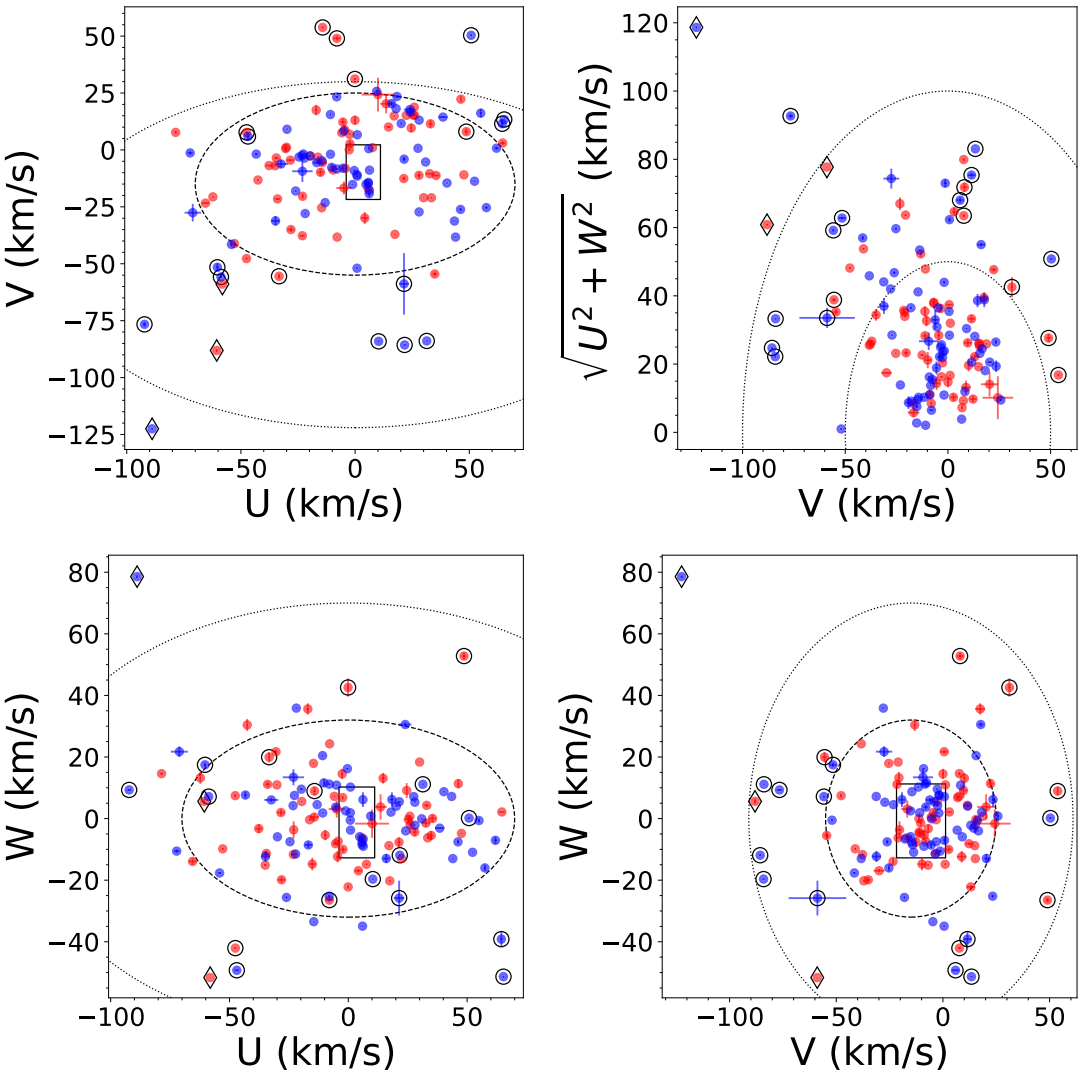

Figure 2.20: Same as Figure 2.11 for the late-M (red) and L dwarfs (blue) in my kinematic sample. The thick disk sources ($P[\mathrm{TD}]/P[\mathrm{D}] > 10$) are highlighted as open diamonds.

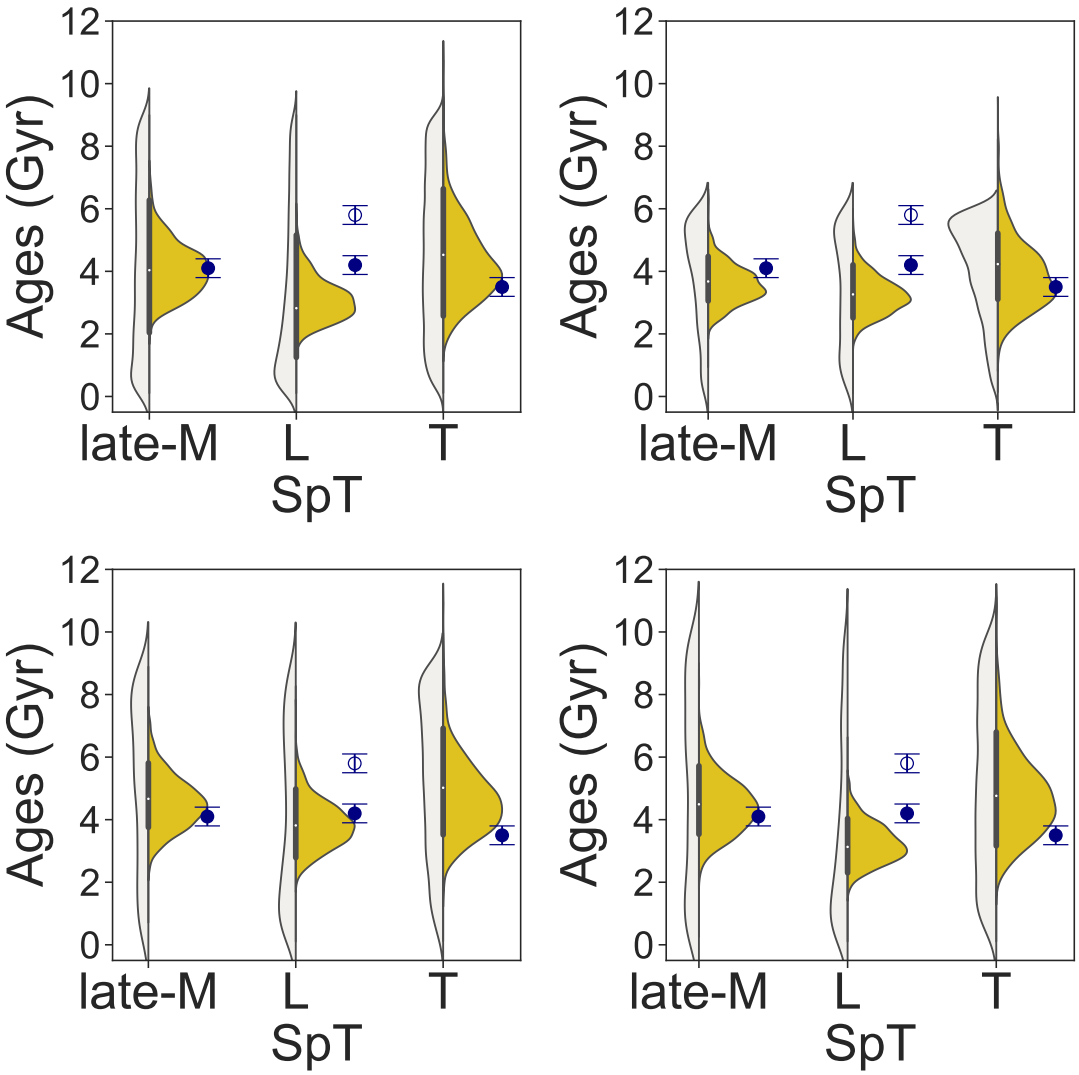

Figure 2.21: Simulated age distributions (white/yellow violin plots for individual/inferred ages, respectively) and measured kinematic ages (offset blue points and sampling uncertainties indicated) for all (empty blue points) and thin disk ($P(\mathrm{TD})/P(\mathrm{D}) \leq 1$; solid blue point) late-M, L, and T dwarfs. Panels are for simulations that assume a mass function $dN/dM \propto M^{-0.5}$, Baraffe et al. (2003) evolutionary models, and the following star formation rates and population ages: *Upper left*: constant birthrate over 9 Gyr (baseline simulation); *Upper right*: Rujopakarn et al. (2013) cosmic birthrate over 6 Gyr; *Lower left*: Aumer & Binney (2009) exponential birthrate over 9 Gyr; *Lower right*: constant birthrate over 12 Gyr.

Table 2.9: Velocity Dispersions and Group Kinematic Ages of Late-M and L Dwarfs at Local 20 pc

Sample	N[a]	$\langle U \rangle$ (km s^{-1})	$\langle V \rangle$ (km s^{-1})	$\langle W \rangle$ (km s^{-1})	σ_U (km s^{-1})	σ_V (km s^{-1})	σ_W (km s^{-1})	σ_{tot} (km s^{-1})	Age (Gyr)	Note
late-M dwarfs	65	-4.7 ± 3.9	-6.8 ± 3.0	0.5 ± 2.1	31.9 ± 0.3	24.8 ± 0.4	17.3 ± 0.3	43.9 ± 0.6	4.9 ± 0.3	Unweighted
					34.1 ± 0.5	27.7 ± 0.5	21.2 ± 0.7	48.8 ± 0.5	4.4 ± 0.1	$\|W\|$ Weighted
late-M dwarfs No Youth	60	-4.8 ± 4.2	-6.9 ± 3.3	0.0 ± 2.3	32.5 ± 0.4	25.8 ± 0.4	17.9 ± 0.4	45.2 ± 0.7	5.3 ± 0.3	Unweighted
					33.9 ± 0.6	28.4 ± 0.6	22.2 ± 1.0	49.5 ± 0.7	4.5 ± 0.1	$\|W\|$ Weighted
late-M dwarfs NTD[b]	63	-3.7 ± 3.8	-4.5 ± 2.8	1.0 ± 2.0	30.5 ± 0.4	22.1 ± 0.4	16.3 ± 0.3	41.0 ± 0.6	4.1 ± 0.3	Unweighted
					34.5 ± 0.6	24.5 ± 0.4	18.1 ± 0.4	46.0 ± 0.5	3.9 ± 0.1	$\|W\|$ Weighted
late-M dwarfs D[c]	63	-3.7 ± 3.8	-4.5 ± 2.8	1.0 ± 2.0	30.5 ± 0.3	22.1 ± 0.3	16.3 ± 0.3	41.0 ± 0.6	4.1 ± 0.3	Unweighted
					34.5 ± 0.6	24.4 ± 0.4	18.1 ± 0.4	46.0 ± 0.5	3.9 ± 0.1	$\|W\|$ Weighted
L dwarfs	71	0.6 ± 4.2	-12.8 ± 3.5	-1.4 ± 2.2	35.8 ± 0.4	29.7 ± 0.5	18.7 ± 0.3	50.1 ± 0.7	7.1 ± 0.4	Unweighted
					46.6 ± 0.8	46.8 ± 1.5	24.3 ± 0.5	70.4 ± 1.6	8.3 ± 0.3	$\|W\|$ Weighted
L dwarfs NTD[b]	70	1.9 ± 4.1	-11.2 ± 3.2	-2.6 ± 1.9	34.4 ± 0.4	26.8 ± 0.5	16.2 ± 0.3	46.5 ± 0.7	5.8 ± 0.3	Unweighted
					39.1 ± 0.5	30.8 ± 1.1	18.9 ± 0.4	53.3 ± 0.8	5.2 ± 0.1	$\|W\|$ Weighted
L dwarfs NB[d]	67	3.8 ± 4.0	-10.8 ± 3.2	-3.3 ± 2.0	33.0 ± 0.4	26.0 ± 0.5	16.1 ± 0.3	45.0 ± 0.7	5.3 ± 0.3	Unweighted
					38.4 ± 0.6	30.2 ± 1.1	19.2 ± 0.3	52.5 ± 0.8	5.1 ± 0.1	$\|W\|$ Weighted
L dwarfs No Youth	57	0.9 ± 5.0	-12.4 ± 4.3	-1.7 ± 2.7	38.1 ± 0.5	32.5 ± 0.7	20.4 ± 0.5	54.0 ± 1.0	8.8 ± 0.6	Unweighted
					48.5 ± 1.2	49.8 ± 2.5	25.6 ± 0.8	74.1 ± 2.6	8.9 ± 0.4	$\|W\|$ Weighted
L dwarfs No Binary	63	0.7 ± 4.6	-12.7 ± 3.7	-1.2 ± 2.4	36.7 ± 0.5	29.4 ± 0.7	19.2 ± 0.5	50.8 ± 1.0	7.4 ± 0.5	Unweighted
					47.7 ± 1.2	47.1 ± 2.8	25.3 ± 0.9	71.6 ± 2.8	8.5 ± 0.5	$\|W\|$ Weighted
L dwarfs No Binary D[c]	58	2.0 ± 4.3	-7.7 ± 2.8	-1.8 ± 2.0	33.0 ± 0.4	21.2 ± 0.7	15.4 ± 0.3	42.1 ± 0.9	4.4 ± 0.3	Unweighted
					37.0 ± 0.7	21.5 ± 1.6	18.3 ± 0.4	46.5 ± 1.0	4.0 ± 0.2	$\|W\|$ Weighted
L dwarfs D[c]	65	1.5 ± 4.0	-7.2 ± 2.6	-1.8 ± 1.9	32.5 ± 0.4	20.9 ± 0.6	15.3 ± 0.3	41.5 ± 0.8	4.2 ± 0.3	Unweighted
					36.3 ± 0.6	22.0 ± 1.4	17.6 ± 0.4	46.0 ± 0.9	3.9 ± 0.2	$\|W\|$ Weighted
L0–L5 dwarfs	57	3.3 ± 5.0	-14.3 ± 4.2	-1.3 ± 2.6	37.6 ± 0.5	31.6 ± 0.6	19.9 ± 0.5	53.0 ± 0.9	8.3 ± 0.5	Unweighted
					49.9 ± 1.3	49.6 ± 2.5	26.0 ± 0.9	75.0 ± 2.7	9.0 ± 0.5	$\|W\|$ Weighted
L0–L5 dwarfs D[c]	51	4.8 ± 4.7	-7.3 ± 3.0	-1.8 ± 2.2	33.6 ± 0.5	21.4 ± 0.3	15.9 ± 0.3	42.9 ± 0.7	4.6 ± 0.3	Unweighted
					38.8 ± 0.8	20.3 ± 0.5	18.5 ± 0.4	47.6 ± 0.7	4.1 ± 0.1	$\|W\|$ Weighted
L6–L9 dwarfs	14	-10.5 ± 6.5	-6.7 ± 4.9	-1.9 ± 3.3	24.0 ± 2.1	18.4 ± 3.3	12.6 ± 1.0	32.8 ± 4.0	2.2 ± 0.8	Unweighted
					26.0 ± 1.9	26.8 ± 6.0	15.1 ± 1.8	40.5 ± 4.9	3.0 ± 0.8	$\|W\|$ Weighted
L0–L1 dwarfs	26	10.1 ± 6.9	-12.7 ± 5.3	-4.5 ± 3.7	34.9 ± 1.1	27.2 ± 1.1	18.8 ± 0.7	48.1 ± 1.7	6.4 ± 0.7	Unweighted
					45.7 ± 1.4	31.0 ± 1.8	24.9 ± 0.8	60.6 ± 1.3	6.5 ± 0.2	$\|W\|$ Weighted
L1–L2 dwarfs	28	8.8 ± 6.6	-15.0 ± 4.7	-3.6 ± 3.5	34.8 ± 0.9	25.0 ± 1.0	18.3 ± 0.6	46.6 ± 1.5	5.8 ± 0.6	Unweighted
					43.7 ± 1.3	31.0 ± 1.7	22.4 ± 0.9	58.1 ± 1.4	6.1 ± 0.3	$\|W\|$ Weighted
L2–L3 dwarfs	16	-0.9 ± 8.7	-13.0 ± 4.5	-1.3 ± 3.7	34.5 ± 1.3	18.0 ± 0.8	14.6 ± 0.9	41.6 ± 1.8	4.2 ± 0.6	Unweighted
					35.7 ± 2.0	28.1 ± 1.9	14.4 ± 1.1	47.7 ± 2.1	4.2 ± 0.4	$\|W\|$ Weighted
L3–L4 dwarfs	13	8.6 ± 7.6	-7.4 ± 7.2	-1.1 ± 3.4	27.4 ± 1.3	25.8 ± 1.7	11.9 ± 1.8	39.5 ± 2.8	3.7 ± 0.8	Unweighted
					28.9 ± 1.7	28.6 ± 3.5	15.6 ± 3.3	43.7 ± 2.5	3.5 ± 0.4	$\|W\|$ Weighted

Table 2.9 (*continued*)

Table 2.9 (*continued*)

Sample	N[a]	$\langle U \rangle$ (km s^{-1})	$\langle V \rangle$ (km s^{-1})	$\langle W \rangle$ (km s^{-1})	σ_U (km s^{-1})	σ_V (km s^{-1})	σ_W (km s^{-1})	σ_{tot} (km s^{-1})	Age (Gyr)	Note
L4–L5 dwarfs	15	-3.9 ± 11.0	-18.3 ± 12.0	4.3 ± 6.4	42.2 ± 2.4	46.1 ± 2.6	24.4 ± 2.7	67.1 ± 4.4	16.2 ± 3.0	Unweighted
					57.2 ± 7.3	72.9 ± 11.0	39.5 ± 6.2	100.8 ± 14.3	12.9 ± 2.0	$\|W\|$ Weighted
L4–L5 dwarfs NB[d]	12	11.1 ± 8.1	-7.6 ± 10.3	-3.7 ± 4.2	27.6 ± 2.5	35.5 ± 2.6	14.5 ± 1.4	47.2 ± 3.9	6.1 ± 1.4	Unweighted
					26.6 ± 3.1	32.1 ± 3.9	17.9 ± 2.6	45.6 ± 3.1	3.8 ± 0.5	$\|W\|$ Weighted
L4–L5 dwarfs D[c]	12	8.4 ± 8.2	0.8 ± 7.9	-1.0 ± 4.5	28.2 ± 2.1	27.2 ± 1.8	15.6 ± 1.3	42.2 ± 3.1	4.4 ± 1.0	Unweighted
					25.1 ± 2.4	20.3 ± 2.1	19.4 ± 2.1	37.7 ± 2.3	2.5 ± 0.4	$\|W\|$ Weighted
L5–L6 dwarfs	15	-14.1 ± 11.1	-22.0 ± 11.2	1.4 ± 6.9	42.7 ± 1.8	43.3 ± 2.5	26.7 ± 2.5	66.4 ± 4.0	15.8 ± 2.7	Unweighted
					50.6 ± 5.2	69.0 ± 8.7	32.4 ± 4.5	91.5 ± 10.8	11.6 ± 1.6	$\|W\|$ Weighted
L5–L6 dwarfs NB[d]	11	-3.7 ± 10.5	-8.0 ± 9.2	-5.5 ± 5.1	34.9 ± 2.5	30.0 ± 3.7	16.7 ± 1.4	48.9 ± 4.7	6.8 ± 1.8	Unweighted
					29.7 ± 2.5	30.0 ± 3.4	16.5 ± 0.9	45.5 ± 2.8	3.8 ± 0.5	$\|W\|$ Weighted
L5–L6 dwarfs D[c]	12	-4.4 ± 9.7	-3.8 ± 7.0	-4.5 ± 5.4	33.4 ± 2.3	24.1 ± 3.2	18.6 ± 1.2	45.2 ± 4.2	5.4 ± 1.4	Unweighted
					28.3 ± 1.8	28.3 ± 5.1	17.1 ± 0.8	43.7 ± 3.7	3.5 ± 0.6	$\|W\|$ Weighted
L6–L7 dwarfs	10	-11.8 ± 8.2	-8.7 ± 6.1	-3.5 ± 4.2	25.7 ± 2.9	18.9 ± 4.5	13.3 ± 1.4	34.6 ± 5.5	2.6 ± 1.2	Unweighted
					27.2 ± 2.5	28.6 ± 7.5	16.3 ± 2.2	43.1 ± 6.1	3.4 ± 1.0	$\|W\|$ Weighted
L6–L7 dwarfs NB[d]	9	-15.4 ± 8.2	-3.1 ± 3.5	-1.0 ± 3.9	24.1 ± 3.7	10.2 ± 2.0	11.6 ± 1.2	28.6 ± 4.3	1.5 ± 0.7	Unweighted
					23.1 ± 3.8	14.3 ± 2.9	13.3 ± 2.1	30.6 ± 2.6	1.5 ± 0.3	$\|W\|$ Weighted
L7–L8 dwarfs	7	-11.1 ± 7.4	-1.4 ± 3.5	2.5 ± 3.4	19.1 ± 2.1	8.7 ± 2.7	8.7 ± 1.2	22.8 ± 3.6	0.7 ± 0.4	Unweighted
					21.4 ± 3.3	10.8 ± 3.1	7.6 ± 1.2	25.3 ± 4.0	0.9 ± 0.4	$\|W\|$ Weighted
L7–L8 dwarfs NB[d]	6	-9.7 ± 8.4	-1.2 ± 4.0	1.3 ± 3.7	20.2 ± 2.1	9.3 ± 3.1	8.9 ± 1.3	24.0 ± 3.9	0.8 ± 0.5	Unweighted
					24.5 ± 4.2	11.3 ± 3.6	8.2 ± 1.3	28.3 ± 4.9	1.2 ± 0.6	$\|W\|$ Weighted
L8–L9 dwarfs	4	-7.5 ± 9.7	-1.9 ± 7.1	2.2 ± 4.4	18.1 ± 2.8	12.9 ± 3.9	7.7 ± 3.4	23.6 ± 5.9	0.9 ± 0.7	Unweighted
					20.3 ± 3.1	14.4 ± 3.7	7.6 ± 3.7	26.6 ± 2.7	1.0 ± 0.3	$\|W\|$ Weighted
L8–L9 dwarfs NB[d]	3	-3.4 ± 12.1	-1.7 ± 9.5	-0.2 ± 5.2	15.9 ± 8.3	13.3 ± 5.5	6.8 ± 4.1	21.8 ± 10.8	1.0 ± 1.3	Unweighted
					19.2 ± 8.7	12.6 ± 5.0	5.5 ± 3.6	25.6 ± 4.0	0.9 ± 0.4	$\|W\|$ Weighted

Ages for unweighted velocities are computed from equation (2.8) using the parameters in Aumer & Binney (2009). Ages for $|W|$-weighted velocities are computed from equation (2.6) using the parameters in Wielen (1977).

[a] Number of sources in sample

[b] Excluding thick disk sources

[c] Thin disk sources only

[d] Excluding unusual blue L dwarfs

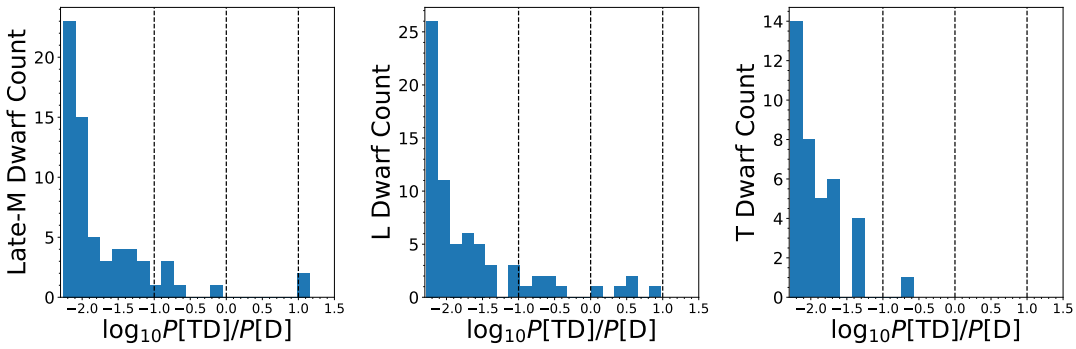

Figure 2.22: Distributions of log probability ratios of thick/thin disk (TD/D) sources for late-M, L, and T dwarfs, respectively. The vertical dashed lines denote the probability ratios of 0.1, 1, and 10, respectively.

2.5.3 Vertical Action Dispersion

Vertical action (J_Z) measures the excursion of momentum perpendicular to the Galactic plane, which is invariant under orbital evolution provided that the Galactic potential is axisymmetric and perturbations are on average planar. The Galactic potential does have non-axisymmetric components, such as the spiral arms, interior bar, and giant molecular clouds above and below the Galactic disk, all of which can perturb J_Z and the planar actions J_R and J_ϕ (Beane et al. 2018; Ting & Rix 2019). Nevertheless, it has been argued that vertical action may be a better physical quantity to probe statistical ages for stellar populations than *UVW* velocities (Kiman et al. 2019; Ting & Rix 2019).

Vertical actions and their dispersion can be computed directly from 6D spatial and velocity coordinates. I used *galpy* (Bovy 2015) to calculate J_Z, using a Galactocentric solar position of $(R_\odot, Z_\odot) = (8.2, 0.025)$ kpc, an LSR Galactic circular velocity at the solar radius of $v_\phi(R_\odot) = 240$ km s^{-1} (Ting & Rix 2019), and the LSR solar velocity vector used above. The position and circular velocity used here differ from my prior assumptions in Section 2.4.2 in order to align my analysis with that of Ting & Rix (2019).

By analyzing the APOGEE-*Gaia* DR2 red clump giant sample (Ting et al. 2018;

Gaia Collaboration et al. 2018b), Ting & Rix (2019) derived an empirical relation to estimate kinematic age from the mean vertical action $\widehat{J_Z}$ (kpc km s^{-1}) as a function of mean Galactic radius $\overline{R}_{GC}$ (kpc) and age τ for a star:

$$\begin{aligned}\widehat{J_Z}(\overline{R}_{GC},\tau) &= \widehat{J}_{Z,0}(\overline{R}_{GC}) + \Delta\widehat{J}_{Z,1}\mathrm{Gyr}\left(\frac{\tau}{1\mathrm{Gyr}}\right)^{\gamma(\overline{R}_{GC})} \\ &= (0.91 + 0.18\Delta R_{GC} + 0.087\Delta R_{GC}^2 \\ &+ 0.014\Delta R_{GC}^3) \\ &+ (1.81 + 0.050\Delta R_{GC})\tau^{1.09+0.060\Delta R_{GC}},\end{aligned} \tag{2.9}$$

where $\Delta R_{GC} = \overline{R}_{GC} - 8$ kpc, $\overline{R}_{GC} = \frac{(R_{GC}+R_{birth})}{2}$, R_{birth} is the birth Galactic radius, and R_{GC} is the current Galactic radius. Since I cannot determine the birth radii for the sample, I simply use $\overline{R}_{GC} = R_{GC}$.

The Ting & Rix (2019) relation turns out to be problematic for this sample, as the zero-age baseline vertical action $\widehat{J}_{Z,0}(\overline{R}_{GC}) = 0.95$ kpc km s^{-1} is greater than the J_Z values of 66% of my sample, resulting in negative ages for these sources. Applying equation (2.9) to the remaining sources yields vertical action ages of 1.9 ± 2.7 Gyr for late-M dwarfs (1.7 ± 2.3 Gyr for thin disk), 2.3 ± 2.5 Gyr for L dwarfs (1.9 ± 2.1 Gyr for thin disk), and 0.9 ± 0.7 Gyr for T dwarfs. These values are similar to the age of 2.7 ± 2.2 Gyr inferred from vertical action analysis of late-M and L dwarfs with SDSS spectra by Kiman et al. (2019), and both are considerably younger than the ages inferred from velocity dispersions. These age estimates are likely in error, as the Ting & Rix (2019) relations produce negative ages for a significant fraction of the stars in my sample. I therefore discard these age determinations as absolute measures, but note that the relative consistency of ages for thin disk late-M, L, and T dwarfs is concurrent with my velocity dispersion analysis.

2.5.4 Comparison to Simulated Populations

Baseline Simulations

To evaluate whether the kinematic ages determined here are consistent with my understanding of the formation and evolution of UCDs, I conducted a Monte-Carlo population simulation for local thin disk late-M, L, and T dwarfs. I simulated 10^5 sources assuming a uniform spatial distribution and a uniform star formation rate over 0.1 Gyr $\leq \tau \leq$ 9 Gyr, with masses sampling the range $0.01\,M_{\odot} \leq M \leq 0.15\,M_{\odot}$[22] drawn according to a power-law initial mass function

$$\frac{dN}{dM} \propto M^{-\alpha}, \tag{2.10}$$

where M is mass, N is the number density of stars in the local volume, and α is a power-law index. I chose a baseline value $\alpha = 0.5$, which is roughly consistent with UCD populations in young clusters (Bastian et al. 2010) and the local Galactic environment (Kirkpatrick et al. 2019, 2021). I used the evolutionary models of Baraffe et al. (2003) to convert ages and masses into effective temperatures ($T_{\rm eff}$), and assigned spectral types (SpT) using the empirical SpT-$T_{\rm eff}$ relation of Filippazzo et al. (2015). *UVW* space velocities in the LSR were then assigned based on age, by assuming[23] $UVW = 0$ at $\tau = 0$ and drawing from normal distributions in all three components using widths based on the Aumer & Binney (2009) age-dispersion relations for each axis of motion. For the *V*

[22]The choice of lowest-mass 0.01 $M_{\odot}$ is limited by evolutionary models for the field sample. Saumon & Marley (2008) models have the lowest-mass 0.01 $M_{\odot}$ that evolve to 10 Gyr. A 10 $M_{\rm Jup}$ T dwarf is relatively young (Baraffe 2003 models for $T_{\rm eff}$ = 953 K and mass = 0.01 $M_{\odot}$ = 100 Myr), so it is unlikely that lower mass objects will be significant contributors to the field sample.

[23]This is consistent with my kinematic analysis for the observed sample; see Sections 2.5.1 and 2.5.2 for more details.

Table 2.10: Simulated UCD Population Parameters

Sample	Simulated Age[a] (Gyr)	$\langle U \rangle$ (km s^{-1})	$\langle V \rangle$ (km s^{-1})	$\langle W \rangle$ (km s^{-1})	Kinematic Age (Gyr)
late-M dwarfs	4.1	1 ± 4	-13 ± 3	0 ± 2	4.1 ± 0.8
L dwarfs	2.8	0 ± 4	-11 ± 3	0.1 ± 1.7	3.1 ± 0.7
T dwarfs	4.6	0 ± 6	-14 ± 4	0 ± 3	4.3 ± 1.2

Note – Ages for simulated populations are computed from equation (2.8) using the parameters in Aumer & Binney (2009), with sampling errors accounted for using a Jackknife test statistic; see Section 2.5.4.
[a] Median simulation age $< \tau >$

velocity, I also added a time-dependent asymmetric drift term (Aumer & Binney 2009):

$$V_a = \frac{-\sigma_U^2(\tau)}{74\,\mathrm{km\,s^{-1}}} = 23.7\Big(\frac{\tau}{10\ \mathrm{Gyr}}\Big)^{0.614}\ \mathrm{km\ s^{-1}}. \tag{2.11}$$

From this simulated (and assumed volume-complete) velocity sample, I computed the kinematic ages of UCD spectral subgroups using the same analysis as that of my observational sample. I simulated sample selection effects by making 1,000 random draws of $N_\mathrm{s} - 1$ sources from the simulated population, where N_s corresponds to the sizes of my late-M, L, and T dwarf RV samples (63, 65, and 36 sources, respectively) and -1 corresponds to the Jackknife sampling. The median values and standard deviations from this sampling are summarized in Table 2.10 and Figure 2.23.

The resulting kinematic ages are 4.1 ± 0.8 Gyr, 3.1 ± 0.7 Gyr, and 4.3 ± 1.2 Gyr for late-M, L, and T dwarfs, respectively. These ages are statistically equivalent, although the L dwarfs are about 1 Gyr younger on average. The relatively large uncertainties highlight the importance of sampling effects. Comparing to the kinematic ages of the observed thin disk sample, I find excellent agreement for the late-M and T dwarfs, but significant disagreement ($\Delta\tau$ = 4.0 Gyr, 5.0σ deviation) compared to the full sample of L dwarfs. However, if I exclude potential thick disk sources ($P[\mathrm{TD}]/P[\mathrm{D}] > 1$), the discrepancy for the L dwarfs is significantly reduced ($\Delta\tau$ = 1.1 Gyr) with only marginal

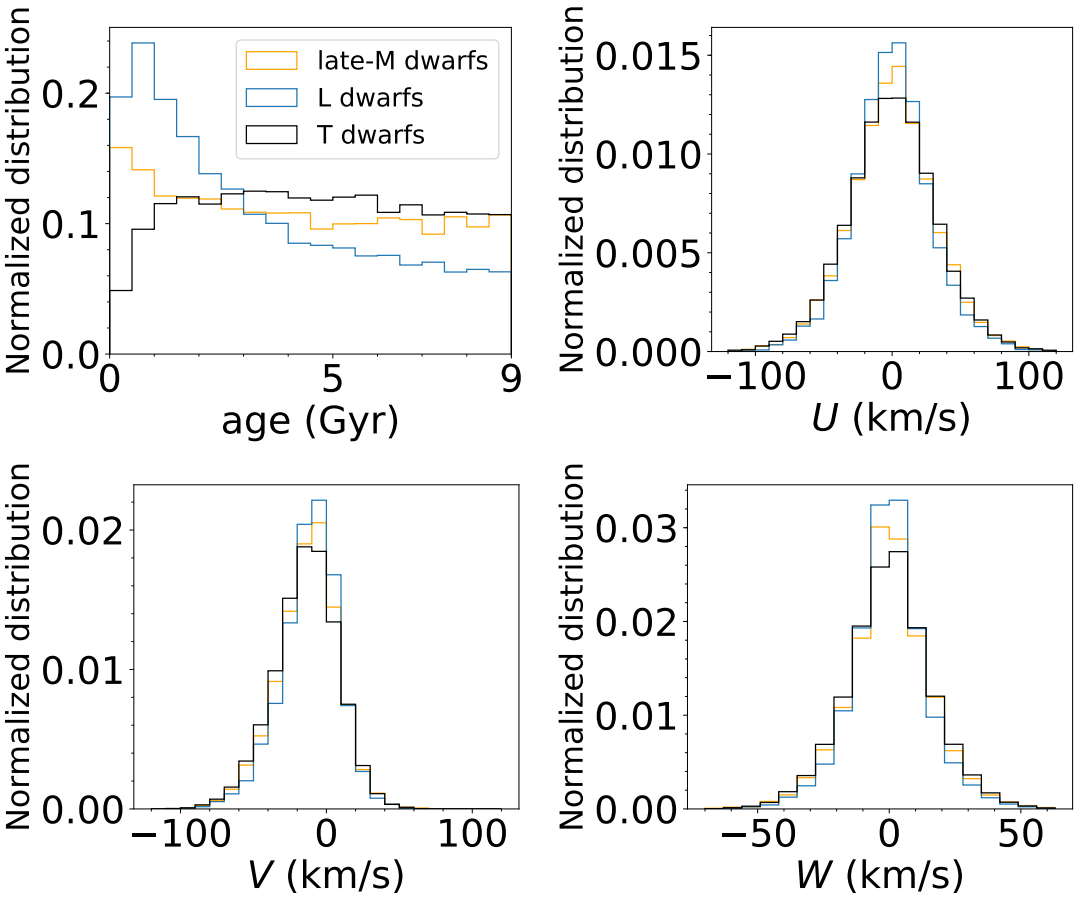

Figure 2.23: Normalized distributions of ages (upper-left) and *UVW* space motions for my baseline simulated population. Distributions are segregated between late-M (orange), L (blue), and T dwarfs (black).

significance of deviation (1.4σ). Again, accounting for potential thick disk sources appears to mostly resolve the previously identified discrepancy between observed and simulated ages for L dwarfs, although my baseline simulations still predict a young L dwarf population compared to late-M and T dwarfs.

Variations on Simulated Populations

The modest disagreement between simulated and observed kinematics suggests the need for some fine-tuning of simulation parameters as they relate to the kinematics of late-M, L, and T dwarfs. To explore this, I evaluated the the influence of following simulation parameters on the ages of the late-M, L, and T dwarf disk population:

- *Star formation rate (SFR)*: In addition to a uniform star formation rate, I examined an exponentially declining birth rate, SFR $\propto e^{\gamma\tau}$, where $\gamma = 0.117$ Gyr^{-1} and τ is age in Gyr (Aumer & Binney 2009); and a star formation rate that reflects cosmic star formation history, SFR $\propto (1+z(\tau))^{\beta}$, where z is the redshift and $\beta = 3.5$ (Rujopakarn et al. 2010; Planck Collaboration et al. 2016).

- *Mass function*: I examined additional power-law relations with $\alpha = -1.5$, -0.5, and +1.5; and two cases of an age-dependent mass function: $\alpha = 0.0 \Rightarrow +1.0$ and $\alpha = +1.0 \Rightarrow 0.0$ 10 Gyr in the past[24] (cf. Burgasser et al. 2015a). I also examined a log-normal mass function from Chabrier (2003).

- *Choice of brown dwarf evolution model*: In addition to the Baraffe et al. (2003) evolutionary models, I evaluated the models of Burrows et al. (2001), Saumon & Marley (2008), Marley et al. (2018), and Phillips et al. (2020).

[24]The cosmological star formation rate peaks at $z \sim 2$, corresponding to a cosmic age of $\sim$3 Gyr ($\sim$10 Gyr in the past) under the standard ΛCDM cosmology (Madau & Dickinson 2014). The star formation rate of the inner Milky Way (R $\leq$ 10 kpc) peaks at $\sim$z = 1–3 ($\sim$8–12 Gyr ago) (Haywood et al. 2016).

- *Maximum simulation age*: In addition to the baseline maximum age of 9 Gyr, I considered maximum ages of 6 Gyr and 12 Gyr.

- *Minimum brown dwarf mass (MBDM)*: The lowest-mass brown dwarfs are also the youngest in the L dwarf phase, which may skew simulated ages downward. I considered additional minimum masses for my simulation of 0.02 $M_\odot$ and 0.03 $M_\odot$ to explore this effect.

For computational expediency, the number of simulated sources used for these simulations was 10^4 versus 10^5 for my baseline simulations. Varying each of these parameters individually, I produced 578 additional simulations. For Marley et al. (2018) and Phillips et al. (2020) models, I only ran the simulations for uniform star formation rate, α = 0.5 and minimum brown dwarf mass of 0.01 $M_\odot$. I quantified the agreement of the simulations to the observations using a χ^2 statistic:

$$\chi^2 = \Sigma_i \frac{(\tau_{\mathrm{obs},i} - \tau_{\mathrm{sim},i})^2}{\sigma^2_{\tau_{\mathrm{obs},i}} + \sigma^2_{\tau_{\mathrm{sim},i}}} \tag{2.12}$$

with τ_{obs} and τ_{sim} being the observed and simulated ages, σ_{obs} and σ_{sim} the observed and simulated age uncertainties, and i = late-M, L, and T dwarf thin disk samples (P[TD]/P[D] $\leq$ 1). A select set of the results discussed here are summarized in Table 2.11. All simulations are fully compiled in Table B.1.

Table 2.11: Select Simulated UCD Population Ages Under Different Assumptions

τ (Gyr)	Star formation (rate)	α	Models	MBDM ($M_\odot$)	late-M dwarf age (Gyr)	L dwarf age (Gyr)	T dwarf age (Gyr)	χ^2
Observations								
ALL SOURCES					4.9 ± 0.3	7.1 ± 0.4	3.5 ± 0.3	···
NOT THICK DISK (P(TD)/P(D) < 10)					4.1 ± 0.3	5.8 ± 0.3	3.5 ± 0.3	···
THIN DISK (P(TD)/P(D) < 1)					4.1 ± 0.3	4.2 ± 0.3	3.5 ± 0.3	···
Simulations								
9[a]	uniform	0.5	B03	0.01	4.1 ± 0.8	3.1 ± 0.7	4.3 ± 1.2	2.1
9	uniform	0.5	B01	0.01	3.5 ± 0.7	3.1 ± 0.6	4.2 ± 1.2	3.0
9	uniform	0.5	S08	0.01	4.3 ± 0.8	3.4 ± 0.7	4.5 ± 1.2	1.7
9	uniform	0.5	M19	0.01	1.6 ± 0.3	3.1 ± 0.6	4.0 ± 1.1	42.1

Table 2.11 (*continued*)

Table 2.11 (*continued*)

τ (Gyr)	Star formation (rate)	α	Models	MBDM ($M_\odot$)	late-M dwarf age (Gyr)	L dwarf age (Gyr)	T dwarf age (Gyr)	χ^2
9	uniform	0.5	P20C	0.01	0.2 ± 0.0	2.6 ± 0.5	4.2 ± 1.2	172.0
9	uniform	0.5	P20NW	0.01	0.3 ± 0.0	2.6 ± 0.6	4.3 ± 1.2	162.3
9	uniform	0.5	P20NS	0.01	0.4 ± 0.0	2.7 ± 0.6	4.1 ± 1.2	154.4
9	exponential	0.5	B03	0.01	4.5 ± 0.8	3.8 ± 0.8	4.7 ± 1.2	1.3
9	exponential	0.5	B01	0.01	3.6 ± 0.6	3.7 ± 0.7	4.9 ± 1.4	1.7
9	exponential	0.5	S08	0.01	4.6 ± 0.8	4.2 ± 0.8	4.8 ± 1.2	1.5
9	log-normal	0.5	B03	0.01	6.8 ± 1.3	6.1 ± 1.0	6.5 ± 1.6	11.6
9	log-normal	0.5	B01	0.01	7.4 ± 1.3	6.0 ± 1.0	6.2 ± 1.5	12.7
9	log-normal	0.5	S08	0.01	6.4 ± 1.0	6.2 ± 1.1	6.4 ± 1.6	11.3
9[b]	exponential	0.0/1.0/3.0	B03	0.01	5.3 ± 1.0	5.0 ± 0.9	4.2 ± 1.2	2.5
9[c]	exponential	1.0/0.0/3.0	B03	0.01	4.2 ± 0.7	4.8 ± 0.8	5.2 ± 1.3	2.3
9[d]	uniform	0.5	B03	0.01	4.0 ± 0.8	3.0 ± 0.6	3.8 ± 1.1	2.8
9[e]	uniform	0.5	B03*	0.01	4.1 ± 0.8	4.1 ± 0.8	4.4 ± 1.2	0.5
9[c]	uniform	1.5/−0.5/3.0	B03	0.01	3.4 ± 0.6	3.5 ± 0.7	5.0 ± 1.2	3.2
9[c]	uniform	1.5/−0.5/4.5	B03	0.01	2.9 ± 0.6	3.5 ± 0.7	5.4 ± 1.4	5.6
9[c]	uniform	1.5/−0.5/6.0	B03	0.01	3.2 ± 0.7	3.4 ± 0.7	4.3 ± 1.1	2.7

Note −− Kinematics ages computed using the Aumer & Binney (2009) relation and the procedure described in Section 2.5.4. τ is the maximum age of the sample, α is the mass function power law index ($\frac{dN}{dM} = M^{-\alpha}$), MBDM is the minimum brown dwarf mass. Evolving mass functions are labeled in the order of early α, late α, and age (in Gyr) of transition. A log-normal mass function from Chabrier (2003) is labeled as "log-normal". Star formation rates considered in my simulations: uniform, exponential (Aumer & Binney 2009), and cosmic star formation rate (Rujopakarn et al. 2010). Brown dwarf evolution models are B03 (Baraffe et al. 2003), B01 (Burrows et al. 2001), S08 (Saumon & Marley 2008), M19 (Marley et al. 2018), and P20 (Phillips et al. 2020). For the last model set, C, NW, and NS stand for chemical equilibrium, weak, and strong chemical disequilibrium, respectively. Note that only substellar models are available in the P20 set. See Table B.1 in Appendix B for the full list of simulations.

[a] Baseline simulation

[b] Simulations with an evolving mass function from top-heavy to bottom-heavy over time using Baraffe et al. (2003) evolutionary models. See Section 2.5.4 for details.

[c] Simulations with an evolving mass function from bottom-heavy to top-heavy over time using Baraffe et al. (2003) evolutionary models. See Section 2.5.4 for details.

[d] Baseline simulation with selection within 20 pc and J or $K < 15.5$. See Section 2.6.1 for details.

[e] Simulation with an artificial decrease in the HBMM for the Baraffe et al. (2003) evolutionary models by fixing the temperatures of brown dwarfs down to masses of 0.060 $M_\odot$ to their 1 Gyr values. See Section 2.5.4 for details.

Several simulations are consistent with the observed ages, which provides some constraints on the local UCD formation history. To explore these, I first compared the results for a fixed power-law mass function with α = 0.5 and MBDM = 0.01 $M_\odot$. Figure 2.24 shows the χ^2 distribution for different SFRs and evolved ages for each of the Baraffe et al. (2003), Burrows et al. (2001), and Saumon & Marley (2008) models. The diagonal elements of the simulations show the best agreements with the observed ages, which are cosmic/6 Gyr, exponential/9 Gyr, and uniform/12 Gyr, with the second of these being consistently best between the models. These parameters generally produce similar ages for late-M, L, T populations, with L dwarfs being slightly younger and T dwarfs being slightly older. The agreement between these parameter sets indicates a clear degeneracy between the SFR and population age that cannot be resolved by this coarse kinematic age

comparison, although I are able to strongly rule out some combinations. For example, the cosmic/12 Gyr SFR/age combination can be ruled out to high probability using a BIC test (ΔBIC > 10, highly significant).

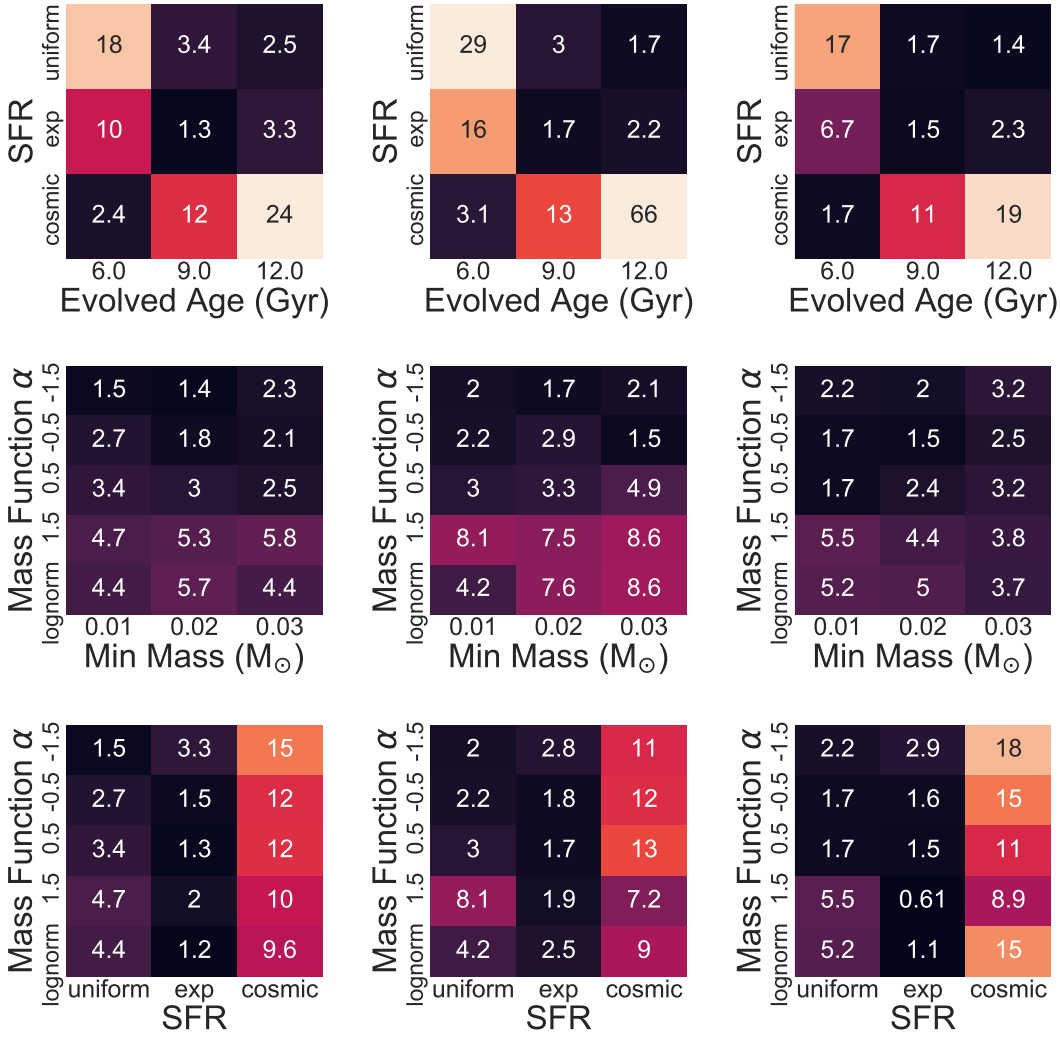

Figure 2.24: χ^2 distributions of simulated populations as a function of (1) *top row:* star formation rate (SFR) and evolved age; (2) *middle row:* minimum brown dwarf mass and mass function; (3) *bottom row:* star formation rate (SFR) and mass function across brown dwarf evolution models: *left column:* Baraffe et al. (2003); *middle column:* Burrows et al. (2001); *right column:* Saumon & Marley (2008). Lower χ^2 values have darker color.

Holding the SFR and sample age fixed to my baseline parameters, I compared the mass function power-law index to the MBDM (Figure 2.24 middle panels). The mass

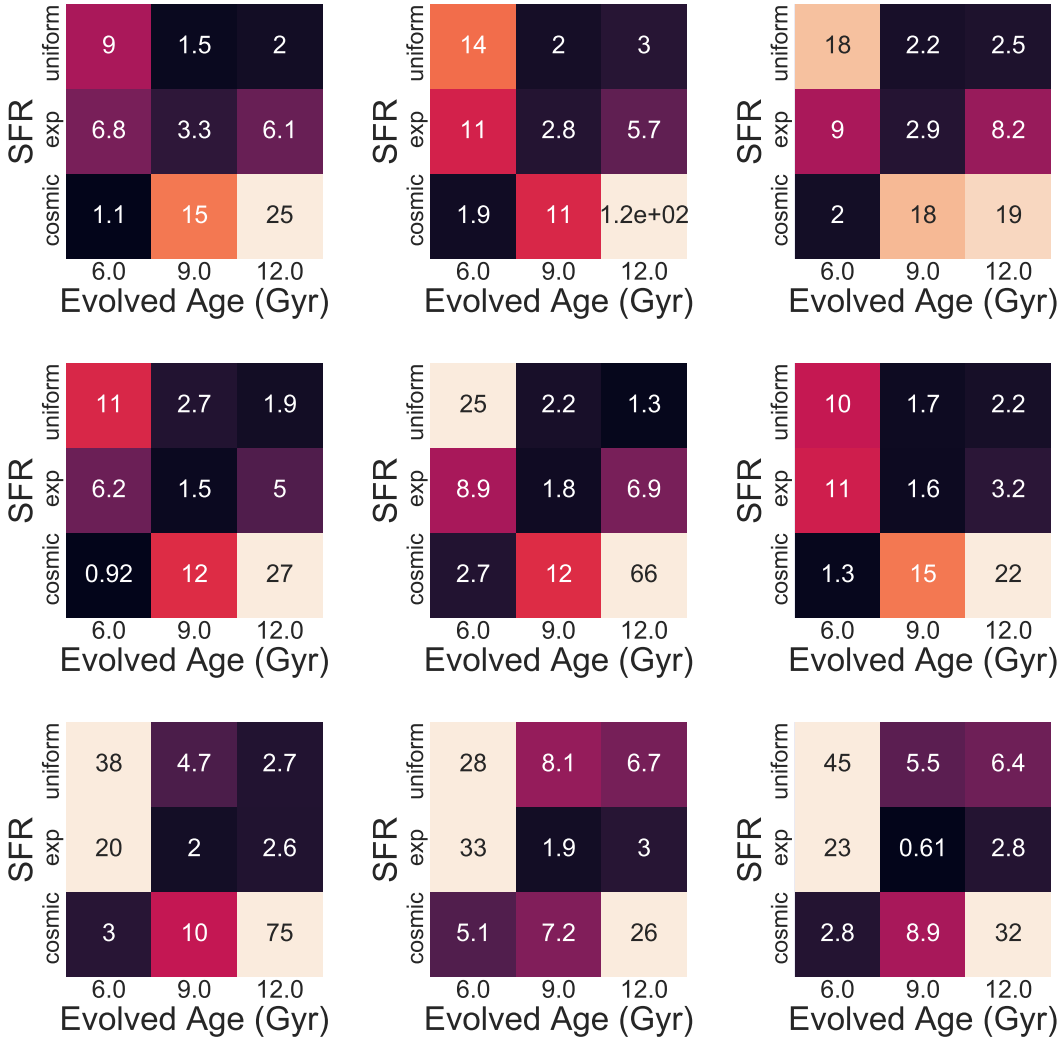

Figure 2.25: Same as Figure 2.24 top panel for $\alpha = -1.5$ (top), -0.5 (middle) and 1.5 (bottom).

functions with α = 0.5, -0.5, and -1.5 are statistically equivalent, while the bottom-heavy α = 1.5 and log-normal mass functions are not favored (ΔBIC > 2, positive; also see Figure 2.25). The results are insensitive to MBDM or evolutionary models. I also compared the SFR and mass function for a fixed age of 9 Gyr and MBDM = 0.01 $M_\odot$ (Figure 2.24 bottom panels). Models using the cosmic star formation rate are significantly worse than other models. Again, the mass functions α = 0.5, -0.5, and -1.5 are statistically equivalent, while α = 1.5 and log-normal mass functions using the uniform star formation rate are not favored (ΔBIC > 2, positive).

Burgasser et al. (2015a) considered whether the observed older L dwarfs in their sample could be the outcome of a mass function that evolves from bottom-heavy to top-heavy over time (i.e., α decreasing over time). Figure 2.26 shows that the original hypothesis $\alpha = 1.5 \rightarrow -0.5$ at 4.5 Gyr is not consistent with the observed ages of late-MLT dwarfs (χ^2 = 5.6; ΔBIC = 3.5), overestimating in particular the ages of T dwarfs (5.4 $\pm$ 1.4 Gyr). However, scenarios with the same transition in at different transition ages (3 Gyr and 6 Gyr) are consistent (ΔBIC ≤ 2). Similarly, a narrower range of mass function of evolution, either $\alpha = 0 \rightarrow 1$ or $\alpha = 1 \rightarrow 0$ with uniform and exponential birth rates cannot be ruled out (ΔBIC ≤ 2; Figure 2.27).

Comparing the outcomes of different evolutionary models, I found the predictions of the Burrows et al. (2001), Saumon & Marley (2008), and Baraffe et al. (2003) models yield roughly identical results. Late-M dwarf ages using the Marley et al. (2018) and Phillips et al. (2020) cloudless atmosphere models were too young compared to L and T dwarfs, likely due to temperature limits in the model parameter space. I also found that increasing the maximum age or minimum brown dwarf mass in the simulations increased the mean ages of ultracool dwarfs, but retained the relative ages for late-M, L, and T dwarfs.

Errors in evolutionary models could contribute to the marginal age discrepancy

between simulations and observations for the L dwarfs. The ratio of L-type stars and brown dwarfs and the thermal evolution of the most massive brown dwarfs depends on the efficiency of hydrogen fusion reactions close to the critical temperature. An offset in the HBMM, particularly toward lower masses so that more L dwarfs are stars, could potentially increase the ages of L dwarfs in the simulations. To explore this effect, I imposed an artificial decrease in the HBMM for the Baraffe et al. (2003) evolutionary models by fixing the temperatures of brown dwarfs with masses $M \geq 0.06$ $M_{\odot}$ to their 1 Gyr values. The resulting ages for late-M, L, and T dwarfs in these simulations are 4.1 ± 0.8 Gyr, 4.1 ± 0.8 Gyr, 4.4 ± 1.2 Gyr, respectively, fully consistent with my observed ages (Figure 2.28). The fact that this adjustment provides the best match between the simulations and observed sources is suggestive of potential evolutionary model issues, which have also been raised with mass and luminosity measurements of brown dwarf companions to age-dated stars (Dupuy & Liu 2017) and the surprisingly high masses T-type brown dwarfs in binaries (e.g. Dupuy et al. 2019; Brandt et al. 2020; Sahlmann et al. 2020, 2021). These studies suggest that evolutionary model predictions of the temperatures and luminosities of objects around the HBMM may not align with the observed properties of these systems. However, with only a marginal age discrepancy, potential selection biases in my L dwarf kinematic sample (see below), and the degeneracies present among other simulation parameters, further work is needed to confirm this result. I note that increasing the timescale of cooling could also produce older L-type brown dwarfs, but also drives up the ages of T dwarfs and is therefore an unlikely scenario.

In summary, several variations in simulation parameters were able to reproduce the observed kinematic ages of the local late-M, L, and T dwarf populations self-consistently, and highlight some degeneracies in this approach. Nevertheless, I are able to rule out several parameter sets, and identify a potential indicator of a lower

HBMM.

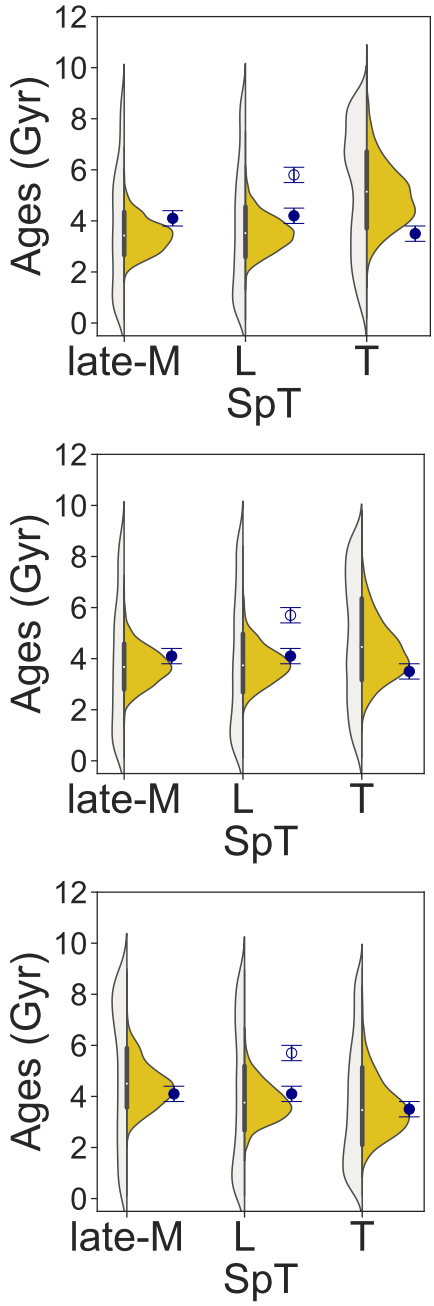

Figure 2.26: Same as Figure 2.21 comparing three simulations with baseline parameters and mass functions that evolve over time: (Top) $\alpha = 1.5 \rightarrow -0.5$ (bottom-heavy to top-heavy; same model as Burgasser et al. 2015a); (Middle) $\alpha = 1 \rightarrow 0$ (bottom-heavy to top-heavy); and (Bottom) $\alpha = 0 \rightarrow 1$ (top-heavy to bottom-heavy).

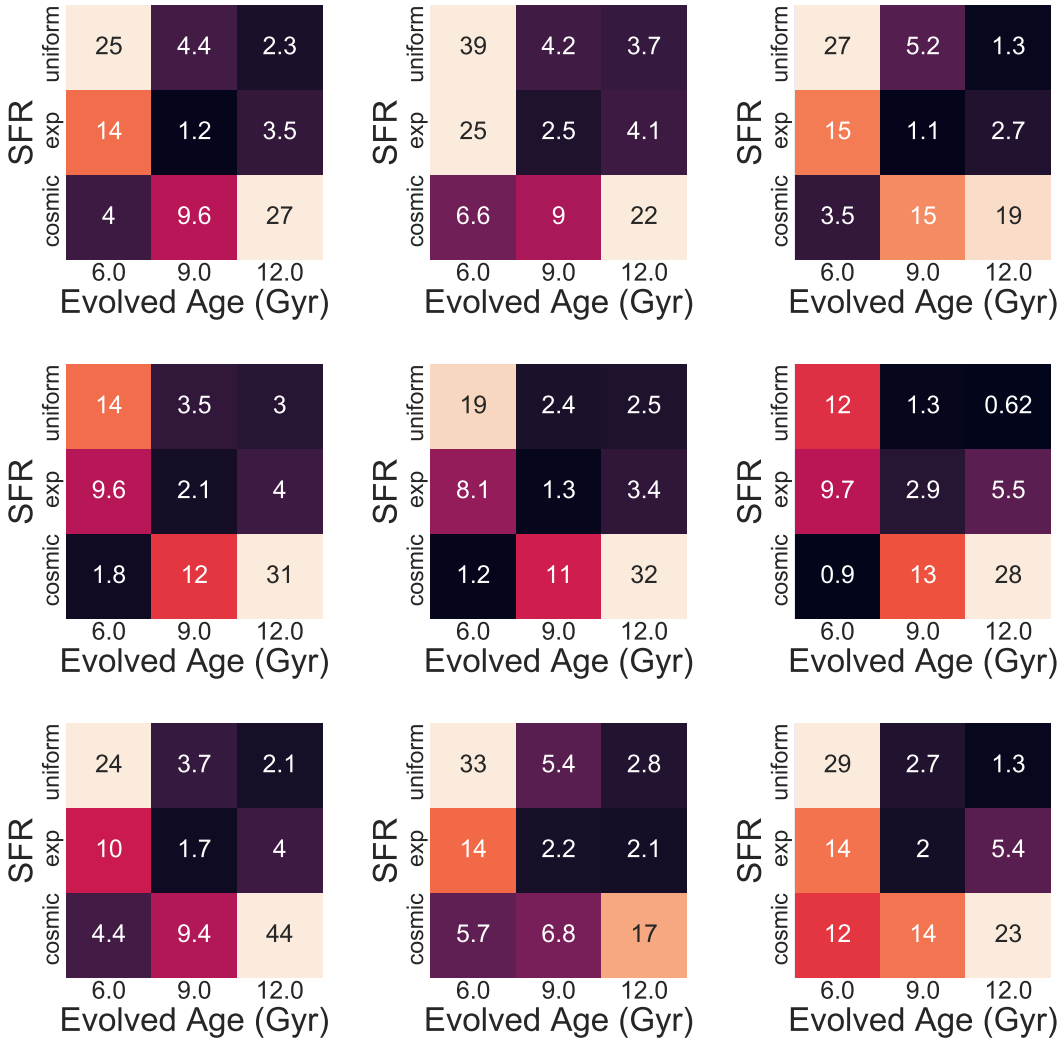

Figure 2.27: Same as Figure 2.24 top panel for the Chabrier et al. (2000) log-normal mass function (top), and for evolving mass functions $\alpha = 0 \rightarrow 1$ at 3 Gyr (middle) and $\alpha = 1 \rightarrow 0$ at 3 Gyr (bottom).

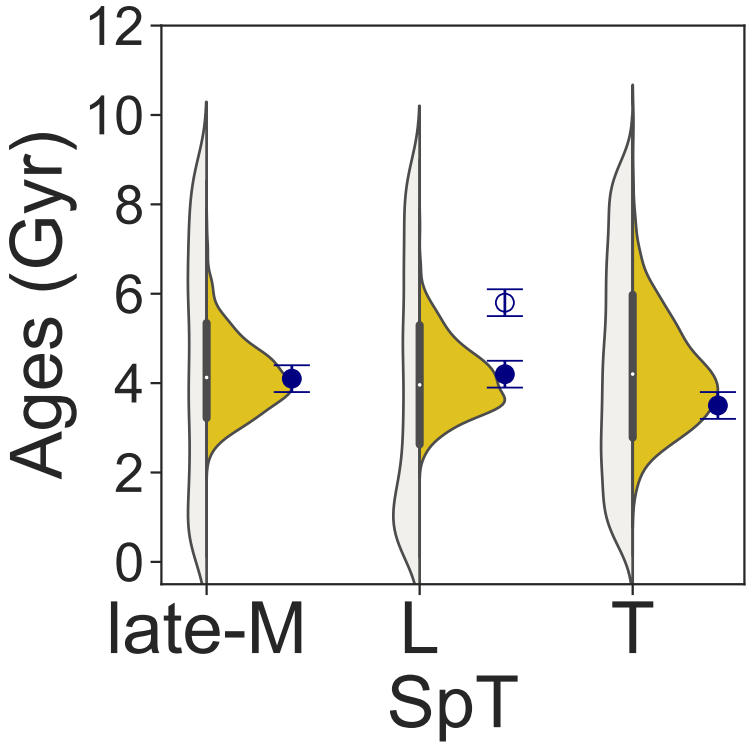

Figure 2.28: Same as Figure 2.21, comparing observed kinematic ages to a simulation assuming baseline parameters and a hydrogen burning minimum mass with an artificial decrease for the Baraffe et al. (2003) evolutionary models by fixing the temperatures of brown dwarfs with masses $M \geq 0.06$ $M_{\odot}$ to their 1 Gyr values.

2.6 Discussion

While my simulations are able to reproduce the kinematic ages of UCDs in the local thin disk population, the origin of the relatively high fraction of local thick disk L dwarfs remains unclear. As L dwarfs span the HBMM, in the local Galactic environment they consist of a mixed population of stars and (young) brown dwarfs. Accurate characterization of this population is therefore critical for validating brown dwarf evolutionary models and measuring brown dwarf formation history in the Galaxy. Here I explore some possible explanation as to why the local L dwarf sample studied in this paper are less well-modeled as compared to local late-M and T dwarfs.

2.6.1 Sample incompleteness

The kinematic sample examined in this study, while larger than previous studies and limited to $d < 20$ pc, is not uniformly volume complete. One primary reason for this is that fainter late-L and T dwarfs are detected at smaller distances for a given sensitivity limit. For Keck/NIRSPEC, an effective magnitude limit of 15 restricts observations of L5 dwarfs to 22 pc (K-band) and T5 dwarfs to 14 pc (J-band). RV measurements from the literature are also not volume- or magnitude-complete, as measurements were obtained with different optical and near-infrared spectrographs with varying sensitivity thresholds.

The underlying target sample is itself not volume-complete, either, particularly in the Galactic plane where nearby ultracool dwarfs sample smaller scale heights, and are hence younger, but where source contamination and crowding is high. Bardalez Gagliuffi et al. (2019b) determined that the sample of late-M and early- to mid-L dwarfs is 62^{+8}_{-7}% and 83^{+10}_{-9}% complete within 20 pc, and new nearby sources are still being uncovered in wide-field surveys such as PanSTARRS (Best et al. 2020), *Gaia* (Faherty et al. 2018; Reylé 2018; Scholz 2020), and *WISE* (Meisner et al. 2020; Kirkpatrick

et al. 2021). Figure 2.19 compares my simulated population to the 20 pc samples of Bardalez Gagliuffi et al. (2019b, hereafter BG19), Best et al. (2020, hereafter B20), and Kirkpatrick et al. (2021, hereafter K21). While these UCD samples are the most volume-complete constructed to date, there remain gaps particularly among the late-M, late-L, and T dwarfs. My kinematic sample contains 48%–52% of the 20 pc UCDs in the BG19 and B20 samples, and based on these studies' completeness estimates, only 32%–42% of M7–T8 dwarfs within 20 pc. Compared to K21, my sample contains only 27% of L0–T8 dwarfs within 20 pc.

One way this incompleteness can produce an age discrepancy is if the fraction of early-type and late-type L dwarfs in my sample is imbalanced. Early-type L dwarfs are predominantly low-mass stars of all ages and very young brown dwarfs, while late-type L dwarfs are predominantly young brown dwarfs, according to my simulations and the data. Figure 2.29 illustrates this trend in my kinematic sample, which shows a clear decline in velocity dispersion and inferred age as a function of L dwarf spectral subclass, with the exception of the L4–L6 subtypes (discussed in further detail below). More coarsely, while the overall kinematic age of thin disk L dwarfs is 4.2 ± 0.3 Gyr, the kinematic age of 14 L6–L9 dwarfs is only 2.2 ± 0.8 Gyr. I computed the ratio of L0–L5 to L5–L9 dwarfs in my baseline simulation sample, my kinematic sample, the samples of B20 and K21, and the combined sample of BG19 and B20. These ratios were found to be 1.3 (simulated), 4.1 (kinematic sample, L0–L5:L5–L9 = 57:14), 1.0 (B20, L0–L5:L5–L9 = 21:22), 1.3 (K21, L0–L5:L5–L9 = 96:75), and 3.3 (B19+B20, L0–L5:L5–L9 = 105:32), respectively. My kinematic sample is clearly biased toward early L dwarfs compared to the simulated, B20, and K21 samples, but not compared to the combined B19 and B20 sample. However, if I try to reproduce the kinematic sample asymmetry through forced random draws from my baseline simulation, I find an average age for thin disk L dwarfs (3.0 ± 0.6 Gyr) that is still younger than observed. Similarly, sampling with replacement

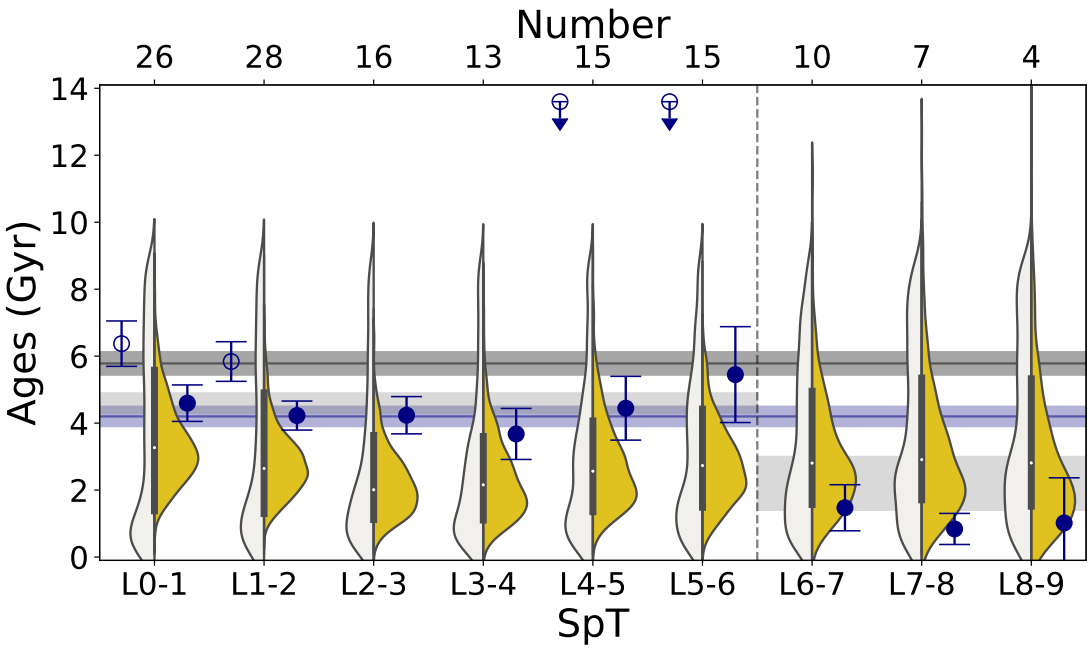

Figure 2.29: Age distributions of L dwarfs from the baseline simulation binned in groupings of two subtypes compared to measured kinematic ages with similar binning. Simulated age distributions are shown as individual source ages (white violin plots) and derived kinematic ages (yellow violin plots). Observed kinematic ages are shown with (open blue points) and without (solid blue points) L dwarfs for $P[\mathrm{TD}]/P[\mathrm{D}] > 1$. My derived kinematic ages and uncertainties (5.8±0.3 Gyr, 4.2±0.3 Gyr) for my nominal L dwarf sample ($P[\mathrm{TD}]/P[\mathrm{D}] < 10$) are indicated by the black line, and for my constrained thin disk sample ($P[\mathrm{TD}]/P[\mathrm{D}] < 1$) by the blue line. I also show the average kinematic ages for early- and late-L dwarfs separately as grey bands. The number of sources in each subtype bin is labeled at top. The ages of the discrepant L4–L5 and L5–L6 subtype bins are due to four unusually blue L dwarfs within these groups. Note that the very old tails of inferred ages for L6–L9 are due to small sampling effect.

the thin disk L dwarfs from my kinematic sample to force a ratio of early-to-late L dwarfs of 1.3 (simulations) or 1.0 (B20) results a nearly identical age (4.1 ± 0.8 Gyr) as the original sample.

My sample is also biased toward early T dwarfs due to the intrinsic faintness of later subtypes, with an early-to-late T dwarf ratio (T0–T4/T5–T8) of 1.0, much higher than the most recent T dwarf sample from K21 (0.14) and my baseline population simulation (0.22). Again, if I randomly draw from the simulation to match the spectral type ratio of the observed kinematic sample, I find an older but statistically equivalent age of 4.3 ± 1.2 Gyr. Drawing from the kinematic sample to match the simulation T dwarf spectral type ratio yields a nearby identical age of 3.5 ± 0.2 Gyr.

Another selection bias is the magnitude limit of the observed kinematic sample, which can similarly skew the number of early-type and later-type L dwarfs. I modeled this in my baseline simulation by assigning distances up to 20 pc over a uniform-density volume, assigning apparent magnitudes using the Dupuy & Liu (2012) absolute magnitude-spectral type relations, and constraining the simulated sample to be brighter than J or $K < 15$. The resulting magnitude-limited simulated late-M, L, and T dwarf kinematic ages are 4.0 ± 0.8 Gyr, 3.0 ± 0.6 Gyr, and 3.8 ± 1.1 Gyr, respectively, fully consistent with my baseline simulation. Hence, a magnitude limit does not explain the older age for L dwarfs in the kinematic sample. A magnitude-limited sample can preferentially select younger sources, which haven't fully contracted to their fully degenerate radii. This would affect all sources in my sample, but particularly those subgroups whose limiting magnitudes place them within the volume limit. This bias may explain the slightly younger kinematic age of T dwarfs compared to the simulations, but does not explain the presence of older L dwarfs in the kinematic sample.

2.6.2 Contamination by Distinct Sub-populations

My kinematic L dwarf sample contains eight L-type binaries, fourteen young L dwarfs and four unusually blue L dwarfs, the latter based on the color outlier criteria of Faherty et al. (2009)[25]. Like the thick disk population, these distinct sub-populations have the potential of skewing the kinematic dispersions and ages of the overall sample, so I re-evaluated the velocity dispersions and kinematic ages of the L dwarfs after removing each of these subgroups (Table 2.9). Removal of young L dwarfs and binaries increases the age of the total population to 8.8 ± 0.6 Gyr and 7.4 ± 0.5 Gyr. The former is expected as removal of young sources makes the population older while the latter is consistent with no change (when thick disk stars are left in). Removal of blue L dwarfs reduces the kinematic age to 5.3 ± 0.3 Gyr, consistent with removal of thick disk stars. This result confirms the interpretation that unusually blue features are associated with higher surface gravities and/or lower metallicities, both of which correlate with older ages. I also examined whether removing L dwarfs with ages younger than 500 Myr in my baseline simulation would elevate the ages of the remaining sources; only a marginal shift to 3.4 ± 0.7 Gyr was found. Finally, I considered the age without the binaries (8 sources) for my thin disk L dwarf sample, which results in a slightly older but statistically consistent age of 4.4 ± 0.3 Gyr.

2.6.3 Evidence of a Kinematic Indicator of the Main Sequence Terminus

Kinematic variations as a function of spectral type, rather that across whole subclasses, provides a finer examination of UCD ages. Prior simulation work has predicted

[25]The blue L dwarfs in my sample are 2MASS J05395200−0059019 (Geballe et al. 2002), DENIS J112639.9−500355 (Phan-Bao et al. 2008), 2MASSI J1721039+334415 (Bardalez Gagliuffi et al. 2014), and 2MASS J05395200−0059019 (Fan et al. 2000).

subtype age structure particularly among the L dwarfs due to brown dwarf evolutionary effects and the changing mixture of stars and brown dwarfs with spectral type (cf. Burgasser 2004). At late-M and early L subtypes, only the youngest and most massive brown dwarfs will have temperatures consistent with these types, restricting their representation among the overall sample and resulting in a relatively low brown dwarf-to-star ratio. As I proceed to later types, the mass range of stars with the appropriate temperatures declines, while both the age and mass range of allowed brown dwarfs expands, increasing the brown dwarf-to-star ratio. Since these brown dwarfs are preferentially young, this changing ratio drives down the average age of the population. At late enough spectral types, temperatures become sufficiently low that stars are not present, resulting in a "pure" brown dwarf sample that is relatively young but increases in mean age through the T and Y dwarf sequences.

As a preliminary assessment of these effects, I examined a more refined breakdown of L dwarfs by subtype. Figure 2.29 displays the observed kinematic ages and simulation predictions of thin disk L dwarfs broken down in bins of two subtypes. Both observations and simulations confirm an overall downward trend of age with later spectral type, declining from 5.8 ± 0.6 Gyr at L1–L2 to 0.9 ± 0.7 Gyr for L8–L9. However, in the L4–L5 and L5–L6 subtypes this downward trend briefly reverses, with the latter having an average age of 5.4 ± 1.4 Gyr. I note that this increase is present even with the removal of both thick-disk and unusually blue L dwarfs, which are clustered among these mid-L subtypes. The simulations show a concurrent reversal in average kinematic age, skewed by an older population of stars near the HBMM. By spectral type L6–L7, the observed kinematic ages drop back to the downward trend line, while the simulations show a more modest decrease in mean age and a broadened distribution of ages overall.

I interpret this newly-discerned "kinematic break" around spectral types L5–L6 to be an observable of the terminus of the stellar Main Sequence. The effective temperature

range of L5–L6 dwarfs, 1500 K $\lesssim T_{\rm eff} \lesssim$ 1600 K (Filippazzo et al. 2015), corresponds to evolutionary model predictions for the HBMM at ages of 4–5 Gyr (Baraffe et al. 2003), in rough agreement with the average age of the local UCD population. Dupuy & Liu (2017) identify a similar HBMM boundary at slightly earlier spectral types of L3–L5 based on the distribution of 38 dynamical mass measurements from binaries; while Dieterich et al. (2014) anchor the HBMM at $\sim$2075 K, corresponding to L1–L2 subtypes, based on an inferred radius minimum. The differences among these empirical indicators of the HBMM may reflect both sample variations and sensitivity to specific brown dwarf indicators. For example, the L1–L2 range may represent a threshold in the brown dwarf-to-star ratio in the field population, while the L5-L6 range represents the disappearance of stars entirely. I emphasize that all of these subtype samples are small and need to be expanded to confirm and quantify these empirical indicators of the transition between stars and brown dwarfs in the Galactic field population.

2.6.4 Refining Constraints on UCD Population Parameters

The segregation of kinematic ages by subtype also provides an opportunity to more finely constrain population parameters, albeit with lower statistical accuracy. In particular, the age distribution of the underlying population plays a specific role in setting the relative balance of stars and brown dwarfs, and the terminus of the Main Sequence, within the L dwarf class. To explore these effects, I compared a subset of my simulations to two subtype breakdowns of my kinematic sample. Following Section 2.5.4, I evaluated variations in SFR and population age with the MF, minimum mass, and evolutionary model fixed to my baseline assumptions. Here I compare these to my thin disk L dwarf sample in groups of two subtypes, and my overall sample in groups of three subtypes to account for the small sample for T dwarfs. Figures 2.30 and 2.31 shows the χ^2 distributions and best-fit distributions of simulated kinematic ages for these comparisons.

For the L dwarf sample, I find the cosmic/9 Gyr SFR/age combination provides the best overall fit, exceeding my baseline model (ΔBIC > 10, highly significant) but consistent with the exponential/9 Gyr (ΔBIC = 2.3, positive) and exponential/12 Gyr (ΔBIC = 1.0, not significant). I can now rule out the cosmic/6 Gyr SFR/age combination by a BIC test (ΔBIC > 10, highly significant). For the UCD sample, the exponential/9 Gyr SFR/age combination provides the best overall fit, exceeding my baseline model (ΔBIC = 3.2, positive) but consistent with the uniform/12 Gyr model (ΔBIC = 1.4, not significant). Therefore, exponential/9 Gyr combination gives consistently the best fit for both forms of sample binning.

The refinement of the population parameters from this analysis is clearly limited, a consequence of the small sample statistics and the necessity to average over spectral types. Nevertheless, these outcomes show that a larger and more complete kinematic sample broken down by subtype could break some of the simulation parameter degeneracies and lead to a well-constrained assessment of the local UCD population properties, particularly in conjunction with other observable distributions such as the luminosity function and independent age or mass diagnostics.

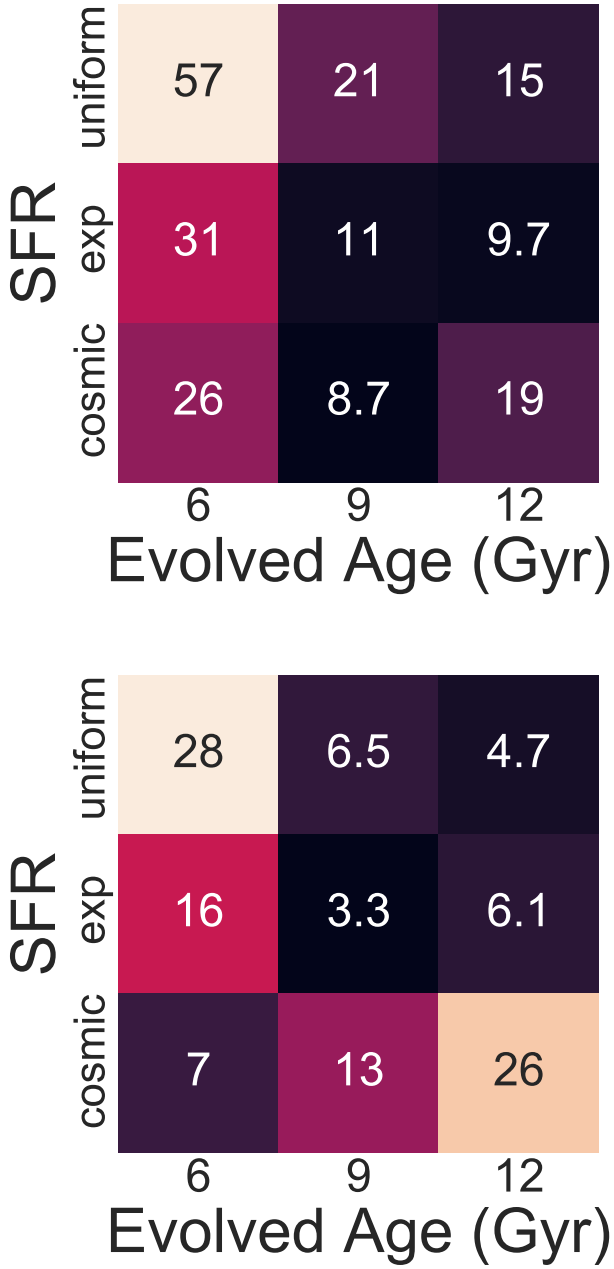

Figure 2.30: χ^2 distributions of simulated populations as a function of star formation rate (SFR) and evolved age for the L dwarf subtype (top) and UCD subtype samples (bottom). All simulations assume a power-law mass function with $\alpha = 0.5$, Baraffe et al. (2003) evolutionary models, and minimum mass of 0.01 $M_{\odot}$.

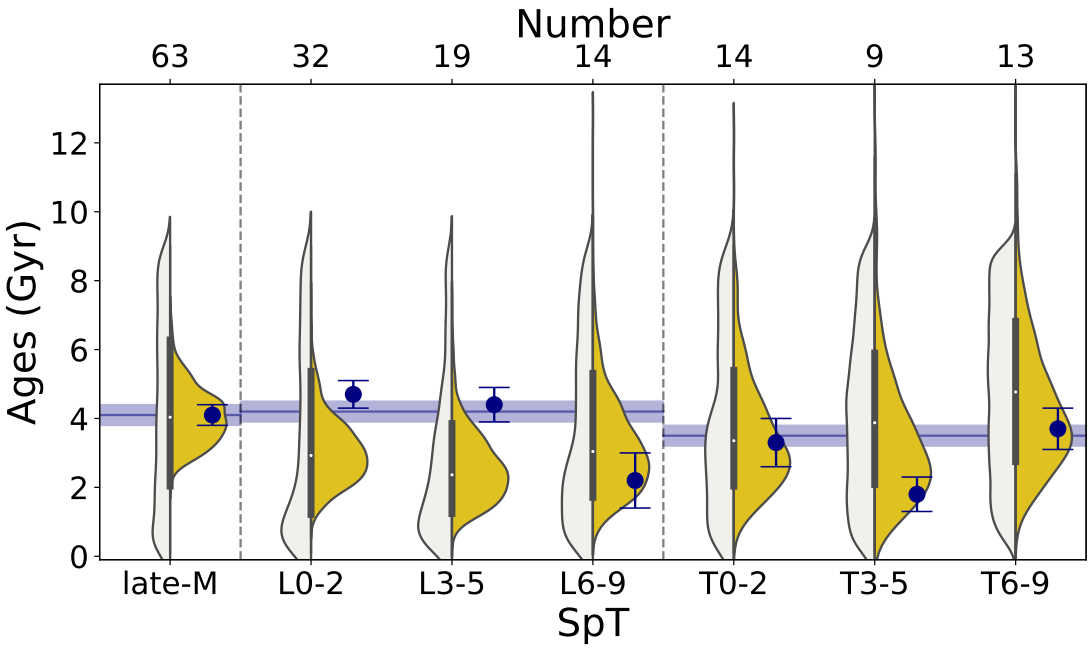

Figure 2.31: Observed kinematic ages of thin-disk UCDs in my kinematic sample grouped into bins of three subtypes (solid blue points) compared to similarly-binned best-fit simulation predictions using a power-law mass function with $\alpha = 0.5$, Baraffe et al. (2003) evolutionary models, minimum mass of 0.01 $M_{\odot}$, the Aumer & Binney (2009) exponential SFR, and a population age of 9 Gyr (white/yellow violin plots for simulated ages/inferred population kinematic ages). The derived kinematic ages and uncertainties for the late-M, L, and T dwarf subgroups are indicated by blue bands. The number of sources in each subtype bin is labeled at top.

Chapter 2, in full, is a reprint of the material as it appears in the Astrophysical Journal Supplement Series 2021, Volume 257, Number 45. Hsu, Chih-Chun; Burgasser, Adam J.; Theissen, Christopher A.; Gelino, Christopher R.; Birky, Jessica L.; Diamant, Sharon J. M.; Bardalez Gagliuffi, Daniella C.; Aganze, Christian; Blake, Cullen H., Faherty, Jacqueline K. The thesis author was the primary investigator and author of this paper.

Chapter 3

SDSS/APOGEE

3.1 APOGEE Sample

My ML dwarf sample is curated from SDSS/APOGEE DR17 (Abdurro'uf et al. 2022) based on observations obtained with the 2.5m Sloan Foundation Telescope at the Apache Point Observatory (Gunn et al. 2006) and 2.5m-meter du Pont Telescope at the Las Campanas Observatory (Bowen & Vaughan 1973). My targets were proposed from SDSS-III Project 176 (PI: Suvrath Mahadevan and Cullen Blake) titled "A Radial Velocity Survey of Bright M Dwarfs with APOGEE: Companions, vsini, Fe/H" and SDSS-IV Project 0288 (PI: Adam Burgasser) titled "APOGEE-2 and eBOSS Observations of the Lowest-Mass Stars and Brown Dwarfs in the Solar Neighborhood" as the M dwarf Ancillary Program. I start with `allStar-dr17-synspec.fits` to curate my sample (while I fit individual apVisit spectra; see Section 3.2). I constructed two UCD samples for my analysis: a comprehensive sample selected using color and magnitude criteria, and a "gold" sample based on sources with literature classifications of M6 and later. The full sample was constructed by matching APOGEE sources to 2MASS (Skrutskie et al. 2006) and *Gaia* EDR3 (Gaia Collaboration et al. 2021) photometry and astrometry. Using the

Gaia $G - G_{\rm RP}$ relation Kiman et al. (2019) and the *Gaia* color-magnitude distribution with the known UCDs in my gold sample, I conservatively selected sources with

- *Gaia* parallaxes $\pi > 2.5$ mas (distances < 400 pc),
- *Gaia* $\mathrm{M}_G > 10$,
- *Gaia* $2.2 > G - G_{\rm RP} > 1.25$, and
- Galactic latitude $|b| > 15^\circ$.

The *Gaia* absolute magnitude and color criteria correspond to spectral types $\gtrsim$M4–M5, while the last criterion is aimed at reducing contamination from reddened background sources. Additionally, I also used 2MASS photometric information and an empirically determined 2MASS J, K and *Gaia* G, $G_{\rm RP}$ color and magnitudes criterion to remove reddened sources:

- $4 > \mathrm{M}_J > 20$,
- $J - K > 0$,
- $$1.25 \times G - G_{\rm RP} + \frac{23}{16} - (G - J) > 0$$

  ,

The reddening cut also removed potentially young sources, but the known young sources with spectral classifications are included in my gold sample.

This sample of 8,055 spectra of 1,563 sources with further reduced by selecting only those APOGEE spectra with median signal-to-noise ratios (SNRs) > 10, resulting in 7,915 spectra of 1,468 sources. My full sample is summarized in Table B.2.

I also created a high-fidelity "gold sample" of APOGEE sources selected on the basis of previous published spectral types of M6 or later, as reported in SIMBAD

(Wenger et al. 2000), the Late-Type Extension to MoVeRS (LaTE-MoVeRS; Theissen et al. 2016, 2017), Reylé (2018), and Best et al. (2021). For my gold sample, I visually inspected each of these sources' SIMBAD and 2MASS coordinates to confirm their UCD status, in particular examining their location on color-magnitude and color-color diagrams combining 2MASS and *Gaia* data (Figure 3.3). Published spectral types are a mixture of photometric and spectroscopic measurements; as discussed below, follow-up spectroscopy of a subset of these sources revealed 28 to be classified earlier than M6 (see below). For the remainder of this study I use the most recent, preferably spectroscopic, classification as my adopted value. The gold sample includes sources in the full sample, plus additional sources that do not satisfy all of the criteria given above, including sources not present in *Gaia*. Indeed, there are 70 sources out of 182 in my gold sample not included in the full sample because of (1) lack of *Gaia* parallax (so no M_G and M_J), (2) sources near the Galactic plane (Galactic $|b| \leq 15°$), (3) removal from the reddening cut (mostly for sources in the Upper Scorpius young cluster. With the SNR > 10 cut, the gold sample is composed of 671 spectra of 182 sources as summarized in Table 3.2.

Figures 3.1, 3.2, and 3.3 summarize the observable properties of my full and gold samples. The distribution of my targets across the sky is highly dependent on APOGEE's survey pointings. Notably, one-third of the gold sample includes known members of nearby young moving groups, targeted as part of the programs listed below (Zasowski et al. 2013, 2017; Beaton et al. 2021; Santana et al. 2021)[1]:

- 'APOGEE_ANCILLARY': Ancillary target,
- 'APOGEE_MDWARF': RVs of M Dwarfs (Blake, Mahadevan, Hearty, Deshpande, Nidever, Bender, Crepp, Carlberg, Terrien, Schneider),
- 'APOGEE2_ANCILLARY': Ancillary target,

[1] https://www.sdss.org/dr17/irspec/apogee-bitmasks/

- ‘APOGEE2_APOKASC’: Ancillary APOKASC faint giants (Pinsonneault),
- ‘APOGEE2_CALIB_CLUSTER’: Selected as calibration cluster member,
- ‘APOGEE2_CIS’: Carnegie program target,
- ‘APOGEE2_CNTAC’: Chilean community target,
- ‘APOGEE2_GAIA_OVERLAP’: Overlap with Gaia,
- ‘APOGEE2_K2’: K2 Galactic Archeology Program Star,
- ‘APOGEE2_MANGA_LED’: Star on a shared MaNGA-led design,
- ‘APOGEE2_MDWARF’: Selected as part of the M dwarf study,
- ‘APOGEE2_NORMAL_SAMPLE’: Selected as part of the random sample,
- ‘APOGEE2_ONEBIN_GT_0_3’: Selected in single $(J-K_{\rm s})o > 0.3$ color bin,
- ‘APOGEE2_SFD_DERED’: Selected with SFD_EBV dereddening,
- ‘APOGEE2_SHORT’: Selected as part of a short cohort,
- ‘APOGEE2_ULTRACOOL’: Ancillary Ultracool Dwarfs Program (Burgasser)
- ‘APOGEE2_YOUNG_CLUSTER’: Selected as part of the young cluster study (IN-SYNC; Covey & Tan)

(see section 3.4.3). My full sample has 19% of the sources previously identified as members of nearby young clusters of moving groups, but it should be noted that only 5.3% of the full sample has spectral classifications in the literature. There are also a handful of gold sample sources located close to the Galactic plane. The majority of my full (92%) and gold sample (70%) sources have distances larger than 30 pc, with the M6.5Ve G 51−15 (2MASS J08294949+2646348) being the closest sources in the

sample at a distance of 3.5810±0.0008 pc. In terms of brightness, the apparent H-band magnitudes of my targets extend to 14.57, which is slightly fainter than the APOGEE magnitude limit of 13.8 for S/N of 100. For the gold sample, spectral types range from M4 to L2, and generally decreases from M6 to later types, with a total of 155 late-M dwarfs and 6 L dwarfs. For the full sample, I used the *Gaia* $G - G_{\rm RP}$ color to spectral type relation in Kiman et al. (2019) to derive their spectral types, which range from M4 to L5, with a total of 268 late-M dwarfs and 61 L dwarfs. Figure 3.3 shows the color-magnitude and color-color relations, as well as the apparent H magnitude distribution. There are two sources with $G - G_{\rm RP} < 1.25$, which are M4 2MASS J15175638+0656388 and M7 2MASS J15512179+2931062. The full sample follows the trend for the gold sample in M_G vs. $G - G_{\rm RP}$, M_G vs. $G - J$, M_G vs. $J - K$, and $G - J$ vs. $J - K$, but has more earlier type dwarfs due to my more conservative selection criteria described above. A similar trend is found in $G - J$ vs. $G - G_{\rm RP}$ with more reddened sources present in the lower corner.

The majority (75%) of my sample have spectral observations taken over multiple epochs, enabling more precise determinations of radial velocities and the possibility of measuring radial velocity variations. I define multi-epoch subsamples in my full and gold samples as those sources with at least four observations satisfying SNR > 10 separated by a day or more. These subsamples include 527 sources in the full sample and 52 sources in the gold sample.

Note that the requirement for a *Gaia* detection likely resulted in the rejection of true UCDs in the APOGEE DR17 sample due to sensitivity limitations (Theissen 2018), while APOGEE targeting was not intended to be uniform across the sky (Zasowski et al. 2013). My APOGEE UCD sample is therefore not expected to be area- or volume-complete, but rather representative of the broader UCD population.

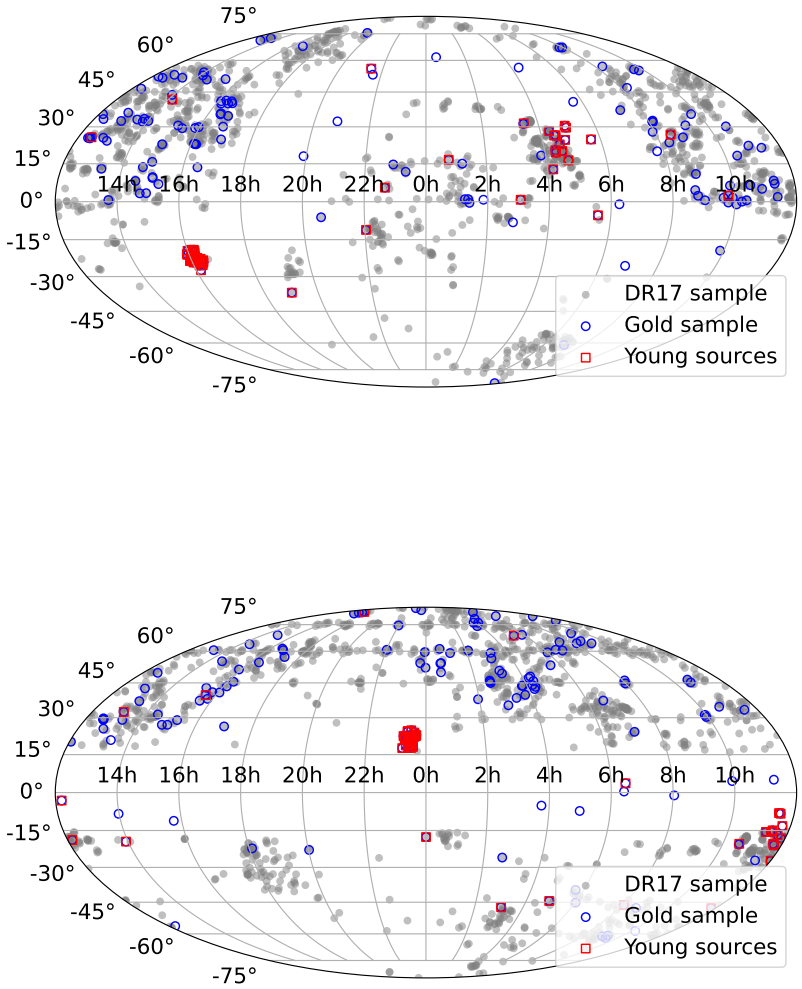

Figure 3.1: Sky distribution of my sample. My DR17 full ML dwarf and DR17 gold sample are labeled in grey and blue, respectively. Young sources in my gold sample are labeled in red squares. *Top*: Equatorial coordinate system projection. *Bottom*: Galactic coordinate system projection.

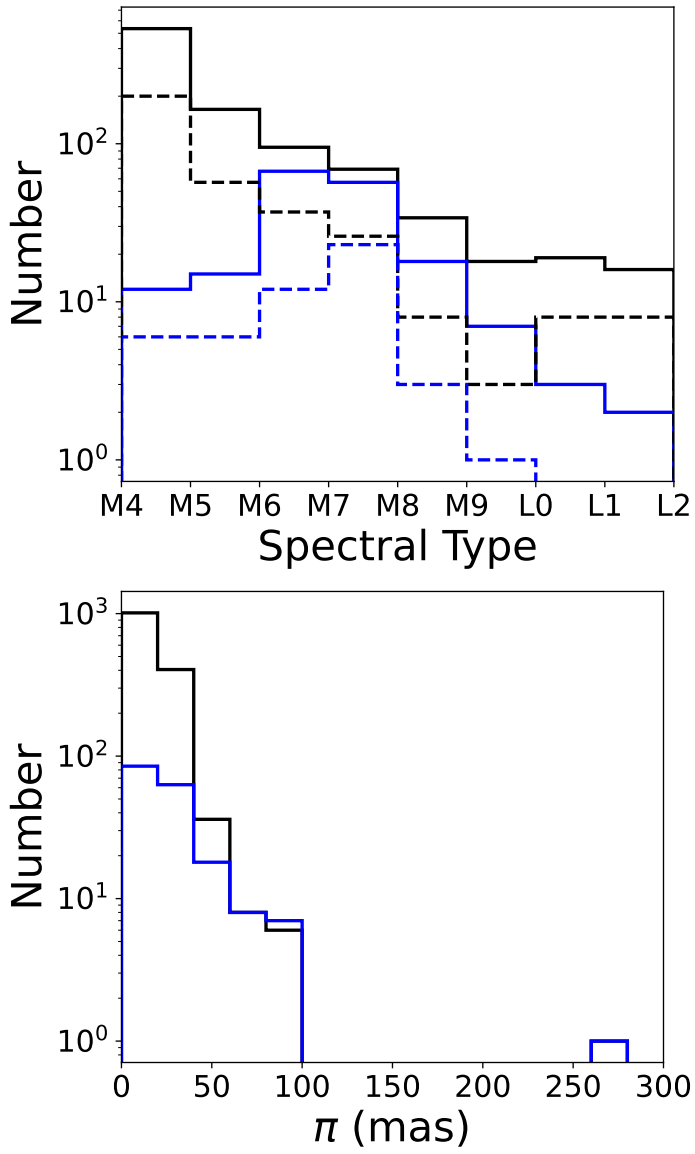

Figure 3.2: Observable properties of my UCD APOGEE sample. *Top*: Spectral type distribution for my full DR17 ML dwarf sample (black) and my DR17 gold sample (blue). The spectral types of my DR17 full sample are estimated from *Gaia* color and magnitude selection criteria (see Section 3.1 for details), while the gold sample literature type is drawn from the literature (see Table 3.2 for references). The dashed lines indicate the sources with the number of visits greater than or equal to 4. There are 527 sources in the DR17 full sample and 52 sources in the gold sample with at least four epochs of observations. *Bottom*: Parallax distribution for my DR17 late-M/L sample (black) and my DR17 gold sample (blue).

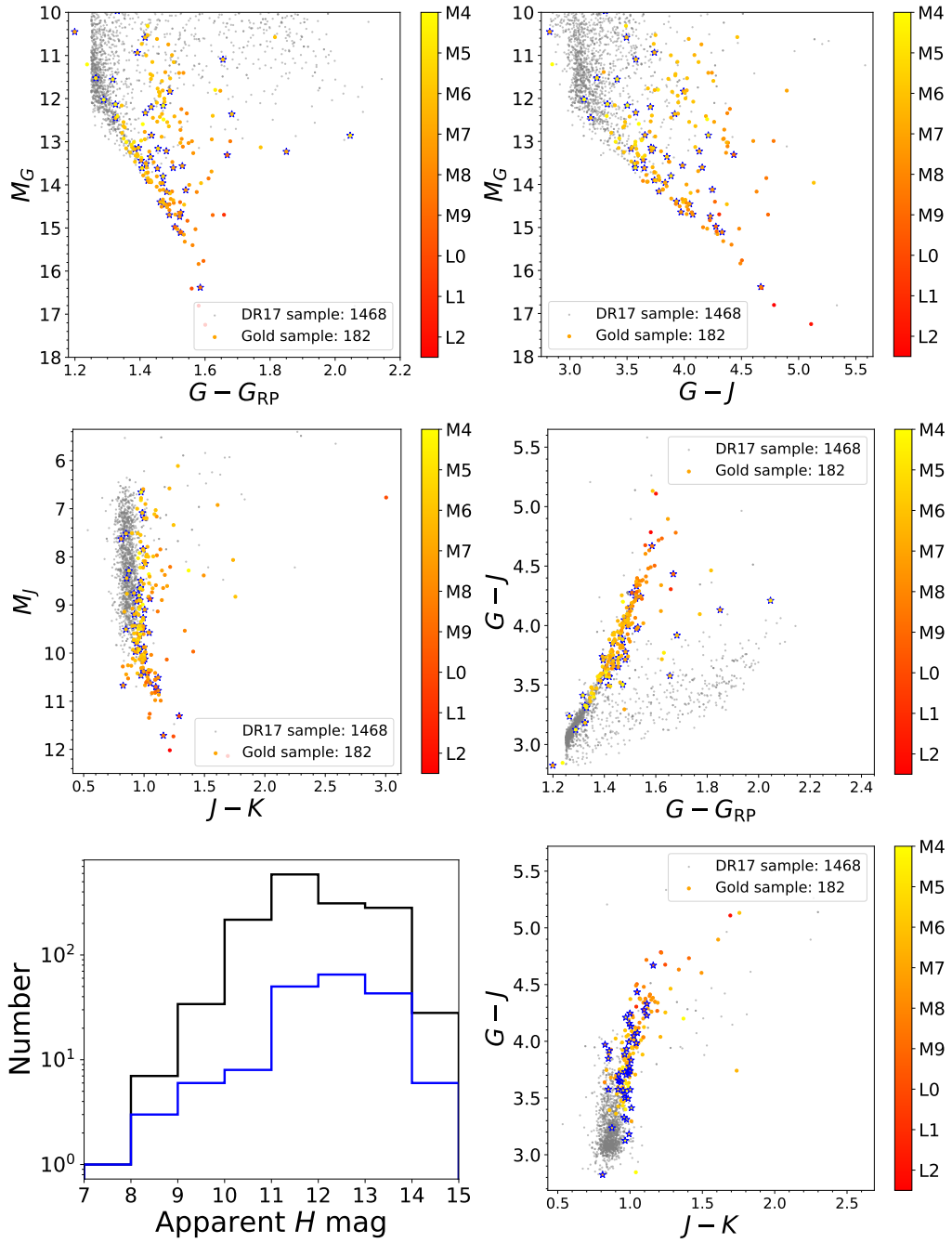

Figure 3.3: Color-magnitude properties of the UCD APOGEE sample. The full sample is indicated in grey dots, and the gold sample in color dots color-coded with spectral type. Blue stars indicate binary candidates. (top left): M_G versus $G - G_{RP}$ color-magnitude diagram. (top right): M_G versus $G - J$ color-magnitude diagram. (middle left): M_J versus $J - K$ color-magnitude diagram. (middle right): $G - J$ versus $G - G_{RP}$ color-color diagram. (bottom left): Apparent H magnitude distribution for my gold (blue) and full DR17 sample (black). (bottom right): $G - J$ versus $J - K$ color-color diagram.

3.1.1 Supporting Observations

A number of sources in my sample lack spectroscopic classifications[2], which hinder precise spectral characterization of the sample. I obtained additional low-resolution optical spectra with the Kast Double Spectrograph (Miller & Stone 1994) on the Shane 3-m Telescope at the Lick Observatory. I used the 600/7500 grating and 2.″ slit to obtain 6000-9000 Å spectra at an average resolution of $\lambda/\Delta\lambda \approx 1800$. Data acquisition included observations of flat-field and arc lamps for pixel response and wavelength calibration, nightly observations of a spectral flux standard from Hamuy et al. (1992, 1994) for relative flux calibration, and observations of a nearby G2 V or A0 V star at similar airmass for telluric absorption and continuum correction. All data were reduced using the `kastredux` package[3]. An example spectrum of the M9 dwarf 2M21272531+5553150 (aka LSPM J2127+5553) is shown in Figure 3.4. Table 3.1 summarizes the observations and corresponding measurements, including classifications based on comparison to SDSS templates from Bochanski et al. (2007b); Schmidt et al. (2014), and Kesseli et al. (2017); measurements of the metallicity index ζ defined by Lépine et al. (2007), all indicating dwarf metallicity classifications; and relative luminosity in Hα emission ($\log_{10} L_{H\alpha}/L_{bol}$) using the χ factor relations of Douglas et al. (2014) and Schmidt et al. (2014), all indicating these sources are magnetically active.

Table 3.1: Shane/Kast Observations of APOGEE Targets

Source	Obs. Date (UT)	Airmass	Exp. Time (s)	S/N[a]	SpT	ζ[b]	$\log_{10} L_{H\alpha}/L_{bol}$[c]
J07552256+2755318	2021 Nov 27	1.02	3000	130	M6.0	1.118±0.002	−4.01±0.09
J08080189+3157054	2021 Jan 17	1.11	3000	55	M7.0	1.007±0.003	−4.22±0.16
J11210854+2126274	2021 May 15	1.05	2400	97	M6.0	1.048±0.002	−4.11±0.09
J12215013+4632447	2018 Jan 21	1.02	2400	156	M7.0	1.008±0.001	−4.17±0.16
J12493960+5255340	2021 May 16	1.06	3000	16	M9.0	1.506±0.043	−4.93±0.14
J13342918+3303043	2020 Feb 05	1.02	3600	84	M7.0	1.031±0.002	−4.91±0.12
J14554964+0321420	2021 May 15	1.21	2400	73	M5.0	1.195±0.004	−4.81±0.12
J15042797+0942464	2021 May 15	1.42	3000	47	M5.0	1.093±0.007	−3.75±0.08
J16572919+2448509	2022 Mar 11	1.06	3000	113	M7.0	0.919±0.002	−4.05±0.13

Table 3.1 (*continued*)

[2]High-resolution spectra are not ideal for spectral classifications (See Section 3.3.3).
[3]https://github.com/aburgasser/kastredux

Table 3.1 (*continued*)

Source	Obs. Date (UT)	Airmass	Exp. Time (s)	S/N[a]	SpT	ζ[b]	$\log_{10} L_{H\alpha}/L_{bol}$[c]
J19544358+1801581	2020 Aug 14	1.07	3600	98	M9.0	1.207±0.003	−4.70±0.11
J21272531+5553150	2020 Aug 14	1.06	3600	96	M9.0	1.080±0.003	−4.78±0.10
J21381698+5257188	2020 Dec 14	1.22	3000	85	M7.0	1.005±0.002	−4.17±0.14

[a] Median signal-to-noise ratio in the 7200–7400 Å region.
[b] Metallicity index defined in Lépine et al. (2007), where $\zeta > 0.875$ indicates a dwarf metallicity classification.
[c] Relative luminosity in Hα emission based on the measured Hα equivalent width and χ correction factors compiled by Douglas et al. (2014) and Schmidt et al. (2014).

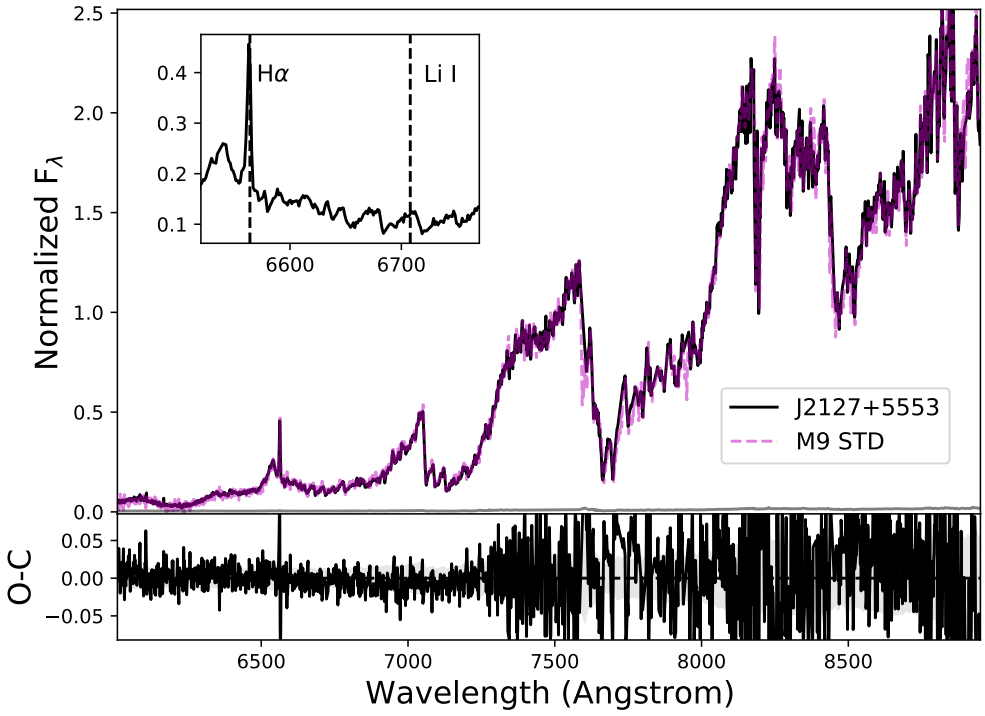

Figure 3.4: Normalized Shane/Kast spectrum of J21272531+5553150 (black line) compared to the best-match M9 spectral template from Bochanski et al. (2007b, magenta line). The lower panel compares the difference between these spectra to the measurement uncertainty (grey band). The inset box highlights the region around Hα emission at 6563 Å and Li I absorption at 6708 Å.

Table 3.2: APOGEE DR17 Sample

APOGEE ID	RA (deg)	Dec (deg)	*Gaia* eDR3 Source ID	SpT	SpT Ref	$N_{\rm obs}$	2MASS H (mag)	μ_α (mas yr^{-1})	μ_δ (mas yr^{-1})	μ Ref	π (mas)	π Ref
2M00312793+6139333	7.866401	+61.659252	430215470915266560	M7	(59, 71)	6	12.483 ± 0.028	369.52 ± 0.07	158.0 ± 0.07	(72)	27.86 ± 0.07	(72)
2M00452143+1634446	11.339304	+16.579082	2781513733917711616	L2beta	(31)	3	12.059 ± 0.035	359.07 ± 0.2	−47.91 ± 0.14	(72)	65.41 ± 0.18	(72)
2M01120002+1502170	18.000108	+15.038074	2591201534008672256	M5.5e	(14)	3	11.351 ± 0.02	166.12 ± 0.15	−317.0 ± 0.09	(72)	35.08 ± 0.1	(72)
2M01154176+0059317	18.924037	+0.992157	2535273088355573120	M6	(76)	2	12.651 ± 0.027	163.82 ± 0.15	24.1 ± 0.13	(72)	15.77 ± 0.13	(72)
2M01215816+0101007	20.492347	+1.016877	2535133209860543616	M6.5	(76)	2	12.429 ± 0.026	161.94 ± 0.16	−78.8 ± 0.09	(72)	26.49 ± 0.12	(72)
2M01243124-0027556	21.130173	−0.465459	2533946665015570304	M7	(35)	2	11.506 ± 0.029	66.72 ± 0.32	−170.47 ± 0.18	(72)	29.17 ± 0.25	(72)
2M01514363+0046188	27.931833	+0.771889	2510880216734767232	M7	(65)	3	12.431 ± 0.023	126.98 ± 0.12	30.41 ± 0.08	(72)	26.32 ± 0.1	(72)
2M02500239-0808417	42.509966	−8.144931	5174318457801944448	M5.5	(13)	2	11.186 ± 0.023	567.33 ± 0.07	101.0 ± 0.07	(72)	41.9 ± 0.06	(72)
2M03040207+0045512	46.008629	+0.76423	3266760032372995072	M6	(36)	16	11.216 ± 0.027	251.94 ± 0.06	34.3 ± 0.05	(72)	33.49 ± 0.05	(72)
2M03282839+3116273	52.118321	+31.274265	121029704500767488	M6.9	(41)	10	13.927 ± 0.049	6.34 ± 0.23	−9.72 ± 0.17	(72)	3.27 ± 0.22	(72)
2M03293053+3127280	52.377236	+31.457779	121412953022160256	M6.9	(41)	2	13.014 ± 0.034	6.61 ± 0.18	−10.18 ± 0.14	(72)	3.58 ± 0.15	(72)
2M03505737+1818069	57.739064	+18.30192	50667699128858624	M9	(40)	1	12.213 ± 0.022	179.42 ± 0.14	−37.58 ± 0.1	(72)	27.12 ± 0.12	(72)
2M04110642+1247481	62.776762	+12.796713	3304478125929665152	M6	(24)	2	12.128 ± 0.038	132.35 ± 0.13	−13.39 ± 0.1	(72)	23.07 ± 0.1	(72)
2M04185115+2814332	64.713151	+28.242567	164495323291866624	M7.5e	(10)	1	13.241 ± 0.029	8.48 ± 0.25	−24.69 ± 0.18	(72)	7.77 ± 0.22	(72)
2M04204796+5624202	65.199861	+56.405624	276870604275149568	M8	(68)	7	12.313 ± 0.023	511.73 ± 0.12	−120.26 ± 0.09	(72)	30.75 ± 0.11	(72)
2M04214435+2024105	65.434833	+20.402943	49131681384221184	M7	(59)	2	12.862 ± 0.027	104.08 ± 0.14	−33.6 ± 0.1	(72)	20.28 ± 0.12	(72)
2M04214955+1929086	65.456494	+19.485744	48190739948429184	M7+M9.5	(32)	1	12.06 ± 0.022	125.41 ± 0.34	−35.86 ± 0.24	(72)	23.62 ± 0.3	(72)
2M04262939+2624137	66.622465	+26.40383	151283870746458496	M6e	(10)	3	12.501 ± 0.022	11.28 ± 0.19	−17.67 ± 0.14	(72)	6.36 ± 0.16	(72)
2M04294568+2630468	67.440334	+26.513002	151327159721125888	M7.5e	(10)	3	11.918 ± 0.024	7.4 ± 0.18	−21.02 ± 0.12	(72)	8.02 ± 0.16	(72)
2M04330945+2246487	68.289405	+22.780195	145947077527182848	M7	(61)	3	12.142 ± 0.021	12.3 ± 0.36	−17.85 ± 0.28	(72)	5.67 ± 0.31	(72)
2M04351354+2008014	68.806455	+20.133726	3410856112139584000	M7.5	(59)	2	12.986 ± 0.021	101.48 ± 0.17	−41.8 ± 0.12	(72)	21.95 ± 0.14	(72)
2M04440164+1621324	71.006848	+16.359003	3406128761895775872	M6	(46)	2	12.768 ± 0.022	11.54 ± 0.14	−18.99 ± 0.1	(72)	6.89 ± 0.12	(72)
2M04464498+2436404	71.687455	+24.611223	147258180719392512	M7	(59)	1	12.493 ± 0.024	100.12 ± 0.1	−62.3 ± 0.07	(72)	23.95 ± 0.08	(72)
2M04552333+3027366	73.84721	+30.460171	156915290131026816	M6e	(17)	4	12.384 ± 0.023	4.74 ± 0.14	−24.96 ± 0.1	(72)	6.22 ± 0.13	(72)
2M04565141+2939310	74.214224	+29.658638	156629039151059328	M7	(57)	4	13.167 ± 0.027	4.94 ± 0.16	−24.65 ± 0.11	(72)	6.61 ± 0.13	(72)
2M05350162-0521489	83.75676	−5.363606	0	L0	(19)	2	13.065 ± 0.051	0.0 ± 44.0	0.0 ± 40.0	(50)	2.42 ± 0.04	(23)
2M05392474+4038437	84.853102	+40.645485	191109281417914880	M8e	(12)	3	10.446 ± 0.021	646.15 ± 0.09	−834.49 ± 0.05	(72)	87.97 ± 0.08	(72)
2M05402570+2448090	85.107108	+24.802505	0	M7	(44)	4	8.384 ± 0.023	107.0 ± 8.0	−376.0 ± 8.0	(42)	97.6 ± 2.8	(48)
2M06154934-0100415	93.955603	−1.01155	3121200807575320448	L2.5	(30)	6	12.984 ± 0.023	198.85 ± 0.25	−56.7 ± 0.24	(72)	44.97 ± 0.23	(72)
2M06521977-2534505	103.082387	−25.580719	2920995300823950720	L0	(30)	3	12.02 ± 0.022	−235.57 ± 0.07	87.92 ± 0.09	(72)	62.26 ± 0.09	(72)
2M07025026-6102482	105.70944	−61.046738	5479255432103480320	M6.5e	(16)	1	9.854 ± 0.024	520.13 ± 0.28	597.17 ± 0.24	(72)	57.02 ± 0.2	(72)
2M07140394+3702459	108.516439	+37.046108	898275195732381440	M8	(25)	3	11.252 ± 0.03	−89.02 ± 0.12	−182.52 ± 0.11	(72)	63.41 ± 0.14	(72)
2M07464256+2000321	116.677342	+20.00894	0	L0+L1.5	(58)	2	11.007 ± 0.022	−370.0 ± 4.0	−42.0 ± 1.0	(11)	81.2 ± 0.2	(70)
2M07475737+6653337	116.989056	+66.892715	1096135130646349568	M7	(59)	18	13.599 ± 0.029	23.59 ± 0.08	−0.79 ± 0.14	(72)	16.73 ± 0.16	(72)
2M07552256+2755318	118.844027	+27.925526	874683391345874816	M6	(73)	3	11.616 ± 0.023	−286.55 ± 0.06	−29.3 ± 0.04	(72)	31.17 ± 0.07	(72)
2M07564895+6649595	119.203963	+66.833221	1095345479434185984	M7.5	(59)	17	13.309 ± 0.036	161.93 ± 0.07	−212.0 ± 0.11	(72)	23.5 ± 0.12	(72)
2M08072607+3213101	121.858652	+32.21949	901941452829250560	M8	(25)	4	11.455 ± 0.03	−372.94 ± 0.1	−253.51 ± 0.08	(72)	52.75 ± 0.09	(72)
2M08080189+3157054	122.007879	+31.951508	901922932930351872	M7	(73)	4	12.082 ± 0.018	−23.97 ± 0.09	−139.0 ± 0.08	(72)	38.82 ± 0.09	(72)
2M08092892+3235226	122.370536	+32.589619	901979660858285824	M4	(67)	4	12.657 ± 0.018	−28.52 ± 0.33	1.78 ± 0.27	(72)	11.92 ± 0.38	(72)
2M08144389+4650522	123.682914	+46.847851	929639800000008832	M4	(67)	2	12.236 ± 0.021	−42.43 ± 0.07	−77.9 ± 0.06	(72)	16.7 ± 0.07	(72)
2M08185804+2333522	124.741863	+23.564503	677439114220735616	M7e	(4)	4	11.552 ± 0.023	−259.12 ± 0.08	−331.58 ± 0.06	(72)	44.32 ± 0.08	(72)
2M08211639+5658358	125.318327	+56.97662	1034818738715797760	M6.5	(76)	3	12.805 ± 0.019	20.92 ± 0.1	−30.9 ± 0.11	(72)	11.52 ± 0.13	(72)
2M08294949+2646348	127.456242	+26.776339	703790044252850688	M6.5e	(16)	5	7.617 ± 0.018	−1113.69 ± 0.06	−612.19 ± 0.05	(72)	279.25 ± 0.06	(72)
2M08440350+0434356	131.014597	+4.576577	582212198844172928	M9	(35)	2	12.827 ± 0.031	−329.09 ± 0.17	272.84 ± 0.13	(72)	36.38 ± 0.16	(72)
2M08490052+0220155	132.252168	+2.337659	577960765337401856	M7.3	(47)	9	12.299 ± 0.021	−92.65 ± 0.1	−105.93 ± 0.07	(72)	32.52 ± 0.09	(72)
2M08501918+1056436	132.579937	+10.945469	598656696613099648	M5e+M6e	(34)	23	10.675 ± 0.022	−172.16 ± 0.03	−64.68 ± 0.02	(72)	25.19 ± 0.03	(72)
2M08522464+2540591	133.102704	+25.683105	690896346271732480	M7	(35)	1	11.56 ± 0.031	−205.52 ± 0.31	−74.91 ± 0.22	(72)	24.04 ± 0.31	(72)
2M09020690+0033195	135.528784	+0.555434	576506489410890752	M6	(2)	2	11.538 ± 0.023	−465.14 ± 0.09	−97.98 ± 0.06	(72)	46.01 ± 0.07	(72)
2M09130162+3037583	138.256788	+30.632866	699795277990242176	M7	(64)	8	12.82 ± 0.025	−109.82 ± 0.1	−224.0 ± 0.09	(72)	17.26 ± 0.11	(72)
2M09373349+5534057	144.389577	+55.568275	1021744377229927040	M6	(35)	20	13.674 ± 0.043	−33.88 ± 0.12	−13.14 ± 0.11	(72)	7.78 ± 0.12	(72)
2M09381783+0132490	144.574292	+1.546969	3847224106513033472	M4	(55)	7	12.266 ± 0.033	−25.95 ± 0.05	−52.3 ± 0.04	(72)	5.66 ± 0.05	(72)
2M09442625+3521233	146.109388	+35.356476	794874515210822144	M5	(55)	6	12.65 ± 0.023	−220.98 ± 0.09	58.7 ± 0.08	(72)	21.89 ± 0.11	(72)

Table 3.2 (*continued*)

Table 3.2 (*continued*)

APOGEE ID	RA (deg)	Dec (deg)	*Gaia* eDR3 Source ID	SpT	SpT Ref	N_{obs}	2MASS H (mag)	μ_α (mas yr^{-1})	μ_δ (mas yr^{-1})	μ Ref	π (mas)	π Ref
2M09453388+5458511	146.391184	+54.980881	1021788250320230016	M7	(59)	10	13.777 ± 0.037	−14.08 ± 0.14	−35.7 ± 0.15	(72)	13.69 ± 0.15	(72)
2M09472006-0020093	146.833623	−0.335939	3833990796878014720	M7	(65)	2	11.63 ± 0.024	−214.15 ± 0.06	47.85 ± 0.06	(72)	37.29 ± 0.06	(72)
2M09474477+0224327	146.93657	+2.409108	3847024132835801344	M8.2	(47)	2	12.485 ± 0.024	−106.83 ± 0.17	−162.4 ± 0.12	(72)	29.85 ± 0.15	(72)
2M09522188-1924319	148.091198	−19.408888	5671384265738137984	M7e	(6)	3	11.256 ± 0.024	−73.0 ± 0.1	−99.48 ± 0.1	(72)	35.32 ± 0.1	(72)
2M09524622+0620410	148.192586	+6.344746	3850426468488570624	M7.3	(47)	4	11.832 ± 0.022	−87.56 ± 0.11	−67.43 ± 0.12	(72)	25.08 ± 0.09	(72)
2M09560888+0134128	149.037012	+1.570232	3834702043462197504	M5	(71)	4	12.397 ± 0.023	−245.45 ± 0.09	0.68 ± 0.09	(72)	25.36 ± 0.08	(72)
2M10031918-0105079	150.829957	−1.085538	3830128624846458752	M7e	(9)	2	11.667 ± 0.023	−498.71 ± 0.09	46.9 ± 0.1	(72)	50.14 ± 0.1	(72)
2M10134315+0000406	153.42981	+0.011291	3831671274019947648	M6	(5)	2	11.953 ± 0.022	323.86 ± 0.06	−281.51 ± 0.07	(72)	27.33 ± 0.07	(72)
2M10225090+0032169	155.712113	+0.538033	3831375157499435648	M8	(64)	3	12.613 ± 0.023	−85.11 ± 0.45	−215.0 ± 0.6	(72)	28.03 ± 0.3	(72)
2M10240997+1815533	156.041547	+18.26482	624312666575349888	M7e	(4)	3	11.62 ± 0.021	−161.85 ± 0.33	−76.98 ± 0.37	(72)	28.76 ± 0.31	(72)
2M10323297+0630074	158.137415	+6.502077	3862117335108574848	M6	(44)	2	9.901 ± 0.022	−232.2 ± 0.03	−193.22 ± 0.03	(72)	51.45 ± 0.03	(72)
2M10372897+3011117	159.370735	+30.186594	735453264711448064	M8	(53)	2	11.286 ± 0.022	−819.76 ± 0.05	−572.97 ± 0.04	(72)	49.84 ± 0.05	(72)
2M10541102-8505023	163.545954	−85.083984	5190838276414527872	M8	(9)	2	12.071 ± 0.024	−427.83 ± 0.14	285.33 ± 0.1	(72)	53.7 ± 0.1	(72)
2M10543366+0503467	163.640277	+5.062998	3816081539168125696	L1	(76)	2	12.712 ± 0.022	153.7 ± 0.47	−257.0 ± 0.42	(72)	25.64 ± 0.4	(72)
2M10570380+2217203	164.265858	+22.28899	3988944695702883584	M6	(44)	2	10.693 ± 0.02	−154.93 ± 0.04	−131.21 ± 0.03	(72)	37.56 ± 0.03	(72)
2M11194647+0820356	169.943658	+8.343246	3818676249170081408	M8	(35)	3	12.22 ± 0.025	371.4 ± 0.1	−351.6 ± 0.1	(72)	35.64 ± 0.09	(72)
2M11203609+0704135	170.1504	+7.070432	3817502486148556032	M6	(35)	3	12.363 ± 0.025	12.09 ± 0.07	−245.67 ± 0.06	(72)	22.91 ± 0.07	(72)
2M11210854+2126274	170.285592	+21.440952	3990812761663064960	M6	(74)	1	11.105 ± 0.023	−240.04 ± 0.06	−2.85 ± 0.07	(72)	38.18 ± 0.07	(72)
2M11232934+0154040	170.872272	+1.901134	3810750831918988928	M7	(49)	3	11.739 ± 0.026	−168.06 ± 0.35	16.2 ± 0.27	(72)	33.38 ± 0.3	(72)
2M12080810+3520281	182.033775	+35.341141	4029757983210057088	M7V	(35)	2	11.791 ± 0.021	−607.68 ± 0.06	−70.85 ± 0.08	(72)	32.19 ± 0.09	(72)
2M12153877+5205050	183.911576	+52.084747	0	M4.5	(55)	1	11.024 ± 0.032	−45.5 ± 3.7	3.8 ± 6.6	(52)	18.0 ± 6.0	(73)
2M12201166+3315379	185.048621	+33.260536	4016348232027455104	M8	(35)	2	12.8 ± 0.022	118.93 ± 0.12	−219.31 ± 0.12	(72)	27.06 ± 0.13	(72)
2M12205439+2525568	185.226666	+25.432447	4008305476265035136	M6	(39)	1	14.309 ± 0.049	−64.98 ± 0.36	1.16 ± 0.27	(72)	11.17 ± 0.32	(72)
2M12215013+4632447	185.458875	+46.545753	0	M8	(73)	2	10.599 ± 0.028	78.0 ± 3.0	−24.0 ± 3.0	(62)	34.0 ± 7.0	(62)
2M12235346+2534559	185.97279	+25.582199	4008273903960972416	M6	(39)	4	14.117 ± 0.044	1.04 ± 0.15	61.7 ± 0.16	(72)	7.86 ± 0.15	(72)
2M12252076+2517082	186.336518	+25.28562	0	M7	(35)	7	13.5 ± 0.039	−82.6 ± 3.1	26.32 ± 2.55	(69)	51.35 ± 5.09	(56)
2M12270429+2541012	186.767875	+25.683676	3960341892843205248	M6.4	(26)	7	13.395 ± 0.04	−12.31 ± 0.16	−8.11 ± 0.16	(72)	11.22 ± 0.17	(72)
2M12315462+5130389	187.977594	+51.510822	1568728631543924608	M6.5	(13)	1	12.601 ± 0.023	−215.1 ± 0.06	14.56 ± 0.08	(72)	21.37 ± 0.08	(72)
2M12493960+5255340	192.415014	+52.926117	1569931222385549056	M9	(73)	3	12.857 ± 0.024	−181.71 ± 0.1	−242.0 ± 0.11	(72)	26.19 ± 0.12	(72)
2M12522354+2528469	193.098115	+25.479712	3958025913333963648	M7	(35)	1	12.592 ± 0.035	−68.92 ± 0.11	−186.66 ± 0.09	(72)	26.79 ± 0.1	(72)
2M13004379+3557591	195.182489	+35.966442	1516374663831829888	M6	(35)	4	11.611 ± 0.02	−345.3 ± 0.02	−7.29 ± 0.03	(72)	27.93 ± 0.04	(72)
2M13022083+3227103	195.586829	+32.452881	1467167257881586816	M6	(35)	3	11.641 ± 0.02	−194.11 ± 0.03	45.95 ± 0.02	(72)	31.57 ± 0.04	(72)
2M13034100+2414020	195.920837	+24.2339	3957137988975049088	M7	(22)	4	12.079 ± 0.031	−349.34 ± 0.1	77.42 ± 0.11	(72)	31.64 ± 0.09	(72)
2M13065141+7056376	196.714226	+70.943779	1686366029137264128	M7	(59)	12	13.585 ± 0.038	186.98 ± 0.14	−103.0 ± 0.12	(72)	19.01 ± 0.11	(72)
2M13192677+1301119	199.861563	+13.019995	3742613512230508288	M4.8	(71)	3	12.107 ± 0.023	−303.51 ± 0.08	−200.0 ± 0.08	(72)	25.23 ± 0.07	(72)
2M13202007+7213140	200.08364	+72.220581	1687938811801144832	M7.5	(59)	12	13.222 ± 0.033	1.72 ± 0.18	−16.7 ± 0.18	(72)	20.2 ± 0.15	(72)
2M13232423+5132272	200.850979	+51.54089	1562758730081761152	M6	(35)	7	11.096 ± 0.022	−163.1 ± 0.06	48.95 ± 0.07	(72)	22.78 ± 0.07	(72)
2M13342918+3303043	203.621597	+33.051212	1469086764666230912	M7	(73)	1	11.928 ± 0.033	−657.08 ± 0.05	−36.4 ± 0.04	(72)	35.63 ± 0.08	(72)
2M13430646+0038442	205.776953	+0.645635	3663165619505342976	M4	(76)	15	13.779 ± 0.039	−55.56 ± 0.14	−17.7 ± 0.1	(72)	7.68 ± 0.13	(72)
2M13482307+3321508	207.096155	+33.364117	1458504515004327168	M4.5	(76)	7	13.792 ± 0.029	−19.72 ± 0.07	−31.0 ± 0.07	(72)	5.5 ± 0.1	(72)
2M13500476+3207596	207.519873	+32.133228	1457430910619077632	M4.5	(55)	15	13.315 ± 0.027	10.48 ± 0.05	−70.3 ± 0.06	(72)	9.18 ± 0.08	(72)
2M13564148+4342587	209.172854	+43.716324	1502523188143833088	M8	(53)	3	11.043 ± 0.021	−445.85 ± 0.44	45.15 ± 0.5	(72)	46.3 ± 0.58	(72)
2M13573443+5408223	209.393463	+54.139549	1561218520448360448	M5	(55)	2	12.4 ± 0.021	−208.78 ± 0.05	−19.1 ± 0.07	(72)	18.23 ± 0.06	(72)
2M14005977+3226109	210.249064	+32.436386	1457632808444461056	M7	(35)	16	13.562 ± 0.028	−176.56 ± 0.08	23.0 ± 0.1	(72)	14.46 ± 0.12	(72)
2M14081562+5236281	212.065096	+52.607822	1512826058772467712	M4.5	(67)	3	12.319 ± 0.029	36.33 ± 0.04	−202.0 ± 0.05	(72)	16.96 ± 0.04	(72)
2M14093200+4138080	212.38335	+41.635582	1498145551317166336	M6	(44)	1	10.187 ± 0.016	−217.32 ± 0.02	72.55 ± 0.02	(72)	40.96 ± 0.03	(72)
2M14320849+0811313	218.035409	+8.192037	1172618435080418176	M6	(44)	3	9.529 ± 0.022	−477.1 ± 0.04	10.06 ± 0.04	(72)	78.56 ± 0.04	(72)
2M14340140+5039480	218.505854	+50.663361	1603770170199226368	M7	(59)	9	13.035 ± 0.031	−100.67 ± 0.07	39.9 ± 0.08	(72)	21.34 ± 0.08	(72)
2M14402293+1339230	220.09555	+13.656391	1179654519224224640	M7	(35)	3	11.71 ± 0.02	−145.08 ± 0.09	−306.07 ± 0.07	(72)	39.13 ± 0.08	(72)
2M14432796+0316543	220.866533	+3.281762	3655776282891553664	M7	(28)	1	12.632 ± 0.027	−211.74 ± 0.15	7.41 ± 0.13	(72)	32.59 ± 0.12	(72)
2M14553384+1545593	223.891033	+15.766495	1187077906338788736	M4.5	(55)	3	11.968 ± 0.028	−8.2 ± 0.41	−116.0 ± 0.4	(72)	12.01 ± 0.41	(72)
2M14554964+0321420	223.956845	+3.361681	1154963095836913920	M5	(73)	2	11.108 ± 0.025	−171.34 ± 0.05	−545.0 ± 0.04	(72)	35.82 ± 0.05	(72)
2M15010818+2250020	225.284113	+22.8339	1262763648230973440	M8.5	(7)	5	11.181 ± 0.03	−43.12 ± 0.11	−65.1 ± 0.14	(72)	93.17 ± 0.14	(72)

Table 3.2 (*continued*)

Table 3.2 (*continued*)

APOGEE ID	RA (deg)	Dec (deg)	*Gaia* eDR3 Source ID	SpT	SpT Ref	N_{obs}	2MASS H (mag)	μ_α (mas yr^{-1})	μ_δ (mas yr^{-1})	μ Ref	π (mas)	π Ref
2M15041028+0923232	226.042873	+9.3898	1167876585027341184	M7.5	(64)	3	12.5 ± 0.028	−257.35 ± 0.14	64.2 ± 0.13	(72)	20.01 ± 0.12	(72)
2M15042797+0942464	226.116574	+9.712908	1167903832299960576	M5	(73)	1	12.493 ± 0.027	−67.07 ± 0.07	15.2 ± 0.06	(72)	5.36 ± 0.06	(72)
2M15115124+3033065	227.963533	+30.551817	1276260600140069888	M5	(13)	2	12.243 ± 0.018	−392.57 ± 0.03	−262.0 ± 0.04	(72)	20.17 ± 0.05	(72)
2M15175638+0656388	229.484941	+6.944124	1163173320960323968	M4	(76)	2	12.402 ± 0.025	−31.06 ± 0.05	−25.7 ± 0.05	(72)	11.02 ± 0.05	(72)
2M15210103+5053230	230.254331	+50.889729	1595520568815311744	M7.5	(25)	1	11.327 ± 0.015	54.19 ± 0.07	−173.13 ± 0.08	(72)	62.04 ± 0.06	(72)
2M15242475+2925318	231.103156	+29.425508	1272178319624018816	M7.5	(38)	4	10.535 ± 0.021	−56.77 ± 0.03	−629.24 ± 0.04	(72)	76.46 ± 0.04	(72)
2M15512179+2931062	237.840811	+29.518406	1320795047312113152	M7	(1)	4	8.38 ± 0.04	−226.53 ± 0.02	−443.61 ± 0.03	(72)	54.11 ± 0.03	(72)
2M15555600-2045187	238.98336	−20.755199	6246820788606409600	M6.5	(15)	2	12.807 ± 0.023	−13.64 ± 0.18	−22.48 ± 0.12	(72)	6.85 ± 0.15	(72)
2M15560104-2338081	239.004338	−23.635588	6237048805996330624	M6.5	(15)	1	13.242 ± 0.025	−18.69 ± 0.16	−26.98 ± 0.1	(72)	8.14 ± 0.14	(72)
2M15560497-2106461	239.020713	−21.112816	6246606452553143296	M7	(15)	2	13.41 ± 0.033	−13.48 ± 0.23	−22.43 ± 0.2	(72)	6.8 ± 0.22	(72)
2M15574011+2952379	239.417144	+29.877197	1320476498177466368	M4.5	(71)	4	11.943 ± 0.022	−35.06 ± 0.03	−158.0 ± 0.04	(72)	25.54 ± 0.04	(72)
2M15592591-2305081	239.857994	−23.085611	6237173192548569600	M6e	(8)	2	11.908 ± 0.022	−12.05 ± 0.08	−24.45 ± 0.05	(72)	7.04 ± 0.07	(72)
2M15594439-1928191	239.934967	−19.471992	6247395008547695488	M7.5	(60)	1	13.817 ± 0.068	−10.98 ± 0.38	−21.92 ± 0.19	(72)	6.54 ± 0.25	(72)
2M16001944-2256287	240.081011	−22.941326	6243186456003514752	M8	(15)	2	13.83 ± 0.037	−11.35 ± 0.4	−24.58 ± 0.24	(72)	6.88 ± 0.31	(72)
2M16002844-2209228	240.118537	−22.156357	6243438347235850112	M6	(8)	3	12.847 ± 0.033	−48.21 ± 0.13	−22.0 ± 0.08	(72)	6.75 ± 0.12	(72)
2M16003023-2334457	240.125981	−23.579365	6237098906793775744	M6e	(8)	3	12.203 ± 0.026	−12.7 ± 0.1	−24.57 ± 0.06	(72)	6.97 ± 0.08	(72)
2M16014955-2351082	240.456488	−23.852278	6236326362439449728	M6e	(3)	1	12.293 ± 0.026	−11.68 ± 0.15	−23.36 ± 0.08	(72)	6.84 ± 0.12	(72)
2M16022585-2414081	240.607737	−24.235594	6236235373548191360	M7.25	(60)	1	13.509 ± 0.032	−13.57 ± 0.33	−24.96 ± 0.2	(72)	7.72 ± 0.28	(72)
2M16044026-2254323	241.167776	−22.908993	6242403771219113216	M6	(60)	1	13.755 ± 0.032	−13.31 ± 0.27	−22.88 ± 0.13	(72)	6.65 ± 0.2	(72)
2M16045199-2224108	241.216658	−22.403019	6243263383155595392	M8	(60)	1	13.314 ± 0.028	−9.73 ± 0.27	−23.02 ± 0.16	(72)	6.26 ± 0.2	(72)
2M16055178-2206212	241.465754	−22.10589	6243298911123311616	M6	(60)	1	13.34 ± 0.024	−10.99 ± 0.17	−23.44 ± 0.09	(72)	6.53 ± 0.14	(72)
2M16055380+2303058	241.474204	+23.051626	1206719582058487552	M7	(35)	11	12.829 ± 0.031	11.99 ± 0.06	24.02 ± 0.08	(72)	18.83 ± 0.08	(72)
2M16063110-1904576	241.629617	−19.08268	6248770050921318656	M6	(60)	2	13.067 ± 0.027	−9.49 ± 0.18	−24.46 ± 0.14	(72)	7.11 ± 0.15	(72)
2M16063390+4054216	241.64125	+40.906013	1380293091823646720	M6e	(14)	3	10.423 ± 0.015	−716.3 ± 0.04	162.49 ± 0.05	(72)	63.42 ± 0.03	(72)
2M16081226+2252548	242.051112	+22.881889	1206516511708372608	M5.5	(55)	4	13.485 ± 0.028	39.75 ± 0.09	−33.4 ± 0.1	(72)	11.36 ± 0.12	(72)
2M16090197-2151225	242.258238	−21.85626	6242933877561854848	M6	(60)	1	13.079 ± 0.036	−11.32 ± 0.2	−24.1 ± 0.16	(72)	7.34 ± 0.16	(72)
2M16090451-2224523	242.268814	−22.414553	6242480432095204480	M7	(29)	3	12.363 ± 0.024	−9.88 ± 0.18	−23.86 ± 0.12	(72)	6.86 ± 0.13	(72)
2M16090568-2245166	242.273669	−22.754614	6242453734573995520	M8.25	(60)	1	14.463 ± 0.041	−9.86 ± 0.76	−23.51 ± 0.51	(72)	6.88 ± 0.57	(72)
2M16093019-2059536	242.375792	−20.998228	6243843994013465088	M6	(21)	1	13.354 ± 0.024	−7.04 ± 0.17	−21.68 ± 0.12	(72)	6.76 ± 0.14	(72)
2M16095107-2722418	242.462817	−27.3783	6042503181382356352	M6	(15)	1	12.743 ± 0.028	−13.05 ± 0.19	−25.55 ± 0.13	(72)	6.78 ± 0.13	(72)
2M16095852-2345186	242.493853	−23.755169	6242136284955026176	M6.5	(15)	1	11.996 ± 0.024	−10.47 ± 0.17	−23.85 ± 0.13	(72)	7.14 ± 0.14	(72)
2M16095990-2155424	242.499612	−21.928471	6242943498288490752	M6.5	(21)	1	13.646 ± 0.035	−10.6 ± 0.25	−24.46 ± 0.18	(72)	7.11 ± 0.21	(72)
2M16100608-2127440	242.525341	−21.462229	6242973459980548608	M8.5	(15)	1	14.15 ± 0.045	−10.06 ± 0.49	−23.29 ± 0.34	(72)	7.09 ± 0.38	(72)
2M16103014-2315167	242.625606	−23.254652	6242235958259504256	M7.5	(15)	1	13.783 ± 0.03	−10.34 ± 0.39	−24.8 ± 0.25	(72)	7.02 ± 0.25	(72)
2M16103040+3954258	242.62668	+39.907169	0	M5	(55)	2	11.191 ± 0.028	110.0 ± 3.0	−245.0 ± 3.0	(73)	19.0 ± 6.0	(73)
2M16103232-1913085	242.634701	−19.219044	6245761404854620416	M8.5-9.5	(43)	1	13.18 ± 0.098	−7.98 ± 0.38	−24.89 ± 0.25	(72)	7.13 ± 0.26	(72)
2M16103232+2249116	242.634684	+22.819895	1206545927940917888	M7	(35)	11	13.286 ± 0.032	21.0 ± 0.13	22.13 ± 0.14	(72)	12.9 ± 0.15	(72)
2M16104714-2239492	242.69642	−22.663685	6242645251461275136	M9	(33)	1	14.573 ± 0.054	−10.79 ± 0.87	−26.76 ± 0.66	(72)	8.08 ± 0.59	(72)
2M16113837-2307072	242.909892	−23.118687	6242198265623040896	M6.25	(33)	2	13.208 ± 0.029	−11.76 ± 0.18	−24.23 ± 0.13	(72)	6.74 ± 0.13	(72)
2M16114261-2525511	242.927582	−25.430885	6049537169580902272	M7	(60)	2	11.719 ± 0.023	−10.06 ± 0.14	−26.56 ± 0.09	(72)	7.39 ± 0.09	(72)
2M16115439-2236491	242.976644	−22.613663	6242649340270424704	M6.25	(33)	1	13.608 ± 0.027	−10.94 ± 0.28	−21.43 ± 0.24	(72)	7.01 ± 0.25	(72)
2M16122703-2013250	243.112661	−20.223621	6245446154254329216	M6	(60)	1	12.608 ± 0.023	−9.64 ± 0.11	−22.63 ± 0.07	(72)	7.16 ± 0.08	(72)
2M16124726-1903531	243.196957	−19.064766	6245819786343951744	M6e	(8)	2	12.15 ± 0.024	−7.96 ± 0.1	−24.74 ± 0.07	(72)	7.18 ± 0.08	(72)
2M16132665-2230348	243.361072	−22.509678	6242661061238878592	M6.25	(33)	1	12.95 ± 0.024	−9.62 ± 0.16	−26.24 ± 0.11	(72)	7.2 ± 0.13	(72)
2M16132809-1924524	243.367055	−19.414564	6245601945603400960	M6	(29)	2	12.26 ± 0.024	−7.96 ± 0.12	−23.76 ± 0.09	(72)	7.2 ± 0.1	(72)
2M16134027-2233192	243.417794	−22.555353	6242613022028649600	M6.5	(60)	1	12.937 ± 0.033	−9.62 ± 0.15	−24.73 ± 0.1	(72)	6.91 ± 0.12	(72)
2M16134079-2219459	243.41998	−22.329437	6242671777180877312	M7.5	(33)	1	14.185 ± 0.04	−8.61 ± 0.48	−24.04 ± 0.31	(72)	6.56 ± 0.35	(72)
2M16134264-2301279	243.427696	−23.02442	6242562861106321024	M6.25	(33)	1	13.123 ± 0.023	−9.34 ± 0.16	−22.08 ± 0.11	(72)	6.09 ± 0.13	(72)
2M16143287-2242133	243.636959	−22.703707	6242595876516326400	M6.5	(29)	1	13.664 ± 0.033	−8.11 ± 0.23	−23.9 ± 0.16	(72)	6.28 ± 0.18	(72)
2M16172079+4113032	244.336648	+41.217567	1380878856643833984	M5	(55)	3	11.855 ± 0.02	−130.24 ± 0.04	−158.0 ± 0.05	(72)	25.08 ± 0.04	(72)
2M16183317-2517504	244.638232	−25.297361	6048838533014900992	M6	(15)	2	11.709 ± 0.023	−10.92 ± 0.19	−20.07 ± 0.16	(72)	5.1 ± 0.16	(72)
2M16195143-2241332	244.964321	−22.692577	6050500784144963712	M6.75	(60)	2	13.868 ± 0.036	−7.88 ± 0.37	−22.29 ± 0.24	(72)	6.77 ± 0.29	(72)
2M16204144-2425491	245.172688	−24.430326	6049278745688783232	M7.5	(15)	1	13.419 ± 0.027	−10.01 ± 0.42	−21.93 ± 0.29	(72)	6.28 ± 0.28	(72)

Table 3.2 (*continued*)

Table 3.2 (*continued*)

APOGEE ID	RA (deg)	Dec (deg)	*Gaia* eDR3 Source ID	SpT	SpT Ref	N_{obs}	2MASS H (mag)	μ_α (mas yr^{-1})	μ_δ (mas yr^{-1})	μ Ref	π (mas)	π Ref
2M16222304-2407108	245.59603	−24.119675	6049395706238205440	M6	(60)	1	13.858 ± 0.041	−12.2 ± 0.79	−20.23 ± 0.57	(72)	6.07 ± 0.66	(72)
2M16222521-2405139	245.605058	−24.087208	6049407594709184256	M9+M9.5	(27)	1	13.804 ± 0.049	−15.98 ± 0.34	−24.61 ± 0.24	(72)	7.6 ± 0.29	(72)
2M16235155-2317270	245.964832	−23.290842	6050211681303674368	M8	(21)	1	12.894 ± 0.024	−7.73 ± 0.19	−27.34 ± 0.13	(72)	7.23 ± 0.16	(72)
2M16265698+3954482	246.73745	+39.913391	1332811575531596800	M7.5	(13)	12	12.664 ± 0.022	41.76 ± 0.13	−16.75 ± 0.15	(72)	20.89 ± 0.12	(72)
2M16271693+3514132	246.820553	+35.237011	1329273106595583872	M6	(35)	3	12.546 ± 0.025	22.14 ± 0.1	−37.86 ± 0.14	(72)	9.44 ± 0.11	(72)
2M16271825+3538347	246.82605	+35.642998	1329300388227708800	M7	(65)	4	11.73 ± 0.024	−105.33 ± 0.04	162.12 ± 0.05	(72)	36.57 ± 0.04	(72)
2M16281707+1334204	247.071157	+13.572345	4460652192092375040	M6	(53)	2	10.997 ± 0.021	−184.05 ± 0.21	−100.99 ± 0.18	(72)	25.38 ± 0.27	(72)
2M16311879+4051516	247.828309	+40.864334	1332966881549315456	M6	(44)	12	8.869 ± 0.023	−143.43 ± 0.03	306.27 ± 0.03	(72)	88.82 ± 0.03	(72)
2M16360984+4000243	249.041036	+40.00676	1331933581137007104	M5	(55)	4	11.965 ± 0.022	−6.97 ± 0.11	−85.6 ± 0.12	(72)	16.17 ± 0.1	(72)
2M16402068+6736046	250.086172	+67.601295	1648484868558988544	M7	(44)	1	9.294 ± 0.021	−273.27 ± 0.29	365.31 ± 0.28	(72)	69.82 ± 0.23	(72)
2M16463154+3434554	251.631453	+34.582073	1326893351115617024	M6	(51)	4	9.968 ± 0.017	−383.68 ± 0.03	−383.5 ± 0.03	(72)	84.01 ± 0.03	(72)
2M16485878+3005366	252.244945	+30.093517	1311338590181283584	M6	(63)	2	12.646 ± 0.033	−136.61 ± 0.16	−25.5 ± 0.17	(72)	13.37 ± 0.15	(72)
2M16572919+2448509	254.371656	+24.814152	4572719468075516288	M5	(71)	4	11.705 ± 0.019	71.55 ± 0.33	387.0 ± 0.46	(72)	33.39 ± 0.42	(72)
2M19005974-3647109	285.248946	−36.786385	6731215545363943296	M4	(37)	2	13.333 ± 0.035	3.86 ± 0.21	−28.94 ± 0.17	(72)	6.59 ± 0.19	(72)
2M19241634+7533121	291.068089	+75.553368	2289304297045379456	M6	(53)	2	9.28 ± 0.026	369.42 ± 0.02	592.28 ± 0.03	(72)	94.07 ± 0.02	(72)
2M19544358+1801581	298.681615	+18.032827	1821315795663331456	M8	(59)	6	11.517 ± 0.024	−40.2 ± 0.08	−454.0 ± 0.08	(72)	49.91 ± 0.1	(72)
2M20353517-0608285	308.896554	−6.141258	6908281142715616640	M7	(76)	3	12.596 ± 0.035	23.61 ± 0.09	18.2 ± 0.07	(72)	9.23 ± 0.08	(72)
2M20491376+3216514	312.307335	+32.28096	1859954695858413184	M6	(45)	3	11.179 ± 0.021	−158.69 ± 0.03	−268.41 ± 0.04	(72)	42.84 ± 0.04	(72)
2M21272531+5553150	321.855489	+55.887512	2177877452238559104	M8	(73)	3	11.327 ± 0.018	308.52 ± 0.08	264.0 ± 0.06	(72)	57.55 ± 0.06	(72)
2M21381698+5257188	324.57076	+52.955242	2173367633501430272	M7.5[a]	(59, 71)	3	11.169 ± 0.028	218.43 ± 0.05	26.9 ± 0.05	(72)	55.01 ± 0.05	(72)
2M22021125-1109461	330.546894	−11.162809	2613754712222934656	M6/6.5e	(18)	3	11.713 ± 0.022	130.75 ± 0.09	−188.45 ± 0.08	(72)	35.98 ± 0.08	(72)
2M22400144+0532162	340.006039	+5.537857	2706200898267171328	M6pec	(54)	3	11.087 ± 0.022	113.85 ± 0.12	−130.01 ± 0.09	(72)	29.1 ± 0.09	(72)
2M22551142+1442456	343.79761	+14.712685	2816270602141797760	M6	(76)	5	12.587 ± 0.023	45.14 ± 0.12	−25.8 ± 0.09	(72)	11.74 ± 0.1	(72)
2M23200703+1150071	350.029308	+11.835315	2810945804767773440	M6.5e	(20)	3	11.815 ± 0.024	406.67 ± 0.13	−433.83 ± 0.09	(72)	37.41 ± 0.09	(72)

[a] Lick/KAST spectra were obtained on 2020 August 15 with a low signal-to-noise ratio, giving a spectral type of M5.

References: (1) Stephenson (1986); (2) Kirkpatrick et al. (1991); (3) Ardila et al. (2000); (4) Gizis et al. (2000); (5) Jahreiß et al. (2001); (6) McCaughrean et al. (2002); (7) Henry et al. (2002); (8) Preibisch et al. (2002); (9) Gizis (2002); (10) Briceño et al. (2002); (11) Monet et al. (2003); (12) Lépine et al. (2003); (13) Cruz et al. (2003); (14) Reid et al. (2003); (15) Martín et al. (2004); (16) Henry et al. (2004); (17) Luhman (2004); (18) Crifo et al. (2005); (19) Meeus & McCaughrean (2005); (20) Reid & Gizis (2005); (21) Slesnick et al. (2006); (22) Law et al. (2006); (23) Menten et al. (2007); (24) Cruz et al. (2007); (25) Schmidt et al. (2007); (26) Kraus & Hillenbrand (2007); (27) Close et al. (2007); (28) Reid et al. (2008); (29) Slesnick et al. (2008); (30) Phan-Bao et al. (2008); (31) Cruz et al. (2009); (32) Konopacky et al. (2010); (33) Lodieu et al. (2011); (34) Faherty et al. (2011); (35) West et al. (2011); (36) Becker et al. (2011); (37) Sicilia-Aguilar et al. (2011); (38) Kirkpatrick et al. (2011); (39) Melnikov & Eislöffel (2012); (40) Deshpande et al. (2012); (41) Scholz et al. (2012); (42) Zacharias et al. (2012); (43) Aller et al. (2013); (44) Newton et al. (2014); (45) Mann et al. (2014); (46) Esplin et al. (2014); (47) Bardalez Gagliuffi et al. (2014); (48) Dittmann et al. (2014); (49) Schmidt et al. (2014); (50) Cutri et al. (2021); (51) Alonso-Floriano et al. (2015); (52) Gagné et al. (2015a); (53) West et al. (2015); (54) Gagné et al. (2015b); (55) Cook et al. (2016); (56) Theissen et al. (2017); (57) Esplin & Luhman (2017); (58) Dupuy & Liu (2017); (59) Reylé (2018); (60) Luhman et al. (2018); (61) Zhang et al. (2018); (62) Theissen (2018); (63) Bai et al. (2018); (64) Ahmed & Warren (2019); (65) Kiman et al. (2019); (66) Lu et al. (2019); (67) Zhong et al. (2019); (68) Cabello et al. (2019); (69) Tian et al. (2020); (70) Best et al. (2021); (71) Sebastian et al. (2021); (72) Gaia Collaboration et al. (2021); (73) this work.

3.2 APOGEE Spectral Analysis

3.2.1 Spectral Data

My APOGEE spectra were selected from APOGEE single epoch, individual visit spectra (apVisit) files (Abdurro'uf et al. 2022), covering chip a (1.657–1.696 μm), chip b (1.585–1.644 μm), and chip c (1.514–1.581 μm).

The data reduction has been described in detail in Nidever et al. (2015); Holtzman et al. (2018); Jönsson et al. (2020); Abdurro'uf et al. (2022). Each apVisit spectrum underwent dark, flat-field, cosmic ray, flux, sky and telluric corrections, as well as wavelength calibrations. In particular, the wavelength solutions were derived from a combination of sky lines and ThArNe and UNe hollow-cathode lamps (Nidever et al. 2015). Each spectrum was applied with pixel to wavelength solution (HDU4), flux (HDU1), and noise (HDU2). Bad pixels were masked out using the bit mask from HDU3 for each chip, including the "0" (BADPIX; bad pixel mask or pixels from strong persistence jump), "1" (CRPIX; cosmic ray contaminated pixel), "2" (SATPIX; saturated pixel), "3" (UNFIXABLE; unfixable pixel), "4" in (BADDARK; bad pixels from dark frames), "5" (BADFLAT bad pixels from flat-field lamp frames), "6" (BADERR; pixels with high error), "12" (SIG_SKYLINE; pixels near the large flux from sky lines), "14" (NOT_ENOUGH_PSF; less than 50% of point-spread function in good pixels). In order to simultaneously calibrate the wavelength solution imprinted in the spectra, the earth telluric absorption profile has been included in each reduced apVisit spectrum (HDU7). I fit each apVisit spectrum using a forward-modeling method which models the stellar and telluric features simultaneously (see Section 3.2.2).

3.2.2 Forward Modeling

To infer the physical properties of my sources—effective temperature ($T_{\rm eff}$), surface gravity ($\log g$), radial velocity (RV), and rotational velocity ($v \sin i$)—I employed a Markov chain Monte Carlo (MCMC) forward-modeling technique that simultaneously models the telluric and stellar absorption present in the APOGEE data. I used the `Spectral Modeling Analysis and RV Tool` (`SMART`; Hsu et al. 2021), which follows methods previously described in Blake et al. (2010); Burgasser et al. (2016); Theissen et al. (2021); and Hsu et al. (2021).

Each APOGEE spectrum is forward-modeled using the following model:

$$D[p] = \Bigg(C[p] \times \Bigg[\Bigg(M\Big[p^*\big(\lambda\big[1+\frac{RV^*}{c}\big]\big), T_{\rm eff}, \log g\Big] * \kappa_D(v_{\rm micro}) * \kappa_R(v \sin i) \Bigg) \times T\big[p^*(\lambda, {\rm AM}, {\rm PWV})\big] \Bigg] * \kappa_G(\Delta v_{\rm inst}) \Bigg) + C_{\rm flux}\,, \tag{3.1}$$

Here, $D[p]$ is the data model as a function of pixel p; $C[p]$ is a fifth-order polynomial representing the continuum emission; $M[p]$ is the stellar solar-metallicity atmosphere model parameterized by $T_{\rm eff}$ and $\log g$; $p^*(\lambda)$ is a wavelength-to-pixel conversion function, initially provided by the APOGEE reduction pipeline with an additional constant offset parameter $C_{\Delta\lambda}$ to adjust for chip-to-chip variations; $RV^* = RV + v_{\rm bary}$ is the radial velocity of the source plus barycentric motion of the Earth at the observed epoch; c is the speed of light; κ_D is a Gaussian convolution kernel that applies a microturbulence velocity broadening $v_{\rm micro}$, modeled as $2.478 - 0.325 \times \log g$ km s^{-1} (Zamora et al. 2015) ; κ_R is a rotational line broadening convolution kernel based, with the limb-darkening coefficient ε of 0.6 (Gray 1992) for projected rotational velocity $v \sin i$ is projected rotational velocity; $T[p]$ is the telluric absorption model based on the model grid of Moehler et al. (2014) and parameterized by airmass (AM) and precipitable water vapor (PWV); κ_G

is a Gauss-Hermite convolution kernel used to account for the instrumental line spread function (LSF), with the width $v_{\rm inst}$ obtained from the APOGEE pipeline (Nidever et al. 2015; Bovy 2016); and $C_{\rm flux}$ is an constant additive flux offset.

The log-likelihood function of my model fit was defined as

$$\ln \mathscr{L} = -0.5 \times \left[\sum \chi^2 / C_{\rm noise}^2 + \sum \ln(2\pi (C_{\rm noise}\sigma)^2) \right], \tag{3.2}$$

where the statistic

$$\chi^2 = \sum_{i=1}^{N} \frac{(S[p] - \alpha D[p])^2}{\sigma[p]^2} \tag{3.3}$$

compares the observed spectrum $S[p]$ and uncertainty $\sigma[p]$ to the scaled forward model $D[p]$, with the scale factor α determined to minimize χ^2. I include the constant scaling factor $C_{\rm noise}$ to account for under- or overestimation of observational noise, as well as systematic errors such as missing line features. With the 18 continuum parameters, LSF broadening $v_{\rm micro}$, and $v_{\rm bary}$ computed outside the MCMC loop, there are 13 parameters fit by the forward-modeling routine. These parameters are summarized in Table 3.3, including the assumed parameter prior and bound ranges. All priors were assumed to be uniformly distributed between state ranges, which were chosen to match the expected values for late-M and L dwarfs.

Cool dwarfs have abundant molecular absorption lines in their infrared spectra, and hence careful consideration must be made for the choice of stellar model. I explored for my APOGEE sample stellar and substellar synthetic model grids from Baraffe et al. (2015, BT-Settl models), Husser et al. (2013, ACES models), Mészáros et al. (2012, MARCS models), and Marley et al. (2018, Sonora models). For the lowest-temperature dwarfs (L dwarfs), I found that the Sonora models outperform other model sets, particular redward of 1.58 μm where FeH absorption is an important source of opacity (Cushing et al. 2003; Souto et al. 2017), although there are still some missing

features in chip c. Figures 3.5, 3.6 and 3.7 show the best-fit models using Sonora and BT-Settl models for L2β 2MASS J00452143+1634446, M9 2MASS J08440350+0434356, and M7+M9.5 2MASS J04214955+1929086. The best-fit model with Sonora models clearly outperforms (from the spectral fit, residual, and χ^2) the rest models even though the best-fit $T_{\rm eff}$ reaches the $T_{\rm eff}$ ceiling of the Sonora model grid. The best-fit models of the BT-Settl, ACES, and MARCS models give similar results, with missing opacities of FeH redder than 1.58 μm. Compared to Sonora models, the other three models give lower $\log g$ and high $v \sin i$, which can be interpreted as compensation of missing opacities. Such effect has been also found in Keck/NIRSPEC J-band spectra of T dwarfs (Hsu et al. 2021). For warmer sources (late-M dwarfs) the BT-Settl models provided superior fits to Sonora and other models, although telluric absorption strengths are higher for these model fits, suggesting compensation for missing opacity. I therefore focused my analysis on these two model sets, with an "optimal model" transition around 2700 K $\lesssim T_{\rm eff} \lesssim$ 3000 K of BT-Settl models. Among these transition temperatures, the Sonora models can give a better fit (based on χ^2 and visual inspection) with its $T_{\rm eff} \leq$ 2400 K.

For each source and model set, I fit all three chips simultaneously, with the nuisance parameters $C_{\rm flux}$, $C_{\Delta\lambda}$, and continuum parameters modeled separately for each chip. I used the `emcee` code (Foreman-Mackey et al. 2013) to run the MCMC with a kernel-density estimator (KDE) for step size determination, and deployed 100 chains of 1,000 steps each, with the first 800 steps removed for "burn-in". I also used a 3-sigma-clipping mask at the step of 600 to remove outliers. Chains were visually inspected to ensure convergence, and the typical integrated auto-correlation range was $\sim$17 steps. An illustrative fit to data for the L2β 2MASS J00452143+1634446 and M7 2MASS J15512179+2931062 (G 168-14) using the Sonora and BT-Settl models are shown in Figures 3.8 and 3.9, respectively.

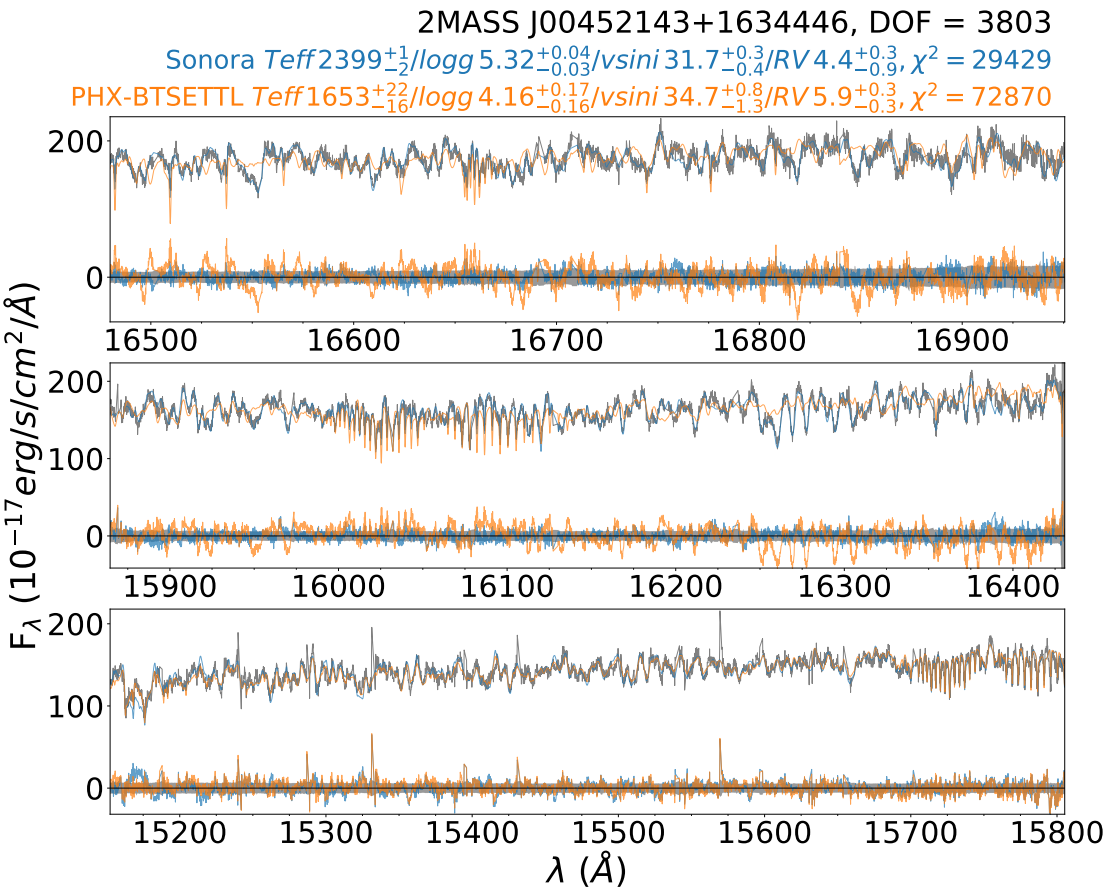

Figure 3.5: Spectrum and best-fit forward models for L2β 2MASS J00452143+1634446, observed on JD of 2456587.736. The APOGEE data are labeled in grey, and the best-fit forward models with Sonora and BT-Settl models are labeled in blue and orange, respectively. The noise and residual (data−model) are depicted in grey-shaded regions and colored lines corresponding to the models, respectively.

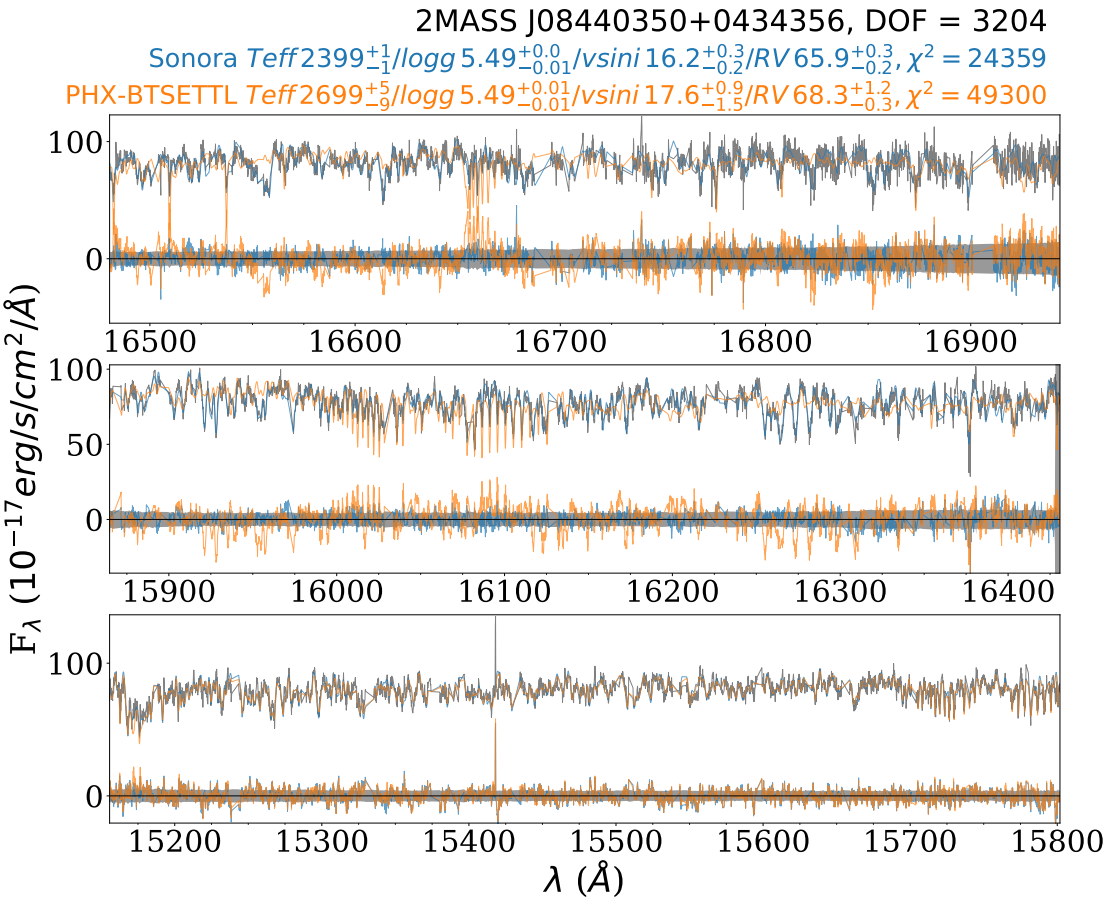

Figure 3.6: Spectrum and best-fit forward models for M9 2MASS J08440350+0434356, observed on JD of 2458198.659. The APOGEE data are labeled in grey, and the best-fit forward models with Sonora and BT-Settl models are labeled in blue and orange, respectively. The noise and residual (data−model) are depicted in grey-shaded regions and colored lines corresponding to the models, respectively.

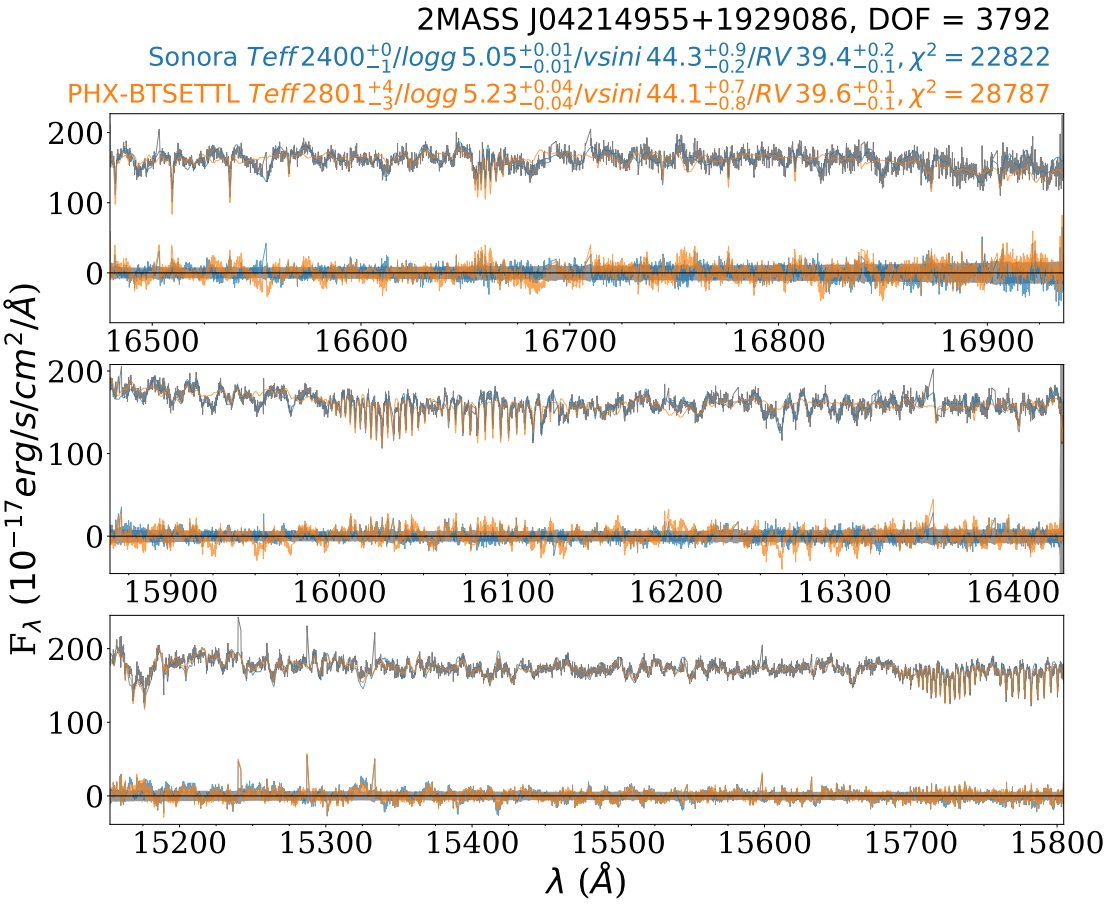

Figure 3.7: Spectrum and best-fit forward models for M7+M9.5 2MASS J04214955+1929086, observed on JD of 2458820.725. The APOGEE data are labeled in grey, and the best-fit forward models with Sonora and BT-Settl models are labeled in blue and orange, respectively. The noise and residual (data−model) are depicted in grey-shaded regions and colored lines corresponding to the models, respectively.

Table 3.3: Modeling Parameter Ranges

Description	Symbol (unit)	Priors[a]	Bounds
Effective Temp.	$T_{\rm eff}$ (K)	(1800, 4000)[b]	(1200, 7000)[b]
...	...	(1,500, 2,400)[c]	(200, 2400)[c]
Surface Grav.	$\log g$ (cm s^{-2})	(3.5, 5.5)	(3.5, 5.5)
Rot. Vel.	$v \sin i$ (km s^{-1})	(0, 50)	(0, 100)
Radial Vel.	RV (km s^{-1})	($-$100, +200)	($-$100, +200)
Flux Offset[d]	$C_{\rm flux}$	($-$0.01, +0.01)	(-10^4, $+10^4$)
Wave Offset[d]	$C_{\Delta\lambda}$ (Å)	($-$0.1, +0.1)	($-$0.5, +0.5)
Airmass	AM	(1.0, 3.0)	(1.0, 3.0)
Water Vapor	PWV (mm)	(0.5, 20.0)	(0.5, 20.0)
Noise Factor	$C_{\rm noise}$	(1.0, 5.0)	(1.0, 10.0)

[a] All priors assume a uniform distribution over range specified
[b] $T_{\rm eff}$ range for BT-Settl (Phoenix) models
[c] $T_{\rm eff}$ range for Sonora models
[d] Three chips are fitted individually.

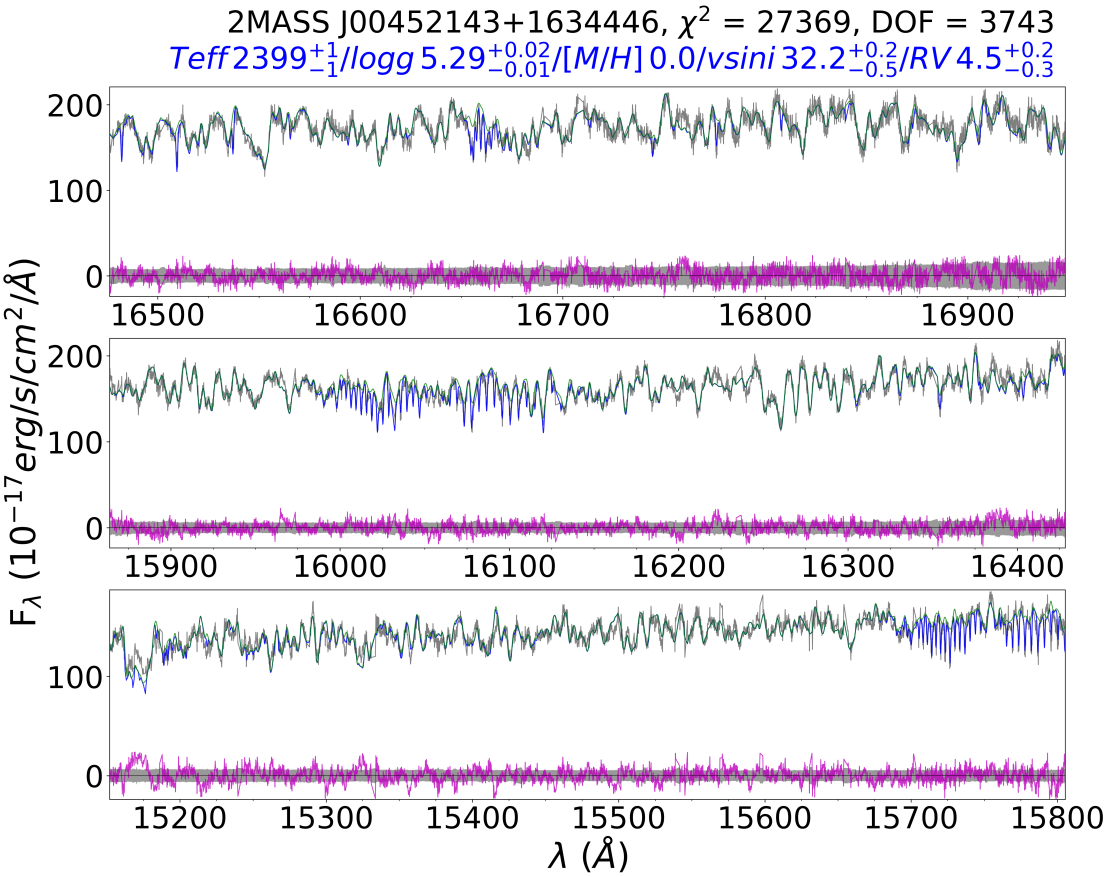

Figure 3.8: Spectrum and best-fit forward model for L2β 2MASS J00452143+1634446, observed on JD of 2456587.736. The APOGEE data, and the best-fit forward model with/without telluric absorption are labeled in grey, blue, and green, respectively. The noise and residual (data−model) are depicted in grey-shaded regions and magenta lines, respectively. The residual highlights some missing molecular opacities, including H_2O and FeH.

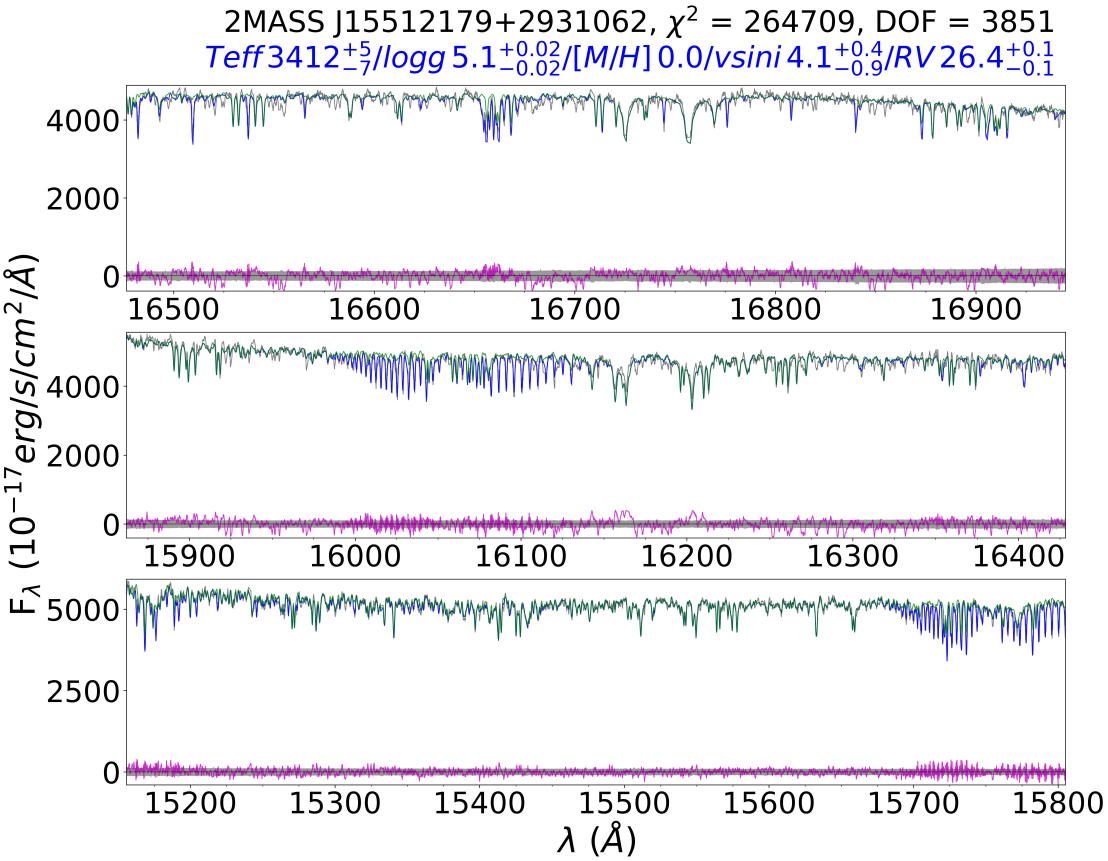

Figure 3.9: Spectrum and best-fit forward model for M7 2MASS J15512179+2931062 (G 168-14), observed on JD of 2458258.85130. The APOGEE data, and the best-fit forward model with/without telluric absorption are labeled in grey, blue, and green, respectively. The noise and residual (data−model) are depicted in grey-shaded regions and magenta lines, respectively. The residual highlights some missing molecular opacities, including H_2O and FeH .

3.3 Results of APOGEE M and L Dwarfs

In this section, I review my RV, $v \sin i$, $T_{\rm eff}$, and $\log g$ measurements, all of which are compiled in Table 3.4.

3.3.1 Radial Velocities

My RV measurements span the range -61.43 km s^{-1} to $+66.68$ km s^{-1} with a median value of -2.1 km s^{-1} and a median measurement uncertainty of 23 km s^{-1}. To assess sources of systematic uncertainty, I evaluated the scatter in measurements inferred from 13 epochs of observations of the M2 2MASS J16495034+4745402, one of the RV standards in the Deshpande et al. (2013) APOGEE sample. I compared fits based on MARCS, BT-Settl, and ACES models, which had internal per-epoch scatter of 0.18 km s^{-1}, 0.19 km s^{-1}, and 0.16 km s^{-1}, respectively; and an overall scatter between models of 0.18 km s^{-1}. I therefore conservatively assume an overall systematic RV uncertainty of 0.19 km s^{-1}, which has been added to the reported RV measurements for all sources, resulting in a final median RV precision of 0.3 km s^{-1}.

I explored whether this precision could be improved by modeling restricted wavelength regions where strong telluric absorption can be used to improve the wavelength calibration. This was motivated by higher fitting scatter in these regions caused by slight mismatches between the observed and modeled spectra, which may be due to offsets in the wavelength calibrations derived from arc lamp lines. I explored fitting individual regions of strong telluric absorption of 16560–16700 Å on chip a, 15980–16160 Å on chip b, and 15100–15500 Å and 15500–16800 Å on chip c (see Figure 3.8), and included an additional pixel-to-wavelength zero-point offset term in my model. Unfortunately, the variance in RV measurements between the regions (0.23–0.56 km s^{-1}) was worse than fitting all three chips simultaneously, likely due to the lack of stellar lines. I conjecture

that slight improvements in the APOGEE pipeline wavelength calibration could be realized by combining arc lines, sky emission lines, and telluric absorption lines to compute the overall wavelength calibration.

I quantified the validity of my RV measurements by comparing my measured RVs with those reported in the literature, summarized in Table 3.5. A total of 59 sources in my sample have reported RVs in the literature, 43 of which include RV uncertainties. Figure 3.10 compares these values. 77% of these sources have consistent RVs to within 3σ deviation, while ten sources are significant outliers. Three of these outliers, 2MASS J08294949+2646348 (ΔRV = 5.5 km s^{-1}), 2MASS J15512179+2931062 (ΔRV = 8.7 km s^{-1}), and 2MASS J16311879+4051516 (ΔRV = 4.4 km s^{-1}), are based on measurements made with lower-resolution data ($\lambda/\Delta\lambda \approx 2000$) reported in Terrien et al. (2015), and may reflect underestimated uncertainties. Three other outliers, 2MASS J04262939+2624137, 2MASS J04294568+2630468, and 2MASS J04330945+2246487 are all members of the Taurus Complex star-forming region and have prior APOGEE measurements reported by Kounkel et al. (2019) that are 2–3 km s^{-1} offset lower than my measurements. Both Cook et al. (2014) and Kounkel et al. (2019) report a systematic red-shift in RV measurements among the lowest temperature sources in their samples ($T_{\rm eff} \leq 3,400$ K) compared to the higher-mass stars in clusters, and the latter study proposes a systematic correction of $\Delta\text{RV} = 12.84 - 0.0038 \times T_{\rm eff}$. Accounting for this offset brings my measurements fully in line with RVs reported in Kounkel et al. (2019). Two of the outliers, 2MASS J03505737+1818069 (LP 413$-$53) and 2MASS J08501918+1056436 appear to be RV-variable binaries based on the high scatter of individual epoch measurements; these are discussed in further detail in Section 3.4.5. Of the remaining two outliers, the M8 2MASS J07140394+3702459 appears to be poorly fit by BT-Settl models due to a lack of FeH opacities, whereas the Sonora models provide a much better fit, resulting in a shift of 2–4 km s^{-1} (depending on the epoch) and bringing

my measurement in line with that from the APOGEE pipeline. As the literature measurement from Deshpande et al. (2013) utilized BT-Settl models, I attribute this difference to modeling systematics. Finally, the M6 2MASS J16093019−2059536, a reported member of the Upper Scorpius Association (Slesnick et al. 2006), has a significantly different RV from my measurements (RV$= -1.3 \pm 0.6$ km s^{-1}) compared to that reported in Dahm et al. (2012) (RV$= -5.1 \pm 0.6$ km s^{-1}). The latter is based on Keck/HIRES optical high-resolution spectra and cross-correlation with the M8 standard VB 10. On the other hand, my measurement is fully consistent with that reported in Jönsson et al. (2020, -0.98 ± 0.09 km s^{-1}), using the cross-correlation method with the DR16 APOGEE spectra. The variance between these measurements could be due to the same RV offset found for Taurus members in near-infrared spectra noted above, or variability induced by a binary (only one epoch of APOGEE data was available for this source).

For completeness, I also compared my measured RVs with those provided by the APOGEE DR17 pipeline `Doppler` (Nidever 2021), which uses cross-correlation with `The Cannon` models (Ness et al. 2015). While performing well for warmer stars, the pipeline is known to have systematic issues with M dwarfs with $T_{\rm eff} \lesssim 3{,}500$ K (Abdurro'uf et al. 2022). Indeed, roughly half of the sources in my sample with literature measurements show a $>3\sigma$ discrepancy with APOGEE pipeline RVs, and 16 sources in my sample have pipeline RVs > 250 km s^{-1}. In general, I thus consider APOGEE pipeline RVs to be unreliable for these low-temperature objects. While all of my APOGEE sources have radial velocities from the APOGEE DR17 pipeline (182 sources), there are 121 sources as more than 3-σ outliers (66% of the sample) compared to my RV measurements.

In summary, all of the significant outliers between my and literature measurements can be explained by methodological or astrophysical causes, and I conclude that my RV measurements are robust to a precision of 0.3 km s^{-1}.

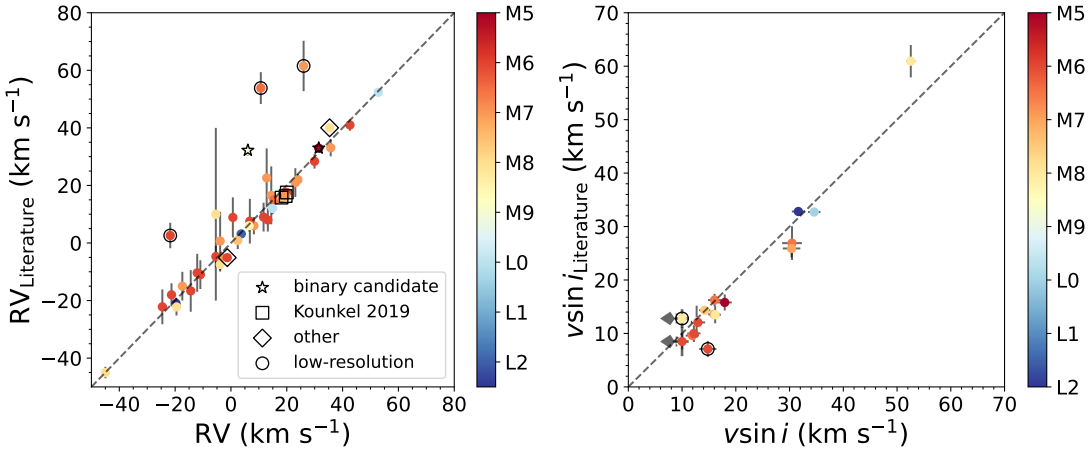

Figure 3.10: Comparison of RV (left) and $v \sin i$ (right) measurements from my APOGEE data to previous values reported in the literature (see Table 3.5). The black dashed line delineates perfect agreement. Sources are color-coded by spectral types. RV outliers are labeled with large symbols indicating binary candidates (stars), young sources with systematic RV offsets (Kounkel et al. 2019; squares), measurements based on low-resolution SpeX spectra (Terrien et al. 2015, circles), and other issues (diamonds). $v \sin i$ outliers are also highlighted by larger symbols, and are largely attributed to the systematic differences between Sonora and BT-Settl models.

3.3.2 Projected Rotational Velocities

Measured $v \sin i$ values for my sample range from 0.4 km s^{-1} to 96.1 km s^{-1}, with a median value of 16 km s^{-1}. The distribution of my measurements is shown in Figure 3.11. To determine my $v \sin i$ detection limit, I compared the distribution of all of my $v \sin i$ for both the Sonora and BT-Settl models and determined my $v \sin i$ detection limit as 10 km s^{-1}, which is more conservative than the $v \sin i = 8$ km s^{-1} floor in Gilhool et al. (2018) and $v \sin i = 5$ km s^{-1} floor in Deshpande et al. 2013), and I set my weighted average $\langle v \sin i \rangle = 10$ km s^{-1} for sources with $\langle v \sin i \rangle < 10$ km s^{-1}. My median $v \sin i$ measurement precision is 1.0 km s^{-1}. In addition to MCMC uncertainty for $v \sin i$, I compared multi-epoch measurements ($N_{obs} \geq 3$) for all of my non-binary sources, and I found that the median scatter (STD) distribution for these sources to be 0.95 km s^{-1}, which I determined as my systematic $v \sin i$ uncertainty and therefore conservatively

added 0.95 km s^{-1} to all of my weighted average $v \sin i$ measurements.

Again, I assess the reliability of my $v \sin i$ measurements being compared to literature values (Figure 3.10). There are 17 sources with literature measurements, two of which are identified as $>3\sigma$ outliers: 2MASS J07140394+3702459 ($<$ 10 km s^{-1}; best-fit $v \sin i = 7.3 \pm 1.1$ km s^{-1} vs. 12.8 ± 0.5 km s^{-1} in Deshpande et al. 2013) and 2MASS J16311879+4051516 (14.8 ± 1.6 km s^{-1} vs. 7.1 ± 1.5 km s^{-1} in Reiners et al. 2018). In these two cases, I find that Sonora models provide a better fit to the APOGEE data, whereas the literature values are based on comparisons to BT-Settl models. I therefore attribute these deviations to systematics associated with model choice, and conjecture that my measured $v \sin i$ values are robust.

The distribution of $v \sin i$ measurements of my sample as a function of spectral type is shown in Figure 3.12. Median values are approximately constant over the M6–L2 range of 16^{+17}_{-7} km s^{-1} (uncertainties computed from the 84$^{\text{th}}$ and 16$^{\text{th}}$ percentiles), which is consistent with trends previously reported in the literature (Crossfield 2014; Tannock et al. 2021; Hsu et al. 2021; Figure 3.13). Median $v \sin i$ values for the full APOGEE plus literature sample are 14^{+16}_{-6} km s^{-1} for M5-L0 dwarfs, 19^{+19}_{-8} km s^{-1} for L0-L5 dwarfs, 22^{+11}_{-4} km s^{-1} for L5-T0 dwarfs, and 28^{+15}_{-17} km s^{-1} for T0-T9 dwarfs, consistent with previous findings showing reduced angular momentum loss toward lower temperature stars and brown dwarfs (Mohanty & Basri 2003; Reiners & Basri 2010; Irwin et al. 2011). It should be noted that my sample and the literature sample are both biased toward young sources, particularly for late M and L dwarfs; and the young cluster members in my sample do show a statistically consistent median $v \sin i = 20^{+25}_{-6}$ km s^{-1} (uncertainties computed from the 84$^{\text{th}}$ and 16$^{\text{th}}$ percentiles). While the majority of my sources have $v \sin i < 40$ km s^{-1}, there are six sources with $v \sin i > 60$ km s^{-1}. Four sources identified as young sources have likely not had time to lose angular momentum. These include three sources previously identified as members of the 10 Myr Upper

Scorpius moving group (M7 2MASS J15560497−2106461, M6 2M16003023−2334457, and M8 2MASS J16045199−2224108; Pecaut & Mamajek 2016). The fourth source appears to be a member of the Orion Nebular Cluster (L0 2MASS J05350162−0521489; Meeus & McCaughrean 2005). The other two sources are likely binaries. The M5 2MASS J09381783+0132490 is spatially resolved binary ($1\farcs7$) in both PanSTARRS and *Gaia* data, with both components having a common parallax and proper motion. 2MASS J15010818+2250020 (aka TVLM 513-46546) is a source with known periodic radio variability (Hallinan et al. 2006) and a potential giant planet companion identified by radio astrometry (Curiel et al. 2020), which I also identify as an RV variable in my sample ($\Delta RV_{max} \sim 2$ km s^{-1}). This source is discussed in further detail below.

3.3.3 Effective Temperatures and Surface Gravities

I examined the modeled effective temperatures and surface gravities for my APOGEE sample. Of the 180 spectra modeled, 160 were best-fit by the Sonora models while 20 were best-fit by the BT-Settl models. The Sorona grid has a $T_{\rm eff}$ ceiling of 2,400 K, which corresponds to a spectral type of approximately M9 (Filippazzo et al. 2015). As this encompasses the majority of my sample, all of the inferred best-fit temperatures were close to the maximum limit, making any inference of $T_{\rm eff}$ trends impossible. On the other hand, $T_{\rm eff}$s inferred from BT-Settl models ranged between 2798 K and 3644 K, with a median of 3162 K. Figure 3.14 shows the $T_{\rm eff}$ trend as a function of spectral type. While the best-fit $T_{\rm eff}$s from the Sonora models almost all reach the $T_{\rm eff}$ ceiling, the best-fit $T_{\rm eff}$s from the BT-Settl models show a general decreasing trend toward later spectral types from M4 to M7. The two outliers in this trend are the binary M7 2M15512179+2931062 (G 168-14; $T_{\rm eff}$ = 3426±9 K; *Gaia* RUWE = 1.521) and the young source L0 2MASS J05350162−0521489 (V V2113 Ori; $T_{\rm eff}$ = 3162±13 K). Comparing to empirical spectral type to $T_{\rm eff}$ relations from Pecaut & Mamajek (2013)

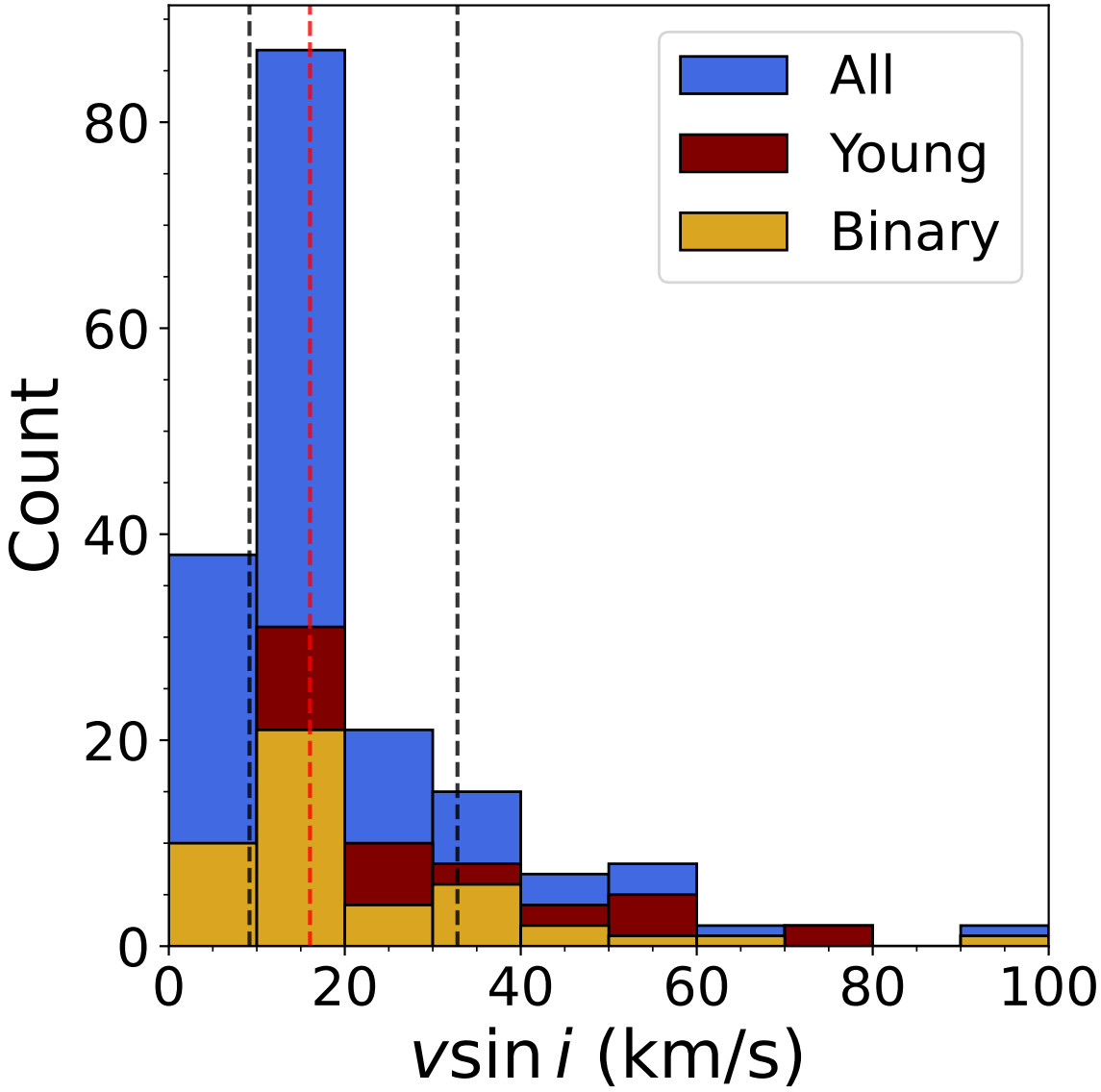

Figure 3.11: Histogram of $v \sin i$ measurements. The median and 16%/84% quantiles are indicated by vertical dashed lines, respectively. Binaries, young cluster members, and overall sample are indicated by stacked yellow, red and blue histograms, respectively.

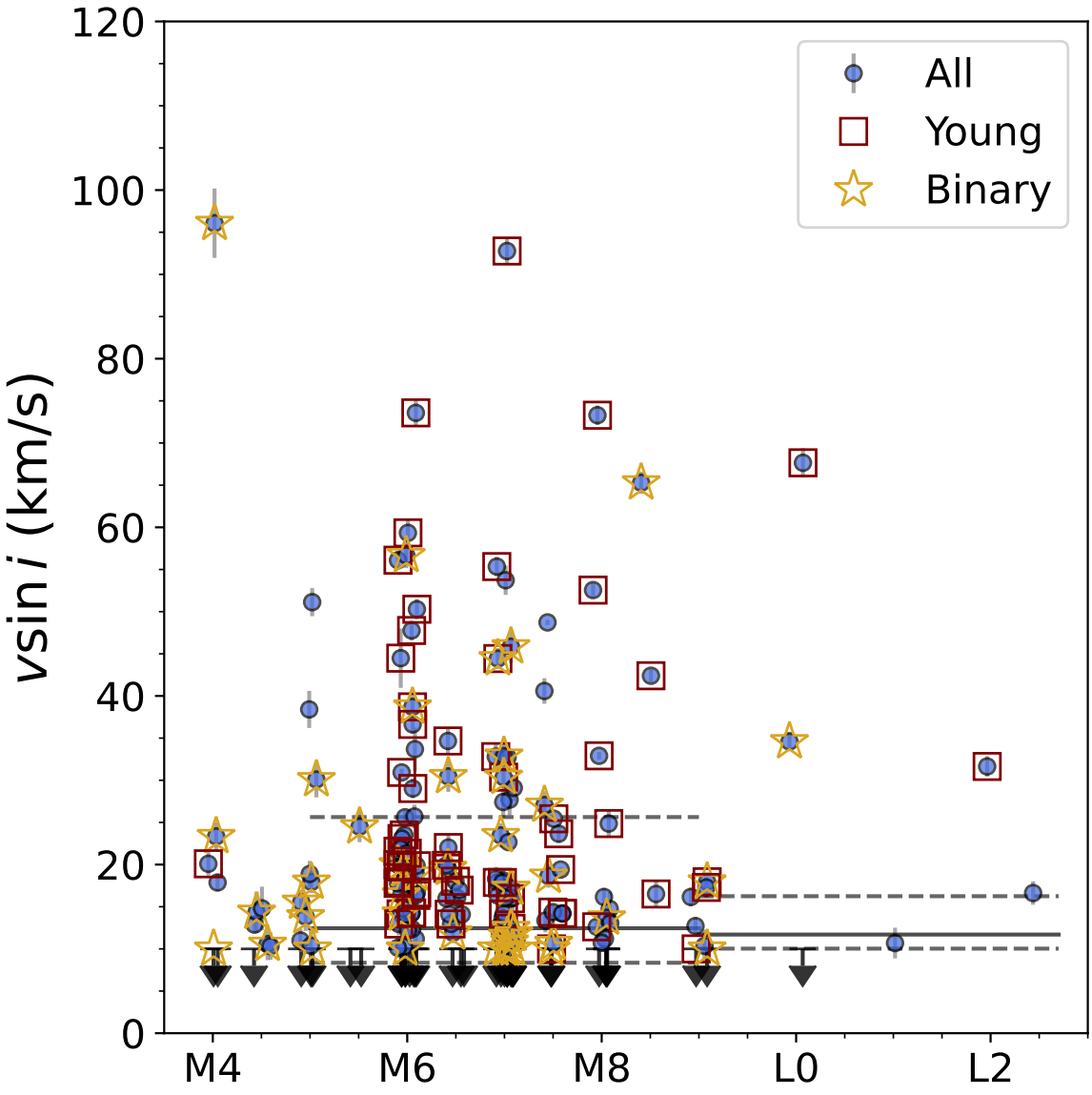

Figure 3.12: Distribution of $v \sin i$ measurements as a function of spectral type. The overall sample are indicated by blue dots, the binary candidates are indicated by yellow stars, and young sources are indicated by red squares. Sources with $v \sin i \leq 10$ km s^{-1} (below my measurement limit) are indicated by downward black arrows. The median and the 84$^{\rm th}$/16$^{\rm th}$ percentiles are labeled in solid and dashed grey lines for M5–M8 and M9–L2 subtypes, respectively.

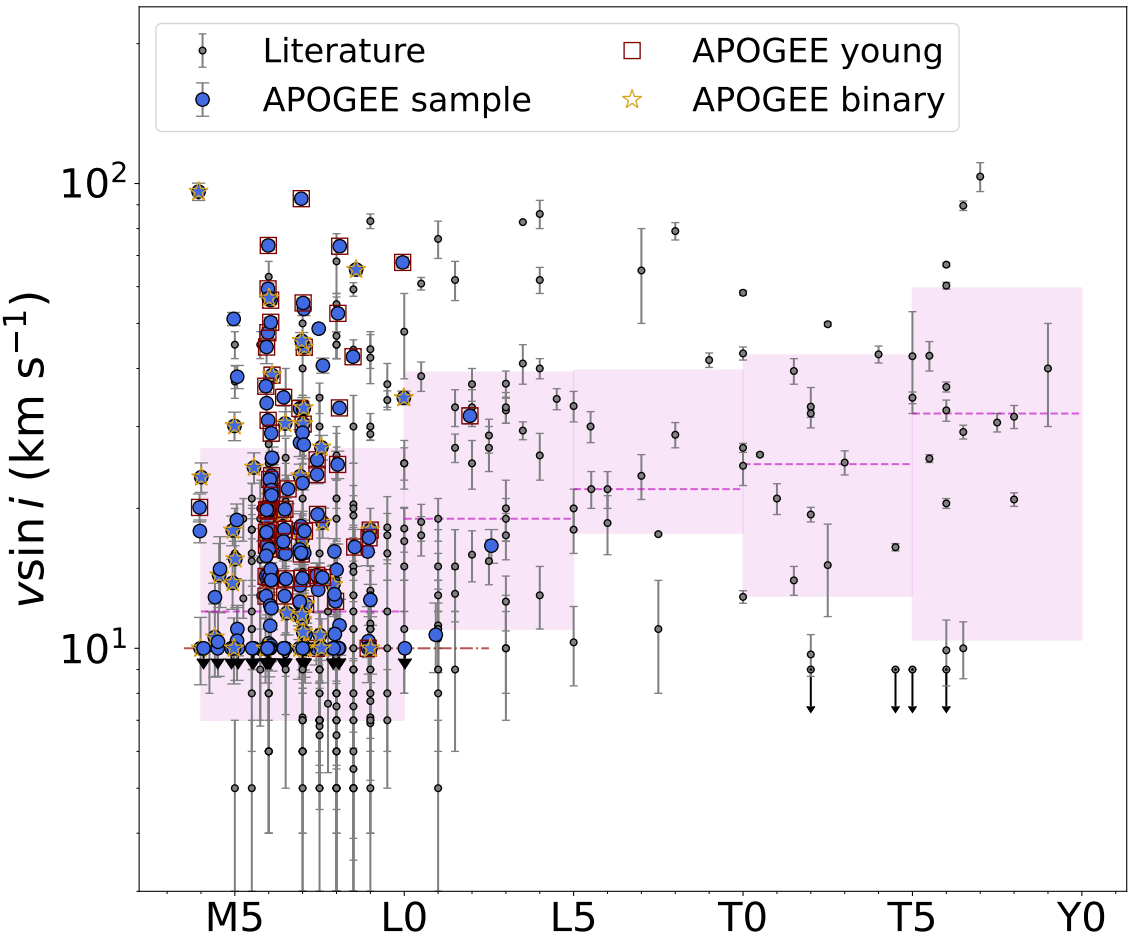

Figure 3.13: Comparison of APOGEE $v \sin i$ measurements (blue large dots) to reported literature measurements (grey small dots) as a function of spectral type. The binary candidates and known young sources are denoted in yellow stars and red squares, respectively. Median values and 16%/84% quantiles in 5-subtype bins are indicated by horizontal magenta bands. The minimum $v \sin i$ limit for my APOGEE sample is indicated by the yellow dashed line, and sources with measurements below this limit are denoted by downward black arrows. The median $v \sin i$s are 12^{+15}_{-5} km s^{-1}, 19^{+20}_{-8} km s^{-1}, 22^{+18}_{-4} km s^{-1}, 25^{+18}_{-12} km s^{-1}, and 32^{+28}_{-22} km s^{-1} in the bins of M4–L0, L0–L5, L5–T0, T0–T5, and T5–Y0, respectively.

and Filippazzo et al. (2015), my best-fit $T_{\rm eff}$s with BT-Settl are higher than the empirical $T_{\rm eff}$s, which can be attributed to the model discrepancy in H-band and/or young sources and binaries in my sample. Surface gravities from the Sonora model fits scatter across the full model parameter range of $3.5 \leq \log g \leq 5.5$, with members of young clusters typically having $\log g$ values closer to the minimum. Surface gravities from the BT-Settl model fits have the narrower range of $4.4 \leq \log g \leq 5.5$, with the young cluster members again having values in the bottom half of this range. These can be shown in Figure 3.15. Finally, I compare the distribution between $T_{\rm eff}$ and $\log g$ between Sonora and BT-Settl models, shown in Figure 3.16. As expected, $T_{\rm eff}$s from the Sonora models are stacked at $T_{\rm eff}$ = 2400 K with $\log g$ spanning across the whole parameter space of $\log g$, while $T_{\rm eff}$s from the BT-Settl models span from 2798 K to 3644 K with narrower $\log g$s. The young sources with the BT-Settl models locate at the lower end of the $\log g$ distribution. Given the limited temperature fit range for the Sonora models and large scatter in inferred surface gravities for both models, I do not regard these values as realistic estimates, and do not further investigate their trends. However, I verified that variations in $T_{\rm eff}$ and $\log g$ about the optimal values had minimal influence on derived RV and $v \sin i$ values, as did the choice of model. I focus the remainder of my analysis on these velocities.

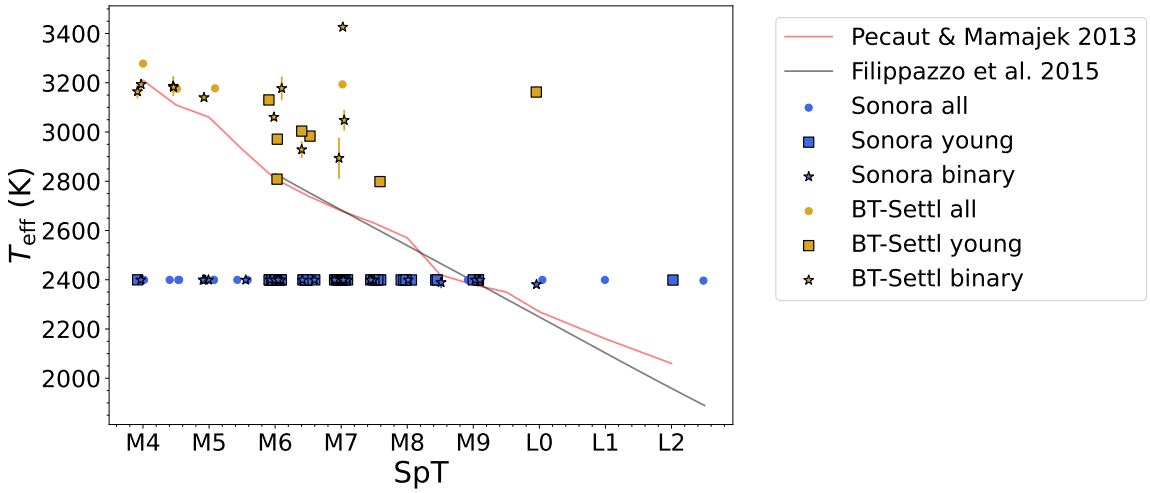

Figure 3.14: Comparison of my best-fit $T_{\rm eff}$s as a function of spectral type between the Sonora (blue) and BT-Settl (yellow) models. The young sources and binaries are depicted in square boxes and stars, respectively. Over-plotted is empirical $T_{\rm eff}$-spectral type relations from Pecaut & Mamajek (2013, red line) and Filippazzo et al. (2015, black line). The uncertainty of. the Filippazzo et al. (2015) relation is 113 K.

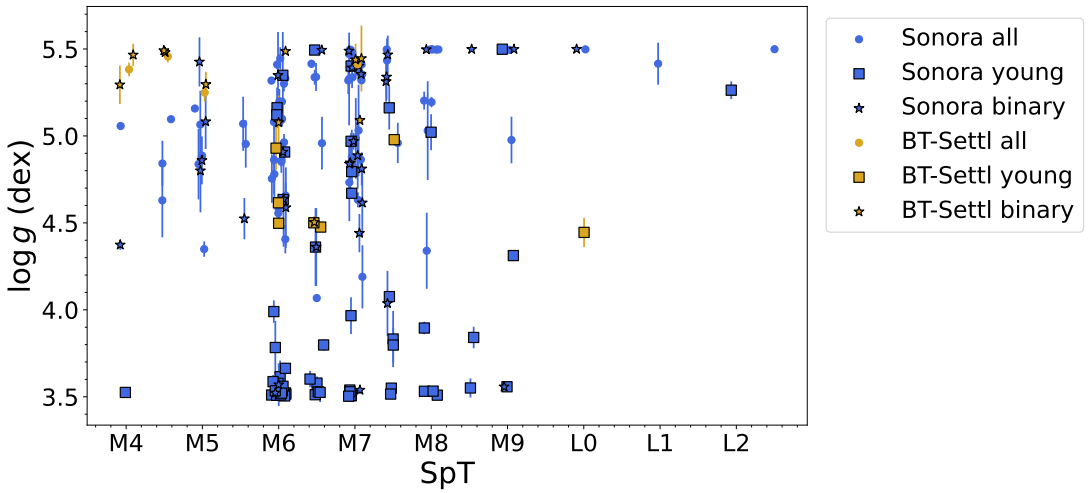

Figure 3.15: Comparison of my best-fit log gs as a function of spectral type between the Sonora (blue) and BT-Settl (yellow) models. The young sources and binaries are depicted in square boxes and stars, respectively.

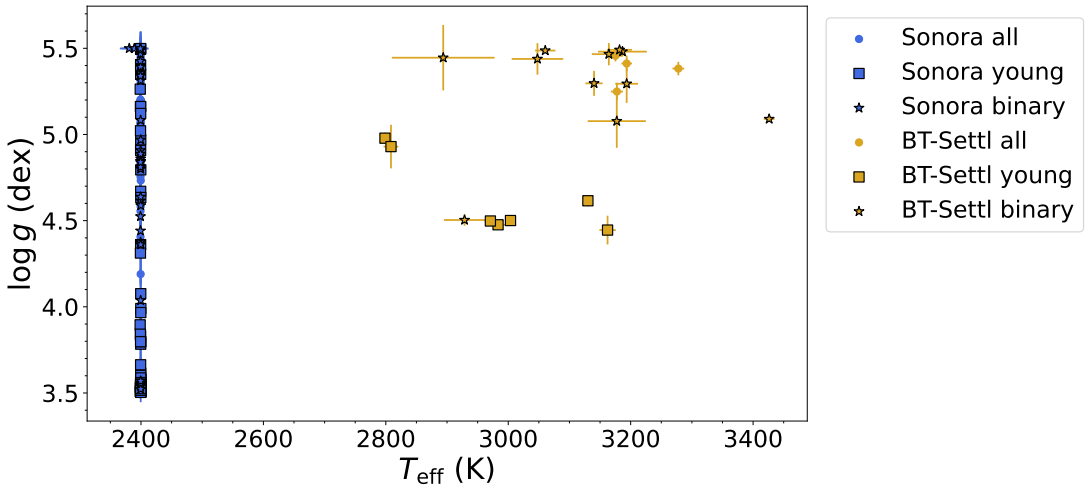

Figure 3.16: Comparison of my best-fit $T_{\rm eff}$s and $\log g$s between the Sonora (blue) and BT-Settl (yellow) models. The young sources and binaries are depicted in square boxes and stars, respectively.

Table 3.4: Spectral Model Fit Parameters

APOGEE ID	Plate	Loc. ID	Fiber ID	JD (day)	bary.[a] ($km\ s^{-1}$)	S/N	RV ($km\ s^{-1}$)	$\langle RV \rangle$[b] ($km\ s^{-1}$)	$v \sin i$ ($km\ s^{-1}$)	$\langle v \sin i \rangle$[b,c] ($km\ s^{-1}$)	$T_{\rm eff}$ (K)	$\langle T_{\rm eff} \rangle$[b] (K)	$\log g$ ($cm\ s^{-2}$)	$\langle \log g \rangle$[b] ($cm\ s^{-2}$)	Mdl[d]
2M00312793+6139333	6228	4243	131	2456171.848	16.15	29.4	$-34.5^{+0.1}_{-0.1}$	$-34.4^{+0.2}_{-0.2}$	$9.0^{+0.4}_{-0.4}$	< 10	$2399.6^{+0.7}_{-0.3}$	$2399.6^{+0.3}_{-0.2}$	$4.81^{+0.02}_{-0.02}$	$4.73^{+0.19}_{-0.22}$	S
⋯	6229	4243	134	2456172.852	15.99	27.9	$-34.3^{+0.2}_{-0.2}$	⋯	$10.3^{+1.5}_{-0.7}$	⋯	$2399.7^{+0.6}_{-0.3}$	⋯	$4.67^{+0.04}_{-0.04}$	⋯	S
⋯	6228	4243	122	2456177.838	15.18	32.4	$-34.6^{+0.2}_{-0.2}$	⋯	$3.5^{+1.4}_{-0.9}$	⋯	$2399.3^{+1.0}_{-0.5}$	⋯	$5.12^{+0.03}_{-0.03}$	⋯	S
⋯	6228	4243	125	2456202.709	9.62	28.1	$-34.0^{+0.3}_{-0.2}$	⋯	$8.6^{+0.2}_{-0.9}$	⋯	$2399.5^{+0.6}_{-0.4}$	⋯	$4.68^{+0.02}_{-0.02}$	⋯	S
⋯	6229	4243	137	2456203.752	9.28	33.7	$-34.6^{+0.3}_{-0.2}$	⋯	$7.9^{+1.0}_{-0.9}$	⋯	$2399.5^{+0.5}_{-0.3}$	⋯	$4.83^{+0.02}_{-0.03}$	⋯	S
⋯	6229	4243	137	2456223.734	3.27	26.6	$-34.8^{+0.4}_{-0.3}$	⋯	$10.6^{+0.2}_{-0.9}$	⋯	$2399.7^{+0.5}_{-0.2}$	⋯	$4.38^{+0.03}_{-0.02}$	⋯	S
2M00452143+1634446	6561	4476	131	2456587.736	−6.46	34.1	$4.5^{+0.3}_{-0.2}$	$3.7^{+0.4}_{-0.6}$	$32.2^{+0.5}_{-0.2}$	$31.6^{+1.1}_{-1.2}$	$2399.0^{+1.4}_{-0.7}$	$2398.8^{+1.1}_{-0.6}$	$5.29^{+0.01}_{-0.02}$	$5.26^{+0.05}_{-0.05}$	S
⋯	6561	4476	125	2456607.662	−15.84	33.8	$3.4^{+0.1}_{-0.2}$	⋯	$31.2^{+0.4}_{-0.5}$	⋯	$2398.8^{+2.0}_{-1.0}$	⋯	$5.32^{+0.04}_{-0.01}$	⋯	S
⋯	6561	4476	131	2456616.665	−19.61	35.9	$3.6^{+0.2}_{-0.3}$	⋯	$31.2^{+0.2}_{-0.4}$	⋯	$2398.2^{+2.3}_{-1.2}$	⋯	$5.2^{+0.01}_{-0.02}$	⋯	S
2M01120002+1502170	12094	2778	200	2458814.659	−20.29	42.9	$-44.6^{+0.2}_{-0.2}$	$-44.3^{+0.3}_{-0.3}$	$7.4^{+0.7}_{-0.4}$	< 10	$2399.5^{+1.0}_{-0.4}$	$2399.4^{+0.6}_{-0.3}$	$5.08^{+0.02}_{-0.02}$	$4.95^{+0.13}_{-0.14}$	S
⋯	12094	2778	200	2458819.652	−22.17	32.5	$-44.1^{+0.3}_{-0.2}$	⋯	$8.2^{+1.2}_{-0.9}$	⋯	$2399.3^{+0.8}_{-0.5}$	⋯	$4.99^{+0.04}_{-0.07}$	⋯	S
⋯	12094	2778	158	2458868.575	−30.01	20.3	$-44.1^{+0.3}_{-0.3}$	⋯	$10.4^{+0.7}_{-0.6}$	⋯	$2399.3^{+1.1}_{-0.5}$	⋯	$4.8^{+0.2}_{-0.02}$	⋯	S
2M01154176+0059317	12075	2759	277	2458779.803	−6.49	22.2	$11.4^{+0.3}_{-0.3}$	$10.8^{+0.8}_{-1.2}$	$33.0^{+0.4}_{-1.6}$	$33.7^{+2.2}_{-2.6}$	$2399.3^{+1.0}_{-0.5}$	$2399.2^{+0.8}_{-0.3}$	$4.68^{+0.07}_{-0.09}$	$4.56^{+0.08}_{-0.04}$	S
⋯	12075	2759	277	2458780.716	−6.74	20.7	$9.1^{+1.6}_{-0.3}$	⋯	$42.4^{+1.8}_{-2.0}$	⋯	$2399.2^{+1.3}_{-0.5}$	⋯	$4.54^{+0.05}_{-0.02}$	⋯	S
2M01215816+0101007	12075	2759	258	2458779.803	−5.72	28.8	$10.3^{+0.1}_{-0.2}$	$10.3^{+0.1}_{-0.1}$	$9.0^{+0.6}_{-0.6}$	< 10	$2399.3^{+1.3}_{-0.5}$	$2399.2^{+1.0}_{-0.5}$	$5.4^{+0.03}_{-0.06}$	$5.34^{+0.04}_{-0.04}$	S
⋯	12075	2759	258	2458780.716	−5.98	28.1	$10.2^{+0.1}_{-0.2}$	⋯	$9.7^{+1.1}_{-1.0}$	⋯	$2399.0^{+1.5}_{-0.7}$	⋯	$5.32^{+0.02}_{-0.02}$	⋯	S
2M01243124−0027556	12075	2759	77	2458779.803	−5.68	48.8	$-3.8^{+0.2}_{-0.1}$	$-3.9^{+0.2}_{-0.2}$	$27.4^{+0.2}_{-1.3}$	$27.7^{+1.1}_{-1.8}$	$2399.5^{+0.7}_{-0.3}$	$2399.5^{+0.5}_{-0.2}$	$5.47^{+0.02}_{-0.02}$	$5.46^{+0.02}_{-0.02}$	S
⋯	12075	2759	77	2458780.716	−5.93	44.8	$-4.0^{+0.2}_{-0.2}$	⋯	$30.4^{+1.1}_{-0.6}$	⋯	$2399.6^{+0.8}_{-0.3}$	⋯	$5.46^{+0.02}_{-0.02}$	⋯	S
2M01514363+0046188	12078	2762	283	2458837.620	−26.23	12.4	$13.5^{+0.4}_{-0.4}$	$14.4^{+0.6}_{-0.7}$	$19.7^{+0.4}_{-0.3}$	$18.1^{+1.0}_{-1.4}$	$2399.2^{+1.0}_{-0.6}$	$2399.3^{+0.6}_{-0.3}$	$4.93^{+0.03}_{-0.03}$	$4.83^{+0.1}_{-0.11}$	S
⋯	12078	2762	283	2458838.668	−26.61	11.7	$15.0^{+0.3}_{-0.2}$	⋯	$18.0^{+0.2}_{-0.4}$	⋯	$2399.3^{+1.0}_{-0.5}$	⋯	$4.83^{+0.02}_{-0.02}$	⋯	S
⋯	12078	2762	283	2458840.666	−27.09	10.2	$14.2^{+0.4}_{-0.5}$	⋯	$17.9^{+0.1}_{-0.3}$	⋯	$2399.4^{+1.3}_{-0.5}$	⋯	$4.58^{+0.04}_{-0.04}$	⋯	S
2M02500239−0808417	10222	2475	19	2458861.574	−26.73	15.7	$26.3^{+0.3}_{-0.3}$	$25.6^{+0.6}_{-0.7}$	$11.1^{+0.7}_{-0.9}$	< 10	$2399.4^{+0.8}_{-0.4}$	$2399.4^{+0.7}_{-0.4}$	$4.78^{+0.07}_{-0.05}$	$5.07^{+0.13}_{-0.16}$	S
⋯	10222	2475	19	2458862.596	−26.92	29.7	$25.1^{+0.3}_{-0.3}$	⋯	$7.1^{+1.1}_{-0.8}$	⋯	$2399.2^{+1.1}_{-0.7}$	⋯	$5.14^{+0.03}_{-0.03}$	⋯	S
2M03040207+0045512	9193	2394	295	2457691.823	2.91	42.2	$29.6^{+0.1}_{-0.2}$	$29.9^{+0.3}_{-0.3}$	$16.3^{+0.2}_{-1.3}$	$20.0^{+2.4}_{-1.7}$	$2399.3^{+1.0}_{-0.5}$	$2399.5^{+0.2}_{-0.2}$	$5.49^{+0.01}_{-0.01}$	$5.35^{+0.25}_{-0.21}$	S
⋯	9193	2394	295	2457692.844	2.34	25.6	$30.3^{+0.2}_{-0.2}$	⋯	$19.8^{+0.1}_{-0.2}$	⋯	$2399.4^{+0.8}_{-0.5}$	⋯	$4.96^{+0.02}_{-0.09}$	⋯	S
⋯	9193	2394	295	2457693.850	1.82	57.0	$30.0^{+0.2}_{-0.2}$	⋯	$16.0^{+0.1}_{-0.2}$	⋯	$2399.4^{+0.9}_{-0.4}$	⋯	$5.47^{+0.02}_{-0.02}$	⋯	S
⋯	9193	2394	246	2457776.624	−28.66	32.6	$30.5^{+0.2}_{-0.2}$	⋯	$19.7^{+1.6}_{-0.2}$	⋯	$2399.2^{+1.1}_{-0.6}$	⋯	$5.2^{+0.04}_{-0.13}$	⋯	S
⋯	9193	2394	246	2457778.616	−28.83	28.8	$30.1^{+0.2}_{-0.2}$	⋯	$20.0^{+0.3}_{-1.6}$	⋯	$2399.4^{+0.8}_{-0.5}$	⋯	$4.88^{+0.06}_{-0.07}$	⋯	S
⋯	9193	2394	246	2457779.581	−28.82	37.6	$29.9^{+0.5}_{-0.3}$	⋯	$20.2^{+0.5}_{-1.5}$	⋯	$2399.5^{+0.6}_{-0.3}$	⋯	$5.39^{+0.04}_{-0.06}$	⋯	S
⋯	9194	2395	289	2457779.629	−28.94	37.4	$30.2^{+0.1}_{-0.1}$	⋯	$19.7^{+0.1}_{-0.2}$	⋯	$2399.7^{+0.4}_{-0.3}$	⋯	$4.92^{+0.02}_{-0.02}$	⋯	S
⋯	9193	2394	246	2457780.576	−28.88	24.0	$30.3^{+0.4}_{-0.2}$	⋯	$25.5^{+0.2}_{-1.7}$	⋯	$2399.5^{+0.7}_{-0.4}$	⋯	$4.81^{+0.04}_{-0.02}$	⋯	S
⋯	9194	2395	289	2457780.615	−28.98	40.8	$30.4^{+0.2}_{-0.2}$	⋯	$18.0^{+0.2}_{-1.7}$	⋯	$2399.4^{+0.8}_{-0.5}$	⋯	$5.17^{+0.02}_{-0.02}$	⋯	S
⋯	9194	2395	289	2457782.614	−29.09	37.7	$29.6^{+0.2}_{-0.3}$	⋯	$23.5^{+0.1}_{-0.1}$	⋯	$2399.6^{+0.5}_{-0.3}$	⋯	$4.84^{+0.02}_{-0.02}$	⋯	S
⋯	9194	2395	289	2457783.614	−29.13	37.9	$29.9^{+0.1}_{-0.1}$	⋯	$19.7^{+0.1}_{-0.1}$	⋯	$2399.5^{+0.6}_{-0.4}$	⋯	$5.01^{+0.05}_{-0.08}$	⋯	S
⋯	9192	2393	180	2457785.587	−29.12	41.1	$29.6^{+0.1}_{-0.2}$	⋯	$17.9^{+0.1}_{-0.2}$	⋯	$2399.4^{+1.2}_{-0.4}$	⋯	$5.46^{+0.02}_{-0.02}$	⋯	S
⋯	9192	2393	180	2457786.587	−29.13	40.3	$30.1^{+0.1}_{-0.1}$	⋯	$17.9^{+0.1}_{-0.2}$	⋯	$2399.2^{+0.9}_{-0.5}$	⋯	$5.39^{+0.03}_{-0.02}$	⋯	S
⋯	9192	2393	180	2457787.588	−29.14	26.7	$29.6^{+0.3}_{-0.3}$	⋯	$19.7^{+0.1}_{-0.2}$	⋯	$2399.6^{+0.7}_{-0.3}$	⋯	$4.85^{+0.03}_{-0.03}$	⋯	S
⋯	9192	2393	259	2458014.929	21.00	82.3	$29.5^{+0.1}_{-0.2}$	⋯	$16.0^{+1.7}_{-0.3}$	⋯	$2399.2^{+1.1}_{-0.6}$	⋯	$5.39^{+0.02}_{-0.04}$	⋯	S
⋯	9192	2393	259	2458015.960	20.58	28.8	$29.5^{+0.2}_{-0.3}$	⋯	$15.9^{+0.5}_{-0.5}$	⋯	$2399.2^{+1.1}_{-0.6}$	⋯	$5.39^{+0.01}_{-0.02}$	⋯	S
2M03282839+3116273	6225	4587	55	2456236.727	7.15	10.5	$15.9^{+0.3}_{-1.3}$	$15.4^{+0.8}_{-0.9}$	$34.7^{+1.4}_{-0.8}$	$30.5^{+2.5}_{-1.8}$	$2837.0^{+18.0}_{-32.6}$	$2928.6^{+33.6}_{-28.7}$	$4.18^{+0.1}_{-0.14}$	$4.5^{+0.03}_{-0.03}$	B
⋯	6226	4587	234	2456315.637	−26.94	12.4	$14.3^{+0.2}_{-0.2}$	⋯	$32.9^{+1.6}_{-1.8}$	⋯	$2964.2^{+17.1}_{-14.0}$	⋯	$4.51^{+0.02}_{-0.03}$	⋯	B
⋯	6224	4587	222	2456561.814	23.56	10.1	$15.7^{+0.5}_{-0.5}$	⋯	$31.3^{+1.3}_{-0.9}$	⋯	$2925.3^{+17.4}_{-18.6}$	⋯	$4.56^{+0.05}_{-0.06}$	⋯	B

Table 3.4 (*continued*)

Table 3.4 (*continued*)

APOGEE ID	Plate	Loc. ID	Fiber ID	JD (day)	bary.[a] ($km\ s^{-1}$)	S/N	RV ($km\ s^{-1}$)	$\langle RV \rangle$[b] ($km\ s^{-1}$)	$v \sin i$ ($km\ s^{-1}$)	$\langle v \sin i \rangle$[b,c] ($km\ s^{-1}$)	$T_{\rm eff}$ (K)	$\langle T_{\rm eff} \rangle$[b] (K)	$\log g$ ($cm\ s^{-2}$)	$\langle \log g \rangle$[b] ($cm\ s^{-2}$)	Mdl[d]
⋯	11425	5925	234	2458447.665	−2.69	10.4	$16.8^{+0.9}_{-0.3}$	⋯	$31.9^{+1.0}_{-1.2}$	⋯	$2922.9^{+13.8}_{-13.8}$	⋯	$4.52^{+0.03}_{-0.04}$	⋯	B
⋯	11425	5925	228	2458527.600	−29.54	13.1	$14.9^{+0.2}_{-0.2}$	⋯	$28.4^{+0.8}_{-0.9}$	⋯	$2980.5^{+18.4}_{-12.9}$	⋯	$4.49^{+0.03}_{-0.03}$	⋯	B
⋯	11425	5925	234	2458744.878	25.67	13.7	$15.9^{+0.3}_{-1.2}$	⋯	$30.9^{+1.4}_{-0.8}$	⋯	$2916.4^{+17.5}_{-13.8}$	⋯	$4.51^{+0.02}_{-0.04}$	⋯	B
⋯	11425	5925	234	2458773.830	16.09	12.1	$15.3^{+0.3}_{-0.3}$	⋯	$26.7^{+1.1}_{-0.8}$	⋯	$2944.3^{+11.4}_{-9.4}$	⋯	$4.49^{+0.02}_{-0.02}$	⋯	B
⋯	11425	5925	234	2458796.752	5.45	10.2	$16.0^{+0.3}_{-0.4}$	⋯	$30.3^{+1.2}_{-0.9}$	⋯	$2924.4^{+12.9}_{-10.5}$	⋯	$4.45^{+0.05}_{-0.05}$	⋯	B
⋯	11425	5925	240	2458803.745	1.90	13.7	$16.4^{+0.2}_{-0.2}$	⋯	$28.7^{+1.0}_{-0.7}$	⋯	$2894.3^{+11.7}_{-11.4}$	⋯	$4.5^{+0.02}_{-0.03}$	⋯	B
⋯	11425	5925	234	2458820.666	−6.70	10.8	$15.1^{+0.3}_{-0.5}$	⋯	$32.9^{+1.0}_{-1.3}$	⋯	$2945.4^{+18.3}_{-32.6}$	⋯	$4.52^{+0.02}_{-0.03}$	⋯	B
2M03293053+3127280	7070	4587	293	2456671.555	−24.26	18.7	$16.7^{+0.4}_{-0.4}$	$15.8^{+0.5}_{-0.5}$	$15.3^{+1.1}_{-0.6}$	$16.0^{+1.0}_{-1.2}$	$2992.4^{+7.9}_{-4.8}$	$2983.3^{+11.4}_{-10.5}$	$4.49^{+0.03}_{-0.02}$	$4.48^{+0.02}_{-0.02}$	B
⋯	7071	4587	230	2456674.559	−25.12	21.6	$15.5^{+0.2}_{-0.2}$	⋯	$16.1^{+0.2}_{-0.5}$	⋯	$2972.4^{+6.7}_{-6.1}$	⋯	$4.47^{+0.03}_{-0.02}$	⋯	B
2M03505737+1818069	12138	6179	19	2459159.856	7.51	26.2	$6.0^{+0.2}_{-0.1}$	$6.0^{+0.2}_{-0.1}$	$12.7^{+0.4}_{-1.0}$	$12.7^{+0.4}_{-1.0}$	$2399.3^{+0.8}_{-0.5}$	$2399.3^{+0.8}_{-0.5}$	$5.49^{+0.01}_{-0.0}$	$5.49^{+0.01}_{-0.0}$	S
2M04110642+1247481	12146	6187	121	2458793.799	9.82	23.9	$39.4^{+0.1}_{-0.2}$	$39.3^{+0.2}_{-0.2}$	$14.2^{+0.2}_{-0.4}$	$14.2^{+1.0}_{-1.1}$	$2399.4^{+1.0}_{-0.5}$	$2399.4^{+0.6}_{-0.3}$	$4.88^{+0.02}_{-0.02}$	$4.91^{+0.05}_{-0.05}$	S
⋯	12146	6187	121	2458796.862	8.15	32.1	$39.0^{+0.3}_{-0.2}$	⋯	$13.9^{+0.4}_{-0.4}$	⋯	$2399.4^{+0.7}_{-0.4}$	⋯	$5.0^{+0.03}_{-0.06}$	⋯	S
2M04185115+2814332	11592	5962	31	2458744.995	27.93	16.4	$21.1^{+0.2}_{-0.2}$	$21.1^{+0.2}_{-0.2}$	$9.2^{+0.6}_{-0.8}$	< 10	$2798.6^{+4.3}_{-3.3}$	$2798.6^{+4.3}_{-3.3}$	$4.98^{+0.03}_{-0.02}$	$4.98^{+0.03}_{-0.02}$	B
2M04204796+5624202	6238	4153	293	2456170.993	24.33	10.3	$-29.5^{+0.4}_{-0.3}$	$-29.5^{+0.3}_{-0.2}$	$16.0^{+0.1}_{-0.2}$	$14.7^{+2.7}_{-2.0}$	$2399.5^{+0.7}_{-0.4}$	$2399.5^{+0.3}_{-0.2}$	$4.63^{+0.03}_{-0.02}$	$5.03^{+0.25}_{-0.28}$	S
⋯	6238	4153	293	2456173.956	24.45	12.5	$-29.8^{+0.2}_{-0.2}$	⋯	$14.1^{+1.5}_{-0.3}$	⋯	$2399.5^{+0.9}_{-0.4}$	⋯	$4.69^{+0.04}_{-0.05}$	⋯	S
⋯	6239	4153	193	2456175.987	24.43	22.4	$-29.4^{+0.2}_{-0.2}$	⋯	$4.0^{+1.0}_{-1.5}$	⋯	$2399.1^{+1.3}_{-0.7}$	⋯	$5.37^{+0.02}_{-0.02}$	⋯	S
⋯	6238	4153	293	2456203.871	21.86	22.6	$-29.3^{+0.2}_{-0.2}$	⋯	$9.0^{+0.4}_{-0.7}$	⋯	$2399.5^{+0.7}_{-0.4}$	⋯	$5.07^{+0.02}_{-0.02}$	⋯	S
⋯	6238	4153	293	2456227.799	15.56	20.9	$-29.5^{+0.3}_{-0.2}$	⋯	$12.5^{+0.3}_{-1.5}$	⋯	$2399.6^{+0.6}_{-0.2}$	⋯	$4.84^{+0.03}_{-0.03}$	⋯	S
⋯	6239	4153	198	2456228.805	15.22	28.6	$-29.9^{+0.2}_{-0.2}$	⋯	$4.7^{+1.2}_{-1.1}$	⋯	$2399.1^{+1.3}_{-0.6}$	⋯	$5.34^{+0.04}_{-0.04}$	⋯	S
⋯	6239	4153	252	2456232.789	13.86	26.9	$-29.4^{+0.2}_{-0.2}$	⋯	$7.1^{+0.8}_{-0.7}$	⋯	$2399.3^{+1.0}_{-0.5}$	⋯	$5.16^{+0.04}_{-0.05}$	⋯	S
2M04214435+2024105	12148	6189	91	2458797.847	9.72	13.3	$41.0^{+0.2}_{-0.2}$	$40.8^{+0.4}_{-0.4}$	$32.8^{+1.5}_{-0.6}$	$32.8^{+1.5}_{-1.1}$	$2399.2^{+1.3}_{-0.6}$	$2399.5^{+0.7}_{-0.3}$	$4.66^{+0.04}_{-0.03}$	$4.67^{+0.03}_{-0.02}$	S
⋯	12148	6189	60	2458802.840	7.22	16.9	$40.1^{+0.4}_{-0.2}$	⋯	$32.8^{+1.7}_{-0.3}$	⋯	$2399.6^{+0.8}_{-0.3}$	⋯	$4.69^{+0.06}_{-0.04}$	⋯	S
2M04214955+1929086	12143	6184	294	2458820.725	−2.02	31.4	$39.4^{+0.2}_{-0.2}$	$39.4^{+0.2}_{-0.2}$	$44.4^{+0.3}_{-1.2}$	$44.4^{+0.3}_{-1.2}$	$2399.6^{+0.5}_{-0.2}$	$2399.6^{+0.5}_{-0.2}$	$4.97^{+0.02}_{-0.05}$	$4.97^{+0.02}_{-0.05}$	S
2M04262939+2624137	9287	5223	233	2457710.833	6.36	20.6	$20.7^{+0.2}_{-0.1}$	$20.0^{+0.4}_{-0.5}$	$14.2^{+0.2}_{-0.3}$	$13.0^{+1.3}_{-1.3}$	$2399.6^{+0.6}_{-0.3}$	$2399.6^{+0.4}_{-0.2}$	$3.6^{+0.02}_{-0.02}$	$3.78^{+0.12}_{-0.15}$	S
⋯	9287	5223	185	2457737.680	−7.44	33.8	$20.0^{+0.1}_{-0.2}$	⋯	$12.3^{+0.1}_{-0.2}$	⋯	$2399.6^{+0.8}_{-0.3}$	⋯	$3.86^{+0.01}_{-0.03}$	⋯	S
⋯	9287	5223	188	2457761.707	−18.91	42.4	$19.7^{+0.1}_{-0.1}$	⋯	$12.4^{+0.2}_{-0.3}$	⋯	$2399.6^{+0.7}_{-0.3}$	⋯	$3.93^{+0.03}_{-0.03}$	⋯	S
2M04294568+2630468	9287	5223	199	2457710.833	6.74	37.1	$17.7^{+0.1}_{-0.2}$	$18.1^{+0.2}_{-0.2}$	$14.2^{+0.2}_{-0.3}$	$14.2^{+1.0}_{-1.0}$	$2399.6^{+0.6}_{-0.3}$	$2399.6^{+0.3}_{-0.2}$	$4.07^{+0.01}_{-0.04}$	$4.08^{+0.01}_{-0.02}$	S
⋯	9287	5223	253	2457737.680	−7.06	52.7	$18.3^{+0.1}_{-0.1}$	⋯	$14.3^{+0.2}_{-0.4}$	⋯	$2399.6^{+0.5}_{-0.2}$	⋯	$4.08^{+0.02}_{-0.03}$	⋯	S
⋯	9287	5223	199	2457761.707	−18.60	57.4	$18.1^{+0.1}_{-0.1}$	⋯	$14.2^{+0.1}_{-0.3}$	⋯	$2399.7^{+0.5}_{-0.2}$	⋯	$4.08^{+0.02}_{-0.03}$	⋯	S
2M04330945+2246487	9259	5222	102	2457683.865	19.33	42.9	$19.5^{+0.2}_{-0.2}$	$19.6^{+0.4}_{-0.4}$	$16.0^{+0.1}_{-0.1}$	$16.0^{+1.0}_{-1.1}$	$2399.7^{+0.3}_{-0.2}$	$2399.6^{+0.3}_{-0.2}$	$3.5^{+0.0}_{-0.01}$	$3.51^{+0.0}_{-0.01}$	S
⋯	9259	5222	91	2457712.842	5.82	38.8	$20.0^{+0.2}_{-0.2}$	⋯	$14.4^{+0.3}_{-1.0}$	⋯	$2399.5^{+0.7}_{-0.3}$	⋯	$3.52^{+0.01}_{-0.02}$	⋯	S
⋯	9259	5222	91	2458010.981	28.98	40.7	$19.1^{+0.3}_{-0.2}$	⋯	$16.1^{+0.1}_{-0.2}$	⋯	$2399.6^{+0.6}_{-0.3}$	⋯	$3.51^{+0.01}_{-0.01}$	⋯	S
2M04351354+2008014	12152	6193	217	2458853.674	−16.81	20.2	$39.9^{+0.4}_{-0.3}$	$40.0^{+0.3}_{-0.2}$	$23.6^{+0.2}_{-0.2}$	$23.7^{+1.0}_{-1.1}$	$2398.9^{+1.1}_{-0.8}$	$2399.1^{+0.8}_{-0.5}$	$5.2^{+0.02}_{-0.02}$	$5.16^{+0.12}_{-0.07}$	S
⋯	12152	6193	222	2458880.638	−26.43	10.6	$40.1^{+0.3}_{-0.2}$	⋯	$23.7^{+0.2}_{-0.4}$	⋯	$2399.2^{+1.1}_{-0.5}$	⋯	$4.95^{+0.03}_{-0.06}$	⋯	S
2M04440164+1621324	12155	6196	139	2458886.664	−27.41	10.1	$21.9^{+0.3}_{-0.3}$	$21.8^{+0.2}_{-0.2}$	$14.4^{+0.7}_{-1.1}$	$14.3^{+1.2}_{-1.2}$	$2822.9^{+17.5}_{-15.3}$	$2808.5^{+11.2}_{-12.1}$	$4.99^{+0.04}_{-0.04}$	$4.93^{+0.12}_{-0.13}$	B
⋯	12155	6196	144	2458915.585	−29.89	10.3	$21.8^{+0.3}_{-0.3}$	⋯	$14.1^{+1.3}_{-0.7}$	⋯	$2803.6^{+9.0}_{-9.9}$	⋯	$4.73^{+0.07}_{-0.07}$	⋯	B
2M04464498+2436404	12150	6191	254	2458854.651	−15.74	30.0	$42.2^{+0.5}_{-0.3}$	$42.2^{+0.5}_{-0.3}$	$17.9^{+0.1}_{-0.2}$	$17.9^{+0.1}_{-0.2}$	$2399.7^{+0.4}_{-0.3}$	$2399.7^{+0.4}_{-0.3}$	$4.79^{+0.04}_{-0.03}$	$4.79^{+0.04}_{-0.03}$	S
2M04552333+3027366	11426	5926	42	2458417.855	20.15	33.8	$17.4^{+0.2}_{-0.2}$	$17.5^{+0.2}_{-0.1}$	$14.2^{+0.1}_{-0.3}$	$14.2^{+1.0}_{-1.0}$	$2399.6^{+0.5}_{-0.3}$	$2399.6^{+0.2}_{-0.1}$	$3.78^{+0.04}_{-0.02}$	$3.62^{+0.09}_{-0.09}$	S
⋯	11427	5926	60	2458438.787	11.14	26.0	$16.9^{+0.3}_{-0.6}$	⋯	$14.2^{+0.1}_{-0.4}$	⋯	$2399.6^{+0.5}_{-0.3}$	⋯	$3.64^{+0.05}_{-0.03}$	⋯	S
⋯	11427	5926	60	2458439.758	10.72	25.1	$17.6^{+0.1}_{-0.1}$	⋯	$14.4^{+0.3}_{-0.8}$	⋯	$2399.6^{+0.6}_{-0.3}$	⋯	$3.57^{+0.03}_{-0.02}$	⋯	S
⋯	11428	5926	47	2458444.753	8.25	36.0	$17.4^{+0.1}_{-0.2}$	⋯	$14.2^{+0.1}_{-0.2}$	⋯	$2399.6^{+0.4}_{-0.2}$	⋯	$3.55^{+0.02}_{-0.03}$	⋯	S
2M04565141+2939310	11426	5926	96	2458417.855	20.28	20.9	$17.1^{+0.2}_{-0.2}$	$17.9^{+0.4}_{-0.4}$	$12.1^{+0.4}_{-0.6}$	$12.4^{+1.0}_{-1.1}$	$2399.5^{+0.7}_{-0.3}$	$2399.4^{+0.4}_{-0.2}$	$3.53^{+0.02}_{-0.04}$	$3.54^{+0.02}_{-0.02}$	S
⋯	11427	5926	98	2458438.787	11.27	14.6	$18.3^{+0.1}_{-0.1}$	⋯	$12.5^{+0.3}_{-0.5}$	⋯	$2399.2^{+1.1}_{-0.6}$	⋯	$3.57^{+0.02}_{-0.02}$	⋯	S
⋯	11427	5926	98	2458439.758	10.85	13.7	$17.9^{+0.2}_{-0.2}$	⋯	$12.8^{+0.5}_{-1.3}$	⋯	$2399.3^{+1.0}_{-0.5}$	⋯	$3.52^{+0.02}_{-0.02}$	⋯	S

Table 3.4 (*continued*)

Table 3.4 (*continued*)

APOGEE ID	Plate	Loc. ID	Fiber ID	JD (day)	bary.[a] ($km\ s^{-1}$)	S/N	RV ($km\ s^{-1}$)	$\langle RV \rangle$[b] ($km\ s^{-1}$)	$v \sin i$ ($km\ s^{-1}$)	$\langle v \sin i \rangle$[b,c] ($km\ s^{-1}$)	$T_{\rm eff}$ (K)	$\langle T_{\rm eff} \rangle$[b] (K)	$\log g$ ($cm\ s^{-2}$)	$\langle \log g \rangle$[b] ($cm\ s^{-2}$)	Mdl[d]
⋯	11428	5926	91	2458444.753	8.39	23.2	$17.9^{+0.2}_{-0.1}$	⋯	$12.5^{+0.2}_{-0.4}$	⋯	$2399.5^{+0.6}_{-0.3}$	⋯	$3.53^{+0.02}_{-0.03}$	⋯	S
2M05350162−0521489	12274	7043	201	2458882.634	−20.28	34.0	$25.0^{+0.3}_{-1.5}$	$25.1^{+0.3}_{-0.6}$	$66.7^{+1.0}_{-0.9}$	$67.7^{+2.4}_{-1.6}$	$3169.7^{+8.3}_{-7.6}$	$3162.3^{+13.4}_{-12.8}$	$4.39^{+0.03}_{-0.04}$	$4.45^{+0.08}_{-0.08}$	B
⋯	12274	7043	201	2458883.686	−20.72	24.7	$25.2^{+1.4}_{-0.7}$	⋯	$70.8^{+1.5}_{-2.0}$	⋯	$3145.2^{+11.9}_{-12.0}$	⋯	$4.55^{+0.05}_{-0.05}$	⋯	B
2M05392474+4038437	6541	4559	164	2456257.734	10.58	65.6	$-5.6^{+0.1}_{-0.1}$	$-5.4^{+0.2}_{-0.2}$	$5.9^{+0.8}_{-0.4}$	< 10	$2399.3^{+0.8}_{-0.5}$	$2399.3^{+0.5}_{-0.3}$	$5.5^{+0.0}_{-0.0}$	$5.5^{+0.0}_{-0.0}$	S
⋯	6541	4559	164	2456261.793	8.55	55.3	$-5.1^{+0.2}_{-0.2}$	⋯	$7.5^{+0.5}_{-0.4}$	⋯	$2399.2^{+1.1}_{-0.6}$	⋯	$5.49^{+0.01}_{-0.0}$	⋯	S
⋯	6541	4559	164	2456313.573	−16.28	57.8	$-5.4^{+0.1}_{-0.1}$	⋯	$7.5^{+0.2}_{-0.2}$	⋯	$2399.4^{+1.0}_{-0.4}$	⋯	$5.5^{+0.01}_{-0.0}$	⋯	S
2M05402570+2448090	6761	4564	250	2456291.683	−6.75	92.3	$25.8^{+0.9}_{-0.3}$	$23.1^{+0.6}_{-0.9}$	$29.1^{+0.1}_{-0.2}$	$30.4^{+2.0}_{-1.6}$	$2399.3^{+0.9}_{-0.5}$	$2399.4^{+0.4}_{-0.2}$	$5.45^{+0.02}_{-0.02}$	$5.4^{+0.03}_{-0.02}$	S
⋯	6761	4564	249	2456559.992	29.54	208.8	$23.8^{+0.2}_{-0.2}$	⋯	$29.3^{+0.8}_{-0.4}$	⋯	$2399.4^{+0.8}_{-0.4}$	⋯	$5.41^{+0.02}_{-0.04}$	⋯	S
⋯	6761	4564	256	2456582.932	26.09	259.7	$22.2^{+0.1}_{-0.1}$	⋯	$32.1^{+1.1}_{-0.8}$	⋯	$2399.5^{+0.8}_{-0.4}$	⋯	$5.41^{+0.02}_{-0.02}$	⋯	S
⋯	6761	4564	249	2456586.926	25.04	193.0	$23.1^{+0.1}_{-0.1}$	⋯	$33.0^{+0.7}_{-0.2}$	⋯	$2399.4^{+0.7}_{-0.5}$	⋯	$5.38^{+0.02}_{-0.01}$	⋯	S
2M06154934−0100415	6358	4123	181	2456202.997	27.01	18.0	$-19.5^{+0.2}_{-0.2}$	$-19.7^{+0.2}_{-0.2}$	$16.3^{+0.3}_{-1.0}$	$16.6^{+1.1}_{-1.4}$	$2335.6^{+8.4}_{-12.9}$	$2396.4^{+14.7}_{-6.5}$	$5.5^{+0.0}_{-0.0}$	$5.5^{+0.0}_{-0.0}$	S
⋯	6359	4123	57	2456206.003	26.81	11.3	$-19.6^{+0.4}_{-0.3}$	⋯	$19.0^{+1.1}_{-0.7}$	⋯	$2398.4^{+1.8}_{-1.2}$	⋯	$5.5^{+0.0}_{-0.0}$	⋯	S
⋯	6358	4123	288	2456206.993	26.77	17.1	$-19.8^{+0.1}_{-0.2}$	⋯	$17.3^{+0.9}_{-0.3}$	⋯	$2392.6^{+7.7}_{-4.9}$	⋯	$5.5^{+0.0}_{-0.0}$	⋯	S
⋯	6359	4123	58	2456209.985	26.52	17.7	$-19.8^{+0.2}_{-0.2}$	⋯	$16.3^{+0.3}_{-1.1}$	⋯	$2396.0^{+5.6}_{-3.0}$	⋯	$5.5^{+0.0}_{-0.0}$	⋯	S
⋯	6358	4123	186	2456233.931	21.93	28.4	$-19.5^{+0.2}_{-0.2}$	⋯	$15.8^{+0.4}_{-0.4}$	⋯	$2283.2^{+20.7}_{-30.2}$	⋯	$5.5^{+0.0}_{-0.0}$	⋯	S
⋯	6359	4123	58	2456235.942	21.32	26.3	$-19.9^{+0.1}_{-0.2}$	⋯	$16.5^{+0.4}_{-0.9}$	⋯	$2395.1^{+7.0}_{-3.3}$	⋯	$5.5^{+0.0}_{-0.0}$	⋯	S
2M06521977−2534505	6333	4292	73	2456228.989	18.93	30.9	$14.8^{+0.1}_{-0.2}$	$14.9^{+0.2}_{-0.2}$	$8.0^{+1.2}_{-0.3}$	< 10	$2399.5^{+0.8}_{-0.4}$	$2399.4^{+0.5}_{-0.3}$	$5.5^{+0.0}_{-0.0}$	$5.5^{+0.0}_{-0.0}$	S
⋯	6333	4292	73	2456232.983	18.46	42.1	$14.8^{+0.1}_{-0.1}$	⋯	$7.8^{+1.2}_{-0.4}$	⋯	$2399.3^{+1.0}_{-0.5}$	⋯	$5.5^{+0.0}_{-0.0}$	⋯	S
⋯	6333	4292	73	2456264.875	11.83	25.7	$15.2^{+0.1}_{-0.2}$	⋯	$9.2^{+0.3}_{-0.3}$	⋯	$2399.5^{+0.8}_{-0.4}$	⋯	$5.5^{+0.0}_{-0.0}$	⋯	S
2M07025026−6102482	12298	7067	179	2458884.720	1.09	84.5	$21.3^{+0.1}_{-0.1}$	$21.3^{+0.1}_{-0.1}$	$16.0^{+0.1}_{-0.1}$	$16.0^{+0.1}_{-0.1}$	$2399.8^{+0.3}_{-0.1}$	$2399.8^{+0.3}_{-0.1}$	$4.07^{+0.02}_{-0.02}$	$4.07^{+0.02}_{-0.02}$	S
2M07140394+3702459	5586	4221	62	2455881.005	22.79	64.0	$35.3^{+0.1}_{-0.1}$	$35.3^{+0.2}_{-0.2}$	$5.3^{+0.4}_{-1.0}$	< 10	$2399.6^{+0.7}_{-0.3}$	$2399.5^{+0.4}_{-0.2}$	$5.5^{+0.0}_{-0.0}$	$5.5^{+0.0}_{-0.0}$	S
⋯	5586	4221	62	2455939.845	−3.70	39.7	$35.2^{+0.1}_{-0.2}$	⋯	$7.4^{+0.2}_{-0.1}$	⋯	$2399.4^{+0.9}_{-0.4}$	⋯	$5.5^{+0.0}_{-0.0}$	⋯	S
⋯	5586	4221	62	2455960.754	−13.78	54.4	$35.8^{+0.2}_{-0.2}$	⋯	$7.4^{+0.3}_{-0.4}$	⋯	$2399.4^{+0.6}_{-0.4}$	⋯	$5.5^{+0.0}_{-0.0}$	⋯	S
2M07464256+2000321	9492	2406	290	2457783.744	−7.73	85.4	$52.7^{+0.2}_{-0.2}$	$52.8^{+0.1}_{-0.1}$	$34.7^{+0.1}_{-0.1}$	$34.6^{+1.0}_{-1.1}$	$2392.8^{+4.3}_{-5.1}$	$2380.9^{+12.5}_{-12.8}$	$5.5^{+0.0}_{-0.0}$	$5.5^{+0.0}_{-0.0}$	S
⋯	9497	2411	113	2457786.730	−9.23	86.7	$52.8^{+0.1}_{-0.1}$	⋯	$33.0^{+0.2}_{-0.9}$	⋯	$2368.4^{+3.8}_{-7.1}$	⋯	$5.5^{+0.0}_{-0.0}$	⋯	S
2M07475737+6653337	9539	5246	204	2457708.002	16.46	12.2	$8.6^{+1.3}_{-0.5}$	$7.4^{+0.7}_{-0.8}$	$49.6^{+1.7}_{-1.8}$	$45.9^{+3.0}_{-1.9}$	$2398.9^{+1.3}_{-0.8}$	$2399.2^{+0.3}_{-0.2}$	$4.62^{+0.03}_{-0.02}$	$4.62^{+0.17}_{-0.19}$	S
⋯	9515	5246	246	2457735.959	8.18	15.7	$8.2^{+0.4}_{-0.2}$	⋯	$44.2^{+0.5}_{-0.5}$	⋯	$2399.1^{+1.1}_{-0.7}$	⋯	$4.75^{+0.02}_{-0.04}$	⋯	S
⋯	9515	5246	294	2457742.880	5.80	17.2	$7.2^{+1.0}_{-0.4}$	⋯	$46.0^{+1.5}_{-1.1}$	⋯	$2399.3^{+1.0}_{-0.5}$	⋯	$4.68^{+0.03}_{-0.02}$	⋯	S
⋯	9539	5246	210	2457761.839	−1.28	11.9	$4.7^{+0.6}_{-0.8}$	⋯	$49.9^{+0.3}_{-0.7}$	⋯	$2399.1^{+1.3}_{-0.6}$	⋯	$4.46^{+0.04}_{-0.09}$	⋯	S
⋯	9515	5246	246	2457789.758	−11.15	22.3	$7.2^{+0.3}_{-0.5}$	⋯	$40.8^{+0.5}_{-1.3}$	⋯	$2399.1^{+1.1}_{-0.5}$	⋯	$4.82^{+0.14}_{-0.02}$	⋯	S
⋯	9515	5246	205	2457793.801	−12.45	10.1	$7.6^{+1.7}_{-0.3}$	⋯	$57.3^{+1.7}_{-1.2}$	⋯	$2398.9^{+1.2}_{-0.8}$	⋯	$3.57^{+0.05}_{-0.04}$	⋯	S
⋯	9539	5246	204	2457795.722	−12.95	13.5	$6.6^{+0.3}_{-0.4}$	⋯	$45.3^{+0.8}_{-0.7}$	⋯	$2399.1^{+1.1}_{-0.6}$	⋯	$4.58^{+0.02}_{-0.02}$	⋯	S
⋯	9539	5246	210	2457821.654	−18.96	14.4	$8.7^{+1.3}_{-0.4}$	⋯	$43.7^{+1.0}_{-0.6}$	⋯	$2399.1^{+1.0}_{-0.6}$	⋯	$4.66^{+0.02}_{-0.03}$	⋯	S
⋯	9539	5246	162	2457825.630	−19.54	22.7	$8.1^{+0.9}_{-0.5}$	⋯	$44.2^{+0.5}_{-0.9}$	⋯	$2399.0^{+1.3}_{-0.7}$	⋯	$4.87^{+0.05}_{-0.03}$	⋯	S
⋯	9666	5246	245	2457827.608	−19.79	18.5	$7.7^{+0.2}_{-0.3}$	⋯	$44.6^{+0.5}_{-1.2}$	⋯	$2399.3^{+0.8}_{-0.5}$	⋯	$4.76^{+0.06}_{-0.02}$	⋯	S
⋯	9726	5246	205	2457878.628	−18.37	16.7	$8.0^{+0.9}_{-1.2}$	⋯	$46.8^{+0.8}_{-1.0}$	⋯	$2399.1^{+1.2}_{-0.6}$	⋯	$4.64^{+0.02}_{-0.03}$	⋯	S
⋯	9666	5246	245	2458054.982	19.85	14.0	$7.1^{+0.6}_{-0.7}$	⋯	$44.2^{+0.8}_{-0.8}$	⋯	$2399.1^{+1.2}_{-0.5}$	⋯	$4.57^{+0.04}_{-0.07}$	⋯	S
⋯	9666	5246	242	2458059.998	19.10	12.8	$5.3^{+1.4}_{-0.4}$	⋯	$46.2^{+1.3}_{-1.6}$	⋯	$2399.1^{+1.1}_{-0.6}$	⋯	$4.35^{+0.05}_{-0.05}$	⋯	S
⋯	9666	5246	242	2458067.965	17.67	17.4	$8.1^{+0.3}_{-0.3}$	⋯	$43.9^{+1.2}_{-0.6}$	⋯	$2399.3^{+0.7}_{-0.5}$	⋯	$4.69^{+0.04}_{-0.05}$	⋯	S
⋯	9726	5246	199	2458097.019	9.57	18.1	$6.0^{+0.4}_{-0.7}$	⋯	$47.8^{+1.6}_{-0.6}$	⋯	$2399.2^{+1.0}_{-0.6}$	⋯	$4.66^{+0.02}_{-0.02}$	⋯	S
⋯	9666	5246	242	2458097.886	9.40	15.7	$7.2^{+0.2}_{-0.3}$	⋯	$46.4^{+0.4}_{-0.9}$	⋯	$2399.4^{+0.7}_{-0.4}$	⋯	$4.6^{+0.02}_{-0.02}$	⋯	S
⋯	9726	5246	241	2458123.962	−0.19	22.4	$8.0^{+1.0}_{-0.6}$	⋯	$44.8^{+0.6}_{-1.1}$	⋯	$2399.4^{+0.7}_{-0.5}$	⋯	$4.6^{+0.03}_{-0.04}$	⋯	S
⋯	9726	5246	241	2458126.947	−1.30	15.2	$7.1^{+0.6}_{-0.7}$	⋯	$48.5^{+0.6}_{-1.2}$	⋯	$2399.3^{+1.1}_{-0.6}$	⋯	$4.37^{+0.03}_{-0.03}$	⋯	S
2M07552256+2755318	8986	2337	18	2458072.998	26.28	16.6	$-3.8^{+0.2}_{-0.2}$	$-3.9^{+0.3}_{-0.2}$	$10.8^{+0.4}_{-1.4}$	< 10	$2399.4^{+0.9}_{-0.4}$	$2399.4^{+0.5}_{-0.3}$	$4.78^{+0.02}_{-0.02}$	$4.86^{+0.07}_{-0.07}$	S

Table 3.4 (*continued*)

Table 3.4 (*continued*)

APOGEE ID	Plate	Loc. ID	Fiber ID	JD (day)	bary.[a] ($km\ s^{-1}$)	S/N	RV ($km\ s^{-1}$)	$\langle RV \rangle$[b] ($km\ s^{-1}$)	$v \sin i$ ($km\ s^{-1}$)	$\langle v \sin i \rangle$[b,c] ($km\ s^{-1}$)	$T_{\rm eff}$ (K)	$\langle T_{\rm eff} \rangle$[b] (K)	$\log g$ ($cm\ s^{-2}$)	$\langle \log g \rangle$[b] ($cm\ s^{-2}$)	Mdl[d]
⋯	8986	2337	18	2458074.877	26.05	27.6	$-3.7^{+0.2}_{-0.2}$	⋯	$7.3^{+0.6}_{-0.3}$	⋯	$2399.3^{+0.7}_{-0.6}$	⋯	$4.93^{+0.02}_{-0.02}$	⋯	S
⋯	8986	2337	18	2458077.997	24.94	28.7	$-4.4^{+0.2}_{-0.4}$	⋯	$9.2^{+0.4}_{-0.3}$	⋯	$2399.5^{+0.7}_{-0.4}$	⋯	$4.87^{+0.03}_{-0.03}$	⋯	S
2M07564895+6649595	9539	5246	179	2457708.002	16.69	10.4	$0.2^{+0.4}_{-0.4}$	$0.2^{+0.4}_{-0.4}$	$11.4^{+0.9}_{-0.6}$	$10.7^{+1.0}_{-1.3}$	$2399.0^{+1.5}_{-0.7}$	$2399.4^{+0.2}_{-0.2}$	$3.64^{+0.04}_{-0.06}$	$4.04^{+0.19}_{-0.15}$	S
⋯	9515	5246	176	2457735.959	8.57	15.0	$0.1^{+0.2}_{-0.3}$	⋯	$10.6^{+0.4}_{-0.4}$	⋯	$2399.3^{+1.0}_{-0.5}$	⋯	$4.08^{+0.03}_{-0.04}$	⋯	S
⋯	9515	5246	155	2457742.880	6.22	17.3	$-0.1^{+0.2}_{-0.2}$	⋯	$10.9^{+0.4}_{-0.4}$	⋯	$2399.5^{+0.8}_{-0.4}$	⋯	$4.12^{+0.03}_{-0.03}$	⋯	S
⋯	9539	5246	260	2457761.839	−0.82	12.0	$0.1^{+0.3}_{-0.3}$	⋯	$10.8^{+0.4}_{-0.8}$	⋯	$2399.3^{+1.1}_{-0.5}$	⋯	$3.6^{+0.04}_{-0.06}$	⋯	S
⋯	9515	5246	176	2457789.758	−10.72	22.4	$0.2^{+0.2}_{-0.2}$	⋯	$10.6^{+0.2}_{-0.4}$	⋯	$2399.6^{+0.6}_{-0.3}$	⋯	$4.09^{+0.03}_{-0.04}$	⋯	S
⋯	9539	5246	179	2457795.722	−12.54	13.3	$0.6^{+0.3}_{-0.2}$	⋯	$10.7^{+0.3}_{-0.8}$	⋯	$2399.4^{+0.8}_{-0.4}$	⋯	$3.91^{+0.06}_{-0.05}$	⋯	S
⋯	9539	5246	161	2457821.654	−18.69	13.1	$0.6^{+0.2}_{-0.2}$	⋯	$12.4^{+0.6}_{-0.5}$	⋯	$2399.3^{+1.0}_{-0.5}$	⋯	$3.56^{+0.03}_{-0.04}$	⋯	S
⋯	9539	5246	266	2457825.630	−19.30	20.6	$0.6^{+0.2}_{-0.2}$	⋯	$10.5^{+0.2}_{-0.9}$	⋯	$2399.5^{+0.7}_{-0.4}$	⋯	$4.11^{+0.03}_{-0.04}$	⋯	S
⋯	9666	5246	259	2457827.608	−19.56	18.6	$1.1^{+0.2}_{-0.2}$	⋯	$11.7^{+1.2}_{-0.5}$	⋯	$2399.5^{+0.6}_{-0.4}$	⋯	$3.93^{+0.04}_{-0.07}$	⋯	S
⋯	9726	5246	163	2457878.628	−18.53	15.6	$0.4^{+0.5}_{-0.4}$	⋯	$10.6^{+0.2}_{-1.0}$	⋯	$2399.5^{+0.8}_{-0.4}$	⋯	$4.05^{+0.03}_{-0.02}$	⋯	S
⋯	9666	5246	270	2458054.982	19.96	13.4	$-0.2^{+0.2}_{-0.2}$	⋯	$10.9^{+0.5}_{-0.4}$	⋯	$2399.0^{+1.5}_{-0.8}$	⋯	$3.88^{+0.2}_{-0.07}$	⋯	S
⋯	9666	5246	175	2458059.998	19.24	14.2	$0.1^{+0.3}_{-0.3}$	⋯	$10.1^{+1.4}_{-0.9}$	⋯	$2399.3^{+0.9}_{-0.5}$	⋯	$4.1^{+0.05}_{-0.03}$	⋯	S
⋯	9666	5246	175	2458067.965	17.87	19.4	$0.1^{+0.3}_{-0.2}$	⋯	$9.8^{+1.2}_{-0.3}$	⋯	$2399.2^{+1.0}_{-0.6}$	⋯	$4.18^{+0.02}_{-0.02}$	⋯	S
⋯	9726	5246	175	2458097.019	9.95	14.2	$-0.4^{+0.2}_{-0.3}$	⋯	$10.8^{+0.4}_{-0.6}$	⋯	$2399.3^{+0.8}_{-0.5}$	⋯	$3.74^{+0.09}_{-0.11}$	⋯	S
⋯	9666	5246	259	2458097.886	9.78	20.7	$-0.5^{+0.2}_{-0.2}$	⋯	$10.6^{+0.2}_{-0.5}$	⋯	$2399.6^{+0.6}_{-0.3}$	⋯	$4.11^{+0.03}_{-0.02}$	⋯	S
⋯	9726	5246	180	2458123.962	0.27	22.3	$0.0^{+0.2}_{-0.2}$	⋯	$10.7^{+0.3}_{-0.4}$	⋯	$2399.6^{+0.6}_{-0.3}$	⋯	$4.12^{+0.03}_{-0.05}$	⋯	S
⋯	9726	5246	180	2458126.947	−0.84	15.7	$0.2^{+0.2}_{-0.2}$	⋯	$9.9^{+1.2}_{-0.6}$	⋯	$2399.3^{+1.0}_{-0.5}$	⋯	$4.09^{+0.02}_{-0.02}$	⋯	S
2M08072607+3213101	10220	2473	43	2458130.771	2.99	32.4	$34.4^{+0.1}_{-0.2}$	$34.4^{+0.2}_{-0.2}$	$12.4^{+0.2}_{-0.4}$	$13.7^{+1.3}_{-1.3}$	$2398.4^{+2.0}_{-1.2}$	$2399.1^{+0.6}_{-0.4}$	$5.5^{+0.0}_{-0.0}$	$5.5^{+0.0}_{-0.0}$	S
⋯	10220	2473	43	2458138.702	−1.05	31.4	$34.4^{+0.1}_{-0.2}$	⋯	$14.3^{+0.2}_{-0.3}$	⋯	$2399.2^{+0.9}_{-0.5}$	⋯	$5.5^{+0.01}_{-0.0}$	⋯	S
⋯	10220	2473	43	2458142.686	−3.10	30.3	$34.2^{+0.1}_{-0.2}$	⋯	$14.2^{+0.3}_{-0.5}$	⋯	$2399.1^{+1.0}_{-0.6}$	⋯	$5.5^{+0.0}_{-0.0}$	⋯	S
⋯	10220	2473	43	2458143.869	−4.07	30.5	$34.8^{+0.2}_{-0.3}$	⋯	$13.5^{+1.1}_{-0.4}$	⋯	$2399.1^{+1.6}_{-0.6}$	⋯	$5.5^{+0.01}_{-0.0}$	⋯	S
2M08080189+3157054	10220	2473	139	2458130.771	3.09	16.3	$30.2^{+0.3}_{-0.4}$	$30.6^{+0.3}_{-0.3}$	$14.0^{+1.1}_{-0.5}$	$12.5^{+1.4}_{-1.4}$	$2398.8^{+1.8}_{-0.8}$	$2399.0^{+0.7}_{-0.4}$	$5.29^{+0.05}_{-0.06}$	$5.35^{+0.03}_{-0.02}$	S
⋯	10220	2473	139	2458138.702	−0.95	18.1	$31.0^{+0.2}_{-0.1}$	⋯	$14.5^{+0.4}_{-0.5}$	⋯	$2398.8^{+1.3}_{-1.0}$	⋯	$5.34^{+0.03}_{-0.02}$	⋯	S
⋯	10220	2473	139	2458142.686	−3.01	16.0	$30.4^{+0.2}_{-0.2}$	⋯	$12.7^{+0.4}_{-0.4}$	⋯	$2399.0^{+1.5}_{-0.8}$	⋯	$5.36^{+0.05}_{-0.01}$	⋯	S
⋯	10220	2473	139	2458143.869	−3.98	17.8	$30.4^{+0.3}_{-0.3}$	⋯	$11.9^{+0.2}_{-0.2}$	⋯	$2399.2^{+1.1}_{-0.6}$	⋯	$5.36^{+0.03}_{-0.02}$	⋯	S
2M08092892+3235226	10220	2473	31	2458130.771	3.17	14.5	$-7.4^{+0.2}_{-0.2}$	$-6.7^{+0.6}_{-0.5}$	$23.6^{+0.2}_{-0.4}$	$23.3^{+1.3}_{-1.7}$	$2399.3^{+0.9}_{-0.5}$	$2399.3^{+0.5}_{-0.3}$	$4.37^{+0.03}_{-0.04}$	$4.37^{+0.03}_{-0.03}$	S
⋯	10220	2473	31	2458138.702	−0.86	13.8	$-6.1^{+0.2}_{-0.2}$	⋯	$23.5^{+1.4}_{-0.4}$	⋯	$2399.4^{+0.9}_{-0.4}$	⋯	$4.36^{+0.03}_{-0.03}$	⋯	S
⋯	10220	2473	31	2458142.686	−2.91	13.3	$-6.5^{+0.3}_{-0.2}$	⋯	$24.9^{+1.3}_{-0.6}$	⋯	$2399.4^{+1.0}_{-0.4}$	⋯	$4.43^{+0.07}_{-0.11}$	⋯	S
⋯	10220	2473	31	2458143.869	−3.88	13.2	$-7.0^{+0.3}_{-0.2}$	⋯	$17.6^{+1.2}_{-0.7}$	⋯	$2399.1^{+1.3}_{-0.6}$	⋯	$4.42^{+0.08}_{-0.2}$	⋯	S
2M08144389+4650522	10495	2469	120	2458546.687	−19.74	38.4	$23.7^{+0.3}_{-0.6}$	$24.4^{+0.5}_{-0.3}$	$17.9^{+0.1}_{-0.2}$	$17.9^{+1.0}_{-1.0}$	$2399.2^{+1.1}_{-0.5}$	$2399.3^{+0.8}_{-0.4}$	$5.06^{+0.04}_{-0.03}$	$5.06^{+0.02}_{-0.02}$	S
⋯	10495	2469	120	2458547.653	−19.99	40.5	$24.6^{+0.2}_{-0.2}$	⋯	$17.9^{+0.1}_{-0.1}$	⋯	$2399.3^{+1.2}_{-0.5}$	⋯	$5.05^{+0.03}_{-0.02}$	⋯	S
2M08185804+2333522	8939	2318	7	2457484.651	−28.66	29.4	$36.0^{+0.1}_{-0.2}$	$35.7^{+0.3}_{-0.3}$	$7.3^{+0.6}_{-0.8}$	< 10	$2399.2^{+1.3}_{-0.6}$	$2399.2^{+0.6}_{-0.3}$	$5.42^{+0.02}_{-0.03}$	$5.39^{+0.12}_{-0.1}$	S
⋯	8939	2318	7	2457485.642	−28.77	25.9	$36.0^{+0.3}_{-0.3}$	⋯	$8.5^{+1.1}_{-0.9}$	⋯	$2398.7^{+1.5}_{-1.0}$	⋯	$5.36^{+0.03}_{-0.04}$	⋯	S
⋯	8939	2318	7	2457488.617	−29.06	22.4	$35.5^{+0.1}_{-0.1}$	⋯	$10.7^{+0.3}_{-0.4}$	⋯	$2399.3^{+0.8}_{-0.5}$	⋯	$5.23^{+0.02}_{-0.02}$	⋯	S
⋯	10219	2472	300	2458107.876	16.47	30.1	$36.1^{+0.2}_{-0.2}$	⋯	$7.3^{+0.5}_{-0.7}$	⋯	$2399.2^{+1.0}_{-0.6}$	⋯	$5.48^{+0.02}_{-0.01}$	⋯	S
2M08211639+5658358	10492	2466	157	2458191.636	−20.71	22.1	$7.1^{+0.2}_{-0.2}$	$7.2^{+0.2}_{-0.3}$	$10.7^{+0.6}_{-1.0}$	$14.1^{+1.2}_{-1.3}$	$2399.4^{+0.9}_{-0.4}$	$2399.5^{+0.5}_{-0.2}$	$5.19^{+0.03}_{-0.03}$	$4.96^{+0.15}_{-0.14}$	S
⋯	10492	2466	157	2458196.700	−21.79	18.0	$6.8^{+0.5}_{-0.3}$	⋯	$14.2^{+0.1}_{-0.3}$	⋯	$2399.4^{+0.7}_{-0.5}$	⋯	$4.85^{+0.03}_{-0.02}$	⋯	S
⋯	10492	2466	157	2458197.594	−21.80	16.9	$7.4^{+0.2}_{-0.2}$	⋯	$14.2^{+0.2}_{-0.4}$	⋯	$2399.6^{+0.8}_{-0.3}$	⋯	$4.96^{+0.04}_{-0.05}$	⋯	S
2M08294949+2646348	9507	2421	226	2457830.640	−23.73	126.8	$10.8^{+0.1}_{-0.2}$	$10.7^{+0.3}_{-0.3}$	$10.6^{+0.2}_{-0.5}$	$11.9^{+1.1}_{-1.1}$	$2399.1^{+1.3}_{-0.6}$	$2399.4^{+0.5}_{-0.3}$	$5.5^{+0.0}_{-0.0}$	$5.49^{+0.02}_{-0.01}$	S
⋯	9508	2422	154	2457833.643	−24.63	144.0	$10.6^{+0.1}_{-0.1}$	⋯	$12.1^{+0.1}_{-0.1}$	⋯	$2399.5^{+0.6}_{-0.3}$	⋯	$5.48^{+0.02}_{-0.01}$	⋯	S
⋯	9508	2422	154	2457834.610	−24.83	115.4	$10.4^{+0.1}_{-0.1}$	⋯	$11.7^{+1.1}_{-0.3}$	⋯	$2399.4^{+1.0}_{-0.4}$	⋯	$5.49^{+0.03}_{-0.01}$	⋯	S

Table 3.4 (*continued*)

Table 3.4 (*continued*)

APOGEE ID	Plate	Loc. ID	Fiber ID	JD (day)	bary.[a] ($km\ s^{-1}$)	S/N	RV ($km\ s^{-1}$)	$\langle RV \rangle$[b] ($km\ s^{-1}$)	$v \sin i$ ($km\ s^{-1}$)	$\langle v \sin i \rangle$[b,c] ($km\ s^{-1}$)	$T_{\rm eff}$ (K)	$\langle T_{\rm eff} \rangle$[b] (K)	$\log g$ ($cm\ s^{-2}$)	$\langle \log g \rangle$[b] ($cm\ s^{-2}$)	Mdl[d]
⋯	9510	2424	141	2457860.640	−29.30	30.0	$11.1^{+0.1}_{-0.2}$	⋯	$10.9^{+0.5}_{-0.6}$	⋯	$2399.1^{+1.4}_{-0.7}$	⋯	$5.43^{+0.02}_{-0.03}$	⋯	S
⋯	9510	2424	141	2457861.640	−29.36	29.1	$11.2^{+0.1}_{-0.2}$	⋯	$12.4^{+0.5}_{-0.5}$	⋯	$2398.9^{+1.3}_{-0.9}$	⋯	$5.42^{+0.04}_{-0.03}$	⋯	S
2M08440350+0434356	10511	2485	276	2458198.659	−21.33	23.9	$66.0^{+0.3}_{-0.3}$	$66.7^{+0.5}_{-0.5}$	$16.1^{+0.2}_{-0.3}$	$16.2^{+1.0}_{-1.1}$	$2398.9^{+1.1}_{-0.8}$	$2399.0^{+0.8}_{-0.5}$	$5.49^{+0.01}_{-0.01}$	$5.49^{+0.01}_{-0.01}$	S
⋯	10511	2485	276	2458211.626	−25.08	12.6	$67.0^{+0.2}_{-0.2}$	⋯	$16.3^{+0.3}_{-0.7}$	⋯	$2399.2^{+1.1}_{-0.6}$	⋯	$5.49^{+0.01}_{-0.01}$	⋯	S
2M08490052+0220155	10511	2485	150	2458198.659	−20.51	31.3	$22.5^{+0.2}_{-1.0}$	$22.4^{+0.4}_{-0.6}$	$53.7^{+0.6}_{-1.0}$	$53.7^{+2.1}_{-1.7}$	$2399.2^{+1.2}_{-0.6}$	$2399.2^{+0.4}_{-0.3}$	$5.07^{+0.02}_{-0.03}$	$4.99^{+0.23}_{-0.19}$	S
⋯	10511	2485	150	2458200.654	−21.18	10.6	$21.4^{+1.9}_{-1.5}$	⋯	$64.6^{+2.2}_{-2.6}$	⋯	$2398.9^{+1.6}_{-0.8}$	⋯	$3.6^{+0.07}_{-0.09}$	⋯	S
⋯	10511	2485	145	2458211.626	−24.40	18.4	$22.8^{+0.2}_{-0.5}$	⋯	$56.8^{+3.0}_{-1.4}$	⋯	$2398.8^{+1.4}_{-0.9}$	⋯	$4.9^{+0.04}_{-0.03}$	⋯	S
⋯	10839	2497	276	2458572.628	−23.24	26.3	$23.5^{+1.5}_{-0.3}$	⋯	$53.5^{+0.8}_{-0.5}$	⋯	$2399.2^{+1.3}_{-0.5}$	⋯	$5.13^{+0.03}_{-0.02}$	⋯	S
⋯	10839	2497	276	2458573.625	−23.52	15.0	$21.3^{+1.4}_{-0.4}$	⋯	$55.7^{+1.9}_{-1.3}$	⋯	$2398.9^{+1.7}_{-0.8}$	⋯	$4.83^{+0.03}_{-0.03}$	⋯	S
⋯	10839	2497	276	2458575.639	−24.12	28.0	$22.2^{+1.4}_{-0.5}$	⋯	$50.9^{+0.9}_{-0.9}$	⋯	$2399.4^{+0.9}_{-0.4}$	⋯	$5.08^{+0.03}_{-0.02}$	⋯	S
⋯	10839	2497	276	2458576.685	−24.51	19.5	$22.2^{+0.2}_{-0.2}$	⋯	$54.0^{+0.5}_{-1.3}$	⋯	$2399.2^{+1.2}_{-0.6}$	⋯	$5.1^{+0.04}_{-0.03}$	⋯	S
⋯	10839	2497	276	2458577.670	−24.73	17.6	$22.3^{+0.2}_{-0.9}$	⋯	$55.4^{+1.3}_{-1.1}$	⋯	$2399.1^{+1.5}_{-0.7}$	⋯	$4.85^{+0.02}_{-0.02}$	⋯	S
⋯	10839	2497	276	2458578.678	−25.01	21.9	$21.5^{+0.3}_{-0.3}$	⋯	$51.8^{+1.1}_{-1.2}$	⋯	$2399.3^{+1.0}_{-0.4}$	⋯	$5.1^{+0.04}_{-0.05}$	⋯	S
2M08501918+1056436	5564	4162	105	2455903.978	24.72	81.8	$31.5^{+0.2}_{-0.1}$	$31.4^{+0.4}_{-0.4}$	$19.8^{+0.3}_{-0.3}$	$17.9^{+1.1}_{-1.3}$	$3125.1^{+5.0}_{-7.5}$	$3140.2^{+14.0}_{-14.1}$	$5.43^{+0.02}_{-0.02}$	$5.3^{+0.07}_{-0.07}$	B
⋯	5564	4162	94	2455930.889	14.41	73.1	$32.3^{+0.1}_{-0.1}$	⋯	$17.2^{+0.9}_{-0.8}$	⋯	$3128.3^{+4.4}_{-4.6}$	⋯	$5.36^{+0.02}_{-0.02}$	⋯	B
⋯	5564	4162	99	2455934.880	12.53	93.4	$32.2^{+0.1}_{-0.1}$	⋯	$18.1^{+0.3}_{-0.6}$	⋯	$3115.9^{+3.1}_{-2.8}$	⋯	$5.42^{+0.02}_{-0.02}$	⋯	B
⋯	7269	4162	93	2456650.992	18.80	110.6	$31.3^{+0.1}_{-0.1}$	⋯	$17.8^{+0.4}_{-0.3}$	⋯	$3153.4^{+6.4}_{-8.4}$	⋯	$5.36^{+0.02}_{-0.03}$	⋯	B
⋯	7270	4162	93	2456652.000	18.37	98.9	$30.9^{+0.3}_{-0.2}$	⋯	$18.1^{+0.3}_{-0.4}$	⋯	$3147.3^{+6.8}_{-5.6}$	⋯	$5.34^{+0.03}_{-0.04}$	⋯	B
⋯	7267	4162	106	2456654.922	17.30	89.9	$31.6^{+0.1}_{-0.1}$	⋯	$18.0^{+0.2}_{-0.2}$	⋯	$3156.2^{+3.7}_{-6.0}$	⋯	$5.34^{+0.02}_{-0.02}$	⋯	B
⋯	7267	4162	99	2456668.864	10.87	81.2	$31.2^{+0.2}_{-0.5}$	⋯	$16.3^{+0.3}_{-0.7}$	⋯	$3148.2^{+5.0}_{-7.1}$	⋯	$5.37^{+0.02}_{-0.02}$	⋯	B
⋯	7269	4162	94	2456671.924	9.20	76.4	$31.0^{+0.1}_{-0.1}$	⋯	$18.0^{+0.3}_{-0.4}$	⋯	$3149.5^{+5.0}_{-3.8}$	⋯	$5.3^{+0.02}_{-0.02}$	⋯	B
⋯	7268	4162	142	2456672.858	8.88	77.7	$30.8^{+0.1}_{-0.1}$	⋯	$16.3^{+0.3}_{-0.7}$	⋯	$3157.1^{+6.1}_{-11.7}$	⋯	$5.34^{+0.02}_{-0.03}$	⋯	B
⋯	7268	4162	142	2456677.875	6.26	86.8	$31.8^{+0.1}_{-0.1}$	⋯	$16.2^{+0.2}_{-0.4}$	⋯	$3156.1^{+5.2}_{-9.2}$	⋯	$5.38^{+0.02}_{-0.02}$	⋯	B
⋯	7269	4162	141	2456678.898	5.68	73.3	$31.4^{+0.1}_{-0.1}$	⋯	$18.0^{+0.2}_{-0.4}$	⋯	$3131.5^{+2.8}_{-3.2}$	⋯	$5.32^{+0.01}_{-0.02}$	⋯	B
⋯	7267	4162	94	2456698.749	−4.47	51.5	$30.4^{+0.2}_{-0.2}$	⋯	$18.1^{+0.3}_{-0.4}$	⋯	$3140.6^{+4.9}_{-6.2}$	⋯	$5.36^{+0.03}_{-0.02}$	⋯	B
⋯	7268	4162	100	2456700.761	−5.54	74.9	$30.9^{+0.1}_{-0.1}$	⋯	$18.2^{+0.3}_{-0.7}$	⋯	$3130.9^{+6.5}_{-2.9}$	⋯	$5.23^{+0.01}_{-0.03}$	⋯	B
⋯	7270	4162	142	2456703.818	−7.25	87.9	$31.1^{+0.2}_{-0.2}$	⋯	$17.8^{+0.5}_{-0.4}$	⋯	$3148.2^{+11.1}_{-4.5}$	⋯	$5.22^{+0.02}_{-0.02}$	⋯	B
⋯	7269	4162	94	2456707.766	−9.12	68.8	$31.3^{+0.1}_{-0.1}$	⋯	$18.0^{+0.2}_{-0.3}$	⋯	$3132.9^{+3.6}_{-3.0}$	⋯	$5.2^{+0.01}_{-0.02}$	⋯	B
⋯	7269	4162	93	2456727.670	−18.07	110.1	$30.7^{+0.1}_{-0.2}$	⋯	$18.0^{+0.1}_{-0.3}$	⋯	$3136.4^{+4.5}_{-5.3}$	⋯	$5.19^{+0.02}_{-0.02}$	⋯	B
⋯	7268	4162	141	2456734.662	−20.76	75.8	$31.4^{+0.1}_{-0.1}$	⋯	$18.0^{+0.1}_{-0.3}$	⋯	$3157.5^{+5.7}_{-2.8}$	⋯	$5.24^{+0.02}_{-0.02}$	⋯	B
⋯	7269	4162	141	2456759.687	−27.76	60.6	$31.8^{+0.1}_{-0.1}$	⋯	$18.0^{+0.2}_{-0.2}$	⋯	$3150.2^{+5.6}_{-5.1}$	⋯	$5.21^{+0.03}_{-0.02}$	⋯	B
⋯	7269	4162	141	2456761.703	−28.13	73.9	$31.7^{+0.1}_{-0.1}$	⋯	$17.9^{+0.1}_{-0.3}$	⋯	$3161.1^{+5.5}_{-4.6}$	⋯	$5.23^{+0.02}_{-0.02}$	⋯	B
⋯	7268	4162	142	2456762.633	−28.12	83.5	$31.6^{+1.1}_{-0.3}$	⋯	$17.7^{+0.8}_{-0.4}$	⋯	$3153.9^{+7.4}_{-6.5}$	⋯	$5.28^{+0.02}_{-0.03}$	⋯	B
⋯	7269	4162	93	2456765.617	−28.51	74.7	$31.2^{+0.2}_{-0.2}$	⋯	$19.7^{+0.5}_{-0.2}$	⋯	$3127.2^{+4.9}_{-4.8}$	⋯	$5.23^{+0.02}_{-0.03}$	⋯	B
⋯	7270	4162	147	2456787.631	−29.34	82.5	$31.9^{+1.4}_{-0.1}$	⋯	$18.2^{+0.3}_{-0.9}$	⋯	$3158.6^{+6.6}_{-5.3}$	⋯	$5.25^{+0.03}_{-0.02}$	⋯	B
⋯	10424	5653	227	2458183.562	−15.64	86.0	$31.4^{+0.1}_{-0.1}$	⋯	$17.9^{+0.1}_{-0.2}$	⋯	$3155.3^{+5.1}_{-5.5}$	⋯	$5.26^{+0.02}_{-0.02}$	⋯	B
2M08522464+2540591	9500	2414	258	2457831.660	−22.36	83.3	$29.6^{+0.2}_{-0.2}$	$29.6^{+0.2}_{-0.2}$	$9.2^{+0.5}_{-0.6}$	< 10	$2399.5^{+0.6}_{-0.4}$	$2399.5^{+0.6}_{-0.4}$	$5.35^{+0.02}_{-0.03}$	$5.35^{+0.02}_{-0.03}$	S
2M09020690+0033195	12511	2812	133	2458895.785	−4.21	23.0	$42.5^{+0.3}_{-0.3}$	$42.6^{+0.3}_{-0.2}$	$9.0^{+0.4}_{-1.1}$	< 10	$2399.3^{+0.8}_{-0.5}$	$2399.3^{+0.6}_{-0.4}$	$4.91^{+0.03}_{-0.02}$	$4.78^{+0.14}_{-0.14}$	S
⋯	12511	2812	133	2458896.700	−4.48	12.2	$42.8^{+0.4}_{-0.2}$	⋯	$13.6^{+1.3}_{-0.4}$	⋯	$2399.3^{+0.9}_{-0.5}$	⋯	$4.63^{+0.02}_{-0.02}$	⋯	S
2M09130162+3037583	11749	2662	115	2458866.787	7.41	16.4	$52.0^{+0.3}_{-0.2}$	$51.8^{+0.6}_{-0.5}$	$9.3^{+0.7}_{-0.7}$	< 10	$3076.4^{+5.6}_{-6.4}$	$3047.7^{+41.6}_{-42.1}$	$5.49^{+0.02}_{-0.01}$	$5.44^{+0.09}_{-0.07}$	B
⋯	11749	2662	115	2458867.778	6.92	22.7	$51.5^{+0.2}_{-0.2}$	⋯	$7.6^{+0.8}_{-0.7}$	⋯	$3080.5^{+6.5}_{-5.0}$	⋯	$5.48^{+0.02}_{-0.01}$	⋯	B
⋯	11749	2662	115	2458872.787	4.34	15.3	$51.9^{+0.3}_{-0.9}$	⋯	$10.2^{+1.1}_{-1.1}$	⋯	$3068.2^{+17.4}_{-13.9}$	⋯	$5.4^{+0.05}_{-0.04}$	⋯	B
⋯	11748	2661	217	2458874.791	3.30	11.1	$51.6^{+0.3}_{-0.3}$	⋯	$9.1^{+0.7}_{-0.7}$	⋯	$3078.7^{+13.0}_{-14.6}$	⋯	$5.46^{+0.04}_{-0.03}$	⋯	B

Table 3.4 (*continued*)

Table 3.4 (*continued*)

APOGEE ID	Plate	Loc. ID	Fiber ID	JD (day)	bary.[a] ($km\ s^{-1}$)	S/N	RV ($km\ s^{-1}$)	$\langle RV \rangle$[b] ($km\ s^{-1}$)	$v \sin i$ ($km\ s^{-1}$)	$\langle v \sin i \rangle$[b,c] ($km\ s^{-1}$)	$T_{\rm eff}$ (K)	$\langle T_{\rm eff} \rangle$[b] (K)	$\log g$ ($cm\ s^{-2}$)	$\langle \log g \rangle$[b] ($cm\ s^{-2}$)	Mdl[d]
⋯	11748	2661	217	2458923.625	−19.44	12.3	$51.8^{+0.2}_{-0.2}$	⋯	$6.5^{+1.5}_{-1.5}$	⋯	$3087.5^{+16.9}_{-10.3}$	⋯	$5.47^{+0.03}_{-0.02}$	⋯	B
⋯	12487	2788	293	2458924.631	−19.83	18.8	$51.1^{+0.2}_{-0.2}$	⋯	$9.3^{+0.7}_{-0.6}$	⋯	$3035.7^{+8.0}_{-6.3}$	⋯	$5.31^{+0.04}_{-0.03}$	⋯	B
⋯	12487	2788	293	2458925.620	−20.16	22.1	$52.6^{+0.1}_{-0.2}$	⋯	$10.8^{+0.4}_{-1.0}$	⋯	$2952.4^{+8.7}_{-8.2}$	⋯	$5.28^{+0.02}_{-0.02}$	⋯	B
⋯	12487	2788	293	2458928.783	−21.60	14.3	$51.9^{+0.3}_{-0.2}$	⋯	$10.8^{+0.5}_{-0.7}$	⋯	$3017.1^{+6.3}_{-11.2}$	⋯	$5.38^{+0.02}_{-0.03}$	⋯	B
2M09373349+5534057	8911	5179	174	2457435.783	−8.43	15.9	$1.3^{+0.2}_{-0.2}$	$0.7^{+0.5}_{-0.4}$	$19.8^{+0.1}_{-0.3}$	$19.4^{+2.9}_{-2.0}$	$2399.3^{+1.1}_{-0.5}$	$2399.4^{+0.3}_{-0.2}$	$4.58^{+0.04}_{-0.03}$	$4.64^{+0.26}_{-0.27}$	S
⋯	8911	5179	151	2457444.753	−11.69	17.5	$0.6^{+0.2}_{-0.2}$	⋯	$17.9^{+0.1}_{-0.2}$	⋯	$2399.3^{+0.9}_{-0.5}$	⋯	$4.89^{+0.03}_{-0.04}$	⋯	S
⋯	8911	5179	180	2457472.676	−19.65	14.6	$0.9^{+0.4}_{-0.4}$	⋯	$16.0^{+1.1}_{-1.8}$	⋯	$2399.3^{+1.0}_{-0.5}$	⋯	$4.67^{+0.02}_{-0.05}$	⋯	S
⋯	8911	5179	151	2457493.620	−22.65	21.1	$0.4^{+0.5}_{-0.5}$	⋯	$15.1^{+0.9}_{-1.0}$	⋯	$2399.3^{+0.9}_{-0.5}$	⋯	$4.92^{+0.07}_{-0.03}$	⋯	S
⋯	9540	5179	38	2457707.016	22.51	10.9	$4.5^{+0.4}_{-0.4}$	⋯	$21.6^{+0.6}_{-0.5}$	⋯	$2398.2^{+1.8}_{-1.3}$	⋯	$3.94^{+0.04}_{-0.03}$	⋯	S
⋯	9540	5179	38	2457711.998	21.87	18.0	$0.8^{+0.2}_{-0.2}$	⋯	$23.5^{+1.8}_{-0.3}$	⋯	$2399.5^{+0.8}_{-0.4}$	⋯	$3.62^{+0.04}_{-0.04}$	⋯	S
⋯	9541	5179	210	2457713.013	21.69	13.1	$0.7^{+0.3}_{-0.2}$	⋯	$19.8^{+0.1}_{-0.2}$	⋯	$2399.5^{+0.9}_{-0.4}$	⋯	$4.68^{+0.02}_{-0.02}$	⋯	S
⋯	9540	5179	41	2457742.946	14.27	17.8	$1.2^{+0.3}_{-0.3}$	⋯	$17.9^{+1.3}_{-0.3}$	⋯	$2399.3^{+0.7}_{-0.5}$	⋯	$4.55^{+0.03}_{-0.04}$	⋯	S
⋯	9540	5179	32	2457761.901	7.35	13.3	$0.6^{+0.3}_{-0.3}$	⋯	$19.6^{+1.7}_{-0.3}$	⋯	$2399.6^{+0.7}_{-0.2}$	⋯	$4.12^{+0.17}_{-0.05}$	⋯	S
⋯	9541	5179	175	2457762.941	6.88	15.9	$0.8^{+0.3}_{-0.3}$	⋯	$16.3^{+0.3}_{-0.9}$	⋯	$2399.3^{+1.0}_{-0.6}$	⋯	$4.83^{+0.07}_{-0.04}$	⋯	S
⋯	9540	5179	32	2457765.872	5.80	11.1	$-0.2^{+0.3}_{-0.3}$	⋯	$23.5^{+1.6}_{-0.7}$	⋯	$2399.5^{+0.7}_{-0.4}$	⋯	$4.36^{+0.05}_{-0.04}$	⋯	S
⋯	9541	5179	156	2457791.827	−4.84	14.6	$1.0^{+0.2}_{-0.3}$	⋯	$16.1^{+0.2}_{-0.3}$	⋯	$2399.2^{+1.2}_{-0.6}$	⋯	$4.86^{+0.03}_{-0.04}$	⋯	S
⋯	9541	5179	156	2457792.826	−5.24	15.2	$-0.4^{+0.5}_{-0.5}$	⋯	$21.7^{+0.2}_{-0.3}$	⋯	$2399.2^{+0.9}_{-0.6}$	⋯	$4.8^{+0.06}_{-0.03}$	⋯	S
⋯	9541	5179	210	2457795.839	−6.46	16.3	$0.7^{+0.2}_{-0.3}$	⋯	$17.9^{+0.1}_{-0.3}$	⋯	$2399.2^{+1.2}_{-0.5}$	⋯	$4.83^{+0.1}_{-0.02}$	⋯	S
⋯	9541	5179	151	2457820.712	−15.19	18.8	$0.9^{+0.2}_{-0.2}$	⋯	$18.0^{+0.1}_{-0.3}$	⋯	$2399.5^{+1.0}_{-0.4}$	⋯	$4.85^{+0.03}_{-0.03}$	⋯	S
⋯	9689	5179	179	2457821.716	−15.50	14.6	$0.4^{+0.5}_{-0.6}$	⋯	$25.4^{+1.8}_{-0.3}$	⋯	$2399.4^{+0.9}_{-0.4}$	⋯	$4.53^{+0.1}_{-0.06}$	⋯	S
⋯	9689	5179	152	2457825.747	−16.72	12.6	$-0.5^{+0.3}_{-0.3}$	⋯	$33.1^{+0.3}_{-1.4}$	⋯	$2399.2^{+1.2}_{-0.6}$	⋯	$4.33^{+0.04}_{-0.02}$	⋯	S
⋯	9689	5179	203	2457829.764	−17.83	12.0	$0.9^{+0.5}_{-0.5}$	⋯	$21.7^{+0.3}_{-0.3}$	⋯	$2399.3^{+0.9}_{-0.5}$	⋯	$4.56^{+0.03}_{-0.03}$	⋯	S
⋯	9689	5179	152	2457849.608	−21.62	15.8	$0.8^{+0.5}_{-1.1}$	⋯	$23.7^{+1.8}_{-1.8}$	⋯	$2399.2^{+1.2}_{-0.5}$	⋯	$4.64^{+0.04}_{-0.06}$	⋯	S
⋯	9689	5179	161	2458098.947	17.14	13.6	$0.4^{+0.4}_{-0.3}$	⋯	$23.5^{+1.8}_{-0.3}$	⋯	$2399.2^{+1.1}_{-0.6}$	⋯	$4.61^{+0.04}_{-0.16}$	⋯	S
2M09381783+0132490	10514	2488	108	2458115.966	22.47	27.2	$-16.5^{+1.2}_{-0.8}$	$-16.8^{+1.5}_{-1.0}$	$61.8^{+1.8}_{-1.7}$	$96.1^{+16.0}_{-3.5}$	$3187.1^{+11.5}_{-12.4}$	$3193.5^{+15.6}_{-18.7}$	$5.32^{+0.05}_{-0.05}$	$5.29^{+0.11}_{-0.11}$	B
⋯	10514	2488	108	2458116.935	22.21	18.9	$-18.7^{+2.1}_{-2.8}$	⋯	$99.6^{+0.6}_{-0.3}$	⋯	$3172.6^{+20.6}_{-24.5}$	⋯	$5.2^{+0.08}_{-0.06}$	⋯	B
⋯	11752	2678	180	2458839.925	24.68	15.1	$-16.9^{+1.3}_{-0.4}$	⋯	$49.7^{+2.0}_{-1.4}$	⋯	$3182.5^{+10.7}_{-17.2}$	⋯	$5.44^{+0.04}_{-0.04}$	⋯	B
⋯	11752	2678	180	2458844.916	23.14	15.1	$-7.9^{+4.0}_{-3.1}$	⋯	$99.3^{+0.9}_{-0.5}$	⋯	$3211.8^{+18.3}_{-18.1}$	⋯	$5.36^{+0.07}_{-0.09}$	⋯	B
⋯	11752	2678	180	2458848.897	21.80	19.2	$-15.9^{+3.2}_{-2.4}$	⋯	$97.1^{+3.7}_{-2.0}$	⋯	$3167.5^{+15.4}_{-11.5}$	⋯	$5.17^{+0.08}_{-0.06}$	⋯	B
⋯	11759	2679	228	2458898.795	−1.44	27.1	$-15.3^{+1.1}_{-1.3}$	⋯	$99.4^{+0.9}_{-0.5}$	⋯	$3201.8^{+8.0}_{-11.1}$	⋯	$5.2^{+0.05}_{-0.05}$	⋯	B
⋯	11759	2679	228	2458899.800	−1.98	19.5	$-17.9^{+0.6}_{-1.4}$	⋯	$44.0^{+2.1}_{-1.7}$	⋯	$3216.9^{+13.4}_{-11.4}$	⋯	$5.17^{+0.04}_{-0.16}$	⋯	B
2M09442625+3521233	11751	2660	37	2458566.610	−19.84	22.5	$51.1^{+0.4}_{-0.3}$	$51.2^{+0.9}_{-0.8}$	$14.6^{+0.4}_{-1.5}$	$13.8^{+1.4}_{-1.7}$	$2399.5^{+0.7}_{-0.3}$	$2399.6^{+0.4}_{-0.2}$	$4.41^{+0.02}_{-0.02}$	$4.8^{+0.24}_{-0.24}$	S
⋯	11751	2660	37	2458567.623	−20.20	28.7	$50.4^{+0.2}_{-0.2}$	⋯	$10.9^{+0.5}_{-0.3}$	⋯	$2399.1^{+1.1}_{-0.7}$	⋯	$5.08^{+0.02}_{-0.02}$	⋯	S
⋯	10838	2496	271	2458569.635	−20.87	17.1	$52.7^{+0.2}_{-0.2}$	⋯	$14.3^{+0.2}_{-0.5}$	⋯	$2399.1^{+1.0}_{-0.6}$	⋯	$4.78^{+0.03}_{-0.02}$	⋯	S
⋯	10838	2496	271	2458576.619	−22.91	16.4	$50.6^{+0.2}_{-0.2}$	⋯	$15.7^{+0.9}_{-0.5}$	⋯	$2399.5^{+0.9}_{-0.3}$	⋯	$4.62^{+0.05}_{-0.05}$	⋯	S
⋯	10838	2496	271	2458577.610	−23.16	21.4	$51.5^{+0.4}_{-0.5}$	⋯	$14.2^{+0.3}_{-0.5}$	⋯	$2399.4^{+0.9}_{-0.5}$	⋯	$4.86^{+0.04}_{-0.03}$	⋯	S
⋯	10838	2496	271	2458578.612	−23.43	28.5	$51.3^{+0.3}_{-0.2}$	⋯	$14.4^{+0.3}_{-1.6}$	⋯	$2399.7^{+0.7}_{-0.2}$	⋯	$4.84^{+0.02}_{-0.03}$	⋯	S
2M09453388+5458511	8911	5179	61	2457435.783	−7.79	13.4	$-3.4^{+0.5}_{-0.5}$	$-3.7^{+0.7}_{-0.6}$	$25.4^{+0.7}_{-0.4}$	$23.5^{+1.4}_{-1.4}$	$2399.2^{+1.1}_{-0.6}$	$2399.2^{+0.4}_{-0.2}$	$4.81^{+0.03}_{-0.03}$	$4.81^{+0.08}_{-0.09}$	S
⋯	8911	5179	67	2457444.753	−11.10	13.4	$-3.1^{+0.4}_{-0.2}$	⋯	$21.9^{+0.3}_{-1.5}$	⋯	$2399.4^{+1.0}_{-0.5}$	⋯	$4.77^{+0.04}_{-0.02}$	⋯	S
⋯	8911	5179	67	2457467.657	−18.08	10.1	$-3.1^{+0.6}_{-0.4}$	⋯	$24.6^{+1.4}_{-0.9}$	⋯	$2399.0^{+1.6}_{-0.7}$	⋯	$4.66^{+0.05}_{-0.05}$	⋯	S
⋯	8911	5179	66	2457472.676	−19.29	11.1	$-3.5^{+0.3}_{-0.4}$	⋯	$23.4^{+1.5}_{-0.6}$	⋯	$2398.9^{+1.7}_{-0.9}$	⋯	$4.68^{+0.03}_{-0.05}$	⋯	S
⋯	8911	5179	61	2457493.620	−22.51	12.9	$-4.1^{+0.4}_{-0.6}$	⋯	$25.0^{+1.4}_{-0.6}$	⋯	$2399.3^{+1.3}_{-0.5}$	⋯	$4.79^{+0.05}_{-0.04}$	⋯	S
⋯	9540	5179	66	2457711.998	22.14	13.3	$-3.9^{+0.3}_{-0.3}$	⋯	$23.8^{+0.4}_{-0.8}$	⋯	$2399.4^{+1.0}_{-0.4}$	⋯	$4.76^{+0.07}_{-0.06}$	⋯	S

Table 3.4 (*continued*)

Table 3.4 (*continued*)

APOGEE ID	Plate	Loc. ID	Fiber ID	JD (day)	bary.[a] ($km\ s^{-1}$)	S/N	RV ($km\ s^{-1}$)	$\langle RV \rangle$[b] ($km\ s^{-1}$)	$v \sin i$ ($km\ s^{-1}$)	$\langle v \sin i \rangle$[b,c] ($km\ s^{-1}$)	$T_{\rm eff}$ (K)	$\langle T_{\rm eff} \rangle$[b] (K)	$\log g$ ($cm\ s^{-2}$)	$\langle \log g \rangle$[b] ($cm\ s^{-2}$)	Mdl[d]
⋯	9540	5179	66	2457742.946	14.83	11.3	$-3.9^{+0.3}_{-0.2}$	⋯	$21.9^{+0.4}_{-1.5}$	⋯	$2399.2^{+0.9}_{-0.6}$	⋯	$4.85^{+0.03}_{-0.03}$	⋯	S
⋯	9541	5179	72	2457795.839	−5.80	10.2	$-5.4^{+0.4}_{-0.4}$	⋯	$23.8^{+0.3}_{-0.6}$	⋯	$2399.1^{+1.7}_{-0.6}$	⋯	$4.78^{+0.06}_{-0.08}$	⋯	S
⋯	9541	5179	67	2457820.712	−14.68	12.5	$-2.9^{+0.3}_{-0.4}$	⋯	$23.7^{+0.2}_{-0.4}$	⋯	$2399.3^{+1.2}_{-0.6}$	⋯	$4.87^{+0.03}_{-0.03}$	⋯	S
⋯	9689	5179	78	2457821.716	−15.00	10.9	$-4.0^{+0.4}_{-0.4}$	⋯	$23.0^{+1.3}_{-0.7}$	⋯	$2399.2^{+0.9}_{-0.6}$	⋯	$5.03^{+0.08}_{-0.03}$	⋯	S
2M09472006−0020093	12512	2813	37	2458904.762	−2.98	39.7	$15.0^{+0.1}_{-0.1}$	$15.0^{+0.1}_{-0.1}$	$9.0^{+0.3}_{-0.4}$	< 10	$2399.6^{+0.5}_{-0.3}$	$2399.5^{+0.4}_{-0.3}$	$5.29^{+0.01}_{-0.01}$	$5.32^{+0.06}_{-0.08}$	S
⋯	12512	2813	37	2458906.775	−4.05	50.1	$15.0^{+0.2}_{-0.2}$	⋯	$7.4^{+0.4}_{-0.7}$	⋯	$2399.4^{+0.7}_{-0.5}$	⋯	$5.44^{+0.02}_{-0.02}$	⋯	S
2M09474477+0224327	11753	2681	54	2458838.943	25.61	31.1	$8.9^{+0.2}_{-0.2}$	$8.8^{+0.2}_{-0.3}$	$12.1^{+0.2}_{-0.8}$	$12.6^{+1.4}_{-1.6}$	$2399.2^{+1.4}_{-0.5}$	$2399.3^{+0.9}_{-0.4}$	$5.11^{+0.03}_{-0.03}$	$5.02^{+0.1}_{-0.1}$	S
⋯	11753	2681	48	2458923.716	−12.69	11.3	$8.5^{+0.3}_{-0.3}$	⋯	$14.6^{+0.5}_{-0.8}$	⋯	$2399.3^{+1.1}_{-0.5}$	⋯	$4.91^{+0.04}_{-0.03}$	⋯	S
2M09522188−1924319	11739	6022	68	2458562.563	−8.56	57.9	$-17.7^{+0.1}_{-0.1}$	$-17.1^{+0.9}_{-0.9}$	$14.2^{+0.1}_{-0.4}$	$16.0^{+1.9}_{-1.8}$	$2399.6^{+0.6}_{-0.3}$	$2399.6^{+0.3}_{-0.2}$	$5.34^{+0.02}_{-0.01}$	$5.37^{+0.05}_{-0.05}$	S
⋯	11739	6022	71	2458565.638	−9.97	28.7	$-17.5^{+0.1}_{-0.1}$	⋯	$16.0^{+0.1}_{-0.2}$	⋯	$2399.6^{+0.5}_{-0.3}$	⋯	$5.47^{+0.03}_{-0.02}$	⋯	S
⋯	11739	6022	71	2458591.535	−19.01	39.8	$-15.4^{+0.1}_{-0.2}$	⋯	$21.3^{+0.3}_{-0.3}$	⋯	$2399.6^{+0.7}_{-0.3}$	⋯	$5.35^{+0.02}_{-0.02}$	⋯	S
2M09524622+0620410	10515	2489	247	2458824.013	28.84	15.5	$12.2^{+0.3}_{-0.3}$	$12.8^{+0.4}_{-0.5}$	$19.8^{+0.3}_{-0.4}$	$17.2^{+1.7}_{-1.7}$	$2399.3^{+1.1}_{-0.4}$	$2399.3^{+0.6}_{-0.3}$	$4.21^{+0.04}_{-0.05}$	$4.44^{+0.09}_{-0.11}$	S
⋯	10515	2489	247	2458824.965	28.81	15.6	$12.5^{+0.3}_{-0.3}$	⋯	$18.1^{+0.3}_{-0.9}$	⋯	$2399.1^{+1.5}_{-0.6}$	⋯	$4.37^{+0.02}_{-0.03}$	⋯	S
⋯	10515	2489	247	2458879.845	9.27	25.3	$13.2^{+0.2}_{-0.3}$	⋯	$16.2^{+0.2}_{-0.4}$	⋯	$2399.2^{+1.1}_{-0.5}$	⋯	$4.61^{+0.05}_{-0.02}$	⋯	S
⋯	10515	2489	247	2458880.834	8.80	21.0	$13.1^{+0.2}_{-0.3}$	⋯	$16.2^{+0.2}_{-0.6}$	⋯	$2399.4^{+0.8}_{-0.4}$	⋯	$4.42^{+0.01}_{-0.01}$	⋯	S
2M09560888+0134128	10845	2503	108	2458582.654	−21.44	30.4	$21.4^{+0.2}_{-0.2}$	$21.1^{+0.6}_{-0.5}$	$27.5^{+0.3}_{-0.7}$	$30.1^{+2.7}_{-2.1}$	$2399.5^{+0.9}_{-0.3}$	$2399.4^{+0.5}_{-0.2}$	$4.93^{+0.02}_{-0.02}$	$4.86^{+0.14}_{-0.13}$	S
⋯	10845	2503	108	2458583.659	−21.79	16.8	$21.4^{+0.2}_{-0.2}$	⋯	$28.3^{+0.9}_{-0.8}$	⋯	$2399.3^{+1.1}_{-0.5}$	⋯	$4.79^{+0.02}_{-0.03}$	⋯	S
⋯	11866	2683	223	2458867.863	16.03	21.8	$20.8^{+0.2}_{-0.3}$	⋯	$29.4^{+0.3}_{-0.8}$	⋯	$2399.3^{+1.2}_{-0.5}$	⋯	$4.95^{+0.02}_{-0.02}$	⋯	S
⋯	11866	2683	223	2458872.834	13.82	12.0	$18.9^{+0.5}_{-0.7}$	⋯	$34.7^{+0.4}_{-0.4}$	⋯	$2399.2^{+1.3}_{-0.5}$	⋯	$4.56^{+0.03}_{-0.03}$	⋯	S
2M10031918−0105079	11836	2682	96	2458849.914	23.73	40.4	$24.4^{+0.3}_{-0.2}$	$24.0^{+0.3}_{-0.3}$	$33.0^{+0.2}_{-0.7}$	$32.7^{+1.0}_{-1.2}$	$2399.2^{+1.4}_{-0.6}$	$2399.3^{+0.9}_{-0.4}$	$5.5^{+0.01}_{-0.0}$	$5.5^{+0.0}_{-0.0}$	S
⋯	11836	2682	96	2458854.961	21.91	42.3	$23.8^{+0.2}_{-0.1}$	⋯	$32.3^{+0.4}_{-0.3}$	⋯	$2399.3^{+1.2}_{-0.5}$	⋯	$5.5^{+0.01}_{-0.0}$	⋯	S
2M10134315+0000406	10846	2504	186	2458900.805	2.19	40.3	$3.7^{+0.2}_{-0.2}$	$3.9^{+0.3}_{-0.4}$	$8.5^{+1.6}_{-0.8}$	$10.2^{+1.3}_{-1.6}$	$2399.4^{+1.1}_{-0.4}$	$2399.4^{+0.7}_{-0.3}$	$5.01^{+0.03}_{-0.02}$	$4.86^{+0.2}_{-0.16}$	S
⋯	10846	2504	186	2458904.828	0.03	24.2	$4.3^{+0.2}_{-0.2}$	⋯	$10.9^{+0.5}_{-1.0}$	⋯	$2399.4^{+0.9}_{-0.4}$	⋯	$4.65^{+0.02}_{-0.05}$	⋯	S
2M10225090+0032169	11838	2685	203	2458873.866	16.38	14.8	$30.7^{+0.2}_{-0.2}$	$34.0^{+6.0}_{-5.9}$	$10.8^{+0.4}_{-0.8}$	$11.2^{+1.6}_{-1.5}$	$2399.2^{+1.4}_{-0.6}$	$2399.2^{+0.7}_{-0.4}$	$5.27^{+0.08}_{-0.03}$	$5.2^{+0.04}_{-0.05}$	S
⋯	11838	2685	203	2458874.872	15.92	14.2	$46.6^{+0.3}_{-0.3}$	⋯	$9.1^{+0.6}_{-0.9}$	⋯	$2399.0^{+1.3}_{-0.7}$	⋯	$5.21^{+0.02}_{-0.03}$	⋯	S
⋯	11838	2685	203	2458877.817	14.69	12.2	$31.8^{+0.2}_{-0.2}$	⋯	$12.6^{+0.4}_{-0.6}$	⋯	$2399.3^{+1.0}_{-0.5}$	⋯	$5.16^{+0.02}_{-0.04}$	⋯	S
2M10240997+1815533	11707	6011	231	2458510.886	12.50	67.3	$8.3^{+0.2}_{-0.1}$	$8.2^{+0.1}_{-0.1}$	$4.0^{+0.5}_{-0.3}$	< 10	$2399.5^{+0.9}_{-0.4}$	$2399.5^{+0.5}_{-0.2}$	$5.48^{+0.01}_{-0.01}$	$5.48^{+0.01}_{-0.01}$	S
⋯	11707	6011	184	2458527.793	4.12	59.5	$8.2^{+0.1}_{-0.1}$	⋯	$5.6^{+0.3}_{-0.2}$	⋯	$2399.6^{+0.5}_{-0.3}$	⋯	$5.48^{+0.01}_{-0.01}$	⋯	S
⋯	11707	6011	231	2458560.787	−12.66	59.2	$8.2^{+0.2}_{-0.1}$	⋯	$5.1^{+1.7}_{-0.7}$	⋯	$2399.2^{+1.1}_{-0.5}$	⋯	$5.45^{+0.04}_{-0.03}$	⋯	S
2M10323297+0630074	10520	2494	242	2458580.635	−18.34	114.0	$13.3^{+0.1}_{-0.1}$	$13.2^{+0.1}_{-0.1}$	$9.8^{+1.3}_{-0.3}$	< 10	$2399.6^{+0.6}_{-0.3}$	$2399.6^{+0.4}_{-0.2}$	$5.2^{+0.01}_{-0.02}$	$5.2^{+0.01}_{-0.02}$	S
⋯	10520	2494	242	2458581.665	−18.82	105.5	$12.9^{+0.2}_{-0.2}$	⋯	$10.6^{+0.4}_{-0.6}$	⋯	$2399.6^{+0.6}_{-0.3}$	⋯	$5.2^{+0.02}_{-0.07}$	⋯	S
2M10372897+3011117	6770	4506	260	2456402.619	−24.00	12.2	$8.2^{+0.2}_{-0.3}$	$8.0^{+0.2}_{-0.2}$	$14.1^{+1.7}_{-0.3}$	$13.1^{+1.2}_{-1.4}$	$2399.4^{+1.0}_{-0.4}$	$2399.5^{+0.6}_{-0.3}$	$3.52^{+0.01}_{-0.03}$	$3.52^{+0.01}_{-0.02}$	S
⋯	6770	4506	158	2456407.688	−25.26	13.6	$7.9^{+0.1}_{-0.2}$	⋯	$12.5^{+0.3}_{-0.5}$	⋯	$2399.6^{+0.7}_{-0.4}$	⋯	$3.52^{+0.02}_{-0.02}$	⋯	S
2M10541102−8505023	9464	5231	193	2458116.869	4.00	27.9	$-11.3^{+0.1}_{-0.1}$	$-10.8^{+0.8}_{-1.1}$	$10.8^{+0.3}_{-0.8}$	$10.7^{+1.0}_{-1.1}$	$2399.4^{+0.8}_{-0.4}$	$2399.4^{+0.5}_{-0.3}$	$5.5^{+0.01}_{-0.0}$	$5.5^{+0.0}_{-0.0}$	S
⋯	9464	5231	192	2458213.609	10.23	34.4	$-9.1^{+0.2}_{-0.1}$	⋯	$10.7^{+0.3}_{-0.3}$	⋯	$2399.5^{+0.7}_{-0.4}$	⋯	$5.5^{+0.0}_{-0.0}$	⋯	S
2M10543366+0503467	11828	2658	270	2458877.908	17.20	30.1	$-20.2^{+0.1}_{-0.1}$	$-20.2^{+0.1}_{-0.1}$	$9.0^{+0.4}_{-0.8}$	< 10	$2399.3^{+1.3}_{-0.5}$	$2399.2^{+1.1}_{-0.4}$	$5.48^{+0.02}_{-0.01}$	$5.42^{+0.12}_{-0.11}$	S
⋯	11828	2658	270	2458880.906	15.84	11.0	$-20.2^{+0.3}_{-0.3}$	⋯	$13.4^{+0.9}_{-0.5}$	⋯	$2399.2^{+1.7}_{-0.6}$	⋯	$5.19^{+0.03}_{-0.03}$	⋯	S
2M10570380+2217203	8448	2165	215	2457123.784	−19.84	45.4	$11.7^{+0.1}_{-0.1}$	$11.7^{+0.1}_{-0.1}$	$9.5^{+0.9}_{-1.0}$	< 10	$2399.4^{+0.8}_{-0.5}$	$2399.5^{+0.5}_{-0.3}$	$5.25^{+0.03}_{-0.02}$	$5.3^{+0.04}_{-0.04}$	S
⋯	8448	2165	215	2457129.723	−21.76	85.4	$11.7^{+0.1}_{-0.2}$	⋯	$8.9^{+0.3}_{-0.8}$	⋯	$2399.6^{+0.6}_{-0.3}$	⋯	$5.33^{+0.02}_{-0.03}$	⋯	S
2M11194647+0820356	7351	4510	265	2456674.908	23.45	33.0	$-45.1^{+0.2}_{-0.1}$	$-45.0^{+0.2}_{-0.2}$	$8.7^{+0.1}_{-1.1}$	< 10	$2399.5^{+0.9}_{-0.4}$	$2399.5^{+0.5}_{-0.2}$	$4.56^{+0.02}_{-0.02}$	$4.34^{+0.22}_{-0.22}$	S
⋯	7351	4510	264	2456706.842	9.71	22.5	$-44.8^{+0.2}_{-0.2}$	⋯	$10.6^{+0.2}_{-1.2}$	⋯	$2399.4^{+0.7}_{-0.5}$	⋯	$4.13^{+0.02}_{-0.02}$	⋯	S
⋯	7351	4510	270	2456726.784	−0.53	17.4	$-45.0^{+0.2}_{-0.2}$	⋯	$10.9^{+0.5}_{-1.4}$	⋯	$2399.5^{+0.8}_{-0.4}$	⋯	$4.11^{+0.02}_{-0.03}$	⋯	S
2M11203609+0704135	7351	4510	72	2456674.908	23.71	37.9	$-15.1^{+0.2}_{-0.2}$	$-14.4^{+0.6}_{-0.6}$	$9.2^{+0.2}_{-0.3}$	< 10	$2399.5^{+0.8}_{-0.3}$	$2399.5^{+0.4}_{-0.2}$	$5.11^{+0.02}_{-0.03}$	$5.1^{+0.04}_{-0.04}$	S

Table 3.4 (*continued*)

Table 3.4 (*continued*)

APOGEE ID	Plate	Loc. ID	Fiber ID	JD (day)	bary.[a] ($km\ s^{-1}$)	S/N	RV ($km\ s^{-1}$)	$\langle RV \rangle$[b] ($km\ s^{-1}$)	$v \sin i$ ($km\ s^{-1}$)	$\langle v \sin i \rangle$[b,c] ($km\ s^{-1}$)	$T_{\rm eff}$ (K)	$\langle T_{\rm eff} \rangle$[b] (K)	$\log g$ ($cm\ s^{-2}$)	$\langle \log g \rangle$[b] ($cm\ s^{-2}$)	Mdl[d]
⋯	7351	4510	90	2456706.842	10.06	34.3	$-13.8^{+0.1}_{-0.2}$	⋯	$5.7^{+0.6}_{-0.6}$	⋯	$2399.2^{+1.1}_{-0.5}$	⋯	$5.04^{+0.04}_{-0.03}$	⋯	S
⋯	7351	4510	67	2456726.784	−0.17	33.7	$-14.4^{+0.2}_{-0.3}$	⋯	$7.4^{+0.7}_{-0.9}$	⋯	$2399.5^{+0.5}_{-0.3}$	⋯	$5.14^{+0.04}_{-0.04}$	⋯	S
2M11210854+2126274	8450	2167	115	2457405.939	20.66	66.6	$-0.3^{+0.2}_{-0.2}$	$-0.3^{+0.2}_{-0.2}$	$12.4^{+0.1}_{-0.3}$	$12.4^{+0.1}_{-0.3}$	$2399.3^{+0.7}_{-0.5}$	$2399.3^{+0.7}_{-0.5}$	$5.09^{+0.01}_{-0.01}$	$5.09^{+0.01}_{-0.01}$	S
2M11232934+0154040	9758	5306	44	2457878.500	−23.18	69.4	$-0.9^{+0.1}_{-0.2}$	$-0.2^{+0.6}_{-0.6}$	$17.6^{+0.2}_{-0.1}$	$18.3^{+1.1}_{-1.4}$	$2399.0^{+1.4}_{-0.7}$	$2399.1^{+0.6}_{-0.4}$	$5.5^{+0.01}_{-0.0}$	$5.5^{+0.01}_{-0.0}$	S
⋯	9850	5306	53	2458243.588	−23.28	56.5	$0.2^{+0.2}_{-0.2}$	⋯	$19.7^{+0.8}_{-0.1}$	⋯	$2399.3^{+1.0}_{-0.6}$	⋯	$5.49^{+0.01}_{-0.01}$	⋯	S
⋯	9850	5306	47	2458263.529	−27.78	47.6	$0.4^{+0.2}_{-0.2}$	⋯	$17.9^{+0.1}_{-0.2}$	⋯	$2399.1^{+0.9}_{-0.7}$	⋯	$5.49^{+0.03}_{-0.01}$	⋯	S
2M12080810+3520281	8554	2210	115	2457152.746	−22.09	29.7	$28.8^{+0.2}_{-0.2}$	$29.2^{+0.6}_{-0.5}$	$10.8^{+0.4}_{-1.0}$	$13.7^{+1.7}_{-1.5}$	$2399.5^{+0.6}_{-0.4}$	$2399.4^{+0.5}_{-0.3}$	$4.88^{+0.02}_{-0.02}$	$4.86^{+0.03}_{-0.03}$	S
⋯	8554	2210	115	2457159.760	−23.34	18.8	$30.1^{+0.2}_{-0.3}$	⋯	$14.3^{+1.0}_{-0.4}$	⋯	$2399.4^{+1.0}_{-0.4}$	⋯	$4.82^{+0.05}_{-0.03}$	⋯	S
2M12153877+5205050	11957	2719	26	2458852.980	16.22	57.2	$-4.8^{+0.2}_{-0.2}$	$-4.8^{+0.2}_{-0.2}$	$12.9^{+0.6}_{-0.9}$	$12.9^{+0.6}_{-0.9}$	$2399.5^{+0.7}_{-0.3}$	$2399.5^{+0.7}_{-0.3}$	$5.1^{+0.02}_{-0.01}$	$5.1^{+0.02}_{-0.01}$	S
2M12201166+3315379	12483	2784	1	2458928.890	−4.21	16.4	$11.1^{+0.3}_{-0.3}$	$11.2^{+0.3}_{-0.2}$	$9.1^{+0.9}_{-0.5}$	< 10	$2399.1^{+1.1}_{-0.7}$	$2399.1^{+0.8}_{-0.5}$	$5.18^{+0.04}_{-0.04}$	$5.19^{+0.03}_{-0.03}$	S
⋯	12483	2784	1	2458929.883	−4.63	14.4	$11.2^{+0.3}_{-0.3}$	⋯	$8.9^{+0.4}_{-1.0}$	⋯	$2399.1^{+1.3}_{-0.7}$	⋯	$5.21^{+0.04}_{-0.04}$	⋯	S
2M12205439+2525568	7437	4216	109	2456815.666	−26.41	10.9	$14.8^{+0.2}_{-0.2}$	$14.8^{+0.2}_{-0.2}$	$25.6^{+0.3}_{-0.8}$	$25.6^{+0.3}_{-0.8}$	$2399.2^{+1.1}_{-0.5}$	$2399.2^{+1.1}_{-0.5}$	$4.85^{+0.03}_{-0.02}$	$4.85^{+0.03}_{-0.02}$	S
2M12215013+4632447	8263	2118	186	2457121.699	−12.60	49.2	$-10.4^{+0.3}_{-0.2}$	$-10.4^{+0.3}_{-0.2}$	$29.1^{+0.1}_{-0.2}$	$29.1^{+1.0}_{-1.6}$	$2398.6^{+1.7}_{-0.9}$	$2399.0^{+1.0}_{-0.5}$	$5.43^{+0.03}_{-0.04}$	$5.03^{+0.26}_{-0.23}$	S
⋯	8263	2118	186	2457122.753	−13.01	43.5	$-10.7^{+0.5}_{-0.4}$	⋯	$47.9^{+3.6}_{-1.9}$	⋯	$2399.2^{+1.2}_{-0.6}$	⋯	$4.88^{+0.02}_{-0.02}$	⋯	S
2M12235346+2534559	7435	4216	109	2456761.646	−12.53	10.1	$7.9^{+0.4}_{-0.8}$	$7.0^{+0.8}_{-0.6}$	$15.4^{+1.3}_{-1.4}$	$16.4^{+1.7}_{-1.5}$	$3045.2^{+18.8}_{-13.2}$	$3060.5^{+16.6}_{-15.4}$	$5.48^{+0.02}_{-0.01}$	$5.49^{+0.01}_{-0.01}$	B
⋯	7438	4216	43	2456814.643	−26.15	10.3	$-22.2^{+5.3}_{-3.9}$	⋯	$97.4^{+3.4}_{-2.0}$	⋯	$3062.8^{+24.4}_{-20.0}$	⋯	$5.38^{+0.1}_{-0.09}$	⋯	B
⋯	7438	4216	7	2456818.645	−26.40	14.3	$-7.1^{+2.6}_{-1.2}$	⋯	$84.7^{+3.0}_{-2.6}$	⋯	$2899.6^{+20.1}_{-15.7}$	⋯	$4.64^{+0.07}_{-0.1}$	⋯	B
⋯	7437	4216	49	2456824.642	−26.55	10.3	$6.6^{+0.5}_{-0.3}$	⋯	$17.5^{+1.4}_{-1.4}$	⋯	$3070.7^{+14.0}_{-11.5}$	⋯	$5.49^{+0.02}_{-0.01}$	⋯	B
2M12252076+2517082	7435	4216	31	2456756.676	−10.34	16.0	$7.5^{+0.2}_{-0.3}$	$7.2^{+0.7}_{-0.8}$	$32.9^{+0.4}_{-0.3}$	$32.9^{+2.3}_{-1.7}$	$2399.3^{+1.1}_{-0.5}$	$2399.3^{+0.5}_{-0.3}$	$4.86^{+0.04}_{-0.03}$	$4.85^{+0.16}_{-0.1}$	S
⋯	7438	4216	31	2456790.632	−22.04	12.7	$7.1^{+1.0}_{-0.6}$	⋯	$34.7^{+1.7}_{-2.0}$	⋯	$2399.3^{+1.2}_{-0.5}$	⋯	$4.81^{+0.11}_{-0.05}$	⋯	S
⋯	7438	4216	144	2456814.643	−26.14	16.0	$8.9^{+0.8}_{-0.3}$	⋯	$29.3^{+0.3}_{-0.5}$	⋯	$2399.1^{+1.2}_{-0.6}$	⋯	$5.07^{+0.03}_{-0.05}$	⋯	S
⋯	7437	4216	43	2456815.666	−26.27	12.7	$6.7^{+0.4}_{-0.5}$	⋯	$34.9^{+0.2}_{-0.5}$	⋯	$2399.1^{+1.3}_{-0.7}$	⋯	$4.65^{+0.02}_{-0.03}$	⋯	S
⋯	7438	4216	43	2456818.645	−26.40	13.9	$6.7^{+0.6}_{-0.7}$	⋯	$32.9^{+0.8}_{-0.4}$	⋯	$2399.3^{+1.0}_{-0.5}$	⋯	$4.9^{+0.03}_{-0.02}$	⋯	S
⋯	7437	4216	126	2456819.640	−26.44	11.6	$7.2^{+0.2}_{-0.2}$	⋯	$30.1^{+1.0}_{-1.1}$	⋯	$2398.6^{+2.0}_{-1.0}$	⋯	$4.95^{+0.06}_{-0.07}$	⋯	S
⋯	7437	4216	37	2456824.642	−26.58	15.8	$5.6^{+0.3}_{-0.6}$	⋯	$33.1^{+0.3}_{-1.6}$	⋯	$2399.4^{+0.9}_{-0.4}$	⋯	$4.83^{+0.04}_{-0.06}$	⋯	S
2M12270429+2541012	7435	4216	84	2456756.676	−10.21	17.3	$2.4^{+0.2}_{-0.3}$	$2.6^{+0.6}_{-0.6}$	$21.7^{+0.2}_{-1.7}$	$19.6^{+2.7}_{-2.1}$	$2399.4^{+0.9}_{-0.4}$	$2399.5^{+0.3}_{-0.2}$	$3.9^{+0.09}_{-0.17}$	$4.36^{+0.19}_{-0.22}$	S
⋯	7435	4216	84	2456761.646	−12.21	15.6	$2.3^{+0.3}_{-0.3}$	⋯	$27.1^{+3.3}_{-0.2}$	⋯	$2399.5^{+0.7}_{-0.4}$	⋯	$4.12^{+0.03}_{-0.03}$	⋯	S
⋯	7438	4216	80	2456790.632	−21.89	14.4	$2.2^{+0.4}_{-0.9}$	⋯	$25.4^{+0.2}_{-1.8}$	⋯	$2399.3^{+0.6}_{-0.5}$	⋯	$4.12^{+0.05}_{-0.05}$	⋯	S
⋯	7438	4216	89	2456814.643	−26.00	19.6	$3.5^{+0.2}_{-0.2}$	⋯	$17.9^{+0.1}_{-0.3}$	⋯	$2399.6^{+0.6}_{-0.3}$	⋯	$4.35^{+0.04}_{-0.03}$	⋯	S
⋯	7437	4216	73	2456815.666	−26.13	18.1	$3.0^{+0.4}_{-0.3}$	⋯	$19.7^{+1.4}_{-0.2}$	⋯	$2399.3^{+0.8}_{-0.5}$	⋯	$4.82^{+0.04}_{-0.03}$	⋯	S
⋯	7438	4216	32	2456818.645	−26.27	18.3	$1.9^{+0.6}_{-0.7}$	⋯	$19.7^{+1.7}_{-0.2}$	⋯	$2399.4^{+0.9}_{-0.4}$	⋯	$4.39^{+0.02}_{-0.03}$	⋯	S
⋯	7437	4216	36	2456824.642	−26.46	16.4	$2.0^{+0.2}_{-0.2}$	⋯	$17.9^{+0.1}_{-0.2}$	⋯	$2399.5^{+1.0}_{-0.4}$	⋯	$4.38^{+0.02}_{-0.03}$	⋯	S
2M12315462+5130389	11832	2668	186	2458607.681	−17.29	43.9	$8.9^{+0.3}_{-0.1}$	$8.9^{+0.3}_{-0.1}$	$7.8^{+1.0}_{-0.6}$	< 10	$2399.3^{+0.9}_{-0.6}$	$2399.3^{+0.9}_{-0.6}$	$5.41^{+0.02}_{-0.02}$	$5.41^{+0.02}_{-0.02}$	S
2M12493960+5255340	11019	2523	283	2458542.878	1.00	19.0	$-56.1^{+0.2}_{-0.2}$	$-56.8^{+0.4}_{-0.4}$	$10.2^{+1.3}_{-0.6}$	$10.4^{+3.0}_{-1.7}$	$2399.5^{+0.7}_{-0.4}$	$2399.4^{+0.6}_{-0.3}$	$4.92^{+0.02}_{-0.02}$	$4.98^{+0.13}_{-0.12}$	S
⋯	11019	2523	283	2458543.899	0.63	15.4	$-57.0^{+0.2}_{-0.1}$	⋯	$11.1^{+0.4}_{-0.2}$	⋯	$2399.3^{+1.2}_{-0.5}$	⋯	$4.9^{+0.02}_{-0.02}$	⋯	S
⋯	11761	2670	60	2458578.766	−9.92	24.9	$-57.0^{+0.2}_{-0.2}$	⋯	$3.8^{+0.8}_{-0.6}$	⋯	$2399.2^{+1.7}_{-0.6}$	⋯	$5.22^{+0.03}_{-0.03}$	⋯	S
2M12522354+2528469	11871	2647	42	2458627.681	−22.59	33.6	$9.4^{+0.3}_{-0.2}$	$9.4^{+0.3}_{-0.2}$	$12.6^{+0.3}_{-0.7}$	$12.6^{+0.3}_{-0.7}$	$2399.3^{+1.1}_{-0.5}$	$2399.3^{+1.1}_{-0.5}$	$5.41^{+0.02}_{-0.02}$	$5.41^{+0.02}_{-0.02}$	S
2M13004379+3557591	8323	2133	217	2457888.641	−19.08	18.0	$-24.6^{+0.4}_{-0.4}$	$-24.6^{+0.2}_{-0.3}$	$19.7^{+1.8}_{-0.3}$	$17.7^{+1.8}_{-1.7}$	$2399.2^{+1.0}_{-0.6}$	$2399.2^{+0.5}_{-0.3}$	$4.5^{+0.04}_{-0.05}$	$4.41^{+0.08}_{-0.08}$	S
⋯	8323	2133	217	2457889.742	−19.51	10.6	$-24.6^{+0.3}_{-0.3}$	⋯	$16.2^{+0.3}_{-0.9}$	⋯	$2399.3^{+0.7}_{-0.5}$	⋯	$4.34^{+0.03}_{-0.03}$	⋯	S
⋯	8323	2133	217	2457891.776	−19.99	11.7	$-24.2^{+0.6}_{-0.5}$	⋯	$18.1^{+1.7}_{-0.9}$	⋯	$2398.9^{+1.8}_{-0.9}$	⋯	$4.5^{+0.09}_{-0.08}$	⋯	S
⋯	8323	2133	217	2457892.727	−20.10	15.2	$-24.8^{+0.4}_{-0.5}$	⋯	$15.6^{+1.3}_{-0.7}$	⋯	$2399.2^{+1.2}_{-0.6}$	⋯	$4.4^{+0.05}_{-0.11}$	⋯	S
2M13022083+3227103	12484	2785	186	2458898.897	12.47	18.0	$7.2^{+0.4}_{-0.3}$	$6.8^{+0.3}_{-0.3}$	$25.5^{+0.2}_{-0.9}$	$25.7^{+1.0}_{-1.4}$	$2399.4^{+0.8}_{-0.4}$	$2399.4^{+0.4}_{-0.3}$	$4.46^{+0.02}_{-0.03}$	$4.58^{+0.09}_{-0.08}$	S
⋯	12484	2785	186	2458899.883	12.13	19.5	$7.2^{+0.3}_{-0.5}$	⋯	$27.1^{+1.7}_{-0.2}$	⋯	$2399.3^{+0.7}_{-0.5}$	⋯	$4.63^{+0.04}_{-0.02}$	⋯	S

Table 3.4 (*continued*)

Table 3.4 (*continued*)

APOGEE ID	Plate	Loc. ID	Fiber ID	JD (day)	bary.[a] ($km\ s^{-1}$)	S/N	RV ($km\ s^{-1}$)	$\langle RV \rangle$[b] ($km\ s^{-1}$)	$v \sin i$ ($km\ s^{-1}$)	$\langle v \sin i \rangle$[b,c] ($km\ s^{-1}$)	$T_{\rm eff}$ (K)	$\langle T_{\rm eff} \rangle$[b] (K)	$\log g$ ($cm\ s^{-2}$)	$\langle \log g \rangle$[b] ($cm\ s^{-2}$)	Mdl[d]
⋯	12484	2785	186	2458904.980	9.95	29.9	$6.6^{+0.2}_{-0.2}$	⋯	$25.4^{+0.1}_{-0.3}$	⋯	$2399.6^{+0.7}_{-0.3}$	⋯	$4.64^{+0.02}_{-0.02}$	⋯	S
2M13034100+2414020	11009	2513	132	2458579.871	−5.02	21.7	$-9.5^{+0.6}_{-0.3}$	$-9.3^{+0.3}_{-0.3}$	$29.2^{+0.2}_{-0.3}$	$27.4^{+2.7}_{-1.7}$	$2398.8^{+1.6}_{-0.8}$	$2399.1^{+0.8}_{-0.5}$	$5.39^{+0.09}_{-0.05}$	$5.33^{+0.21}_{-0.27}$	S
⋯	11009	2513	132	2458580.728	−5.09	29.3	$-9.3^{+0.7}_{-0.5}$	⋯	$25.4^{+0.1}_{-0.3}$	⋯	$2398.7^{+1.3}_{-1.0}$	⋯	$5.47^{+0.03}_{-0.02}$	⋯	S
⋯	11010	2514	19	2458599.723	−13.03	18.7	$-8.9^{+0.2}_{-0.2}$	⋯	$29.1^{+0.1}_{-0.2}$	⋯	$2399.4^{+0.9}_{-0.4}$	⋯	$4.9^{+0.03}_{-0.01}$	⋯	S
⋯	11010	2514	19	2458601.759	−13.90	43.9	$-9.5^{+0.1}_{-0.2}$	⋯	$21.8^{+0.2}_{-0.9}$	⋯	$2397.6^{+3.1}_{-1.7}$	⋯	$5.48^{+0.02}_{-0.01}$	⋯	S
2M13065141+7056376	8913	5181	29	2457445.846	−4.33	12.0	$15.0^{+0.2}_{-0.2}$	$15.3^{+0.3}_{-0.4}$	$10.8^{+0.4}_{-0.8}$	$11.8^{+1.3}_{-1.3}$	$2399.4^{+0.8}_{-0.5}$	$2399.4^{+0.3}_{-0.2}$	$4.28^{+0.09}_{-0.06}$	$4.19^{+0.18}_{-0.13}$	S
⋯	8913	5181	119	2457448.840	−4.94	11.3	$15.2^{+0.2}_{-0.3}$	⋯	$11.7^{+1.1}_{-0.7}$	⋯	$2399.3^{+1.3}_{-0.5}$	⋯	$4.34^{+0.04}_{-0.05}$	⋯	S
⋯	8913	5181	29	2457463.788	−7.77	11.3	$15.1^{+0.4}_{-0.3}$	⋯	$10.5^{+0.6}_{-0.6}$	⋯	$2399.5^{+1.3}_{-0.4}$	⋯	$4.12^{+0.05}_{-0.05}$	⋯	S
⋯	8913	5181	26	2457493.689	−11.60	11.2	$15.4^{+0.3}_{-0.3}$	⋯	$11.3^{+0.9}_{-1.1}$	⋯	$2399.4^{+0.8}_{-0.4}$	⋯	$3.87^{+0.07}_{-0.05}$	⋯	S
⋯	9012	5181	26	2457497.758	−11.96	12.4	$15.0^{+0.3}_{-0.2}$	⋯	$10.9^{+0.4}_{-0.6}$	⋯	$2399.4^{+0.9}_{-0.4}$	⋯	$4.37^{+0.06}_{-0.04}$	⋯	S
⋯	9012	5181	113	2457503.703	−12.26	11.0	$14.6^{+0.3}_{-0.4}$	⋯	$12.7^{+0.4}_{-0.8}$	⋯	$2399.2^{+1.2}_{-0.6}$	⋯	$3.68^{+0.05}_{-0.11}$	⋯	S
⋯	9012	5181	113	2457522.629	−12.44	11.4	$14.9^{+0.3}_{-0.2}$	⋯	$12.3^{+0.8}_{-0.7}$	⋯	$2399.3^{+1.0}_{-0.5}$	⋯	$4.17^{+0.04}_{-0.03}$	⋯	S
⋯	9067	5181	113	2457795.965	−1.10	14.2	$15.3^{+0.2}_{-0.2}$	⋯	$12.4^{+0.8}_{-0.4}$	⋯	$2399.5^{+0.8}_{-0.4}$	⋯	$4.28^{+0.1}_{-0.04}$	⋯	S
⋯	9067	5181	113	2457801.949	−2.42	14.5	$15.6^{+0.2}_{-0.2}$	⋯	$10.8^{+0.3}_{-0.6}$	⋯	$2399.5^{+0.7}_{-0.4}$	⋯	$4.16^{+0.03}_{-0.04}$	⋯	S
⋯	9068	5181	29	2457820.885	−6.34	13.2	$15.3^{+0.2}_{-0.2}$	⋯	$10.9^{+0.6}_{-1.1}$	⋯	$2399.4^{+0.7}_{-0.4}$	⋯	$4.24^{+0.03}_{-0.05}$	⋯	S
⋯	9068	5181	26	2457827.854	−7.60	11.2	$15.5^{+0.2}_{-0.2}$	⋯	$10.8^{+0.3}_{-0.6}$	⋯	$2399.6^{+0.7}_{-0.3}$	⋯	$4.11^{+0.04}_{-0.06}$	⋯	S
⋯	9068	5181	26	2457831.885	−8.32	10.2	$16.5^{+1.2}_{-0.3}$	⋯	$12.5^{+0.3}_{-0.5}$	⋯	$2399.2^{+1.0}_{-0.6}$	⋯	$3.67^{+0.09}_{-0.18}$	⋯	S
2M13192677+1301119	6777	4492	139	2456324.014	25.04	48.0	$6.3^{+0.2}_{-0.2}$	$6.3^{+0.1}_{-0.1}$	$5.3^{+0.4}_{-0.8}$	< 10	$2399.4^{+0.8}_{-0.5}$	$2399.4^{+0.5}_{-0.3}$	$5.06^{+0.02}_{-0.01}$	$4.84^{+0.2}_{-0.19}$	S
⋯	6777	4492	42	2456346.961	17.75	15.3	$6.2^{+0.2}_{-0.2}$	⋯	$8.9^{+0.3}_{-0.8}$	⋯	$2399.3^{+1.2}_{-0.5}$	⋯	$4.63^{+0.01}_{-0.01}$	⋯	S
⋯	6777	4492	138	2456351.896	15.92	39.3	$6.3^{+0.1}_{-0.1}$	⋯	$7.3^{+0.9}_{-0.2}$	⋯	$2399.5^{+0.6}_{-0.4}$	⋯	$4.96^{+0.03}_{-0.01}$	⋯	S
2M13202007+7213140	9067	5181	195	2457771.026	3.84	16.6	$-28.1^{+0.2}_{-0.2}$	$-27.3^{+0.5}_{-0.5}$	$18.0^{+0.9}_{-0.4}$	$18.6^{+1.4}_{-1.4}$	$2399.4^{+0.9}_{-0.4}$	$2399.3^{+0.4}_{-0.2}$	$5.3^{+0.11}_{-0.03}$	$5.31^{+0.12}_{-0.11}$	S
⋯	9067	5181	195	2457795.965	−1.40	21.3	$-27.8^{+0.2}_{-0.2}$	⋯	$18.0^{+0.2}_{-0.4}$	⋯	$2399.3^{+1.2}_{-0.5}$	⋯	$5.38^{+0.02}_{-0.03}$	⋯	S
⋯	9067	5181	196	2457801.949	−2.64	21.1	$-26.9^{+0.2}_{-0.2}$	⋯	$17.4^{+1.2}_{-0.5}$	⋯	$2399.2^{+1.0}_{-0.5}$	⋯	$5.4^{+0.02}_{-0.04}$	⋯	S
⋯	9067	5181	195	2457819.881	−6.11	22.1	$-27.0^{+0.2}_{-0.2}$	⋯	$19.8^{+0.1}_{-0.2}$	⋯	$2399.4^{+0.8}_{-0.4}$	⋯	$5.12^{+0.03}_{-0.02}$	⋯	S
⋯	9068	5181	190	2457820.885	−6.30	25.6	$-27.1^{+0.2}_{-0.1}$	⋯	$16.3^{+0.3}_{-0.8}$	⋯	$2399.5^{+0.8}_{-0.4}$	⋯	$5.44^{+0.02}_{-0.02}$	⋯	S
⋯	9067	5181	195	2457820.927	−6.34	17.0	$-27.0^{+0.2}_{-0.2}$	⋯	$17.4^{+0.9}_{-0.4}$	⋯	$2399.3^{+0.9}_{-0.5}$	⋯	$5.37^{+0.02}_{-0.02}$	⋯	S
⋯	9067	5181	201	2457824.915	−7.02	12.0	$-28.0^{+0.3}_{-0.3}$	⋯	$19.1^{+1.1}_{-0.7}$	⋯	$2399.1^{+1.6}_{-0.6}$	⋯	$5.18^{+0.02}_{-0.02}$	⋯	S
⋯	9068	5181	189	2457827.854	−7.46	25.2	$-27.9^{+0.3}_{-0.4}$	⋯	$18.0^{+0.1}_{-0.2}$	⋯	$2399.5^{+0.9}_{-0.4}$	⋯	$5.4^{+0.03}_{-0.03}$	⋯	S
⋯	9068	5181	202	2457831.885	−8.12	19.0	$-27.3^{+0.3}_{-0.3}$	⋯	$17.8^{+0.5}_{-0.3}$	⋯	$2399.3^{+1.1}_{-0.5}$	⋯	$5.31^{+0.05}_{-0.04}$	⋯	S
⋯	9068	5181	190	2457848.828	−10.29	10.1	$-27.5^{+0.2}_{-0.4}$	⋯	$20.2^{+0.5}_{-1.0}$	⋯	$2398.7^{+1.1}_{-0.9}$	⋯	$5.28^{+0.09}_{-0.05}$	⋯	S
⋯	9068	5181	196	2457851.792	−10.56	12.7	$-28.3^{+0.6}_{-0.4}$	⋯	$18.1^{+0.4}_{-0.6}$	⋯	$2399.0^{+1.4}_{-0.7}$	⋯	$5.16^{+0.02}_{-0.05}$	⋯	S
⋯	9068	5181	189	2457854.797	−10.83	10.3	$-26.2^{+0.3}_{-0.2}$	⋯	$19.8^{+0.3}_{-0.5}$	⋯	$2399.0^{+1.3}_{-0.8}$	⋯	$5.39^{+0.05}_{-0.03}$	⋯	S
2M13232423+5132272	11017	2521	284	2458547.967	1.76	37.6	$-5.5^{+0.3}_{-0.2}$	$-5.4^{+0.5}_{-0.5}$	$16.0^{+0.1}_{-0.2}$	$18.9^{+1.9}_{-1.7}$	$2399.6^{+0.6}_{-0.3}$	$2399.6^{+0.2}_{-0.2}$	$4.55^{+0.01}_{-0.03}$	$4.59^{+0.18}_{-0.23}$	S
⋯	11017	2521	284	2458548.911	1.54	25.0	$-4.6^{+0.2}_{-0.2}$	⋯	$14.4^{+0.3}_{-0.4}$	⋯	$2399.5^{+0.8}_{-0.4}$	⋯	$4.62^{+0.02}_{-0.02}$	⋯	S
⋯	11017	2521	284	2458549.947	1.17	13.7	$-5.9^{+0.5}_{-0.3}$	⋯	$16.4^{+0.3}_{-0.7}$	⋯	$2399.2^{+1.4}_{-0.7}$	⋯	$4.38^{+0.03}_{-0.05}$	⋯	S
⋯	11017	2521	296	2458568.777	−4.35	36.7	$-5.7^{+0.2}_{-0.4}$	⋯	$19.7^{+0.1}_{-0.1}$	⋯	$2399.7^{+0.4}_{-0.2}$	⋯	$4.38^{+0.03}_{-0.03}$	⋯	S
⋯	11017	2521	296	2458572.885	−5.72	30.9	$-5.5^{+0.3}_{-0.2}$	⋯	$16.0^{+0.5}_{-0.2}$	⋯	$2399.6^{+0.6}_{-0.3}$	⋯	$4.38^{+0.02}_{-0.02}$	⋯	S
⋯	11017	2521	296	2458575.838	−6.51	34.8	$-6.3^{+0.2}_{-0.2}$	⋯	$19.7^{+0.1}_{-0.1}$	⋯	$2399.6^{+0.4}_{-0.2}$	⋯	$4.34^{+0.04}_{-0.03}$	⋯	S
⋯	11758	2666	119	2458605.755	−13.59	64.3	$-5.3^{+0.1}_{-0.2}$	⋯	$9.3^{+0.6}_{-0.9}$	⋯	$2399.4^{+1.1}_{-0.5}$	⋯	$4.95^{+0.02}_{-0.02}$	⋯	S
2M13342918+3303043	8444	2161	163	2457863.729	−8.61	19.2	$-18.0^{+0.3}_{-0.3}$	$-18.0^{+0.3}_{-0.3}$	$10.7^{+0.3}_{-0.4}$	$10.7^{+0.3}_{-0.4}$	$2399.3^{+1.0}_{-0.5}$	$2399.3^{+1.0}_{-0.5}$	$4.63^{+0.04}_{-0.04}$	$4.63^{+0.04}_{-0.04}$	S
2M13430646+0038442	8266	5121	294	2457058.007	27.68	13.7	$-12.4^{+0.3}_{-0.3}$	$-11.9^{+0.7}_{-0.7}$	$9.6^{+0.9}_{-1.0}$	< 10	$3157.5^{+9.5}_{-11.1}$	$3164.4^{+27.8}_{-23.9}$	$5.44^{+0.03}_{-0.03}$	$5.47^{+0.06}_{-0.04}$	B
⋯	8266	5121	187	2457060.971	27.15	13.4	$-12.4^{+0.3}_{-0.3}$	⋯	$8.1^{+1.0}_{-1.3}$	⋯	$3152.1^{+10.2}_{-10.5}$	⋯	$5.47^{+0.04}_{-0.02}$	⋯	B
⋯	8266	5121	187	2457092.891	16.61	14.9	$-13.3^{+0.2}_{-0.2}$	⋯	$9.9^{+1.0}_{-0.9}$	⋯	$3142.9^{+17.2}_{-8.7}$	⋯	$5.45^{+0.04}_{-0.03}$	⋯	B
⋯	8267	5121	187	2457093.913	16.12	13.5	$-13.2^{+0.3}_{-0.3}$	⋯	$9.8^{+1.2}_{-1.2}$	⋯	$3121.9^{+10.6}_{-16.1}$	⋯	$5.22^{+0.03}_{-0.05}$	⋯	B

Table 3.4 (*continued*)

Table 3.4 (*continued*)

APOGEE ID	Plate	Loc. ID	Fiber ID	JD (day)	bary.[a] ($km\ s^{-1}$)	S/N	RV ($km\ s^{-1}$)	$\langle RV \rangle$[b] ($km\ s^{-1}$)	$v \sin i$ ($km\ s^{-1}$)	$\langle v \sin i \rangle$[b,c] ($km\ s^{-1}$)	$T_{\rm eff}$ (K)	$\langle T_{\rm eff} \rangle$[b] (K)	$\log g$ ($cm\ s^{-2}$)	$\langle \log g \rangle$[b] ($cm\ s^{-2}$)	Mdl[d]
⋯	8266	5121	192	2457110.844	8.32	13.7	$-11.7^{+0.4}_{-0.4}$	⋯	$9.6^{+0.9}_{-0.8}$	⋯	$3152.8^{+12.1}_{-14.8}$	⋯	$5.43^{+0.04}_{-0.05}$	⋯	B
⋯	8266	5121	181	2457113.869	6.76	11.0	$-12.8^{+0.4}_{-0.4}$	⋯	$9.3^{+0.8}_{-1.0}$	⋯	$3176.9^{+8.3}_{-11.4}$	⋯	$5.47^{+0.03}_{-0.02}$	⋯	B
⋯	8267	5121	271	2457114.854	6.31	13.0	$-12.2^{+0.3}_{-0.4}$	⋯	$11.8^{+1.3}_{-1.1}$	⋯	$3171.1^{+16.4}_{-12.8}$	⋯	$5.49^{+0.01}_{-0.01}$	⋯	B
⋯	8267	5121	198	2457123.840	1.82	12.6	$-11.5^{+0.2}_{-0.2}$	⋯	$9.1^{+1.3}_{-1.2}$	⋯	$3186.4^{+15.2}_{-11.7}$	⋯	$5.31^{+0.08}_{-0.05}$	⋯	B
⋯	8581	5121	235	2457142.796	−7.57	12.4	$-11.2^{+0.2}_{-0.2}$	⋯	$13.3^{+1.0}_{-1.0}$	⋯	$3107.2^{+8.0}_{-15.6}$	⋯	$5.25^{+0.04}_{-0.04}$	⋯	B
⋯	9684	5121	295	2457794.010	26.47	11.1	$-12.6^{+0.6}_{-0.3}$	⋯	$8.3^{+1.6}_{-1.5}$	⋯	$3205.6^{+13.4}_{-18.7}$	⋯	$5.48^{+0.04}_{-0.02}$	⋯	B
⋯	9684	5121	192	2457802.011	24.31	12.7	$-11.6^{+0.6}_{-0.3}$	⋯	$12.8^{+0.7}_{-1.0}$	⋯	$3143.0^{+10.8}_{-10.6}$	⋯	$5.44^{+0.05}_{-0.03}$	⋯	B
⋯	9685	5121	239	2457849.892	3.95	14.3	$-12.2^{+0.6}_{-0.8}$	⋯	$9.1^{+1.0}_{-0.7}$	⋯	$3183.9^{+10.9}_{-9.5}$	⋯	$5.38^{+0.04}_{-0.04}$	⋯	B
⋯	9685	5121	239	2457857.896	−0.10	12.9	$-11.5^{+0.1}_{-0.2}$	⋯	$7.4^{+0.9}_{-0.6}$	⋯	$3178.9^{+7.3}_{-6.5}$	⋯	$5.45^{+0.03}_{-0.02}$	⋯	B
⋯	9684	5121	289	2458150.014	28.36	12.8	$-12.8^{+0.3}_{-0.7}$	⋯	$8.9^{+1.6}_{-1.0}$	⋯	$3210.0^{+10.8}_{-9.6}$	⋯	$5.49^{+0.01}_{-0.01}$	⋯	B
⋯	9684	5121	289	2458176.962	21.14	14.2	$-11.4^{+0.2}_{-0.2}$	⋯	$8.9^{+1.6}_{-0.9}$	⋯	$3166.4^{+6.8}_{-9.8}$	⋯	$5.38^{+0.03}_{-0.04}$	⋯	B
2M13482307+3321508	8912	5180	216	2457499.666	−7.57	12.8	$-4.7^{+1.0}_{-0.6}$	$-19.2^{+3.6}_{-4.5}$	$12.6^{+0.8}_{-0.9}$	$14.4^{+5.1}_{-2.4}$	$3146.9^{+17.9}_{-13.2}$	$3186.6^{+39.8}_{-39.4}$	$5.49^{+0.02}_{-0.01}$	$5.48^{+0.03}_{-0.02}$	B
⋯	9778	5180	223	2457856.849	−4.91	10.7	$-11.6^{+2.1}_{-1.7}$	⋯	$28.0^{+9.3}_{-5.8}$	⋯	$3154.9^{+15.7}_{-16.3}$	⋯	$5.45^{+0.05}_{-0.03}$	⋯	B
⋯	9665	5180	222	2457858.851	−5.67	13.8	$-21.9^{+0.2}_{-0.2}$	⋯	$20.9^{+1.3}_{-1.1}$	⋯	$3220.4^{+9.0}_{-9.5}$	⋯	$5.46^{+0.04}_{-0.03}$	⋯	B
⋯	9683	5180	216	2457859.838	−6.01	12.8	$-20.8^{+0.4}_{-0.8}$	⋯	$11.8^{+1.1}_{-1.0}$	⋯	$3172.9^{+15.5}_{-14.7}$	⋯	$5.49^{+0.02}_{-0.01}$	⋯	B
⋯	9778	5180	222	2457860.873	−6.47	11.9	$-17.2^{+0.4}_{-0.4}$	⋯	$14.2^{+1.0}_{-1.0}$	⋯	$3217.1^{+10.2}_{-15.0}$	⋯	$5.47^{+0.04}_{-0.02}$	⋯	B
⋯	9778	5180	228	2457878.798	−12.56	11.8	$-15.0^{+0.4}_{-0.2}$	⋯	$12.4^{+2.0}_{-1.0}$	⋯	$3201.8^{+24.2}_{-14.7}$	⋯	$5.43^{+0.07}_{-0.04}$	⋯	B
⋯	9777	5180	222	2457886.711	−14.76	10.2	$14.8^{+2.9}_{-3.7}$	⋯	$63.2^{+6.1}_{-5.6}$	⋯	$3098.5^{+17.0}_{-17.3}$	⋯	$5.2^{+0.14}_{-0.09}$	⋯	B
2M13500476+3207596	8912	5180	118	2457499.666	−7.24	19.1	$-5.8^{+0.2}_{-0.3}$	$-5.8^{+0.5}_{-0.6}$	$10.9^{+1.4}_{-1.1}$	$10.6^{+2.9}_{-1.8}$	$3158.3^{+10.4}_{-11.3}$	$3181.8^{+19.5}_{-20.3}$	$5.49^{+0.02}_{-0.01}$	$5.49^{+0.01}_{-0.01}$	B
⋯	9544	5180	112	2457743.012	22.87	11.7	$-6.7^{+0.3}_{-0.3}$	⋯	$10.1^{+1.3}_{-1.3}$	⋯	$3183.8^{+14.5}_{-21.5}$	⋯	$5.48^{+0.04}_{-0.02}$	⋯	B
⋯	9544	5180	117	2457823.794	8.55	10.8	$-4.7^{+1.3}_{-0.4}$	⋯	$12.9^{+1.3}_{-1.6}$	⋯	$3181.7^{+25.3}_{-9.8}$	⋯	$5.48^{+0.02}_{-0.01}$	⋯	B
⋯	9665	5180	27	2457852.871	−3.03	12.2	$-5.2^{+0.6}_{-0.3}$	⋯	$13.2^{+1.0}_{-1.2}$	⋯	$3233.2^{+18.9}_{-13.2}$	⋯	$5.47^{+0.04}_{-0.02}$	⋯	B
⋯	9778	5180	111	2457856.849	−4.53	11.5	$-5.7^{+0.2}_{-0.2}$	⋯	$5.9^{+2.6}_{-1.9}$	⋯	$3179.2^{+8.7}_{-11.9}$	⋯	$5.48^{+0.02}_{-0.01}$	⋯	B
⋯	8912	5180	112	2457857.710	−4.58	11.4	$-6.6^{+0.5}_{-0.5}$	⋯	$10.8^{+1.9}_{-1.2}$	⋯	$3159.9^{+12.9}_{-23.5}$	⋯	$5.48^{+0.03}_{-0.01}$	⋯	B
⋯	9665	5180	27	2457858.851	−5.30	12.4	$-4.6^{+0.4}_{-0.4}$	⋯	$13.5^{+1.0}_{-1.1}$	⋯	$3174.2^{+10.7}_{-9.3}$	⋯	$5.49^{+0.01}_{-0.01}$	⋯	B
⋯	9777	5180	28	2457859.770	−5.48	17.5	$-6.4^{+0.1}_{-0.2}$	⋯	$10.1^{+1.1}_{-1.0}$	⋯	$3171.1^{+13.8}_{-11.0}$	⋯	$5.46^{+0.04}_{-0.03}$	⋯	B
⋯	9683	5180	27	2457859.838	−5.65	12.9	$-4.6^{+0.2}_{-0.2}$	⋯	$9.5^{+1.0}_{-1.0}$	⋯	$3173.8^{+7.2}_{-11.7}$	⋯	$5.45^{+0.03}_{-0.03}$	⋯	B
⋯	9778	5180	112	2457860.873	−6.11	13.9	$-5.8^{+0.3}_{-0.3}$	⋯	$6.1^{+1.4}_{-1.4}$	⋯	$3183.6^{+10.0}_{-9.5}$	⋯	$5.5^{+0.01}_{-0.0}$	⋯	B
⋯	9665	5180	27	2457876.710	−11.48	10.9	$-5.5^{+0.5}_{-0.6}$	⋯	$8.2^{+1.2}_{-1.2}$	⋯	$3251.2^{+9.4}_{-10.0}$	⋯	$5.49^{+0.02}_{-0.01}$	⋯	B
⋯	9778	5180	10	2457878.798	−12.35	11.0	$-6.1^{+0.4}_{-0.4}$	⋯	$6.1^{+1.3}_{-1.4}$	⋯	$3176.1^{+19.2}_{-9.6}$	⋯	$5.48^{+0.02}_{-0.01}$	⋯	B
⋯	9730	5180	28	2457879.689	−12.41	18.3	$-4.8^{+0.3}_{-0.3}$	⋯	$7.2^{+1.7}_{-1.7}$	⋯	$3201.1^{+11.2}_{-10.8}$	⋯	$5.49^{+0.01}_{-0.01}$	⋯	B
⋯	9725	5180	112	2457884.700	−13.99	11.8	$-6.7^{+0.4}_{-0.5}$	⋯	$11.7^{+1.1}_{-1.2}$	⋯	$3157.4^{+11.4}_{-16.6}$	⋯	$5.49^{+0.02}_{-0.01}$	⋯	B
⋯	9777	5180	27	2457886.711	−14.61	12.2	$-6.1^{+0.1}_{-0.2}$	⋯	$10.4^{+1.2}_{-1.0}$	⋯	$3220.3^{+16.9}_{-14.1}$	⋯	$5.48^{+0.02}_{-0.02}$	⋯	B
2M13564148+4342587	5752	4233	259	2455999.860	4.11	66.0	$-19.7^{+0.2}_{-0.2}$	$-19.5^{+0.6}_{-0.6}$	$16.1^{+0.2}_{-0.3}$	$16.2^{+1.0}_{-1.1}$	$2399.0^{+1.0}_{-0.7}$	$2399.0^{+0.7}_{-0.4}$	$5.5^{+0.0}_{-0.0}$	$5.5^{+0.0}_{-0.0}$	S
⋯	5752	4233	199	2456018.858	−2.16	95.1	$-20.2^{+0.2}_{-0.2}$	⋯	$16.2^{+0.2}_{-0.3}$	⋯	$2399.1^{+1.2}_{-0.6}$	⋯	$5.5^{+0.0}_{-0.0}$	⋯	S
⋯	5752	4233	205	2456345.942	9.92	44.8	$-18.8^{+0.2}_{-0.2}$	⋯	$16.2^{+0.2}_{-0.8}$	⋯	$2398.8^{+2.0}_{-0.9}$	⋯	$5.5^{+0.0}_{-0.0}$	⋯	S
2M13573443+5408223	11013	2517	121	2458581.869	−6.16	12.6	$-40.2^{+1.3}_{-0.5}$	$-43.2^{+0.7}_{-1.0}$	$36.6^{+0.5}_{-0.4}$	$38.4^{+4.0}_{-1.9}$	$2399.2^{+1.0}_{-0.5}$	$2399.4^{+0.6}_{-0.4}$	$4.4^{+0.03}_{-0.02}$	$4.35^{+0.04}_{-0.04}$	S
⋯	11013	2517	121	2458582.854	−6.38	21.7	$-43.5^{+0.3}_{-0.2}$	⋯	$44.2^{+0.6}_{-1.1}$	⋯	$2399.5^{+0.7}_{-0.4}$	⋯	$4.32^{+0.02}_{-0.02}$	⋯	S
2M14005977+3226109	8912	5180	77	2457499.666	−6.15	16.6	$-18.1^{+0.3}_{-0.3}$	$-17.9^{+0.7}_{-0.8}$	$7.7^{+1.0}_{-0.7}$	$11.5^{+2.3}_{-1.8}$	$2946.4^{+14.6}_{-11.7}$	$2893.8^{+82.0}_{-83.9}$	$5.29^{+0.04}_{-0.04}$	$5.45^{+0.19}_{-0.11}$	B
⋯	9544	5180	71	2457743.012	22.20	12.4	$-18.4^{+0.4}_{-0.3}$	⋯	$10.3^{+0.4}_{-1.0}$	⋯	$2917.7^{+12.8}_{-13.5}$	⋯	$5.48^{+0.03}_{-0.01}$	⋯	B
⋯	9665	5180	77	2457852.871	−1.98	12.2	$-18.1^{+0.3}_{-0.5}$	⋯	$9.5^{+0.8}_{-0.7}$	⋯	$2937.9^{+22.3}_{-13.0}$	⋯	$5.1^{+0.05}_{-0.03}$	⋯	B
⋯	9778	5180	76	2457853.901	−2.44	11.6	$-18.9^{+0.2}_{-0.3}$	⋯	$15.4^{+1.2}_{-1.0}$	⋯	$2931.9^{+15.7}_{-16.3}$	⋯	$5.48^{+0.02}_{-0.01}$	⋯	B
⋯	9778	5180	76	2457856.849	−3.46	17.0	$-18.1^{+0.2}_{-0.2}$	⋯	$12.4^{+1.1}_{-0.6}$	⋯	$2930.5^{+7.9}_{-10.1}$	⋯	$5.49^{+0.01}_{-0.01}$	⋯	B

Table 3.4 (*continued*)

Table 3.4 (*continued*)

APOGEE ID	Plate	Loc. ID	Fiber ID	JD (day)	bary.[a] ($km\ s^{-1}$)	S/N	RV ($km\ s^{-1}$)	$\langle RV \rangle$[b] ($km\ s^{-1}$)	$v \sin i$ ($km\ s^{-1}$)	$\langle v \sin i \rangle$[b,c] ($km\ s^{-1}$)	$T_{\rm eff}$ (K)	$\langle T_{\rm eff} \rangle$[b] (K)	$\log g$ ($cm\ s^{-2}$)	$\langle \log g \rangle$[b] ($cm\ s^{-2}$)	Mdl[d]
⋯	9665	5180	68	2457858.851	−4.22	11.8	$-18.1^{+0.4}_{-0.2}$	⋯	$10.1^{+1.3}_{-1.4}$	⋯	$2848.1^{+14.8}_{-26.9}$	⋯	$4.97^{+0.06}_{-0.07}$	⋯	B
⋯	9777	5180	75	2457859.770	−4.40	18.5	$-18.4^{+0.2}_{-0.2}$	⋯	$14.4^{+0.3}_{-1.5}$	⋯	$2878.1^{+33.9}_{-23.1}$	⋯	$4.79^{+0.12}_{-0.15}$	⋯	B
⋯	9683	5180	75	2457859.838	−4.57	13.1	$-17.9^{+0.2}_{-0.3}$	⋯	$10.7^{+0.3}_{-0.8}$	⋯	$2815.9^{+10.1}_{-13.5}$	⋯	$4.99^{+0.04}_{-0.03}$	⋯	B
⋯	9778	5180	75	2457860.873	−5.03	18.1	$-18.7^{+0.2}_{-0.3}$	⋯	$10.8^{+0.5}_{-0.9}$	⋯	$2946.3^{+10.0}_{-14.9}$	⋯	$5.45^{+0.05}_{-0.03}$	⋯	B
⋯	9665	5180	71	2457876.710	−10.39	11.5	$-17.2^{+0.3}_{-0.7}$	⋯	$9.4^{+0.8}_{-1.2}$	⋯	$2896.9^{+20.6}_{-17.9}$	⋯	$5.21^{+0.09}_{-0.07}$	⋯	B
⋯	9778	5180	76	2457878.798	−11.26	13.1	$-16.1^{+0.4}_{-0.3}$	⋯	$10.7^{+1.5}_{-1.0}$	⋯	$3068.3^{+13.8}_{-11.5}$	⋯	$5.49^{+0.02}_{-0.01}$	⋯	B
⋯	9730	5180	128	2457879.689	−11.33	11.5	$-18.2^{+0.3}_{-0.2}$	⋯	$6.9^{+1.7}_{-1.0}$	⋯	$2968.0^{+20.3}_{-24.7}$	⋯	$5.47^{+0.05}_{-0.02}$	⋯	B
⋯	9725	5180	76	2457884.700	−12.93	10.7	$-16.6^{+0.3}_{-0.4}$	⋯	$11.0^{+0.9}_{-1.0}$	⋯	$2892.5^{+21.3}_{-17.9}$	⋯	$5.25^{+0.07}_{-0.04}$	⋯	B
⋯	9777	5180	70	2457886.711	−13.55	14.3	$-17.9^{+0.8}_{-0.4}$	⋯	$13.6^{+1.2}_{-0.9}$	⋯	$2806.6^{+5.6}_{-12.2}$	⋯	$4.99^{+0.03}_{-0.04}$	⋯	B
⋯	9725	5180	64	2457909.698	−19.19	10.7	$-17.5^{+0.3}_{-0.4}$	⋯	$10.5^{+0.9}_{-0.7}$	⋯	$2807.2^{+6.9}_{-11.4}$	⋯	$5.08^{+0.05}_{-0.06}$	⋯	B
⋯	9683	5180	76	2457915.628	−20.05	10.4	$-16.1^{+0.3}_{-0.3}$	⋯	$15.1^{+1.2}_{-1.1}$	⋯	$3056.2^{+13.3}_{-15.4}$	⋯	$5.49^{+0.02}_{-0.01}$	⋯	B
2M14081562+5236281	6857	4499	43	2456376.906	−1.67	32.9	$-43.7^{+0.2}_{-0.3}$	$-43.5^{+0.1}_{-0.1}$	$9.2^{+0.6}_{-0.9}$	< 10	$3180.0^{+8.9}_{-7.7}$	$3175.2^{+11.3}_{-12.2}$	$5.48^{+0.02}_{-0.02}$	$5.46^{+0.03}_{-0.03}$	B
⋯	6857	4499	91	2456383.847	−3.40	37.6	$-43.5^{+0.2}_{-0.2}$	⋯	$3.8^{+1.4}_{-1.6}$	⋯	$3184.8^{+11.5}_{-7.1}$	⋯	$5.41^{+0.03}_{-0.03}$	⋯	B
⋯	6857	4499	91	2456402.802	−7.98	40.5	$-43.4^{+0.2}_{-0.2}$	⋯	$7.4^{+0.8}_{-0.6}$	⋯	$3159.2^{+14.4}_{-6.9}$	⋯	$5.45^{+0.03}_{-0.03}$	⋯	B
2M14093200+4138080	8334	2144	296	2458253.726	−13.09	77.0	$-11.0^{+0.2}_{-0.2}$	$-11.0^{+0.2}_{-0.2}$	$19.7^{+0.1}_{-0.2}$	$19.7^{+0.1}_{-0.2}$	$2399.7^{+0.5}_{-0.2}$	$2399.7^{+0.5}_{-0.2}$	$4.63^{+0.02}_{-0.01}$	$4.63^{+0.02}_{-0.01}$	S
2M14320849+0811313	5672	4436	143	2456439.692	−14.57	135.2	$-21.2^{+0.3}_{-0.1}$	$-21.3^{+0.1}_{-0.1}$	$9.1^{+0.3}_{-0.5}$	< 10	$2399.5^{+0.7}_{-0.4}$	$2399.5^{+0.4}_{-0.2}$	$5.4^{+0.02}_{-0.01}$	$5.41^{+0.03}_{-0.03}$	S
⋯	5672	4436	89	2456461.665	−21.97	135.0	$-21.4^{+0.1}_{-0.1}$	⋯	$9.1^{+0.3}_{-0.4}$	⋯	$2399.5^{+0.9}_{-0.3}$	⋯	$5.39^{+0.02}_{-0.03}$	⋯	S
⋯	5672	4436	41	2456468.649	−23.69	137.6	$-21.3^{+0.1}_{-0.2}$	⋯	$9.5^{+0.7}_{-0.6}$	⋯	$2399.5^{+0.7}_{-0.4}$	⋯	$5.45^{+0.03}_{-0.02}$	⋯	S
2M14340140+5039480	9005	5186	206	2457498.739	−5.69	26.9	$-6.5^{+0.2}_{-0.1}$	$-6.4^{+0.3}_{-0.3}$	$16.0^{+0.1}_{-0.2}$	$16.3^{+1.5}_{-1.6}$	$2399.5^{+0.7}_{-0.4}$	$2399.3^{+0.3}_{-0.2}$	$4.92^{+0.02}_{-0.02}$	$4.88^{+0.15}_{-0.16}$	S
⋯	9006	5186	158	2457499.883	−6.18	22.3	$-6.3^{+0.1}_{-0.2}$	⋯	$16.1^{+0.2}_{-0.3}$	⋯	$2399.3^{+0.9}_{-0.4}$	⋯	$4.93^{+0.02}_{-0.02}$	⋯	S
⋯	9006	5186	158	2457522.738	−10.66	17.3	$-6.8^{+0.2}_{-0.3}$	⋯	$16.1^{+0.1}_{-0.3}$	⋯	$2398.9^{+1.4}_{-0.8}$	⋯	$4.87^{+0.02}_{-0.02}$	⋯	S
⋯	9005	5186	206	2457524.644	−10.85	17.1	$-6.4^{+0.2}_{-0.2}$	⋯	$16.1^{+0.1}_{-0.3}$	⋯	$2399.3^{+1.0}_{-0.6}$	⋯	$4.69^{+0.02}_{-0.02}$	⋯	S
⋯	9005	5186	206	2457528.725	−11.62	15.9	$-6.0^{+0.2}_{-0.2}$	⋯	$16.3^{+0.3}_{-1.5}$	⋯	$2399.4^{+1.0}_{-0.5}$	⋯	$4.78^{+0.04}_{-0.05}$	⋯	S
⋯	9006	5186	206	2457529.774	−11.85	29.7	$-6.3^{+0.2}_{-0.2}$	⋯	$14.1^{+1.2}_{-0.5}$	⋯	$2399.2^{+1.0}_{-0.6}$	⋯	$5.01^{+0.07}_{-0.13}$	⋯	S
⋯	9006	5186	254	2457532.698	−12.16	27.1	$-6.0^{+0.2}_{-0.2}$	⋯	$12.6^{+0.3}_{-0.8}$	⋯	$2399.1^{+0.8}_{-0.7}$	⋯	$5.19^{+0.02}_{-0.02}$	⋯	S
⋯	9006	5186	206	2457553.647	−14.20	23.4	$-6.6^{+0.3}_{-0.3}$	⋯	$16.1^{+0.1}_{-0.3}$	⋯	$2399.3^{+1.0}_{-0.5}$	⋯	$4.81^{+0.02}_{-0.03}$	⋯	S
⋯	9006	5186	161	2457556.694	−14.43	13.4	$-6.9^{+0.3}_{-0.2}$	⋯	$19.8^{+0.2}_{-0.3}$	⋯	$2399.2^{+1.2}_{-0.6}$	⋯	$4.63^{+0.04}_{-0.02}$	⋯	S
2M14402293+1339230	6842	4493	272	2456469.649	−22.80	45.7	$-3.3^{+0.2}_{-0.2}$	$-3.5^{+0.2}_{-0.2}$	$4.2^{+1.0}_{-0.4}$	< 10	$2399.1^{+1.1}_{-0.6}$	$2399.1^{+0.7}_{-0.4}$	$5.49^{+0.01}_{-0.01}$	$5.47^{+0.03}_{-0.03}$	S
⋯	6842	4493	278	2456701.025	25.03	27.3	$-3.7^{+0.3}_{-0.3}$	⋯	$5.9^{+0.7}_{-1.0}$	⋯	$2398.6^{+1.2}_{-1.0}$	⋯	$5.41^{+0.06}_{-0.02}$	⋯	S
⋯	6842	4493	224	2456709.004	23.50	34.7	$-3.7^{+0.2}_{-0.2}$	⋯	$3.9^{+0.9}_{-0.8}$	⋯	$2399.3^{+1.0}_{-0.5}$	⋯	$5.44^{+0.02}_{-0.03}$	⋯	S
2M14432796+0316543	11835	2675	155	2458629.742	−12.45	22.2	$-38.4^{+0.3}_{-0.3}$	$-38.4^{+0.3}_{-0.3}$	$22.7^{+0.8}_{-0.4}$	$22.7^{+0.8}_{-0.4}$	$2399.2^{+1.3}_{-0.6}$	$2399.2^{+1.3}_{-0.6}$	$5.34^{+0.02}_{-0.02}$	$5.34^{+0.02}_{-0.02}$	S
2M14553384+1545593	6844	4494	150	2456432.761	−9.70	17.4	$19.4^{+0.2}_{-0.2}$	$19.3^{+0.2}_{-0.2}$	$12.4^{+0.2}_{-1.2}$	$14.8^{+2.7}_{-2.6}$	$2399.2^{+0.9}_{-0.6}$	$2399.2^{+0.6}_{-0.3}$	$4.85^{+0.04}_{-0.04}$	$4.63^{+0.15}_{-0.21}$	S
⋯	6844	4494	102	2456470.651	−21.60	16.2	$19.2^{+0.2}_{-0.2}$	⋯	$13.8^{+1.3}_{-0.6}$	⋯	$2399.2^{+1.2}_{-0.6}$	⋯	$4.67^{+0.03}_{-0.03}$	⋯	S
⋯	6844	4494	150	2456703.995	24.34	12.2	$19.2^{+0.3}_{-0.6}$	⋯	$21.7^{+1.5}_{-0.4}$	⋯	$2399.2^{+1.5}_{-0.5}$	⋯	$4.34^{+0.08}_{-0.03}$	⋯	S
2M14554964+0321420	11824	2673	119	2458634.771	−13.24	60.5	$-39.9^{+0.3}_{-0.3}$	$-39.9^{+0.2}_{-0.1}$	$8.8^{+0.7}_{-0.4}$	< 10	$2399.5^{+0.5}_{-0.4}$	$2399.5^{+0.4}_{-0.2}$	$4.87^{+0.03}_{-0.02}$	$4.89^{+0.02}_{-0.02}$	S
⋯	11824	2673	119	2458635.775	−13.68	56.2	$-39.9^{+0.2}_{-0.1}$	⋯	$7.6^{+0.9}_{-0.8}$	⋯	$2399.5^{+0.6}_{-0.3}$	⋯	$4.89^{+0.01}_{-0.01}$	⋯	S
2M15010818+2250020	5673	4437	293	2456702.002	22.44	60.2	$7.6^{+0.1}_{-0.1}$	$6.5^{+0.7}_{-0.7}$	$65.9^{+0.5}_{-0.4}$	$65.3^{+1.2}_{-1.3}$	$2395.6^{+5.2}_{-3.0}$	$2389.1^{+23.6}_{-15.9}$	$5.5^{+0.0}_{-0.0}$	$5.5^{+0.0}_{-0.0}$	S
⋯	5673	4437	284	2456706.009	21.78	48.6	$6.8^{+0.1}_{-0.2}$	⋯	$65.0^{+0.5}_{-0.5}$	⋯	$2387.4^{+3.9}_{-5.3}$	⋯	$5.5^{+0.0}_{-0.0}$	⋯	S
⋯	5673	4437	239	2456727.907	16.74	51.8	$7.1^{+0.1}_{-0.1}$	⋯	$64.6^{+0.7}_{-0.6}$	⋯	$2341.1^{+13.3}_{-13.5}$	⋯	$5.5^{+0.0}_{-0.0}$	⋯	S
⋯	5673	4437	191	2456733.940	14.78	69.8	$5.7^{+0.1}_{-0.1}$	⋯	$64.1^{+0.8}_{-0.4}$	⋯	$2309.6^{+9.2}_{-11.0}$	⋯	$5.5^{+0.0}_{-0.0}$	⋯	S
⋯	5673	4437	293	2456780.843	−3.03	73.1	$6.3^{+0.1}_{-0.1}$	⋯	$66.3^{+0.4}_{-0.7}$	⋯	$2396.1^{+4.6}_{-2.6}$	⋯	$5.5^{+0.0}_{-0.0}$	⋯	S
2M15041028+0923232	11970	2732	132	2458928.974	17.78	15.9	$-53.5^{+0.2}_{-0.2}$	$-53.3^{+0.3}_{-0.3}$	$15.0^{+0.8}_{-0.8}$	$13.4^{+1.4}_{-1.4}$	$2399.3^{+0.9}_{-0.6}$	$2399.2^{+0.6}_{-0.4}$	$4.85^{+0.02}_{-0.02}$	$4.96^{+0.11}_{-0.12}$	S
⋯	11970	2732	132	2458930.898	17.25	14.9	$-53.5^{+0.2}_{-0.2}$	⋯	$12.7^{+0.4}_{-0.5}$	⋯	$2399.1^{+1.2}_{-0.6}$	⋯	$5.08^{+0.02}_{-0.02}$	⋯	S
⋯	11962	2724	247	2458932.911	16.47	16.5	$-52.9^{+0.2}_{-0.3}$	⋯	$14.1^{+1.4}_{-0.7}$	⋯	$2399.2^{+1.2}_{-0.6}$	⋯	$5.07^{+0.04}_{-0.04}$	⋯	S

Table 3.4 (*continued*)

Table 3.4 (*continued*)

APOGEE ID	Plate	Loc. ID	Fiber ID	JD (day)	bary.[a] ($km\ s^{-1}$)	S/N	RV ($km\ s^{-1}$)	$\langle RV \rangle$[b] ($km\ s^{-1}$)	$v \sin i$ ($km\ s^{-1}$)	$\langle v \sin i \rangle$[b,c] ($km\ s^{-1}$)	$T_{\rm eff}$ (K)	$\langle T_{\rm eff} \rangle$[b] (K)	$\log g$ ($cm\ s^{-2}$)	$\langle \log g \rangle$[b] ($cm\ s^{-2}$)	Mdl[d]
2M15042797+0942464	11970	2732	73	2458928.974	17.72	22.6	$-35.6^{+1.3}_{-0.8}$	$-35.6^{+1.3}_{-0.8}$	$51.1^{+1.1}_{-1.7}$	$51.1^{+1.1}_{-1.7}$	$3177.5^{+7.8}_{-9.7}$	$3177.5^{+7.8}_{-9.7}$	$5.25^{+0.05}_{-0.04}$	$5.25^{+0.05}_{-0.04}$	B
2M15115124+3033065	6848	4496	127	2456411.747	−1.39	19.9	$-61.4^{+0.1}_{-0.2}$	$-61.4^{+0.1}_{-0.1}$	$18.3^{+0.4}_{-0.7}$	$18.9^{+1.3}_{-1.6}$	$2399.3^{+1.3}_{-0.5}$	$2399.4^{+0.7}_{-0.3}$	$4.89^{+0.04}_{-0.04}$	$4.88^{+0.03}_{-0.02}$	S
⋯	6848	4496	150	2456433.710	−8.76	19.4	$-61.5^{+0.2}_{-0.2}$	⋯	$20.9^{+1.1}_{-0.7}$	⋯	$2399.4^{+0.8}_{-0.4}$	⋯	$4.87^{+0.04}_{-0.03}$	⋯	S
2M15175638+0656388	11968	2730	78	2459010.740	−15.06	30.0	$-20.0^{+0.1}_{-0.1}$	$-19.8^{+0.3}_{-0.3}$	$5.9^{+1.0}_{-1.4}$	< 10	$3292.9^{+7.9}_{-11.5}$	$3277.9^{+9.2}_{-9.6}$	$5.43^{+0.03}_{-0.03}$	$5.38^{+0.04}_{-0.04}$	B
⋯	11968	2730	78	2459011.672	−15.25	32.0	$-19.3^{+0.2}_{-0.3}$	⋯	$7.4^{+0.6}_{-0.7}$	⋯	$3273.4^{+4.4}_{-5.9}$	⋯	$5.36^{+0.02}_{-0.02}$	⋯	B
2M15210103+5053230	8596	2226	294	2458607.834	−5.09	58.5	$2.4^{+0.2}_{-0.1}$	$2.4^{+0.2}_{-0.1}$	$48.7^{+0.3}_{-0.3}$	$48.7^{+0.3}_{-0.3}$	$2399.2^{+1.1}_{-0.6}$	$2399.2^{+1.1}_{-0.6}$	$5.5^{+0.0}_{-0.0}$	$5.5^{+0.0}_{-0.0}$	S
2M15242475+2925318	9044	2375	131	2457861.767	4.02	40.6	$-14.8^{+0.1}_{-0.1}$	$-15.2^{+0.0}_{-0.1}$	$7.3^{+0.3}_{-0.5}$	< 10	$2399.2^{+1.1}_{-0.6}$	$2399.3^{+0.5}_{-0.3}$	$5.46^{+0.01}_{-0.02}$	$5.47^{+0.11}_{-0.07}$	S
⋯	9044	2375	131	2457862.790	3.62	61.3	$-15.1^{+0.2}_{-0.1}$	⋯	$6.4^{+1.4}_{-1.1}$	⋯	$2399.4^{+0.8}_{-0.5}$	⋯	$5.48^{+0.02}_{-0.01}$	⋯	S
⋯	9043	2374	245	2457921.713	−15.07	46.9	$-15.0^{+0.2}_{-0.1}$	⋯	$7.3^{+0.4}_{-0.7}$	⋯	$2399.2^{+1.2}_{-0.6}$	⋯	$5.49^{+0.01}_{-0.0}$	⋯	S
⋯	9043	2374	245	2457922.650	−15.15	21.6	$-15.2^{+0.0}_{-0.0}$	⋯	$10.5^{+0.4}_{-0.6}$	⋯	$2399.3^{+1.2}_{-0.5}$	⋯	$5.14^{+0.02}_{-0.02}$	⋯	S
2M15512179+2931062	9887	2458	285	2458258.851	−4.32	196.6	$26.4^{+0.1}_{-0.1}$	$26.0^{+0.2}_{-0.2}$	$4.1^{+0.9}_{-0.4}$	< 10	$3412.1^{+6.8}_{-5.1}$	$3426.3^{+8.7}_{-8.8}$	$5.1^{+0.02}_{-0.02}$	$5.09^{+0.01}_{-0.01}$	B
⋯	9887	2458	238	2458271.707	−8.11	149.8	$26.2^{+0.1}_{-0.1}$	⋯	$4.1^{+0.7}_{-0.4}$	⋯	$3428.7^{+6.4}_{-5.0}$	⋯	$5.09^{+0.02}_{-0.02}$	⋯	B
⋯	9887	2458	238	2458277.835	−10.20	165.0	$26.0^{+0.1}_{-0.1}$	⋯	$3.9^{+0.6}_{-0.4}$	⋯	$3418.8^{+4.5}_{-4.3}$	⋯	$5.07^{+0.02}_{-0.02}$	⋯	B
⋯	9887	2458	238	2458280.655	−10.64	211.9	$25.8^{+0.0}_{-0.1}$	⋯	$3.8^{+0.5}_{-0.6}$	⋯	$3434.1^{+3.7}_{-2.9}$	⋯	$5.09^{+0.01}_{-0.01}$	⋯	B
2M15555600−2045187	9851	5371	294	2458176.820	30.22	37.2	$-3.7^{+0.2}_{-0.2}$	$-4.1^{+0.5}_{-0.5}$	$19.9^{+0.2}_{-0.4}$	$19.9^{+1.0}_{-1.1}$	$3007.7^{+4.8}_{-3.7}$	$3003.7^{+8.4}_{-6.8}$	$4.49^{+0.01}_{-0.01}$	$4.5^{+0.01}_{-0.01}$	B
⋯	9851	5371	289	2458243.639	9.32	30.0	$-4.7^{+0.2}_{-0.2}$	⋯	$20.1^{+0.4}_{-0.8}$	⋯	$2992.6^{+6.2}_{-7.8}$	⋯	$4.51^{+0.01}_{-0.02}$	⋯	B
2M15560104−2338081	10944	5785	264	2458350.477	−29.14	15.4	$1.5^{+0.3}_{-0.2}$	$1.5^{+0.3}_{-0.2}$	$13.0^{+0.6}_{-0.9}$	$13.0^{+0.6}_{-0.9}$	$2399.4^{+0.8}_{-0.4}$	$2399.4^{+0.8}_{-0.4}$	$3.58^{+0.04}_{-0.02}$	$3.58^{+0.04}_{-0.02}$	S
2M15560497−2106461	9851	5371	283	2458176.820	30.23	19.6	$-3.5^{+1.7}_{-1.8}$	$-4.1^{+1.4}_{-0.6}$	$93.0^{+2.9}_{-3.3}$	$92.8^{+1.8}_{-1.5}$	$2399.1^{+1.3}_{-0.7}$	$2399.1^{+0.9}_{-0.5}$	$3.51^{+0.0}_{-0.01}$	$3.51^{+0.0}_{-0.01}$	S
⋯	9851	5371	283	2458243.639	9.37	16.1	$-4.3^{+1.9}_{-0.5}$	⋯	$92.7^{+1.7}_{-1.6}$	⋯	$2399.1^{+1.2}_{-0.7}$	⋯	$3.51^{+0.01}_{-0.01}$	⋯	S
2M15574011+2952379	9887	2458	179	2458258.851	−3.65	32.8	$1.1^{+0.2}_{-0.2}$	$1.1^{+0.2}_{-0.2}$	$10.6^{+0.3}_{-0.9}$	$10.3^{+1.8}_{-1.6}$	$2399.5^{+0.7}_{-0.3}$	$2399.4^{+0.4}_{-0.2}$	$4.89^{+0.03}_{-0.02}$	$4.84^{+0.13}_{-0.09}$	S
⋯	9887	2458	176	2458271.707	−7.42	23.6	$0.9^{+0.8}_{-0.3}$	⋯	$14.8^{+0.7}_{-1.1}$	⋯	$2399.5^{+0.8}_{-0.4}$	⋯	$4.6^{+0.02}_{-0.04}$	⋯	S
⋯	9887	2458	176	2458277.835	−9.52	28.2	$1.3^{+0.2}_{-0.2}$	⋯	$9.1^{+0.3}_{-0.4}$	⋯	$2399.2^{+1.1}_{-0.6}$	⋯	$4.89^{+0.01}_{-0.02}$	⋯	S
⋯	9887	2458	176	2458280.655	−9.96	35.7	$0.9^{+0.2}_{-0.4}$	⋯	$10.9^{+0.4}_{-1.0}$	⋯	$2399.4^{+0.7}_{-0.4}$	⋯	$4.95^{+0.08}_{-0.05}$	⋯	S
2M15592591−2305081	9781	5331	186	2458177.782	30.22	60.1	$-3.3^{+0.1}_{-0.1}$	$-3.3^{+0.1}_{-0.1}$	$23.5^{+0.4}_{-0.1}$	$23.5^{+1.0}_{-1.0}$	$2399.7^{+0.4}_{-0.2}$	$2399.7^{+0.3}_{-0.1}$	$4.06^{+0.03}_{-0.03}$	$3.99^{+0.06}_{-0.06}$	S
⋯	9781	5331	186	2458261.573	1.09	56.3	$-3.4^{+0.2}_{-0.2}$	⋯	$23.5^{+0.1}_{-0.2}$	⋯	$2399.7^{+0.4}_{-0.2}$	⋯	$3.94^{+0.03}_{-0.02}$	⋯	S
2M15594439−1928191	11629	6001	229	2458913.801	29.70	13.9	$-2.6^{+0.4}_{-0.2}$	$-2.6^{+0.4}_{-0.2}$	$14.4^{+0.2}_{-0.9}$	$14.4^{+0.2}_{-0.9}$	$2399.4^{+0.7}_{-0.5}$	$2399.4^{+0.7}_{-0.5}$	$3.83^{+0.16}_{-0.04}$	$3.83^{+0.16}_{-0.04}$	S
2M16001944−2256287	9781	5331	48	2458177.782	30.23	10.9	$-3.1^{+0.4}_{-1.2}$	$-4.3^{+0.7}_{-0.5}$	$23.6^{+0.2}_{-0.4}$	$24.9^{+2.1}_{-1.7}$	$2399.3^{+1.1}_{-0.5}$	$2399.2^{+0.8}_{-0.4}$	$3.54^{+0.03}_{-0.02}$	$3.53^{+0.02}_{-0.02}$	S
⋯	9781	5331	49	2458261.573	1.18	12.4	$-4.6^{+0.2}_{-0.3}$	⋯	$27.7^{+0.3}_{-0.5}$	⋯	$2399.2^{+1.2}_{-0.5}$	⋯	$3.53^{+0.02}_{-0.04}$	⋯	S
2M16002844−2209228	9781	5331	67	2458177.782	30.24	17.2	$-4.7^{+0.7}_{-0.2}$	$-3.7^{+0.7}_{-0.8}$	$9.1^{+0.7}_{-0.8}$	< 10	$3226.5^{+20.4}_{-20.3}$	$3177.3^{+47.5}_{-36.1}$	$5.06^{+0.12}_{-0.08}$	$5.08^{+0.15}_{-0.13}$	B
⋯	9781	5331	90	2458261.573	1.12	12.7	$-3.0^{+0.2}_{-0.2}$	⋯	$6.3^{+1.3}_{-1.2}$	⋯	$3171.8^{+23.3}_{-13.8}$	⋯	$5.18^{+0.05}_{-0.04}$	⋯	B
⋯	11627	5999	224	2458565.809	26.51	13.2	$-3.4^{+0.2}_{-0.2}$	⋯	$10.6^{+1.0}_{-0.8}$	⋯	$3117.4^{+22.3}_{-27.7}$	⋯	$4.87^{+0.06}_{-0.07}$	⋯	B
2M16003023−2334457	9781	5331	211	2458177.782	30.22	24.6	$-3.6^{+1.4}_{-0.5}$	$-3.7^{+0.5}_{-0.4}$	$75.8^{+1.2}_{-1.8}$	$73.6^{+1.8}_{-1.5}$	$2399.5^{+0.6}_{-0.4}$	$2399.5^{+0.4}_{-0.2}$	$3.51^{+0.01}_{-0.01}$	$3.51^{+0.0}_{-0.01}$	S
⋯	9781	5331	211	2458261.573	1.26	36.1	$-4.5^{+0.3}_{-0.4}$	⋯	$73.4^{+1.1}_{-1.0}$	⋯	$2399.5^{+0.6}_{-0.4}$	⋯	$3.52^{+0.01}_{-0.02}$	⋯	S
⋯	10944	5785	85	2458350.477	−29.09	38.6	$-3.5^{+0.3}_{-0.2}$	⋯	$72.5^{+0.9}_{-1.3}$	⋯	$2399.6^{+0.7}_{-0.3}$	⋯	$3.51^{+0.01}_{-0.01}$	⋯	S
2M16014955−2351082	10944	5785	139	2458350.477	−29.07	35.0	$-3.5^{+0.1}_{-0.1}$	$-3.5^{+0.1}_{-0.1}$	$38.7^{+0.3}_{-1.5}$	$38.7^{+0.3}_{-1.5}$	$2399.6^{+0.6}_{-0.3}$	$2399.6^{+0.6}_{-0.3}$	$3.52^{+0.02}_{-0.02}$	$3.52^{+0.02}_{-0.02}$	S
2M16022585−2414081	10944	5785	103	2458350.477	−29.05	16.6	$-2.1^{+0.4}_{-0.3}$	$-2.1^{+0.4}_{-0.3}$	$17.9^{+0.2}_{-0.2}$	$17.9^{+0.2}_{-0.2}$	$2399.4^{+1.0}_{-0.4}$	$2399.4^{+1.0}_{-0.4}$	$3.53^{+0.02}_{-0.02}$	$3.53^{+0.02}_{-0.02}$	S
2M16044026−2254323	10945	5786	246	2458320.473	−23.56	13.2	$-1.2^{+0.4}_{-0.5}$	$-1.2^{+0.4}_{-0.5}$	$19.8^{+0.1}_{-0.2}$	$19.8^{+0.1}_{-0.2}$	$2399.4^{+1.1}_{-0.4}$	$2399.4^{+1.1}_{-0.4}$	$3.66^{+0.03}_{-0.03}$	$3.66^{+0.03}_{-0.03}$	S
2M16045199−2224108	10945	5786	157	2458320.473	−23.58	17.9	$-1.1^{+0.8}_{-1.3}$	$-1.1^{+0.8}_{-1.3}$	$73.3^{+1.1}_{-1.2}$	$73.3^{+1.1}_{-1.2}$	$2399.1^{+1.2}_{-0.7}$	$2399.1^{+1.2}_{-0.7}$	$3.51^{+0.01}_{-0.01}$	$3.51^{+0.01}_{-0.01}$	S
2M16055178−2206212	10945	5786	170	2458320.473	−23.53	15.5	$-3.8^{+0.3}_{-0.2}$	$-3.8^{+0.3}_{-0.2}$	$21.6^{+0.3}_{-0.2}$	$21.6^{+0.3}_{-0.2}$	$2399.3^{+0.9}_{-0.5}$	$2399.3^{+0.9}_{-0.5}$	$3.52^{+0.01}_{-0.02}$	$3.52^{+0.01}_{-0.02}$	S
2M16055380+2303058	8969	5125	23	2457468.950	17.52	30.5	$-40.7^{+0.2}_{-0.2}$	$-40.3^{+0.4}_{-0.4}$	$7.9^{+1.1}_{-0.4}$	$10.8^{+2.6}_{-1.8}$	$2399.4^{+0.9}_{-0.4}$	$2399.4^{+0.3}_{-0.2}$	$5.12^{+0.03}_{-0.04}$	$4.89^{+0.19}_{-0.19}$	S
⋯	8969	5125	23	2457474.939	16.04	24.1	$-40.5^{+0.1}_{-0.1}$	⋯	$10.9^{+0.5}_{-0.4}$	⋯	$2399.3^{+1.0}_{-0.5}$	⋯	$4.91^{+0.02}_{-0.03}$	⋯	S
⋯	8969	5125	26	2457500.888	7.96	23.1	$-40.9^{+0.2}_{-0.2}$	⋯	$7.7^{+0.6}_{-0.4}$	⋯	$2399.3^{+1.0}_{-0.5}$	⋯	$5.1^{+0.02}_{-0.01}$	⋯	S
⋯	8969	5125	23	2457506.874	5.85	18.4	$-40.5^{+0.2}_{-0.3}$	⋯	$12.4^{+1.3}_{-0.5}$	⋯	$2399.4^{+1.0}_{-0.4}$	⋯	$4.67^{+0.03}_{-0.03}$	⋯	S
⋯	8969	5125	20	2457524.785	−0.61	15.2	$-40.2^{+0.4}_{-0.3}$	⋯	$11.6^{+1.0}_{-0.5}$	⋯	$2399.3^{+0.9}_{-0.5}$	⋯	$4.71^{+0.04}_{-0.02}$	⋯	S

Table 3.4 (*continued*)

Table 3.4 (*continued*)

APOGEE ID	Plate	Loc. ID	Fiber ID	JD (day)	bary.[a] ($km\ s^{-1}$)	S/N	RV ($km\ s^{-1}$)	$\langle RV \rangle$[b] ($km\ s^{-1}$)	$v \sin i$ ($km\ s^{-1}$)	$\langle v \sin i \rangle$[b,c] ($km\ s^{-1}$)	$T_{\rm eff}$ (K)	$\langle T_{\rm eff} \rangle$[b] (K)	$\log g$ ($cm\ s^{-2}$)	$\langle \log g \rangle$[b] ($cm\ s^{-2}$)	Mdl[d]
⋯	8969	5125	14	2457530.805	−2.88	11.5	$-40.0^{+0.3}_{-0.2}$	⋯	$14.2^{+0.5}_{-0.4}$	⋯	$2399.3^{+0.6}_{-0.5}$	⋯	$4.65^{+0.03}_{-0.03}$	⋯	S
⋯	8970	5125	23	2457532.763	−3.50	20.4	$-40.2^{+0.2}_{-0.3}$	⋯	$8.9^{+0.4}_{-0.9}$	⋯	$2399.4^{+0.9}_{-0.4}$	⋯	$4.88^{+0.04}_{-0.06}$	⋯	S
⋯	8970	5125	20	2457535.782	−4.64	23.9	$-40.2^{+0.1}_{-0.1}$	⋯	$9.5^{+0.9}_{-0.7}$	⋯	$2399.5^{+0.7}_{-0.4}$	⋯	$5.02^{+0.03}_{-0.02}$	⋯	S
⋯	8970	5125	26	2457552.704	−10.32	26.2	$-39.9^{+0.1}_{-0.1}$	⋯	$7.7^{+0.9}_{-0.7}$	⋯	$2399.4^{+0.8}_{-0.4}$	⋯	$4.93^{+0.02}_{-0.02}$	⋯	S
⋯	8970	5125	26	2457555.675	−11.20	16.7	$-40.3^{+0.3}_{-0.2}$	⋯	$10.7^{+0.3}_{-1.5}$	⋯	$2399.4^{+0.5}_{-0.5}$	⋯	$4.75^{+0.04}_{-0.02}$	⋯	S
⋯	8970	5125	110	2457558.751	−12.31	12.2	$-39.0^{+0.4}_{-0.3}$	⋯	$14.5^{+0.3}_{-0.7}$	⋯	$2399.1^{+1.3}_{-0.7}$	⋯	$4.59^{+0.02}_{-0.02}$	⋯	S
2M16063110−1904576	9782	5332	67	2458176.882	30.26	16.8	$-5.0^{+0.2}_{-0.2}$	$-4.9^{+0.2}_{-0.2}$	$16.1^{+0.1}_{-0.3}$	$16.7^{+1.2}_{-1.8}$	$2399.5^{+0.6}_{-0.4}$	$2399.5^{+0.5}_{-0.3}$	$3.51^{+0.01}_{-0.01}$	$3.51^{+0.0}_{-0.01}$	S
⋯	9782	5332	67	2458177.833	30.26	11.6	$-4.8^{+0.7}_{-0.6}$	⋯	$19.7^{+1.5}_{-0.3}$	⋯	$2399.3^{+1.0}_{-0.6}$	⋯	$3.51^{+0.01}_{-0.01}$	⋯	S
2M16063390+4054216	8313	2123	32	2457166.793	−4.49	28.8	$-40.7^{+0.2}_{-0.2}$	$-41.0^{+0.2}_{-0.2}$	$0.7^{+0.5}_{-1.2}$	< 10	$2398.9^{+1.7}_{-0.7}$	$2399.1^{+0.8}_{-0.5}$	$5.3^{+0.03}_{-0.03}$	$5.32^{+0.02}_{-0.01}$	S
⋯	8979	2330	116	2457464.950	11.21	64.1	$-41.1^{+0.1}_{-0.1}$	⋯	$0.7^{+0.4}_{-1.3}$	⋯	$2399.3^{+0.8}_{-0.5}$	⋯	$5.32^{+0.02}_{-0.01}$	⋯	S
2M16081226+2252548	8468	5125	104	2457122.864	12.58	11.3	$14.5^{+0.4}_{-0.2}$	$14.4^{+0.8}_{-0.5}$	$24.1^{+0.6}_{-1.3}$	$24.5^{+2.2}_{-1.8}$	$2399.3^{+1.0}_{-0.5}$	$2399.2^{+0.6}_{-0.3}$	$4.54^{+0.08}_{-0.06}$	$4.52^{+0.12}_{-0.11}$	S
⋯	8468	5125	8	2457151.784	2.59	11.3	$13.1^{+0.5}_{-0.9}$	⋯	$28.2^{+0.9}_{-0.9}$	⋯	$2399.0^{+1.4}_{-0.7}$	⋯	$4.63^{+0.03}_{-0.04}$	⋯	S
⋯	8469	5125	116	2457175.720	−6.10	10.6	$15.4^{+0.4}_{-0.4}$	⋯	$22.8^{+1.1}_{-1.0}$	⋯	$2399.2^{+0.9}_{-0.6}$	⋯	$4.45^{+0.05}_{-0.08}$	⋯	S
⋯	8969	5125	53	2457500.888	8.23	11.1	$14.3^{+0.3}_{-0.3}$	⋯	$22.7^{+1.0}_{-1.0}$	⋯	$2399.2^{+1.4}_{-0.6}$	⋯	$4.36^{+0.04}_{-0.06}$	⋯	S
2M16090197−2151225	11628	6000	175	2458565.865	26.88	26.9	$-6.4^{+0.2}_{-1.1}$	$-6.4^{+0.2}_{-1.1}$	$47.8^{+1.2}_{-0.4}$	$47.8^{+1.2}_{-0.4}$	$2399.7^{+0.6}_{-0.2}$	$2399.7^{+0.6}_{-0.2}$	$3.52^{+0.01}_{-0.02}$	$3.52^{+0.01}_{-0.02}$	S
2M16090451−2224523	9852	5372	19	2458243.753	10.73	31.4	$-5.8^{+0.1}_{-0.1}$	$-5.2^{+0.9}_{-0.8}$	$14.2^{+0.1}_{-0.3}$	$14.1^{+1.0}_{-1.0}$	$2399.7^{+0.6}_{-0.2}$	$2399.7^{+0.3}_{-0.1}$	$4.14^{+0.03}_{-0.02}$	$3.97^{+0.1}_{-0.11}$	S
⋯	10945	5786	125	2458320.473	−23.29	34.8	$-3.8^{+0.2}_{-0.2}$	⋯	$14.1^{+0.1}_{-0.1}$	⋯	$2399.7^{+0.5}_{-0.2}$	⋯	$3.88^{+0.02}_{-0.02}$	⋯	S
⋯	11628	6000	251	2458565.865	26.90	43.8	$-4.7^{+0.2}_{-0.2}$	⋯	$14.1^{+0.1}_{-0.2}$	⋯	$2399.7^{+0.4}_{-0.2}$	⋯	$3.95^{+0.02}_{-0.02}$	⋯	S
2M16090568−2245166	11628	6000	295	2458565.865	26.91	10.5	$-3.0^{+0.2}_{-0.2}$	$-3.0^{+0.2}_{-0.2}$	$32.9^{+0.3}_{-0.4}$	$32.9^{+0.3}_{-0.4}$	$2398.7^{+2.0}_{-1.0}$	$2398.7^{+2.0}_{-1.0}$	$3.9^{+0.04}_{-0.04}$	$3.9^{+0.04}_{-0.04}$	S
2M16093019−2059536	9852	5372	132	2458243.753	10.66	22.0	$-1.3^{+0.2}_{-0.2}$	$-1.3^{+0.2}_{-0.2}$	$17.9^{+0.1}_{-0.3}$	$17.9^{+0.1}_{-0.3}$	$2399.6^{+0.5}_{-0.3}$	$2399.6^{+0.5}_{-0.3}$	$3.55^{+0.02}_{-0.02}$	$3.55^{+0.02}_{-0.02}$	S
2M16095107−2722418	10952	5793	151	2458350.594	−29.04	21.9	$-1.5^{+0.2}_{-0.2}$	$-1.5^{+0.2}_{-0.2}$	$56.1^{+0.9}_{-1.1}$	$56.1^{+0.7}_{-1.1}$	$2399.5^{+0.7}_{-0.4}$	$2399.5^{+0.7}_{-0.4}$	$3.5^{+0.0}_{-0.01}$	$3.5^{+0.0}_{-0.01}$	S
2M16095852−2345186	10591	5655	131	2458243.821	10.77	29.5	$-2.4^{+0.2}_{-0.2}$	$-2.4^{+0.2}_{-0.2}$	$34.7^{+1.5}_{-0.1}$	$34.7^{+1.5}_{-0.1}$	$2399.6^{+0.5}_{-0.3}$	$2399.6^{+0.5}_{-0.3}$	$3.51^{+0.01}_{-0.01}$	$3.51^{+0.01}_{-0.01}$	S
2M16095990−2155424	11628	6000	157	2458565.865	26.94	19.0	$-3.8^{+0.5}_{-0.5}$	$-3.8^{+0.5}_{-0.5}$	$22.0^{+0.4}_{-1.5}$	$22.0^{+0.4}_{-1.5}$	$2399.5^{+0.7}_{-0.4}$	$2399.5^{+0.7}_{-0.4}$	$3.6^{+0.04}_{-0.05}$	$3.6^{+0.04}_{-0.05}$	S
2M16100608−2127440	11628	6000	164	2458565.865	26.93	10.7	$-5.4^{+0.3}_{-1.3}$	$-5.4^{+0.3}_{-1.3}$	$16.5^{+0.5}_{-1.5}$	$16.5^{+0.5}_{-1.5}$	$2399.1^{+1.3}_{-0.7}$	$2399.1^{+1.3}_{-0.7}$	$3.84^{+0.06}_{-0.04}$	$3.84^{+0.06}_{-0.04}$	S
2M16103014−2315167	9783	5333	247	2458560.866	28.10	19.9	$-3.9^{+0.2}_{-0.2}$	$-3.9^{+0.2}_{-0.2}$	$14.2^{+0.1}_{-0.3}$	$14.2^{+0.1}_{-0.3}$	$2399.6^{+0.5}_{-0.3}$	$2399.6^{+0.5}_{-0.3}$	$3.55^{+0.03}_{-0.03}$	$3.55^{+0.03}_{-0.03}$	S
2M16103040+3954258	8314	2124	204	2458282.788	−8.74	35.3	$14.6^{+0.3}_{-0.2}$	$14.2^{+0.1}_{-0.2}$	$12.3^{+0.6}_{-0.5}$	$11.0^{+1.1}_{-1.4}$	$2399.4^{+1.1}_{-0.4}$	$2399.5^{+0.7}_{-0.3}$	$5.17^{+0.03}_{-0.03}$	$5.16^{+0.02}_{-0.02}$	S
⋯	8314	2124	204	2458287.786	−9.76	76.8	$14.2^{+0.1}_{-0.1}$	⋯	$10.7^{+0.2}_{-0.5}$	⋯	$2399.6^{+0.8}_{-0.3}$	⋯	$5.15^{+0.02}_{-0.02}$	⋯	S
2M16103232−1913085	10595	5659	258	2458242.662	11.26	16.7	$-6.2^{+1.3}_{-0.3}$	$-6.2^{+1.3}_{-0.3}$	$42.4^{+0.3}_{-0.8}$	$42.4^{+0.3}_{-0.8}$	$2399.3^{+1.0}_{-0.5}$	$2399.3^{+1.0}_{-0.5}$	$3.55^{+0.04}_{-0.05}$	$3.55^{+0.04}_{-0.05}$	S
2M16103232+2249116	8468	5125	50	2457116.907	14.49	10.8	$-3.6^{+0.5}_{-0.4}$	$-4.0^{+0.5}_{-0.5}$	$10.8^{+1.4}_{-1.0}$	$11.8^{+1.4}_{-1.9}$	$2399.1^{+1.3}_{-0.7}$	$2399.3^{+0.3}_{-0.2}$	$4.78^{+0.03}_{-0.03}$	$4.84^{+0.14}_{-0.13}$	S
⋯	8468	5125	140	2457119.850	13.75	14.8	$-4.6^{+0.4}_{-0.4}$	⋯	$12.2^{+1.5}_{-2.0}$	⋯	$2399.1^{+1.3}_{-0.7}$	⋯	$4.8^{+0.05}_{-0.04}$	⋯	S
⋯	8469	5125	38	2457121.883	13.06	15.1	$-3.9^{+0.2}_{-0.2}$	⋯	$12.1^{+0.2}_{-0.7}$	⋯	$2399.2^{+1.0}_{-0.6}$	⋯	$4.72^{+0.03}_{-0.04}$	⋯	S
⋯	8468	5125	140	2457122.864	12.80	16.2	$-4.2^{+0.2}_{-0.2}$	⋯	$10.9^{+0.4}_{-0.5}$	⋯	$2399.4^{+1.6}_{-0.5}$	⋯	$4.96^{+0.03}_{-0.03}$	⋯	S
⋯	8468	5125	92	2457148.752	4.04	12.8	$-4.7^{+0.2}_{-0.3}$	⋯	$16.0^{+1.6}_{-0.3}$	⋯	$2399.4^{+0.7}_{-0.4}$	⋯	$4.59^{+0.02}_{-0.02}$	⋯	S
⋯	8468	5125	92	2457151.784	2.86	21.4	$-4.1^{+0.3}_{-0.3}$	⋯	$10.6^{+0.3}_{-0.5}$	⋯	$2399.5^{+0.9}_{-0.4}$	⋯	$4.91^{+0.02}_{-0.03}$	⋯	S
⋯	8468	5125	50	2457168.712	−3.29	16.7	$-3.6^{+0.2}_{-0.2}$	⋯	$10.1^{+1.2}_{-0.8}$	⋯	$2399.2^{+1.1}_{-0.7}$	⋯	$5.15^{+0.11}_{-0.05}$	⋯	S
⋯	8469	5125	140	2457169.698	−3.62	13.1	$-3.2^{+0.3}_{-0.4}$	⋯	$11.4^{+0.9}_{-0.6}$	⋯	$2399.2^{+0.9}_{-0.6}$	⋯	$4.88^{+0.02}_{-0.02}$	⋯	S
⋯	8469	5125	44	2457175.720	−5.82	16.8	$-4.3^{+0.2}_{-0.1}$	⋯	$10.6^{+0.2}_{-0.9}$	⋯	$2399.3^{+0.8}_{-0.5}$	⋯	$4.96^{+0.02}_{-0.02}$	⋯	S
⋯	8469	5125	47	2457412.024	20.84	10.2	$-3.6^{+0.4}_{-0.4}$	⋯	$13.8^{+1.1}_{-0.6}$	⋯	$2399.3^{+1.0}_{-0.5}$	⋯	$4.62^{+0.05}_{-0.04}$	⋯	S
⋯	8469	5125	143	2457415.024	21.21	14.9	$-3.2^{+0.2}_{-0.2}$	⋯	$9.7^{+1.1}_{-1.3}$	⋯	$2398.9^{+1.6}_{-0.8}$	⋯	$4.91^{+0.04}_{-0.02}$	⋯	S
2M16104714−2239492	11628	6000	235	2458565.865	27.00	10.2	$-7.5^{+0.2}_{-0.2}$	$-7.5^{+0.2}_{-0.2}$	$9.2^{+0.5}_{-0.4}$	< 10	$2399.1^{+1.4}_{-0.6}$	$2399.1^{+1.4}_{-0.6}$	$4.31^{+0.03}_{-0.02}$	$4.31^{+0.03}_{-0.02}$	S
2M16113837−2307072	9783	5333	258	2458560.866	28.15	17.8	$-1.9^{+0.2}_{-0.2}$	$-2.2^{+0.5}_{-0.4}$	$35.8^{+1.0}_{-1.1}$	$36.6^{+1.0}_{-1.1}$	$2399.6^{+0.7}_{-0.4}$	$2399.6^{+0.4}_{-0.2}$	$3.51^{+0.01}_{-0.01}$	$3.51^{+0.01}_{-0.01}$	S
⋯	11628	6000	216	2458565.865	27.06	28.2	$-2.9^{+0.3}_{-0.9}$	⋯	$36.6^{+0.1}_{-0.2}$	⋯	$2399.7^{+0.5}_{-0.3}$	⋯	$3.52^{+0.01}_{-0.02}$	⋯	S
2M16114261−2525511	9762	5310	199	2457878.674	11.26	56.4	$-5.3^{+0.2}_{-0.2}$	$-4.7^{+0.6}_{-0.7}$	$55.1^{+0.4}_{-0.4}$	$55.3^{+1.0}_{-1.1}$	$2399.8^{+0.3}_{-0.2}$	$2399.8^{+0.2}_{-0.1}$	$3.5^{+0.0}_{-0.01}$	$3.5^{+0.0}_{-0.0}$	S
⋯	9853	5373	235	2458243.877	10.94	58.4	$-4.0^{+0.2}_{-0.2}$	⋯	$55.5^{+0.2}_{-0.6}$	⋯	$2399.8^{+0.3}_{-0.2}$	⋯	$3.5^{+0.0}_{-0.0}$	⋯	S

Table 3.4 (*continued*)

Table 3.4 (*continued*)

APOGEE ID	Plate	Loc. ID	Fiber ID	JD (day)	bary.[a] ($km\ s^{-1}$)	S/N	RV ($km\ s^{-1}$)	$\langle RV \rangle$[b] ($km\ s^{-1}$)	$v \sin i$ ($km\ s^{-1}$)	$\langle v \sin i \rangle$[b,c] ($km\ s^{-1}$)	$T_{\rm eff}$ (K)	$\langle T_{\rm eff} \rangle$[b] (K)	$\log g$ ($cm\ s^{-2}$)	$\langle \log g \rangle$[b] ($cm\ s^{-2}$)	Mdl[d]
2M16115439−2236491	11628	6000	186	2458565.865	27.06	18.6	$-2.5^{+0.8}_{-0.3}$	$-2.5^{+0.8}_{-0.3}$	$50.3^{+0.5}_{-1.2}$	$50.3^{+0.5}_{-1.2}$	$2399.5^{+0.5}_{-0.3}$	$2399.5^{+0.5}_{-0.3}$	$3.53^{+0.02}_{-0.02}$	$3.53^{+0.02}_{-0.02}$	S
2M16122703−2013250	9763	5311	186	2457878.837	10.56	41.1	$-4.9^{+0.2}_{-0.3}$	$-4.9^{+0.2}_{-0.3}$	$30.9^{+0.4}_{-0.1}$	$30.9^{+0.4}_{-0.1}$	$2399.7^{+0.3}_{-0.2}$	$2399.7^{+0.3}_{-0.2}$	$3.58^{+0.03}_{-0.02}$	$3.58^{+0.03}_{-0.02}$	S
2M16124726−1903531	9763	5311	61	2457878.837	10.49	27.7	$-7.1^{+0.1}_{-0.1}$	$-7.1^{+0.3}_{-0.2}$	$29.2^{+0.5}_{-0.4}$	$29.0^{+1.1}_{-1.2}$	$2977.8^{+9.1}_{-9.9}$	$2970.8^{+9.1}_{-9.5}$	$4.51^{+0.01}_{-0.02}$	$4.5^{+0.02}_{-0.03}$	B
⋯	10595	5659	41	2458242.662	11.50	42.2	$-6.2^{+0.3}_{-0.7}$	⋯	$28.6^{+0.9}_{-0.5}$	⋯	$2964.6^{+8.6}_{-9.4}$	⋯	$4.47^{+0.02}_{-0.02}$	⋯	B
2M16132665−2230348	11628	6000	1	2458565.865	27.14	30.1	$-4.7^{+0.2}_{-0.2}$	$-4.7^{+0.2}_{-0.2}$	$19.9^{+0.1}_{-1.7}$	$19.9^{+0.1}_{-1.7}$	$2399.6^{+0.5}_{-0.3}$	$2399.6^{+0.5}_{-0.3}$	$3.59^{+0.04}_{-0.04}$	$3.59^{+0.04}_{-0.04}$	S
2M16132809−1924524	9763	5311	80	2457878.837	10.60	44.0	$-4.6^{+0.1}_{-0.1}$	$-4.8^{+0.2}_{-0.2}$	$23.5^{+0.1}_{-0.2}$	$23.1^{+1.1}_{-1.4}$	$2399.8^{+0.4}_{-0.2}$	$2399.7^{+0.3}_{-0.1}$	$3.53^{+0.01}_{-0.01}$	$3.56^{+0.06}_{-0.06}$	S
⋯	10595	5659	55	2458242.662	11.61	37.4	$-5.2^{+0.2}_{-0.2}$	⋯	$21.6^{+0.2}_{-0.2}$	⋯	$2399.7^{+0.6}_{-0.2}$	⋯	$3.66^{+0.02}_{-0.03}$	⋯	S
2M16134027−2233192	11628	6000	114	2458565.865	27.15	24.6	$-6.4^{+0.1}_{-0.1}$	$-6.4^{+0.1}_{-0.1}$	$14.1^{+0.2}_{-0.2}$	$14.1^{+0.2}_{-0.2}$	$2399.6^{+0.5}_{-0.3}$	$2399.6^{+0.5}_{-0.3}$	$3.8^{+0.03}_{-0.03}$	$3.8^{+0.03}_{-0.03}$	S
2M16134079−2219459	11628	6000	108	2458565.865	27.15	11.8	$-0.8^{+0.2}_{-0.3}$	$-0.8^{+0.2}_{-0.3}$	$19.4^{+0.2}_{-0.3}$	$19.4^{+0.2}_{-0.3}$	$2399.4^{+1.2}_{-0.4}$	$2399.4^{+1.2}_{-0.4}$	$3.8^{+0.1}_{-0.06}$	$3.8^{+0.1}_{-0.06}$	S
2M16134264−2301279	11628	6000	27	2458565.865	27.17	24.8	$-2.0^{+0.9}_{-1.0}$	$-2.0^{+0.9}_{-1.0}$	$59.3^{+0.4}_{-1.7}$	$59.3^{+0.4}_{-1.7}$	$2399.6^{+0.6}_{-0.3}$	$2399.6^{+0.6}_{-0.3}$	$3.52^{+0.01}_{-0.03}$	$3.52^{+0.01}_{-0.03}$	S
2M16143287−2242133	11628	6000	115	2458565.865	27.20	14.4	$0.2^{+0.2}_{-0.1}$	$0.2^{+0.2}_{-0.1}$	$18.0^{+0.2}_{-0.4}$	$18.0^{+0.2}_{-0.4}$	$2399.4^{+0.9}_{-0.5}$	$2399.4^{+0.9}_{-0.5}$	$3.53^{+0.02}_{-0.04}$	$3.53^{+0.02}_{-0.04}$	S
2M16172079+4113032	8600	2230	97	2457459.007	12.28	24.0	$0.5^{+0.2}_{-0.2}$	$0.5^{+0.4}_{-0.3}$	$11.0^{+0.4}_{-0.2}$	< 10	$2399.5^{+0.8}_{-0.4}$	$2399.4^{+0.5}_{-0.3}$	$4.81^{+0.02}_{-0.02}$	$5.07^{+0.19}_{-0.18}$	S
⋯	8600	2230	97	2457460.922	12.15	34.9	$0.1^{+0.2}_{-0.2}$	⋯	$7.1^{+0.5}_{-0.9}$	⋯	$2399.3^{+1.0}_{-0.5}$	⋯	$4.99^{+0.02}_{-0.01}$	⋯	S
⋯	8979	2330	73	2457464.950	11.47	51.4	$0.9^{+0.2}_{-0.1}$	⋯	$2.6^{+1.4}_{-1.4}$	⋯	$2399.3^{+0.8}_{-0.5}$	⋯	$5.27^{+0.01}_{-0.01}$	⋯	S
2M16183317−2517504	10592	5656	95	2458242.848	12.21	38.0	$-1.2^{+0.5}_{-0.3}$	$-1.0^{+0.1}_{-0.2}$	$18.2^{+0.3}_{-0.5}$	$16.3^{+1.2}_{-1.4}$	$3128.6^{+5.8}_{-5.7}$	$3130.1^{+3.8}_{-3.9}$	$4.59^{+0.03}_{-0.02}$	$4.62^{+0.03}_{-0.03}$	B
⋯	10948	5789	158	2458320.566	−22.60	43.4	$-1.0^{+0.1}_{-0.1}$	⋯	$16.1^{+0.1}_{-0.3}$	⋯	$3131.2^{+4.5}_{-4.8}$	⋯	$4.64^{+0.02}_{-0.03}$	⋯	B
2M16195143−2241332	10594	5658	252	2458242.784	12.33	13.5	$-4.2^{+0.4}_{-0.3}$	$-4.6^{+0.1}_{-0.2}$	$18.0^{+0.7}_{-0.5}$	$17.0^{+1.2}_{-1.4}$	$2399.5^{+0.9}_{-0.3}$	$2399.5^{+0.6}_{-0.2}$	$3.52^{+0.01}_{-0.03}$	$3.53^{+0.02}_{-0.06}$	S
⋯	9855	5317	223	2458243.690	12.07	12.9	$-4.6^{+0.1}_{-0.1}$	⋯	$16.4^{+0.3}_{-0.6}$	⋯	$2399.5^{+0.9}_{-0.3}$	⋯	$3.61^{+0.06}_{-0.04}$	⋯	S
2M16204144−2425491	10947	5788	115	2458560.798	28.63	15.7	$1.5^{+0.6}_{-0.3}$	$1.5^{+0.6}_{-0.3}$	$25.4^{+0.2}_{-0.3}$	$25.4^{+0.2}_{-0.3}$	$2399.6^{+0.6}_{-0.3}$	$2399.6^{+0.6}_{-0.3}$	$3.52^{+0.01}_{-0.02}$	$3.52^{+0.01}_{-0.02}$	S
2M16222304−2407108	10947	5788	127	2458560.798	28.70	15.1	$-1.9^{+0.5}_{-0.5}$	$-1.9^{+0.5}_{-0.5}$	$44.5^{+1.1}_{-3.5}$	$44.5^{+1.1}_{-3.5}$	$2399.4^{+1.0}_{-0.5}$	$2399.4^{+1.0}_{-0.5}$	$3.53^{+0.02}_{-0.04}$	$3.53^{+0.02}_{-0.04}$	S
2M16222521−2405139	10947	5788	131	2458560.798	28.70	16.5	$-1.2^{+0.3}_{-0.4}$	$-1.2^{+0.2}_{-0.4}$	$18.0^{+0.2}_{-0.3}$	$18.0^{+0.2}_{-0.3}$	$2399.4^{+1.0}_{-0.5}$	$2399.4^{+1.0}_{-0.5}$	$3.56^{+0.02}_{-0.02}$	$3.56^{+0.02}_{-0.02}$	S
2M16235155−2317270	10594	5658	216	2458242.784	12.81	27.5	$-3.9^{+0.2}_{-0.8}$	$-3.9^{+0.2}_{-0.8}$	$52.6^{+0.8}_{-0.8}$	$52.6^{+0.8}_{-0.8}$	$2399.6^{+0.8}_{-0.3}$	$2399.6^{+0.8}_{-0.3}$	$3.53^{+0.02}_{-0.02}$	$3.53^{+0.02}_{-0.02}$	S
2M16265698+3954482	11942	2704	120	2458641.850	−5.90	27.0	$3.1^{+0.3}_{-0.3}$	$2.9^{+0.4}_{-0.5}$	$25.3^{+0.5}_{-0.3}$	$27.1^{+1.6}_{-1.7}$	$2399.0^{+1.5}_{-0.8}$	$2399.1^{+0.4}_{-0.2}$	$5.45^{+0.01}_{-0.02}$	$5.34^{+0.13}_{-0.13}$	S
⋯	11942	2704	120	2458642.869	−6.17	19.1	$2.9^{+0.4}_{-0.4}$	⋯	$29.1^{+0.5}_{-0.3}$	⋯	$2398.9^{+1.4}_{-0.8}$	⋯	$5.39^{+0.05}_{-0.03}$	⋯	S
⋯	11943	2705	55	2458643.851	−6.36	22.8	$3.1^{+0.3}_{-0.4}$	⋯	$26.4^{+0.7}_{-0.5}$	⋯	$2399.1^{+1.4}_{-0.6}$	⋯	$5.22^{+0.03}_{-0.07}$	⋯	S
⋯	11943	2705	60	2458656.654	−8.72	22.9	$3.6^{+0.2}_{-0.1}$	⋯	$25.7^{+0.3}_{-1.0}$	⋯	$2399.1^{+1.3}_{-0.7}$	⋯	$5.47^{+0.02}_{-0.02}$	⋯	S
⋯	11941	2703	102	2458656.714	−8.84	15.9	$3.1^{+0.3}_{-0.3}$	⋯	$28.1^{+0.7}_{-0.6}$	⋯	$2398.8^{+1.5}_{-0.9}$	⋯	$5.19^{+0.02}_{-0.02}$	⋯	S
⋯	11941	2703	102	2458657.673	−8.96	20.5	$2.8^{+0.4}_{-0.5}$	⋯	$25.7^{+0.3}_{-0.8}$	⋯	$2399.3^{+1.1}_{-0.5}$	⋯	$5.12^{+0.02}_{-0.04}$	⋯	S
⋯	11941	2703	102	2458658.640	−9.09	17.5	$2.6^{+0.2}_{-0.2}$	⋯	$25.7^{+0.4}_{-1.4}$	⋯	$2399.0^{+1.3}_{-0.7}$	⋯	$5.41^{+0.02}_{-0.02}$	⋯	S
⋯	12674	2871	259	2459022.755	−9.08	14.9	$2.3^{+0.2}_{-0.2}$	⋯	$29.1^{+1.4}_{-0.3}$	⋯	$2399.1^{+1.2}_{-0.6}$	⋯	$5.14^{+0.03}_{-0.02}$	⋯	S
⋯	12674	2871	259	2459023.763	−9.30	20.1	$2.5^{+0.2}_{-0.3}$	⋯	$27.4^{+0.2}_{-0.4}$	⋯	$2399.1^{+1.4}_{-0.6}$	⋯	$5.38^{+0.02}_{-0.04}$	⋯	S
⋯	12673	2870	198	2459078.740	−14.79	12.0	$3.8^{+0.4}_{-0.4}$	⋯	$31.1^{+0.9}_{-0.6}$	⋯	$2398.7^{+1.6}_{-0.9}$	⋯	$5.13^{+0.07}_{-0.06}$	⋯	S
⋯	12673	2870	198	2459080.723	−14.76	15.4	$2.8^{+0.4}_{-0.2}$	⋯	$27.5^{+0.4}_{-0.7}$	⋯	$2399.3^{+1.0}_{-0.5}$	⋯	$5.32^{+0.03}_{-0.04}$	⋯	S
⋯	12673	2870	198	2459084.705	−14.64	18.8	$2.9^{+0.2}_{-0.3}$	⋯	$25.9^{+0.4}_{-0.6}$	⋯	$2399.3^{+1.2}_{-0.5}$	⋯	$5.44^{+0.03}_{-0.02}$	⋯	S
2M16271693+3514132	11940	2702	139	2459042.784	−13.68	17.3	$-12.0^{+0.5}_{-0.4}$	$-12.1^{+0.7}_{-0.7}$	$21.8^{+0.2}_{-0.9}$	$21.9^{+1.3}_{-1.7}$	$2399.3^{+1.2}_{-0.5}$	$2399.3^{+0.7}_{-0.3}$	$4.7^{+0.05}_{-0.12}$	$4.75^{+0.11}_{-0.14}$	S
⋯	11940	2702	139	2459047.746	−14.39	16.5	$-11.3^{+0.3}_{-0.4}$	⋯	$31.1^{+1.5}_{-1.0}$	⋯	$2399.2^{+1.1}_{-0.5}$	⋯	$4.6^{+0.08}_{-0.04}$	⋯	S
⋯	11940	2702	139	2459069.678	−16.42	20.7	$-12.9^{+0.5}_{-0.3}$	⋯	$21.7^{+0.2}_{-0.2}$	⋯	$2399.3^{+1.2}_{-0.5}$	⋯	$4.88^{+0.04}_{-0.04}$	⋯	S
2M16271825+3538347	11940	2702	43	2459042.784	−13.58	26.3	$-9.2^{+0.2}_{-0.2}$	$-8.8^{+0.3}_{-0.4}$	$9.1^{+0.5}_{-0.8}$	< 10	$2399.0^{+1.2}_{-0.8}$	$2398.9^{+0.8}_{-0.5}$	$5.49^{+0.01}_{-0.01}$	$5.49^{+0.02}_{-0.01}$	S
⋯	11940	2702	43	2459047.746	−14.27	25.7	$-8.2^{+0.2}_{-0.2}$	⋯	$7.8^{+1.1}_{-0.5}$	⋯	$2398.7^{+1.7}_{-1.0}$	⋯	$5.45^{+0.02}_{-0.02}$	⋯	S
⋯	11940	2702	43	2459050.735	−14.66	10.7	$-6.3^{+0.3}_{-0.3}$	⋯	$16.3^{+0.3}_{-0.5}$	⋯	$2399.2^{+1.5}_{-0.6}$	⋯	$4.85^{+0.03}_{-0.02}$	⋯	S
⋯	11940	2702	43	2459069.678	−16.26	31.5	$-8.9^{+0.1}_{-0.1}$	⋯	$7.8^{+1.0}_{-0.4}$	⋯	$2399.0^{+1.4}_{-0.8}$	⋯	$5.49^{+0.01}_{-0.01}$	⋯	S
2M16281707+1334204	8609	2239	98	2458633.844	−2.34	51.3	$-36.5^{+0.3}_{-0.2}$	$-36.6^{+0.2}_{-0.1}$	$15.7^{+0.3}_{-0.3}$	$15.8^{+1.0}_{-1.1}$	$2399.6^{+0.5}_{-0.4}$	$2399.5^{+0.5}_{-0.3}$	$5.16^{+0.01}_{-0.01}$	$5.2^{+0.06}_{-0.07}$	S
⋯	8609	2239	98	2458634.838	−2.74	37.4	$-36.6^{+0.2}_{-0.1}$	⋯	$15.9^{+0.5}_{-0.3}$	⋯	$2399.3^{+0.8}_{-0.5}$	⋯	$5.32^{+0.04}_{-0.02}$	⋯	S

Table 3.4 (*continued*)

Table 3.4 (*continued*)

APOGEE ID	Plate	Loc. ID	Fiber ID	JD (day)	bary.[a] ($km\ s^{-1}$)	S/N	RV ($km\ s^{-1}$)	$\langle RV \rangle$[b] ($km\ s^{-1}$)	$v \sin i$ ($km\ s^{-1}$)	$\langle v \sin i \rangle$[b,c] ($km\ s^{-1}$)	$T_{\rm eff}$ (K)	$\langle T_{\rm eff} \rangle$[b] (K)	$\log g$ ($cm\ s^{-2}$)	$\langle \log g \rangle$[b] ($cm\ s^{-2}$)	Mdl[d]
2M16311879+4051516	8312	2122	171	2457160.893	−0.85	241.5	$-21.8^{+0.1}_{-0.1}$	$-21.8^{+0.2}_{-0.2}$	$12.3^{+0.1}_{-0.2}$	$14.8^{+1.8}_{-1.6}$	$2399.6^{+0.5}_{-0.3}$	$2399.6^{+0.2}_{-0.1}$	$5.34^{+0.02}_{-0.02}$	$5.33^{+0.05}_{-0.05}$	S
⋯	8601	2231	214	2457192.686	−7.70	275.2	$-21.6^{+0.3}_{-0.2}$	⋯	$12.4^{+0.2}_{-0.4}$	⋯	$2399.5^{+0.6}_{-0.3}$	⋯	$5.36^{+0.02}_{-0.02}$	⋯	S
⋯	9869	2440	292	2457899.827	−2.76	123.2	$-21.4^{+0.2}_{-0.2}$	⋯	$16.0^{+0.1}_{-0.2}$	⋯	$2399.7^{+0.5}_{-0.2}$	⋯	$5.39^{+0.02}_{-0.02}$	⋯	S
⋯	9869	2440	292	2457900.806	−2.95	184.0	$-21.6^{+0.2}_{-0.2}$	⋯	$13.5^{+0.9}_{-0.3}$	⋯	$2399.6^{+0.6}_{-0.3}$	⋯	$5.29^{+0.05}_{-0.03}$	⋯	S
⋯	11942	2704	195	2458641.850	−5.46	170.9	$-21.7^{+0.2}_{-0.2}$	⋯	$12.6^{+0.4}_{-0.4}$	⋯	$2399.6^{+0.4}_{-0.3}$	⋯	$5.3^{+0.01}_{-0.01}$	⋯	S
⋯	11942	2704	195	2458642.869	−5.72	133.8	$-21.5^{+0.3}_{-0.2}$	⋯	$13.4^{+1.1}_{-0.4}$	⋯	$2399.5^{+0.5}_{-0.4}$	⋯	$5.3^{+0.02}_{-0.02}$	⋯	S
⋯	11943	2705	159	2458643.851	−5.91	199.6	$-21.9^{+0.2}_{-0.2}$	⋯	$14.2^{+0.1}_{-0.2}$	⋯	$2399.5^{+0.4}_{-0.4}$	⋯	$5.29^{+0.01}_{-0.02}$	⋯	S
⋯	11943	2705	159	2458645.863	−6.36	44.7	$-21.8^{+0.2}_{-0.2}$	⋯	$16.1^{+0.2}_{-0.3}$	⋯	$2399.5^{+0.7}_{-0.3}$	⋯	$5.24^{+0.03}_{-0.05}$	⋯	S
⋯	11943	2705	261	2458656.654	−8.20	226.8	$-21.5^{+0.2}_{-0.2}$	⋯	$16.0^{+0.1}_{-0.2}$	⋯	$2399.7^{+0.3}_{-0.2}$	⋯	$5.3^{+0.02}_{-0.02}$	⋯	S
⋯	11941	2703	82	2458656.714	−8.32	145.8	$-21.8^{+0.1}_{-0.2}$	⋯	$12.7^{+0.4}_{-0.8}$	⋯	$2399.5^{+0.5}_{-0.3}$	⋯	$5.41^{+0.03}_{-0.03}$	⋯	S
⋯	11941	2703	82	2458657.673	−8.44	224.8	$-21.9^{+0.1}_{-0.1}$	⋯	$12.5^{+0.2}_{-0.2}$	⋯	$2399.5^{+0.5}_{-0.3}$	⋯	$5.41^{+0.02}_{-0.01}$	⋯	S
⋯	11941	2703	82	2458658.640	−8.56	171.6	$-21.6^{+0.1}_{-0.1}$	⋯	$12.4^{+0.2}_{-0.4}$	⋯	$2399.6^{+0.4}_{-0.2}$	⋯	$5.38^{+0.06}_{-0.04}$	⋯	S
2M16360984+4000243	11942	2704	132	2458641.850	−5.00	33.6	$-11.4^{+0.2}_{-0.2}$	$-11.5^{+0.2}_{-0.2}$	$6.0^{+1.0}_{-1.1}$	< 10	$2399.3^{+0.8}_{-0.5}$	$2399.4^{+0.5}_{-0.2}$	$5.19^{+0.03}_{-0.02}$	$5.08^{+0.13}_{-0.16}$	S
⋯	11942	2704	132	2458642.869	−5.27	24.0	$-11.7^{+0.1}_{-0.1}$	⋯	$9.2^{+0.6}_{-0.7}$	⋯	$2399.4^{+1.0}_{-0.5}$	⋯	$4.86^{+0.03}_{-0.01}$	⋯	S
⋯	11943	2705	90	2458643.851	−5.46	31.0	$-11.1^{+0.1}_{-0.1}$	⋯	$3.7^{+1.1}_{-1.9}$	⋯	$2399.3^{+1.0}_{-0.5}$	⋯	$5.23^{+0.04}_{-0.05}$	⋯	S
⋯	11943	2705	66	2458656.654	−7.86	31.0	$-11.6^{+0.1}_{-0.1}$	⋯	$8.8^{+0.3}_{-0.9}$	⋯	$2399.5^{+0.9}_{-0.3}$	⋯	$5.17^{+0.01}_{-0.01}$	⋯	S
2M16402068+6736046	11922	6078	3	2458893.999	1.41	201.0	$-17.4^{+0.1}_{-0.1}$	$-17.4^{+0.1}_{-0.1}$	$16.0^{+0.1}_{-0.2}$	$16.0^{+0.1}_{-0.2}$	$2399.6^{+0.6}_{-0.3}$	$2399.6^{+0.6}_{-0.3}$	$5.32^{+0.01}_{-0.01}$	$5.32^{+0.01}_{-0.01}$	S
2M16463154+3434554	11947	2709	110	2459019.842	−7.26	75.6	$-52.6^{+0.1}_{-0.1}$	$-52.6^{+0.1}_{-0.1}$	$5.7^{+0.3}_{-0.2}$	< 10	$2399.5^{+0.8}_{-0.4}$	$2399.6^{+0.4}_{-0.2}$	$5.04^{+0.02}_{-0.02}$	$4.96^{+0.05}_{-0.04}$	S
⋯	11947	2709	110	2459020.835	−7.50	68.6	$-52.6^{+0.1}_{-0.1}$	⋯	$6.0^{+1.0}_{-0.4}$	⋯	$2399.5^{+0.8}_{-0.3}$	⋯	$4.96^{+0.02}_{-0.03}$	⋯	S
⋯	11949	2711	274	2459021.842	−7.76	73.8	$-52.5^{+0.1}_{-0.1}$	⋯	$7.5^{+0.3}_{-0.3}$	⋯	$2399.6^{+0.6}_{-0.3}$	⋯	$4.93^{+0.02}_{-0.02}$	⋯	S
⋯	11949	2711	274	2459022.821	−7.97	67.7	$-52.9^{+0.2}_{-0.2}$	⋯	$5.9^{+1.0}_{-1.3}$	⋯	$2399.4^{+0.7}_{-0.4}$	⋯	$4.93^{+0.02}_{-0.02}$	⋯	S
2M16485878+3005366	11950	2712	168	2459084.655	−18.26	10.5	$-46.4^{+0.3}_{-0.5}$	$-44.8^{+0.3}_{-0.3}$	$16.1^{+0.2}_{-0.4}$	$14.0^{+1.7}_{-0.9}$	$2399.0^{+1.4}_{-0.7}$	$2398.6^{+2.4}_{-1.1}$	$4.67^{+0.09}_{-0.05}$	$4.66^{+0.07}_{-0.07}$	S
⋯	11950	2712	168	2459085.653	−18.28	11.5	$-44.8^{+0.3}_{-0.3}$	⋯	$14.0^{+1.7}_{-0.9}$	⋯	$2398.6^{+2.4}_{-1.1}$	⋯	$4.66^{+0.07}_{-0.07}$	⋯	S
2M16572919+2448509	9893	2464	1	2458008.620	−19.95	25.5	$-57.7^{+0.3}_{-0.2}$	$-58.1^{+0.5}_{-0.5}$	$16.0^{+0.2}_{-0.3}$	$15.6^{+1.5}_{-1.3}$	$2399.0^{+1.5}_{-0.7}$	$2398.9^{+0.9}_{-0.6}$	$5.17^{+0.02}_{-0.05}$	$5.43^{+0.14}_{-0.07}$	S
⋯	9893	2464	1	2458009.614	−19.88	27.7	$-57.6^{+0.2}_{-0.1}$	⋯	$15.6^{+1.4}_{-0.5}$	⋯	$2398.5^{+1.6}_{-1.1}$	⋯	$5.38^{+0.02}_{-0.02}$	⋯	S
⋯	9893	2464	1	2458222.897	14.58	35.4	$-57.7^{+0.1}_{-0.1}$	⋯	$15.4^{+1.1}_{-0.4}$	⋯	$2399.2^{+1.1}_{-0.6}$	⋯	$5.4^{+0.02}_{-0.02}$	⋯	S
⋯	11977	2739	37	2458658.727	−7.75	56.1	$-58.6^{+0.1}_{-0.1}$	⋯	$12.8^{+0.5}_{-0.9}$	⋯	$2397.3^{+2.2}_{-1.8}$	⋯	$5.49^{+0.01}_{-0.01}$	⋯	S
2M19005974−3647109	10718	5733	264	2458262.905	18.43	12.8	$1.8^{+0.2}_{-0.2}$	$1.5^{+0.2}_{-0.2}$	$21.6^{+0.5}_{-0.3}$	$20.1^{+1.1}_{-1.4}$	$2399.4^{+0.7}_{-0.4}$	$2399.6^{+0.5}_{-0.2}$	$3.52^{+0.01}_{-0.02}$	$3.53^{+0.01}_{-0.02}$	S
⋯	10718	5733	264	2458263.800	18.28	24.4	$1.4^{+0.2}_{-0.2}$	⋯	$19.8^{+0.1}_{-0.3}$	⋯	$2399.7^{+0.6}_{-0.2}$	⋯	$3.54^{+0.02}_{-0.03}$	⋯	S
2M19241634+7533121	10888	5770	261	2458293.823	2.85	189.8	$-18.5^{+0.2}_{-0.2}$	$-18.6^{+0.2}_{-0.2}$	$7.0^{+0.3}_{-1.1}$	< 10	$2399.6^{+0.4}_{-0.3}$	$2399.5^{+0.3}_{-0.2}$	$5.09^{+0.01}_{-0.01}$	$5.08^{+0.04}_{-0.02}$	S
⋯	10888	5770	172	2458297.825	3.17	157.0	$-18.8^{+0.2}_{-0.2}$	⋯	$8.3^{+1.5}_{-0.9}$	⋯	$2399.5^{+0.6}_{-0.3}$	⋯	$4.97^{+0.03}_{-0.06}$	⋯	S
2M19544358+1801581	5217	4261	131	2456109.911	9.85	65.2	$-18.8^{+0.2}_{-0.1}$	$-18.6^{+0.3}_{-0.3}$	$8.1^{+1.3}_{-0.3}$	< 10	$2398.7^{+1.1}_{-0.9}$	$2398.9^{+0.6}_{-0.4}$	$5.5^{+0.0}_{-0.0}$	$5.5^{+0.0}_{-0.0}$	S
⋯	5217	4261	137	2456164.738	−10.85	71.9	$-18.6^{+0.1}_{-0.1}$	⋯	$9.3^{+0.4}_{-0.3}$	⋯	$2399.0^{+1.2}_{-0.6}$	⋯	$5.5^{+0.0}_{-0.0}$	⋯	S
⋯	5217	4261	128	2456169.695	−12.48	57.2	$-18.4^{+0.1}_{-0.1}$	⋯	$9.3^{+0.2}_{-0.2}$	⋯	$2399.1^{+1.5}_{-0.7}$	⋯	$5.5^{+0.0}_{-0.0}$	⋯	S
⋯	6367	4261	133	2456193.598	−19.30	57.7	$-19.0^{+0.1}_{-0.1}$	⋯	$9.2^{+0.4}_{-0.4}$	⋯	$2398.2^{+2.2}_{-1.3}$	⋯	$5.5^{+0.0}_{-0.0}$	⋯	S
⋯	6367	4261	138	2456224.574	−23.63	22.7	$-18.6^{+0.2}_{-0.2}$	⋯	$10.7^{+0.5}_{-0.8}$	⋯	$2398.4^{+2.2}_{-1.3}$	⋯	$5.49^{+0.02}_{-0.01}$	⋯	S
⋯	6367	4261	133	2456228.567	−23.70	51.5	$-18.3^{+0.2}_{-0.1}$	⋯	$9.0^{+0.2}_{-0.7}$	⋯	$2399.1^{+1.3}_{-0.6}$	⋯	$5.5^{+0.0}_{-0.0}$	⋯	S
2M20353517−0608285	11982	2744	19	2458663.888	15.46	19.8	$8.7^{+0.2}_{-0.2}$	$8.2^{+0.3}_{-0.3}$	$8.6^{+1.2}_{-0.8}$	< 10	$3192.8^{+7.6}_{-7.2}$	$3193.5^{+8.6}_{-8.3}$	$5.44^{+0.04}_{-0.03}$	$5.41^{+0.05}_{-0.04}$	B
⋯	11982	2744	19	2458664.868	15.10	18.0	$8.1^{+0.1}_{-0.1}$	⋯	$10.9^{+1.8}_{-2.0}$	⋯	$3186.1^{+10.1}_{-11.3}$	⋯	$5.35^{+0.05}_{-0.07}$	⋯	B
⋯	11982	2744	19	2458665.873	14.66	13.3	$8.0^{+0.2}_{-0.1}$	⋯	$7.4^{+0.8}_{-1.2}$	⋯	$3205.1^{+11.4}_{-12.8}$	⋯	$5.41^{+0.06}_{-0.04}$	⋯	B
2M20491376+3216514	6081	4297	77	2456604.557	−19.93	45.4	$11.4^{+0.2}_{-0.2}$	$11.5^{+0.3}_{-0.3}$	$11.6^{+0.9}_{-1.1}$	$12.2^{+1.0}_{-1.2}$	$2399.4^{+0.8}_{-0.5}$	$2399.4^{+0.5}_{-0.3}$	$5.48^{+0.01}_{-0.01}$	$5.45^{+0.06}_{-0.05}$	S
⋯	6081	4297	77	2456611.559	−20.32	54.1	$11.0^{+0.3}_{-0.2}$	⋯	$11.1^{+0.6}_{-0.4}$	⋯	$2399.3^{+1.0}_{-0.5}$	⋯	$5.47^{+0.02}_{-0.02}$	⋯	S
⋯	7465	4297	77	2456808.846	19.65	53.3	$11.8^{+0.2}_{-0.2}$	⋯	$12.4^{+0.2}_{-0.2}$	⋯	$2399.5^{+0.8}_{-0.4}$	⋯	$5.36^{+0.01}_{-0.02}$	⋯	S
2M21272531+5553150	6088	4546	40	2456228.635	−7.51	60.4	$-12.7^{+0.2}_{-0.2}$	$-12.2^{+0.2}_{-0.2}$	$17.7^{+0.2}_{-0.1}$	$17.3^{+1.1}_{-1.2}$	$2399.6^{+0.6}_{-0.3}$	$2399.6^{+0.4}_{-0.2}$	$5.5^{+0.0}_{-0.0}$	$5.5^{+0.0}_{-0.0}$	S

Table 3.4 (*continued*)

Table 3.4 (*continued*)

APOGEE ID	Plate	Loc. ID	Fiber ID	JD (day)	bary.[a] ($km\ s^{-1}$)	S/N	RV ($km\ s^{-1}$)	$\langle RV \rangle$[b] ($km\ s^{-1}$)	$v \sin i$ ($km\ s^{-1}$)	$\langle v \sin i \rangle$[b,c] ($km\ s^{-1}$)	$T_{\rm eff}$ (K)	$\langle T_{\rm eff} \rangle$[b] (K)	$\log g$ ($cm\ s^{-2}$)	$\langle \log g \rangle$[b] ($cm\ s^{-2}$)	Mdl[d]
⋯	6088	4546	39	2456233.576	−8.37	58.1	$-12.2^{+0.1}_{-0.1}$	⋯	$16.3^{+0.3}_{-0.3}$	⋯	$2399.6^{+0.8}_{-0.3}$	⋯	$5.5^{+0.0}_{-0.0}$	⋯	S
⋯	6088	4546	40	2456259.550	−12.13	64.9	$-12.1^{+0.1}_{-0.1}$	⋯	$16.6^{+0.4}_{-0.2}$	⋯	$2399.6^{+0.8}_{-0.3}$	⋯	$5.5^{+0.0}_{-0.0}$	⋯	S
2M21381698+5257188	6087	4316	29	2456260.546	−13.78	64.0	$-7.5^{+0.2}_{-0.2}$	$-7.5^{+0.2}_{-0.2}$	$40.4^{+0.1}_{-0.2}$	$40.6^{+1.7}_{-1.4}$	$2399.7^{+0.4}_{-0.2}$	$2399.7^{+0.2}_{-0.1}$	$5.49^{+0.01}_{-0.01}$	$5.43^{+0.13}_{-0.05}$	S
⋯	6087	4316	23	2456582.686	−6.29	59.0	$-7.8^{+0.2}_{-0.2}$	⋯	$39.4^{+0.3}_{-0.3}$	⋯	$2399.6^{+0.5}_{-0.3}$	⋯	$5.4^{+0.01}_{-0.01}$	⋯	S
⋯	6087	4316	29	2456588.628	−7.57	67.9	$-7.4^{+0.1}_{-0.1}$	⋯	$44.3^{+0.3}_{-0.7}$	⋯	$2399.7^{+0.3}_{-0.2}$	⋯	$5.13^{+0.02}_{-0.15}$	⋯	S
2M22021125−1109461	9997	5451	32	2458026.587	−18.56	39.4	$-7.8^{+0.1}_{-0.1}$	$-7.7^{+0.4}_{-0.4}$	$21.6^{+0.1}_{-0.2}$	$21.3^{+1.1}_{-1.4}$	$2399.6^{+0.7}_{-0.3}$	$2399.5^{+0.5}_{-0.2}$	$5.15^{+0.04}_{-0.02}$	$5.16^{+0.12}_{-0.06}$	S
⋯	9997	5451	89	2458028.607	−19.40	26.5	$-8.1^{+0.1}_{-0.1}$	⋯	$21.7^{+0.1}_{-0.3}$	⋯	$2399.5^{+1.0}_{-0.4}$	⋯	$4.96^{+0.03}_{-0.07}$	⋯	S
⋯	9997	5451	206	2458052.514	−26.88	45.1	$-7.0^{+0.2}_{-0.2}$	⋯	$19.6^{+0.2}_{-0.2}$	⋯	$2399.4^{+0.8}_{-0.5}$	⋯	$5.21^{+0.02}_{-0.01}$	⋯	S
2M22400144+0532162	6558	4474	23	2456606.610	−26.53	68.9	$-10.3^{+0.1}_{-0.1}$	$-10.1^{+0.3}_{-0.3}$	$17.8^{+0.3}_{-0.4}$	$17.8^{+1.0}_{-1.1}$	$2399.6^{+0.7}_{-0.3}$	$2399.5^{+0.5}_{-0.3}$	$5.1^{+0.02}_{-0.03}$	$5.12^{+0.03}_{-0.02}$	S
⋯	6558	4474	5	2456628.558	−29.43	52.5	$-9.7^{+0.2}_{-0.1}$	⋯	$17.5^{+0.3}_{-0.2}$	⋯	$2399.3^{+1.1}_{-0.5}$	⋯	$5.19^{+0.04}_{-0.07}$	⋯	S
⋯	6558	4474	5	2456637.545	−29.38	63.3	$-9.9^{+0.2}_{-0.1}$	⋯	$18.0^{+0.2}_{-0.3}$	⋯	$2399.4^{+0.7}_{-0.5}$	⋯	$5.13^{+0.02}_{-0.01}$	⋯	S
2M22551142+1442456	12083	2767	247	2458776.666	−16.55	21.4	$-13.7^{+1.5}_{-0.3}$	$-14.1^{+1.0}_{-0.8}$	$55.6^{+1.7}_{-1.1}$	$56.7^{+1.7}_{-1.5}$	$2399.4^{+0.9}_{-0.4}$	$2399.5^{+0.3}_{-0.2}$	$3.52^{+0.01}_{-0.02}$	$3.57^{+0.1}_{-0.12}$	S
⋯	12083	2767	247	2458777.593	−16.76	24.8	$-13.9^{+1.5}_{-0.3}$	⋯	$57.3^{+0.6}_{-0.9}$	⋯	$2399.4^{+0.7}_{-0.4}$	⋯	$3.55^{+0.03}_{-0.05}$	⋯	S
⋯	12083	2767	247	2458778.572	−17.11	20.0	$-12.6^{+1.0}_{-0.6}$	⋯	$59.0^{+1.8}_{-1.7}$	⋯	$2399.5^{+0.6}_{-0.4}$	⋯	$3.52^{+0.02}_{-0.02}$	⋯	S
⋯	12084	2768	198	2458781.688	−18.58	28.9	$-12.7^{+0.3}_{-0.4}$	⋯	$54.4^{+0.9}_{-1.1}$	⋯	$2399.6^{+0.7}_{-0.3}$	⋯	$3.82^{+0.03}_{-0.02}$	⋯	S
⋯	12084	2768	198	2458782.694	−18.98	34.2	$-14.8^{+0.2}_{-0.2}$	⋯	$57.2^{+0.8}_{-0.6}$	⋯	$2399.6^{+0.5}_{-0.3}$	⋯	$3.62^{+0.06}_{-0.03}$	⋯	S
2M23200703+1150071	6559	4475	36	2456578.743	−12.37	45.2	$-53.9^{+0.2}_{-0.1}$	$-54.5^{+0.4}_{-0.3}$	$0.5^{+0.3}_{-0.3}$	< 10	$2399.4^{+1.1}_{-0.5}$	$2399.5^{+0.4}_{-0.2}$	$5.31^{+0.02}_{-0.02}$	$5.34^{+0.08}_{-0.08}$	S
⋯	6559	4475	79	2456583.743	−14.62	57.7	$-54.8^{+0.1}_{-0.2}$	⋯	$0.4^{+0.2}_{-0.3}$	⋯	$2399.5^{+0.6}_{-0.3}$	⋯	$5.45^{+0.02}_{-0.02}$	⋯	S
⋯	6559	4475	37	2456606.665	−23.27	50.8	$-54.5^{+0.1}_{-0.1}$	⋯	$0.7^{+0.4}_{-1.2}$	⋯	$2399.4^{+0.6}_{-0.4}$	⋯	$5.26^{+0.02}_{-0.02}$	⋯	S

[a] Barycentric correction.

[b] Weighted average over all epochs.

[c] Averaged $v \sin i < 10\ km\ s^{-1}$ is below my $v \sin i$ detection limit; see Section 3.3.2 for details.

[d] Models used: S = Sonora 2018 (Marley et al. 2018); B = BT-Settl (Baraffe et al. 2015).

Note – Measurements from individual spectra over individual or multiple epochs are combined using inverse uncertainty weighting (weight = $1/(\sigma^2_{\rm upper} + \sigma^2_{\rm lower})$); upper and lower uncertainties are also combined using inverse uncertainty-squared weighting. In cases where individual spectra have S/N < 10, spectral data are combined first, then modeled.

3.4 APOGEE M/L Dwarf Analysis

3.4.1 *UVW* Space Motions

Stars near the Sun are representative of the Milky Way's thin disk, thick disk and halo populations in approximate proportions of X:Y:Z (Jurić et al. 2008). Kinematics can be a useful tool for separating these populations, as well as identifying members of young moving groups and associations (Gagné et al. 2015b). I combined my RV measurements with *Gaia* and ground-based astrometry to compute heliocentric *UVW* space motions following Johnson & Soderblom (1987), where the U velocity points to the Galactic center, V velocity follows the direction of the Galactic rotation, and W velocity is in the direction of Galactic North pole. I used the Solar ($U_\odot$, $V_\odot$, $W_\odot$) = (11.1 km s^{-1}, 12.24 km s^{-1}, 7.5 km s^{-1}) measured by Schönrich et al. (2010) to correct these velocities to the local standard of rest (LSR). These values are visualized in Figure 3.17 and listed in Table 3.6. It should be noted that I used heliocentric velocities to assess their cluster membership (see Section 3.4.3). The mean U_{LSR} and V_{LSR} velocities of my sample are consistent with zero ($\langle U_{LSR} \rangle = -2.1 \pm 2.0$ km s^{-1} and $\langle W_{LSR} \rangle = 1.7 \pm 0.9$ km s^{-1}), while the average V_{LSR} velocity is negative ($\langle V_{LSR} \rangle = -9.5 \pm 1.5$ km s^{-1}), which can be attributed to asymmetric drift (Strömberg 1924).

I followed Bensby et al. (2003) to determine the probabilities of kinematic membership for each star to thin disk, thick disk, or halo populations based on the LSR velocities. I specifically separated thin disk, intermediate thin/thick disk, and thick disk membership by using the ratios $P[\mathrm{TD}]/P[\mathrm{D}] < 0.1$, $0.1 \leq P[\mathrm{TD}]/P[\mathrm{D}] \leq 10$, and $P[\mathrm{TD}]/P[\mathrm{D}] > 10$, respectively. As expected, the majority of my sample[4] is thin disk sources (171 sources), with 11 intermediate thin disk/thick disk members and 1 thick disk member (LP 327−24; 2MASS J15115124+3033065), as labeled in Figure 3.17. LP

[4]2MASS J05350162−0521489 was removed for the kinematic analysis due to its large proper motion uncertainties.

327−24 has an optical classification of M5 using the Kitt Peak 4 m telescope with the RC Spectrograph from Cruz et al. (2003), and its magnitudes $M_G = 13.01$ and $M_R = 13.92$ with its colors $G - J = 3.64$ and $R - J = 4.56$ were normal using the empirical color-magnitude relation in (Cifuentes et al. 2020) (empirical $M_G = 13.50$ and $M_R = 13.93$). Correlations between UVW velocities can be useful diagnostics of different Galactic populations (e.g. thin disk and thick disk sources). I did not detect significant correlations between $U_{LSR}W_{LSR}$ or $V_{LSR}W_{LSR}$ velocity pairs (p-value = 0.62 and 0.73, respectively), but did find a significant positive correlation for UV velocities (R = 0.16, p-value < 0.05), driven largely by my intermediate thin/thick disk and thick disk members, likely due to asymmetric drift. Removing these kinematically hot sources eliminates the $U_{LSR}V_{LSR}$ correlation (R = 0.07, p-value = 0.37). I also found significant positive correlations between total velocity-squared v^2_{LSR} and absolute $|W_{LSR}|$-velocity for the full sample (R = 0.53, p-value < 0.001) and thin disk subsample (R = 0.50, p-value < 0.001), implying that my sample show correlations between different metrics of ages. v^2_{LSR} is the square of the magnitude of V_{LSR} velocities, which correlates with the asymmetric drift (Strömberg 1924), while absolute $|W_{LSR}|$-velocity has been used as a proxy of ages (Wielen 1977). While the APOGEE sample selection is not volume-complete, this result is consistent with my prior analysis of the 20 pc UCD sample (Hsu et al. 2021).

3.4.2 Galactic Orbits

Galactic orbits can identify sources with different spatial origins, including stars that had drifted radially inward or outward to the Solar Neighborhood. Starting with the LSR velocities and XYZ spatial coordinates[5] of each source, Galactic orbits were computed using the `galpy` package (Bovy 2015), an ordinary differential equation

[5] XYZ are the transformation from Galactic spherical coordinates to Galactic rectangular coordinates from Galactic longitude l, latitude b, and distance d to the Galactic center following $X = d\cos b\cos l$, $Y = d\cos b\sin l$, and $Z = d\sin b$ (Bovy 2015).

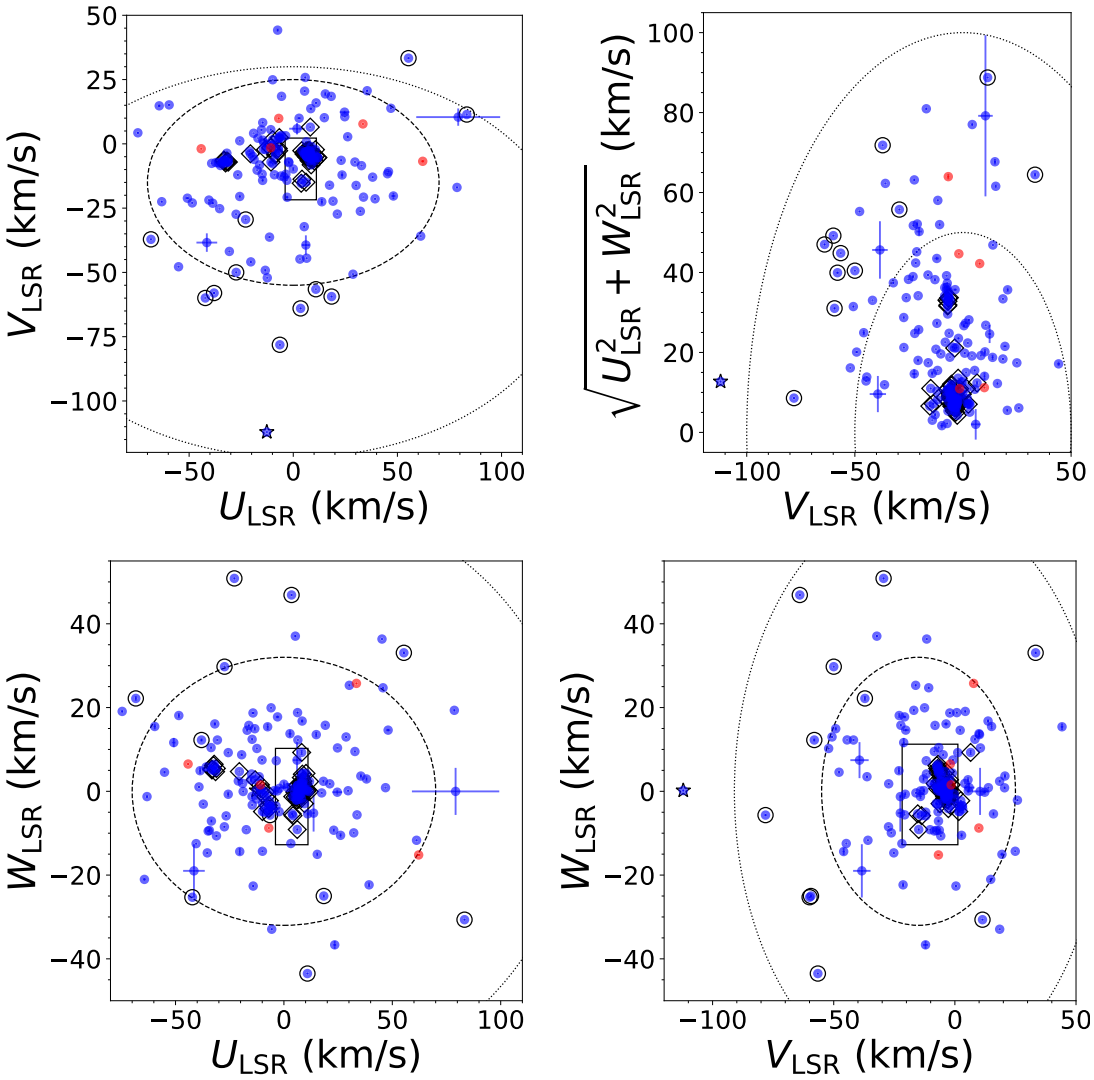

Figure 3.17: Space motions of my sample in the Local Standard of Rest (LSR; Schönrich et al. 2010). The $U_{LSR}V_{LSR}$, $U_{LSR}W_{LSR}$, and $V_{LSR}W_{LSR}$ velocities are shown along with the 2σ uncertainty spheres for the thin disk (dashed lines) and thick disk (dotted lines) populations based on Bensby et al. (2003). M and L dwarfs are labeled as blue and red circles, respectively. The "good box" from Zuckerman & Song (2004) that segregates members of young moving groups is also labeled. The upper-right corner is a Toomre plot, with total velocities $v_{tot} = \sqrt{U_{LSR}^2 + V_{LSR}^2 + W_{LSR}^2}$ indicated in steps of 50 km s^{-1}. Young sources, intermediate thin/thick disk, and thick disk sources are highlighted with open diamonds, open circles, and stars, respectively.

solver that conserves energy and momentum. I used an axisymmetric potential from Miyamoto & Nagai (1975) with spatial coordinates measured relative to a solar coordinate ($R_\odot$, $Z_\odot$) = (8.43 kpc, 0.027 kpc) and azimuthal velocity , v_ϕ = 220 km s^{-1} (Bovy & Tremaine 2012; Chen et al. 2001; Reid et al. 2014). Each orbit was integrated from -5 to $+5$ Gyr in steps of 10 Myr, and 1000 orbit realizations were computed using Monte Carlo sampling of velocity uncertainties assuming normal distributions. I examined the specific orbital parameters of minimum and maximum Galactic cylindrical radius ($R_{\rm min}$, $R_{\rm max}$), maximum Galactic vertical height ($|Z|$), median orbital eccentricity ($e \equiv \langle R_{\rm max} - R_{\rm min}\rangle / \langle R_{\rm max} + R_{\rm min}\rangle$), and median orbital inclination ($\tan i \equiv |Z/\sqrt{X^2+Y^2}|$). These parameters are listed in Table 3.7.

Figure 3.18 shows the distributions of the derived orbital parameters. The majority of my sample exhibit circular ($\langle e\rangle = 0.08^{+0.13}_{-0.04}$) and planar orbits ($\langle i\rangle = 0.6^\circ\ ^{+0.9^\circ}_{-0.2^\circ}$), residing mostly at the Solar Galactic radius ($\langle R_{\rm min}\rangle$ = $7.5^{+0.5}_{-1.3}$ kpc, $\langle R_{\rm max}\rangle$ = $8.6^{+0.7}_{-0.3}$ kpc) and close to the Galactic Plane ($\langle |Z|\rangle$ = $0.09^{+0.12}_{-0.03}$ kpc). There are 31 sources that have $e > 0.2$, 11 of which are intermediate thin/thick disk or thick disk members. There are also 16 sources with non-planar orbits ($i > 2^\circ$), with 9 of these being intermediate thin/thick disk members. $0.6^\circ\ ^{+0.9^\circ}_{-0.2^\circ}$).

3.4.3 Cluster Membership

Kinematics allows me to identify members of young clusters and moving groups, sources which are crucial for testing theoretical brown dwarf evolution models at early ages (Burrows et al. 1997; Baraffe et al. 2003) as well as empirical trends between effective spectral type, temperature, luminosity, mass, and age. I examined my sample for young association membership by comparing their 6D spatial and velocity coordinates (determined from RVs and *Gaia* astrometry) to known nearby systems using the BANYAN Σ web tool (Gagné et al. 2018c). Results are summarized in Table 3.6.

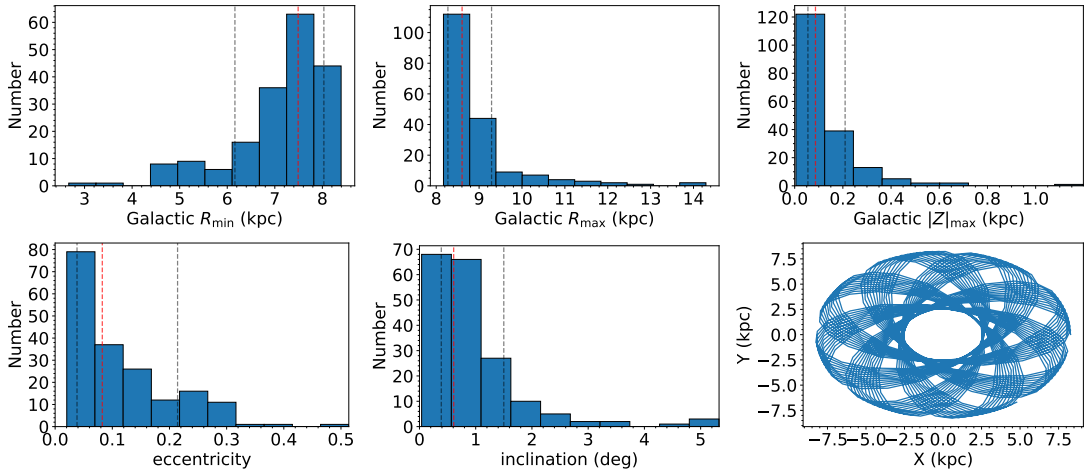

Figure 3.18: The distributions of inferred orbital parameters for my sample. *upper left*: minimum Galactic radius $R_{\rm min}$; *upper middle*: maximum Galactic radius $R_{\rm max}$; *upper right*: minimum vertical displacement $|Z|$; *lower left*: eccentricity e; *lower middle*: inclination i; *lower right*: The Galactic XY orbit of the thick disk source 2MASS J15115124+3033065, integrated between -5 Gyr to $+5$ Gyr. The median values and the $16^{\rm th}$/$84^{\rm th}$ percentiles are shown in red and grey dashed lines, respectively.

My APOGEE DR17 sample is highly biased toward young clusters, which is confirmed in the cluster membership analysis. Out of 66 young sources in my sample, I identified 64 kinematic members of young moving groups, with 61 previously reported in the literature. Two of the young sources were not identified due to their parent clusters not being included in the BANYAN Σ web tool (see below). The majority of cluster members are associated with Upper Scorpius (10±3 Myr, Pecaut & Mamajek 2016; 41 sources), Taurus (1–2 Myr, Kenyon & Hartmann 1995; 7 sources), and the Hyades (750±100 Myr, Brandt & Huang 2015; 6 sources). The three sources not previously reported in the literature are 2MASS J05402570+2448090 (G 100-28; 54.7% Argus moving group, 40-50 Myr, Zuckerman 2019; 43.2% Carina Near moving group, ∼200 Myr, Zuckerman et al. 2006), 2MASS J14093200+4138080 (LP 220-50; 99.6% Argus moving group), and 2MASS J21272531+5553150 (LSPM J2127+5553; 99.3% Carina Near moving group). On the other hand, I ruled out 2MASS J07140394+3702459 (LSPM J0714+3702) as a member of the Argus Moving Group and classified as M7β intermediate gravity class

using the SpeX data reported in (Gagné et al. 2015b), but they did not have the radial velocity information[6] I also ruled out two members of the Coma Berenices Cluster (562^{+98}_{-84} Myr with my full 6D kinematics information, Silaj & Landstreet 2014), 2MASS J12205439+2525568 and 2MASS J12235346+2534559, reported in Melnikov & Eislöffel (2012) with only astrometry and photometry. Melnikov & Eislöffel (2012) used proper motions from the Lépine Shara Proper Motion (LSPM) catalog (Lépine & Shara 2005), but unfortunately these sources were not measured in the LSPM catalog due to their relatively small proper motions. This also highlights the importance of RVs when the proper motions of the cluster as the Coma Berenices Cluster ($\mu_\alpha = -12.0 \pm 0.5$ mas, $\mu_\delta = -9.0 \pm 0.8$ mas) are small. While BANYAN Σ web tool is extremely useful, it does not have all of the young clusters and moving groups, so two young sources were not recovered, including 2MASS J03293053+3127280 and J08294949+2646348. 2MASS J03293053+3127280 was reported as a member in NGC 1333 (Cantat-Gaudin et al. 2018; Yao et al. 2018; Cantat-Gaudin & Anders 2020; Cantat-Gaudin et al. 2020), which is part of the IN-SYNC Survey (Cook et al. 2014; Yao et al. 2018) and identified in *Gaia* DR2 astrometry (without RVs; Cantat-Gaudin et al. 2018; Cantat-Gaudin & Anders 2020; Cantat-Gaudin et al. 2020). 2MASS J08294949+2646348 reported as a member of the Castor Moving Group (>200 Myr, Zuckerman et al. 2013), but the Castor Moving Group does not have a precise age determination (Zuckerman et al. 2013). I include these two sources as young sources in the kinematic analysis in Section 3.4.4.

Finally, I examine the best-fit parameters between the young and the field sample. For $\log g$s, I found significant difference between the young ($\log g = 3.58^{+1.37}_{-0.06}$ cm s^{-2} dex) and field objects ($\log g = 5.08^{+0.40}_{-0.45}$ cm s^{-2} dex) with the Sonora models. For $v \sin i$s, I found more high $v \sin i$s for the young ($v \sin i = 20^{+24}_{-6}$ km s^{-1}) than field objects ($v \sin i$

[6]With the BANYAN Σ web tool (Gagné et al. 2018c), the optimal RV to make 2MASS J07140394+3702459 as a member of the Argus Moving Group is 20.9 km s^{-1}, which is completely ruled out with my RV of 35.3±0.2 km s^{-1}.

$= 13^{+13}_{-5}$ km s^{-1}) for Sonora models, but their distributions overlap. For the BT-Settl models, I found lower $T_{\rm eff}$s and $\log g$ for the young objects ($T_{\rm eff} = 2983^{+148}_{-175}$ K; $\log g = 4.5^{+0.43}_{-0.03}$ cm s^{-2} dex) than the field objects ($T_{\rm eff} = 3177^{+16}_{-126}$ K; $\log g = 5.41^{+0.07}_{-0.28}$ cm s^{-2} dex) and higher $v \sin i$s for the young objects ($v \sin i = 16^{+14}_{-2}$ km s^{-1}) than the field objects ($v \sin i = 11^{+17}_{-3}$ km s^{-1}) but with a much smaller sample size (N=22, including 7 young and 15 field objects).

3.4.4 Kinematic Ages

Ensemble kinematics of a population also provides age information, as stellar velocities become increasingly dispersed through dynamical interactions of Galactic structures (Spitzer & Schwarzschild 1953; Wielen 1977; Aumer & Binney 2009; Ting & Rix 2019; Sharma et al. 2021). The increased dispersion over time has been historically captured in empirical age-velocity dispersion relations (AVRs), which can be inverted to derive mean kinematic ages for stellar samples (Hsu et al. 2021). I considered two functional forms of the AVR in this study: the exponential relation of Wielen (1977), and the power-law relation from Aumer & Binney (2009). I followed the same analysis methodology as described in Hsu et al. (2021), and the results are summarized in Table 3.8. Since 2MASS J05350162−0521489 does not have precise proper motion measurements which give larger *UVW* errors, so I excluded this source for the kinematic age analysis.

The overall velocity dispersion of my sample $\sigma_{\rm tot} = 35.4 \pm 0.4$ km s^{-1}, which corresponds to a kinematic age of $\tau = 2.64 \pm 0.17$ Gyr using the Aumer & Binney (2009) relation. For the Wielen (1977) relation, the W-weighted velocity dispersion $\sigma_{W\text{-tot}} = 45.7 \pm 0.3$ km s^{-1} corresponds to a kinematic age of $\tau = 3.81 \pm 0.05$ Gyr. Compared to the late-M age of 4.0 ± 0.3 Gyr in Hsu et al. (2021) based on the Aumer & Binney (2009) relation, my sample appears to have a younger average age, likely reflecting

the sample bias toward young clusters. Removing the 66[7] identified young cluster members increases the velocity dispersion to $\sigma_{\rm tot} = 42.7 \pm 0.6$ km s^{-1}, corresponding to a kinematic age of 4.5 $\pm$ 0.3 Gyr for the Aumer & Binney (2009) relation, in line with prior results (Reiners & Basri 2009a; Blake et al. 2010; Burgasser et al. 2015a; Hsu et al. 2021). There is a also better agreement in this case with the W-weighted velocity dispersion and Wielen (1977) age of 4.19 $\pm$ 0.05 Gyr. I can also discern the distinct young and field populations using the velocity probability plot, or probit plot, that ranks the individual velocity components in steps of overall sample standard deviation. A normal distribution would be represented as a straight line whose slope equals the sample dispersion (Chambers et al. 1983). Figure 3.19 displays probit plots for each of the UVW velocity components, all of which show two clear linear trends: a shallower "core" sample and a steeper (and hence more dispersed) "wide" sample. A piece-wise linear fit to these trends broken at $\pm 1\sigma$ components yields total velocity dispersions of $\sigma_{\rm tot} = 38.9 \pm 0.4$ km s^{-1}, $\sigma_{\rm tot} = 49.5 \pm 1.7$ km s^{-1}, and $\sigma_{\rm tot} = 53.0 \pm 2.5$ km s^{-1} for the shallow, lower wide, and upper wide sample, respectively, corresponding to kinematic ages of 3.5 $\pm$ 0.2 Gyr, 6.9 $\pm$ 1.7 Gyr, and 8.4 $\pm$ 1.1 Gyr, based on the Aumer & Binney (2009) relation. The core sample is fully consistent with the thin disk without young and binary sources; the wing sample for the upper and lower wide samples both have similar ages and are older than the core sample as expected for thick disk ages. I also examined the removal of sources of 12 thick disk and intermediate thin/thick disk sources and young sources (Section 3.4.1), which slightly reduces the velocity dispersion and sample age to 3.2 ± 0.2 Gyr based on the Aumer & Binney (2009) relation. Segregating thin disk M dwarfs (100 sources) and L dwarfs (4 sources), I find similar kinematic ages (3.1 ± 0.2 Gyr and 4.3 ± 2.4 Gyr, respectively), albeit with large uncertainties for the latter. I also examined removing 36 RV variables from the thin disk sample as likely

[7]This number includes 2MASS J05350162−0521489, which has huge proper motion uncertainties.

binaries; this had minimal influence on the inferred age (3.5 ± 0.3 Gyr).

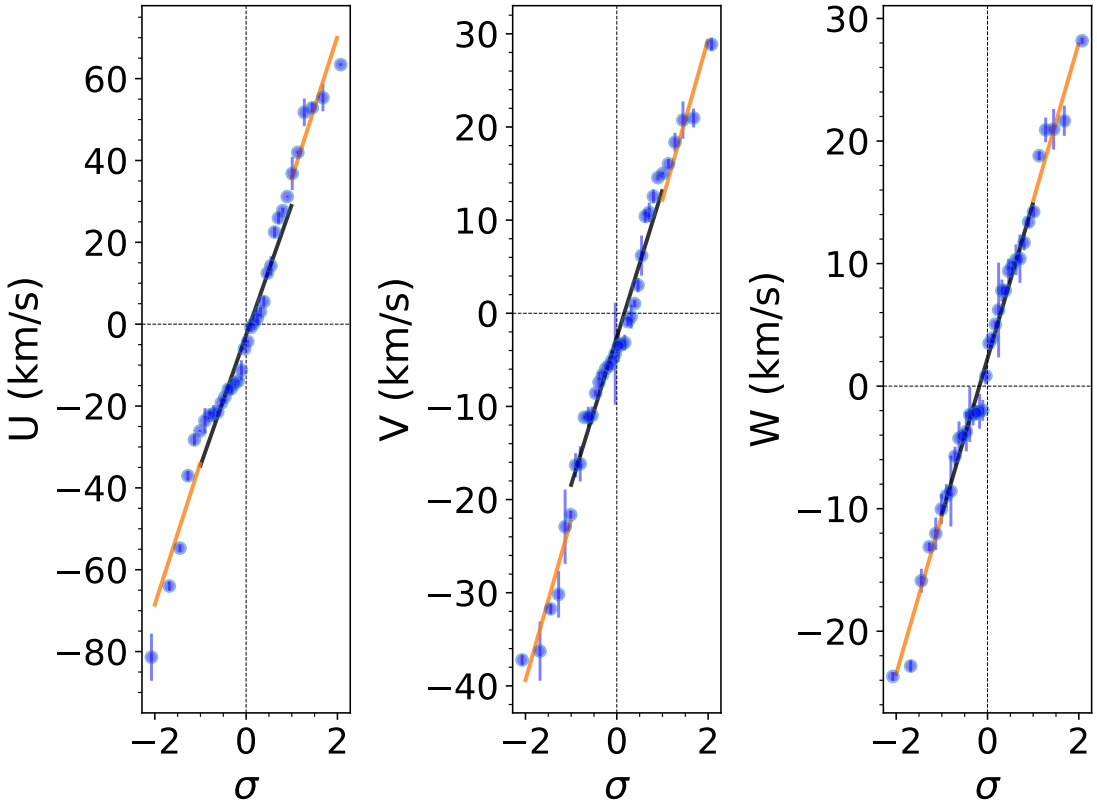

Figure 3.19: Space velocity probit plots of the APOGEE sample. Individual velocities are indicated by blue and red circles for my M and L dwarfs, respectively, while a piece-wise linear fit broken at ± 1 σ is shown (orange dashed lines). Note that 2MASS J05350162−0521489 is not plotted here due to its huge proper motion errors.

3.4.5 Radial Velocity Variables

One of the main stellar science goals of the APOGEE survey is to identify closely-separated binary systems, which are crucial for mass measurements and testing binary formation and evolution models. While the APOGEE ASPCAP pipeline is unable to provide robust RVs in the ultracool dwarf temperature regime, my RV precisions are sufficient to identify binaries at projected separations $\lesssim$0.7 AU from RV variability, assuming the total mass of 0.3 $M_{\odot}$, secondary mass of 5 M_{Jup} and RV precision of 0.3 km

s^{-1}. My sample contains 137 sources with at least two epochs of observations, 51 of which have four or more epochs. Of the latter, 18 exhibit evidence of significant RV variations ($p < 0.01$) based on a χ^2 test,[8] and I consider these high probability binary systems. Among the 90 sources with 2 or 3 epochs of observations, 11 show significant RV variations, and I consider these promising binary candidates. All of the RV variables are listed in Table 3.9.

The majority of the RV variables have too few epochs to full sample a complete orbit, and hence only partial constraints can be made on orbital parameters. I attempted to make these constraints for each RV variable with at least four epochs of observation using `The Joker` (Price-Whelan et al. 2017), a Monte Carlo rejection sampler that quantifies single-line RV orbits in terms of period (P), velocity variation semi-amplitude (K), eccentricity (e), systemic velocity (v_0), the mean anomaly (M_0), and the argument of periastron (ω), and identifies a family of orbits consistent with the measurements. I ran the `The Joker` using its default settings. For each system, I initially selected limiting ranges for the minimum and maximum orbital period ($P_{\rm min}$ and $P_{\rm max}$), the maximum RV semi-amplitude (K_0), and the number of input samplers ($10^5 \leq N_{samp} \leq 5\times10^6$) by optimizing the reasonable number of survival simulated orbital solutions. Initial estimates of v_0 and K were determined from the mean and standard deviation of RV measurements), and both of these quantities were assumed to follow normal distributions with scale factors σ_K, σ_v = 1–4 km s^{-1} constrained from the ΔRV variations in the observed RV time series. The period distribution was assumed to follow $\mathscr{P}(P) \propto P^{-1}$ following Uehara et al. (2016); Price-Whelan et al. (2017); Kipping (2018). The eccentricity distribution was assumed to be a Beta distribution

$$\mathscr{P}(e) = \frac{\Gamma(a+b)}{\Gamma(a)+\Gamma(a)} e^{a-1}\left[1-e\right]^{b-1} \tag{3.4}$$

[8]This includes an assumed systematic RV uncertainty of 0.19 km s^{-1}; see Section 3.3.1)

, where Γ is the Gamma function and $a = 0.867$ and $b = 3.03$ (Kipping 2013). The distributions of mean anomaly and periastron angle were assumed to be uniformly distributed between 0 and 2π. The standard deviation of of the RV semi-amplitude σ_K prior, assumed to be a normal distribution Price-Whelan et al. (2020), is defined as

$$\sigma_K^2 = \sigma_{K,0}^2 \left(\frac{P}{1 \text{ year}} \right)^{-2/3} \left(1 - e^2\right)^{-1}. \tag{3.5}$$

Since RV semi-amplitude of the primary $K_1 = \sqrt{\frac{G}{(1-e^2)}} m_2 \sin i (m_1 + m_2)^{-1/2} a^{-1/2}$, for the gravitational constant G, eccentricity e, masses of the primary m_1 and secondary m_2, inclination i, and semi-major axis a, this form of priors has the advantage that the RV semi-amplitude K has a fixed form of primary mass independent of the period and eccentricity at a fixed primary mass (Price-Whelan et al. 2020). Typical computation time is within 0.5–2 min.

Results for these fits are provided in Table 3.10, and individual fits to all RV variables are provided in Appendix C. Figure 3.20 illustrates an example orbit fit for 2MASS J07564895+6649595, which has 17 epochs of observations. For this fit I were able to constrain its period $P_{\rm fit} = 409^{+120}_{-52}$ day, RV semi-amplitude $K_{\rm fit} = 0.5 \pm 0.2$ km s^{-1}, and eccentricity $e_{\rm fit} = 0.18^{+0.26}_{-0.14}$. There are two sources with orbits less than 2 day (2MASS J13500476+3207596, $P = 1.7^{+0.2}_{-0.7}$ day; and 2MASS J14005977+3226109, $P = 1.4^{+321.9}_{-0.3}$ day[9]) and one source with larger RV semi-amplitude (2MASS J13482307+3321508, $K = 10.8^{+1.6}_{-1.6}$ km s^{-1}). The major limitation of my binary orbital parameter estimates is the eccentricity (median uncertainty = 0.27) as well as the period (median uncertainty = 29 day), which requires complete sampling of the RV orbit to be well-constrained. Finally, I emphasize that given the sparse RVs in my APOGEE sample, more data are required to provide robust constraints of orbital parameters.

[9] not well constrained for the upper bound since long-period solutions are also possible

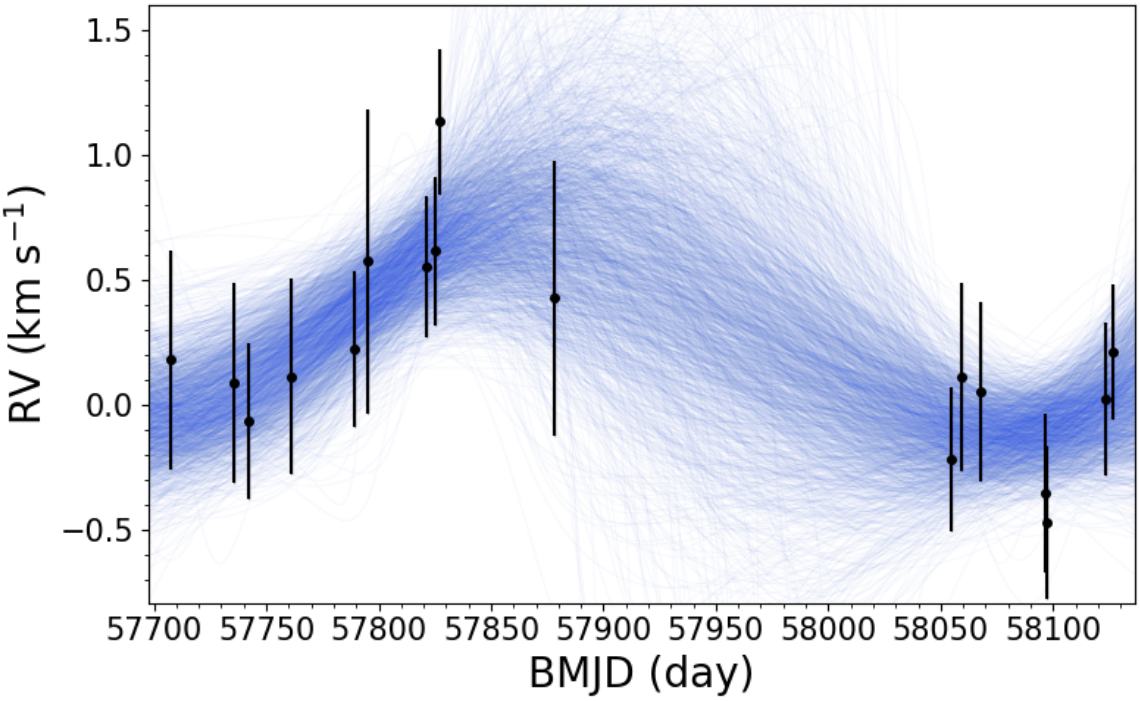

Figure 3.20: Binary orbital fit for 2MASS J07564895+6649595 using the Monte Carlo rejection sampler `The Joker`. The black dots are my measured RVs, and possible binary orbital solutions are labeled in blue lines. The inferred orbital parameters are period $P_{\rm fit} = 409^{+120}_{-52}$ day, the RV semi-amplitude $K_{\rm fit} = 0.5 \pm +0.2$ km s^{-1}, and eccentricity $e_{\rm fit} = 0.18^{+0.26}_{-0.14}$, with the full information summarized in Table 3.10.

3.4.6 Rotation Periods, Projected Radii, and Inclinations

Finally, I examine in some detail the results of my $v \sin i$ analysis, which provides information on the ages, sizes, and viewing geometries of my targets, particularly when an independent measure of rotation period is available. Recalling that roughly one-third of my sample is kinematically associated with a nearby young cluster (Section 3.4.3), such measurements can be used to examine radius evolution as a function of time to test evolutionary models (Jackson & Jeffries 2010). The projected radius $R \sin i$ can be directly inferred from rotational velocity and period using the relation

$$\frac{R \sin i}{R_\odot} = 0.0198 \frac{P}{\mathrm{day}} \frac{v \sin i}{\mathrm{km/s}} \tag{3.6}$$

Thanks to the K2 Mission (Howell et al. 2014), the Transiting Exoplanet Survey Satellite (TESS; Ricker et al. 2015), and other ground-based programs, rotational periods have been measured for several sources in my APOGEE sample, in particular for several members of the Upper Scorpius cluster. I have compiled period measurements from the literature for 53 APOGEE sources, listed in Table 3.11. These include 37 young cluster members and 11 field objects. An initial assessment shows that the young sources (median period of 0.87 days) rotate significantly slower than the field sources (median period of 0.40 days). I computed the projected radii of each source and show the trend with age in Figure 3.21, assuming the uncertainty of periods of 5% for sources without period uncertainties in the literature and the $R \sin i$ uncertainties were propagated through the Monte Carlo method. I also removed five objects with periods > 5 day or $v \sin i$ < 10 km s^{-1} (lower than my $v \sin i$ detection limit; see Section 3.3.2), which are all field objects (2MASS J07140394+3702459, 2MASS J10323297+0630074, 2MASS J10570380+2217203, 2MASS J14320849+0811313, and 2MASS J19241634+7533121). Since the $v \sin i$ close to my detection limit could potentially give overestimated projected

radii, I conservatively constrain my analysis for sources with $v \sin i > 20$ km s^{-1}, which leaves 26 sources in total, including 21 young sources (14 sources in the Upper Scorpius cluster) and 5 field objects. Overall, the projected radii are larger for the young sources (median 0.48 $R_\odot$) compared to the field objects (median 0.15 $R_\odot$), and show a consistent decline with age from Upper Scorpius' 10±3 Myr Pecaut & Mamajek 2016 to Hyades' 750±100 Myr (Brandt & Huang 2015) and field age (assumed as 5 Gyr). In particular, the projected radii are $0.53^{+0.16}_{-0.15}$ $R_\odot$ for the Upper Scorpius cluster and $0.15^{+0.09}_{-0.06}$ $R_\odot$ for the field objects. These radii are slightly larger but consistent with the evolutionary models, which predict radii of 0.39–0.45 $R_\odot$ at 10 Myr, 0.17–0.22 $R_\odot$ at 100 Myr, and 0.12–0.18 $R_\odot$ at 1 Gyr for a 0.10–0.15 $M_\odot$ star (Burrows et al. 2001). It should be noted that the radius inflation of M dwarfs is commonly reported in the literature ($\Delta R/R \sim 14 \pm 2\%$; e.g. Jackson et al. 2018; Kesseli et al. 2018; Parsons et al. 2018; Khata et al. 2020)

As a final assessment, I attempted to infer inclination angles for those sources with robust determinations of $v \sin i$ and period, using model-based radii (cf. Vos et al. 2017). Radii were drawn from the Burrows et al. (2001) evolutionary models, adopting uniform distributions with $T_{\rm eff}$s from the spectral type using Pecaut & Mamajek (2013) relation (assuming ±1 subtype uncertainty) and ages for each cluster (Taurus: 1–2 Myr, Kenyon & Hartmann 1995; Corona Australis: 45^{+11}_{-7} Myr, Bell et al. 2015; Upper Scorpius: 10±3 Myr, Pecaut & Mamajek 2016; Argus: 40–50 Myr, Zuckerman 2019; AB Doradus: 149^{+51}_{19} Myr, Bell et al. 2015; Carina-Near: ∼200 Myr, Zuckerman et al. 2006; Castor: 200∼100 Myr (Barrado y Navascues 1998)[10]; and Hyades: 750±100 Myr, Brandt & Huang 2015) or 5 Gyr for the field, which is a reasonable assumption for field ages between 1–10 Gyr in theoretical models (Burrows et al. 1997; Chabrier et al. 2000; Allard et al. 2001; Baraffe et al. 2003) and observational studies (Burgasser & Blake 2009;

[10]The stars associated with the Castor Moving Group might not share a common age; see the discussion in Mamajek et al. (2013) in their § 2.11.

Burgasser & Mamajek 2017; Dupuy & Liu 2017).[11] I drew 100,000 samples from both measurement distributions in normal distributions and radii in uniform distributions, and propagated uncertainties using the Monte Carlo method. The resulting inclinations are summarized in Table 3.11. Again, I constrained the inclination analysis for sources with P <5 day and $v \sin i$ >20 km s^{-1}. From this select sample of 26 sources, 17 inclinations were found to be non-physical ($\sin i > 1$), leaving 9 sources with realistic measurements: 3 Upper Scorpius sources and 3 field objects. While this is a small sample, I examined the distribution of orientations to assess whether there were any obvious biases in inferred inclinations that may be related to measurement errors. If a given population of stars is randomly oriented, the cumulative distribution function follows $CDF(i) = 1 - \cos i$ (Jackson & Jeffries 2010). I used the Kolmogorov–Smirnov (K-S) test (Massey 1951) to compare the distribution of inclinations in my sample to this random orientation distribution, and found that the Upper Scorpius (K-S statistic = 0.55, p-value = 0.22), field (K-S statistic = 0.20, p-value = 0.99), and the full sample (K-S statistic = 0.28, p-value = 0.39) are all consistent with a random orientation.

[11] The radii were inferred to be 0.518–0.585 $R_\odot$ for 1 source Corona Australis (45^{+11}_{-7} Myr, Bell et al. 2015), 0.226–0.314 $R_\odot$ for 23 sources in Upper Scorpius (10±3 Myr, Pecaut & Mamajek 2016), 0.137–0.141 $R_\odot$ for 1 source in Argus (40–50 Myr, Zuckerman 2019), 0.128–0.157 $R_\odot$ for 1 source in AB Doradus (149^{+51}_{19} Myr, Bell et al. 2015), 0.097–0.111 $R_\odot$ for 6 sources in Hyades (750±100 Myr, Brandt & Huang 2015), and 0.090–0.137 $R_\odot$ for field (5 Gyr, see references in the main text).

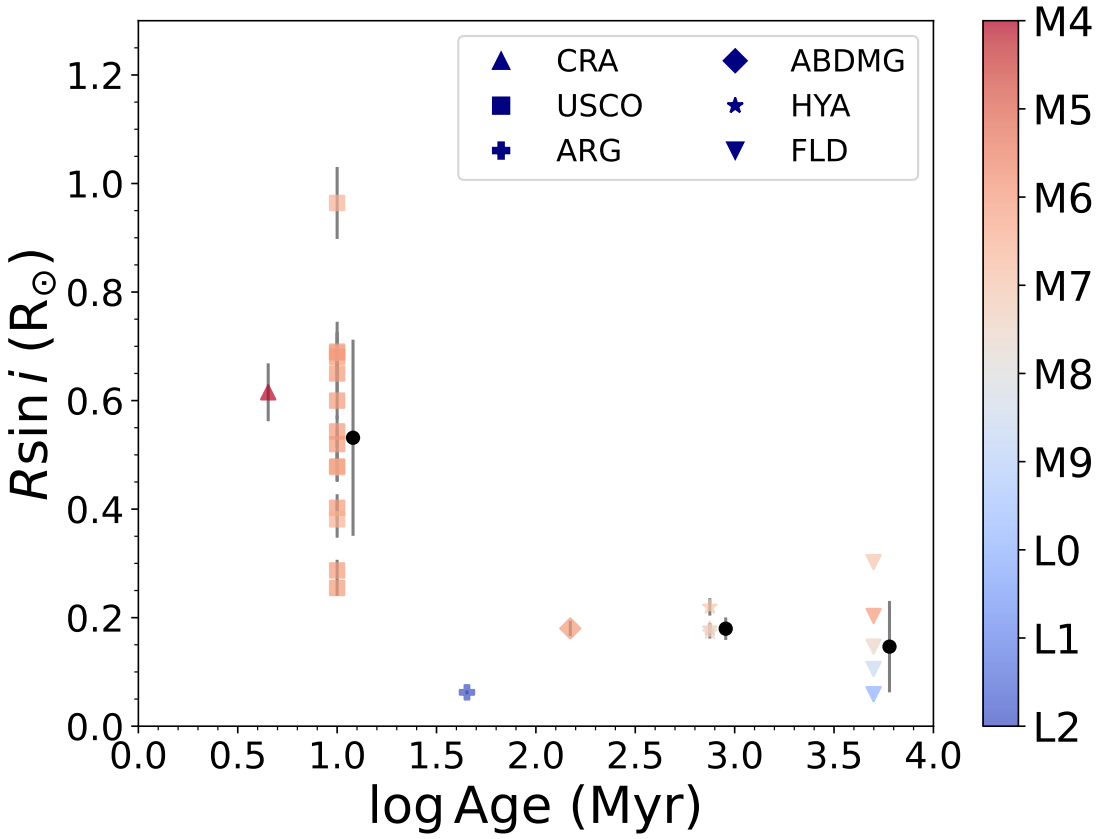

Figure 3.21: Projected radii as a function of ages. The Projected radii ($R \sin i$) for each source are color-coded with their spectral types with shapes corresponding to their clusters, including Corona Australis (CRA; upper triangle), Upper Scorpius (USCO; square), Argus (ARG; plus), AB Doradus (ABDMG; diamond), Hyades (HYA; star), and field objects (FLD; lower triangle). For sources in the Upper Scorpius and Hyades, and field objects, the median, 16$^{\text{th}}$, and 84$^{\text{th}}$ percentiles for the subsamples are plotted in black dots with a slight shift to the right with respect to their ages.

Table 3.5: RV and $v \sin i$ Measurements with ASPCAP and Literature Comparison

APOGEE ID	$\langle \mathrm{RV} \rangle^{a}$ (km s^{-1})	ASPCAP RV^{b} (km s^{-1})	Lit. RV (km s^{-1})	Lit. RV Ref.	$\langle v \sin i \rangle^{a}$ (km s^{-1})	Lit. $v \sin i$ (km s^{-1})	Lit. $v \sin i$ Ref.
2M00312793+6139333	$-34.44^{+0.19}_{-0.2}$	-38.02 ± 0.69	⋯	⋯	< 10	⋯	⋯
2M00452143+1634446	$3.71^{+0.4}_{-0.56}$	555.81 ± 4.96	3.16 ± 0.83	Faherty et al. (2016)	$31.64^{+1.07}_{-1.21}$	32.82 ± 0.17	Blake et al. (2010)
2M01120002+1502170	$-44.31^{+0.28}_{-0.27}$	-45.61 ± 0.44	⋯	⋯	< 10	⋯	⋯
2M01154176+0059317	$10.78^{+0.78}_{-1.18}$	11.7 ± 0.41	⋯	⋯	$33.69^{+2.15}_{-2.57}$	⋯	⋯
2M01215816+0101007	$10.28^{+0.11}_{-0.13}$	586.83 ± 0.92	⋯	⋯	< 10	⋯	⋯
2M01243124−0027556	$-3.88^{+0.17}_{-0.16}$	577.03 ± 1.68	0.69 ± 10.14	Kiman et al. (2019)	$27.7^{+1.11}_{-1.84}$	⋯	⋯
2M01514363+0046188	$14.44^{+0.65}_{-0.67}$	14.49 ± 2.0	16.55 ± 10.07	Kiman et al. (2019)	$18.12^{+1.05}_{-1.35}$	⋯	⋯
2M02500239−0808417	$25.61^{+0.64}_{-0.66}$	25.06 ± 0.81	⋯	⋯	< 10	⋯	⋯
2M03040207+0045512	$29.94^{+0.32}_{-0.31}$	29.18 ± 0.77	28.38 ± 2.52	Kiman et al. (2019)	$19.99^{+2.42}_{-1.73}$	⋯	⋯
2M03282839+3116273	$15.41^{+0.77}_{-0.91}$	14.09 ± 9.08	15.06 ± 2.15	Kounkel et al. (2019)	$30.46^{+2.51}_{-1.83}$	26.9 ± 3.16	Kounkel et al. (2019)
2M03293053+3127280	$15.77^{+0.48}_{-0.54}$	15.83 ± 0.43	14.9 ± 0.8	Cottaar et al. (2015)	$16.05^{+0.97}_{-1.22}$	16.25 ± 1.16	Kounkel et al. (2019)
2M03505737+1818069	$6.05^{+0.16}_{-0.13}$	105.07 ± 0.81	32.2 ± 1.8	Deshpande et al. (2012)	$12.71^{+0.4}_{-1.02}$	12.2 ± 3.0	Deshpande et al. (2012)
2M04110642+1247481	$39.28^{+0.19}_{-0.23}$	37.66 ± 0.63	⋯	⋯	$14.15^{+0.97}_{-1.12}$	⋯	⋯
2M04185115+2814332	$21.13^{+0.23}_{-0.2}$	16.61 ± 1.44	⋯	⋯	< 10	⋯	⋯
2M04204796+5624202	$-29.54^{+0.27}_{-0.24}$	-31.93 ± 1.44	⋯	⋯	$14.75^{+2.7}_{-2.01}$	⋯	⋯
2M04214435+2024105	$40.78^{+0.42}_{-0.45}$	30.36 ± 0.42	⋯	⋯	$32.8^{+1.48}_{-1.06}$	⋯	⋯
2M04214955+1929086	$39.43^{+0.19}_{-0.17}$	636.19 ± 0.61	⋯	⋯	$44.43^{+0.34}_{-1.24}$	⋯	⋯
2M04262939+2624137	$20.01^{+0.37}_{-0.47}$	17.36 ± 0.58	17.55 ± 0.26	Kounkel et al. (2019)	$12.95^{+1.3}_{-1.33}$	12.06 ± 0.66	Kounkel et al. (2019)
2M04294568+2630468	$18.13^{+0.22}_{-0.21}$	16.8 ± 0.38	15.77 ± 0.23	Kounkel et al. (2019)	$14.21^{+0.96}_{-1.05}$	14.34 ± 0.51	Kounkel et al. (2019)
2M04330945+2246487	$19.6^{+0.37}_{-0.39}$	16.04 ± 1.02	16.31 ± 0.29	Kounkel et al. (2019)	$15.96^{+1.0}_{-1.06}$	13.59 ± 0.65	Kounkel et al. (2019)
2M04351354+2008014	$40.01^{+0.28}_{-0.21}$	283.03 ± 0.99	⋯	⋯	$23.66^{+0.96}_{-1.05}$	⋯	⋯
2M04440164+1621324	$21.82^{+0.19}_{-0.21}$	843.02 ± 5.32	⋯	⋯	$14.28^{+1.16}_{-1.24}$	⋯	⋯
2M04464498+2436404	$42.22^{+0.46}_{-0.34}$	40.79 ± 0.45	⋯	⋯	$17.88^{+0.08}_{-0.17}$	⋯	⋯
2M04552333+3027366	$17.46^{+0.19}_{-0.15}$	15.63 ± 2.53	⋯	⋯	$14.22^{+0.95}_{-1.02}$	⋯	⋯
2M04565141+2939310	$17.91^{+0.43}_{-0.37}$	16.65 ± 2.42	⋯	⋯	$12.44^{+0.98}_{-1.11}$	⋯	⋯
2M05350162−0521489	$25.07^{+0.31}_{-0.62}$	53.21 ± 0.77	⋯	⋯	$67.65^{+2.38}_{-1.62}$	⋯	⋯
2M05392474+4038437	$-5.42^{+0.23}_{-0.24}$	524.06 ± 1.22	10.0 ± 30.0	Lépine et al. (2003)	< 10	⋯	⋯
2M05402570+2448090	$23.07^{+0.63}_{-0.93}$	18.67 ± 6.31	21.0 ± 5.0	Newton et al. (2014)	$30.37^{+2.0}_{-1.63}$	25.9 ± 1.7	Gilhool et al. (2018)
2M06154934−0100415	$-19.69^{+0.19}_{-0.2}$	1024.34 ± 3.38	-21.0 ± 2.0	Burgasser et al. (2015a)	$16.62^{+1.14}_{-1.38}$	⋯	⋯
2M06521977−2534505	$14.9^{+0.21}_{-0.22}$	595.94 ± 0.96	12.0 ± 2.0	Burgasser et al. (2015a)	< 10	⋯	⋯
2M07025026−6102482	$21.31^{+0.14}_{-0.13}$	17.85 ± 0.43	⋯	⋯	$15.98^{+0.06}_{-0.1}$	⋯	⋯
2M07140394+3702459	$35.34^{+0.24}_{-0.23}$	618.83 ± 2.03	40.03 ± 0.11	Deshpande et al. (2013)	< 10	12.8 ± 0.5	Deshpande et al. (2013)
2M07464256+2000321	$52.78^{+0.11}_{-0.1}$	635.3 ± 0.91	52.37 ± 0.59	Blake et al. (2010)	$34.59^{+1.04}_{-1.08}$	32.72 ± 0.56	Blake et al. (2010)
2M07475737+6653337	$7.45^{+0.7}_{-0.82}$	116.13 ± 28.51	⋯	⋯	$45.85^{+3.03}_{-1.93}$	⋯	⋯

Table 3.5 (*continued*)

Table 3.5 (*continued*)

APOGEE ID	$\langle$RV$\rangle$[a] (km s^{-1})	ASPCAP RV[b] (km s^{-1})	Lit. RV (km s^{-1})	Lit. RV Ref.	$\langle v \sin i \rangle$[a] (km s^{-1})	Lit. $v \sin i$ (km s^{-1})	Lit. $v \sin i$ Ref.
2M07552256+2755318	$-3.86^{+0.28}_{-0.24}$	-5.72 ± 0.53	⋯	⋯	< 10	⋯	⋯
2M07564895+6649595	$0.19^{+0.42}_{-0.41}$	-215.64 ± 28.35	⋯	⋯	$10.67^{+0.99}_{-1.25}$	⋯	⋯
2M08072607+3213101	$34.41^{+0.22}_{-0.25}$	619.69 ± 2.2	⋯	⋯	$13.68^{+1.29}_{-1.28}$	⋯	⋯
2M08080189+3157054	$30.61^{+0.32}_{-0.33}$	616.38 ± 2.69	⋯	⋯	$12.55^{+1.35}_{-1.36}$	⋯	⋯
2M08092892+3235226	$-6.66^{+0.58}_{-0.54}$	-10.32 ± 1.08	⋯	⋯	$23.35^{+1.32}_{-1.7}$	⋯	⋯
2M08144389+4650522	$24.39^{+0.48}_{-0.3}$	23.56 ± 0.53	⋯	⋯	$17.87^{+0.95}_{-1.01}$	⋯	⋯
2M08185804+2333522	$35.74^{+0.29}_{-0.29}$	617.93 ± 0.78	33.1 ± 3.0	Reiners & Basri (2009a)	< 10	⋯	⋯
2M08211639+5658358	$7.17^{+0.22}_{-0.27}$	4.85 ± 1.16	⋯	⋯	$14.09^{+1.16}_{-1.32}$	⋯	⋯
2M08294949+2646348	$10.69^{+0.32}_{-0.31}$	594.91 ± 1.82	53.84 ± 5.53	Terrien et al. (2015)	$11.91^{+1.12}_{-1.1}$	9.6 ± 0.8	Kesseli et al. (2018)
2M08440350+0434356	$66.68^{+0.5}_{-0.49}$	648.94 ± 1.83	⋯	⋯	$16.16^{+0.97}_{-1.1}$	⋯	⋯
2M08490052+0220155	$22.37^{+0.37}_{-0.64}$	625.5 ± 0.97	⋯	⋯	$53.72^{+2.13}_{-1.73}$	⋯	⋯
2M08501918+1056436	$31.45^{+0.43}_{-0.44}$	821.19 ± 1.74	32.97 ± 0.09	Deshpande et al. (2013)	$17.94^{+1.15}_{-1.32}$	15.8 ± 1.5	Gilhool et al. (2018)
2M08522464+2540591	$29.56^{+0.21}_{-0.2}$	28.14 ± 0.38	⋯	⋯	< 10	⋯	⋯
2M09020690+0033195	$42.63^{+0.25}_{-0.22}$	41.72 ± 0.59	41.0 ± 2.0	Burgasser et al. (2015a)	< 10	⋯	⋯
2M09130162+3037583	$51.79^{+0.55}_{-0.51}$	49.63 ± 0.51	⋯	⋯	< 10	⋯	⋯
2M09373349+5534057	$0.68^{+0.45}_{-0.45}$	-0.68 ± 2.26	8.89 ± 6.97	Kiman et al. (2019)	$19.41^{+2.87}_{-1.95}$	⋯	⋯
2M09381783+0132490	$-16.8^{+1.51}_{-1.04}$	-21.85 ± 57.4	⋯	⋯	$96.07^{+16.05}_{-3.47}$	⋯	⋯
2M09442625+3521233	$51.2^{+0.87}_{-0.78}$	50.47 ± 0.49	⋯	⋯	$13.83^{+1.43}_{-1.7}$	⋯	⋯
2M09453388+5458511	$-3.67^{+0.68}_{-0.63}$	-0.5 ± 15.12	⋯	⋯	$23.46^{+1.4}_{-1.44}$	⋯	⋯
2M09472006−0020093	$15.0^{+0.08}_{-0.09}$	14.31 ± 0.44	⋯	⋯	< 10	⋯	⋯
2M09474477+0224327	$8.76^{+0.2}_{-0.26}$	234.77 ± 0.87	⋯	⋯	$12.62^{+1.36}_{-1.58}$	⋯	⋯
2M09522188−1924319	$-17.11^{+0.91}_{-0.93}$	561.77 ± 1.58	⋯	⋯	$16.04^{+1.87}_{-1.84}$	⋯	⋯
2M09524622+0620410	$12.8^{+0.43}_{-0.45}$	11.65 ± 1.0	22.62 ± 10.24	Kiman et al. (2019)	$17.2^{+1.67}_{-1.66}$	⋯	⋯
2M09560888+0134128	$21.12^{+0.6}_{-0.53}$	605.29 ± 5.22	⋯	⋯	$30.09^{+2.73}_{-2.12}$	⋯	⋯
2M10031918−0105079	$23.99^{+0.27}_{-0.26}$	-818.36 ± 0.78	22.0 ± 2.0	Burgasser et al. (2015a)	$32.73^{+1.01}_{-1.18}$	⋯	⋯
2M10134315+0000406	$3.95^{+0.35}_{-0.35}$	2.3 ± 1.03	⋯	⋯	$10.24^{+1.34}_{-1.56}$	⋯	⋯
2M10225090+0032169	$34.04^{+6.01}_{-5.87}$	744.1 ± 0.88	⋯	⋯	$11.2^{+1.6}_{-1.54}$	⋯	⋯
2M10240997+1815533	$8.22^{+0.09}_{-0.08}$	588.4 ± 0.91	6.0 ± 3.0	Reiners & Basri (2009a)	< 10	⋯	⋯
2M10323297+0630074	$13.22^{+0.15}_{-0.14}$	12.16 ± 0.24	8.0 ± 4.0	Newton et al. (2014)	< 10	⋯	⋯
2M10372897+3011117	$7.97^{+0.17}_{-0.19}$	6.39 ± 1.01	⋯	⋯	$13.07^{+1.16}_{-1.36}$	⋯	⋯
2M10541102−8505023	$-10.8^{+0.82}_{-1.13}$	563.45 ± 36.52	⋯	⋯	$10.73^{+0.97}_{-1.1}$	⋯	⋯
2M10543366+0503467	$-20.17^{+0.1}_{-0.11}$	560.48 ± 1.44	⋯	⋯	< 10	⋯	⋯
2M10570380+2217203	$11.68^{+0.1}_{-0.1}$	10.83 ± 0.24	9.0 ± 5.0	Newton et al. (2014)	< 10	⋯	⋯
2M11194647+0820356	$-44.98^{+0.18}_{-0.17}$	743.33 ± 4.96	-45.0 ± 2.0	Burgasser et al. (2015a)	< 10	⋯	⋯
2M11203609+0704135	$-14.41^{+0.57}_{-0.6}$	-15.62 ± 0.66	-16.65 ± 7.23	Kiman et al. (2019)	< 10	⋯	⋯

Table 3.5 (*continued*)

Table 3.5 (*continued*)

APOGEE ID	$\langle$RV$\rangle$[a] (km s^{-1})	ASPCAP RV[b] (km s^{-1})	Lit. RV (km s^{-1})	Lit. RV Ref.	$\langle v \sin i \rangle$[a] (km s^{-1})	Lit. $v \sin i$ (km s^{-1})	Lit. $v \sin i$ Ref.
2M11210854+2126274	$-0.3^{+0.16}_{-0.16}$	-2.37 ± 0.36	⋯	⋯	$12.36^{+0.14}_{-0.32}$	⋯	⋯
2M11232934+0154040	$-0.21^{+0.62}_{-0.59}$	580.32 ± 0.98	⋯	⋯	$18.32^{+1.1}_{-1.4}$	⋯	⋯
2M12080810+3520281	$29.17^{+0.56}_{-0.54}$	27.76 ± 1.37	⋯	⋯	$13.66^{+1.65}_{-1.48}$	⋯	⋯
2M12153877+5205050	$-4.75^{+0.2}_{-0.23}$	-5.92 ± 0.24	⋯	⋯	$12.88^{+0.58}_{-0.92}$	⋯	⋯
2M12201166+3315379	$11.16^{+0.26}_{-0.24}$	542.27 ± 1.15	⋯	⋯	< 10	⋯	⋯
2M12205439+2525568	$14.81^{+0.22}_{-0.22}$	260.45 ± 20.52	⋯	⋯	$25.61^{+0.28}_{-0.78}$	⋯	⋯
2M12215013+4632447	$-10.44^{+0.27}_{-0.22}$	563.85 ± 0.36	⋯	⋯	$29.1^{+1.0}_{-1.58}$	⋯	⋯
2M12235346+2534559	$7.03^{+0.78}_{-0.56}$	3.44 ± 1.94	⋯	⋯	$16.42^{+1.67}_{-1.52}$	⋯	⋯
2M12252076+2517082	$7.24^{+0.71}_{-0.81}$	-216.12 ± 0.6	⋯	⋯	$32.88^{+2.35}_{-1.65}$	⋯	⋯
2M12270429+2541012	$2.63^{+0.59}_{-0.61}$	0.28 ± 0.93	⋯	⋯	$19.56^{+2.69}_{-2.13}$	⋯	⋯
2M12315462+5130389	$8.92^{+0.26}_{-0.14}$	6.24 ± 0.44	⋯	⋯	< 10	⋯	⋯
2M12493960+5255340	$-56.77^{+0.43}_{-0.36}$	-272.74 ± 0.62	⋯	⋯	$10.36^{+2.98}_{-1.68}$	⋯	⋯
2M12522354+2528469	$9.43^{+0.28}_{-0.24}$	6.23 ± 0.48	⋯	⋯	$12.6^{+0.26}_{-0.7}$	⋯	⋯
2M13004379+3557591	$-24.58^{+0.23}_{-0.26}$	-27.07 ± 1.49	-22.18 ± 6.05	Kiman et al. (2019)	$17.75^{+1.83}_{-1.67}$	⋯	⋯
2M13022083+3227103	$6.77^{+0.33}_{-0.33}$	2.13 ± 1.16	7.58 ± 7.77	Kiman et al. (2019)	$25.7^{+0.99}_{-1.4}$	⋯	⋯
2M13034100+2414020	$-9.3^{+0.25}_{-0.27}$	566.48 ± 0.63	⋯	⋯	$27.42^{+2.72}_{-1.73}$	⋯	⋯
2M13065141+7056376	$15.29^{+0.3}_{-0.42}$	-199.04 ± 4.21	⋯	⋯	$11.75^{+1.26}_{-1.3}$	⋯	⋯
2M13192677+1301119	$6.27^{+0.11}_{-0.1}$	4.66 ± 0.38	⋯	⋯	< 10	⋯	⋯
2M13202007+7213140	$-27.34^{+0.52}_{-0.54}$	574.4 ± 146.73	⋯	⋯	$18.65^{+1.4}_{-1.38}$	⋯	⋯
2M13232423+5132272	$-5.41^{+0.52}_{-0.49}$	-6.29 ± 0.26	-4.69 ± 3.73	Kiman et al. (2019)	$18.91^{+1.88}_{-1.66}$	⋯	⋯
2M13342918+3303043	$-18.03^{+0.3}_{-0.27}$	-28.1 ± 5.22	⋯	⋯	$10.71^{+0.3}_{-0.41}$	⋯	⋯
2M13430646+0038442	$-11.91^{+0.72}_{-0.72}$	-14.72 ± 1.0	⋯	⋯	< 10	⋯	⋯
2M13482307+3321508	$-19.22^{+3.6}_{-4.53}$	-17.38 ± 9.06	⋯	⋯	$14.37^{+5.08}_{-2.44}$	⋯	⋯
2M13500476+3207596	$-5.83^{+0.53}_{-0.61}$	-7.99 ± 2.41	⋯	⋯	$10.56^{+2.86}_{-1.84}$	⋯	⋯
2M13564148+4342587	$-19.51^{+0.62}_{-0.57}$	559.79 ± 1.51	-22.2 ± 3.0	Reiners & Basri (2009a)	$16.16^{+0.96}_{-1.06}$	13.5 ± 1.6	Gilhool et al. (2018)
2M13573443+5408223	$-43.22^{+0.72}_{-0.98}$	-48.07 ± 16.87	⋯	⋯	$38.4^{+4.05}_{-1.87}$	⋯	⋯
2M14005977+3226109	$-17.9^{+0.74}_{-0.82}$	-21.8 ± 1.48	⋯	⋯	$11.53^{+2.27}_{-1.79}$	⋯	⋯
2M14081562+5236281	$-43.49^{+0.14}_{-0.15}$	-45.07 ± 0.31	⋯	⋯	< 10	⋯	⋯
2M14093200+4138080	$-10.96^{+0.22}_{-0.15}$	-13.51 ± 0.27	-11.0 ± 5.0	Newton et al. (2014)	$19.73^{+0.07}_{-0.15}$	⋯	⋯
2M14320849+0811313	$-21.3^{+0.13}_{-0.14}$	-22.66 ± 0.42	-18.0 ± 4.0	Newton et al. (2014)	< 10	8.49 ± 1.5	Gilhool et al. (2018)
2M14340140+5039480	$-6.39^{+0.25}_{-0.27}$	-630.07 ± 0.63	⋯	⋯	$16.32^{+1.5}_{-1.57}$	⋯	⋯
2M14402293+1339230	$-3.49^{+0.24}_{-0.24}$	578.19 ± 0.46	-5.0 ± 2.0	Burgasser et al. (2015a)	< 10	⋯	⋯
2M14432796+0316543	$-38.45^{+0.27}_{-0.29}$	501.09 ± 1.77	⋯	⋯	$22.67^{+0.76}_{-0.44}$	⋯	⋯
2M14553384+1545593	$19.3^{+0.16}_{-0.18}$	17.59 ± 0.6	⋯	⋯	$14.81^{+2.7}_{-2.57}$	⋯	⋯
2M14554964+0321420	$-39.92^{+0.16}_{-0.09}$	-41.88 ± 0.24	⋯	⋯	< 10	⋯	⋯

Table 3.5 (*continued*)

Table 3.5 (*continued*)

APOGEE ID	$\langle$RV$\rangle$[a] (km s^{-1})	ASPCAP RV[b] (km s^{-1})	Lit. RV (km s^{-1})	Lit. RV Ref.	$\langle v \sin i \rangle$[a] (km s^{-1})	Lit. $v \sin i$ (km s^{-1})	Lit. $v \sin i$ Ref.
2M15010818+2250020	$6.53^{+0.69}_{-0.71}$	1014.81 ± 0.67	6.0 ± 2.0	Burgasser et al. (2015a)	$65.29^{+1.25}_{-1.32}$	⋯	⋯
2M15041028+0923232	$-53.33^{+0.29}_{-0.29}$	529.61 ± 6.14	⋯	⋯	$13.36^{+1.38}_{-1.4}$	⋯	⋯
2M15042797+0942464	$-35.61^{+1.26}_{-0.77}$	-52.89 ± 13.56	⋯	⋯	$51.13^{+1.13}_{-1.67}$	⋯	⋯
2M15115124+3033065	$-61.43^{+0.13}_{-0.14}$	-63.94 ± 0.75	⋯	⋯	$18.88^{+1.33}_{-1.55}$	⋯	⋯
2M15175638+0656388	$-19.8^{+0.34}_{-0.33}$	-21.59 ± 0.21	⋯	⋯	< 10	⋯	⋯
2M15210103+5053230	$2.43^{+0.18}_{-0.13}$	564.62 ± 0.83	0.9 ± 3.0	Reiners & Basri (2009a)	$48.72^{+0.31}_{-0.28}$	⋯	⋯
2M15242475+2925318	$-15.15^{+0.03}_{-0.06}$	787.03 ± 1.41	⋯	⋯	< 10	⋯	⋯
2M15512179+2931062	$26.03^{+0.22}_{-0.23}$	25.93 ± 0.13	61.52 ± 8.75	Terrien et al. (2015)	< 10	⋯	⋯
2M15555600−2045187	$-4.1^{+0.47}_{-0.47}$	-6.98 ± 0.28	⋯	⋯	$19.91^{+0.97}_{-1.13}$	⋯	⋯
2M15560104−2338081	$1.51^{+0.28}_{-0.23}$	-2.49 ± 0.42	⋯	⋯	$12.96^{+0.63}_{-0.86}$	⋯	⋯
2M15560497−2106461	$-4.14^{+1.35}_{-0.55}$	529.63 ± 1.02	⋯	⋯	$92.77^{+1.75}_{-1.54}$	⋯	⋯
2M15574011+2952379	$1.06^{+0.19}_{-0.18}$	0.51 ± 0.46	⋯	⋯	$10.33^{+1.76}_{-1.62}$	⋯	⋯
2M15592591−2305081	$-3.31^{+0.11}_{-0.11}$	-6.34 ± 0.78	⋯	⋯	$23.51^{+0.95}_{-1.01}$	⋯	⋯
2M15594439−1928191	$-2.59^{+0.35}_{-0.24}$	-6.27 ± 0.51	⋯	⋯	$14.36^{+0.23}_{-0.88}$	⋯	⋯
2M16001944−2256287	$-4.27^{+0.67}_{-0.53}$	-8.85 ± 5.05	⋯	⋯	$24.86^{+2.09}_{-1.69}$	⋯	⋯
2M16002844−2209228	$-3.66^{+0.66}_{-0.78}$	-4.51 ± 0.24	⋯	⋯	< 10	⋯	⋯
2M16003023−2334457	$-3.74^{+0.51}_{-0.36}$	-10.44 ± 0.37	⋯	⋯	$73.58^{+1.75}_{-1.49}$	⋯	⋯
2M16014955−2351082	$-3.54^{+0.14}_{-0.14}$	-7.03 ± 0.29	⋯	⋯	$38.71^{+0.31}_{-1.5}$	⋯	⋯
2M16022585−2414081	$-2.1^{+0.36}_{-0.27}$	-6.95 ± 0.54	⋯	⋯	$17.87^{+0.19}_{-0.2}$	⋯	⋯
2M16044026−2254323	$-1.17^{+0.44}_{-0.54}$	-5.8 ± 0.58	⋯	⋯	$19.81^{+0.12}_{-0.23}$	⋯	⋯
2M16045199−2224108	$-1.06^{+0.78}_{-1.29}$	-767.13 ± 0.93	⋯	⋯	$73.3^{+1.12}_{-1.16}$	⋯	⋯
2M16055178−2206212	$-3.84^{+0.28}_{-0.22}$	-6.52 ± 0.53	⋯	⋯	$21.59^{+0.35}_{-0.23}$	⋯	⋯
2M16055380+2303058	$-40.3^{+0.36}_{-0.42}$	-41.99 ± 0.7	⋯	⋯	$10.83^{+2.61}_{-1.84}$	⋯	⋯
2M16063110−1904576	$-4.95^{+0.23}_{-0.18}$	-7.62 ± 0.51	⋯	⋯	$16.65^{+1.16}_{-1.79}$	⋯	⋯
2M16063390+4054216	$-41.01^{+0.22}_{-0.22}$	446.63 ± 732.5	⋯	⋯	< 10	⋯	⋯
2M16081226+2252548	$14.45^{+0.76}_{-0.49}$	26.98 ± 23.16	⋯	⋯	$24.49^{+2.18}_{-1.84}$	⋯	⋯
2M16090197−2151225	$-6.38^{+0.23}_{-1.14}$	-24.66 ± 0.53	⋯	⋯	$47.77^{+1.17}_{-0.43}$	⋯	⋯
2M16090451−2224523	$-5.24^{+0.88}_{-0.78}$	-8.63 ± 0.41	⋯	⋯	$14.14^{+0.95}_{-1.0}$	⋯	⋯
2M16090568−2245166	$-3.03^{+0.24}_{-0.2}$	525.72 ± 1.62	⋯	⋯	$32.9^{+0.35}_{-0.44}$	⋯	⋯
2M16093019−2059536	$-1.33^{+0.16}_{-0.16}$	-3.32 ± 0.36	-5.08 ± 0.6	Dahm et al. (2012)	$17.95^{+0.13}_{-0.28}$	⋯	⋯
2M16095107−2722418	$-1.53^{+0.22}_{-0.21}$	7.33 ± 0.5	⋯	⋯	$56.1^{+0.93}_{-1.05}$	⋯	⋯
2M16095852−2345186	$-2.44^{+0.16}_{-0.18}$	-7.03 ± 0.36	⋯	⋯	$34.66^{+1.46}_{-0.13}$	⋯	⋯
2M16095990−2155424	$-3.85^{+0.51}_{-0.41}$	-7.97 ± 0.47	⋯	⋯	$22.02^{+0.43}_{-1.55}$	⋯	⋯
2M16100608−2127440	$-5.44^{+0.31}_{-1.32}$	-214.79 ± 1.2	⋯	⋯	$16.51^{+0.5}_{-1.51}$	⋯	⋯
2M16103014−2315167	$-3.86^{+0.25}_{-0.2}$	-5.21 ± 0.96	⋯	⋯	$14.19^{+0.13}_{-0.29}$	⋯	⋯

Table 3.5 (*continued*)

Table 3.5 (*continued*)

APOGEE ID	$\langle$RV$\rangle$[a] (km s^{-1})	ASPCAP RV[b] (km s^{-1})	Lit. RV (km s^{-1})	Lit. RV Ref.	$\langle v \sin i \rangle$[a] (km s^{-1})	Lit. $v \sin i$ (km s^{-1})	Lit. $v \sin i$ Ref.
2M16103040+3954258	$14.24^{+0.12}_{-0.17}$	13.29 ± 0.85	⋯	⋯	$11.0^{+1.12}_{-1.37}$	⋯	⋯
2M16103232−1913085	$-6.21^{+1.34}_{-0.29}$	-17.48 ± 0.91	⋯	⋯	$42.4^{+0.25}_{-0.78}$	⋯	⋯
2M16103232+2249116	$-3.96^{+0.48}_{-0.47}$	-9.54 ± 4.23	⋯	⋯	$11.8^{+1.42}_{-1.91}$	⋯	⋯
2M16104714−2239492	$-7.54^{+0.22}_{-0.18}$	525.76 ± 1.95	⋯	⋯	< 10	⋯	⋯
2M16113837−2307072	$-2.24^{+0.51}_{-0.42}$	-8.72 ± 0.51	⋯	⋯	$36.63^{+0.96}_{-1.09}$	⋯	⋯
2M16114261−2525511	$-4.69^{+0.64}_{-0.66}$	-10.43 ± 0.42	⋯	⋯	$55.35^{+0.99}_{-1.15}$	⋯	⋯
2M16115439−2236491	$-2.51^{+0.76}_{-0.3}$	-2.2 ± 0.58	⋯	⋯	$50.29^{+0.55}_{-1.21}$	⋯	⋯
2M16122703−2013250	$-4.88^{+0.23}_{-0.29}$	-11.8 ± 0.35	⋯	⋯	$30.93^{+0.43}_{-0.12}$	⋯	⋯
2M16124726−1903531	$-7.06^{+0.31}_{-0.24}$	-15.63 ± 0.32	⋯	⋯	$29.03^{+1.06}_{-1.15}$	⋯	⋯
2M16132665−2230348	$-4.73^{+0.22}_{-0.23}$	-7.95 ± 0.38	⋯	⋯	$19.86^{+0.15}_{-1.66}$	⋯	⋯
2M16132809−1924524	$-4.75^{+0.22}_{-0.25}$	-8.5 ± 0.25	⋯	⋯	$23.09^{+1.14}_{-1.4}$	⋯	⋯
2M16134027−2233192	$-6.45^{+0.13}_{-0.13}$	-209.93 ± 1.29	⋯	⋯	$14.11^{+0.21}_{-0.2}$	⋯	⋯
2M16134079−2219459	$-0.81^{+0.23}_{-0.27}$	-3.83 ± 1.06	⋯	⋯	$19.41^{+0.21}_{-0.27}$	⋯	⋯
2M16134264−2301279	$-1.95^{+0.9}_{-0.99}$	-14.35 ± 0.58	⋯	⋯	$59.35^{+0.4}_{-1.69}$	⋯	⋯
2M16143287−2242133	$0.19^{+0.19}_{-0.14}$	-2.61 ± 0.68	⋯	⋯	$18.02^{+0.18}_{-0.36}$	⋯	⋯
2M16172079+4113032	$0.52^{+0.35}_{-0.33}$	-0.64 ± 0.29	⋯	⋯	< 10	⋯	⋯
2M16183317−2517504	$-0.99^{+0.15}_{-0.16}$	-2.53 ± 0.14	⋯	⋯	$16.35^{+1.17}_{-1.36}$	⋯	⋯
2M16195143−2241332	$-4.57^{+0.14}_{-0.19}$	-4.9 ± 0.97	⋯	⋯	$16.97^{+1.2}_{-1.36}$	⋯	⋯
2M16204144−2425491	$1.46^{+0.61}_{-0.32}$	-2.69 ± 0.45	⋯	⋯	$25.43^{+0.15}_{-0.32}$	⋯	⋯
2M16222304−2407108	$-1.93^{+0.52}_{-0.49}$	241.12 ± 1.13	⋯	⋯	$44.48^{+1.12}_{-3.52}$	⋯	⋯
2M16222521−2405139	$-1.23^{+0.32}_{-0.37}$	-7.69 ± 0.49	⋯	⋯	$17.96^{+0.15}_{-0.26}$	⋯	⋯
2M16235155−2317270	$-3.86^{+0.21}_{-0.8}$	20.42 ± 0.67	-7.47 ± 2.45	Dahm et al. (2012)	$52.56^{+0.81}_{-0.84}$	60.94 ± 3.03	Dahm et al. (2012)
2M16265698+3954482	$2.92^{+0.44}_{-0.48}$	112.51 ± 0.73	⋯	⋯	$27.06^{+1.58}_{-1.65}$	⋯	⋯
2M16271693+3514132	$-12.09^{+0.72}_{-0.7}$	-15.89 ± 6.51	-10.37 ± 6.6	Kiman et al. (2019)	$21.9^{+1.26}_{-1.73}$	⋯	⋯
2M16271825+3538347	$-8.84^{+0.27}_{-0.38}$	567.04 ± 0.65	⋯	⋯	< 10	⋯	⋯
2M16281707+1334204	$-36.56^{+0.16}_{-0.13}$	-38.22 ± 0.35	⋯	⋯	$15.81^{+0.98}_{-1.06}$	⋯	⋯
2M16311879+4051516	$-21.75^{+0.17}_{-0.16}$	-22.82 ± 0.25	2.61 ± 4.43	Terrien et al. (2015)	$14.79^{+1.79}_{-1.59}$	7.1 ± 1.5	Reiners et al. (2018)
2M16360984+4000243	$-11.5^{+0.24}_{-0.23}$	-14.48 ± 0.36	⋯	⋯	< 10	⋯	⋯
2M16402068+6736046	$-17.42^{+0.08}_{-0.1}$	-18.96 ± 0.34	-15.0 ± 5.0	Newton et al. (2014)	$16.04^{+0.09}_{-0.16}$	⋯	⋯
2M16463154+3434554	$-52.64^{+0.13}_{-0.12}$	-56.32 ± 0.36	⋯	⋯	< 10	⋯	⋯
2M16485878+3005366	$-44.79^{+0.33}_{-0.34}$	-49.35 ± 0.64	⋯	⋯	$14.02^{+1.72}_{-0.87}$	⋯	⋯
2M16572919+2448509	$-58.12^{+0.51}_{-0.52}$	524.1 ± 0.6	⋯	⋯	$15.56^{+1.5}_{-1.2}$	⋯	⋯
2M19005974−3647109	$1.55^{+0.24}_{-0.25}$	-1.51 ± 1.09	⋯	⋯	$20.09^{+1.07}_{-1.39}$	⋯	⋯
2M19241634+7533121	$-18.62^{+0.17}_{-0.16}$	-19.93 ± 0.31	⋯	⋯	< 10	⋯	⋯
2M19544358+1801581	$-18.62^{+0.26}_{-0.26}$	365.56 ± 244.7	⋯	⋯	< 10	⋯	⋯

Table 3.5 (*continued*)

Table 3.5 (*continued*)

APOGEE ID	$\langle$RV$\rangle$[a] (km s^{-1})	ASPCAP RV[b] (km s^{-1})	Lit. RV (km s^{-1})	Lit. RV Ref.	$\langle v \sin i \rangle$[a] (km s^{-1})	Lit. $v \sin i$ (km s^{-1})	Lit. $v \sin i$ Ref.
2M20353517−0608285	$8.16^{+0.33}_{-0.25}$	6.06 ± 0.33	···	···	< 10	···	···
2M20491376+3216514	$11.5^{+0.31}_{-0.35}$	9.39 ± 0.91	···	···	$12.2^{+1.04}_{-1.23}$	10 ± 1.6	Gilhool et al. (2018)
2M21272531+5553150	$-12.23^{+0.21}_{-0.24}$	-224.75 ± 1086.03	···	···	$17.29^{+1.12}_{-1.2}$	···	···
2M21381698+5257188	$-7.52^{+0.21}_{-0.19}$	111.53 ± 0.54	···	···	$40.59^{+1.69}_{-1.45}$	···	···
2M22021125−1109461	$-7.72^{+0.37}_{-0.4}$	575.21 ± 1.36	···	···	$21.34^{+1.14}_{-1.38}$	···	···
2M22400144+0532162	$-10.05^{+0.29}_{-0.3}$	-12.35 ± 1.21	···	···	$17.77^{+0.98}_{-1.08}$	···	···
2M22551142+1442456	$-14.08^{+1.01}_{-0.76}$	-16.84 ± 0.51	···	···	$56.68^{+1.67}_{-1.48}$	···	···
2M23200703+1150071	$-54.47^{+0.36}_{-0.34}$	-57.79 ± 0.81	···	···	< 10	···	···

[a] My Weighted average measurements over all epochs.

[b] RV from DR17 ASPCAP Pipeline.

Note – Measurements from individual spectra over individual or multiple epochs are combined usinginverse uncertainty weighting (weight = $1/(\sigma^2_{\rm upper} + \sigma^2_{\rm lower})$); upper and lower uncertainties are also combined using inverse uncertainty-squared weighting. In cases where individual spectra have S/N < 10, spectral data are combined first, then modeled.

Table 3.6: Radial Velocities and Heliocentric Space Motions

APOGEE ID	SpT	Adpoted RV (km s^{-1})	U (km s^{-1})	V (km s^{-1})	W (km s^{-1})	P[TD]/P[D][a]	Population[a]	BANYAN Σ[c]
2M00312793+6139333	M7.0	$-34.44^{+0.19}_{-0.2}$	-27.4 ± 0.2	-50.0 ± 0.2	29.8 ± 0.1	0.18	D/TD	99.9% field
2M00452143+1634446	L2.0	$3.71^{+0.4}_{-0.56}$	-10.8 ± 0.2	-1.5 ± 0.3	1.5 ± 0.4	0.01	D	99.7% ARG
2M01120002+1502170	M5.5	$-44.31^{+0.28}_{-0.27}$	28.7 ± 0.1	-50.7 ± 0.2	13.0 ± 0.2	0.06	D	99.9% field
2M01154176+0059317	M6.0	$10.78^{+0.78}_{-1.18}$	-35.8 ± 0.6	-7.4 ± 0.4	5.8 ± 1.0	0.01	D	99.9% field
2M01215816+0101007	M6.5	$10.28^{+0.11}_{-0.13}$	-9.0 ± 0.1	-12.0 ± 0.1	-5.0 ± 0.1	0.01	D	99.9% field
2M01243124−0027556	M7.0	$-3.88^{+0.17}_{-0.16}$	17.4 ± 0.1	-16.1 ± 0.2	-0.4 ± 0.2	0.01	D	99.9% field
2M01514363+0046188	M7.0	$14.44^{+0.65}_{-0.67}$	-15.3 ± 0.3	5.4 ± 0.2	2.8 ± 0.6	0.01	D	98.3% field
2M02500239−0808417	M5.5	$25.61^{+0.64}_{-0.66}$	-48.5 ± 0.4	-23.0 ± 0.0	18.1 ± 0.6	0.02	D	99.9% field
2M03040207+0045512	M6.0	$29.94^{+0.32}_{-0.31}$	-31.5 ± 0.2	-6.9 ± 0.0	4.7 ± 0.2	0.01	D	77.1% HYA
2M03282839+3116273	M6.5	$15.41^{+0.77}_{-0.91}$	-6.2 ± 0.8	2.2 ± 1.1	-3.6 ± 0.6	0.01	D	99.9% field
2M03293053+3127280[e]	M6.5	$15.77^{+0.48}_{-0.54}$	-6.4 ± 0.5	3.0 ± 0.7	-3.4 ± 0.4	0.01	D	99.9% field
2M03505737+1818069	M9.0	$6.05^{+0.16}_{-0.13}$	-5.9 ± 0.2	-12.5 ± 0.1	19.9 ± 0.1	0.01	D	99.9% field
2M04110642+1247481	M6.0	$39.28^{+0.19}_{-0.23}$	-32.5 ± 0.2	-7.4 ± 0.1	6.1 ± 0.1	0.01	D	99.4% HYA
2M04185115+2814332	M7.5	$21.13^{+0.23}_{-0.2}$	-9.9 ± 0.2	1.6 ± 0.4	-4.8 ± 0.2	0.01	D	98.0% TAU
2M04204796+5624202	M8.0	$-29.54^{+0.27}_{-0.24}$	3.5 ± 0.2	-64.0 ± 0.2	46.9 ± 0.2	4.32	D/TD	99.9% field
2M04214435+2024105	M7.0	$40.78^{+0.42}_{-0.45}$	-33.3 ± 0.4	-6.3 ± 0.1	5.3 ± 0.2	0.01	D	99.9% HYA
2M04214955+1929086	M7.0	$39.43^{+0.19}_{-0.17}$	-32.2 ± 0.2	-6.9 ± 0.3	6.5 ± 0.2	0.01	D	99.9% HYA
2M04262939+2624137	M6.0	$20.01^{+0.37}_{-0.47}$	-9.6 ± 0.4	-0.3 ± 0.4	-0.6 ± 0.2	0.01	D	70.8% TAU
2M04294568+2630468	M7.5	$18.13^{+0.22}_{-0.21}$	-6.7 ± 0.2	2.4 ± 0.3	-2.2 ± 0.1	0.01	D	99.8% TAU
2M04330945+2246487	M7.0	$19.6^{+0.37}_{-0.39}$	-8.5 ± 0.4	-4.3 ± 1.0	-0.2 ± 0.3	0.01	D	17.1% TAU
2M04351354+2008014	M7.5	$40.01^{+0.28}_{-0.21}$	-31.2 ± 0.3	-7.1 ± 0.1	5.5 ± 0.1	0.01	D	99.9% HYA
2M04440164+1621324	M6.0	$21.82^{+0.19}_{-0.21}$	-8.4 ± 0.2	-3.8 ± 0.3	-1.3 ± 0.1	0.01	D	86.9% TAU
2M04464498+2436404	M7.0	$42.22^{+0.46}_{-0.34}$	-33.2 ± 0.4	-6.7 ± 0.1	5.1 ± 0.1	0.01	D	99.2% HYA
2M04552333+3027366	M6.0	$17.46^{+0.19}_{-0.15}$	-7.0 ± 0.2	-2.7 ± 0.4	-4.1 ± 0.2	0.01	D	34.2% TAU
2M04565141+2939310	M7.0	$17.91^{+0.43}_{-0.37}$	-7.2 ± 0.4	-1.8 ± 0.3	-3.4 ± 0.2	0.01	D	87.2% TAU
2M05350162−0521489	L0.0	$25.07^{+0.31}_{-0.62}$	-9.6 ± 44.4	0.8 ± 72.5	-1.1 ± 80.0	0.01	D	99.9% field
2M05392474+4038437	M8.0	$-5.42^{+0.23}_{-0.24}$	6.4 ± 0.2	-44.5 ± 0.1	12.3 ± 0.0	0.03	D	99.9% field
2M05402570+2448090	M7.0	$23.07^{+0.63}_{-0.93}$	-10.7 ± 0.9	-7.1 ± 0.6	0.6 ± 0.4	0.01	D	54.7% ARG, 43.2% CARN[d]
2M06154934−0100415	L2.5	$-19.69^{+0.19}_{-0.2}$	33.4 ± 0.2	7.7 ± 0.1	25.8 ± 0.1	0.02	D	99.9% field
2M06521977−2534505	L0.0	$14.9^{+0.21}_{-0.22}$	-7.0 ± 0.1	9.9 ± 0.2	-8.8 ± 0.0	0.01	D	99.9% field
2M07025026−6102482	M6.5	$21.31^{+0.14}_{-0.13}$	-22.9 ± 0.1	-29.4 ± 0.2	50.8 ± 0.2	0.6	D/TD	99.9% field
2M07140394+3702459	M8.0	$35.34^{+0.24}_{-0.23}$	-25.7 ± 0.2	1.2 ± 0.0	9.2 ± 0.1	0.01	D	99.9% field
2M07464256+2000321	L0.0	$52.78^{+0.11}_{-0.1}$	-44.2 ± 0.1	-1.9 ± 0.1	6.5 ± 0.2	0.01	D	99.9% field
2M07475737+6653337	M7.0	$7.45^{+0.7}_{-0.82}$	8.4 ± 0.6	13.7 ± 0.4	16.8 ± 0.4	0.01	D	99.9% field

Table 3.6 (*continued*)

Table 3.6 (*continued*)

APOGEE ID	SpT	Adpoted RV (km s^{-1})	U (km s^{-1})	V (km s^{-1})	W (km s^{-1})	P[TD]/P[D][a]	Population[a]	BANYAN Σ[c]
2M07552256+2755318	M5.5	$-3.86^{+0.28}_{-0.24}$	-5.6 ± 0.2	18.5 ± 0.1	-32.9 ± 0.2	0.04	D	99.9% field
2M07564895+6649595	M7.5	$0.19^{+0.41}_{-0.42}$	5.3 ± 0.3	-32.2 ± 0.3	37.0 ± 0.3	0.09	D	99.9% field
2M08072607+3213101	M8.0	$34.41^{+0.22}_{-0.25}$	-34.9 ± 0.2	-8.4 ± 0.0	-9.5 ± 0.1	0.01	D	99.9% field
2M08080189+3157054	M7.5	$30.61^{+0.32}_{-0.33}$	-16.2 ± 0.3	-8.2 ± 0.1	15.7 ± 0.2	0.01	D	99.9% field
2M08092892+3235226	M4.0	$-6.66^{+0.58}_{-0.54}$	11.0 ± 0.5	15.9 ± 0.2	-5.4 ± 0.4	0.01	D	99.9% field
2M08144389+4650522	M6.0	$24.39^{+0.48}_{-0.3}$	-19.5 ± 0.4	-4.8 ± 0.1	8.7 ± 0.3	0.01	D	99.9% field
2M08185804+2333522	M7.0	$35.74^{+0.29}_{-0.29}$	-27.5 ± 0.2	-27.4 ± 0.1	-8.5 ± 0.2	0.01	D	99.9% field
2M08211639+5658358	M6.5	$7.17^{+0.22}_{-0.27}$	6.3 ± 0.2	0.8 ± 0.2	18.8 ± 0.2	0.01	D	99.9% field
2M08294949+2646348[f]	M6.5	$10.69^{+0.32}_{-0.31}$	-7.0 ± 0.3	2.0 ± 0.1	-4.8 ± 0.2	0.01	D	99.9% field
2M08440350+0434356	M9.0	$66.68^{+0.5}_{-0.49}$	-74.6 ± 0.4	4.3 ± 0.3	19.1 ± 0.2	0.05	D	99.9% field
2M08490052+0220155	M7.0	$22.37^{+0.37}_{-0.64}$	-4.4 ± 0.4	-12.9 ± 0.4	0.2 ± 0.3	0.01	D	99.9% field
2M08501918+1056436	M5.0	$31.45^{+0.43}_{-0.44}$	-26.6 ± 0.3	-12.0 ± 0.2	-5.9 ± 0.2	0.01	D	99.9% field
2M08522464+2540591	M7.0	$29.56^{+0.21}_{-0.2}$	-34.4 ± 0.3	-7.6 ± 0.2	-9.3 ± 0.5	0.01	D	99.9% field
2M09020690+0033195	M6.0	$42.63^{+0.25}_{-0.22}$	-40.5 ± 0.2	-21.9 ± 0.2	-12.5 ± 0.1	0.01	D	99.9% field
2M09130162+3037583	M7.0	$51.79^{+0.55}_{-0.51}$	-38.0 ± 0.4	-58.0 ± 0.4	12.2 ± 0.4	0.15	D/TD	99.9% field
2M09373349+5534057	M6.0	$0.68^{+0.45}_{-0.45}$	-5.6 ± 0.4	3.2 ± 0.2	-4.2 ± 0.4	0.01	D	99.9% field
2M09381783+0132490	M5.0	$-16.8^{+1.51}_{-1.04}$	23.4 ± 0.7	-12.1 ± 1.0	-36.7 ± 1.0	0.05	D	99.9% field
2M09442625+3521233	M6.0	$51.2^{+0.87}_{-0.78}$	-59.6 ± 0.6	15.2 ± 0.1	15.5 ± 0.7	0.03	D	99.9% field
2M09453388+5458511	M7.0	$-3.67^{+0.68}_{-0.63}$	8.7 ± 0.4	-1.0 ± 0.2	4.4 ± 0.5	0.01	D	99.9% field
2M09472006−0020093	M7.0	$15.0^{+0.08}_{-0.09}$	-19.0 ± 0.0	4.1 ± 0.1	1.9 ± 0.1	0.01	D	99.9% field
2M09474477+0224327	M8.0	$8.76^{+0.2}_{-0.26}$	6.2 ± 0.1	-14.9 ± 0.2	-9.1 ± 0.2	0.01	D	98.6% ABDMG
2M09522188−1924319	M7.0	$-17.11^{+0.91}_{-0.93}$	15.4 ± 0.2	19.4 ± 0.8	-15.0 ± 0.4	0.01	D	99.9% field
2M09524622+0620410	M7.0	$12.8^{+0.43}_{-0.45}$	-2.1 ± 0.2	-7.3 ± 0.3	0.7 ± 0.3	0.01	D	98.9% field
2M09560888+0134128	M5.0	$21.12^{+0.6}_{-0.53}$	-33.4 ± 0.3	-6.8 ± 0.4	-7.1 ± 0.4	0.01	D	99.9% field
2M10031918−0105079	M7.0	$23.99^{+0.27}_{-0.26}$	-37.2 ± 0.1	-7.3 ± 0.2	-3.1 ± 0.2	0.01	D	99.9% field
2M10134315+0000406	M6.0	$3.95^{+0.35}_{-0.35}$	78.6 ± 0.2	-17.0 ± 0.2	19.3 ± 0.2	0.07	D	99.9% field
2M10225090+0032169	M8.0	$34.04^{+6.01}_{-5.87}$	6.0 ± 1.9	-39.4 ± 3.8	7.4 ± 4.3	0.02	D	99.9% field
2M10240997+1815533	M7.0	$8.22^{+0.09}_{-0.08}$	-9.8 ± 0.2	-7.7 ± 0.2	-2.9 ± 0.2	0.01	D	10% CARN, 90% field
2M10323297+0630074	M6.0	$13.22^{+0.15}_{-0.14}$	-3.0 ± 0.0	-14.2 ± 0.1	0.1 ± 0.1	0.01	D	99.9% field
2M10372897+3011117	M8.0	$7.97^{+0.17}_{-0.19}$	-42.2 ± 0.1	-60.0 ± 0.1	-25.3 ± 0.2	0.43	D/TD	99.9% field
2M10541102−8505023	M8.0	$-10.8^{+0.82}_{-1.13}$	-31.9 ± 0.5	-3.6 ± 0.9	16.1 ± 0.4	0.01	D	99.9% field
2M10543366+0503467	L1.0	$-20.17^{+0.1}_{-0.11}$	62.2 ± 0.7	-6.8 ± 0.5	-15.2 ± 0.1	0.02	D	99.9% field
2M10570380+2217203	M6.0	$11.68^{+0.1}_{-0.1}$	-3.5 ± 0.0	-11.8 ± 0.0	7.3 ± 0.1	0.01	D	99.9% field
2M11194647+0820356	M8.0	$-44.98^{+0.18}_{-0.17}$	83.3 ± 0.2	11.4 ± 0.1	-30.6 ± 0.2	0.21	D/TD	99.9% field
2M11203609+0704135	M6.0	$-14.41^{+0.57}_{-0.6}$	39.3 ± 0.1	-21.4 ± 0.3	-22.3 ± 0.5	0.02	D	99.9% field

Table 3.6 (*continued*)

Table 3.6 (*continued*)

APOGEE ID	SpT	Adpoted RV (km s^{-1})	U (km s^{-1})	V (km s^{-1})	W (km s^{-1})	P[TD]/P[D][a]	Population[a]	BANYAN Σ[c]
2M11210854+2126274	M4.5	$-0.3^{+0.16}_{-0.16}$	-14.6 ± 0.1	1.4 ± 0.0	-3.3 ± 0.2	0.01	D	99.9% field
2M11232934+0154040	M7.0	$-0.21^{+0.62}_{-0.59}$	-10.8 ± 0.2	5.5 ± 0.3	0.1 ± 0.5	0.01	D	99.6% field
2M12080810+3520281	M7.0	$29.17^{+0.56}_{-0.54}$	-68.3 ± 0.2	-37.1 ± 0.2	22.2 ± 0.6	0.12	D/TD	99.9% field
2M12153877+5205050	M4.5	$-4.75^{+0.2}_{-0.23}$	1.8 ± 3.8	5.9 ± 2.2	0.9 ± 1.0	0.01	D	99.9% field
2M12201166+3315379	M8.0	$11.16^{+0.26}_{-0.24}$	45.7 ± 0.2	-10.8 ± 0.1	24.7 ± 0.3	0.03	D	99.9% field
2M12205439+2525568	M6.0	$14.81^{+0.22}_{-0.22}$	-14.3 ± 0.7	-2.1 ± 0.4	18.7 ± 0.2	0.01	D	99.9% field
2M12215013+4632447	M8.0	$-10.44^{+0.27}_{-0.22}$	24.6 ± 2.3	12.3 ± 0.7	-0.2 ± 0.6	0.01	D	99.9% field
2M12235346+2534559	M6.0	$7.03^{+0.78}_{-0.56}$	-7.5 ± 0.4	44.2 ± 0.6	15.4 ± 0.8	0.06	D	99.9% field
2M12252076+2517082	M7.0	$7.24^{+0.71}_{-0.81}$	2.8 ± 0.8	10.0 ± 0.3	13.8 ± 0.8	0.01	D	99.9% field
2M12270429+2541012	M6.5	$2.63^{+0.59}_{-0.61}$	8.2 ± 0.1	6.5 ± 0.1	9.3 ± 0.6	0.01	D	99.7% CBER
2M12315462+5130389	M6.5	$8.92^{+0.26}_{-0.14}$	-33.6 ± 0.2	-6.7 ± 0.1	10.4 ± 0.2	0.01	D	99.9% field
2M12493960+5255340	M7.5	$-56.77^{+0.43}_{-0.36}$	18.4 ± 0.1	-59.4 ± 0.3	-25.0 ± 0.4	0.26	D/TD	99.9% field
2M12522354+2528469	M7.0	$9.43^{+0.28}_{-0.24}$	19.1 ± 0.0	-22.3 ± 0.1	15.8 ± 0.3	0.01	D	99.9% field
2M13004379+3557591	M6.0	$-24.58^{+0.23}_{-0.26}$	-35.3 ± 0.1	-25.2 ± 0.1	-14.7 ± 0.3	0.02	D	99.9% field
2M13022083+3227103	M6.0	$6.77^{+0.33}_{-0.33}$	-17.0 ± 0.0	2.2 ± 0.0	14.6 ± 0.3	0.01	D	99.9% field
2M13034100+2414020	M7.0	$-9.3^{+0.25}_{-0.27}$	-39.2 ± 0.1	-7.6 ± 0.1	1.0 ± 0.3	0.01	D	99.9% field
2M13065141+7056376	M7.0	$15.29^{+0.3}_{-0.42}$	55.3 ± 0.3	33.3 ± 0.3	33.1 ± 0.3	0.23	D/TD	99.9% field
2M13192677+1301119	M5.0	$6.27^{+0.11}_{-0.1}$	-12.5 ± 0.1	-52.1 ± 0.2	10.2 ± 0.1	0.05	D	99.9% field
2M13202007+7213140	M7.5	$-27.34^{+0.52}_{-0.54}$	23.0 ± 0.2	-6.4 ± 0.3	-9.3 ± 0.4	0.01	D	99.9% field
2M13232423+5132272	M6.0	$-5.41^{+0.52}_{-0.49}$	-21.0 ± 0.1	-2.9 ± 0.2	2.5 ± 0.5	0.01	D	99.9% field
2M13342918+3303043	M7.0	$-18.03^{+0.3}_{-0.27}$	-55.1 ± 0.1	-47.8 ± 0.1	4.6 ± 0.3	0.08	D	99.9% field
2M13430646+0038442	M4.0	$-11.91^{+0.72}_{-0.72}$	-14.7 ± 0.5	-14.2 ± 0.5	-1.2 ± 0.6	0.01	D	99.9% field
2M13482307+3321508	M4.5	$-19.22^{+3.6}_{-4.33}$	13.7 ± 0.5	-22.5 ± 1.1	-5.2 ± 4.4	0.01	D	99.9% field
2M13500476+3207596	M4.5	$-5.83^{+0.53}_{-0.61}$	38.1 ± 0.2	-13.0 ± 0.2	3.0 ± 0.6	0.01	D	99.9% field
2M13564148+4342587	M8.0	$-19.51^{+0.62}_{-0.57}$	-25.7 ± 0.5	-20.5 ± 0.4	-0.7 ± 0.6	0.01	D	99.9% field
2M13573443+5408223	M5.0	$-43.22^{+0.72}_{-0.98}$	-20.4 ± 0.2	-45.9 ± 0.5	-14.4 ± 0.8	0.04	D	99.9% field
2M14005977+3226109	M7.0	$-17.9^{+0.74}_{-0.82}$	-38.7 ± 0.4	-23.1 ± 0.3	4.9 ± 0.8	0.01	D	99.9% field
2M14081562+5236281	M4.5	$-43.49^{+0.14}_{-0.15}$	61.2 ± 0.1	-35.9 ± 0.1	-11.7 ± 0.1	0.05	D	99.9% field
2M14093200+4138080	M6.0	$-10.96^{+0.22}_{-0.15}$	-13.3 ± 0.0	-2.2 ± 0.1	2.8 ± 0.2	0.01	D	99.6% ARG[d]
2M14320849+0811313	M6.0	$-21.3^{+0.13}_{-0.14}$	-18.8 ± 0.1	-6.1 ± 0.0	-0.0 ± 0.1	0.01	D	99.9% field
2M14340140+5039480	M7.0	$-6.39^{+0.25}_{-0.27}$	-10.1 ± 0.1	-0.8 ± 0.1	7.5 ± 0.2	0.01	D	55.9% ARG, 44.1% field
2M14402293+1339230	M7.0	$-3.49^{+0.24}_{-0.24}$	21.2 ± 0.1	-27.3 ± 0.1	1.8 ± 0.2	0.01	D	99.9% field
2M14432796+0316543	M7.0	$-38.45^{+0.27}_{-0.29}$	-31.1 ± 0.2	-5.8 ± 0.1	-10.6 ± 0.2	0.01	D	99.9% field
2M14553384+1545593	M4.5	$19.3^{+0.16}_{-0.18}$	48.1 ± 1.0	-20.3 ± 1.2	14.6 ± 0.4	0.02	D	99.9% field
2M14554964+0321420	M4.5	$-39.92^{+0.16}_{-0.09}$	10.8 ± 0.1	-56.6 ± 0.1	-43.5 ± 0.1	1.29	D/TD	99.9% field

Table 3.6 (*continued*)

Table 3.6 (*continued*)

APOGEE ID	SpT	Adpoted RV (km s^{-1})	U (km s^{-1})	V (km s^{-1})	W (km s^{-1})	P[TD]/P[D][a]	Population[a]	BANYAN Σ[c]
2M15010818+2250020	M8.5	$6.53^{+0.69}_{-0.71}$	14.9 ± 0.3	10.2 ± 0.2	13.5 ± 0.6	0.01	D	99.9% field
2M15041028+0923232	M7.5	$-53.33^{+0.29}_{-0.29}$	-63.2 ± 0.3	-22.5 ± 0.2	-1.3 ± 0.3	0.02	D	99.9% field
2M15042797+0942464	M6.0	$-35.61^{+1.26}_{-0.77}$	-50.8 ± 0.9	-21.1 ± 0.4	11.6 ± 1.1	0.02	D	99.9% field
2M15115124+3033065	M5.0	$-61.43^{+0.13}_{-0.14}$	-12.7 ± 0.0	-112.1 ± 0.3	0.2 ± 0.2	243.5	TD	99.9% field
2M15175638+0656388	M4.0	$-19.8^{+0.34}_{-0.33}$	-2.2 ± 0.2	-7.0 ± 0.1	-4.9 ± 0.3	0.01	D	99.9% field
2M15210103+5053230	M7.5	$2.43^{+0.18}_{-0.13}$	24.7 ± 0.0	10.5 ± 0.1	10.4 ± 0.1	0.01	D	99.9% field
2M15242475+2925318	M7.5	$-15.15^{+0.03}_{-0.06}$	33.7 ± 0.0	-20.7 ± 0.0	-5.6 ± 0.0	0.01	D	99.9% field
2M15512179+2931062	M7.0	$26.03^{+0.22}_{-0.23}$	45.2 ± 0.1	-11.6 ± 0.1	36.4 ± 0.2	0.08	D	99.9% field
2M15555600−2045187	M6.5	$-4.1^{+0.47}_{-0.47}$	6.4 ± 0.4	-4.9 ± 0.4	1.5 ± 0.2	0.01	D	99.9% USCO
2M15560104−2338081	M6.5	$1.51^{+0.28}_{-0.23}$	10.2 ± 0.3	-6.7 ± 0.3	4.3 ± 0.1	0.01	D	93.5% USCO
2M15560497−2106461	M7.0	$-4.14^{+1.35}_{-0.55}$	6.3 ± 1.2	-4.9 ± 0.6	1.4 ± 0.6	0.01	D	99.9% USCO
2M15574011+2952379	M4.5	$1.06^{+0.19}_{-0.18}$	32.8 ± 0.1	-8.5 ± 0.1	9.5 ± 0.2	0.01	D	99.9% field
2M15592591−2305081	M6.0	$-3.31^{+0.11}_{-0.11}$	7.2 ± 0.1	-4.7 ± 0.2	0.4 ± 0.1	0.01	D	99.9% USCO
2M15594439−1928191	M7.5	$-2.59^{+0.35}_{-0.24}$	8.8 ± 0.3	-4.5 ± 0.7	1.2 ± 0.3	0.01	D	99.8% USCO
2M16001944−2256287	M8.0	$-4.27^{+0.67}_{-0.53}$	6.6 ± 0.6	-4.7 ± 0.8	-0.4 ± 0.4	0.01	D	99.9% USCO
2M16002844−2209228	M6.0	$-3.66^{+0.66}_{-0.78}$	-2.9 ± 0.7	-20.8 ± 0.6	17.8 ± 0.4	0.01	D	99.9% field
2M16003023−2334457	M6.0	$-3.74^{+0.51}_{-0.36}$	6.5 ± 0.5	-5.1 ± 0.2	0.4 ± 0.2	0.01	D	99.9% USCO
2M16014955−2351082	M6.0	$-3.54^{+0.14}_{-0.14}$	6.8 ± 0.1	-4.4 ± 0.3	0.5 ± 0.1	0.01	D	99.9% USCO
2M16022585−2414081	M7.0	$-2.1^{+0.36}_{-0.27}$	7.8 ± 0.4	-4.1 ± 0.6	1.8 ± 0.3	0.01	D	99.8% USCO
2M16044026−2254323	M6.0	$-1.17^{+0.44}_{-0.54}$	8.8 ± 0.5	-5.9 ± 0.6	2.4 ± 0.3	0.01	D	99.8% USCO
2M16045199−2224108	M8.0	$-1.06^{+0.78}_{-1.29}$	10.0 ± 1.2	-5.4 ± 0.6	0.4 ± 0.5	0.01	D	99.7% USCO
2M16055178−2206212	M6.0	$-3.84^{+0.28}_{-0.22}$	7.2 ± 0.3	-5.1 ± 0.4	0.1 ± 0.2	0.01	D	99.9% USCO
2M16055380+2303058	M7.0	$-40.3^{+0.36}_{-0.42}$	-14.2 ± 0.2	0.4 ± 0.2	-22.6 ± 0.3	0.01	D	99.9% field
2M16063110−1904576	M6.0	$-4.95^{+0.23}_{-0.18}$	7.5 ± 0.2	-3.7 ± 0.4	-0.7 ± 0.2	0.01	D	99.9% USCO
2M16063390+4054216	M6.0	$-41.01^{+0.22}_{-0.22}$	-30.7 ± 0.1	-41.8 ± 0.1	12.2 ± 0.2	0.03	D	99.9% field
2M16081226+2252548	M5.5	$14.45^{+0.76}_{-0.49}$	35.5 ± 0.4	20.7 ± 0.3	3.6 ± 0.6	0.01	D	99.9% field
2M16090197−2151225	M6.0	$-6.38^{+0.23}_{-1.14}$	5.0 ± 1.0	-3.4 ± 0.4	-0.2 ± 0.4	0.01	D	99.9% USCO
2M16090451−2224523	M7.0	$-5.24^{+0.88}_{-0.78}$	6.2 ± 0.8	-3.8 ± 0.4	-0.7 ± 0.4	0.01	D	99.9% USCO
2M16090568−2245166	M8.0	$-3.03^{+0.24}_{-0.2}$	8.1 ± 0.3	-3.9 ± 1.4	0.2 ± 0.6	0.01	D	99.9% USCO
2M16093019−2059536	M6.0	$-1.33^{+0.16}_{-0.16}$	10.7 ± 0.2	-2.3 ± 0.3	0.4 ± 0.2	0.01	D	99.8% USCO
2M16095107−2722418	M6.0	$-1.53^{+0.22}_{-0.21}$	7.6 ± 0.2	-6.5 ± 0.4	0.9 ± 0.2	0.01	D	98.8% USCO
2M16095852−2345186	M6.5	$-2.44^{+0.16}_{-0.18}$	8.3 ± 0.2	-3.8 ± 0.3	0.8 ± 0.2	0.01	D	99.9% USCO
2M16095990−2155424	M6.5	$-3.85^{+0.51}_{-0.41}$	7.5 ± 0.5	-4.1 ± 0.5	0.2 ± 0.3	0.01	D	99.9% USCO
2M16100608−2127440	M8.5	$-5.44^{+0.31}_{-1.32}$	6.2 ± 1.2	-3.2 ± 0.9	-0.2 ± 0.6	0.01	D	99.9% USCO
2M16103014−2315167	M7.5	$-3.86^{+0.25}_{-0.2}$	7.2 ± 0.2	-4.3 ± 0.6	-0.2 ± 0.3	0.01	D	99.9% USCO

Table 3.6 (*continued*)

Table 3.6 (*continued*)

APOGEE ID	SpT	Adpoted RV (km s^{-1})	U (km s^{-1})	V (km s^{-1})	W (km s^{-1})	P[TD]/P[D][a]	Population[a]	BANYAN Σ[c]
2M16103040+3954258	M5.0	$14.24^{+0.12}_{-0.17}$	79.2 ± 20.2	10.4 ± 3.4	-0.0 ± 5.6	0.04	D	99.9% field
2M16103232−1913085	M8.5	$-6.21^{+1.34}_{-0.29}$	6.8 ± 1.2	-3.2 ± 0.6	-1.9 ± 0.6	0.01	D	99.8% USCO
2M16103232+2249116	M7.0	$-3.96^{+0.48}_{-0.47}$	5.4 ± 0.3	20.5 ± 0.2	0.8 ± 0.3	0.01	D	99.9% field
2M16104714−2239492	M9.0	$-7.54^{+0.22}_{-0.18}$	4.1 ± 0.3	-2.7 ± 1.2	-1.3 ± 0.6	0.01	D	99.9% USCO
2M16113837−2307072	M6.0	$-2.24^{+0.51}_{-0.42}$	8.4 ± 0.5	-5.6 ± 0.4	1.1 ± 0.2	0.01	D	99.9% USCO
2M16114261−2525511	M7.0	$-4.69^{+0.64}_{-0.66}$	6.1 ± 0.6	-3.8 ± 0.2	-1.1 ± 0.2	0.01	D	99.9% USCO
2M16115439−2236491	M6.0	$-2.51^{+0.76}_{-0.3}$	8.2 ± 0.7	-3.1 ± 0.6	2.1 ± 0.4	0.01	D	99.9% USCO
2M16122703−2013250	M6.0	$-4.88^{+0.23}_{-0.29}$	7.1 ± 0.3	-2.8 ± 0.2	0.4 ± 0.1	0.01	D	99.9% USCO
2M16124726−1903531	M6.0	$-7.06^{+0.31}_{-0.24}$	6.0 ± 0.3	-3.0 ± 0.2	-2.0 ± 0.2	0.01	D	99.9% USCO
2M16132665−2230348	M6.0	$-4.73^{+0.22}_{-0.23}$	7.0 ± 0.2	-4.3 ± 0.3	-1.1 ± 0.2	0.01	D	99.9% USCO
2M16132809−1924524	M6.0	$-4.75^{+0.22}_{-0.25}$	7.9 ± 0.2	-2.6 ± 0.2	-0.7 ± 0.1	0.01	D	99.9% USCO
2M16134027−2233192	M6.5	$-6.45^{+0.13}_{-0.13}$	5.2 ± 0.1	-4.0 ± 0.3	-1.4 ± 0.2	0.01	D	99.9% USCO
2M16134079−2219459	M7.5	$-0.81^{+0.23}_{-0.27}$	10.7 ± 0.3	-4.8 ± 1.0	0.1 ± 0.5	0.01	D	99.7% USCO
2M16134264−2301279	M6.0	$-1.95^{+0.9}_{-0.99}$	9.1 ± 0.9	-5.2 ± 0.4	0.5 ± 0.4	0.01	D	99.8% USCO
2M16143287−2242133	M6.5	$0.19^{+0.19}_{-0.14}$	11.7 ± 0.2	-5.3 ± 0.5	-0.0 ± 0.3	0.01	D	99.2% USCO
2M16172079+4113032	M5.0	$0.52^{+0.35}_{-0.33}$	30.2 ± 0.1	-16.2 ± 0.2	25.3 ± 0.2	0.02	D	99.9% field
2M16183317−2517504	M6.0	$-0.99^{+0.15}_{-0.16}$	8.6 ± 0.2	-8.2 ± 0.6	1.9 ± 0.2	0.01	D	70.7% USCO
2M16195143−2241332	M6.5	$-4.57^{+0.14}_{-0.19}$	7.1 ± 0.2	-2.7 ± 0.7	-0.3 ± 0.3	0.01	D	99.9% USCO
2M16204144−2425491	M7.5	$1.46^{+0.61}_{-0.32}$	11.8 ± 0.6	-5.3 ± 0.8	2.3 ± 0.4	0.01	D	89.6% USCO, 9.5% UCL
2M16222304−2407108	M6.0	$-1.93^{+0.52}_{-0.49}$	8.0 ± 0.6	-5.6 ± 2.0	3.3 ± 0.7	0.01	D	97.5% USCO
2M16222521−2405139	M9.0	$-1.23^{+0.32}_{-0.37}$	8.5 ± 0.4	-5.6 ± 0.7	4.1 ± 0.2	0.01	D	89.6% USCO, 9.5% UCL
2M16235155−2317270	M8.0	$-3.86^{+0.21}_{-0.8}$	8.1 ± 0.8	-4.3 ± 0.4	-1.7 ± 0.3	0.01	D	99.6% USCO
2M16265698+3954482	M7.5	$2.92^{+0.44}_{-0.48}$	18.2 ± 0.2	18.5 ± 0.3	2.4 ± 0.3	0.01	D	99.9% field
2M16271693+3514132	M6.0	$-12.09^{+0.72}_{-0.7}$	26.1 ± 0.4	2.8 ± 0.4	-10.5 ± 0.5	0.01	D	99.9% field
2M16271825+3538347	M7.0	$-8.84^{+0.27}_{-0.38}$	-14.7 ± 0.2	8.3 ± 0.2	12.4 ± 0.3	0.01	D	99.9% field
2M16281707+1334204	M6.0	$-36.56^{+0.16}_{-0.13}$	-11.4 ± 0.1	-36.3 ± 0.4	3.5 ± 0.2	0.01	D	99.9% field
2M16311879+4051516	M6.0	$-21.75^{+0.17}_{-0.16}$	-12.6 ± 0.0	-0.1 ± 0.1	-1.8 ± 0.1	0.01	D	30.5% ARG, 69.5% field
2M16360984+4000243	M5.0	$-11.5^{+0.24}_{-0.23}$	29.6 ± 0.2	-7.1 ± 0.2	0.1 ± 0.2	0.01	D	99.9% field
2M16402068+6736046	M7.0	$-17.42^{+0.08}_{-0.1}$	-14.9 ± 0.1	-11.7 ± 0.1	4.1 ± 0.1	0.01	D	99.9% field
2M16463154+3434554	M6.0	$-52.64^{+0.13}_{-0.12}$	3.2 ± 0.1	-44.8 ± 0.1	-12.5 ± 0.1	0.03	D	99.9% field
2M16485878+3005366	M6.0	$-44.79^{+0.33}_{-0.34}$	-13.4 ± 0.2	-49.2 ± 0.4	15.0 ± 0.4	0.05	D	99.9% field
2M16572919+2448509	M5.0	$-58.12^{+0.51}_{-0.52}$	-64.4 ± 0.6	14.8 ± 0.6	-21.0 ± 0.3	0.05	D	99.9% field
2M19005974−3647109	M7.0	$1.55^{+0.24}_{-0.25}$	9.5 ± 0.3	-6.1 ± 0.6	-2.9 ± 0.3	0.01	D	64.9% CRA, 35.1% UCRA
2M19241634+7533121	M6.0	$-18.62^{+0.17}_{-0.16}$	-17.4 ± 0.0	-10.2 ± 0.2	-9.2 ± 0.1	0.01	D	99.9% field
2M19544358+1801581	M8.0	$-18.62^{+0.26}_{-0.26}$	32.2 ± 0.2	-26.2 ± 0.2	-9.9 ± 0.0	0.01	D	99.9% field

Table 3.6 (*continued*)

Table 3.6 (*continued*)

APOGEE ID	SpT	Adpoted RV (km s^{-1})	U (km s^{-1})	V (km s^{-1})	W (km s^{-1})	P[TD]/P[D][a]	Population[a]	BANYAN Σ[c]
2M20353517−0608285	M7.0	$8.16^{+0.33}_{-0.25}$	5.7 ± 0.2	25.8 ± 0.2	-2.1 ± 0.2	0.01	D	99.9% field
2M20491376+3216514	M6.0	$11.5^{+0.31}_{-0.35}$	46.9 ± 0.1	13.8 ± 0.3	0.9 ± 0.0	0.01	D	99.9% field
2M21272531+5553150	M8.0	$-12.23^{+0.21}_{-0.24}$	-20.6 ± 0.0	-3.8 ± 0.2	4.7 ± 0.0	0.01	D	99.3% CARN[d]
2M21381698+5257188	M7.5	$-7.52^{+0.21}_{-0.19}$	-3.7 ± 0.0	3.2 ± 0.2	-3.5 ± 0.0	0.01	D	99.9% field
2M22021125−1109461	M6.0	$-7.72^{+0.37}_{-0.4}$	3.8 ± 0.2	-15.3 ± 0.2	-5.4 ± 0.3	0.01	D	99.9% ABDMG
2M22400144+0532162	M6.0	$-10.05^{+0.29}_{-0.3}$	4.2 ± 0.1	-13.8 ± 0.2	-5.8 ± 0.2	0.01	D	99.6% ABDMG
2M22551142+1442456	M6.0	$-14.08^{+1.01}_{-0.76}$	0.0 ± 0.1	-9.8 ± 0.8	1.7 ± 0.6	0.01	D	99.9% field
2M23200703+1150071	M6.5	$-54.47^{+0.36}_{-0.34}$	-6.4 ± 0.0	-78.2 ± 0.3	-5.7 ± 0.3	0.87	D/TD	99.9% field

[a] Galactic thin disk (D), thick disk (TD), intermediate populations (D/TD) are assigned according to probability ratios $P(\mathrm{TD})/P(\mathrm{D}) < 0.1$, $P(\mathrm{TD})/P(\mathrm{D}) > 10$, and $0.1 < P(\mathrm{TD})/P(\mathrm{D}) < 10$, respectively, following Bensby et al. (2003).
[b] Known or candidate binary.
[c] BANYAN Σ young moving group name abbreviation follows those defined in Gagné et al. (2018c): AB Doradus (ABDMG), Argus (ARG), Coma Berenices (CBER), Corona Australis (CRA), Hyades (HYA), Taurus (TAU), Upper Scorpius (USCO).
[d] Not reported in the literature as a member of young moving groups.
[e] Reported as a member of NGC 1333 in Cantat-Gaudin et al. (2018); Yao et al. (2018); Cantat-Gaudin & Anders (2020); Cantat-Gaudin et al. (2020), but I did not identify because NGC 1333 is not included in BANYAN Σ.
[f] Reported as a member of the Castor Moving Group in Zuckerman et al. (2013), but I did not identify it because the Castor Moving Group is not included in BANYAN Σ.

Table 3.7: Galactic Orbital Parameters

APOGEE ID	$R_{\rm min}$ (kpc)	$R_{\rm max}$ (kpc)	$Z_{\rm max}$ (kpc)	e	i (deg)
2M00312793+6139333	5.0023 ± 0.0083	8.4886 ± 0.0024	0.3386 ± 0.0008	0.25838 ± 0.00076	2.86473 ± 0.01438
2M00452143+1634446	7.897 ± 0.013	8.5567 ± 0.0171	0.023 ± 0.0029	0.0401 ± 0.00034	0.1593 ± 0.02005
2M01120002+1502170	4.9281 ± 0.0091	8.4791 ± 0.0012	0.1345 ± 0.0025	0.26487 ± 0.0009	1.17157 ± 0.02209
2M01154176+0059317	7.0465 ± 0.0194	9.1796 ± 0.0265	0.0713 ± 0.0096	0.13147 ± 0.00161	0.49604 ± 0.06816
2M01215816+0101007	7.2423 ± 0.0102	8.3797 ± 0.0009	0.0494 ± 0.0011	0.07279 ± 0.00072	0.35879 ± 0.00781
2M01243124−0027556	6.8832 ± 0.0156	8.4725 ± 0.0015	0.0052 ± 0.0015	0.1035 ± 0.00109	0.03824 ± 0.01075
2M01514363+0046188	8.0498 ± 0.0047	9.1008 ± 0.0204	0.0309 ± 0.0057	0.06126 ± 0.00136	0.20332 ± 0.0383
2M02500239−0808417	6.1155 ± 0.0086	9.1541 ± 0.0101	0.202 ± 0.0063	0.199 ± 0.00119	1.49417 ± 0.04583
2M03040207+0045512	7.1719 ± 0.0048	9.039 ± 0.0074	0.0514 ± 0.0025	0.11517 ± 0.00072	0.35808 ± 0.01773
2M03282839+3116273	8.394 ± 0.0253	9.0218 ± 0.0602	0.0908 ± 0.008	0.03639 ± 0.00337	0.59335 ± 0.05366
2M03293053+3127280	8.3922 ± 0.0139	9.047 ± 0.0381	0.0796 ± 0.0047	0.03765 ± 0.00209	0.5192 ± 0.0313
2M03505737+1818069	7.2998 ± 0.0081	8.3618 ± 0.0014	0.2116 ± 0.0011	0.06783 ± 0.00058	1.52736 ± 0.00901
2M04110642+1247481	7.1471 ± 0.0065	9.0766 ± 0.0067	0.0675 ± 0.0013	0.11893 ± 0.00067	0.46931 ± 0.00948
2M04185115+2814332	8.1789 ± 0.0132	8.8298 ± 0.021	0.0496 ± 0.0025	0.03834 ± 0.00089	0.33173 ± 0.01676
2M04204796+5624202	4.5228 ± 0.0108	8.3366 ± 0.0003	0.6019 ± 0.0028	0.29658 ± 0.0011	5.32751 ± 0.0333
2M04214435+2024105	7.1898 ± 0.01	9.1533 ± 0.0153	0.0599 ± 0.0017	0.12018 ± 0.00135	0.41249 ± 0.01683
2M04214955+1929086	7.1772 ± 0.0154	9.0849 ± 0.0084	0.0719 ± 0.002	0.1173 ± 0.00089	0.49901 ± 0.01477
2M04262939+2624137	8.1481 ± 0.019	8.7549 ± 0.0209	0.0158 ± 0.0013	0.03595 ± 0.00152	0.1067 ± 0.00867
2M04294568+2630468	8.2917 ± 0.0065	8.7776 ± 0.0166	0.0225 ± 0.0016	0.02846 ± 0.00095	0.15037 ± 0.01061
2M04330945+2246487	7.9775 ± 0.0581	8.6105 ± 0.0136	0.0237 ± 0.0027	0.03823 ± 0.00328	0.16216 ± 0.01901
2M04351354+2008014	7.1949 ± 0.0085	9.0485 ± 0.0093	0.0614 ± 0.0014	0.11417 ± 0.0009	0.42658 ± 0.00978
2M04440164+1621324	7.9852 ± 0.0155	8.5697 ± 0.0061	0.0228 ± 0.001	0.03532 ± 0.00092	0.15652 ± 0.00684
2M04464498+2436404	7.1636 ± 0.0086	9.1264 ± 0.0162	0.0592 ± 0.001	0.1205 ± 0.0014	0.41023 ± 0.00748
2M04552333+3027366	8.0943 ± 0.0212	8.5972 ± 0.0075	0.0414 ± 0.0021	0.03014 ± 0.00111	0.28294 ± 0.01485
2M04565141+2939310	8.1333 ± 0.0176	8.6132 ± 0.0157	0.034 ± 0.0018	0.02866 ± 0.00147	0.23168 ± 0.01258
2M05350162−0521489	8.0894 ± 1.9855	11.3578 ± 16.7989	1.1982 ± 2.9632	0.31558 ± 0.29099	5.18459 ± 7.03864
2M05392474+4038437	5.2928 ± 0.0037	8.3211 ± 0.0007	0.1327 ± 0.0003	0.22245 ± 0.00035	1.11604 ± 0.01083
2M05402570+2448090	7.5608 ± 0.0469	8.4345 ± 0.0203	0.0279 ± 0.0012	0.05461 ± 0.00334	0.19782 ± 0.00814
2M06154934−0100415	7.7023 ± 0.0029	9.983 ± 0.0151	0.314 ± 0.0014	0.12893 ± 0.00078	1.96352 ± 0.0141
2M06521977−2534505	8.269 ± 0.002	9.2708 ± 0.0153	0.0978 ± 0.0004	0.05712 ± 0.00071	0.63112 ± 0.00333
2M07025026−6102482	6.2392 ± 0.0087	8.5044 ± 0.0025	0.6552 ± 0.0034	0.15361 ± 0.00069	4.89985 ± 0.0261
2M07140394+3702459	7.6589 ± 0.0055	9.1737 ± 0.0076	0.106 ± 0.0009	0.08999 ± 0.00076	0.71042 ± 0.00585
2M07464256+2000321	7.1091 ± 0.004	9.6899 ± 0.0083	0.0802 ± 0.002	0.15364 ± 0.00051	0.53629 ± 0.01383
2M07475737+6653337	8.3071 ± 0.0068	9.7905 ± 0.0347	0.2035 ± 0.0054	0.08198 ± 0.00136	1.26241 ± 0.0295
2M07552256+2755318	8.3147 ± 0.0011	10.4023 ± 0.007	0.4325 ± 0.0025	0.11155 ± 0.00028	2.54506 ± 0.01308
2M07564895+6649595	6.0959 ± 0.0182	8.3439 ± 0.0009	0.4414 ± 0.0039	0.15567 ± 0.00149	3.40782 ± 0.02954
2M08072607+3213101	7.022 ± 0.0059	9.0858 ± 0.0057	0.1071 ± 0.0014	0.12813 ± 0.00072	0.74881 ± 0.00919

Table 3.7 (*continued*)

Table 3.7 (*continued*)

APOGEE ID	$R_{\rm min}$ (kpc)	$R_{\rm max}$ (kpc)	$Z_{\rm max}$ (kpc)	e	i (deg)
2M08080189+3157054	7.4324 ± 0.008	8.5594 ± 0.006	0.1714 ± 0.0017	0.0705 ± 0.00087	1.21252 ± 0.01212
2M08092892+3235226	8.302 ± 0.0074	10.0865 ± 0.0243	0.0982 ± 0.0043	0.09705 ± 0.00132	0.60058 ± 0.02155
2M08144389+4650522	7.5669 ± 0.0087	8.7618 ± 0.0141	0.1116 ± 0.0024	0.0732 ± 0.00122	0.77359 ± 0.01662
2M08185804+2333522	6.1116 ± 0.008	8.5718 ± 0.0037	0.0943 ± 0.0016	0.16755 ± 0.00084	0.72993 ± 0.01274
2M08211639+5658358	8.2479 ± 0.0088	8.6016 ± 0.0085	0.2183 ± 0.002	0.02099 ± 0.0006	1.47567 ± 0.01356
2M08294949+2646348	8.158 ± 0.0091	8.5857 ± 0.0026	0.0568 ± 0.0015	0.02552 ± 0.00071	0.38711 ± 0.00985
2M08440350+0434356	6.7342 ± 0.0148	11.5646 ± 0.0213	0.2508 ± 0.0031	0.26396 ± 0.00116	1.5062 ± 0.02061
2M08490052+0220155	7.2227 ± 0.0297	8.3305 ± 0.0018	0.0412 ± 0.0002	0.07123 ± 0.00215	0.3004 ± 0.0014
2M08501918+1056436	7.0091 ± 0.0182	8.7437 ± 0.0036	0.078 ± 0.0019	0.1101 ± 0.00148	0.55992 ± 0.0134
2M08522464+2540591	7.0985 ± 0.014	9.1092 ± 0.0068	0.1139 ± 0.0046	0.12406 ± 0.00134	0.79184 ± 0.04135
2M09020690+0033195	6.2619 ± 0.0105	8.9221 ± 0.0015	0.1389 ± 0.0015	0.17518 ± 0.00087	1.0339 ± 0.01102
2M09130162+3037583	4.5784 ± 0.0193	8.6047 ± 0.0061	0.1474 ± 0.004	0.30535 ± 0.00208	1.33019 ± 0.03699
2M09373349+5534057	8.2936 ± 0.0086	8.777 ± 0.0173	0.1297 ± 0.0023	0.02832 ± 0.00126	0.86488 ± 0.01592
2M09381783+0132490	7.1498 ± 0.0465	8.8668 ± 0.0456	0.4725 ± 0.0149	0.10738 ± 0.00096	3.27406 ± 0.08562
2M09442625+3521233	7.323 ± 0.0136	11.7527 ± 0.0273	0.2134 ± 0.0093	0.23222 ± 0.00194	1.22742 ± 0.05159
2M09453388+5458511	8.0507 ± 0.0205	8.5448 ± 0.0097	0.0934 ± 0.0026	0.02976 ± 0.00169	0.6416 ± 0.01747
2M09472006−0020093	7.9328 ± 0.0028	9.0964 ± 0.0032	0.0501 ± 0.0002	0.06832 ± 0.00014	0.33294 ± 0.0018
2M09474477+0224327	7.065 ± 0.0134	8.3437 ± 0.0012	0.104 ± 0.0018	0.08298 ± 0.00087	0.76524 ± 0.01327
2M09522188−1924319	8.194 ± 0.0016	10.4839 ± 0.1024	0.1838 ± 0.0063	0.12261 ± 0.0047	1.09275 ± 0.03033
2M09524622+0620410	7.6573 ± 0.0209	8.3214 ± 0.0007	0.0546 ± 0.0004	0.04156 ± 0.00141	0.38904 ± 0.0035
2M09560888+0134128	7.1534 ± 0.0238	9.0782 ± 0.0059	0.0943 ± 0.0035	0.11858 ± 0.00139	0.6525 ± 0.02229
2M10031918−0105079	7.031 ± 0.0104	9.1817 ± 0.0037	0.0536 ± 0.0012	0.13264 ± 0.0006	0.37301 ± 0.00755
2M10134315+0000406	5.91 ± 0.008	10.511 ± 0.015	0.2471 ± 0.003	0.28017 ± 0.00061	1.68303 ± 0.02346
2M10225090+0032169	5.5556 ± 0.1953	8.3225 ± 0.0078	0.0918 ± 0.0347	0.19935 ± 0.01645	0.7599 ± 0.29988
2M10240997+1815533	7.5469 ± 0.0165	8.4103 ± 0.0022	0.063 ± 0.0012	0.0541 ± 0.00119	0.44809 ± 0.00896
2M10323297+0630074	7.119 ± 0.0076	8.3114 ± 0.001	0.0422 ± 0.0	0.07727 ± 0.00062	0.31027 ± 0.00046
2M10372897+3011117	4.4813 ± 0.0042	8.6312 ± 0.0014	0.2838 ± 0.0021	0.3165 ± 0.00048	2.51617 ± 0.05486
2M10541102−8505023	7.3148 ± 0.0282	9.1477 ± 0.0564	0.17 ± 0.0055	0.11135 ± 0.00124	1.15997 ± 0.03233
2M10543366+0503467	6.5581 ± 0.0295	10.231 ± 0.0107	0.1894 ± 0.0018	0.21874 ± 0.00255	1.25859 ± 0.01507
2M10570380+2217203	7.3002 ± 0.0026	8.3183 ± 0.0002	0.0899 ± 0.0008	0.06519 ± 0.00019	0.65433 ± 0.00549
2M11194647+0820356	6.7624 ± 0.0051	12.8571 ± 0.012	0.466 ± 0.0034	0.31061 ± 0.00056	2.52436 ± 0.01898
2M11203609+0704135	6.3093 ± 0.0165	8.9276 ± 0.0086	0.257 ± 0.0066	0.17182 ± 0.00087	1.89255 ± 0.04352
2M11210854+2126274	7.9455 ± 0.0032	8.7966 ± 0.001	0.0628 ± 0.0007	0.05083 ± 0.00019	0.42594 ± 0.00545
2M11232934+0154040	8.1569 ± 0.0088	8.9374 ± 0.0246	0.0547 ± 0.0004	0.04566 ± 0.00104	0.36335 ± 0.00275
2M12080810+3520281	5.2464 ± 0.0081	9.4749 ± 0.0063	0.2656 ± 0.0067	0.28721 ± 0.00091	2.05799 ± 0.05055
2M12153877+5205050	8.3045 ± 0.0262	8.8757 ± 0.2157	0.0815 ± 0.0152	0.03333 ± 0.01266	0.54241 ± 0.10651
2M12201166+3315379	6.7351 ± 0.0084	9.3994 ± 0.0026	0.2981 ± 0.0032	0.16513 ± 0.00073	2.05415 ± 0.02156
2M12205439+2525568	7.8265 ± 0.0328	8.6605 ± 0.0088	0.2363 ± 0.0024	0.05057 ± 0.00251	1.62106 ± 0.01652

Table 3.7 (*continued*)

Table 3.7 (*continued*)

APOGEE ID	$R_{\rm min}$ (kpc)	$R_{\rm max}$ (kpc)	$Z_{\rm max}$ (kpc)	e	i (deg)
2M12215013+4632447	7.9789 ± 0.0361	9.9355 ± 0.1285	0.061 ± 0.0066	0.10935 ± 0.0083	0.3826 ± 0.0396
2M12235346+2534559	8.3003 ± 0.0007	14.29 ± 0.1367	0.3291 ± 0.011	0.26514 ± 0.00445	1.54487 ± 0.04595
2M12252076+2517082	8.2943 ± 0.0043	9.2443 ± 0.0333	0.1579 ± 0.0086	0.05419 ± 0.00198	1.01879 ± 0.05521
2M12270429+2541012	8.2195 ± 0.0016	8.9937 ± 0.0106	0.1588 ± 0.0042	0.04498 ± 0.00058	1.04662 ± 0.02797
2M12315462+5130389	7.1298 ± 0.0073	9.1229 ± 0.0063	0.1344 ± 0.0023	0.12262 ± 0.00061	0.92913 ± 0.01394
2M12493960+5255340	4.5924 ± 0.0122	8.3709 ± 0.0008	0.2798 ± 0.0051	0.29147 ± 0.00122	2.52634 ± 0.04295
2M12522354+2528469	6.4863 ± 0.0087	8.4524 ± 0.0005	0.1784 ± 0.0028	0.13162 ± 0.00064	1.35024 ± 0.02079
2M13004379+3557591	6.149 ± 0.0033	8.7497 ± 0.0011	0.1696 ± 0.0027	0.17456 ± 0.0003	1.2868 ± 0.02025
2M13022083+3227103	7.9079 ± 0.002	8.9367 ± 0.0029	0.1687 ± 0.0032	0.06108 ± 0.00013	1.13299 ± 0.02127
2M13034100+2414020	6.9639 ± 0.0054	9.2448 ± 0.003	0.0634 ± 0.0005	0.14072 ± 0.00051	0.44132 ± 0.00354
2M13065141+7056376	7.7469 ± 0.0068	14.0929 ± 0.0509	0.5604 ± 0.0079	0.29057 ± 0.00156	2.66023 ± 0.02791
2M13192677+1301119	4.8972 ± 0.008	8.3229 ± 0.0017	0.1241 ± 0.0009	0.25913 ± 0.00097	1.09808 ± 0.00889
2M13202007+7213140	7.4014 ± 0.0226	8.7591 ± 0.0037	0.1161 ± 0.0035	0.08399 ± 0.00134	0.81221 ± 0.02494
2M13232423+5132272	7.5775 ± 0.0098	8.8365 ± 0.0105	0.0737 ± 0.0018	0.07669 ± 0.00042	0.50807 ± 0.01152
2M13342918+3303043	4.8876 ± 0.0068	8.9437 ± 0.002	0.0746 ± 0.0021	0.29326 ± 0.00073	0.63382 ± 0.01766
2M13430646+0038442	6.9919 ± 0.0358	8.3663 ± 0.0063	0.1424 ± 0.002	0.08949 ± 0.00258	1.04984 ± 0.01637
2M13482307+3321508	6.5186 ± 0.0637	8.3518 ± 0.0072	0.2129 ± 0.0133	0.12326 ± 0.00443	1.60962 ± 0.11316
2M13500476+3207596	6.7381 ± 0.016	9.0094 ± 0.0063	0.1444 ± 0.002	0.14424 ± 0.00115	1.03309 ± 0.01385
2M13564148+4342587	6.5066 ± 0.0264	8.5898 ± 0.0065	0.0486 ± 0.0008	0.13799 ± 0.00223	0.36592 ± 0.00631
2M13573443+5408223	5.1874 ± 0.0236	8.4076 ± 0.002	0.1695 ± 0.0083	0.23687 ± 0.00206	1.43876 ± 0.07293
2M14005977+3226109	6.1934 ± 0.0219	8.8512 ± 0.0062	0.1097 ± 0.0039	0.17669 ± 0.00205	0.82459 ± 0.02858
2M14081562+5236281	5.3636 ± 0.005	9.2403 ± 0.0024	0.1513 ± 0.0013	0.26545 ± 0.00051	1.18993 ± 0.01061
2M14093200+4138080	7.7965 ± 0.0047	8.6023 ± 0.0023	0.058 ± 0.001	0.04914 ± 0.00017	0.40192 ± 0.00706
2M14320849+0811313	7.4594 ± 0.002	8.6388 ± 0.0016	0.0389 ± 0.0	0.07326 ± 0.00022	0.27407 ± 0.00011
2M14340140+5039480	7.9455 ± 0.0076	8.5756 ± 0.0055	0.103 ± 0.0018	0.03814 ± 0.0003	0.70906 ± 0.01337
2M14402293+1339230	6.1427 ± 0.0047	8.4405 ± 0.0017	0.0534 ± 0.0008	0.15756 ± 0.00037	0.41685 ± 0.00608
2M14432796+0316543	7.2042 ± 0.0057	9.0191 ± 0.006	0.1252 ± 0.0023	0.11186 ± 0.00058	0.8688 ± 0.01543
2M14553384+1545593	6.2066 ± 0.071	9.1128 ± 0.0066	0.1955 ± 0.0022	0.18967 ± 0.00557	1.43656 ± 0.01336
2M14554964+0321420	4.7885 ± 0.0041	8.3107 ± 0.0004	0.531 ± 0.0021	0.26888 ± 0.00041	4.59087 ± 0.02197
2M15010818+2250020	8.1285 ± 0.0031	9.4614 ± 0.0265	0.1545 ± 0.007	0.07578 ± 0.00158	0.9911 ± 0.04642
2M15041028+0923232	5.8786 ± 0.0111	9.5897 ± 0.0066	0.075 ± 0.0006	0.23992 ± 0.00116	0.55289 ± 0.00385
2M15042797+0942464	6.0613 ± 0.0303	9.1392 ± 0.0198	0.2293 ± 0.0075	0.20238 ± 0.00338	1.69649 ± 0.05449
2M15115124+3033065	2.6677 ± 0.0077	8.3032 ± 0.0002	0.0697 ± 0.0002	0.51367 ± 0.00107	0.94247 ± 0.00338
2M15175638+0656388	7.6036 ± 0.0076	8.2505 ± 0.0014	0.1078 ± 0.0013	0.04081 ± 0.00054	0.77359 ± 0.00936
2M15210103+5053230	7.9371 ± 0.0019	9.7724 ± 0.0104	0.1247 ± 0.0017	0.10363 ± 0.0004	0.78984 ± 0.00905
2M15242475+2925318	6.3859 ± 0.0014	8.7472 ± 0.0009	0.0691 ± 0.0004	$0.15603 \pm 9e-05$	0.51866 ± 0.00314
2M15512179+2931062	6.7431 ± 0.004	9.3673 ± 0.0085	0.4574 ± 0.0036	0.16289 ± 0.00017	3.12668 ± 0.02221
2M15555600−2045187	7.62 ± 0.0337	8.2369 ± 0.0091	0.0892 ± 0.0013	0.0389 ± 0.0021	0.64042 ± 0.01034

Table 3.7 (*continued*)

Table 3.7 (*continued*)

APOGEE ID	$R_{\rm min}$ (kpc)	$R_{\rm max}$ (kpc)	$Z_{\rm max}$ (kpc)	e	i (deg)
2M15560104−2338081	7.4612 ± 0.0228	8.3113 ± 0.0079	0.0864 ± 0.0007	0.05394 ± 0.00134	0.62239 ± 0.00594
2M15560497−2106461	7.6189 ± 0.059	8.2346 ± 0.0217	0.089 ± 0.0021	0.03875 ± 0.00413	0.63899 ± 0.01651
2M15574011+2952379	7.0505 ± 0.0039	8.9616 ± 0.0056	0.1183 ± 0.0011	0.11938 ± 0.00017	0.83323 ± 0.00745
2M15592591−2305081	7.6206 ± 0.0135	8.2566 ± 0.0037	0.0812 ± 0.0005	0.04007 ± 0.00073	0.58174 ± 0.00405
2M15594439−1928191	7.5982 ± 0.0527	8.2791 ± 0.0175	0.0925 ± 0.0022	0.04298 ± 0.00265	0.66316 ± 0.01838
2M16001944−2256287	7.6322 ± 0.0686	8.2427 ± 0.0182	0.082 ± 0.0027	0.03865 ± 0.00382	0.58799 ± 0.02188
2M16002844−2209228	6.5676 ± 0.0402	8.1692 ± 0.0028	0.2032 ± 0.0039	0.10859 ± 0.00288	1.5591 ± 0.03383
2M16003023−2334457	7.6 ± 0.0222	8.2386 ± 0.0087	0.0804 ± 0.0006	0.04035 ± 0.00165	0.57787 ± 0.00556
2M16014955−2351082	7.6424 ± 0.0244	8.2477 ± 0.0066	0.0805 ± 0.0009	0.03811 ± 0.00125	0.57725 ± 0.00705
2M16022585−2414081	7.6634 ± 0.0461	8.2879 ± 0.0152	0.0758 ± 0.0013	0.03921 ± 0.00235	0.54201 ± 0.01128
2M16044026−2254323	7.5041 ± 0.045	8.2645 ± 0.0146	0.0862 ± 0.0014	0.04818 ± 0.00256	0.62279 ± 0.01178
2M16045199−2224108	7.5062 ± 0.0523	8.2844 ± 0.0262	0.0873 ± 0.0019	0.04926 ± 0.00391	0.62833 ± 0.01611
2M16055178−2206212	7.5774 ± 0.0306	8.239 ± 0.0082	0.0843 ± 0.0012	0.04186 ± 0.00172	0.60646 ± 0.0102
2M16055380+2303058	7.8874 ± 0.0123	8.7477 ± 0.0022	0.2568 ± 0.0035	0.0517 ± 0.00074	1.74634 ± 0.02441
2M16063110−1904576	7.6907 ± 0.0275	8.2726 ± 0.0086	0.0844 ± 0.0012	0.03645 ± 0.00143	0.60138 ± 0.01006
2M16063390+4054216	5.3283 ± 0.007	8.5303 ± 0.0003	0.1329 ± 0.0016	0.23105 ± 0.00064	1.10681 ± 0.01188
2M16081226+2252548	7.8531 ± 0.0044	11.0419 ± 0.0523	0.1173 ± 0.0028	0.16879 ± 0.00252	0.68996 ± 0.01519
2M16090197−2151225	7.7547 ± 0.0425	8.2281 ± 0.0197	0.0771 ± 0.0011	0.02965 ± 0.00333	0.55001 ± 0.00932
2M16090451−2224523	7.6929 ± 0.0349	8.2382 ± 0.0155	0.0798 ± 0.0012	0.03427 ± 0.00269	0.57095 ± 0.00911
2M16090568−2245166	7.6511 ± 0.109	8.2775 ± 0.0344	0.0795 ± 0.004	0.03929 ± 0.0051	0.56741 ± 0.03336
2M16093019−2059536	7.7001 ± 0.0225	8.3716 ± 0.0112	0.0835 ± 0.001	0.04179 ± 0.00091	0.59146 ± 0.00844
2M16095107−2722418	7.4732 ± 0.0302	8.2394 ± 0.0076	0.0723 ± 0.0007	0.04867 ± 0.00167	0.52292 ± 0.00621
2M16095852−2345186	7.6634 ± 0.0252	8.2899 ± 0.0088	0.0759 ± 0.0008	0.03928 ± 0.00124	0.54141 ± 0.00676
2M16095990−2155424	7.6554 ± 0.0444	8.2653 ± 0.0139	0.0784 ± 0.0015	0.03848 ± 0.00248	0.56068 ± 0.0121
2M16100608−2127440	7.742 ± 0.0778	8.25 ± 0.0293	0.0792 ± 0.0027	0.03174 ± 0.00487	0.56469 ± 0.02163
2M16103014−2315167	7.6464 ± 0.049	8.2569 ± 0.0131	0.0766 ± 0.0018	0.03834 ± 0.00257	0.54844 ± 0.01441
2M16103040+3954258	6.7999 ± 0.4649	12.1867 ± 0.8937	0.0954 ± 0.0262	0.2826 ± 0.06471	0.54909 ± 0.14659
2M16103232−1913085	7.7378 ± 0.0553	8.2611 ± 0.0274	0.084 ± 0.0025	0.03266 ± 0.0041	0.59867 ± 0.02
2M16103232+2249116	8.2486 ± 0.0012	10.3314 ± 0.0319	0.0944 ± 0.001	0.1121 ± 0.00159	0.56913 ± 0.00486
2M16104714−2239492	7.8411 ± 0.1062	8.2321 ± 0.0237	0.0714 ± 0.004	0.02432 ± 0.00531	0.50746 ± 0.03177
2M16113837−2307072	7.5279 ± 0.03	8.2581 ± 0.0109	0.0794 ± 0.0009	0.04625 ± 0.00195	0.57238 ± 0.00727
2M16114261−2525511	7.6996 ± 0.0264	8.2466 ± 0.0117	0.071 ± 0.0007	0.03434 ± 0.00203	0.50706 ± 0.0054
2M16115439−2236491	7.7031 ± 0.048	8.2948 ± 0.0212	0.0805 ± 0.0016	0.037 ± 0.00293	0.57269 ± 0.01292
2M16122703−2013250	7.7578 ± 0.0153	8.2746 ± 0.0075	0.0799 ± 0.0005	0.03226 ± 0.00099	0.56737 ± 0.00448
2M16124726−1903531	7.7642 ± 0.0164	8.2483 ± 0.0064	0.0832 ± 0.0008	0.03022 ± 0.00106	0.59219 ± 0.00625
2M16132665−2230348	7.6555 ± 0.0254	8.2536 ± 0.007	0.076 ± 0.001	0.03758 ± 0.00142	0.54402 ± 0.00809
2M16132809−1924524	7.7502 ± 0.0178	8.2964 ± 0.0079	0.0806 ± 0.0008	0.0341 ± 0.00102	0.57235 ± 0.00649
2M16134027−2233192	7.6961 ± 0.0246	8.2184 ± 0.0052	0.078 ± 0.0011	0.03285 ± 0.00132	0.55815 ± 0.00823

Table 3.7 (*continued*)

Table 3.7 (*continued*)

APOGEE ID	$R_{\rm min}$ (kpc)	$R_{\rm max}$ (kpc)	$Z_{\rm max}$ (kpc)	e	i (deg)
2M16134079−2219459	7.5347 ± 0.0664	8.313 ± 0.0223	0.0809 ± 0.0026	0.04914 ± 0.00315	0.57913 ± 0.02159
2M16134264−2301279	7.5359 ± 0.0345	8.2619 ± 0.0191	0.0836 ± 0.001	0.04595 ± 0.0029	0.60217 ± 0.00871
2M16143287−2242133	7.4773 ± 0.0376	8.3209 ± 0.0133	0.0821 ± 0.0015	0.0534 ± 0.00181	0.59063 ± 0.01343
2M16172079+4113032	6.74 ± 0.0119	8.7278 ± 0.0066	0.2895 ± 0.0031	0.12851 ± 0.00052	2.09666 ± 0.02115
2M16183317−2517504	7.2968 ± 0.0474	8.1951 ± 0.0113	0.0886 ± 0.0014	0.05802 ± 0.00262	0.64909 ± 0.01201
2M16195143−2241332	7.7478 ± 0.0511	8.2684 ± 0.0186	0.0757 ± 0.002	0.03254 ± 0.00234	0.53861 ± 0.01661
2M16204144−2425491	7.4677 ± 0.0616	8.3203 ± 0.0248	0.0804 ± 0.0017	0.05412 ± 0.00311	0.5786 ± 0.01409
2M16222304−2407108	7.5178 ± 0.1607	8.2354 ± 0.0429	0.0845 ± 0.0043	0.04551 ± 0.00809	0.61046 ± 0.03743
2M16222521−2405139	7.5415 ± 0.0569	8.2727 ± 0.0148	0.0794 ± 0.0014	0.0463 ± 0.00298	0.57107 ± 0.01151
2M16235155−2317270	7.6352 ± 0.0348	8.2731 ± 0.0168	0.0718 ± 0.0013	0.04008 ± 0.00253	0.5134 ± 0.01026
2M16265698+3954482	8.1485 ± 0.0007	10.3335 ± 0.0396	0.0741 ± 0.0019	0.11823 ± 0.00189	0.44965 ± 0.0098
2M16271693+3514132	7.6989 ± 0.0096	9.1588 ± 0.0352	0.1548 ± 0.0039	0.08661 ± 0.0016	1.03471 ± 0.02832
2M16271825+3538347	8.0893 ± 0.0066	9.2988 ± 0.017	0.1435 ± 0.0031	0.06954 ± 0.00048	0.93242 ± 0.01747
2M16281707+1334204	5.6796 ± 0.024	8.3118 ± 0.0011	0.0628 ± 0.0014	0.18813 ± 0.00201	0.51201 ± 0.01109
2M16311879+4051516	7.9132 ± 0.0063	8.6581 ± 0.0032	0.0402 ± 0.0005	0.04495 ± 0.00021	0.27612 ± 0.00383
2M16360984+4000243	7.1885 ± 0.0093	8.8825 ± 0.0078	0.0716 ± 0.0003	0.10539 ± 0.00057	0.50319 ± 0.00237
2M16402068+6736046	7.187 ± 0.0062	8.4705 ± 0.0019	0.0535 ± 0.0006	0.08199 ± 0.00043	0.38752 ± 0.00375
2M16463154+3434554	5.2644 ± 0.004	8.2972 ± 0.0001	0.1307 ± 0.0008	0.22363 ± 0.00035	1.11318 ± 0.00767
2M16485878+3005366	5.022 ± 0.0206	8.3096 ± 0.0009	0.1726 ± 0.0046	0.2466 ± 0.00193	1.50168 ± 0.04089
2M16572919+2448509	7.1748 ± 0.0127	11.9375 ± 0.0749	0.2897 ± 0.0043	0.2492 ± 0.00292	1.64757 ± 0.02741
2M19005974−3647109	7.4711 ± 0.0398	8.2562 ± 0.0121	0.0342 ± 0.0033	0.04999 ± 0.00206	0.24731 ± 0.02447
2M19241634+7533121	7.263 ± 0.0083	8.5401 ± 0.0033	0.1042 ± 0.0005	0.08081 ± 0.00038	0.74711 ± 0.00533
2M19544358+1801581	6.1137 ± 0.0095	8.6403 ± 0.0051	0.1041 ± 0.0005	0.17125 ± 0.00054	0.80147 ± 0.01437
2M20353517−0608285	8.2203 ± 0.0011	10.9198 ± 0.0288	0.0352 ± 0.0016	0.14086 ± 0.00133	0.20511 ± 0.00879
2M20491376+3216514	7.5309 ± 0.0059	10.8981 ± 0.036	0.0307 ± 0.0001	0.18272 ± 0.0012	0.18041 ± 0.00184
2M21272531+5553150	7.5343 ± 0.0118	8.7775 ± 0.0095	0.0557 ± 0.0002	0.07624 ± 0.00028	0.38642 ± 0.0019
2M21381698+5257188	8.2525 ± 0.0023	8.5949 ± 0.0173	0.0454 ± 0.0001	0.02033 ± 0.00087	0.30758 ± 0.00067
2M22021125−1109461	7.0154 ± 0.0147	8.2945 ± 0.0009	0.0536 ± 0.0029	0.08355 ± 0.00099	0.3974 ± 0.02182
2M22400144+0532162	7.1407 ± 0.0153	8.3018 ± 0.0012	0.0578 ± 0.0029	0.07514 ± 0.00109	0.42499 ± 0.01606
2M22551142+1442456	7.4411 ± 0.0547	8.2977 ± 0.0003	0.0319 ± 0.0031	0.05443 ± 0.00368	0.22999 ± 0.02316
2M23200703+1150071	3.8072 ± 0.0112	8.3068 ± 0.0001	0.0575 ± 0.0029	0.37144 ± 0.00126	0.59684 ± 0.02957

Table 3.8: Velocity Dispersions and Group Kinematic Ages

Sample	N	$\langle U \rangle$ (km s^{-1})	$\langle V \rangle$ (km s^{-1})	$\langle W \rangle$ (km s^{-1})	σ_U (km s^{-1})	σ_V (km s^{-1})	σ_W (km s^{-1})	$\sigma_{\rm tot}$ (km s^{-1})	Age (Gyr)	Note
All	181	-1.8 ± 2.0	-9.5 ± 1.5	1.9 ± 0.9	26.5 ± 0.4	19.7 ± 0.1	12.7 ± 0.1	35.4 ± 0.4	2.6 ± 0.2	Unweighted
					34.0 ± 0.4	25.6 ± 0.2	16.7 ± 0.1	45.7 ± 0.3	3.81 ± 0.05	$\lvert W \rvert$ Weighted
Not Young	116	-3.1 ± 2.9	-12.4 ± 2.2	2.8 ± 1.4	31.7 ± 0.5	23.9 ± 0.2	15.6 ± 0.1	42.7 ± 0.6	4.5 ± 0.3	Unweighted
					35.5 ± 0.4	26.7 ± 0.2	17.7 ± 0.2	47.8 ± 0.3	4.19 ± 0.05	$\lvert W \rvert$ Weighted
Thin Disk	104	-3.0 ± 3.0	-8.5 ± 1.8	2.5 ± 1.3	30.5 ± 0.6	18.2 ± 0.2	12.8 ± 0.1	37.8 ± 0.6	3.2 ± 0.2	Unweighted
& Not Young					33.7 ± 0.4	19.2 ± 0.2	13.9 ± 0.2	41.2 ± 0.4	3.0 ± 0.1	$\lvert W \rvert$ Weighted
M Dwarfs	100	-3.5 ± 3.0	-8.9 ± 1.8	2.6 ± 1.3	30.0 ± 0.6	18.4 ± 0.2	12.7 ± 0.1	37.4 ± 0.7	3.1 ± 0.2	Unweighted
(Thin Disk)					33.4 ± 0.5	19.5 ± 0.2	13.9 ± 0.2	41.1 ± 0.4	3.0 ± 0.1	$\lvert W \rvert$ Weighted
L Dwarfs	4	11.1 ± 20.1	2.2 ± 3.4	2.1 ± 7.9	37.4 ± 7.4	6.4 ± 0.9	14.5 ± 3.4	40.7 ± 8.2	4.3 ± 2.4	Unweighted
(Thin Disk)					47.2 ± 10.6	6.9 ± 1.0	12.3 ± 3.8	49.7 ± 9.4	4.6 ± 1.6	$\lvert W \rvert$ Weighted
Thin Disk &	75	-1.3 ± 3.6	-9.6 ± 2.3	4.1 ± 1.5	31.6 ± 0.8	19.6 ± 0.2	12.8 ± 0.2	39.3 ± 0.8	3.6 ± 0.3	Unweighted
Not Young, Binary					33.6 ± 0.6	20.2 ± 0.3	14.0 ± 0.2	41.6 ± 0.5	3.1 ± 0.1	$\lvert W \rvert$ Weighted
Shallow[a]	80	-4.6 ± 1.9	-9.7 ± 1.2	2.8 ± 0.8	30.5 ± 0.4	20.0 ± 0.4	13.6 ± 0.2	38.9 ± 0.4	3.5 ± 0.2	Unweighted
Wide Lower[a]	16	-45.5 ± 2.5	-50.1 ± 1.9	-18.6 ± 1.7	34.2 ± 2.1	26.3 ± 1.5	24.3 ± 1.1	49.5 ± 1.7	6.9 ± 0.7	Unweighted
Wide Upper[a]	16	44.9 ± 3.3	15.7 ± 1.1	23.9 ± 1.6	45.4 ± 2.8	15.1 ± 0.7	22.7 ± 1.3	53.0 ± 2.5	8.4 ± 1.1	Unweighted

Note – Ages for unweighted velocities are computed from Aumer & Binney (2009) using the parameters in Aumer & Binney (2009). Ages for $|W|$-weighted velocities are computed from Wielen (1977) using the parameters in Wielen (1977), following the implementation in Hsu et al. (2021).

[a] Piece-wise linear fits to unweighted velocities, broken at $\sigma = \pm 1$; see Section 3.4.4.

Table 3.9: Radial Velocity Variations for Multi-epoch Observations

APOGEE ID	N_{obs}	Mean RV (km s^{-1})	χ^2	p-value	Significance Type[a]
2M03282839+3116273	10	+15.25	39.8	< 0.001	$N \geq 4$ significant
2M05402570+2448090	4	+22.93	28.17	< 0.001	$N \geq 4$ significant
2M08092892+3235226	4	−6.65	11.52	0.009	$N \geq 4$ significant
2M08501918+1056436	23	+31.45	82.19	< 0.001	$N \geq 4$ significant
2M09373349+5534057	20	+0.8	109.65	< 0.001	$N \geq 4$ significant
2M09442625+3521233	6	+51.18	36.42	< 0.001	$N \geq 4$ significant
2M09453388+5458511	10	−3.78	22.9	0.006	$N \geq 4$ significant
2M09522188−1924319	3	−17.09	53.22	< 0.001	$N < 4$ significant
2M09560888+0134128	4	+21.15	12.68	0.005	$N \geq 4$ significant
2M10225090+0032169	3	+34.09	1172.27	< 0.001	$N < 4$ significant
2M10541102−8505023	2	−10.55	45.52	< 0.001	$N < 4$ significant
2M11203609+0704135	3	−14.47	11.74	0.003	$N < 4$ significant
2M11232934+0154040	3	−0.13	14.16	0.001	$N < 4$ significant
2M12080810+3520281	2	+29.19	8.46	0.004	$N < 4$ significant
2M13202007+7213140	12	−27.34	35.62	< 0.001	$N \geq 4$ significant
2M13232423+5132272	7	−5.39	17.91	0.006	$N \geq 4$ significant
2M13430646+0038442	15	−11.9	63.8	< 0.001	$N \geq 4$ significant
2M13482307+3321508	6	−19.82	558.78	< 0.001	$N \geq 4$ significant
2M13500476+3207596	15	−5.77	52.01	< 0.001	$N \geq 4$ significant
2M13564148+4342587	3	−19.5	13.18	0.001	$N < 4$ significant
2M14005977+3226109	16	−17.89	70.77	< 0.001	$N \geq 4$ significant
2M15010818+2250020	5	+6.55	44.72	< 0.001	$N \geq 4$ significant
2M16002844−2209228	3	−3.56	19.69	< 0.001	$N < 4$ significant
2M16090451−2224523	3	−5.15	43.57	< 0.001	$N < 4$ significant
2M16114261−2525511	2	−4.78	10.0	0.002	$N < 4$ significant
2M16271825+3538347	4	−8.56	48.52	< 0.001	$N \geq 4$ significant
2M16572919+2448509	4	−58.04	14.52	0.002	$N \geq 4$ significant
2M22551142+1442456	5	−14.27	18.55	0.001	$N \geq 4$ significant

[a] I regard sources with numbers of observations < 4 promising candidates; see Section 3.4.5for more details.

Table 3.10: Binary Orbital Parameter Estimate

APOGEE ID	$N_{\rm obs}$	$P_{\rm Prior}$ (day)	$K_{0,\rm Prior}$ (km s^{-1})	σ_{K_0} (km s^{-1})	σ_v (km s^{-1})	$N_{\rm sam,in}$	$P_{\rm fit}$ (day)	$K_{\rm fit}$ (km s^{-1})	$e_{\rm fit}$	*Gaia* RUWE
2M03282839+3116273	10	1–300	3.0	2.0	2.0	1000000	$24.1^{+86.9}_{-21.8}$	$1.0^{+0.3}_{-0.2}$	$0.175^{+0.245}_{-0.132}$	0.995
2M05402570+2448090	4	1–800	4.0	3.0	3.0	1000000	$27.8^{+49.5}_{-24.8}$	$2.3^{+1.2}_{-0.9}$	$0.186^{+0.268}_{-0.143}$	⋯
2M08092892+3235226	4	6–100	1.5	1.0	1.0	100000	$17.7^{+11.9}_{-4.6}$	$0.9^{+0.5}_{-0.3}$	$0.199^{+0.255}_{-0.151}$	4.424
2M08501918+1056436	23	1–300	4.0	3.0	3.0	5000000	$26.0^{+17.4}_{-24.0}$	$0.7^{+0.3}_{-0.1}$	$0.365^{+0.43}_{-0.232}$	1.154 & 1.185
2M09373349+5534057	20	1–100	4.0	3.0	2.0	5000000	$5.7^{+13.5}_{-3.9}$	$0.4^{+0.3}_{-0.2}$	$0.271^{+0.297}_{-0.199}$	1.103 & ⋯
2M09442625+3521233	6	1–100	1.5	1.0	1.0	1000000	$4.8^{+5.2}_{-3.4}$	$1.2^{+0.5}_{-0.3}$	$0.227^{+0.273}_{-0.179}$	0.994
2M09453388+5458511	10	1–800	4.0	3.0	2.0	5000000	$15.1^{+119.8}_{-12.7}$	$1.0^{+0.5}_{-0.5}$	$0.315^{+0.298}_{-0.244}$	0.947
2M09560888+0134128	4	15–800	1.5	1.0	1.0	100000	$47.1^{+188.3}_{-25.4}$	$1.4^{+0.7}_{-0.7}$	$0.177^{+0.262}_{-0.14}$	0.929
2M13202007+7213140	12	20–150	3.0	2.0	3.0	5000000	$52.6^{+4.1}_{-16.0}$	$0.9^{+0.6}_{-0.5}$	$0.338^{+0.268}_{-0.213}$	1.332
2M13232423+5132272	7	1–50	3.0	2.0	2.0	1000000	$3.6^{+8.0}_{-2.0}$	$0.7^{+0.4}_{-0.3}$	$0.207^{+0.332}_{-0.154}$	1.090 & 0.918
2M13430646+0038442	15	20–200	3.0	2.0	2.0	5000000	$106.7^{+40.4}_{-2.0}$	$1.1^{+0.2}_{-0.2}$	$0.124^{+0.207}_{-0.096}$	1.022
2M13482307+3321508	6	1–200	15.0	4.0	3.0	5000000	$10.7^{+0.1}_{-3.4}$	$10.8^{+3.6}_{-1.6}$	$0.101^{+0.182}_{-0.066}$	1.030
2M13500476+3207596	15	1–100	4.0	3.0	3.0	5000000	$1.7^{+0.2}_{-0.7}$	$1.1^{+0.9}_{-0.2}$	$0.655^{+0.093}_{-0.177}$	1.054
2M14005977+3226109	16	1–600	3.0	3.0	3.0	5000000	$1.4^{+321.0}_{-0.3}$	$1.5^{+1.0}_{-0.4}$	$0.419^{+0.258}_{-0.255}$	0.986
2M15010818+2250020	5	5–50	3.0	3.0	2.0	1000000	$23.3^{+1.3}_{-11.0}$	$1.2^{+0.7}_{-0.3}$	$0.189^{+0.284}_{-0.142}$	1.661
2M16271825+3538347	4	60–200	5.0	4.0	3.0	5000000	$69.7^{+17.6}_{-7.4}$	$3.4^{+2.1}_{-1.3}$	$0.524^{+0.175}_{-0.238}$	0.976
2M16572919+2448509	4	100–3000	3.0	3.0	3.0	100000	$989.0^{+1158.0}_{-800.9}$	$0.8^{+0.6}_{-0.3}$	$0.195^{+0.29}_{-0.15}$	7.898
2M22551142+1442456	5	1–50	3.0	3.0	2.0	100000	$2.8^{+4.8}_{-1.1}$	$1.6^{+0.9}_{-0.5}$	$0.178^{+0.256}_{-0.135}$	1.091

[a] The *Gaia* Renormalised Unit Weight Error (RUWE) (Gaia Collaboration et al. 2018a) is a common used of binary indicator. The RUWEs of two resolved sources with consistent proper motions and parallaxes in *Gaia* are both listed.

Table 3.11: Inferred Projected Radii, Inclination and Literature Period Measurements

APOGEE ID	BANYAN Σ[a]	$v \sin i$ (km s^{-1})	Period[b] (day)	$R \sin i$ ($R_\odot$)	inclination (deg)	Period Ref
2M00452143+1634446	99.7% ARG	31.64 ± 1.21	0.1 ± 0.004	0.06 ± 0.0	26.7 ± 1.1	(14)
2M01243124−0027556	99.9% field	27.7 ± 1.84	0.555	0.3 ± 0.03	···	(2)
2M03040207+0045512	77.1% HYA	19.99 ± 1.77	1.293	0.51 ± 0.06	···	(6)
2M04110642+1247481	99.4% HYA	14.15 ± 1.12	0.897	0.25 ± 0.02	···	(5)
2M04214435+2024105	99.9% HYA	32.8 ± 1.43	0.34	0.22 ± 0.02	···	(9), (11)
2M04214955+1929086	99.9% HYA	44.43 ± 1.24	0.205	0.18 ± 0.01	···	(5)
2M04330945+2246487	17.1% TAU	15.96 ± 1.1	3.492	1.11 ± 0.1	···	(13)
2M04351354+2008014	99.9% HYA	23.66 ± 1.05	0.37	0.17 ± 0.01	···	(9), (11)
2M04440164+1621324	86.9% TAU	14.28 ± 1.25	2.172	0.61 ± 0.07	···	(13)
2M04464498+2436404	99.2% HYA	17.88 ± 0.17	0.66	0.23 ± 0.01	···	(9), (11)
2M05402570+2448090	54.7% ARG, 43.2% CARN	30.37 ± 1.63	0.294	0.18 ± 0.01	···	(6)
2M07140394+3702459	99.9% field	7.31 ± 1.23	60.2	8.76 ± 1.58	···	(6)
2M07464256+2000321	99.9% field	34.59 ± 1.16	0.086	0.06 ± 0.0	31.3 ± 5.9	(3)
2M08072607+3213101	99.9% field	13.68 ± 1.33	0.345	0.09 ± 0.01	···	(6)
2M08294949+2646348	99.9% field[c]	11.91 ± 1.22	0.459	0.11 ± 0.01	···	(6)
2M10323297+0630074	99.9% field	10.13 ± 1.2	16.52	3.29 ± 0.42	···	(6)
2M10372897+3011117	99.9% field	13.07 ± 1.36	1.012	0.26 ± 0.03	···	(6)
2M10570380+2217203	99.9% field	8.96 ± 1.27	23.7	4.19 ± 0.66	···	(6)
2M13022083+3227103	99.9% field	25.7 ± 1.4	0.4	0.2 ± 0.02	···	(6)
2M13564148+4342587	99.9% field	16.16 ± 1.06	0.477	0.15 ± 0.01	···	(6)
2M14320849+0811313	99.9% field	9.17 ± 1.09	0.757	0.14 ± 0.02	···	(6)
2M15010818+2250020	99.9% field	65.29 ± 1.32	0.082	0.11 ± 0.01	60.4 ± 12.2	(4)
2M15555600−2045187	99.9% USCO	19.91 ± 1.13	1.7	0.67 ± 0.05	···	(7)
2M15560104−2338081	93.5% USCO	12.96 ± 0.86	1.505	0.39 ± 0.03	···	(7)
2M15560497−2106461	99.9% USCO	92.77 ± 1.54	0.26	0.48 ± 0.03	···	(1)
2M15592591−2305081	99.9% USCO	23.51 ± 1.01	0.62	0.29 ± 0.02	72.2 ± 7.8	(7)
2M16003023−2334457	99.9% USCO	73.58 ± 1.54	0.448	0.65 ± 0.04	···	(7)
2M16014955−2351082	99.9% USCO	38.71 ± 1.5	0.527	0.4 ± 0.02	···	(7)
2M16063110−1904576	99.9% USCO	16.65 ± 1.79	2.301	0.76 ± 0.09	···	(7)
2M16090197−2151225	99.9% USCO	47.77 ± 1.17	0.269	0.25 ± 0.01	63.4 ± 11.1	(7)
2M16090451−2224523	99.9% USCO	14.14 ± 1.0	2.181	0.61 ± 0.06	···	(7)
2M16093019−2059536	99.8% USCO	17.95 ± 0.28	1.593	0.57 ± 0.03	···	(7)
2M16095107−2722418	98.8% USCO	56.1 ± 1.05	0.543	0.6 ± 0.03	···	(7)
2M16095852−2345186	99.9% USCO	34.66 ± 1.46	1.411	0.96 ± 0.07	···	(7)
2M16095990−2155424	99.9% USCO	22.02 ± 1.55	0.874	0.38 ± 0.03	78.4 ± 5.2	(7)
2M16113837−2307072	99.9% USCO	36.63 ± 1.09	0.72	0.52 ± 0.03	···	(7)
2M16114261−2525511	99.9% USCO	55.35 ± 1.15	0.629	0.69 ± 0.04	···	(7)

Table 3.11 (*continued*)

Table 3.11 (*continued*)

APOGEE ID	BANYAN Σ[a]	$v \sin i$ (km s^{-1})	Period[b] (day)	$R \sin i$ ($R_\odot$)	inclination (deg)	Period Ref
2M16115439−2236491	99.9% USCO	50.29 ± 1.21	0.484	0.48 ± 0.03	···	(7)
2M16122703−2013250	99.9% USCO	30.93 ± 0.43	0.888	0.54 ± 0.03	···	(7)
2M16124726−1903531	99.9% USCO	29.03 ± 1.17	1.188	0.68 ± 0.05	···	(7)
2M16132665−2230348	99.9% USCO	19.86 ± 1.66	1.532	0.6 ± 0.06	···	(7)
2M16132809−1924524	99.9% USCO	23.09 ± 1.4	1.512	0.69 ± 0.06	···	(7)
2M16134027−2233192	99.9% USCO	14.11 ± 0.21	1.716	0.48 ± 0.02	···	(1)
2M16134079−2219459	99.7% USCO	19.41 ± 0.27	1.336	0.51 ± 0.03	···	(7)
2M16143287−2242133	99.2% USCO	18.02 ± 0.36	1.823	0.65 ± 0.03	···	(7)
2M16281707+1334204	99.9% field	15.81 ± 1.07	0.603	0.19 ± 0.02	···	(6)
2M16311879+4051516	30.5% ARG, 69.5% field	14.79 ± 1.59	0.512	0.15 ± 0.02	···	(6)
2M16402068+6736046	99.9% field	16.04 ± 0.16	0.378	0.12 ± 0.01	···	(6)
2M19005974−3647109	64.9% CRA, 35.1% UCRA	20.09 ± 1.39	1.552	0.62 ± 0.05	76.3 ± 7.6	(12)
2M19241634+7533121	99.9% field	7.18 ± 1.41	162.7	23.46 ± 4.76	···	(6)
2M21272531+5553150	99.3% CARN	17.29 ± 1.22	0.54	0.18 ± 0.02	···	(6)
2M21381698+5257188	99.9% field	40.59 ± 1.52	0.183	0.15 ± 0.01	82.1 ± 5.1	(6)
2M22021125−1109461	99.9% ABDMG	21.34 ± 1.38	0.428	0.18 ± 0.01	68.3 ± 9.5	(1)

[a] BANYAN Σ young moving group name abbreviation follows those defined in Gagné et al. (2018c):
AB Doradus (ABDMG), Argus (ARG), Coma Berenices (CBER), Corona Australis (CRA), Hyades (HYA), Taurus (TAU), Upper Scorpius (USCO).

[b] I assume 5% uncertainty for each period without reported uncertainty. See Section 3.4.6 for details.

[c] This source is a confirmed member of the Castor Moving Group ("CMG") but the CMG is not included in BANYAN Σ, see Section 3.4.3.

References – (1) Watson et al. (2006), (2) Ivezić et al. (2007), (3) Berger et al. (2009), (4) Crossfield (2014), (5) Douglas et al. (2019), (6) Newton et al. (2016), (7) Rebull et al. (2018), (8) Reiners et al. (2018), (9) Douglas et al. (2019), (10) Vos et al. (2019), (11) Freund et al. (2020), (12) Nardiello (2020), (13) Rebull et al. (2020), (14) Vos et al. (2020)

Chapter 3, in full is currently being prepared for submission for publication of the material. Hsu, Chih-Chun; Burgasser, Adam J.; Theissen, Christopher A.; Birky, Jessica L.; Aganze, C.; Gerasimov, R.; Covey K. R.; Blake, Cullen H.; Moreno-Hilario, E. The thesis author was the primary investigator and author of this paper.

Chapter 4

Conclusions and Future Work

4.1 Summary of the Thesis Work

In this thesis work, I have measured and compiled the largest sample of high-resolution spectral observations for 385 local ultracool dwarfs. In particular, I presented multi-epoch, precise radial and projected rotational velocity measurements for 175 late-M/L/T dwarfs with NIRSPEC and 182 M4–L2 dwarfs with APOGEE, as well as determinations of their effective temperatures and surface gravities, for a total of 352 sources with 1194 epochs. I summarize the key findings of the Keck/NIRSPEC T dwarf, the SDSS/APOGEE M/L dwarf, and the Keck/NISPEC late-M/L dwarf samples as follows.

4.1.1 NIRSPEC T Dwarfs

Drawing from the new and archival observations , I have measured new and refined multi-epoch RV and $v \sin i$ measurements for a total of 37 T dwarfs. In addition to 23 sources without previously reported RV or $v \sin i$ measurements, I improved the measurements of 14 T dwarfs by reducing RV uncertainties by an average factor of 5 and

$v \sin i$ uncertainties by an average factor of 3 using a forward-modeling approach. The key scientific results are summarized as follows:

1. Most of the local T dwarfs are fast rotators, with a median $v \sin i$ of 27 km s^{-1} independent of T dwarf spectral type. This is larger than the median rotational velocities of late-M dwarfs (12 km s^{-1}) and L dwarfs (20 km s^{-1}), a trend that supports prior work indicating that the angular momenta of brown dwarfs are not lost effectively to magnetic winds. In addition, T dwarfs with larger space velocities, which are likely older and more massive, have larger $v \sin i$ values, which may reflect their larger moments of inertia (resistance to angular momentum loss) or more compact radii (greater spin-up).

2. Combining my RVs with published and *Gaia* astrometry, I calculated the Galactic *UVW* velocities and orbits for my sample. I found that all of my T dwarfs are in the thin disk population; the one exception in my sample, 2MASS J1331−0116, is an unusually blue L dwarf.

3. I kinematically confirmed two previously-identified, planetary-mass, young moving group members SIMP J0136+0933 (Carina-Near; Gagné et al. 2017) and 2MASS J1324+6358 (AB Doradus; Gagné et al. 2018a). The T4 dwarf 2MASS J0819−0335 and the T6.5+T7.5 binary J1553+1532AB are identified as candidate kinematic members of β Pictoris and Carina-Near moving groups, respectively, but the absence of spectral indicators of youth suggest that these are coincident field brown dwarfs.

4. Among 5 T dwarfs with multiple-epoch RV measurements, I found that two objects exhibited statistically significant RV variability consistent with binary orbital motion: the T0.0+T4.5 spectral binary 2MASS J1106+2754, which has an orbital period of $3.92^{+0.07}_{-0.09}$ yr and semi-amplitude of 6.30 ± 0.05 km s^{-1}; and the L7+T3.5

spectral binary 2MASS J2126+7617 which has an orbit period of $12^{+1.5}_{-1.2}$ yr and semi-amplitude of $3.0^{+0.7}_{-0.6}$ km s^{-1}. In addition, 2MASS J0559−1404, a suspected overluminous T4.5, shows evidence of RV variability over the course of 20 years, but no clear periodic signal; future observations are needed to confirm and assess the origin of these variations.

5. Using empirical age-velocity dispersion relations, I determined the kinematic age of local T dwarfs to be 3.5 ± 0.3 Gyr, which is consistent with the kinematic age of local late-M dwarfs (4.1 ± 0.3 Gyr), but considerably younger than the kinematic age of local L dwarfs (5.8 ± 0.3 Gyr). By excluding likely thick disk population members ($P(\mathrm{TD})/P(\mathrm{D}) > 1$), the kinematic age of local L dwarfs is lowered to 4.2 ± 0.3 Gyr, in line with late-M and T dwarfs. This analysis appears to partly resolve the long-standing kinematic anomaly of local L dwarfs.

6. Population simulations reproduce the measured ages of local thin-disk late-M, L, and T dwarfs, although L dwarf ages are predicted to be younger than observed. Varying the star formation history, mass function, evolutionary models, maximum age, and minimum mass of these simulations and comparing to my kinematic sample allows me to constrain some of these population parameters, but several degeneracies remain. I am able to rule out mass function evolution (bottom-heavy to top-heavy) as an explanation for old L dwarfs due to disagreement with the T dwarf velocity dispersion, but find tentative evidence of a lower hydrogen burning minimum mass (HBMM). A more refined breakdown in spectral type can improve this analysis, but will require larger samples to make robust constraints.

7. A detailed evaluation of kinematic age as a function of spectral type for L dwarfs reveals a linear trend of decreasing mean age with spectral type, as predicted by population simulations. I also identify an age upturn and sudden break in ages at

subtypes L4–L6 which likely reflects the terminus of the stellar Main Sequence. This spectral type range aligns with evolutionary model predictions for the HBMM at an age of 4–5 Gyr.

The work reported in Chapter 2 provides a significant expansion in the number and spectral type range of UCDs with precise 6D coordinates, and the inclusion of T dwarfs in particular allows me to constrain many of the underlying population parameters. It has also allowed me to resolve the L dwarf age anomaly and identify empirical diagnostics of brown dwarf evolution and the Main Sequence terminus. However, the size of the current sample remains the primary limitation in precisely quantifying key aspects of this analysis, notably the contaminating fraction of thick disk/blue L dwarfs in the local population, the location and sharpness of the stellar Main Sequence, and degeneracies among simulation parameters. There is considerable capacity to increase the size of the kinematic sample even in the local volume, which is necessary to properly address issues related to completeness, resolution and accuracy in per-spectral-type analyses, as well as the sample bias induced by distinct subpopulations such as blue L dwarfs. Moreover, even a volume-complete 20 pc sample represents a tiny fraction of the Milky Way environment, and it is possible that the immediate local volume around the Sun is not representative of the Galactic disk, a form of cosmic scatter. This motivates a deeper kinematic survey, to 50 pc or 100 pc for example, which may be feasible with future spectroscopic survey facilities or through a more restricted analysis of 2D kinematics (cf. Faherty et al. 2009). Improvements can also be made to the characterization of the UCD kinematic sample. While I specifically evaluated the contributions of young, binary, and unusually blue UCDs, I did not explicitly evaluate model metallicity or cloud variations, or inclination angle, which are of particular importance for the L dwarfs and can influence both empirical calibrations and the underlying evolution of brown dwarfs. There are also improvements to made to the population simulations. I have not explicitly taken into

account thick disk or halo populations in the simulation, which are likely well-mixed and not easily separable from the thin disk sample based on simple probability thresholds. There are also spatial-temporal correlations to consider, since sources found closer to the Sun (smaller scaleheights) will be preferentially younger than the broader Milky Way population (cf. Ryan et al. 2017). All of these considerations are open for exploration in future studies.

4.1.2 SDSS/APOGEE M and L Dwarfs

I summarize my main results for SDSS/APOGEE (Chapter 3) as follows:

1. I constructed a robust UCD sample of 182 ultracool dwarfs with 671 epochs of observations from APOGEE DR17, with spectral types ranging from M4 to L2. This is a subset of the full DR17 sample of 1563 candidate UCDs with 8055 epochs based on color magnitude selection criteria with photometry and astrometry from 2MASS and *Gaia* EDR3. I focused my analysis on the smaller "gold" sample to assure accurate assessment of source properties. I obtained additional low-resolution optical spectra using the Lick Shane KAST spectrograph to classify eleven sources with spectral types ranging from M5 to M9.

2. I employed a Markov Chain Monte Carlo forward-modeling method to measure RVs and $v \sin i$s with precisions of 0.3 km s^{-1} and 1.0 km s^{-1}, respectively, using the BT-Settl models (Baraffe et al. 2015) for higher-temperature sources and Sonora models (Marley et al. 2018; Marley et al. 2021), for lower-temperature sources.

3. The $v \sin i$ measurements of my sample have a median value of 16 km s^{-1}, and the distribution is consistent with literature M4–M9 dwarf measurements (median $v \sin i$ of 12.1 km s^{-1}).

4. I examined both individual and population 6D kinematics for my sample, facilitated by my RV measurements. Using the BANYAN Σ tool, I found roughly one third of my sample (66 sources) are known members of nearby young clusters or moving groups. The majority are previously reported in the literature, and I add three new sources 2MASS J05402570+2448090 (54.7% 40–50 Myr Argus moving group, 43.2% ∼200 Myr Carina Near moving group), 2MASS J14093200+4138080 (99.6% 40–50 Myr Argus moving group), and 2MASS J21272531+5553150 (99.3% ∼200 Myr Carina Near moving group). I also determined their Galactic orbits of the sample, most of which show are circular and planar (e ≤ 0.1, $i \leq 2\%$). There are 11 sources with intermediate thin/thick disk kinematics and 1 source with thick disk kinematics.

5. I computed the kinematic ages of the sample using empirical age-velocity dispersion relations. After removal of known young cluster members, I found a total velocity dispersion of 42.7 ± 0.6 km s^{-1}, corresponding to a kinematic age of 4.5 ± 0.3 Gyr using the empirical age-velocity dispersion relation, consistent with measurements of the 20 pc late-M dwarfs in the literature and my NIRSPEC analysis.

6. The averaged RV precision is sufficient for the identification of binaries in the sample with multi-epoch observations. I identified 29 sources with significant RV variability. For a subset of these sources with more than four epochs, I estimated their possible orbital parameters using the sparse RV and the Monte Carlo rejection sampler `The Joker`. Follow-up observations of these sources are needed to robustly determine their true orbital parameters.

7. Combining literature measurements of rotation periods from the *Kepler* K2 mission and other ground-based facilities, I computed the projected radii ($R \sin i$) for 26

sources, including 21 young and 5 field objects. $R \sin i$ shows a general decline with age as expected for pre-degeneracy contraction. The inferred $R \sin i$s for the Upper Scorpius cluster ($0.53^{+0.16}_{-0.15}$ $R_\odot$) and the field objects ($0.15^{+0.09}_{-0.06}$ $R_\odot$) are consistent with the Burrows et al. (2001) evolutionary models.

8. I computed the inclinations for a subset of my sample (9 sources) with robust periods and $v \sin i$. I found the Upper Scorpius (3 sources), field objects (3 sources), and the full sample (9 sources) are all consistent with randomly orientated distribution, although the sample size is small.

This work illustrates the need for improvements in the theoretical stellar atmosphere and evolutionary models, particularly for temperatures $\leq$ 3,500 K in H-band spectra. While the Sonora models provided better fits in numerous cases compared to BT-Settl models even for earlier spectral types, a better model that has updated opacities across the mid-M to early-L dwarfs will fully utilize the APOGEE spectra to their maximum scientific content, and allow for robust determination of $T_{\rm eff}$ and $\log g$ in addition to RV and $v \sin i$.

4.2 Future Work

The process of measuring and compiling of the largest RV and $v \sin i$ velocity sample for local ultracool dwarfs has revealed several new directions to improve my understanding of kinematics, rotation, and multiplicity of ultracool dwarfs.

First, despite the substantial increase in measurements, high-resolution spectral coverage of ultracool dwarfs is still very incomplete. This sample is largely limited to $<$20 pc, and remains only partly complete for late-M and L dwarfs, and largely incomplete for T dwarfs. A volume-complete high-resolution spectroscopic sample is necessary to robustly determine ultracool dwarf population statistics with subtype

resolution to clarify features related to brown dwarf evolution. This work requires next-generation high-resolution spectrometer on larger aperture telescopes such as the High resolution Infrared Spectrograph for Exoplanet Characterization (HISPEC; Mawet et al. 2019) on the Thirty Meter Telescope (TMT) or the Immersion Grating Near Infrared Spectrograph (IGNIS) on the W. M. Keck Telescope.

While multi-epoch NIRSPEC and APOGEE observations identified several promising RV binary candidates, I need follow-up high-resolution spectral observations to confirm and characterize these sources and increase the close-in binary sample. RV binaries yield the orbital parameters (periods, eccentricities, and separations) that can be compared to statistics for wider resolved brown dwarf binaries, as well as gas giant extrasolar planets sharing similar temperature ranges and atmospheric properties (Bowler et al. 2020). Binary statistics provide insight into their formation pathways (capture, in-situ formation, tertiary interactions), which also serving as benchmarks for theoretical models and tests of their long-term dynamical stability.

Higher precision wavelength calibration will be essential for identifying very-low mass companions around ultracool dwarfs, pushing into the exoplanet regime. Exoplanets around ultracool dwarfs are starting to be discovered, including the TRAPPIST-1 system (Gillon et al. 2017; transit method) and the Teegarden Star system (Zechmeister et al. 2019; RV method). Examination of the occurrence rate of exoplanets around ultracool dwarfs require more precise and sensitive high-resolution near-infrared spectrometers mounted on large aperture telescopes. For example, the laser frequency comb offers wavelength precision of $\sim$1 m s^{-1}. Such precision can allow me to detect a Neptune mass 17.0 M_{earth} exoplanet orbiting a 0.08 $M_{\odot}$ ultracool dwarf host at 0.01 AU.

Improved theoretical atmosphere model grids for low-mass stars and brown dwarfs are also needed. With updated molecular opacities and line lists, the Sonora model has provided significantly better fits for Keck/NIRSPEC T dwarf spectra in *J*-band

(demonstrated in Chapter 2) and late-M and early-L dwarf SDSS/APOGEE spectra in H-band (demonstrated in Chapter 3). However, the Sonora model is limited to its upper $T_{\rm eff}$ ceiling of 2,400 K, hindering comprehensive assessment of associated stellar atmospheric parameters including $T_{\rm eff}$ and $\log g$. Furthermore, the Sonora model does not include clouds, which are especially important for L-type ultracool dwarfs. Even in its applicable temperature regimes, the Sonora model fits show residuals in both CH_4 in J-band (Hsu et al. 2021), and H-band and CO in K-band (Tannock et al. 2022). Retrieval and forward-modeling methods are useful in identifying these missing molecular features and inaccurate molecular opacities.

An important next step for building on the high-resolution kinematic sample is to obtain detailed and precise abundance measurements. Coarse metallicity measurements are possible using low-resolution optical or infrared spectra, but precise and detailed abundances are needed, which can be used to probe different formation environments for single or multiple systems (e.g. C/O and D/H ratios, CO isotopes; Crossfield et al. 2019; Zhang et al. 2021a; Souto et al. 2022) as well as to compare with exoplanets (Mollière & Snellen 2019; Line et al. 2021). Abundance studies on higher mass stars have identified different Galactic populations such as streams (Ji et al. 2020) and dwarf galaxies (Escala et al. 2018), work that can be extended to ultracool dwarfs with sensitive high-resolution spectrometers on larger telescopes and accurate atmosphere models.

Finally, the hundreds of lines and molecular transitions provided by high-resolution spectra offers an opportunity to measure magnetic fields, especially for slow rotators identified in this thesis. With S/N $\sim$200, detailed line profiles, including pressure, rotation broadening and Zeeman effects can be studied. With possible variability period measurements with light curves and transit surveys (e.g. The Perkins INfrared Exosatellite Survey (PINES) survey; Tamburo et al. 2022), orientations inferred from inclinations can be examined with magnetic emission diagnostics to constrain magnetic field geometries.

For rapid rotators, line profile variability can be used to probe Doppler maps probing magnetic spots and clouds of different heights in the atmosphere. All of the measurements will enrich my understanding of the physical, evolutionary, and statistical properties of the UCD population.

A Minimum $v \sin i$ Determination

In Section 2.2.1, I described my method to determine the minimum $v \sin i$. Here I provide the corresponding diagnostic plots on the minimum $v \sin i$ values as a function of $T_{\rm eff}$ and S/N.

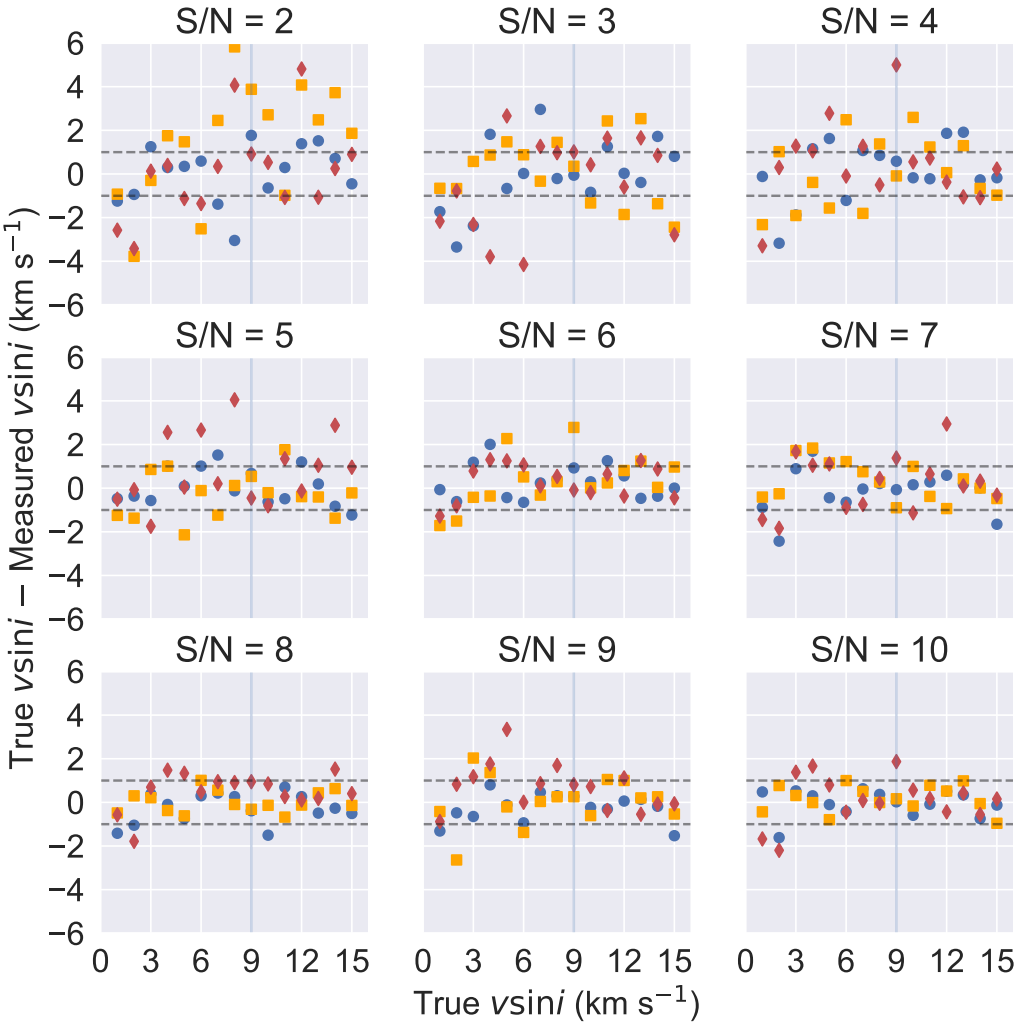

Figure A.1: The difference between true and measured $v \sin i$ compared to true $v \sin i$ values as a function of S/N and $T_{\rm eff}$ for BT-Settl models. The $T_{\rm eff}$ grid points are 900 K (blue), 1200 K (orange), and 1500 K (red). The grey horizontal dash lines represent $v \sin i$ difference = 1 km s^{-1}. The vertical blue line indicates the $v \sin i$ = 9 km s^{-1}

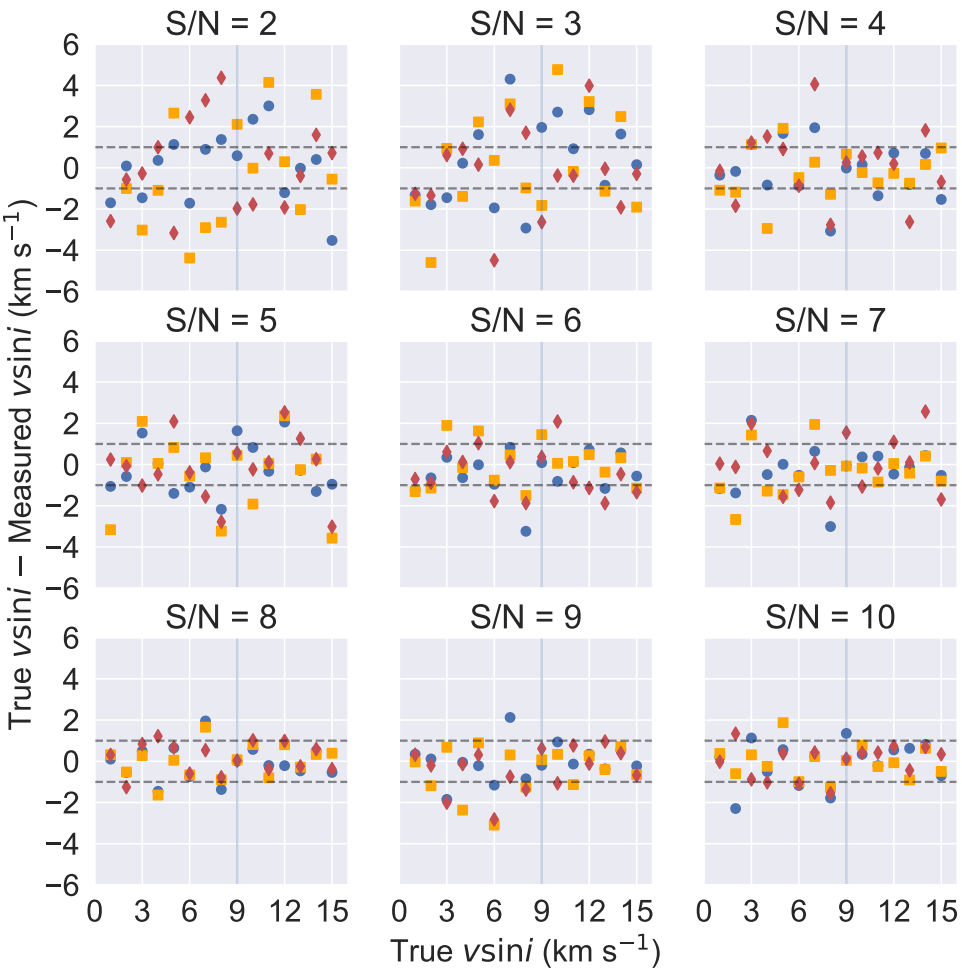

Figure A.2: Same as Figure A.1 for Sonora models.

B Simulated UCD Population Ages Under Different Assumptions

This Appendix supplements the analysis in Sectoin 2.5.4 by providing the full list of parameters and corresponding χ^2 fit values for the population simulation examined. Select visualizations of the age distributions and comparative χ^2 plots are provided in the main text.

Table B.1: Simulated UCD Population Ages Under Different Assumptions

τ (Gyr)	Star formation (rate)	α	Models	MBDM ($M_\odot$)	late-M dwarf age (Gyr)	L dwarf age (Gyr)	T dwarf age (Gyr)	χ^2
Observations								
ALL SOURCES					4.9 ± 0.3	7.1 ± 0.4	3.5 ± 0.3	···
NOT THICK DISK (P(TD)/P(D) < 10)					4.1 ± 0.3	5.8 ± 0.3	3.5 ± 0.3	···
THIN DISK (P(TD)/P(D) < 1)					4.1 ± 0.3	4.2 ± 0.3	3.5 ± 0.3	···
Simulations								
9[a]	uniform	0.5	B03	0.01	4.1 ± 0.8	3.1 ± 0.7	4.3 ± 1.2	2.1
9	uniform	0.5	B01	0.01	3.5 ± 0.7	3.1 ± 0.6	4.2 ± 1.2	3.0
9	uniform	0.5	S08	0.01	4.3 ± 0.8	3.4 ± 0.7	4.5 ± 1.2	1.7
9	uniform	0.5	M19	0.01	1.6 ± 0.3	3.1 ± 0.6	4.0 ± 1.1	42.1
9	uniform	0.5	P20C	0.01	0.2 ± 0.0	2.6 ± 0.5	4.2 ± 1.2	172.0
9	uniform	0.5	P20NW	0.01	0.3 ± 0.0	2.6 ± 0.6	4.3 ± 1.2	162.3
9	uniform	0.5	P20NS	0.01	0.4 ± 0.0	2.7 ± 0.6	4.1 ± 1.2	154.4
9	exponential	0.5	B03	0.01	4.5 ± 0.8	3.8 ± 0.8	4.7 ± 1.2	1.3
9	exponential	0.5	B01	0.01	3.6 ± 0.6	3.7 ± 0.7	4.9 ± 1.4	1.7
9	exponential	0.5	S08	0.01	4.6 ± 0.8	4.2 ± 0.8	4.8 ± 1.2	1.5
9	log-normal	0.5	B03	0.01	6.8 ± 1.3	6.1 ± 1.0	6.5 ± 1.6	11.6
9	log-normal	0.5	B01	0.01	7.4 ± 1.3	6.0 ± 1.0	6.2 ± 1.5	12.7
9	log-normal	0.5	S08	0.01	6.4 ± 1.0	6.2 ± 1.1	6.4 ± 1.6	11.3
9	uniform	-1.5	B03	0.01	4.1 ± 0.7	3.6 ± 0.7	5.0 ± 1.3	1.5
9	uniform	-1.5	B01	0.01	3.6 ± 0.7	3.7 ± 0.7	5.1 ± 1.3	2.0
9	uniform	-1.5	S08	0.01	3.9 ± 0.6	3.9 ± 0.7	5.3 ± 1.2	2.2
9	uniform	-0.5	B03	0.01	4.0 ± 0.8	3.3 ± 0.6	5.1 ± 1.4	2.7
9	uniform	-0.5	B01	0.01	4.0 ± 0.8	3.2 ± 0.6	4.6 ± 1.3	2.2
9	uniform	-0.5	S08	0.01	3.5 ± 0.6	3.7 ± 0.7	4.7 ± 1.3	1.7
9	uniform	1.5	B03	0.01	3.8 ± 0.7	2.7 ± 0.6	3.6 ± 1.0	4.7
9	uniform	1.5	B01	0.01	3.6 ± 0.6	2.4 ± 0.5	3.6 ± 1.1	8.1
9	uniform	1.5	S08	0.01	3.5 ± 0.5	2.8 ± 0.6	3.6 ± 1.0	5.5
9[b]	uniform	0.0/1.0/3.0	B03	0.01	4.4 ± 0.9	3.8 ± 0.7	3.5 ± 1.0	0.3
9	uniform	0.0/1.0/3.0	B01	0.01	3.6 ± 0.7	3.1 ± 0.6	4.0 ± 1.1	2.6
9	uniform	0.0/1.0/3.0	S08	0.01	5.4 ± 1.0	3.6 ± 0.7	3.8 ± 1.0	2.2
9[c]	uniform	1.0/0.0/3.0	B03	0.01	3.7 ± 0.7	3.8 ± 0.7	4.3 ± 1.1	0.9
9	uniform	1.0/0.0/3.0	B01	0.01	3.1 ± 0.7	3.0 ± 0.6	4.4 ± 1.2	4.9
9	uniform	1.0/0.0/3.0	S08	0.01	3.8 ± 0.6	3.1 ± 0.6	4.8 ± 1.2	3.3
9	uniform	C03	B03	0.01	3.7 ± 0.7	2.8 ± 0.6	4.1 ± 1.1	4.4
9	uniform	C03	B01	0.01	3.6 ± 0.7	2.8 ± 0.6	4.0 ± 1.2	4.2
9	uniform	C03	S08	0.01	3.6 ± 0.6	2.8 ± 0.6	4.2 ± 1.2	5.2
9	exponential	-1.5	B03	0.01	5.2 ± 0.9	4.6 ± 0.9	5.5 ± 1.4	3.3
9	exponential	-1.5	B01	0.01	4.4 ± 0.8	4.8 ± 0.9	5.8 ± 1.6	2.8
9	exponential	-1.5	S08	0.01	4.8 ± 0.8	4.6 ± 0.8	5.2 ± 1.2	2.9
9	exponential	-0.5	B03	0.01	4.5 ± 0.8	4.2 ± 0.7	5.2 ± 1.5	1.5
9	exponential	-0.5	B01	0.01	4.1 ± 0.8	3.9 ± 0.8	5.4 ± 1.4	1.8

Table B.1 (*continued*)

Table B.1 (*continued*)

τ (Gyr)	Star formation (rate)	α	Models	MBDM ($M_\odot$)	late-M dwarf age (Gyr)	L dwarf age (Gyr)	T dwarf age (Gyr)	χ^2
9	exponential	-0.5	S08	0.01	4.3 ± 0.8	4.4 ± 0.8	5.2 ± 1.4	1.6
9	exponential	1.5	B03	0.01	5.1 ± 0.9	3.6 ± 0.7	4.2 ± 1.2	2.0
9	exponential	1.5	B01	0.01	4.7 ± 1.0	3.3 ± 0.7	4.3 ± 1.2	1.9
9	exponential	1.5	S08	0.01	4.0 ± 0.5	3.8 ± 0.8	4.4 ± 1.2	0.6
9	exponential	0.0/1.0/3.0	B03	0.01	5.3 ± 1.0	5.0 ± 0.9	4.2 ± 1.2	2.5
9	exponential	0.0/1.0/3.0	B01	0.01	3.9 ± 0.7	3.6 ± 0.7	4.5 ± 1.2	1.2
9	exponential	0.0/1.0/3.0	S08	0.01	5.8 ± 0.9	4.2 ± 0.8	4.5 ± 1.2	3.9
9	exponential	1.0/0.0/3.0	B03	0.01	4.2 ± 0.7	4.8 ± 0.8	5.2 ± 1.3	2.3
9	exponential	1.0/0.0/3.0	B01	0.01	4.6 ± 1.0	3.6 ± 0.7	5.1 ± 1.4	2.0
9	exponential	1.0/0.0/3.0	S08	0.01	4.3 ± 0.8	3.8 ± 0.7	5.5 ± 1.4	2.1
9	exponential	C03	B03	0.01	4.5 ± 0.9	3.8 ± 0.8	4.8 ± 1.3	1.2
9	exponential	C03	B01	0.01	3.6 ± 0.7	3.2 ± 0.6	4.6 ± 1.2	2.5
9	exponential	C03	S08	0.01	4.5 ± 0.7	3.9 ± 0.8	4.6 ± 1.3	1.1
9	log-normal	-1.5	B03	0.01	7.1 ± 1.2	6.2 ± 0.9	7.0 ± 1.7	14.6
9	log-normal	-1.5	B01	0.01	6.4 ± 1.1	5.8 ± 0.8	6.6 ± 1.6	11.3
9	log-normal	-1.5	S08	0.01	7.2 ± 1.0	6.9 ± 1.2	6.7 ± 1.6	17.5
9	log-normal	-0.5	B03	0.01	6.9 ± 1.2	6.0 ± 1.0	6.4 ± 1.5	11.6
9	log-normal	-0.5	B01	0.01	6.9 ± 1.2	6.0 ± 1.1	6.2 ± 1.5	11.6
9	log-normal	-0.5	S08	0.01	7.1 ± 1.1	6.0 ± 0.9	6.8 ± 1.8	14.6
9	log-normal	1.5	B03	0.01	6.5 ± 1.0	5.7 ± 1.0	6.1 ± 1.6	10.2
9	log-normal	1.5	B01	0.01	5.7 ± 0.8	5.1 ± 0.8	6.2 ± 1.6	7.2
9	log-normal	1.5	S08	0.01	5.7 ± 0.8	5.6 ± 0.9	6.3 ± 1.6	8.9
9	log-normal	0.0/1.0/3.0	B03	0.01	7.4 ± 1.2	6.0 ± 0.9	6.1 ± 1.6	13.9
9	log-normal	0.0/1.0/3.0	B01	0.01	6.3 ± 1.0	6.3 ± 1.0	6.2 ± 1.5	12.0
9	log-normal	0.0/1.0/3.0	S08	0.01	6.2 ± 0.9	6.3 ± 1.1	6.2 ± 1.5	11.9
9	log-normal	1.0/0.0/3.0	B03	0.01	6.4 ± 1.1	6.1 ± 0.9	6.4 ± 1.6	11.6
9	log-normal	1.0/0.0/3.0	B01	0.01	5.7 ± 0.9	5.8 ± 1.0	6.6 ± 1.8	8.4
9	log-normal	1.0/0.0/3.0	S08	0.01	6.1 ± 1.0	5.8 ± 1.0	6.3 ± 1.5	10.3
9	log-normal	C03	B03	0.01	6.5 ± 1.1	5.6 ± 0.9	6.4 ± 1.6	9.6
9	log-normal	C03	B01	0.01	6.3 ± 1.0	5.1 ± 0.8	6.2 ± 1.5	9.0
9	log-normal	C03	S08	0.01	6.7 ± 0.8	6.1 ± 1.0	6.6 ± 1.6	15.4
9	uniform	-1.5	B03	0.02	4.0 ± 0.8	3.9 ± 0.7	5.0 ± 1.3	1.4
9	uniform	-1.5	B03	0.03	4.0 ± 0.8	3.5 ± 0.6	5.1 ± 1.3	2.3
9	uniform	-1.5	B01	0.02	3.6 ± 0.7	3.9 ± 0.7	4.8 ± 1.3	1.7
9	uniform	-1.5	B01	0.03	3.9 ± 0.7	4.1 ± 0.7	5.2 ± 1.2	2.1
9	uniform	-1.5	S08	0.02	4.1 ± 0.7	4.0 ± 0.7	5.5 ± 1.4	2.0
9	uniform	-1.5	S08	0.03	3.4 ± 0.6	3.6 ± 0.7	5.6 ± 1.5	3.2
9	uniform	0.5	B03	0.02	4.2 ± 0.8	3.1 ± 0.6	4.9 ± 1.4	3.0
9	uniform	0.5	B03	0.03	4.0 ± 0.8	3.3 ± 0.7	5.2 ± 1.4	2.5
9	uniform	0.5	B01	0.02	3.4 ± 0.7	3.1 ± 0.6	4.5 ± 1.2	3.3
9	uniform	0.5	B01	0.03	3.2 ± 0.7	3.0 ± 0.6	4.7 ± 1.3	4.9
9	uniform	0.5	S08	0.02	4.1 ± 0.8	3.1 ± 0.6	4.5 ± 1.2	2.4
9	uniform	0.5	S08	0.03	3.6 ± 0.7	3.3 ± 0.6	5.0 ± 1.3	3.2
9	uniform	-0.5	B03	0.02	4.2 ± 0.8	3.5 ± 0.7	5.0 ± 1.3	1.8
9	uniform	-0.5	B03	0.03	4.2 ± 0.8	3.6 ± 0.7	5.2 ± 1.3	2.1
9	uniform	-0.5	B01	0.02	3.3 ± 0.7	3.5 ± 0.7	4.9 ± 1.3	2.9
9	uniform	-0.5	B01	0.03	4.1 ± 0.9	3.6 ± 0.8	4.9 ± 1.3	1.5
9	uniform	-0.5	S08	0.02	4.0 ± 0.8	3.7 ± 0.7	4.9 ± 1.3	1.5
9	uniform	-0.5	S08	0.03	3.6 ± 0.6	3.8 ± 0.7	5.5 ± 1.4	2.5
9	uniform	1.5	B03	0.02	4.0 ± 0.8	2.6 ± 0.6	4.3 ± 1.2	5.3
9	uniform	1.5	B03	0.03	4.1 ± 0.8	2.7 ± 0.6	4.8 ± 1.3	5.8
9	uniform	1.5	B01	0.02	3.3 ± 0.7	2.5 ± 0.6	4.1 ± 1.2	7.5
9	uniform	1.5	B01	0.03	3.1 ± 0.6	2.6 ± 0.6	4.7 ± 1.2	8.6
9	uniform	1.5	S08	0.02	3.3 ± 0.6	3.0 ± 0.6	4.2 ± 1.2	4.4
9	uniform	1.5	S08	0.03	4.0 ± 0.8	3.0 ± 0.6	4.8 ± 1.2	3.8
9	uniform	0.0/1.0/3.0	B03	0.02	4.5 ± 0.9	3.2 ± 0.6	4.1 ± 1.1	2.1
9	uniform	0.0/1.0/3.0	B03	0.03	4.2 ± 0.9	3.6 ± 0.7	4.4 ± 1.1	0.9
9	uniform	0.0/1.0/3.0	B01	0.02	3.7 ± 0.8	3.1 ± 0.6	4.2 ± 1.2	2.6
9	uniform	0.0/1.0/3.0	B01	0.03	3.3 ± 0.7	2.8 ± 0.6	4.4 ± 1.2	5.9
9	uniform	0.0/1.0/3.0	S08	0.02	3.5 ± 0.6	3.0 ± 0.6	4.3 ± 1.2	3.4
9	uniform	0.0/1.0/3.0	S08	0.03	4.2 ± 0.8	3.2 ± 0.6	4.4 ± 1.1	2.2

Table B.1 (*continued*)

Table B.1 (*continued*)

τ (Gyr)	Star formation (rate)	α	Models	MBDM ($M_\odot$)	late-M dwarf age (Gyr)	L dwarf age (Gyr)	T dwarf age (Gyr)	χ^2
9	uniform	1.0/0.0/3.0	B03	0.02	3.7 ± 0.7	3.8 ± 0.7	5.2 ± 1.4	2.0
9	uniform	1.0/0.0/3.0	B03	0.03	3.8 ± 0.8	4.0 ± 0.7	5.5 ± 1.4	2.0
9	uniform	1.0/0.0/3.0	B01	0.02	3.0 ± 0.6	3.0 ± 0.6	4.8 ± 1.3	5.8
9	uniform	1.0/0.0/3.0	B01	0.03	3.5 ± 0.7	3.3 ± 0.7	5.4 ± 1.4	3.5
9	uniform	1.0/0.0/3.0	S08	0.02	3.4 ± 0.6	3.4 ± 0.6	4.9 ± 1.2	3.7
9	uniform	1.0/0.0/3.0	S08	0.03	3.8 ± 0.7	3.6 ± 0.7	5.6 ± 1.4	2.6
9	uniform	C03	B03	0.02	3.6 ± 0.7	2.7 ± 0.6	4.6 ± 1.2	5.7
9	uniform	C03	B03	0.03	4.0 ± 0.8	2.9 ± 0.6	5.0 ± 1.3	4.4
9	uniform	C03	B01	0.02	3.5 ± 0.7	2.5 ± 0.6	4.2 ± 1.2	7.6
9	uniform	C03	B01	0.03	3.2 ± 0.7	2.6 ± 0.5	4.6 ± 1.2	8.6
9	uniform	C03	S08	0.02	3.2 ± 0.5	3.0 ± 0.6	4.4 ± 1.2	5.0
9	uniform	C03	S08	0.03	4.2 ± 0.8	3.1 ± 0.6	5.0 ± 1.3	3.7
9	exponential	-1.5	B03	0.02	4.8 ± 0.9	4.5 ± 0.8	5.9 ± 1.5	3.3
9	exponential	-1.5	B03	0.03	5.1 ± 1.0	4.8 ± 0.8	5.5 ± 1.4	3.7
9	exponential	-1.5	B01	0.02	4.7 ± 0.9	4.0 ± 0.7	5.4 ± 1.3	2.4
9	exponential	-1.5	B01	0.03	3.7 ± 0.6	4.3 ± 0.8	5.2 ± 1.2	2.2
9	exponential	-1.5	S08	0.02	4.6 ± 0.7	4.4 ± 0.8	5.3 ± 1.2	2.5
9	exponential	-1.5	S08	0.03	4.2 ± 0.7	4.9 ± 0.8	5.9 ± 1.5	3.4
9	exponential	0.5	B03	0.02	4.6 ± 0.9	4.2 ± 0.8	5.1 ± 1.3	1.6
9	exponential	0.5	B03	0.03	4.9 ± 1.0	3.9 ± 0.8	5.4 ± 1.3	2.6
9	exponential	0.5	B01	0.02	4.5 ± 0.7	4.1 ± 0.7	5.0 ± 1.4	1.4
9	exponential	0.5	B01	0.03	4.2 ± 0.9	4.0 ± 0.8	5.3 ± 1.3	1.8
9	exponential	0.5	S08	0.02	4.7 ± 0.7	4.1 ± 0.8	5.3 ± 1.4	2.2
9	exponential	0.5	S08	0.03	4.5 ± 0.9	4.0 ± 0.7	5.6 ± 1.4	2.4
9	exponential	-0.5	B03	0.02	4.8 ± 0.9	4.5 ± 0.8	5.6 ± 1.5	2.6
9	exponential	-0.5	B03	0.03	4.9 ± 1.0	4.4 ± 0.8	5.5 ± 1.3	3.1
9	exponential	-0.5	B01	0.02	4.0 ± 0.7	4.2 ± 0.8	5.3 ± 1.4	1.5
9	exponential	-0.5	B01	0.03	4.1 ± 0.8	3.8 ± 0.7	5.6 ± 1.4	2.3
9	exponential	-0.5	S08	0.02	5.1 ± 0.9	4.0 ± 0.7	5.2 ± 1.4	2.7
9	exponential	-0.5	S08	0.03	4.5 ± 0.8	4.4 ± 0.8	6.1 ± 1.6	3.1
9	exponential	1.5	B03	0.02	4.2 ± 0.8	3.5 ± 0.6	4.8 ± 1.3	1.8
9	exponential	1.5	B03	0.03	4.8 ± 0.9	3.5 ± 0.8	5.3 ± 1.4	2.9
9	exponential	1.5	B01	0.02	3.6 ± 0.6	3.0 ± 0.6	4.8 ± 1.3	4.4
9	exponential	1.5	B01	0.03	4.4 ± 0.8	3.3 ± 0.6	5.2 ± 1.3	3.1
9	exponential	1.5	S08	0.02	4.7 ± 0.6	3.7 ± 0.7	4.8 ± 1.3	1.8
9	exponential	1.5	S08	0.03	5.5 ± 1.1	3.7 ± 0.7	5.6 ± 1.5	3.8
9	exponential	0.0/1.0/3.0	B03	0.02	4.9 ± 0.8	4.3 ± 0.8	4.6 ± 1.2	1.5
9	exponential	0.0/1.0/3.0	B03	0.03	4.8 ± 0.9	4.2 ± 0.8	4.8 ± 1.2	1.6
9	exponential	0.0/1.0/3.0	B01	0.02	4.2 ± 0.8	3.7 ± 0.7	4.8 ± 1.3	1.3
9	exponential	0.0/1.0/3.0	B01	0.03	4.4 ± 0.9	3.6 ± 0.7	5.3 ± 1.4	2.0
9	exponential	0.0/1.0/3.0	S08	0.02	5.4 ± 0.9	4.0 ± 0.7	4.9 ± 1.3	2.8
9	exponential	0.0/1.0/3.0	S08	0.03	4.7 ± 0.8	4.0 ± 0.8	5.3 ± 1.4	1.9
9	exponential	1.0/0.0/3.0	B03	0.02	4.7 ± 0.9	4.7 ± 0.8	5.6 ± 1.4	3.0
9	exponential	1.0/0.0/3.0	B03	0.03	4.7 ± 0.8	4.9 ± 0.9	5.8 ± 1.5	3.4
9	exponential	1.0/0.0/3.0	B01	0.02	4.2 ± 0.8	3.6 ± 0.8	5.3 ± 1.3	2.3
9	exponential	1.0/0.0/3.0	B01	0.03	4.2 ± 0.8	3.9 ± 0.7	5.5 ± 1.3	2.3
9	exponential	1.0/0.0/3.0	S08	0.02	4.6 ± 0.8	4.1 ± 0.8	5.8 ± 1.5	2.7
9	exponential	1.0/0.0/3.0	S08	0.03	3.7 ± 0.6	4.2 ± 0.8	6.4 ± 1.6	3.7
9	exponential	C03	B03	0.02	4.4 ± 0.9	3.5 ± 0.7	4.9 ± 1.3	1.9
9	exponential	C03	B03	0.03	4.6 ± 0.9	3.9 ± 0.8	5.6 ± 1.4	2.4
9	exponential	C03	B01	0.02	4.8 ± 0.9	3.4 ± 0.6	5.0 ± 1.4	2.5
9	exponential	C03	B01	0.03	4.3 ± 0.9	3.2 ± 0.6	5.4 ± 1.4	3.2
9	exponential	C03	S08	0.02	3.4 ± 0.6	3.9 ± 0.8	5.1 ± 1.3	2.7
9	exponential	C03	S08	0.03	4.5 ± 0.7	3.9 ± 0.8	5.6 ± 1.4	2.4
9	log-normal	-1.5	B03	0.02	6.6 ± 1.2	6.1 ± 1.0	6.7 ± 1.6	11.8
9	log-normal	-1.5	B03	0.03	6.5 ± 1.1	6.2 ± 1.0	6.9 ± 1.7	12.0
9	log-normal	-1.5	B01	0.02	6.6 ± 1.1	6.1 ± 1.0	6.9 ± 1.6	12.3
9	log-normal	-1.5	B01	0.03	6.2 ± 1.1	6.4 ± 1.0	6.7 ± 1.7	11.2
9	log-normal	-1.5	S08	0.02	6.9 ± 1.1	6.6 ± 1.0	6.5 ± 1.5	15.9
9	log-normal	-1.5	S08	0.03	6.7 ± 1.0	6.2 ± 1.0	6.6 ± 1.6	13.8
9	log-normal	0.5	B03	0.02	6.8 ± 1.1	5.8 ± 0.9	6.2 ± 1.5	11.8

Table B.1 (*continued*)

Table B.1 (*continued*)

τ (Gyr)	Star formation (rate)	α	Models	MBDM ($M_\odot$)	late-M dwarf age (Gyr)	L dwarf age (Gyr)	T dwarf age (Gyr)	χ^2
9	log-normal	0.5	B03	0.03	5.9 ± 0.9	6.2 ± 1.0	6.9 ± 1.7	10.8
9	log-normal	0.5	B01	0.02	5.7 ± 0.8	5.8 ± 0.9	6.3 ± 1.5	9.9
9	log-normal	0.5	B01	0.03	6.2 ± 1.0	6.0 ± 1.0	6.6 ± 1.6	11.1
9	log-normal	0.5	S08	0.02	6.7 ± 1.0	6.0 ± 1.0	6.6 ± 1.6	12.9
9	log-normal	0.5	S08	0.03	5.7 ± 0.8	6.4 ± 1.1	6.6 ± 1.6	11.0
9	log-normal	-0.5	B03	0.02	6.2 ± 1.1	6.5 ± 1.0	6.6 ± 1.7	12.0
9	log-normal	-0.5	B03	0.03	6.5 ± 1.0	6.2 ± 0.9	6.6 ± 1.6	13.0
9	log-normal	-0.5	B01	0.02	6.6 ± 1.2	6.5 ± 1.1	6.5 ± 1.6	11.8
9	log-normal	-0.5	B01	0.03	5.8 ± 0.9	6.3 ± 1.0	6.9 ± 1.7	11.6
9	log-normal	-0.5	S08	0.02	5.5 ± 0.9	6.2 ± 0.9	6.4 ± 1.6	9.8
9	log-normal	-0.5	S08	0.03	6.4 ± 1.0	6.5 ± 1.2	6.8 ± 1.7	12.1
9	log-normal	1.5	B03	0.02	6.6 ± 1.2	5.7 ± 1.0	6.2 ± 1.6	9.7
9	log-normal	1.5	B03	0.03	6.5 ± 1.1	5.6 ± 0.9	6.8 ± 1.6	11.0
9	log-normal	1.5	B01	0.02	6.0 ± 1.0	6.0 ± 0.9	6.3 ± 1.6	10.4
9	log-normal	1.5	B01	0.03	5.2 ± 0.9	5.8 ± 1.0	6.4 ± 1.6	7.3
9	log-normal	1.5	S08	0.02	6.9 ± 1.2	5.4 ± 0.9	6.2 ± 1.6	9.7
9	log-normal	1.5	S08	0.03	6.5 ± 1.0	6.1 ± 1.0	6.8 ± 1.7	12.4
9	log-normal	0.0/1.0/3.0	B03	0.02	7.0 ± 1.3	6.4 ± 1.0	6.0 ± 1.5	12.3
9	log-normal	0.0/1.0/3.0	B03	0.03	6.6 ± 1.1	6.7 ± 1.1	6.3 ± 1.6	12.8
9	log-normal	0.0/1.0/3.0	B01	0.02	6.8 ± 1.1	5.8 ± 0.8	6.0 ± 1.5	12.0
9	log-normal	0.0/1.0/3.0	B01	0.03	6.0 ± 0.9	5.7 ± 1.0	6.4 ± 1.6	9.0
9	log-normal	0.0/1.0/3.0	S08	0.02	5.7 ± 0.9	6.1 ± 1.1	6.2 ± 1.5	9.1
9	log-normal	0.0/1.0/3.0	S08	0.03	7.8 ± 1.3	5.8 ± 1.0	6.6 ± 1.5	14.6
9	log-normal	1.0/0.0/3.0	B03	0.02	6.2 ± 1.0	6.4 ± 1.0	6.4 ± 1.6	11.6
9	log-normal	1.0/0.0/3.0	B03	0.03	6.6 ± 1.1	6.8 ± 1.1	7.0 ± 1.7	14.9
9	log-normal	1.0/0.0/3.0	B01	0.02	5.5 ± 0.8	5.6 ± 0.9	6.5 ± 1.6	8.6
9	log-normal	1.0/0.0/3.0	B01	0.03	6.4 ± 1.0	5.7 ± 0.9	7.2 ± 1.8	11.5
9	log-normal	1.0/0.0/3.0	S08	0.02	6.3 ± 0.9	5.8 ± 1.0	6.7 ± 1.6	11.6
9	log-normal	1.0/0.0/3.0	S08	0.03	7.4 ± 1.3	6.2 ± 1.0	7.0 ± 1.7	14.5
9	log-normal	C03	B03	0.02	6.1 ± 1.1	5.4 ± 0.9	6.4 ± 1.5	8.5
9	log-normal	C03	B03	0.03	6.3 ± 1.1	5.8 ± 1.0	6.9 ± 1.7	10.2
9	log-normal	C03	B01	0.02	6.7 ± 1.1	5.0 ± 0.8	6.5 ± 1.7	9.7
9	log-normal	C03	B01	0.03	6.8 ± 1.2	6.0 ± 1.1	6.6 ± 1.6	11.5
9	log-normal	C03	S08	0.02	5.6 ± 0.9	5.6 ± 0.9	6.3 ± 1.6	7.9
9	log-normal	C03	S08	0.03	5.7 ± 0.9	5.9 ± 1.0	6.8 ± 1.7	9.8
6	uniform	0.5	B03	0.01	2.8 ± 0.6	2.2 ± 0.4	3.0 ± 0.8	18.1
6	uniform	0.5	B01	0.01	1.9 ± 0.4	2.4 ± 0.5	3.0 ± 0.9	28.6
6	uniform	0.5	S08	0.01	2.7 ± 0.5	2.2 ± 0.5	3.0 ± 0.9	16.5
6	uniform	0.5	M19	0.01	1.2 ± 0.2	2.2 ± 0.4	2.9 ± 0.8	72.8
6	uniform	0.5	P20C	0.01	0.4 ± 0.0	2.0 ± 0.4	3.0 ± 0.8	164.1
6	uniform	0.5	P20NW	0.01	0.3 ± 0.0	2.0 ± 0.4	3.0 ± 0.8	173.3
6	uniform	0.5	P20NS	0.01	0.2 ± 0.0	1.8 ± 0.4	2.9 ± 0.8	189.3
6	exponential	0.5	B03	0.01	3.0 ± 0.6	2.5 ± 0.5	3.2 ± 0.9	10.4
6	exponential	0.5	B01	0.01	2.6 ± 0.6	2.4 ± 0.4	3.2 ± 0.9	16.2
6	exponential	0.5	S08	0.01	3.2 ± 0.6	2.7 ± 0.6	3.2 ± 0.9	6.7
6	log-normal	0.5	B03	0.01	3.6 ± 0.6	3.2 ± 0.6	3.9 ± 1.1	2.4
6	log-normal	0.5	B01	0.01	3.4 ± 0.6	3.2 ± 0.6	3.7 ± 1.0	3.1
6	log-normal	0.5	S08	0.01	3.7 ± 0.7	3.3 ± 0.6	3.5 ± 0.9	1.7
6	uniform	-1.5	B03	0.01	2.8 ± 0.6	2.8 ± 0.5	3.8 ± 1.0	9.0
6	uniform	-1.5	B01	0.01	2.5 ± 0.5	2.6 ± 0.5	3.8 ± 1.1	14.2
6	uniform	-1.5	S08	0.01	2.3 ± 0.4	2.7 ± 0.5	3.8 ± 1.1	17.9
6	uniform	-0.5	B03	0.01	2.8 ± 0.6	2.5 ± 0.5	3.4 ± 1.0	11.3
6	uniform	-0.5	B01	0.01	2.1 ± 0.5	2.3 ± 0.4	3.1 ± 0.9	24.7
6	uniform	-0.5	S08	0.01	2.6 ± 0.5	2.8 ± 0.6	3.4 ± 0.9	10.2
6	uniform	1.5	B03	0.01	2.2 ± 0.4	1.7 ± 0.4	2.5 ± 0.7	38.3
6	uniform	1.5	B01	0.01	2.4 ± 0.6	1.8 ± 0.4	2.6 ± 0.8	27.5
6	uniform	1.5	S08	0.01	1.7 ± 0.4	2.0 ± 0.4	2.6 ± 0.8	44.9
6	uniform	0.0/1.0/3.0	B03	0.01	2.9 ± 0.6	2.6 ± 0.5	2.4 ± 0.7	12.5
6	uniform	0.0/1.0/3.0	B01	0.01	2.3 ± 0.4	2.4 ± 0.5	2.6 ± 0.8	20.4
6	uniform	0.0/1.0/3.0	S08	0.01	3.1 ± 0.6	2.3 ± 0.5	2.6 ± 0.8	12.3
6	uniform	1.0/0.0/3.0	B03	0.01	2.4 ± 0.5	2.4 ± 0.5	3.2 ± 0.8	18.1

Table B.1 (*continued*)

Table B.1 (*continued*)

τ (Gyr)	Star formation (rate)	α	Models	MBDM ($M_\odot$)	late-M dwarf age (Gyr)	L dwarf age (Gyr)	T dwarf age (Gyr)	χ^2
6	uniform	1.0/0.0/3.0	B01	0.01	2.0 ± 0.4	2.2 ± 0.4	3.1 ± 0.8	31.8
6	uniform	1.0/0.0/3.0	S08	0.01	2.1 ± 0.4	2.3 ± 0.5	3.4 ± 1.0	23.8
6	uniform	C03	B03	0.01	2.4 ± 0.6	1.9 ± 0.4	2.8 ± 0.8	24.7
6	uniform	C03	B01	0.01	2.0 ± 0.4	1.8 ± 0.4	2.9 ± 0.8	38.7
6	uniform	C03	S08	0.01	2.4 ± 0.4	2.1 ± 0.4	3.0 ± 0.9	27.3
6	exponential	-1.5	B03	0.01	2.9 ± 0.6	3.0 ± 0.5	3.8 ± 0.9	6.8
6	exponential	-1.5	B01	0.01	2.8 ± 0.5	2.7 ± 0.5	3.9 ± 1.0	11.0
6	exponential	-1.5	S08	0.01	2.6 ± 0.5	3.1 ± 0.6	4.0 ± 1.0	9.0
6	exponential	-0.5	B03	0.01	3.1 ± 0.6	2.8 ± 0.6	3.8 ± 1.0	6.2
6	exponential	-0.5	B01	0.01	2.7 ± 0.6	2.9 ± 0.6	3.4 ± 0.9	8.9
6	exponential	-0.5	S08	0.01	2.7 ± 0.5	2.7 ± 0.5	3.8 ± 0.9	10.7
6	exponential	1.5	B03	0.01	2.9 ± 0.5	2.1 ± 0.4	2.9 ± 0.8	20.2
6	exponential	1.5	B01	0.01	2.2 ± 0.4	1.9 ± 0.4	2.7 ± 0.8	33.1
6	exponential	1.5	S08	0.01	2.5 ± 0.4	2.2 ± 0.4	2.9 ± 0.9	22.8
6	exponential	0.0/1.0/3.0	B03	0.01	3.1 ± 0.6	3.0 ± 0.6	2.7 ± 0.8	5.6
6	exponential	0.0/1.0/3.0	B01	0.01	2.6 ± 0.5	2.4 ± 0.5	2.9 ± 0.8	16.2
6	exponential	0.0/1.0/3.0	S08	0.01	3.6 ± 0.6	2.5 ± 0.5	2.9 ± 0.8	8.5
6	exponential	1.0/0.0/3.0	B03	0.01	2.6 ± 0.5	2.5 ± 0.5	3.6 ± 1.0	14.2
6	exponential	1.0/0.0/3.0	B01	0.01	2.2 ± 0.4	2.5 ± 0.5	3.4 ± 0.9	18.8
6	exponential	1.0/0.0/3.0	S08	0.01	2.9 ± 0.5	2.6 ± 0.5	3.7 ± 1.0	10.3
6	exponential	C03	B03	0.01	3.1 ± 0.6	2.3 ± 0.4	3.1 ± 0.9	14.1
6	exponential	C03	B01	0.01	2.3 ± 0.5	2.0 ± 0.4	3.0 ± 0.8	25.3
6	exponential	C03	S08	0.01	2.9 ± 0.5	2.3 ± 0.5	3.2 ± 0.9	14.8
6	log-normal	-1.5	B03	0.01	3.8 ± 0.8	3.6 ± 0.6	4.2 ± 1.0	1.1
6	log-normal	-1.5	B01	0.01	3.5 ± 0.6	3.5 ± 0.6	4.1 ± 1.0	1.9
6	log-normal	-1.5	S08	0.01	3.5 ± 0.6	3.5 ± 0.6	4.2 ± 1.0	2.0
6	log-normal	-0.5	B03	0.01	3.7 ± 0.7	3.6 ± 0.6	4.0 ± 1.1	0.9
6	log-normal	-0.5	B01	0.01	3.4 ± 0.6	3.4 ± 0.6	4.0 ± 1.0	2.7
6	log-normal	-0.5	S08	0.01	3.6 ± 0.6	3.6 ± 0.6	4.0 ± 1.0	1.3
6	log-normal	1.5	B03	0.01	4.1 ± 0.7	3.0 ± 0.5	3.5 ± 1.0	3.0
6	log-normal	1.5	B01	0.01	3.2 ± 0.6	2.9 ± 0.6	3.5 ± 1.0	5.1
6	log-normal	1.5	S08	0.01	3.7 ± 0.5	3.1 ± 0.6	3.4 ± 0.9	2.8
6	log-normal	0.0/1.0/3.0	B03	0.01	3.9 ± 0.7	4.0 ± 0.7	3.5 ± 0.9	0.1
6	log-normal	0.0/1.0/3.0	B01	0.01	3.3 ± 0.6	3.0 ± 0.6	3.7 ± 1.0	4.5
6	log-normal	0.0/1.0/3.0	S08	0.01	3.8 ± 0.6	3.4 ± 0.6	3.4 ± 0.9	1.1
6	log-normal	1.0/0.0/3.0	B03	0.01	3.4 ± 0.6	3.5 ± 0.6	3.8 ± 1.0	1.7
6	log-normal	1.0/0.0/3.0	B01	0.01	3.0 ± 0.5	2.9 ± 0.5	4.1 ± 1.1	7.3
6	log-normal	1.0/0.0/3.0	S08	0.01	3.0 ± 0.6	3.2 ± 0.6	4.1 ± 1.0	5.2
6	log-normal	C03	B03	0.01	3.3 ± 0.7	3.0 ± 0.6	3.8 ± 1.0	4.0
6	log-normal	C03	B01	0.01	3.3 ± 0.5	2.8 ± 0.5	3.6 ± 1.0	6.6
6	log-normal	C03	S08	0.01	3.8 ± 0.7	2.9 ± 0.6	3.8 ± 1.0	3.5
6	uniform	-1.5	B03	0.02	2.7 ± 0.6	2.7 ± 0.5	3.8 ± 1.1	10.2
6	uniform	-1.5	B03	0.03	2.7 ± 0.5	2.5 ± 0.4	3.6 ± 0.9	14.5
6	uniform	-1.5	B01	0.02	2.4 ± 0.5	2.7 ± 0.5	3.5 ± 0.9	12.8
6	uniform	-1.5	B01	0.03	2.4 ± 0.5	2.7 ± 0.5	3.7 ± 0.9	16.0
6	uniform	-1.5	S08	0.02	2.6 ± 0.5	2.7 ± 0.5	3.5 ± 0.9	12.2
6	uniform	-1.5	S08	0.03	3.0 ± 0.5	2.8 ± 0.5	3.6 ± 0.9	8.6
6	uniform	0.5	B03	0.02	2.7 ± 0.6	2.3 ± 0.5	3.4 ± 0.9	15.8
6	uniform	0.5	B03	0.03	2.6 ± 0.5	2.3 ± 0.5	3.4 ± 0.9	16.1
6	uniform	0.5	B01	0.02	2.0 ± 0.5	2.2 ± 0.5	3.3 ± 0.9	25.3
6	uniform	0.5	B01	0.03	2.3 ± 0.5	2.2 ± 0.5	3.4 ± 0.9	22.6
6	uniform	0.5	S08	0.02	2.2 ± 0.4	2.2 ± 0.5	3.6 ± 0.9	24.4
6	uniform	0.5	S08	0.03	2.1 ± 0.4	2.2 ± 0.4	3.6 ± 0.9	28.8
6	uniform	-0.5	B03	0.02	2.7 ± 0.5	2.3 ± 0.5	3.6 ± 0.9	15.5
6	uniform	-0.5	B03	0.03	2.8 ± 0.6	2.6 ± 0.5	3.5 ± 0.8	10.4
6	uniform	-0.5	B01	0.02	2.4 ± 0.5	2.4 ± 0.5	3.6 ± 1.0	17.4
6	uniform	-0.5	B01	0.03	2.4 ± 0.5	2.6 ± 0.5	3.6 ± 1.0	16.7
6	uniform	-0.5	S08	0.02	2.3 ± 0.4	2.6 ± 0.5	3.4 ± 0.9	17.6
6	uniform	-0.5	S08	0.03	2.9 ± 0.6	2.6 ± 0.5	3.5 ± 1.0	10.0
6	uniform	1.5	B03	0.02	2.6 ± 0.5	2.0 ± 0.4	3.1 ± 0.8	23.4
6	uniform	1.5	B03	0.03	2.6 ± 0.6	2.0 ± 0.4	3.4 ± 0.9	21.5

Table B.1 (*continued*)

Table B.1 (*continued*)

τ (Gyr)	Star formation (rate)	α	Models	MBDM ($M_\odot$)	late-M dwarf age (Gyr)	L dwarf age (Gyr)	T dwarf age (Gyr)	χ^2
6	uniform	1.5	B01	0.02	2.5 ± 0.6	1.7 ± 0.4	3.0 ± 0.9	31.5
6	uniform	1.5	B01	0.03	1.7 ± 0.4	1.9 ± 0.4	3.4 ± 0.9	44.0
6	uniform	1.5	S08	0.02	2.1 ± 0.4	2.0 ± 0.4	3.1 ± 0.9	32.7
6	uniform	1.5	S08	0.03	2.3 ± 0.5	2.1 ± 0.5	3.6 ± 1.0	23.2
6	uniform	0.0/1.0/3.0	B03	0.02	2.8 ± 0.6	2.3 ± 0.5	2.6 ± 0.7	15.5
6	uniform	0.0/1.0/3.0	B03	0.03	2.8 ± 0.6	2.3 ± 0.4	2.9 ± 0.8	15.0
6	uniform	0.0/1.0/3.0	B01	0.02	2.6 ± 0.6	2.3 ± 0.5	2.7 ± 0.7	16.4
6	uniform	0.0/1.0/3.0	B01	0.03	2.3 ± 0.5	2.1 ± 0.4	3.0 ± 0.8	25.0
6	uniform	0.0/1.0/3.0	S08	0.02	2.7 ± 0.5	2.2 ± 0.5	2.9 ± 0.8	17.6
6	uniform	0.0/1.0/3.0	S08	0.03	2.2 ± 0.4	2.3 ± 0.4	3.2 ± 0.8	24.3
6	uniform	1.0/0.0/3.0	B03	0.02	2.8 ± 0.6	2.7 ± 0.5	3.5 ± 1.0	9.2
6	uniform	1.0/0.0/3.0	B03	0.03	2.8 ± 0.6	3.0 ± 0.6	3.6 ± 0.9	6.7
6	uniform	1.0/0.0/3.0	B01	0.02	2.2 ± 0.5	2.1 ± 0.4	3.5 ± 0.9	28.3
6	uniform	1.0/0.0/3.0	B01	0.03	1.9 ± 0.4	2.5 ± 0.5	3.7 ± 1.0	27.0
6	uniform	1.0/0.0/3.0	S08	0.02	2.0 ± 0.4	2.3 ± 0.4	3.7 ± 1.0	28.1
6	uniform	1.0/0.0/3.0	S08	0.03	2.8 ± 0.6	2.2 ± 0.4	3.9 ± 1.0	16.4
6	uniform	C03	B03	0.02	2.5 ± 0.5	2.0 ± 0.5	3.2 ± 0.8	22.6
6	uniform	C03	B03	0.03	2.6 ± 0.6	2.2 ± 0.4	3.3 ± 0.9	18.2
6	uniform	C03	B01	0.02	1.9 ± 0.4	1.8 ± 0.4	3.2 ± 0.9	39.4
6	uniform	C03	B01	0.03	2.2 ± 0.4	1.9 ± 0.4	3.4 ± 0.9	31.1
6	uniform	C03	S08	0.02	2.2 ± 0.4	2.1 ± 0.5	3.4 ± 0.9	26.9
6	uniform	C03	S08	0.03	2.2 ± 0.4	2.2 ± 0.5	3.6 ± 0.9	24.9
6	exponential	-1.5	B03	0.02	2.9 ± 0.6	2.9 ± 0.5	3.5 ± 0.9	8.2
6	exponential	-1.5	B03	0.03	2.9 ± 0.6	3.2 ± 0.6	4.2 ± 1.1	5.7
6	exponential	-1.5	B01	0.02	2.7 ± 0.5	3.0 ± 0.5	3.6 ± 0.9	9.7
6	exponential	-1.5	B01	0.03	2.9 ± 0.6	3.0 ± 0.5	3.5 ± 0.8	6.6
6	exponential	-1.5	S08	0.02	2.9 ± 0.6	3.0 ± 0.6	3.9 ± 0.9	6.3
6	exponential	-1.5	S08	0.03	3.1 ± 0.6	2.8 ± 0.5	4.2 ± 1.1	7.1
6	exponential	0.5	B03	0.02	3.0 ± 0.6	2.6 ± 0.5	3.6 ± 1.0	9.1
6	exponential	0.5	B03	0.03	3.0 ± 0.6	2.7 ± 0.5	3.6 ± 0.9	8.0
6	exponential	0.5	B01	0.02	2.4 ± 0.5	2.3 ± 0.5	3.4 ± 1.0	18.2
6	exponential	0.5	B01	0.03	2.3 ± 0.5	2.7 ± 0.6	3.5 ± 0.9	15.4
6	exponential	0.5	S08	0.02	2.7 ± 0.5	2.6 ± 0.6	3.5 ± 1.0	11.2
6	exponential	0.5	S08	0.03	2.6 ± 0.5	2.6 ± 0.5	3.8 ± 1.0	14.3
6	exponential	-0.5	B03	0.02	3.2 ± 0.6	2.7 ± 0.5	3.5 ± 0.9	6.6
6	exponential	-0.5	B03	0.03	3.0 ± 0.6	2.9 ± 0.6	3.9 ± 1.0	6.5
6	exponential	-0.5	B01	0.02	2.7 ± 0.5	2.6 ± 0.5	3.7 ± 1.0	13.4
6	exponential	-0.5	B01	0.03	2.4 ± 0.5	2.6 ± 0.4	3.7 ± 0.9	17.0
6	exponential	-0.5	S08	0.02	2.6 ± 0.4	2.8 ± 0.6	3.9 ± 1.0	11.9
6	exponential	-0.5	S08	0.03	2.9 ± 0.6	3.1 ± 0.6	3.8 ± 1.0	5.5
6	exponential	1.5	B03	0.02	2.8 ± 0.5	2.2 ± 0.5	3.5 ± 1.0	16.2
6	exponential	1.5	B03	0.03	3.0 ± 0.6	2.5 ± 0.5	3.7 ± 1.0	9.9
6	exponential	1.5	B01	0.02	2.6 ± 0.5	2.3 ± 0.5	3.3 ± 0.9	16.9
6	exponential	1.5	B01	0.03	2.4 ± 0.5	2.2 ± 0.4	3.7 ± 0.9	21.7
6	exponential	1.5	S08	0.02	2.7 ± 0.5	2.3 ± 0.5	3.4 ± 0.9	16.1
6	exponential	1.5	S08	0.03	2.6 ± 0.4	2.4 ± 0.5	3.7 ± 0.9	16.3
6	exponential	0.0/1.0/3.0	B03	0.02	3.1 ± 0.5	2.8 ± 0.5	3.0 ± 0.8	7.6
6	exponential	0.0/1.0/3.0	B03	0.03	3.3 ± 0.7	2.7 ± 0.5	3.4 ± 0.9	6.6
6	exponential	0.0/1.0/3.0	B01	0.02	2.5 ± 0.5	2.6 ± 0.5	3.2 ± 0.9	15.2
6	exponential	0.0/1.0/3.0	B01	0.03	2.6 ± 0.5	2.3 ± 0.5	3.4 ± 0.9	15.9
6	exponential	0.0/1.0/3.0	S08	0.02	2.6 ± 0.5	2.4 ± 0.4	3.2 ± 0.9	18.2
6	exponential	0.0/1.0/3.0	S08	0.03	2.8 ± 0.5	2.5 ± 0.5	3.5 ± 0.8	12.6
6	exponential	1.0/0.0/3.0	B03	0.02	2.9 ± 0.6	2.9 ± 0.5	3.9 ± 1.1	7.4
6	exponential	1.0/0.0/3.0	B03	0.03	3.1 ± 0.6	3.1 ± 0.6	4.1 ± 1.1	4.4
6	exponential	1.0/0.0/3.0	B01	0.02	2.3 ± 0.5	2.7 ± 0.5	3.6 ± 0.9	16.1
6	exponential	1.0/0.0/3.0	B01	0.03	2.6 ± 0.5	2.7 ± 0.5	4.0 ± 1.0	11.8
6	exponential	1.0/0.0/3.0	S08	0.02	2.7 ± 0.5	2.6 ± 0.5	3.9 ± 1.0	11.9
6	exponential	1.0/0.0/3.0	S08	0.03	2.7 ± 0.5	2.9 ± 0.6	4.1 ± 1.0	9.6
6	exponential	C03	B03	0.02	2.8 ± 0.6	2.4 ± 0.5	3.4 ± 0.9	13.1
6	exponential	C03	B03	0.03	2.9 ± 0.6	2.2 ± 0.4	3.6 ± 1.0	16.3
6	exponential	C03	B01	0.02	2.7 ± 0.5	2.3 ± 0.5	3.4 ± 0.9	17.1

Table B.1 (*continued*)

Table B.1 (*continued*)

τ (Gyr)	Star formation (rate)	α	Models	MBDM ($M_\odot$)	late-M dwarf age (Gyr)	L dwarf age (Gyr)	T dwarf age (Gyr)	χ^2
6	exponential	C03	B01	0.03	2.4 ± 0.5	2.5 ± 0.5	3.8 ± 1.0	16.3
6	exponential	C03	S08	0.02	2.4 ± 0.6	2.4 ± 0.5	3.5 ± 0.9	15.6
6	exponential	C03	S08	0.03	3.0 ± 0.6	2.7 ± 0.5	4.0 ± 1.0	8.5
6	log-normal	-1.5	B03	0.02	4.0 ± 0.7	3.4 ± 0.6	4.5 ± 1.1	1.8
6	log-normal	-1.5	B03	0.03	3.6 ± 0.6	3.6 ± 0.7	4.4 ± 1.1	1.7
6	log-normal	-1.5	B01	0.02	3.5 ± 0.6	3.5 ± 0.6	4.1 ± 1.0	2.3
6	log-normal	-1.5	B01	0.03	3.4 ± 0.6	3.7 ± 0.6	4.3 ± 1.1	2.1
6	log-normal	-1.5	S08	0.02	3.2 ± 0.6	3.6 ± 0.6	4.1 ± 1.0	2.5
6	log-normal	-1.5	S08	0.03	3.1 ± 0.6	4.0 ± 0.7	4.1 ± 1.0	2.7
6	log-normal	0.5	B03	0.02	3.5 ± 0.6	3.4 ± 0.6	4.2 ± 1.1	2.4
6	log-normal	0.5	B03	0.03	3.7 ± 0.8	3.5 ± 0.7	4.0 ± 1.0	1.2
6	log-normal	0.5	B01	0.02	3.7 ± 0.7	3.0 ± 0.6	3.9 ± 1.0	3.3
6	log-normal	0.5	B01	0.03	3.3 ± 0.6	3.4 ± 0.6	4.1 ± 1.0	3.1
6	log-normal	0.5	S08	0.02	4.2 ± 0.8	3.3 ± 0.6	4.0 ± 1.1	1.7
6	log-normal	0.5	S08	0.03	3.6 ± 0.6	3.2 ± 0.6	4.1 ± 1.0	2.6
6	log-normal	-0.5	B03	0.02	3.5 ± 0.7	3.6 ± 0.6	4.0 ± 1.0	1.5
6	log-normal	-0.5	B03	0.03	3.9 ± 0.7	3.3 ± 0.6	4.1 ± 1.0	1.9
6	log-normal	-0.5	B01	0.02	3.1 ± 0.6	3.0 ± 0.5	4.2 ± 1.1	5.7
6	log-normal	-0.5	B01	0.03	3.8 ± 0.7	3.3 ± 0.6	4.3 ± 1.1	2.1
6	log-normal	-0.5	S08	0.02	3.6 ± 0.6	3.6 ± 0.6	4.1 ± 1.0	1.4
6	log-normal	-0.5	S08	0.03	4.1 ± 0.7	3.5 ± 0.6	4.2 ± 1.0	1.2
6	log-normal	1.5	B03	0.02	4.0 ± 0.8	3.0 ± 0.6	3.8 ± 0.9	3.1
6	log-normal	1.5	B03	0.03	3.8 ± 0.7	3.1 ± 0.6	4.0 ± 1.0	2.4
6	log-normal	1.5	B01	0.02	3.1 ± 0.5	2.7 ± 0.5	3.7 ± 1.0	7.9
6	log-normal	1.5	B01	0.03	3.3 ± 0.6	2.8 ± 0.5	4.3 ± 1.1	6.2
6	log-normal	1.5	S08	0.02	3.8 ± 0.6	3.1 ± 0.5	3.9 ± 1.0	2.9
6	log-normal	1.5	S08	0.03	3.6 ± 0.6	3.2 ± 0.6	4.0 ± 1.0	2.6
6	log-normal	0.0/1.0/3.0	B03	0.02	3.6 ± 0.7	3.3 ± 0.6	3.5 ± 1.0	1.9
6	log-normal	0.0/1.0/3.0	B03	0.03	3.7 ± 0.6	3.4 ± 0.6	3.6 ± 1.0	1.6
6	log-normal	0.0/1.0/3.0	B01	0.02	3.5 ± 0.6	2.9 ± 0.5	3.7 ± 1.0	4.6
6	log-normal	0.0/1.0/3.0	B01	0.03	3.1 ± 0.6	2.8 ± 0.5	4.1 ± 1.1	7.0
6	log-normal	0.0/1.0/3.0	S08	0.02	3.9 ± 0.7	3.4 ± 0.6	3.6 ± 1.0	1.2
6	log-normal	0.0/1.0/3.0	S08	0.03	3.5 ± 0.6	3.2 ± 0.6	3.8 ± 1.0	2.8
6	log-normal	1.0/0.0/3.0	B03	0.02	3.5 ± 0.6	3.5 ± 0.6	4.1 ± 1.0	1.9
6	log-normal	1.0/0.0/3.0	B03	0.03	3.7 ± 0.6	4.0 ± 0.8	4.6 ± 1.1	1.1
6	log-normal	1.0/0.0/3.0	B01	0.02	2.9 ± 0.5	3.2 ± 0.6	4.1 ± 1.1	6.4
6	log-normal	1.0/0.0/3.0	B01	0.03	2.9 ± 0.6	3.3 ± 0.6	4.5 ± 1.1	5.4
6	log-normal	1.0/0.0/3.0	S08	0.02	3.4 ± 0.6	3.3 ± 0.6	4.3 ± 1.1	3.4
6	log-normal	1.0/0.0/3.0	S08	0.03	3.3 ± 0.5	3.4 ± 0.6	4.4 ± 1.1	3.8
6	log-normal	C03	B03	0.02	3.6 ± 0.6	2.9 ± 0.6	3.9 ± 1.0	4.1
6	log-normal	C03	B03	0.03	3.3 ± 0.7	3.1 ± 0.6	4.1 ± 1.1	3.4
6	log-normal	C03	B01	0.02	2.7 ± 0.5	2.9 ± 0.6	3.7 ± 1.0	9.8
6	log-normal	C03	B01	0.03	3.3 ± 0.6	2.9 ± 0.5	4.1 ± 1.1	5.7
6	log-normal	C03	S08	0.02	2.9 ± 0.5	3.2 ± 0.6	4.0 ± 1.1	6.8
6	log-normal	C03	S08	0.03	3.5 ± 0.6	3.1 ± 0.6	4.2 ± 1.1	3.5
12	uniform	0.5	B03	0.01	4.4 ± 0.9	3.2 ± 0.6	4.7 ± 1.3	2.5
12	uniform	0.5	B01	0.01	4.2 ± 0.9	3.3 ± 0.6	4.4 ± 1.3	1.7
12	uniform	0.5	S08	0.01	3.6 ± 0.7	3.7 ± 0.8	4.7 ± 1.2	1.4
12	uniform	0.5	M19	0.01	2.7 ± 0.4	3.8 ± 0.7	5.4 ± 1.4	10.4
12	uniform	0.5	P20C	0.01	0.3 ± 0.1	2.9 ± 0.6	4.7 ± 1.3	153.5
12	uniform	0.5	P20NW	0.01	0.3 ± 0.1	2.8 ± 0.6	4.7 ± 1.3	150.0
12	uniform	0.5	P20NS	0.01	0.3 ± 0.1	2.7 ± 0.6	4.7 ± 1.3	153.4
12	exponential	0.5	B03	0.01	5.5 ± 1.1	4.3 ± 0.7	5.4 ± 1.5	3.3
12	exponential	0.5	B01	0.01	4.2 ± 0.8	4.4 ± 0.8	5.6 ± 1.4	2.2
12	exponential	0.5	S08	0.01	4.7 ± 0.7	4.2 ± 0.8	5.3 ± 1.4	2.3
12	log-normal	0.5	B03	0.01	7.3 ± 0.9	6.4 ± 0.8	7.3 ± 1.8	23.8
12	log-normal	0.5	B01	0.01	7.3 ± 0.4	7.3 ± 0.8	7.6 ± 1.8	66.0
12	log-normal	0.5	S08	0.01	7.1 ± 1.0	7.0 ± 1.1	7.3 ± 1.9	19.2
12	uniform	-1.5	B03	0.01	4.3 ± 0.8	4.3 ± 0.7	5.5 ± 1.4	2.0
12	uniform	-1.5	B01	0.01	5.0 ± 1.0	4.4 ± 0.8	5.4 ± 1.3	3.0
12	uniform	-1.5	S08	0.01	4.7 ± 0.8	4.2 ± 0.8	5.7 ± 1.5	2.5

Table B.1 (*continued*)

Table B.1 (*continued*)

τ (Gyr)	Star formation (rate)	α	Models	MBDM ($M_\odot$)	late-M dwarf age (Gyr)	L dwarf age (Gyr)	T dwarf age (Gyr)	χ^2
12	uniform	-0.5	B03	0.01	4.3 ± 0.8	3.6 ± 0.6	5.1 ± 1.3	1.9
12	uniform	-0.5	B01	0.01	3.8 ± 0.8	3.8 ± 0.7	4.8 ± 1.2	1.3
12	uniform	-0.5	S08	0.01	4.7 ± 1.0	4.0 ± 0.7	5.2 ± 1.3	2.2
12	uniform	1.5	B03	0.01	4.4 ± 0.8	3.0 ± 0.6	3.8 ± 1.1	2.7
12	uniform	1.5	B01	0.01	2.9 ± 0.5	3.1 ± 0.6	3.8 ± 1.1	6.7
12	uniform	1.5	S08	0.01	3.1 ± 0.4	2.9 ± 0.6	4.0 ± 1.2	6.4
12	uniform	0.0/1.0/3.0	B03	0.01	4.7 ± 0.9	4.2 ± 0.8	4.1 ± 1.2	0.7
12	uniform	0.0/1.0/3.0	B01	0.01	4.1 ± 0.8	2.9 ± 0.7	4.4 ± 1.3	2.8
12	uniform	0.0/1.0/3.0	S08	0.01	3.7 ± 0.6	3.4 ± 0.7	4.2 ± 1.1	1.5
12	uniform	1.0/0.0/3.0	B03	0.01	4.0 ± 0.7	4.3 ± 0.8	4.6 ± 1.3	0.8
12	uniform	1.0/0.0/3.0	B01	0.01	4.0 ± 0.9	3.2 ± 0.6	5.0 ± 1.4	3.0
12	uniform	1.0/0.0/3.0	S08	0.01	3.7 ± 0.6	3.6 ± 0.7	5.2 ± 1.3	2.2
12	uniform	C03	B03	0.01	4.4 ± 0.8	3.2 ± 0.7	4.8 ± 1.4	2.3
12	uniform	C03	B01	0.01	4.2 ± 0.9	2.9 ± 0.6	4.4 ± 1.3	3.7
12	uniform	C03	S08	0.01	3.9 ± 0.6	3.4 ± 0.7	4.4 ± 1.3	1.3
12	exponential	-1.5	B03	0.01	5.5 ± 1.0	5.0 ± 0.8	6.2 ± 1.5	6.1
12	exponential	-1.5	B01	0.01	5.3 ± 0.9	4.8 ± 0.9	6.3 ± 1.5	5.7
12	exponential	-1.5	S08	0.01	5.5 ± 0.8	5.0 ± 0.9	7.0 ± 1.6	8.2
12	exponential	-0.5	B03	0.01	5.9 ± 1.1	4.7 ± 0.9	5.6 ± 1.4	5.0
12	exponential	-0.5	B01	0.01	6.0 ± 1.0	4.8 ± 0.8	6.5 ± 1.7	6.9
12	exponential	-0.5	S08	0.01	4.7 ± 0.7	4.4 ± 0.7	5.8 ± 1.4	3.2
12	exponential	1.5	B03	0.01	5.3 ± 0.9	3.9 ± 0.7	5.0 ± 1.3	2.6
12	exponential	1.5	B01	0.01	5.2 ± 0.8	3.6 ± 0.6	4.9 ± 1.4	3.0
12	exponential	1.5	S08	0.01	4.7 ± 0.4	3.9 ± 0.7	5.3 ± 1.5	2.8
12	exponential	0.0/1.0/3.0	B03	0.01	5.3 ± 1.0	4.8 ± 0.8	4.6 ± 1.3	2.6
12	exponential	0.0/1.0/3.0	B01	0.01	4.6 ± 0.8	3.8 ± 0.7	5.2 ± 1.5	2.0
12	exponential	0.0/1.0/3.0	S08	0.01	4.9 ± 0.7	4.4 ± 0.8	5.1 ± 1.4	2.6
12	exponential	1.0/0.0/3.0	B03	0.01	6.0 ± 1.1	5.3 ± 1.0	5.2 ± 1.4	5.7
12	exponential	1.0/0.0/3.0	B01	0.01	5.4 ± 1.0	3.9 ± 0.7	5.4 ± 1.4	3.4
12	exponential	1.0/0.0/3.0	S08	0.01	4.8 ± 0.8	5.0 ± 0.9	5.6 ± 1.3	4.0
12	exponential	C03	B03	0.01	5.6 ± 1.0	4.1 ± 0.8	5.2 ± 1.4	3.5
12	exponential	C03	B01	0.01	5.7 ± 1.0	3.7 ± 0.8	5.1 ± 1.4	4.1
12	exponential	C03	S08	0.01	4.9 ± 0.7	4.4 ± 0.8	5.1 ± 1.4	2.7
12	log-normal	-1.5	B03	0.01	6.6 ± 0.9	6.5 ± 0.6	7.6 ± 1.7	25.0
12	log-normal	-1.5	B01	0.01	8.9 ± 0.4	9.6 ± 0.9	7.7 ± 1.6	118.9
12	log-normal	-1.5	S08	0.01	6.7 ± 1.0	6.8 ± 1.0	7.9 ± 1.9	19.0
12	log-normal	-0.5	B03	0.01	7.3 ± 0.9	6.4 ± 0.7	7.8 ± 1.7	26.6
12	log-normal	-0.5	B01	0.01	8.6 ± 0.6	8.3 ± 0.9	7.1 ± 1.8	66.4
12	log-normal	-0.5	S08	0.01	7.5 ± 1.0	7.4 ± 1.3	7.9 ± 1.9	21.6
12	log-normal	1.5	B03	0.01	8.0 ± 0.5	6.3 ± 0.4	7.9 ± 1.7	75.2
12	log-normal	1.5	B01	0.01	8.0 ± 1.0	6.8 ± 0.9	7.0 ± 1.8	26.4
12	log-normal	1.5	S08	0.01	8.4 ± 0.9	7.3 ± 1.2	7.3 ± 1.8	32.0
12	log-normal	0.0/1.0/3.0	B03	0.01	9.1 ± 1.3	8.4 ± 1.1	6.7 ± 1.6	31.5
12	log-normal	0.0/1.0/3.0	B01	0.01	7.5 ± 1.0	6.4 ± 1.1	7.6 ± 1.8	19.3
12	log-normal	0.0/1.0/3.0	S08	0.01	8.1 ± 1.3	7.1 ± 1.2	7.1 ± 1.6	20.4
12	log-normal	1.0/0.0/3.0	B03	0.01	7.8 ± 1.0	7.0 ± 1.1	7.6 ± 1.8	24.2
12	log-normal	1.0/0.0/3.0	B01	0.01	7.3 ± 1.3	7.6 ± 1.2	7.6 ± 1.7	18.8
12	log-normal	1.0/0.0/3.0	S08	0.01	7.2 ± 1.2	7.4 ± 1.2	7.5 ± 1.8	18.2
12	log-normal	C03	B03	0.01	7.1 ± 0.8	6.2 ± 0.7	7.9 ± 1.8	26.9
12	log-normal	C03	B01	0.01	7.6 ± 0.9	6.0 ± 0.9	7.4 ± 1.8	21.9
12	log-normal	C03	S08	0.01	7.0 ± 1.0	6.8 ± 1.0	7.3 ± 1.7	19.3
12	uniform	-1.5	B03	0.02	4.5 ± 0.8	4.6 ± 0.9	6.0 ± 1.6	2.6
12	uniform	-1.5	B03	0.03	4.3 ± 0.8	4.7 ± 0.9	5.8 ± 1.5	2.6
12	uniform	-1.5	B01	0.02	4.2 ± 0.8	3.9 ± 0.7	5.6 ± 1.4	2.1
12	uniform	-1.5	B01	0.03	4.0 ± 0.7	4.0 ± 0.8	5.6 ± 1.3	2.4
12	uniform	-1.5	S08	0.02	4.5 ± 0.8	4.2 ± 0.8	5.6 ± 1.4	2.4
12	uniform	-1.5	S08	0.03	4.8 ± 0.8	4.2 ± 0.7	5.9 ± 1.5	3.1
12	uniform	0.5	B03	0.02	4.5 ± 0.9	3.3 ± 0.7	5.2 ± 1.3	3.0
12	uniform	0.5	B03	0.03	4.3 ± 0.8	3.5 ± 0.7	5.5 ± 1.4	2.7
12	uniform	0.5	B01	0.02	3.6 ± 0.7	3.2 ± 0.7	4.9 ± 1.3	2.8
12	uniform	0.5	B01	0.03	3.8 ± 0.7	3.6 ± 0.8	5.2 ± 1.3	2.0

Table B.1 (*continued*)

Table B.1 (*continued*)

τ (Gyr)	Star formation (rate)	α	Models	MBDM ($M_\odot$)	late-M dwarf age (Gyr)	L dwarf age (Gyr)	T dwarf age (Gyr)	χ^2
12	uniform	0.5	S08	0.02	4.0 ± 0.7	3.5 ± 0.6	5.0 ± 1.3	2.0
12	uniform	0.5	S08	0.03	4.1 ± 0.7	3.6 ± 0.7	5.8 ± 1.4	2.8
12	uniform	−0.5	B03	0.02	4.6 ± 1.0	3.9 ± 0.8	5.3 ± 1.4	1.9
12	uniform	−0.5	B03	0.03	4.5 ± 0.9	3.8 ± 0.7	5.5 ± 1.3	2.4
12	uniform	−0.5	B01	0.02	4.1 ± 0.8	3.5 ± 0.6	4.9 ± 1.3	1.9
12	uniform	−0.5	B01	0.03	3.8 ± 0.7	3.8 ± 0.8	5.6 ± 1.4	2.3
12	uniform	−0.5	S08	0.02	3.8 ± 0.6	4.0 ± 0.8	5.5 ± 1.4	2.1
12	uniform	−0.5	S08	0.03	4.2 ± 0.7	4.1 ± 0.8	6.0 ± 1.5	2.6
12	uniform	1.5	B03	0.02	4.3 ± 0.8	2.8 ± 0.7	4.6 ± 1.3	3.4
12	uniform	1.5	B03	0.03	4.5 ± 0.9	3.2 ± 0.7	5.2 ± 1.4	3.1
12	uniform	1.5	B01	0.02	4.5 ± 0.8	2.7 ± 0.6	4.5 ± 1.2	5.0
12	uniform	1.5	B01	0.03	3.8 ± 0.8	2.8 ± 0.6	5.3 ± 1.4	5.9
12	uniform	1.5	S08	0.02	4.7 ± 0.8	3.4 ± 0.7	4.6 ± 1.2	2.1
12	uniform	1.5	S08	0.03	4.8 ± 0.8	3.4 ± 0.7	5.4 ± 1.5	3.3
12	uniform	0.0/1.0/3.0	B03	0.02	4.3 ± 0.8	4.0 ± 0.7	4.6 ± 1.2	0.8
12	uniform	0.0/1.0/3.0	B03	0.03	4.5 ± 0.9	4.2 ± 0.8	5.2 ± 1.4	1.6
12	uniform	0.0/1.0/3.0	B01	0.02	3.7 ± 0.8	3.2 ± 0.7	4.6 ± 1.3	2.4
12	uniform	0.0/1.0/3.0	B01	0.03	3.4 ± 0.6	3.2 ± 0.7	5.2 ± 1.4	3.9
12	uniform	0.0/1.0/3.0	S08	0.02	3.5 ± 0.6	3.5 ± 0.7	4.9 ± 1.3	2.4
12	uniform	0.0/1.0/3.0	S08	0.03	4.0 ± 0.6	3.6 ± 0.7	5.4 ± 1.4	2.2
12	uniform	1.0/0.0/3.0	B03	0.02	4.6 ± 0.8	4.1 ± 0.8	5.2 ± 1.4	1.7
12	uniform	1.0/0.0/3.0	B03	0.03	5.0 ± 1.0	4.1 ± 0.7	5.3 ± 1.2	2.7
12	uniform	1.0/0.0/3.0	B01	0.02	3.6 ± 0.8	3.3 ± 0.6	5.0 ± 1.3	3.2
12	uniform	1.0/0.0/3.0	B01	0.03	3.6 ± 0.7	3.7 ± 0.7	5.4 ± 1.3	2.7
12	uniform	1.0/0.0/3.0	S08	0.02	3.8 ± 0.7	3.7 ± 0.7	5.4 ± 1.4	2.2
12	uniform	1.0/0.0/3.0	S08	0.03	3.9 ± 0.7	3.5 ± 0.7	6.1 ± 1.5	3.3
12	uniform	C03	B03	0.02	4.5 ± 0.9	2.9 ± 0.6	4.8 ± 1.3	4.2
12	uniform	C03	B03	0.03	4.3 ± 0.8	3.0 ± 0.6	5.3 ± 1.3	4.8
12	uniform	C03	B01	0.02	3.5 ± 0.7	2.9 ± 0.7	4.6 ± 1.3	4.1
12	uniform	C03	B01	0.03	3.6 ± 0.7	3.1 ± 0.6	5.2 ± 1.3	3.8
12	uniform	C03	S08	0.02	4.4 ± 0.7	3.3 ± 0.7	4.9 ± 1.4	2.2
12	uniform	C03	S08	0.03	3.8 ± 0.7	3.4 ± 0.7	5.6 ± 1.4	3.0
12	exponential	−1.5	B03	0.02	5.8 ± 1.1	5.2 ± 0.8	6.8 ± 1.7	7.2
12	exponential	−1.5	B03	0.03	5.5 ± 1.0	5.4 ± 0.9	6.1 ± 1.5	6.4
12	exponential	−1.5	B01	0.02	4.9 ± 0.9	4.9 ± 0.9	6.2 ± 1.6	4.2
12	exponential	−1.5	B01	0.03	4.6 ± 0.8	4.5 ± 0.7	6.3 ± 1.6	3.7
12	exponential	−1.5	S08	0.02	4.1 ± 0.6	5.2 ± 0.9	6.3 ± 1.6	4.5
12	exponential	−1.5	S08	0.03	5.6 ± 0.9	5.1 ± 0.9	6.6 ± 1.7	6.8
12	exponential	0.5	B03	0.02	5.5 ± 1.0	4.4 ± 0.8	5.9 ± 1.5	4.2
12	exponential	0.5	B03	0.03	5.6 ± 1.0	4.2 ± 0.8	6.3 ± 1.7	4.6
12	exponential	0.5	B01	0.02	4.8 ± 0.8	4.4 ± 0.9	5.4 ± 1.4	2.5
12	exponential	0.5	B01	0.03	4.9 ± 0.9	4.3 ± 0.8	6.0 ± 1.5	3.5
12	exponential	0.5	S08	0.02	4.6 ± 0.7	5.0 ± 0.9	6.1 ± 1.6	3.8
12	exponential	0.5	S08	0.03	5.4 ± 0.9	4.6 ± 0.9	6.1 ± 1.5	4.7
12	exponential	−0.5	B03	0.02	5.8 ± 1.1	4.3 ± 0.8	5.7 ± 1.4	4.6
12	exponential	−0.5	B03	0.03	5.8 ± 1.1	5.0 ± 0.9	6.1 ± 1.6	6.0
12	exponential	−0.5	B01	0.02	5.3 ± 0.9	5.2 ± 0.9	5.9 ± 1.5	5.4
12	exponential	−0.5	B01	0.03	5.0 ± 0.8	4.7 ± 0.8	6.2 ± 1.6	4.3
12	exponential	−0.5	S08	0.02	5.7 ± 1.0	4.9 ± 0.8	6.1 ± 1.6	5.8
12	exponential	−0.5	S08	0.03	6.1 ± 0.9	5.1 ± 1.0	6.4 ± 1.7	8.7
12	exponential	1.5	B03	0.02	5.5 ± 1.0	4.3 ± 0.9	5.5 ± 1.5	3.5
12	exponential	1.5	B03	0.03	4.9 ± 0.9	3.8 ± 0.6	6.3 ± 1.6	3.9
12	exponential	1.5	B01	0.02	4.7 ± 0.7	3.7 ± 0.8	5.4 ± 1.5	2.5
12	exponential	1.5	B01	0.03	4.2 ± 0.7	3.9 ± 0.7	5.8 ± 1.4	2.7
12	exponential	1.5	S08	0.02	5.4 ± 0.8	4.5 ± 0.9	5.2 ± 1.4	4.4
12	exponential	1.5	S08	0.03	5.6 ± 0.8	4.4 ± 0.8	6.0 ± 1.5	5.8
12	exponential	0.0/1.0/3.0	B03	0.02	5.3 ± 1.0	4.7 ± 0.8	5.4 ± 1.5	3.4
12	exponential	0.0/1.0/3.0	B03	0.03	5.6 ± 1.0	5.2 ± 1.0	6.1 ± 1.6	5.9
12	exponential	0.0/1.0/3.0	B01	0.02	4.1 ± 0.8	3.7 ± 0.7	5.3 ± 1.4	1.9
12	exponential	0.0/1.0/3.0	B01	0.03	4.9 ± 0.9	3.6 ± 0.7	5.7 ± 1.4	3.4
12	exponential	0.0/1.0/3.0	S08	0.02	5.7 ± 0.9	4.3 ± 0.8	5.4 ± 1.4	4.4

Table B.1 (*continued*)

Table B.1 (*continued*)

τ (Gyr)	Star formation (rate)	α	Models	MBDM ($M_\odot$)	late-M dwarf age (Gyr)	L dwarf age (Gyr)	T dwarf age (Gyr)	χ^2
12	exponential	0.0/1.0/3.0	S08	0.03	6.0 ± 0.9	4.4 ± 0.8	6.2 ± 1.7	6.4
12	exponential	1.0/0.0/3.0	B03	0.02	5.4 ± 1.0	5.7 ± 1.0	5.6 ± 1.6	5.4
12	exponential	1.0/0.0/3.0	B03	0.03	5.1 ± 0.9	5.6 ± 1.0	6.2 ± 1.6	6.0
12	exponential	1.0/0.0/3.0	B01	0.02	5.5 ± 0.9	4.3 ± 0.7	6.0 ± 1.5	4.8
12	exponential	1.0/0.0/3.0	B01	0.03	5.1 ± 1.0	4.5 ± 0.8	6.1 ± 1.8	3.1
12	exponential	1.0/0.0/3.0	S08	0.02	5.3 ± 0.9	4.6 ± 0.9	5.8 ± 1.5	4.4
12	exponential	1.0/0.0/3.0	S08	0.03	4.8 ± 0.8	4.7 ± 0.9	6.6 ± 1.7	4.5
12	exponential	C03	B03	0.02	5.6 ± 1.0	4.2 ± 0.8	5.8 ± 1.4	4.3
12	exponential	C03	B03	0.03	5.5 ± 0.9	4.4 ± 0.8	6.2 ± 1.6	5.0
12	exponential	C03	B01	0.02	4.7 ± 0.8	4.2 ± 0.9	5.2 ± 1.4	2.1
12	exponential	C03	B01	0.03	4.4 ± 0.8	4.2 ± 0.8	5.8 ± 1.5	2.5
12	exponential	C03	S08	0.02	5.4 ± 0.9	4.2 ± 0.8	5.6 ± 1.4	3.7
12	exponential	C03	S08	0.03	5.3 ± 0.9	4.3 ± 0.8	6.0 ± 1.6	4.2
12	log-normal	-1.5	B03	0.02	6.9 ± 0.9	6.8 ± 0.8	6.8 ± 1.5	23.6
12	log-normal	-1.5	B03	0.03	8.3 ± 1.0	8.1 ± 0.8	7.8 ± 1.5	47.0
12	log-normal	-1.5	B01	0.02	6.0 ± 0.5	5.6 ± 0.3	7.2 ± 1.5	30.7
12	log-normal	-1.5	B01	0.03	7.2 ± 0.4	7.4 ± 0.7	7.6 ± 1.6	60.8
12	log-normal	-1.5	S08	0.02	7.2 ± 1.0	7.5 ± 1.2	7.6 ± 1.6	22.4
12	log-normal	-1.5	S08	0.03	7.7 ± 1.1	7.6 ± 1.2	7.4 ± 1.8	22.6
12	log-normal	0.5	B03	0.02	6.8 ± 0.9	8.2 ± 1.2	7.6 ± 1.7	23.2
12	log-normal	0.5	B03	0.03	7.4 ± 0.8	8.4 ± 1.0	7.6 ± 1.7	35.3
12	log-normal	0.5	B01	0.02	6.8 ± 0.5	6.3 ± 0.6	7.2 ± 1.6	34.9
12	log-normal	0.5	B01	0.03	7.5 ± 0.6	6.6 ± 0.8	7.4 ± 1.6	42.2
12	log-normal	0.5	S08	0.02	7.8 ± 1.3	7.0 ± 1.1	7.6 ± 1.8	19.1
12	log-normal	0.5	S08	0.03	6.4 ± 0.4	6.6 ± 0.8	8.8 ± 1.9	40.4
12	log-normal	-0.5	B03	0.02	6.6 ± 0.8	7.5 ± 0.8	7.0 ± 1.5	29.4
12	log-normal	-0.5	B03	0.03	6.7 ± 0.9	7.1 ± 0.9	7.4 ± 1.5	24.1
12	log-normal	-0.5	B01	0.02	7.4 ± 0.5	7.6 ± 1.1	7.7 ± 1.7	48.7
12	log-normal	-0.5	B01	0.03	9.1 ± 0.8	8.5 ± 1.1	7.8 ± 1.8	51.7
12	log-normal	-0.5	S08	0.02	8.2 ± 1.4	7.2 ± 1.2	8.1 ± 1.9	20.7
12	log-normal	-0.5	S08	0.03	8.0 ± 1.2	7.2 ± 1.2	8.1 ± 2.0	22.7
12	log-normal	1.5	B03	0.02	8.4 ± 0.9	7.0 ± 0.7	6.9 ± 1.7	39.1
12	log-normal	1.5	B03	0.03	8.2 ± 1.0	7.3 ± 1.1	8.0 ± 1.9	28.6
12	log-normal	1.5	B01	0.02	5.7 ± 0.2	5.1 ± 0.3	7.2 ± 1.9	28.0
12	log-normal	1.5	B01	0.03	9.7 ± 0.0	6.5 ± 0.8	7.6 ± 1.8	359.3
12	log-normal	1.5	S08	0.02	9.3 ± 1.3	7.4 ± 1.3	7.6 ± 1.9	26.1
12	log-normal	1.5	S08	0.03	7.5 ± 1.1	7.4 ± 1.2	7.8 ± 1.9	21.7
12	log-normal	0.0/1.0/3.0	B03	0.02	8.8 ± 1.1	7.5 ± 1.1	7.8 ± 1.9	32.5
12	log-normal	0.0/1.0/3.0	B03	0.03	7.7 ± 1.2	7.4 ± 1.1	7.7 ± 1.8	22.6
12	log-normal	0.0/1.0/3.0	B01	0.02	9.1 ± 0.6	7.2 ± 0.9	7.1 ± 1.6	79.2
12	log-normal	0.0/1.0/3.0	B01	0.03	5.5 ± 0.3	5.8 ± 0.7	8.0 ± 1.8	20.6
12	log-normal	0.0/1.0/3.0	S08	0.02	8.1 ± 1.2	7.6 ± 1.3	7.6 ± 1.7	22.6
12	log-normal	0.0/1.0/3.0	S08	0.03	7.6 ± 1.2	7.5 ± 1.2	7.9 ± 1.9	19.6
12	log-normal	1.0/0.0/3.0	B03	0.02	7.4 ± 1.0	6.8 ± 1.0	6.9 ± 1.5	20.5
12	log-normal	1.0/0.0/3.0	B03	0.03	6.9 ± 1.1	7.7 ± 1.2	7.8 ± 1.8	19.9
12	log-normal	1.0/0.0/3.0	B01	0.02	6.7 ± 0.5	7.4 ± 1.1	7.8 ± 1.8	34.2
12	log-normal	1.0/0.0/3.0	B01	0.03	7.6 ± 1.2	7.0 ± 1.2	7.7 ± 1.8	18.4
12	log-normal	1.0/0.0/3.0	S08	0.02	7.8 ± 1.2	7.2 ± 1.3	7.8 ± 1.8	20.1
12	log-normal	1.0/0.0/3.0	S08	0.03	8.6 ± 1.4	7.2 ± 1.2	7.5 ± 1.8	20.4
12	log-normal	C03	B03	0.02	6.8 ± 0.9	7.4 ± 0.9	8.0 ± 1.9	26.1
12	log-normal	C03	B03	0.03	7.7 ± 1.0	6.2 ± 0.9	7.5 ± 1.9	20.2
12	log-normal	C03	B01	0.02	7.3 ± 0.3	7.4 ± 0.7	7.6 ± 1.8	73.9
12	log-normal	C03	B01	0.03	7.6 ± 0.6	5.9 ± 0.7	7.4 ± 1.7	37.2
12	log-normal	C03	S08	0.02	7.3 ± 1.1	7.0 ± 1.2	7.6 ± 1.9	17.5
12	log-normal	C03	S08	0.03	7.8 ± 1.2	7.5 ± 1.3	7.8 ± 1.8	21.3
9[d]	uniform	0.5	B03	0.01	4.0 ± 0.8	3.0 ± 0.6	3.8 ± 1.1	2.8
9[e]	uniform	0.5	B03*	0.01	4.1 ± 0.8	4.1 ± 0.8	4.4 ± 1.2	0.5
9[c]	uniform	1.5/-0.5/3.0	B03	0.01	3.4 ± 0.6	3.5 ± 0.7	5.0 ± 1.2	3.2
9[c]	uniform	1.5/-0.5/4.5	B03	0.01	2.9 ± 0.6	3.5 ± 0.7	5.4 ± 1.4	5.6
9[c]	uniform	1.5/-0.5/6.0	B03	0.01	3.2 ± 0.7	3.4 ± 0.7	4.3 ± 1.1	2.7

Table B.1 (*continued*)

Table B.1 (*continued*)

τ (Gyr)	Star formation (rate)	α	Models	MBDM ($M_\odot$)	late-M dwarf age (Gyr)	L dwarf age (Gyr)	T dwarf age (Gyr)	χ^2

Note −− Kinematics ages computed using the Aumer & Binney (2009) relation and the procedure described in Section 2.5.4. τ is the maximum age of the sample, α is the mass function power law index ($\frac{dN}{dM} = M^{-\alpha}$), MBDM is the minimum brown dwarf mass. Evolving mass functions are labeled in the order of early α, late α, and age (in Gyr) of transition. A log-normal mass function from Chabrier (2003) is labeled as "log-normal". Star formation rates considered in my simulations: uniform, exponential (Aumer & Binney 2009), and cosmic star formation rate (Rujopakarn et al. 2010). Brown dwarf evolution models are B03 (Baraffe et al. 2003), B01 (Burrows et al. 2001), S08 (Saumon & Marley 2008), M19 (Marley et al. 2018), and P20 (Phillips et al. 2020). For the last model set, C, NW, and NS stand for chemical equilibrium, weak, and strong chemical disequilibrium, respectively. Note that only substellar models are available in the P20 set. See Table B.1 in Appendix B for the full list of simulations.

[a] Baseline simulation

[b] Simulations with an evolving mass function from top-heavy to bottom-heavy over time using Baraffe et al. (2003) evolutionary models. See Section 2.5.4 for details.

[c] Simulations with an evolving mass function from bottom-heavy to top-heavy over time using Baraffe et al. (2003) evolutionary models. See Section 2.5.4 for details.

[d] Baseline simulation with selection within 20 pc and J or $K < 15.5$. See Section 2.6.1 for details.

[e] Simulation with an artificial decrease in the HBMM for the Baraffe et al. (2003) evolutionary models by fixing the temperatures of brown dwarfs down to masses of 0.060 $M_\odot$ to their 1 Gyr values. See Section 2.5.4 for details.

Table B.2: APOGEE DR17 Sample

APOGEE ID	RA (deg)	Dec (deg)	*Gaia* eDR3 Source ID	SpT	$N_{\rm obs}$	2MASS H (mag)	μ_α (mas yr^{-1})	μ_δ (mas yr^{-1})	π (mas)
2M00034394+8606422	0.933088	+86.111732	574059045248283008	4.8	10	11.738 ± 0.031	175.94 ± 0.04	-25.83 ± 0.04	30.81 ± 0.03
2M00050140+0053081	1.255859	+0.885589	2546208620551960064	4.3	3	12.142 ± 0.037	65.1 ± 0.59	7.73 ± 0.31	7.69 ± 0.48
2M00073367-2008192	1.890326	−20.138685	2365564632543830016	10.3	6	12.609 ± 0.031	124.82 ± 0.4	61.89 ± 0.35	8.56 ± 0.4
2M00091064-2116214	2.294345	−21.272621	2364486119011979776	5.1	3	11.53 ± 0.021	-108.87 ± 0.09	-51.74 ± 0.09	21.54 ± 0.09
2M00104654-2003471	2.693939	−20.063097	2364900000000000000	4.4	6	12.865 ± 0.027	-19.99 ± 0.08	-130.0 ± 0.06	14.5 ± 0.07
2M00111055-2021034	2.793974	−20.350962	2364839646360019968	5.9	3	11.616 ± 0.026	71.88 ± 0.07	-44.11 ± 0.05	14.16 ± 0.07
2M00114208-2057129	2.925351	−20.953594	2364524086522970112	5.1	1	12.848 ± 0.025	613.35 ± 0.09	-0.33 ± 0.08	21.2 ± 0.1
2M00124831-2036481	3.201292	−20.613363	2364630601711690240	4.6	6	12.601 ± 0.03	107.25 ± 0.07	-47.19 ± 0.05	16.49 ± 0.07
2M00133672-2110568	3.403002	−21.182453	2364536937064889856	5.8	3	11.616 ± 0.024	37.88 ± 0.68	-0.03 ± 0.52	10.43 ± 0.69
2M00203491-1445567	5.145497	−14.765753	2416897433126550016	5.4	5	11.867 ± 0.024	-3.57 ± 0.47	-48.34 ± 0.41	9.54 ± 0.47
2M00222083+8619567	5.586817	+86.332428	574152263218374976	4.4	10	11.018 ± 0.033	475.44 ± 0.02	29.57 ± 0.03	27.77 ± 0.02
2M00225340+1459299	5.72253	+14.991654	2792262456511220224		3	10.589 ± 0.022	115.05 ± 0.76	-1.82 ± 0.43	14.47 ± 0.53
2M00272223+0104266	6.842657	+1.074072	2546970620766130176		7	8.979 ± 0.03	202.77 ± 0.26	-13.15 ± 0.18	28.82 ± 0.2
2M00272392+1623565	6.849681	+16.399036	2792881000522279936	3.9	3	11.249 ± 0.03	10.16 ± 0.03	13.21 ± 0.03	25.27 ± 0.03
2M00381273+3850323	9.553082	+38.842308	368514898441865984	4.9	6	12.459 ± 0.033	163.84 ± 0.05	12.5 ± 0.05	17.21 ± 0.06
2M00385741+3733423	9.739221	+37.561775	368190405071763968	6.4	6	13.292 ± 0.043	23.1 ± 0.11	-21.1 ± 0.09	4.0 ± 0.12
2M00393995-6717510	9.916475	−67.297523	4703903265535039488	6.0	3	11.871 ± 0.039	-30.98 ± 0.05	25.05 ± 0.06	9.15 ± 0.05
2M00394923+0017110	9.955147	+0.286397	2543281175138169856	4.3	4	11.11 ± 0.023	75.65 ± 0.04	-205.77 ± 0.03	29.51 ± 0.03
2M00403709+0314141	10.15457	+3.23726	2550655290388109824	4.0	3	12.831 ± 0.033	69.37 ± 0.08	1.05 ± 0.06	10.83 ± 0.06
2M00413621+3757173	10.400904	+37.954819	368219984511758016	3.9	6	13.264 ± 0.037	80.13 ± 0.07	5.03 ± 0.05	7.38 ± 0.08
2M00415938+3946340	10.497458	+39.776131	369021906445473024	6.1	3	10.982 ± 0.023	122.19 ± 0.25	-13.85 ± 0.26	13.3 ± 0.31
2M00425211+1416557	10.717128	+14.282163	2779442009197270016	3.9	5	11.369 ± 0.032	165.79 ± 0.04	-111.98 ± 0.03	20.47 ± 0.03
2M00440889+0143590	11.037056	+1.733068	2549540316877960192	3.7	4	11.993 ± 0.03	25.46 ± 0.06	19.07 ± 0.05	8.18 ± 0.05
2M00443289+1853533	11.137077	+18.898144	2783170178249789952		3	11.908 ± 0.017	48.9 ± 0.09	-21.04 ± 0.05	8.53 ± 0.07

Note – The astrometry, proper motions, and parallaxes are compiled from *Gaia* EDR3 (Gaia Collaboration et al. 2021).
Note – The full table is presented in a machine-readable table format.

C Binary Candidate Orbital Fit

In Section 3.4.5, we presented the orbital fits for our binary candidates identified in our sample below.

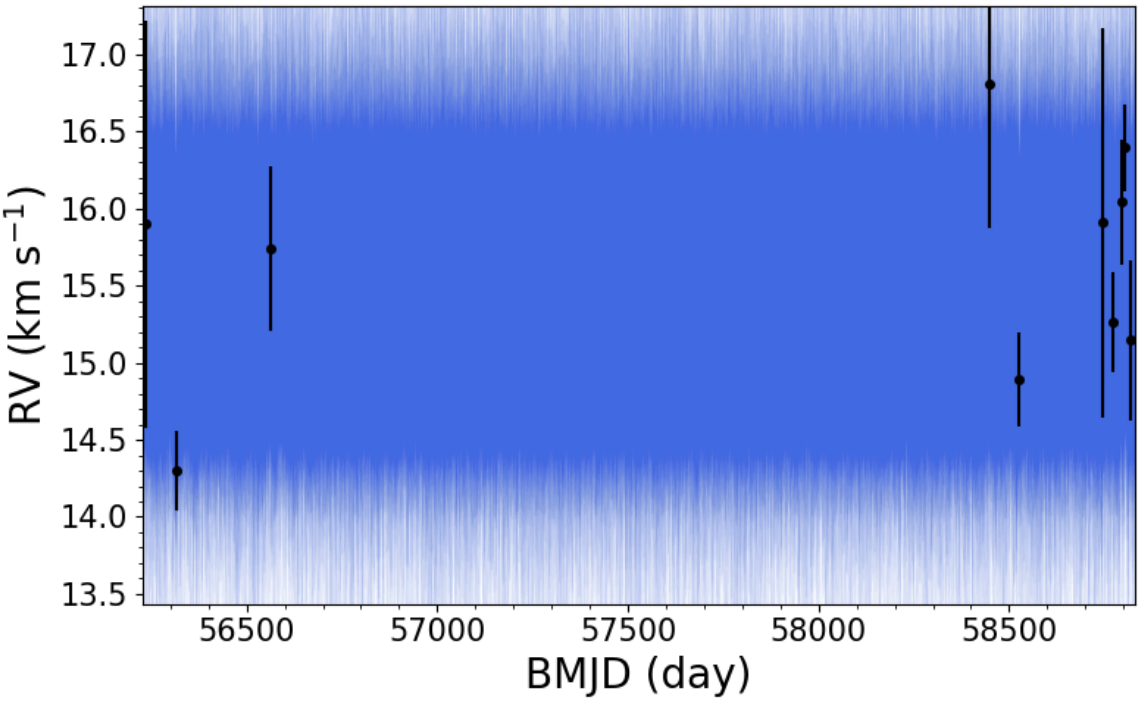

Figure C.1: Binary orbital fit for 2MASS J03282839+3116273. The best-fit orbital parameters are $P_{\rm fit} = 24.1^{+86.9}_{-21.8}$ day, $K_{\rm fit} = 1.0^{+0.3}_{-0.2}$ km s^{-1}, and $e_{\rm fit} = 0.175^{+0.245}_{-0.132}$.

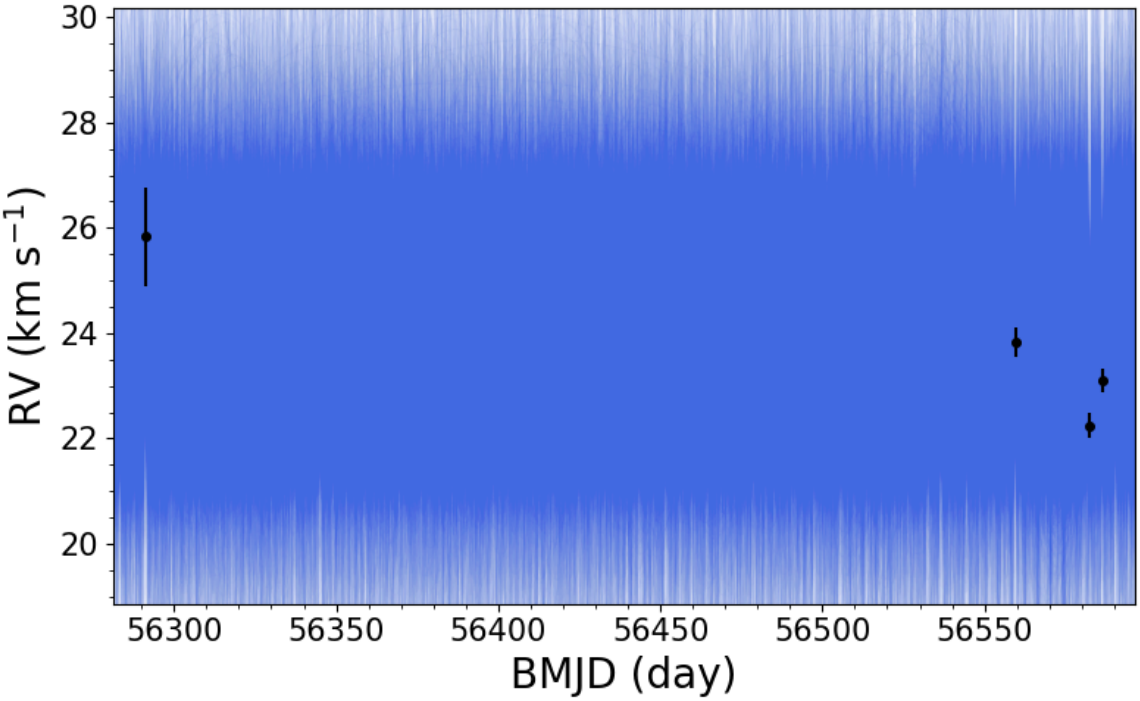

Figure C.2: Binary orbital fit for 2MASS J05402570+2448090. The best-fit orbital parameters are $P_{\rm fit} = 27.8^{+49.5}_{-24.8}$ day, $K_{\rm fit} = 2.3^{+1.2}_{-0.9}$ km s^{-1}, and $e_{\rm fit} = 0.186^{+0.268}_{-0.143}$.

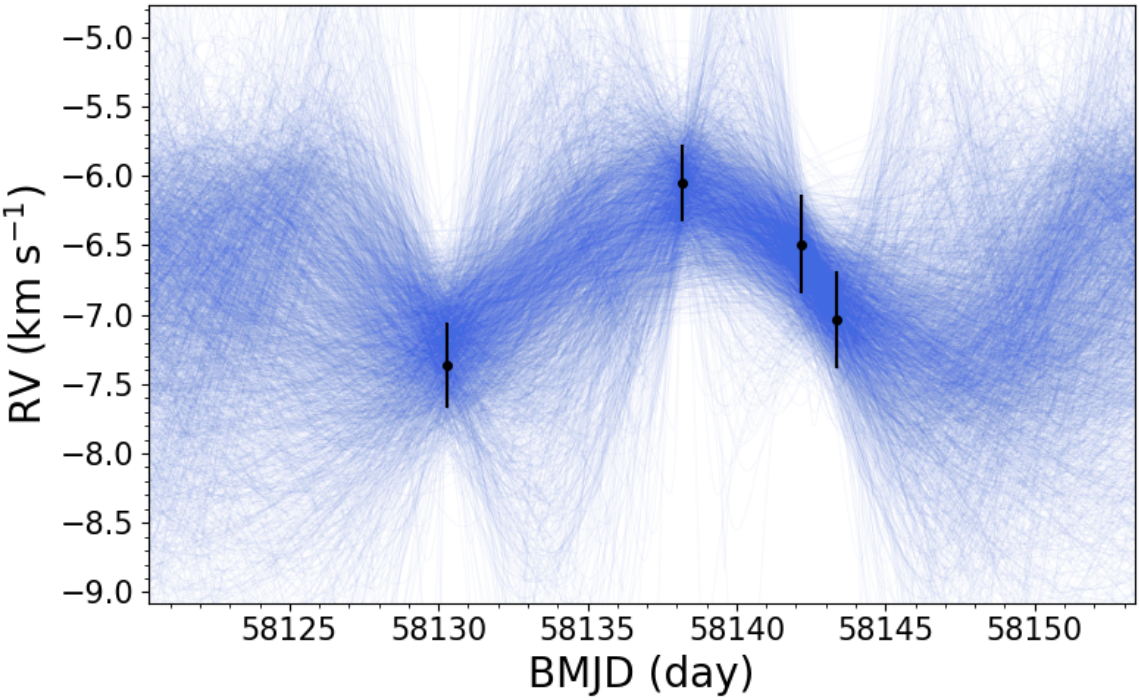

Figure C.3: Binary orbital fit for 2MASS J08092892+3235226. The best-fit orbital parameters are $P_{\rm fit} = 17.7^{+11.9}_{-4.6}$ day, $K_{\rm fit} = 0.9^{+0.5}_{-0.3}$ km s^{-1}, and $e_{\rm fit} = 0.199^{+0.255}_{-0.151}$.

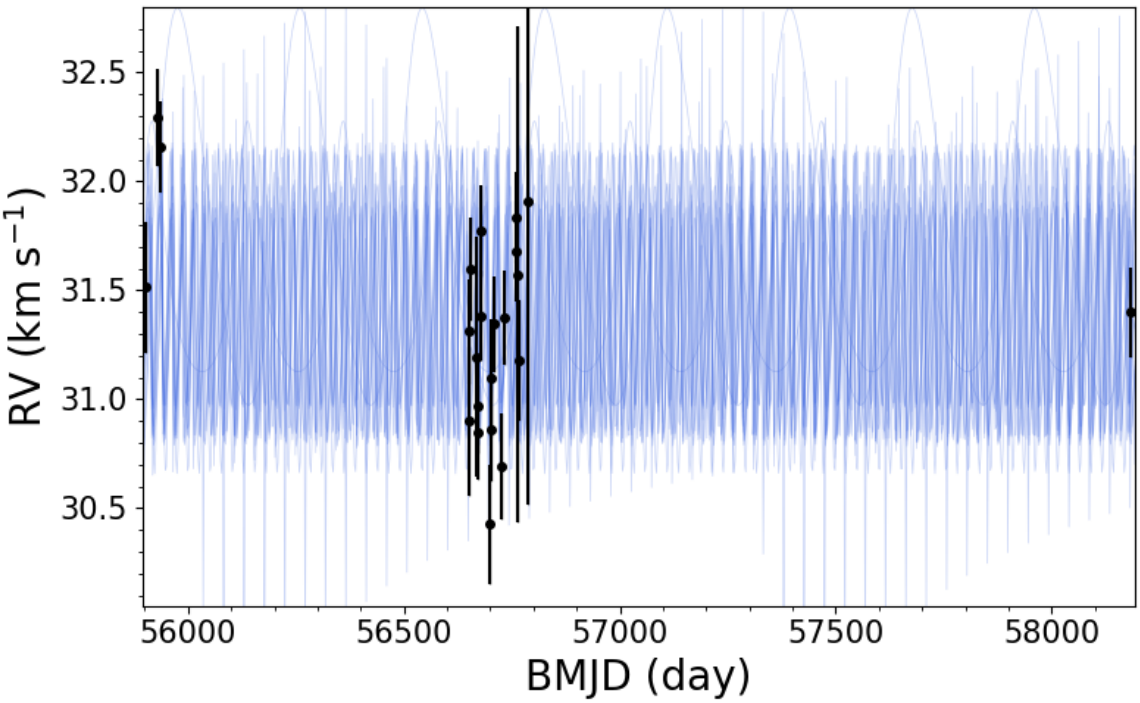

Figure C.4: Binary orbital fit for 2MASS J08501918+1056436. The best-fit orbital parameters are $P_{\rm fit} = 26.0^{+17.4}_{-24.0}$ day, $K_{\rm fit} = 0.7^{+0.3}_{-0.1}$ km s^{-1}, and $e_{\rm fit} = 0.365^{+0.43}_{-0.232}$.

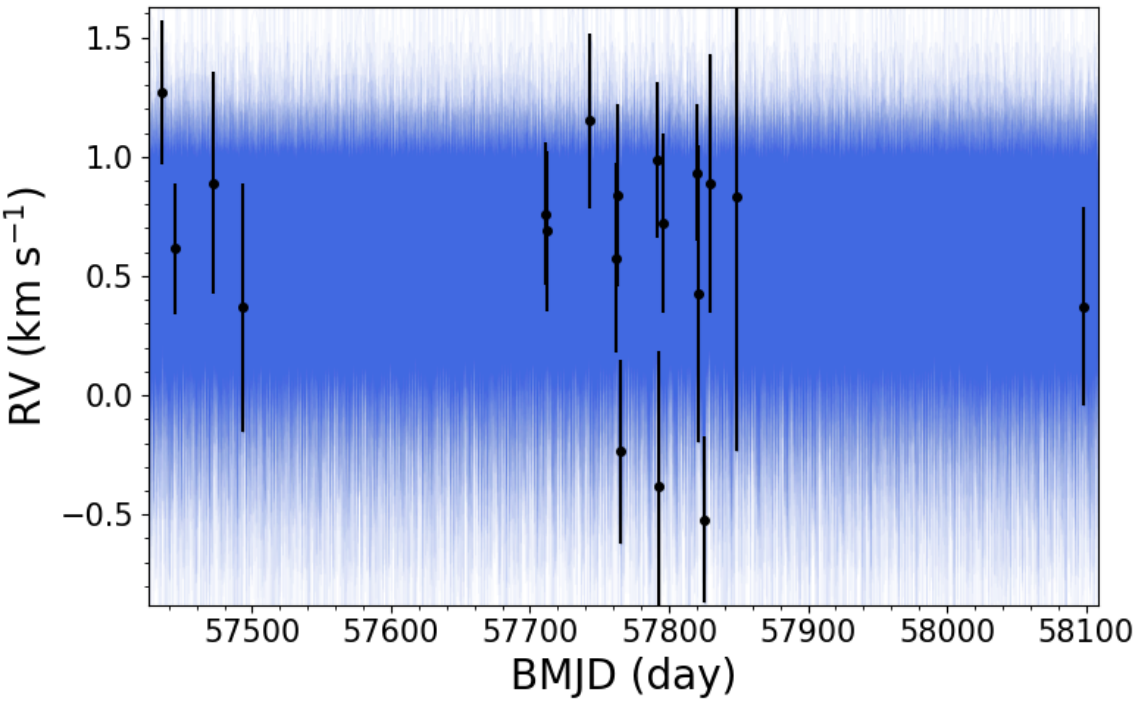

Figure C.5: Binary orbital fit for 2MASS J09373349+5534057. The best-fit orbital parameters are $P_{\rm fit} = 5.7^{+13.5}_{-3.9}$ day, $K_{\rm fit} = 0.4^{+0.3}_{-0.2}$ km s^{-1}, and $e_{\rm fit} = 0.271^{+0.297}_{-0.199}$.

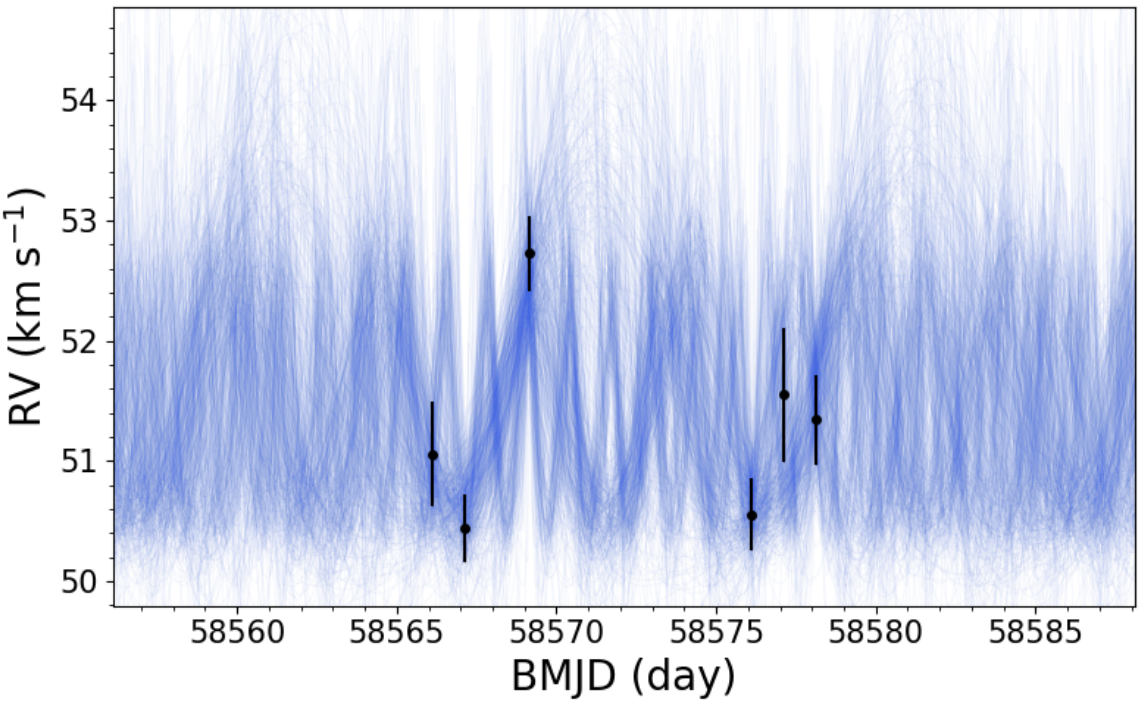

Figure C.6: Binary orbital fit for 2MASS J09442625+3521233. The best-fit orbital parameters are $P_{\rm fit} = 4.8^{+5.2}_{-3.4}$ day, $K_{\rm fit} = 1.2^{+0.5}_{-0.3}$ km s^{-1}, and $e_{\rm fit} = 0.227^{+0.273}_{-0.179}$.

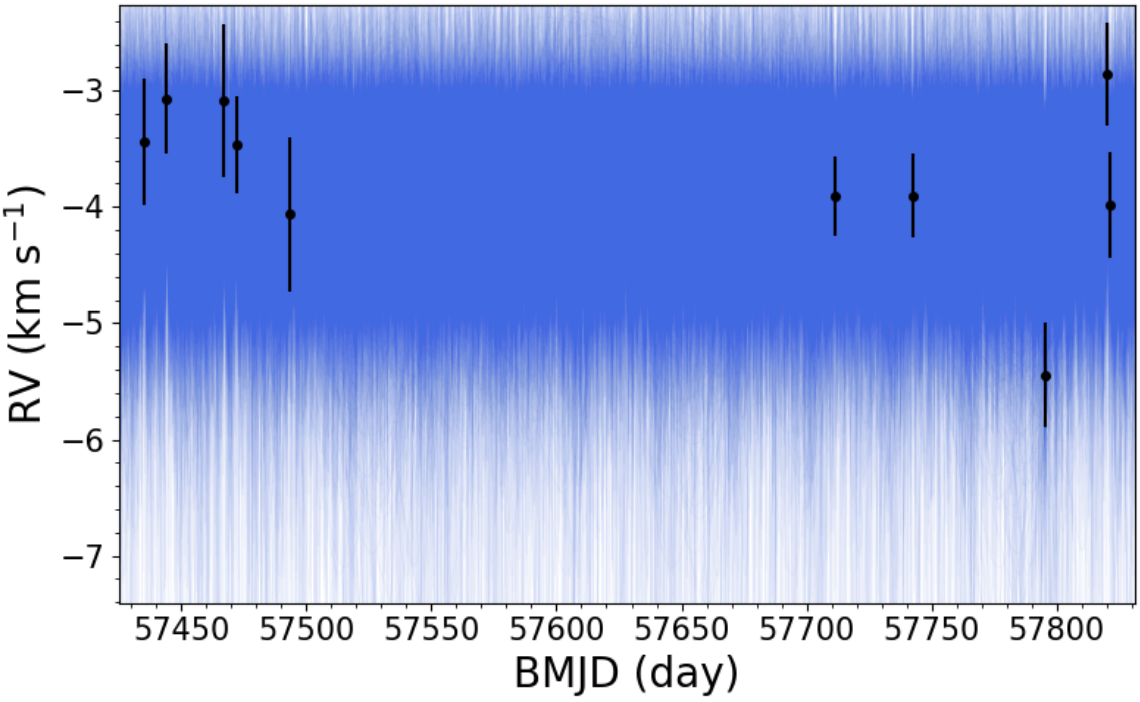

Figure C.7: Binary orbital fit for 2MASS J09453388+5458511. The best-fit orbital parameters are $P_{\rm fit} = 15.1^{+119.8}_{-12.7}$ day, $K_{\rm fit} = 1.0^{+0.5}_{-0.5}$ km s^{-1}, and $e_{\rm fit} = 0.315^{+0.298}_{-0.244}$.

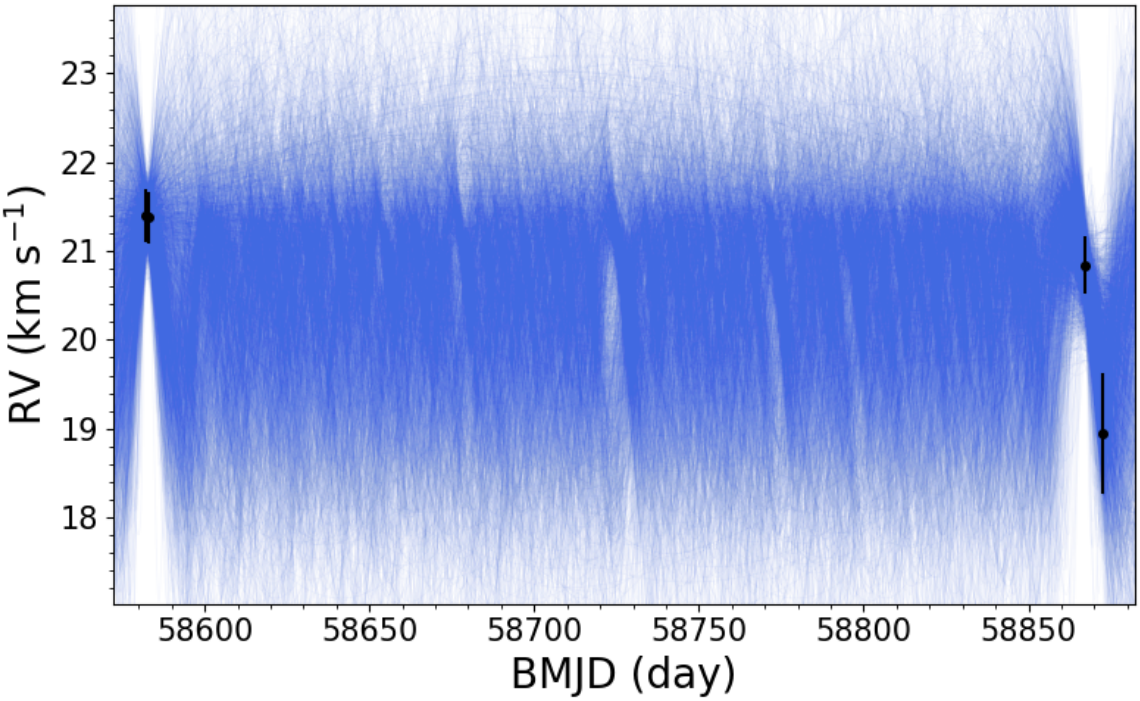

Figure C.8: Binary orbital fit for 2MASS J09560888+0134128. The best-fit orbital parameters are $P_{\rm fit} = 47.1^{+188.3}_{-25.4}$ day, $K_{\rm fit} = 1.4^{+0.7}_{-0.7}$ km s^{-1}, and $e_{\rm fit} = 0.177^{+0.262}_{-0.14}$.

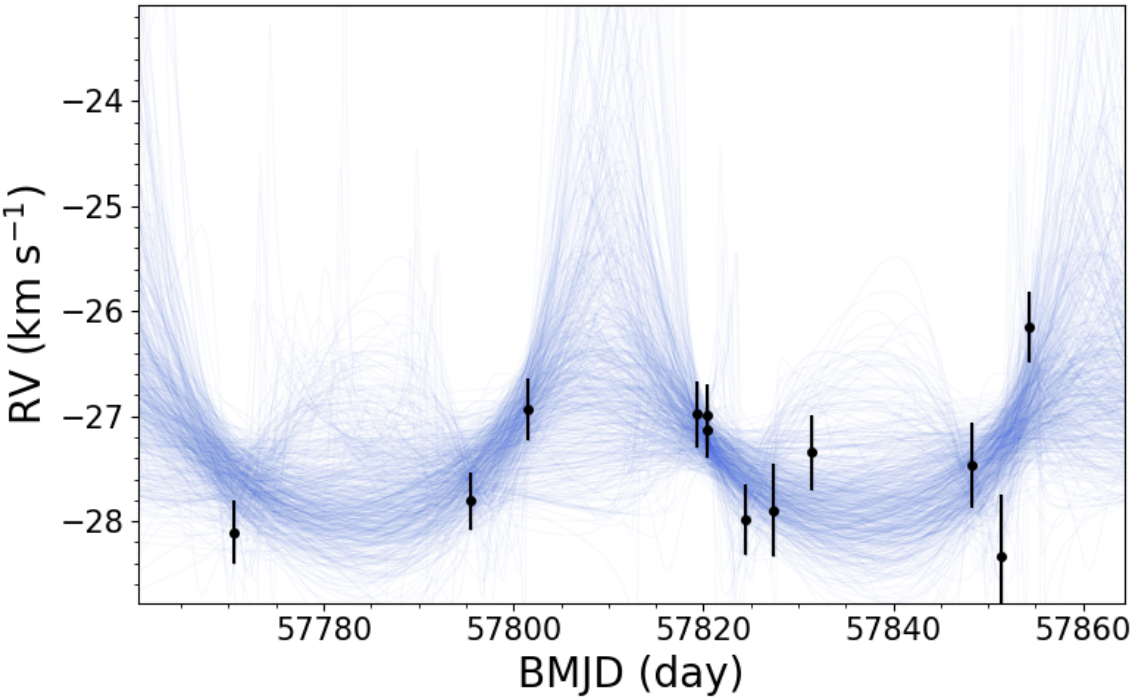

Figure C.9: Binary orbital fit for 2MASS J13202007+7213140. The best-fit orbital parameters are $P_{\rm fit} = 52.6^{+4.1}_{-16.0}$ day, $K_{\rm fit} = 0.9^{+0.6}_{-0.5}$ km s^{-1}, and $e_{\rm fit} = 0.338^{+0.268}_{-0.213}$.

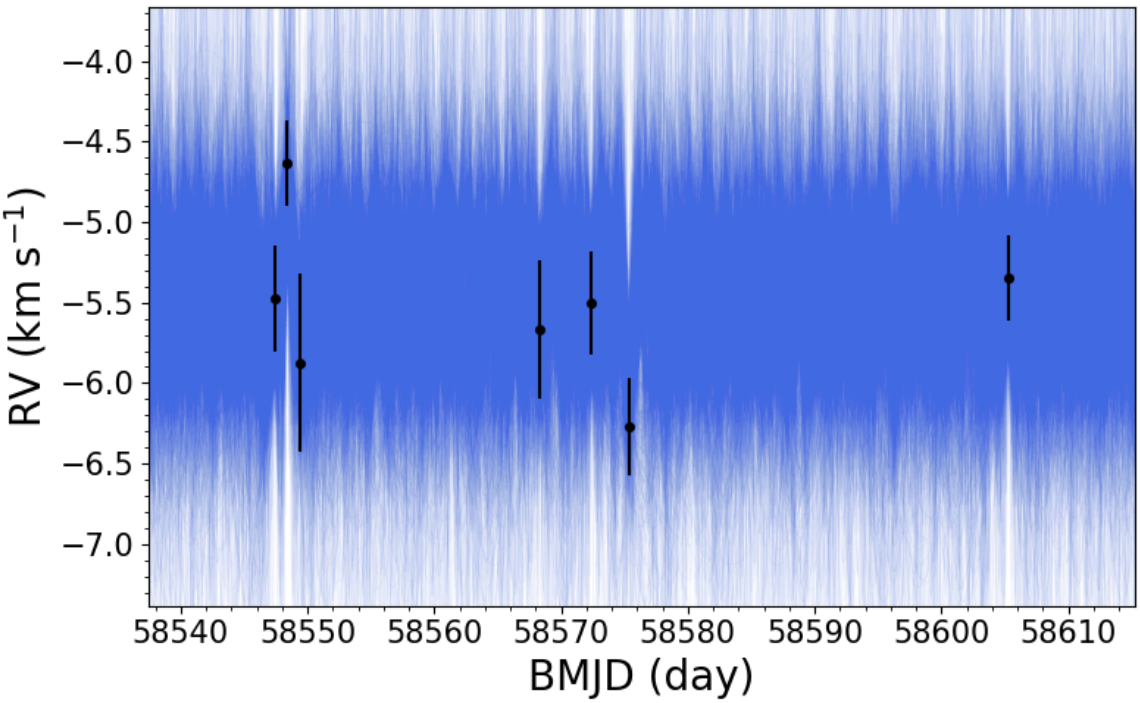

Figure C.10: Binary orbital fit for 2MASS J13232423+5132272. The best-fit orbital parameters are $P_{\rm fit} = 3.6^{+8.0}_{-2.0}$ day, $K_{\rm fit} = 0.7^{+0.4}_{-0.3}$ km s^{-1}, and $e_{\rm fit} = 0.207^{+0.332}_{-0.154}$.

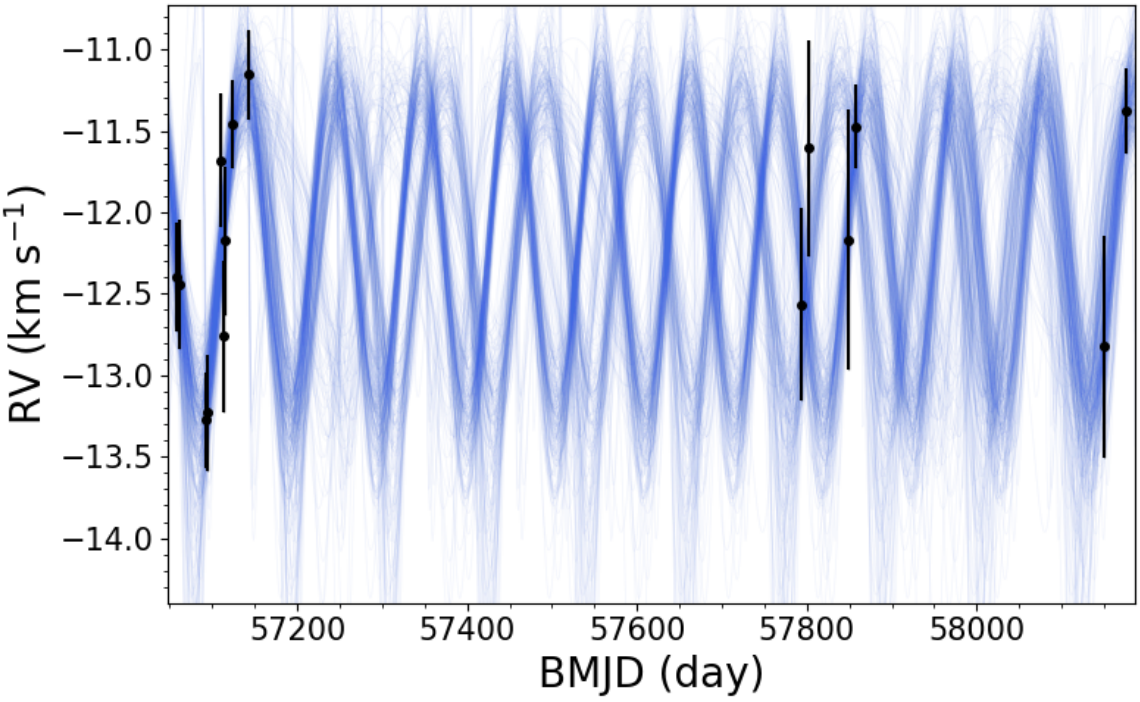

Figure C.11: Binary orbital fit for 2MASS J13430646+0038442. The best-fit orbital parameters are $P_{\rm fit} = 106.7^{+40.4}_{-2.0}$ day, $K_{\rm fit} = 1.1^{+0.2}_{-0.2}$ km s^{-1}, and $e_{\rm fit} = 0.124^{+0.207}_{-0.096}$.

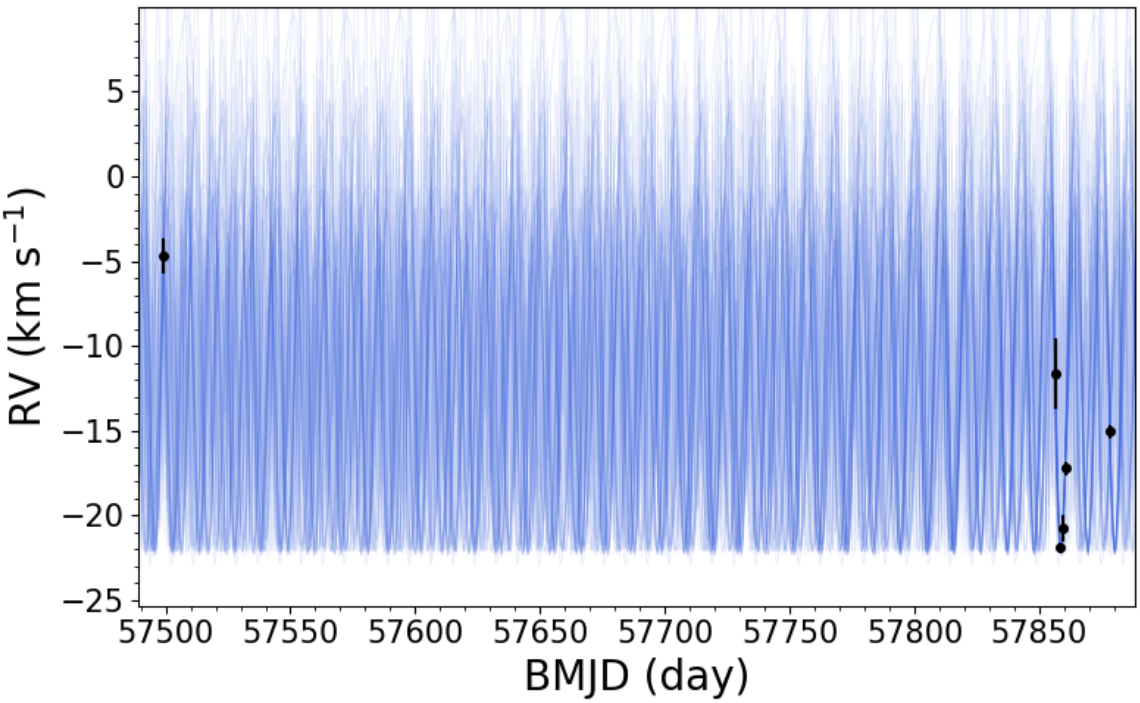

Figure C.12: Binary orbital fit for 2MASS J13482307+3321508. The best-fit orbital parameters are $P_{\rm fit} = 10.7^{+0.1}_{-3.4}$ day, $K_{\rm fit} = 10.8^{+3.6}_{-1.6}$ km s^{-1}, and $e_{\rm fit} = 0.101^{+0.182}_{-0.066}$.

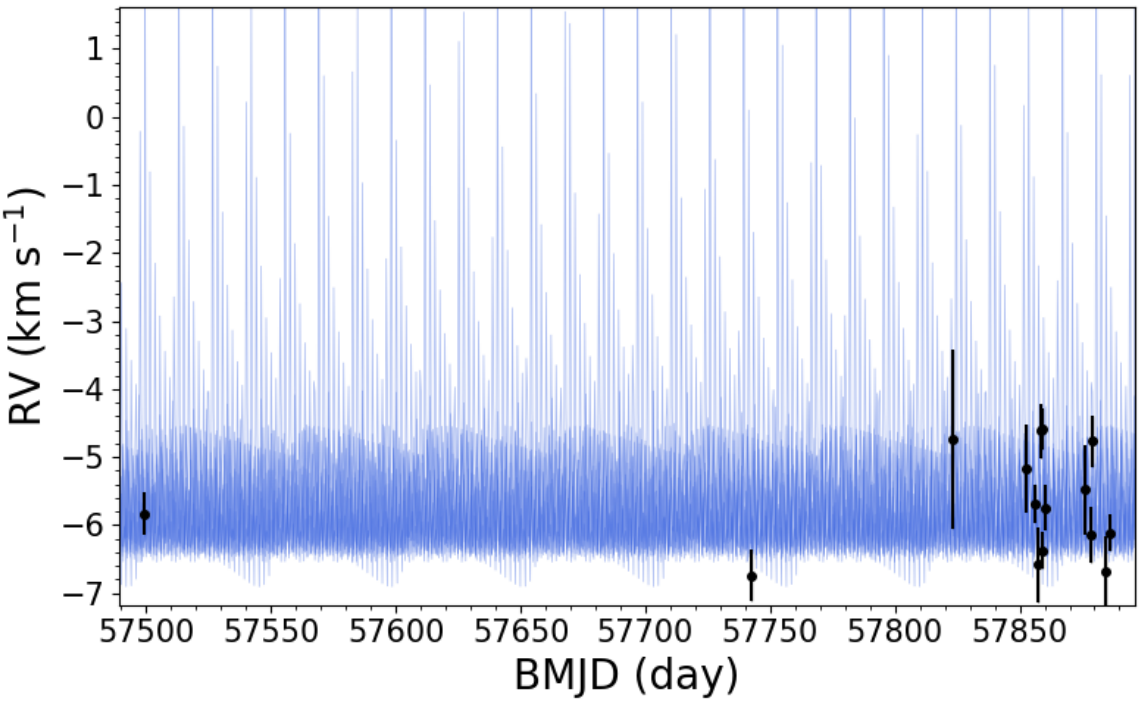

Figure C.13: Binary orbital fit for 2MASS J13500476+3207596. The best-fit orbital parameters are $P_{\rm fit} = 1.7^{+0.2}_{-0.7}$ day, $K_{\rm fit} = 1.1^{+0.9}_{-0.2}$ km s^{-1}, and $e_{\rm fit} = 0.655^{+0.093}_{-0.177}$.

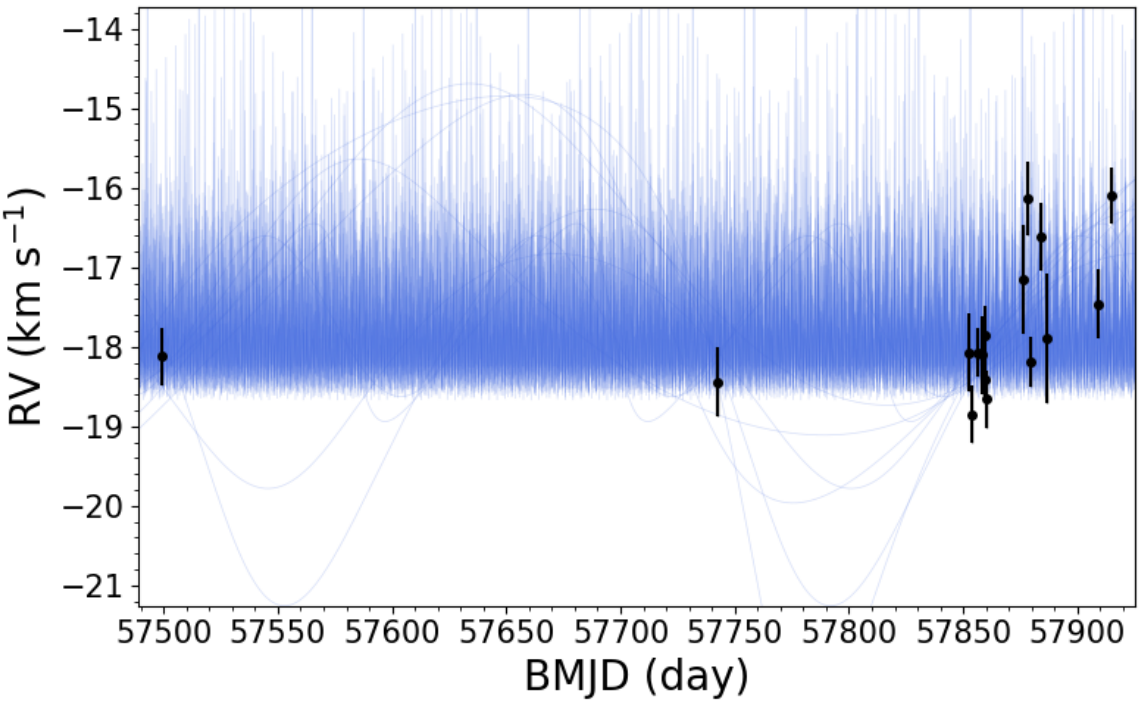

Figure C.14: Binary orbital fit for 2MASS J14005977+3226109. The best-fit orbital parameters are $P_{\rm fit} = 1.4^{+321.0}_{-0.3}$ day, $K_{\rm fit} = 1.5^{+1.0}_{-0.4}$ km s^{-1}, and $e_{\rm fit} = 0.419^{+0.258}_{-0.255}$.

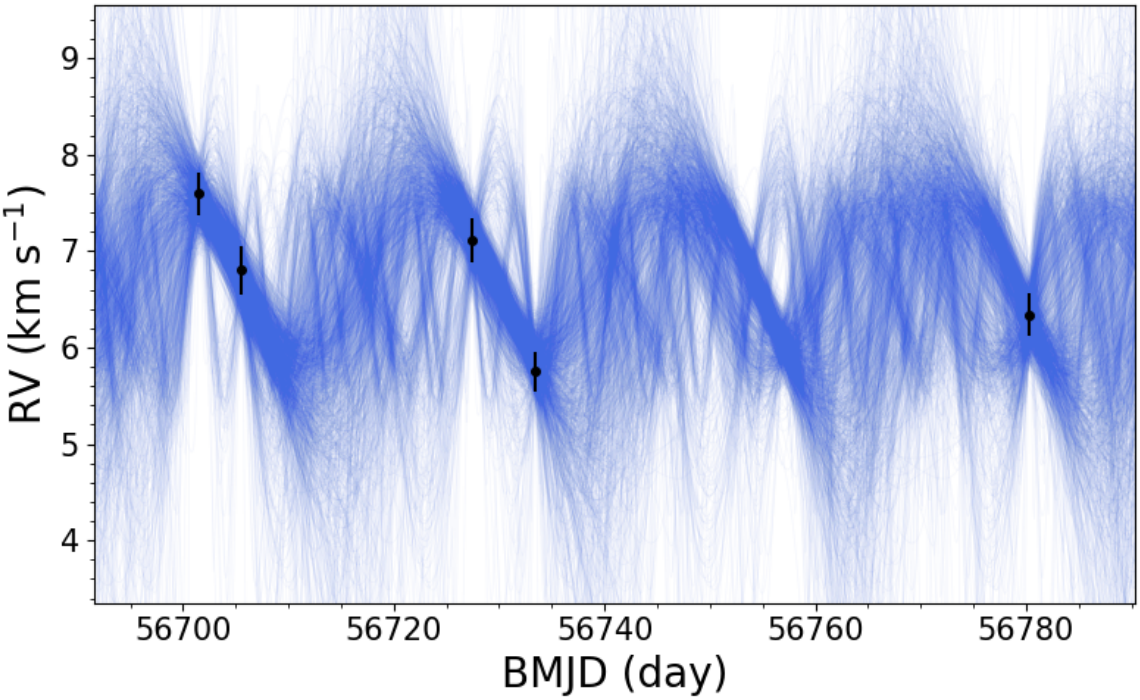

Figure C.15: Binary orbital fit for 2MASS J15010818+2250020. The best-fit orbital parameters are $P_{\rm fit} = 23.3^{+1.3}_{-11.0}$ day, $K_{\rm fit} = 1.2^{+0.7}_{-0.3}$ km s^{-1}, and $e_{\rm fit} = 0.189^{+0.284}_{-0.142}$.

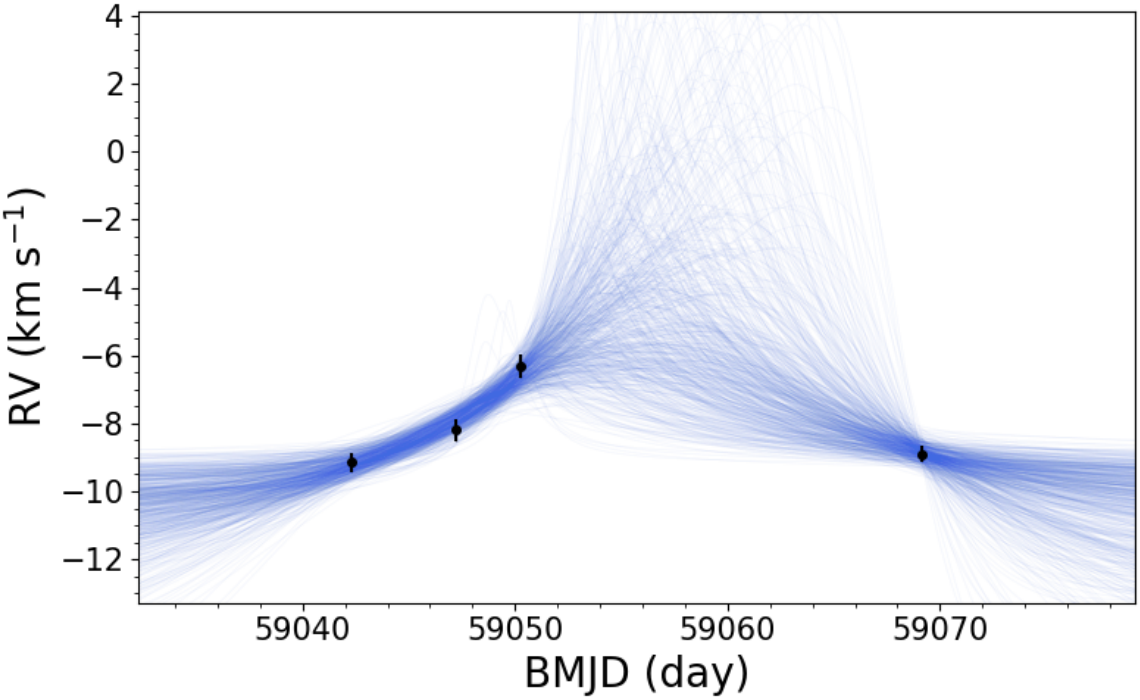

Figure C.16: Binary orbital fit for 2MASS J16271825+3538347. The best-fit orbital parameters are $P_{\rm fit} = 69.7^{+17.6}_{-7.4}$ day, $K_{\rm fit} = 3.4^{+2.1}_{-1.3}$ km s^{-1}, and $e_{\rm fit} = 0.524^{+0.175}_{-0.238}$.

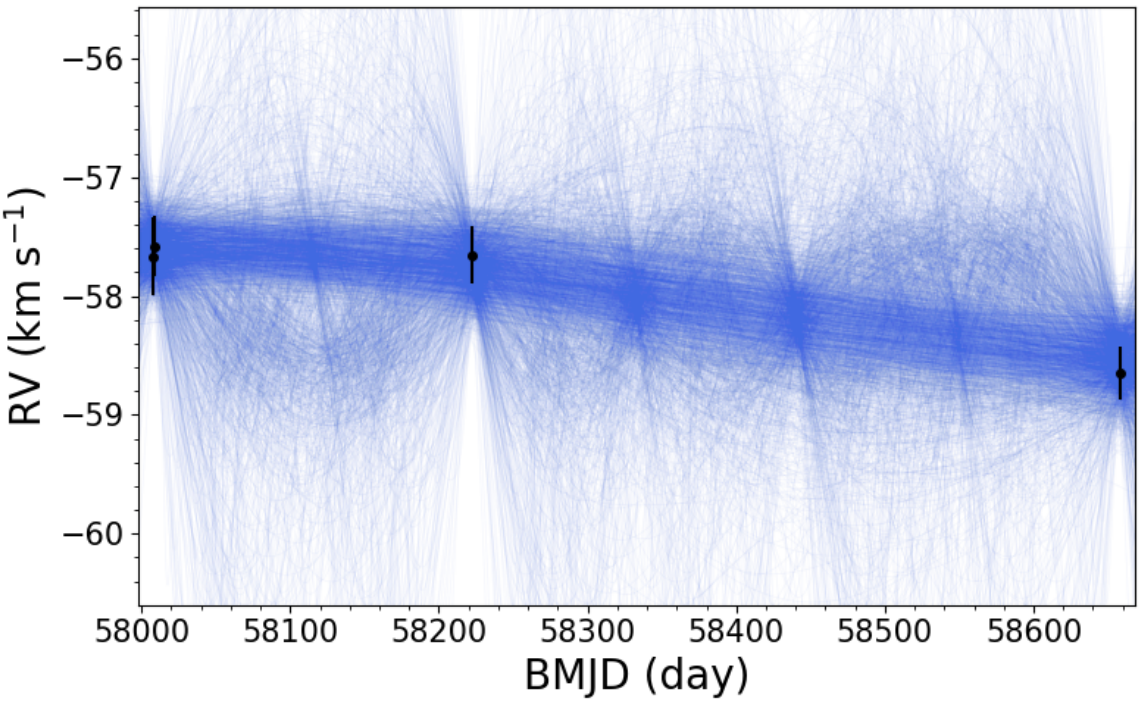

Figure C.17: Binary orbital fit for 2MASS J16572919+2448509. The best-fit orbital parameters are $P_{\rm fit} = 989.0^{+1158.0}_{-800.9}$ day, $K_{\rm fit} = 0.8^{+0.6}_{-0.3}$ km s^{-1}, and $e_{\rm fit} = 0.195^{+0.29}_{-0.15}$.

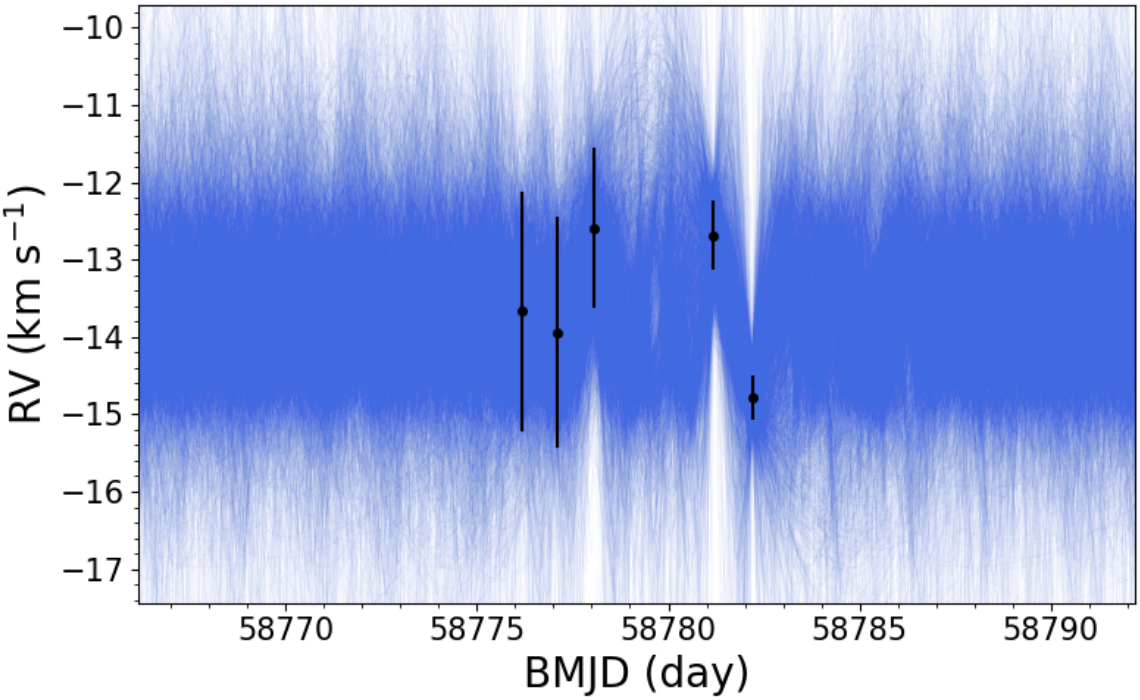

Figure C.18: Binary orbital fit for 2MASS J22551142+1442456. The best-fit orbital parameters are $P_{\rm fit} = 2.8^{+4.8}_{-1.1}$ day, $K_{\rm fit} = 1.6^{+0.9}_{-0.5}$ km s^{-1}, and $e_{\rm fit} = 0.178^{+0.256}_{-0.135}$.

Bibliography

Abdurro'uf, Accetta K., Aerts C., Silva Aguirre V., Ahumada R., Ajgaonkar N., Filiz Ak N., Alam S., Allende Prieto C., Almeida A., et al. 2022, The Seventeenth Data Release of the Sloan Digital Sky Surveys: Complete Release of MaNGA, MaStar, and APOGEE-2 Data, ApJS, 259, 35, doi: 10.3847/1538-4365/ac4414

Acuna M. H., Ness N. F. 1976, The main magnetic field of Jupiter, J. Geophys. Res., 81, 2917, doi: 10.1029/JA081i016p02917

Ahmed S., Warren S. J. 2019, A homogeneous sample of 34 000 M7-M9.5 dwarfs brighter than J = 17.5 with accurate spectral types, A&A, 623, A127, doi: 10.1051/0004-6361/201834591

Allard F., Hauschildt P. H., Alexander D. R., Tamanai A., Schweitzer A. 2001, The Limiting Effects of Dust in Brown Dwarf Model Atmospheres, ApJ, 556, 357, doi: 10.1086/321547

Allard F., Homeier D., Freytag B. 2012, Models of very-low-mass stars, brown dwarfs and exoplanets, Philosophical Transactions of the Royal Society of London Series A, 370, 2765, doi: 10.1098/rsta.2011.0269

Allen P. R. 2007, Star Formation via the Little Guy: A Bayesian Study of Ultracool Dwarf Imaging Surveys for Companions, ApJ, 668, 492, doi: 10.1086/521207

Allen P. R., Koerner D. W., Reid I. N., Trilling D. E. 2005, The Substellar Mass Function: A Bayesian Approach, ApJ, 625, 385, doi: 10.1086/429548

Aller K. M., Kraus A. L., Liu M. C., Burgett W. S., Chambers K. C., Hodapp K. W., Kaiser N., Magnier E. A., Price P. A. 2013, A Pan-STARRS + UKIDSS Search for Young, Wide Planetary-mass Companions in Upper Scorpius, ApJ, 773, 63, doi: 10.1088/0004-637X/773/1/63

Allers K. N., Gallimore J. F., Liu M. C., Dupuy T. J. 2016, The Radial and Rotational Velocities of PSO J318.5338-22.8603, a Newly Confirmed Planetary-mass Member of the β Pictoris Moving Group, ApJ, 819, 133, doi: 10.3847/0004-637X/819/2/133

Allers K. N., Liu M. C. 2013, A Near-infrared Spectroscopic Study of Young Field Ultracool Dwarfs, ApJ, 772, 79, doi: 10.1088/0004-637X/772/2/79

Alonso-Floriano F. J., Morales J. C., Caballero J. A., Montes D., Klutsch A., Mundt R., Cortés-Contreras M., Ribas I., Reiners A., Amado P. J., Quirrenbach A., Jeffers S. V. 2015, CARMENES input catalogue of M dwarfs. I. Low-resolution spectroscopy with CAFOS, A&A, 577, A128, doi: 10.1051/0004-6361/201525803

Angus R., Morton T. D., Foreman-Mackey D., van Saders J., Curtis J., Kane S. R., Bedell M., Kiman R., Hogg D. W., Brewer J. 2019, Toward Precise Stellar Ages: Combining Isochrone Fitting with Empirical Gyrochronology, AJ, 158, 173, doi: 10.3847/1538-3881/ab3c53

Ardila D., Martín E., Basri G. 2000, A Survey for Low-Mass Stars and Brown Dwarfs in the Upper Scorpius OB Association, AJ, 120, 479, doi: 10.1086/301443

Artigau É., Doyon R., Lafrenière D., Nadeau D., Robert J., Albert L. 2006, Discovery of the Brightest T Dwarf in the Northern Hemisphere, ApJ, 651, L57, doi: 10.1086/509146

Aumer M., Binney J. J. 2009, Kinematics and history of the solar neighbourhood revisited, MNRAS, 397, 1286, doi: 10.1111/j.1365-2966.2009.15053.x

Bai Y., Liu J., Wicker J., Wang S., Guo J., Qin Y., He L., Wang J., Wu Y., Dong Y., Zhang Y., Hou Y., Wang Y., Cao Z. 2018, The UV Emission of Stars in the LAMOST Survey. I. Catalogs, ApJS, 235, 16, doi: 10.3847/1538-4365/aaaab9

Bailer-Jones C. A. L. 2004, Spectroscopic rotation velocities of L dwarfs from VLT/UVES and their comparison with periods from photometric monitoring, A&A, 419, 703, doi: 10.1051/0004-6361:20040965

Bannister N. P., Jameson R. F. 2007, L and T dwarfs in the Hyades and Ursa Major moving groups, MNRAS, 378, L24, doi: 10.1111/j.1745-3933.2007.00312.x

Baraffe I., Chabrier G., Barman T. S., Allard F., Hauschildt P. H. 2003, Evolutionary models for cool brown dwarfs and extrasolar giant planets. The case of HD 209458, A&A, 402, 701, doi: 10.1051/0004-6361:20030252

Baraffe I., Homeier D., Allard F., Chabrier G. 2015, New evolutionary models for pre-main sequence and main sequence low-mass stars down to the hydrogen-burning limit, A&A, 577, A42, doi: 10.1051/0004-6361/201425481

Bardalez Gagliuffi D., Ward-Duong K., Faherty J., Greenbaum A., Marocco F., Burgasser A., Bate M., Dupuy T., Gelino C., Sahlmann J., Martinache F., Meyer M., Konopacky Q., Stephens D. 2019a, Substellar Multiplicity Throughout the Ages, BAAS, 51, 285. https://arxiv.org/abs/1903.06699

Bardalez Gagliuffi D. C., Gagné J., Faherty J. K., Burgasser A. J. 2018, An L+T Spectral Binary with Possible AB Doradus Kinematics, ApJ, 854, 101, doi: 10.3847/1538-4357/aaa961

Bardalez Gagliuffi D. C., Gelino C. R., Burgasser A. J. 2015, High Resolution Imaging of Very Low Mass Spectral Binaries: Three Resolved Systems and Detection of Orbital Motion in an L/T Transition Binary, AJ, 150, 163, doi: 10.1088/0004-6256/150/5/163

Bardalez Gagliuffi D. C., Burgasser A. J., Gelino C. R., Looper D. L., Nicholls C. P., Schmidt S. J., Cruz K., West A. A., Gizis J. E., Metchev S. 2014, SpeX Spectroscopy of Unresolved Very Low Mass Binaries. II. Identification of 14 Candidate Binaries with Late-M/Early-L and T Dwarf Components, ApJ, 794, 143, doi: 10.1088/0004-637X/794/2/143

Bardalez Gagliuffi D. C., Burgasser A. J., Schmidt S. J., Theissen C., Gagné J., Gillon M., Sahlmann J., Faherty J. K., Gelino C., Cruz K. L., Skrzypek N., Looper D. 2019b, The Ultracool SpeXtroscopic Survey. I. Volume-limited Spectroscopic Sample and Luminosity Function of M7-L5 Ultracool Dwarfs, ApJ, 883, 205, doi: 10.3847/1538-4357/ab253d

Barnes J. R., Jenkins J. S., Jones H. R. A., Jeffers S. V., Rojo P., Arriagada P., Jordán A., Minniti D., Tuomi M., Pinfield D., Anglada-Escudé G. 2014, Precision radial velocities of 15 M5-M9 dwarfs, MNRAS, 439, 3094, doi: 10.1093/mnras/stu172

Barnes S. A. 2003, On the Rotational Evolution of Solar- and Late-Type Stars, Its Magnetic Origins, and the Possibility of Stellar Gyrochronology, ApJ, 586, 464, doi: 10.1086/367639

Barnes S. A. 2007, Ages for Illustrative Field Stars Using Gyrochronology: Viability, Limitations, and Errors, ApJ, 669, 1167, doi: 10.1086/519295

Barrado y Navascues D. 1998, The Castor moving group. The age of Fomalhaut and VEGA, A&A, 339, 831. https://arxiv.org/abs/astro-ph/9905243

Basri G., Mohanty S., Allard F., Hauschildt P. H., Delfosse X., Martín E. L., Forveille T., Goldman B. 2000, An Effective Temperature Scale for Late-M and L Dwarfs, from Resonance Absorption Lines of Cs I and Rb I, ApJ, 538, 363, doi: 10.1086/309095

Bastian N., Covey K. R., Meyer M. R. 2010, A Universal Stellar Initial Mass Function? A Critical Look at Variations, ARA&A, 48, 339, doi: 10.1146/annurev-astro-082708-101642

Beane A., Ness M. K., Bedell M. 2018, Actions Are Weak Stellar Age Indicators in the Milky Way Disk, ApJ, 867, 31, doi: 10.3847/1538-4357/aae07f

Beaton R. L., Oelkers R. J., Hayes C. R., Covey K. R., Chojnowski S. D., De Lee N., Sobeck J. S., Majewski S. R., Cohen R. E., Fernández-Trincado J., Longa-Peña P., O'Connell J. E., Santana F. A., Stringfellow G. S., Zasowski G., Aerts C., Anguiano B., Bender C., Cañas C. I., Cunha K., Donor J., Fleming S. W., Frinchaboy P. M., Feuillet D., Harding P., Hasselquist S., Holtzman J. A., Johnson J. A., Kollmeier J. A., Kounkel M., Mahadevan S., Price-Whelan A. M., Rojas-Arriagada A., Román-Zúñiga C., Schlafly E. F., Schultheis M., Shetrone M., Simon J. D., Stassun K. G., Stutz A. M., Tayar J., Teske J., Tkachenko A., Troup N., Albareti F. D., Bizyaev D., Bovy J., Burgasser A. J., Comparat J., Downes J. J., Geisler D., Inno L., Manchado A., Ness M. K., Pinsonneault M. H., Prada F., Roman-Lopes A., Simonian G. V. A., Smith V. V., Yan R., Zamora O. 2021, Final Targeting Strategy for the Sloan Digital Sky Survey IV Apache Point Observatory Galactic Evolution Experiment 2 North Survey, AJ, 162, 302, doi: 10.3847/1538-3881/ac260c

Becker A. C., Bochanski J. J., Hawley S. L., Ivezić Ž., Kowalski A. F., Sesar B., West A. A. 2011, Periodic Variability of Low-mass Stars in Sloan Digital Sky Survey Stripe 82, ApJ, 731, 17, doi: 10.1088/0004-637X/731/1/17

Bell C. P. M., Mamajek E. E., Naylor T. 2015, A self-consistent, absolute isochronal age scale for young moving groups in the solar neighbourhood, MNRAS, 454, 593, doi: 10.1093/mnras/stv1981

Bensby T., Feltzing S., Lundström I. 2003, Elemental abundance trends in the Galactic thin and thick disks as traced by nearby F and G dwarf stars, A&A, 410, 527, doi: 10.1051/0004-6361:20031213

Berger E., Rutledge R. E., Phan-Bao N., Basri G., Giampapa M. S., Gizis J. E., Liebert J., Martín E., Fleming T. A. 2009, Periodic Radio and Hα Emission from the L Dwarf Binary 2MASSW J0746425+200032: Exploring the Magnetic Field Topology and Radius Of An L Dwarf, ApJ, 695, 310, doi: 10.1088/0004-637X/695/1/310

Best W. M. J., Liu M. C., Dupuy T. J., Magnier E. A. 2017, The Young L Dwarf 2MASS J11193254-1137466 Is a Planetary-mass Binary, ApJ, 843, L4, doi: 10.3847/2041-8213/aa76df

Best W. M. J., Liu M. C., Magnier E. A., Dupuy T. J. 2020, The Hawaii Infrared Parallax Program. IV. A Comprehensive Parallax Survey of L0-T8 Dwarfs with UKIRT, AJ, 159, 257, doi: 10.3847/1538-3881/ab84f4

Best W. M. J., Liu M. C., Magnier E. A., Dupuy T. J. 2021, A Volume-limited Sample of Ultracool Dwarfs. I. Construction, Space Density, and a Gap in the L/T Transition, AJ, 161, 42, doi: 10.3847/1538-3881/abc893

Best W. M. J., Liu M. C., Magnier E. A., Aller K. M., Deacon N. R., Dupuy T. J., Redstone J., Burgett W. S., Chambers K. C., Hodapp K. W., Kaiser N., Kudritzki R. P., Morgan J. S., Price P. A., Tonry J. L., Wainscoat R. J. 2013, A Search for L/T Transition Dwarfs with Pan-STARRS1 and WISE: Discovery of Seven Nearby Objects Including Two Candidate Spectroscopic Variables, ApJ, 777, 84, doi: 10.1088/0004-637X/777/2/84

Best W. M. J., Magnier E. A., Liu M. C., Aller K. M., Zhang Z., Burgett W. S., Chambers K. C., Draper P., Flewelling H., Kaiser N., Kudritzki R. P., Metcalfe N., Tonry J. L., Wainscoat R. J., Waters C. 2018, Photometry and Proper Motions of M, L, and T Dwarfs from the Pan-STARRS1 3π Survey, ApJS, 234, 1, doi: 10.3847/1538-4365/aa9982

Bird J. 2019, in American Astronomical Society Meeting Abstracts, Vol. 233, American Astronomical Society Meeting Abstracts #233, 231.03

Blake C. H., Charbonneau D., White R. J. 2010, The NIRSPEC Ultracool Dwarf Radial Velocity Survey, ApJ, 723, 684, doi: 10.1088/0004-637X/723/1/684

Blake C. H., Charbonneau D., White R. J., Marley M. S., Saumon D. 2007, Multiepoch Radial Velocity Observations of L Dwarfs, ApJ, 666, 1198, doi: 10.1086/520124

Bochanski J. J., Munn J. A., Hawley S. L., West A. A., Covey K. R., Schneider D. P. 2007a, Exploring the Local Milky Way: M Dwarfs as Tracers of Galactic Populations, AJ, 134, 2418, doi: 10.1086/522053

Bochanski J. J., West A. A., Hawley S. L., Covey K. R. 2007b, Low-Mass Dwarf Template Spectra from the Sloan Digital Sky Survey, AJ, 133, 531, doi: 10.1086/510240

Bovy J. 2015, galpy: A python Library for Galactic Dynamics, ApJS, 216, 29, doi: 10.1088/0067-0049/216/2/29

Bovy J. 2016, The Chemical Homogeneity of Open Clusters, ApJ, 817, 49, doi: 10.3847/0004-637X/817/1/49

Bovy J., Tremaine S. 2012, On the Local Dark Matter Density, ApJ, 756, 89, doi: 10.1088/0004-637X/756/1/89

Bowen I. S., Vaughan A. H. J. 1973, The optical design of the 40-in. telescope and of the Irénée DuPont telescope at Las Campanas Observatory, Chile., Appl. Opt., 12, 1430, doi: 10.1364/AO.12.001430

Bowler B. P., Blunt S. C., Nielsen E. L. 2020, Population-level Eccentricity Distributions of Imaged Exoplanets and Brown Dwarf Companions: Dynamical Evidence for Distinct Formation Channels, AJ, 159, 63, doi: 10.3847/1538-3881/ab5b11

Brandt T. D., Dupuy T. J., Bowler B. P. 2019, Precise Dynamical Masses of Directly Imaged Companions from Relative Astrometry, Radial Velocities, and Hipparcos-Gaia DR2 Accelerations, AJ, 158, 140, doi: 10.3847/1538-3881/ab04a8

Brandt T. D., Dupuy T. J., Bowler B. P., Bardalez Gagliuffi D. C., Faherty J., Brand t G. M., Michalik D. 2020, A Dynamical Mass of 70 $\pm$ 5 M_{Jup} for Gliese 229B, the First T Dwarf, AJ, 160, 196, doi: 10.3847/1538-3881/abb45e

Brandt T. D., Huang C. X. 2015, The Age and Age Spread of the Praesepe and Hyades Clusters: a Consistent, $\sim$800 Myr Picture from Rotating Stellar Models, ApJ, 807, 24, doi: 10.1088/0004-637X/807/1/24

Briceño C., Luhman K. L., Hartmann L., Stauffer J. R., Kirkpatrick J. D. 2002, The Initial Mass Function in the Taurus Star-forming Region, ApJ, 580, 317, doi: 10.1086/343127

Burgasser A. J. 2004, T Dwarfs and the Substellar Mass Function. I. Monte Carlo Simulations, ApJS, 155, 191, doi: 10.1086/424386

Burgasser A. J. 2007, Binaries and the L Dwarf/T Dwarf Transition, ApJ, 659, 655, doi: 10.1086/511027

Burgasser A. J. 2009, in IAU Symposium, Vol. 258, The Ages of Stars, ed. E. E. Mamajek, D. R. Soderblom, R. F. G. Wyse, 317–326, doi: 10.1017/S1743921309031974

Burgasser A. J., Blake C. H. 2009, An Age Constraint for the Very Low Mass Stellar/Brown Dwarf Binary 2MASS J03202839-0446358AB, AJ, 137, 4621, doi: 10.1088/0004-6256/137/6/4621

Burgasser A. J., Blake C. H., Gelino C. R., Sahlmann J., Bardalez Gagliuffi D. 2016, The Orbit of the L Dwarf + T Dwarf Spectral Binary SDSS J080531.84+481233.0, ApJ, 827, 25, doi: 10.3847/0004-637X/827/1/25

Burgasser A. J., Burrows A., Kirkpatrick J. D. 2006a, A Method for Determining the Physical Properties of the Coldest Known Brown Dwarfs, ApJ, 639, 1095, doi: 10.1086/499344

Burgasser A. J., Cruz K. L., Cushing M., Gelino C. R., Looper D. L., Faherty J. K., Kirkpatrick J. D., Reid I. N. 2010, SpeX Spectroscopy of Unresolved Very Low Mass Binaries. I. Identification of 17 Candidate Binaries Straddling the L Dwarf/T Dwarf Transition, ApJ, 710, 1142, doi: 10.1088/0004-637X/710/2/1142

Burgasser A. J., Geballe T. R., Leggett S. K., Kirkpatrick J. D., Golimowski D. A. 2006b, A Unified Near-Infrared Spectral Classification Scheme for T Dwarfs, ApJ, 637, 1067, doi: 10.1086/498563

Burgasser A. J., Kirkpatrick J. D., Cruz K. L., Reid I. N., Leggett S. K., Liebert J., Burrows A., Brown M. E. 2006c, Hubble Space Telescope NICMOS Observations of T Dwarfs: Brown Dwarf Multiplicity and New Probes of the L/T Transition, ApJS, 166, 585, doi: 10.1086/506327

Burgasser A. J., Kirkpatrick J. D., Liebert J., Burrows A. 2003a, The Spectra of T Dwarfs. II. Red Optical Data, ApJ, 594, 510, doi: 10.1086/376756

Burgasser A. J., Kirkpatrick J. D., McElwain M. W., Cutri R. M., Burgasser A. J., Skrutskie M. F. 2003b, The 2Mass Wide-Field T Dwarf Search. I. Discovery of a Bright T Dwarf within 10 Parsecs of the Sun, AJ, 125, 850, doi: 10.1086/345975

Burgasser A. J., Kirkpatrick J. D., Reid I. N., Brown M. E., Miskey C. L., Gizis J. E. 2003c, Binarity in Brown Dwarfs: T Dwarf Binaries Discovered with the Hubble Space Telescope Wide Field Planetary Camera 2, ApJ, 586, 512, doi: 10.1086/346263

Burgasser A. J., Liu M. C., Ireland M. J., Cruz K. L., Dupuy T. J. 2008, Subtle Signatures of Multiplicity in Late-type Dwarf Spectra: The Unresolved M8.5 + T5 Binary 2MASS J03202839-0446358, ApJ, 681, 579, doi: 10.1086/588379

Burgasser A. J., Luk C., Dhital S., Bardalez Gagliuffi D., Nicholls C. P., Prato L., West A. A., Lépine S. 2012, Discovery of a Very Low Mass Triple with Late-M and T Dwarf Components: LP 704-48/SDSS J0006-0852AB, ApJ, 757, 110, doi: 10.1088/0004-637X/757/2/110

Burgasser A. J., Mamajek E. E. 2017, On the Age of the TRAPPIST-1 System, ApJ, 845, 110, doi: 10.3847/1538-4357/aa7fea

Burgasser A. J., McElwain M. W. 2006, Resolved Spectroscopy of M Dwarf/L Dwarf Binaries. I. DENIS J220002.05-303832.9AB, AJ, 131, 1007, doi: 10.1086/499042

Burgasser A. J., McElwain M. W., Kirkpatrick J. D., Cruz K. L., Tinney C. G., Reid I. N. 2004, The 2MASS Wide-Field T Dwarf Search. III. Seven New T Dwarfs and Other Cool Dwarf Discoveries, AJ, 127, 2856, doi: 10.1086/383549

Burgasser A. J., Reid I. N., Siegler N., Close L., Allen P., Lowrance P., Gizis J. 2007, in Protostars and Planets V, ed. B. Reipurth, D. Jewitt, K. Keil, 427. https://arxiv.org/abs/astro-ph/0602122

Burgasser A. J., Sheppard S. S., Luhman K. L. 2013, Resolved Near-infrared Spectroscopy of WISE J104915.57-531906.1AB: A Flux-reversal Binary at the L dwarf/T Dwarf Transition, ApJ, 772, 129, doi: 10.1088/0004-637X/772/2/129

Burgasser A. J., Sitarski B. N., Gelino C. R., Logsdon S. E., Perrin M. D. 2011, The Hyperactive L Dwarf 2MASS J13153094-2649513: Continued Emission and a Brown Dwarf Companion, ApJ, 739, 49, doi: 10.1088/0004-637X/739/1/49

Burgasser A. J., Kirkpatrick J. D., Brown M. E., Reid I. N., Gizis J. E., Dahn C. C., Monet D. G., Beichman C. A., Liebert J., Cutri R. M., Skrutskie M. F. 1999, Discovery of Four Field Methane (T-Type) Dwarfs with the Two Micron All-Sky Survey, ApJ, 522, L65, doi: 10.1086/312221

Burgasser A. J., Kirkpatrick J. D., Cutri R. M., McCallon H., Kopan G., Gizis J. E., Liebert J., Reid I. N., Brown M. E., Monet D. G., Dahn C. C., Beichman C. A., Skrutskie M. F. 2000a, Discovery of a Brown Dwarf Companion to Gliese 570ABC: A 2MASS T Dwarf Significantly Cooler than Gliese 229B, ApJ, 531, L57, doi: 10.1086/312522

Burgasser A. J., Wilson J. C., Kirkpatrick J. D., Skrutskie M. F., Colonno M. R., Enos A. T., Smith J. D., Henderson C. P., Gizis J. E., Brown M. E., Houck J. R. 2000b, Discovery of a Bright Field Methane (T-Type) Brown Dwarf by 2MASS, AJ, 120, 1100, doi: 10.1086/301475

Burgasser A. J., Kirkpatrick J. D., Brown M. E., Reid I. N., Burrows A., Liebert J., Matthews K., Gizis J. E., Dahn C. C., Monet D. G., Cutri R. M., Skrutskie M. F. 2002, The Spectra of T Dwarfs. I. Near-Infrared Data and Spectral Classification, ApJ, 564, 421, doi: 10.1086/324033

Burgasser A. J., Logsdon S. E., Gagné J., Bochanski J. J., Faherty J. K., West A. A., Mamajek E. E., Schmidt S. J., Cruz K. L. 2015a, The Brown Dwarf Kinematics Project (BDKP). IV. Radial Velocities of 85 Late-M and L Dwarfs with MagE, ApJS, 220, 18, doi: 10.1088/0067-0049/220/1/18

Burgasser A. J., Gillon M., Melis C., Bowler B. P., Michelsen E. L., Bardalez Gagliuffi D., Gelino C. R., Jehin E., Delrez L., Manfroid J., Blake C. H. 2015b, WISE J072003.20-084651.2: an Old and Active M9.5 + T5 Spectral Binary 6 pc from the Sun, AJ, 149, 104, doi: 10.1088/0004-6256/149/3/104

Burrows A., Hubbard W. B., Lunine J. I., Liebert J. 2001, The theory of brown dwarfs and extrasolar giant planets, Reviews of Modern Physics, 73, 719, doi: 10.1103/RevModPhys.73.719

Burrows A., Marley M., Hubbard W. B., Lunine J. I., Guillot T., Saumon D., Freedman R., Sudarsky D., Sharp C. 1997, A Nongray Theory of Extrasolar Giant Planets and Brown Dwarfs, ApJ, 491, 856, doi: 10.1086/305002

Cabello C., Csörnyei G., Merc J., Ferreirós Lopez V., Pessev P. 2019, Independent study and spectral classification of a sample of poorly studied high proper motion M-dwarf candidate stars, Contributions of the Astronomical Observatory Skalnate Pleso, 49, 546. https://arxiv.org/abs/1912.10504

Caiazzo I., Heyl J. S., Richer H., Kalirai J. 2017, Globular cluster absolute ages from cooling brown dwarfs, arXiv e-prints, arXiv:1702.00091. https://arxiv.org/abs/1702.00091

Cale B., Plavchan P., LeBrun D., Gagné J., Gao P., Tanner A., Beichman C., Xuesong Wang S., Gaidos E., Teske J., Ciardi D., Vasisht G., Kane S. R., von Braun K. 2019,

Precise Radial Velocities of Cool Low-mass Stars with iSHELL, AJ, 158, 170, doi: 10.3847/1538-3881/ab3b0f

Cantat-Gaudin T., Anders F. 2020, Clusters and mirages: cataloguing stellar aggregates in the Milky Way, A&A, 633, A99, doi: 10.1051/0004-6361/201936691

Cantat-Gaudin T., Jordi C., Vallenari A., Bragaglia A., Balaguer-Núñez L., Soubiran C., Bossini D., Moitinho A., Castro-Ginard A., Krone-Martins A., Casamiquela L., Sordo R., Carrera R. 2018, A Gaia DR2 view of the open cluster population in the Milky Way, A&A, 618, A93, doi: 10.1051/0004-6361/201833476

Cantat-Gaudin T., Anders F., Castro-Ginard A., Jordi C., Romero-Gómez M., Soubiran C., Casamiquela L., Tarricq Y., Moitinho A., Vallenari A., Bragaglia A., Krone-Martins A., Kounkel M. 2020, Painting a portrait of the Galactic disc with its stellar clusters, A&A, 640, A1, doi: 10.1051/0004-6361/202038192

Chabrier G. 2003, Galactic Stellar and Substellar Initial Mass Function, PASP, 115, 763, doi: 10.1086/376392

Chabrier G., Brassard P., Fontaine G., Saumon D. 2000, Cooling Sequences and Color-Magnitude Diagrams for Cool White Dwarfs with Hydrogen Atmospheres, ApJ, 543, 216, doi: 10.1086/317092

Chambers J. M., Cleveland W. S., Kleiner B., Tukey P. A. 1983, Graphical Methods for Data Analysis (Wadsworth)

Chambers K. C., et al. 2017, VizieR Online Data Catalog: The Pan-STARRS release 1 (PS1) Survey - DR1 (Chambers+, 2016), VizieR Online Data Catalog, II/349

Chambers K. C., Magnier E. A., Metcalfe N., Flewelling H. A., Huber M. E., Waters C. Z., Denneau L., Draper P. W., Farrow D., Finkbeiner D. P., Holmberg C., Koppenhoefer J.,

Price P. A., Rest A., Saglia R. P., Schlafly E. F., Smartt S. J., Sweeney W., Wainscoat R. J., Burgett W. S., Chastel S., Grav T., Heasley J. N., Hodapp K. W., Jedicke R., Kaiser N., Kudritzki R. P., Luppino G. A., Lupton R. H., Monet D. G., Morgan J. S., Onaka P. M., Shiao B., Stubbs C. W., Tonry J. L., White R., Bañados E., Bell E. F., Bender R., Bernard E. J., Boegner M., Boffi F., Botticella M. T., Calamida A., Casertano S., Chen W. P., Chen X., Cole S., Deacon N., Frenk C., Fitzsimmons A., Gezari S., Gibbs V., Goessl C., Goggia T., Gourgue R., Goldman B., Grant P., Grebel E. K., Hambly N. C., Hasinger G., Heavens A. F., Heckman T. M., Henderson R., Henning T., Holman M., Hopp U., Ip W. H., Isani S., Jackson M., Keyes C. D., Koekemoer A. M., Kotak R., Le D., Liska D., Long K. S., Lucey J. R., Liu M., Martin N. F., Masci G., McLean B., Mindel E., Misra P., Morganson E., Murphy D. N. A., Obaika A., Narayan G., Nieto-Santisteban M. A., Norberg P., Peacock J. A., Pier E. A., Postman M., Primak N., Rae C., Rai A., Riess A., Riffeser A., Rix H. W., Röser S., Russel R., Rutz L., Schilbach E., Schultz A. S. B., Scolnic D., Strolger L., Szalay A., Seitz S., Small E., Smith K. W., Soderblom D. R., Taylor P., Thomson R., Taylor A. N., Thakar A. R., Thiel J., Thilker D., Unger D., Urata Y., Valenti J., Wagner J., Walder T., Walter F., Watters S. P., Werner S., Wood-Vasey W. M., Wyse R. 2016, The Pan-STARRS1 Surveys, arXiv e-prints, arXiv:1612.05560. https://arxiv.org/abs/1612.05560

Chen B., Stoughton C., Smith J. A., Uomoto A., Pier J. R., Yanny B., Ivezić Ž., York D. G., Anderson J. E., Annis J., Brinkmann J., Csabai I., Fukugita M., Hindsley R., Lupton R., Munn J. A., SDSS Collaboration. 2001, Stellar Population Studies with the SDSS. I. The Vertical Distribution of Stars in the Milky Way, ApJ, 553, 184, doi: 10.1086/320647

Chini R., Hoffmeister V. H., Nasseri A., Stahl O., Zinnecker H. 2012, A spectroscopic

survey on the multiplicity of high-mass stars, MNRAS, 424, 1925, doi: 10.1111/j.1365-2966.2012.21317.x

Chiu K., Fan X., Leggett S. K., Golimowski D. A., Zheng W., Geballe T. R., Schneider D. P., Brinkmann J. 2006, Seventy-One New L and T Dwarfs from the Sloan Digital Sky Survey, AJ, 131, 2722, doi: 10.1086/501431

Cifuentes C., Caballero J. A., Cortés-Contreras M., Montes D., Abellán F. J., Dorda R., Holgado G., Zapatero Osorio M. R., Morales J. C., Amado P. J., Passegger V. M., Quirrenbach A., Reiners A., Ribas I., Sanz-Forcada J., Schweitzer A., Seifert W., Solano E. 2020, CARMENES input catalogue of M dwarfs. V. Luminosities, colours, and spectral energy distributions, A&A, 642, A115, doi: 10.1051/0004-6361/202038295

Claret A. 2000, A new non-linear limb-darkening law for LTE stellar atmosphere models. Calculations for -5.0 <= log[M/H] <= +1, 2000 K <= T_{eff} <= 50000 K at several surface gravities, A&A, 363, 1081

Clark B. M., Blake C. H., Knapp G. R. 2012, The Close Binary Fraction of Dwarf M Stars, ApJ, 744, 119, doi: 10.1088/0004-637X/744/2/119

Close L. M., Zuckerman B., Song I., Barman T., Marois C., Rice E. L., Siegler N., Macintosh B., Becklin E. E., Campbell R., Lyke J. E., Conrad A., Le Mignant D. 2007, The Wide Brown Dwarf Binary Oph 1622-2405 and Discovery of a Wide, Low-Mass Binary in Ophiuchus (Oph 1623-2402): A New Class of Young Evaporating Wide Binaries?, ApJ, 660, 1492, doi: 10.1086/513417

Collins George W. I., Truax R. J. 1995, Classical Rotational Broadening of Spectral Lines, ApJ, 439, 860, doi: 10.1086/175225

Cook B. A., Williams P. K. G., Berger E. 2014, Trends in Ultracool Dwarf Magnetism.

II. The Inverse Correlation Between X-Ray Activity and Rotation as Evidence for a Bimodal Dynamo, ApJ, 785, 10, doi: 10.1088/0004-637X/785/1/10

Cook N. J., Pinfield D. J., Marocco F., Burningham B., Jones H. R. A., Frith J., Zhong J., Luo A. L., Qi Z. X., Lucas P. W., Gromadzki M., Day-Jones A. C., Kurtev R. G., Guo Y. X., Wang Y. F., Bai Y., Yi Z. P., Smart R. L. 2016, A method for selecting M dwarfs with an increased likelihood of unresolved ultracool companionship, MNRAS, 457, 2192, doi: 10.1093/mnras/stw061

Costa E., Méndez R. A., Jao W.-C., Henry T. J., Subasavage J. P., Brown M. A., Ianna P. A., Bartlett J. 2005, The Solar Neighborhood. XIV. Parallaxes from the Cerro Tololo Inter-American Observatory Parallax Investigation-First Results from the 1.5 m Telescope Program, AJ, 130, 337, doi: 10.1086/430473

Cottaar M., Covey K. R., Foster J. B., Meyer M. R., Tan J. C., Nidever D. L., Chojnowski S. D., da Rio N., Flaherty K. M., Frinchaboy P. M., Majewski S., Skrutskie M. F., Wilson J. C., Zasowski G. 2015, IN-SYNC. III. The Dynamical State of IC 348 - A Super-virial Velocity Dispersion and a Puzzling Sign of Convergence, ApJ, 807, 27, doi: 10.1088/0004-637X/807/1/27

Crifo F., Phan-Bao N., Delfosse X., Forveille T., Guibert J., Martín E. L., Reylé C. 2005, New neighbours. VI. Spectroscopy of DENIS nearby stars candidates, A&A, 441, 653, doi: 10.1051/0004-6361:20052998

Crossfield I. J. M. 2014, Doppler imaging of exoplanets and brown dwarfs, A&A, 566, A130, doi: 10.1051/0004-6361/201423750

Crossfield I. J. M., Biller B., Schlieder J. E., Deacon N. R., Bonnefoy M., Homeier D., Allard F., Buenzli E., Henning T., Brandner W., Goldman B., Kopytova T. 2014, A

global cloud map of the nearest known brown dwarf, Nature, 505, 654, doi: 10.1038/nature12955

Crossfield I. J. M., Lothringer J. D., Flores B., Mills E. A. C., Freedman R., Valverde J., Miles B., Guo X., Skemer A. 2019, Unusual Isotopic Abundances in a Fully Convective Stellar Binary, ApJ, 871, L3, doi: 10.3847/2041-8213/aaf9b6

Cruz K. L., Kirkpatrick J. D., Burgasser A. J. 2009, Young L Dwarfs Identified in the Field: A Preliminary Low-Gravity, Optical Spectral Sequence from L0 to L5, AJ, 137, 3345, doi: 10.1088/0004-6256/137/2/3345

Cruz K. L., Reid I. N., Liebert J., Kirkpatrick J. D., Lowrance P. J. 2003, Meeting the Cool Neighbors. V. A 2MASS-Selected Sample of Ultracool Dwarfs, AJ, 126, 2421, doi: 10.1086/378607

Cruz K. L., Reid I. N., Kirkpatrick J. D., Burgasser A. J., Liebert J., Solomon A. R., Schmidt S. J., Allen P. R., Hawley S. L., Covey K. R. 2007, Meeting the Cool Neighbors. IX. The Luminosity Function of M7-L8 Ultracool Dwarfs in the Field, AJ, 133, 439, doi: 10.1086/510132

Curiel S., Ortiz-León G. N., Mioduszewski A. J., Torres R. M. 2020, An Astrometric Planetary Companion Candidate to the M9 Dwarf TVLM 513-46546, AJ, 160, 97, doi: 10.3847/1538-3881/ab9e6e

Cushing M. C., Rayner J. T., Davis S. P., Vacca W. D. 2003, FeH Absorption in the Near-Infrared Spectra of Late M and L Dwarfs, ApJ, 582, 1066, doi: 10.1086/344525

Cushing M. C., Kirkpatrick J. D., Gelino C. R., Griffith R. L., Skrutskie M. F., Mainzer A., Marsh K. A., Beichman C. A., Burgasser A. J., Prato L. A., Simcoe R. A., Marley M. S., Saumon D., Freedman R. S., Eisenhardt P. R., Wright E. L. 2011, The Discovery

of Y Dwarfs using Data from the Wide-field Infrared Survey Explorer (WISE), ApJ, 743, 50, doi: 10.1088/0004-637X/743/1/50

Cutri R. M., et al. 2012, VizieR Online Data Catalog: WISE All-Sky Data Release (Cutri+ 2012), VizieR Online Data Catalog, II/311

Cutri R. M., Wright E. L., Conrow T., Fowler J. W., Eisenhardt P. R. M., Grillmair C., Kirkpatrick J. D., Masci F., McCallon H. L., Wheelock S. L., Fajardo-Acosta S., Yan L., Benford D., Harbut M., Jarrett T., Lake S., Leisawitz D., Ressler M. E., Stanford S. A., Tsai C. W., Liu F., Helou G., Mainzer A., Gettngs D., Gonzalez A., Hoffman D., Marsh K. A., Padgett D., Skrutskie M. F., Beck R., Papin M., Wittman M. 2021, VizieR Online Data Catalog: AllWISE Data Release (Cutri+ 2013), VizieR Online Data Catalog, II/328

Dahm S. E., Slesnick C. L., White R. J. 2012, A Correlation between Circumstellar Disks and Rotation in the Upper Scorpius OB Association, ApJ, 745, 56, doi: 10.1088/0004-637X/745/1/56

Dahn C. C., Harris H. C., Subasavage J. P., Ables H. D., Canzian B. J., Guetter H. H., Harris F. H., Henden A. H., Leggett S. K., Levine S. E., Luginbuhl C. B., Monet A. B., Monet D. G., Munn J. A., Pier J. R., Stone R. C., Vrba F. J., Walker R. L., Tilleman T. M. 2017, CCD Parallaxes for 309 Late-type Dwarfs and Subdwarfs, AJ, 154, 147, doi: 10.3847/1538-3881/aa880b

Davison C. L., White R. J., Henry T. J., Riedel A. R., Jao W.-C., Bailey III J. I., Quinn S. N., Cantrell J. R., Subasavage J. P., Winters J. G. 2015, A 3D Search for Companions to 12 Nearby M Dwarfs, AJ, 149, 106, doi: 10.1088/0004-6256/149/3/106

Deacon N. R., Liu M. C., Magnier E. A., Bowler B. P., Goldman B., Redstone J. A., Burgett W. S., Chambers K. C., Flewelling H., Kaiser N., Lupton R. H., Morgan

J. S., Price P. A., Sweeney W. E., Tonry J. L., Wainscoat R. J., Waters C. 2011, Four New T Dwarfs Identified in Pan-STARRS 1 Commissioning Data, AJ, 142, 77, doi: 10.1088/0004-6256/142/3/77

Deacon N. R., Magnier E. A., Liu M. C., Schlieder J. E., Aller K. M., Best W. M. J., Bowler B. P., Burgett W. S., Chambers K. C., Draper P. W., Flewelling H., Hodapp K. W., Kaiser N., Metcalfe N., Sweeney W. E., Wainscoat R. J., Waters C. 2017, 2MASS 0213+3648 C: A wide T3 benchmark companion to an an active, old M dwarf binary, MNRAS, 467, 1126, doi: 10.1093/mnras/stx065

Del Burgo C., Martín E. L., Zapatero Osorio M. R., Hauschildt P. H. 2009, Physical parameters of T dwarfs derived from high-resolution near-infrared spectra, A&A, 501, 1059, doi: 10.1051/0004-6361/200810752

Deshpande R., Martín E. L., Montgomery M. M., Zapatero Osorio M. R., Rodler F., del Burgo C., Phan Bao N., Lyubchik Y., Tata R., Bouy H., Pavlenko Y. 2012, Intermediate Resolution Near-infrared Spectroscopy of 36 Late M Dwarfs, AJ, 144, 99, doi: 10.1088/0004-6256/144/4/99

Deshpande R., Blake C. H., Bender C. F., Mahadevan S., Terrien R. C., Carlberg J. K., Zasowski G., Crepp J., Rajpurohit A. S., Reylé C., Nidever D. L., Schneider D. P., Allende Prieto C., Bizyaev D., Ebelke G., Fleming S. W., Frinchaboy P. M., Ge J., Hearty F., Hernández J., Malanushenko E., Malanushenko V., Majewski S. R., Marchwinski R., Muna D., Oravetz D., Pan K., Schiavon R. P., Shetrone M., Simmons A., Stassun K. G., Wilson J. C., Wisniewski J. P. 2013, The SDSS-III APOGEE Radial Velocity Survey of M Dwarfs. I. Description of the Survey and Science Goals, AJ, 146, 156, doi: 10.1088/0004-6256/146/6/156

Dhital S., West A. A., Stassun K. G., Bochanski J. J. 2010, Sloan Low-mass Wide Pairs

of Kinematically Equivalent Stars (SLoWPoKES): A Catalog of Very Wide, Low-mass Pairs, AJ, 139, 2566, doi: 10.1088/0004-6256/139/6/2566

Dieterich S. B., Henry T. J., Jao W.-C., Winters J. G., Hosey A. D., Riedel A. R., Subasavage J. P. 2014, The Solar Neighborhood. XXXII. The Hydrogen Burning Limit, AJ, 147, 94, doi: 10.1088/0004-6256/147/5/94

Dittmann J. A., Irwin J. M., Charbonneau D., Berta-Thompson Z. K. 2014, Trigonometric Parallaxes for 1507 Nearby Mid-to-late M Dwarfs, ApJ, 784, 156, doi: 10.1088/0004-637X/784/2/156

Donati J.-F., Forveille T., Collier Cameron A., Barnes J. R., Delfosse X., Jardine M. M., Valenti J. A. 2006, The Large-Scale Axisymmetric Magnetic Topology of a Very-Low-Mass Fully Convective Star, Science, 311, 633, doi: 10.1126/science.1121102

Douglas S. T., Curtis J. L., Agüeros M. A., Cargile P. A., Brewer J. M., Meibom S., Jansen T. 2019, K2 Rotation Periods for Low-mass Hyads and a Quantitative Comparison of the Distribution of Slow Rotators in the Hyades and Praesepe, ApJ, 879, 100, doi: 10.3847/1538-4357/ab2468

Douglas S. T., Agüeros M. A., Covey K. R., Bowsher E. C., Bochanski J. J., Cargile P. A., Kraus A., Law N. M., Lemonias J. J., Arce H. G., Fierroz D. F., Kundert A. 2014, The Factory and the Beehive. II. Activity and Rotation in Praesepe and the Hyades, ApJ, 795, 161, doi: 10.1088/0004-637X/795/2/161

Duchêne G., Kraus A. 2013, Stellar Multiplicity, ARA&A, 51, 269, doi: 10.1146/annurev-astro-081710-102602

Dupuy T. J., Liu M. C. 2012, The Hawaii Infrared Parallax Program. I. Ultracool Binaries and the L/T Transition, ApJS, 201, 19, doi: 10.1088/0067-0049/201/2/19

Dupuy T. J., Liu M. C. 2017, Individual Dynamical Masses of Ultracool Dwarfs, ApJS, 231, 15, doi: 10.3847/1538-4365/aa5e4c

Dupuy T. J., Liu M. C., Best W. M. J., Mann A. W., Tucker M. A., Zhang Z., Baraffe I., Chabrier G., Forveille T., Metchev S. A., Tremblin P., Do A., Payne A. V., Shappee B. J., Bond C. Z., Cetre S., Chun M., Delorme J.-R., Jovanovic N., Lilley S., Mawet D., Ragland S., Wetherell E., Wizinowich P. 2019, WISE J072003.20-084651.2B is a Massive T Dwarf, AJ, 158, 174, doi: 10.3847/1538-3881/ab3cd1

Epchtein N., de Batz B., Capoani L., Chevallier L., Copet E., Fouqué P., Lacombe P., Le Bertre T., Pau S., Rouan D., Ruphy S., Simon G., Tiphène D., Burton W. B., Bertin E., Deul E., Habing H., Borsenberger J., Dennefeld M., Guglielmo F., Loup C., Mamon G., Ng Y., Omont A., Provost L., Renault J. C., Tanguy F., Kimeswenger S., Kienel C., Garzon F., Persi P., Ferrari-Toniolo M., Robin A., Paturel G., Vauglin I., Forveille T., Delfosse X., Hron J., Schultheis M., Appenzeller I., Wagner S., Balazs L., Holl A., Lépine J., Boscolo P., Picazzio E., Duc P. A., Mennessier M. O. 1997, The deep near-infrared southern sky survey (DENIS)., The Messenger, 87, 27

Escala I., Wetzel A., Kirby E. N., Hopkins P. F., Ma X., Wheeler C., Kereš D., Faucher-Giguère C.-A., Quataert E. 2018, Modelling chemical abundance distributions for dwarf galaxies in the Local Group: the impact of turbulent metal diffusion, MNRAS, 474, 2194, doi: 10.1093/mnras/stx2858

Esplin T. L., Luhman K. L. 2017, A Survey For Planetary-mass Brown Dwarfs in the Taurus and Perseus Star-forming Regions, AJ, 154, 134, doi: 10.3847/1538-3881/aa859b

Esplin T. L., Luhman K. L., Mamajek E. E. 2014, A WISE Survey of Circumstellar Disks in Taurus, ApJ, 784, 126, doi: 10.1088/0004-637X/784/2/126

Faherty J. K., Burgasser A. J., Bochanski J. J., Looper D. L., West A. A., van der Bliek N. S. 2011, Identification of a Wide, Low-Mass Multiple System Containing the Brown Dwarf 2MASS J0850359+105716, AJ, 141, 71, doi: 10.1088/0004-6256/141/3/71

Faherty J. K., Burgasser A. J., Cruz K. L., Shara M. M., Walter F. M., Gelino C. R. 2009, The Brown Dwarf Kinematics Project I. Proper Motions and Tangential Velocities for a Large Sample of Late-Type M, L, and T Dwarfs, AJ, 137, 1, doi: 10.1088/0004-6256/137/1/1

Faherty J. K., Gagné J., Burgasser A. J., Mamajek E. E., Gonzales E. C., Bardalez Gagliuffi D. C., Marocco F. 2018, A Late-type L Dwarf at 11 pc Hiding in the Galactic Plane Characterized Using Gaia DR2, ApJ, 868, 44, doi: 10.3847/1538-4357/aadd04

Faherty J. K., Burgasser A. J., Walter F. M., Van der Bliek N., Shara M. M., Cruz K. L., West A. A., Vrba F. J., Anglada-Escudé G. 2012, The Brown Dwarf Kinematics Project (BDKP). III. Parallaxes for 70 Ultracool Dwarfs, ApJ, 752, 56, doi: 10.1088/0004-637X/752/1/56

Faherty J. K., Riedel A. R., Cruz K. L., Gagne J., Filippazzo J. C., Lambrides E., Fica H., Weinberger A., Thorstensen J. R., Tinney C. G., Baldassare V., Lemonier E., Rice E. L. 2016, Population Properties of Brown Dwarf Analogs to Exoplanets, ApJS, 225, 10, doi: 10.3847/0067-0049/225/1/10

Fan X., Knapp G. R., Strauss M. A., Gunn J. E., Lupton R. H., Ivezić Ž., Rockosi C. M., Yanny B., Kent S., Schneider D. P., Kirkpatrick J. D., Annis J., Bastian S., Berman E., Brinkmann J., Csabai I., Federwitz G. R., Fukugita M., Gurbani V. K., Hennessy G. S., Hindsley R. B., Ichikawa T., Lamb D. Q., Lindenmeyer C., Mantsch P. M., McKay T. A., Munn J. A., Nash T., Okamura S., Pauls A. G., Pier J. R., Rechenmacher R., Rivetta C. H., Sergey G., Stoughton C., Szalay A. S., Szokoly G. P., Tucker D. L.,

York D. G., SDSS Collaboration. 2000, L Dwarfs Found in Sloan Digital Sky Survey Commissioning Imaging Data, AJ, 119, 928, doi: 10.1086/301224

Filippazzo J. C., Rice E. L., Faherty J., Cruz K. L., Van Gordon M. M., Looper D. L. 2015, Fundamental Parameters and Spectral Energy Distributions of Young and Field Age Objects with Masses Spanning the Stellar to Planetary Regime, ApJ, 810, 158, doi: 10.1088/0004-637X/810/2/158

Filliben J. J. 1975, The Probability Plot Correlation Coefficient Test for Normality, Technometrics, 17, 111, doi: 10.1080/00401706.1975.10489279

Foreman-Mackey D., Hogg D. W., Lang D., Goodman J. 2013, emcee: The MCMC Hammer, PASP, 125, 306, doi: 10.1086/670067

Freund S., Robrade J., Schneider P. C., Schmitt J. H. M. M. 2020, Updated X-ray view of the Hyades cluster, A&A, 640, A66, doi: 10.1051/0004-6361/201937304

Fulton B. J., Petigura E. A., Blunt S., Sinukoff E. 2018, RadVel: The Radial Velocity Modeling Toolkit, PASP, 130, 044504, doi: 10.1088/1538-3873/aaaaa8

Gagné J., Allers K. N., Theissen C. A., Faherty J. K., Bardalez Gagliuffi D., Artigau É. 2018a, 2MASS J13243553+6358281 Is an Early T-type Planetary-mass Object in the AB Doradus Moving Group, ApJ, 854, L27, doi: 10.3847/2041-8213/aaacfd

Gagné J., Fontaine G., Simon A., Faherty J. K. 2018b, A Young Ultramassive White Dwarf in the AB Doradus Moving Group, ApJ, 861, L13, doi: 10.3847/2041-8213/aacdff

Gagné J., Lafrenière D., Doyon R., Malo L., Artigau É. 2015a, BANYAN. V. A Systematic All-sky Survey for New Very Late-type Low-mass Stars and Brown Dwarfs in Nearby Young Moving Groups, ApJ, 798, 73, doi: 10.1088/0004-637X/798/2/73

Gagné J., Faherty J. K., Cruz K. L., Lafreniére D., Doyon R., Malo L., Burgasser A. J., Naud M.-E., Artigau É., Bouchard S., Gizis J. E., Albert L. 2015b, BANYAN. VII. A New Population of Young Substellar Candidate Members of Nearby Moving Groups from the BASS Survey, ApJS, 219, 33, doi: 10.1088/0067-0049/219/2/33

Gagné J., Faherty J. K., Burgasser A. J., Artigau É., Bouchard S., Albert L., Lafrenière D., Doyon R., Bardalez Gagliuffi D. C. 2017, SIMP J013656.5+093347 Is Likely a Planetary-mass Object in the Carina-Near Moving Group, ApJ, 841, L1, doi: 10.3847/2041-8213/aa70e2

Gagné J., Mamajek E. E., Malo L., Riedel A., Rodriguez D., Lafrenière D., Faherty J. K., Roy-Loubier O., Pueyo L., Robin A. C., Doyon R. 2018c, BANYAN. XI. The BANYAN Σ Multivariate Bayesian Algorithm to Identify Members of Young Associations with 150 pc, ApJ, 856, 23, doi: 10.3847/1538-4357/aaae09

Gaia Collaboration, Babusiaux C., van Leeuwen F., Barstow M. A., Jordi C., Vallenari A., Bossini D., Bressan A., Cantat-Gaudin T., van Leeuwen M., et al. 2018a, Gaia Data Release 2. Observational Hertzsprung-Russell diagrams, A&A, 616, A10, doi: 10.1051/0004-6361/201832843

Gaia Collaboration, Brown A. G. A., Vallenari A., Prusti T., de Bruijne J. H. J., Babusiaux C., Bailer-Jones C. A. L., Biermann M., Evans D. W., Eyer L., et al. 2018b, Gaia Data Release 2. Summary of the contents and survey properties, A&A, 616, A1, doi: 10.1051/0004-6361/201833051

Gaia Collaboration, Brown A. G. A., Vallenari A., Prusti T., de Bruijne J. H. J., Babusiaux C., Biermann M., Creevey O. L., Evans D. W., Eyer L., Hutton A., Jansen F., Jordi C., Klioner S. A., Lammers U., Lindegren L., Luri X., Mignard F., Panem C., Pourbaix D., Randich S., Sartoretti P., Soubiran C., Walton N. A., Arenou F., Bailer-Jones C. A. L.,

Bastian U., Cropper M., Drimmel R., Katz D., Lattanzi M. G., van Leeuwen F., Bakker J., Cacciari C., Castañeda J., De Angeli F., Ducourant C., Fabricius C., Fouesneau M., Frémat Y., Guerra R., Guerrier A., Guiraud J., Jean-Antoine Piccolo A., Masana E., Messineo R., Mowlavi N., Nicolas C., Nienartowicz K., Pailler F., Panuzzo P., Riclet F., Roux W., Seabroke G. M., Sordo R., Tanga P., Thévenin F., Gracia-Abril G., Portell J., Teyssier D., Altmann M., Andrae R., Bellas-Velidis I., Benson K., Berthier J., Blomme R., Brugaletta E., Burgess P. W., Busso G., Carry B., Cellino A., Cheek N., Clementini G., Damerdji Y., Davidson M., Delchambre L., Dell'Oro A., Fernández-Hernández J., Galluccio L., García-Lario P., Garcia-Reinaldos M., González-Núñez J., Gosset E., Haigron R., Halbwachs J. L., Hambly N. C., Harrison D. L., Hatzidimitriou D., Heiter U., Hernández J., Hestroffer D., Hodgkin S. T., Holl B., Janßen K., Jevardat de Fombelle G., Jordan S., Krone-Martins A., Lanzafame A. C., Löffler W., Lorca A., Manteiga M., Marchal O., Marrese P. M., Moitinho A., Mora A., Muinonen K., Osborne P., Pancino E., Pauwels T., Petit J. M., Recio-Blanco A., Richards P. J., Riello M., Rimoldini L., Robin A. C., Roegiers T., Rybizki J., Sarro L. M., Siopis C., Smith M., Sozzetti A., Ulla A., Utrilla E., van Leeuwen M., van Reeven W., Abbas U., Abreu Aramburu A., Accart S., Aerts C., Aguado J. J., Ajaj M., Altavilla G., Álvarez M. A., Álvarez Cid-Fuentes J., Alves J., Anderson R. I., Anglada Varela E., Antoja T., Audard M., Baines D., Baker S. G., Balaguer-Núñez L., Balbinot E., Balog Z., Barache C., Barbato D., Barros M., Barstow M. A., Bartolomé S., Bassilana J. L., Bauchet N., Baudesson-Stella A., Becciani U., Bellazzini M., Bernet M., Bertone S., Bianchi L., Blanco-Cuaresma S., Boch T., Bombrun A., Bossini D., Bouquillon S., Bragaglia A., Bramante L., Breedt E., Bressan A., Brouillet N., Bucciarelli B., Burlacu A., Busonero D., Butkevich A. G., Buzzi R., Caffau E., Cancelliere R., Cánovas H., Cantat-Gaudin T., Carballo R., Carlucci T., Carnerero M. I., Carrasco J. M., Casamiquela L., Castellani M., Castro-Ginard A., Castro Sampol P., Chaoul

L., Charlot P., Chemin L., Chiavassa A., Cioni M. R. L., Comoretto G., Cooper W. J., Cornez T., Cowell S., Crifo F., Crosta M., Crowley C., Dafonte C., Dapergolas A., David M., David P., de Laverny P., De Luise F., De March R., De Ridder J., de Souza R., de Teodoro P., de Torres A., del Peloso E. F., del Pozo E., Delbo M., Delgado A., Delgado H. E., Delisle J. B., Di Matteo P., Diakite S., Diener C., Distefano E., Dolding C., Eappachen D., Edvardsson B., Enke H., Esquej P., Fabre C., Fabrizio M., Faigler S., Fedorets G., Fernique P., Fienga A., Figueras F., Fouron C., Fragkoudi F., Fraile E., Franke F., Gai M., Garabato D., Garcia-Gutierrez A., García-Torres M., Garofalo A., Gavras P., Gerlach E., Geyer R., Giacobbe P., Gilmore G., Girona S., Giuffrida G., Gomel R., Gomez A., Gonzalez-Santamaria I., González-Vidal J. J., Granvik M., Gutiérrez-Sánchez R., Guy L. P., Hauser M., Haywood M., Helmi A., Hidalgo S. L., Hilger T., Hładczuk N., Hobbs D., Holland G., Huckle H. E., Jasniewicz G., Jonker P. G., Juaristi Campillo J., Julbe F., Karbevska L., Kervella P., Khanna S., Kochoska A., Kontizas M., Kordopatis G., Korn A. J., Kostrzewa-Rutkowska Z., Kruszyńska K., Lambert S., Lanza A. F., Lasne Y., Le Campion J. F., Le Fustec Y., Lebreton Y., Lebzelter T., Leccia S., Leclerc N., Lecoeur-Taibi I., Liao S., Licata E., Lindstrøm E. P., Lister T. A., Livanou E., Lobel A., Madrero Pardo P., Managau S., Mann R. G., Marchant J. M., Marconi M., Marcos Santos M. M. S., Marinoni S., Marocco F., Marshall D. J., Martin Polo L., Martín-Fleitas J. M., Masip A., Massari D., Mastrobuono-Battisti A., Mazeh T., McMillan P. J., Messina S., Michalik D., Millar N. R., Mints A., Molina D., Molinaro R., Molnár L., Montegriffo P., Mor R., Morbidelli R., Morel T., Morris D., Mulone A. F., Munoz D., Muraveva T., Murphy C. P., Musella I., Noval L., Ordénovic C., Orrù G., Osinde J., Pagani C., Pagano I., Palaversa L., Palicio P. A., Panahi A., Pawlak M., Peñalosa Esteller X., Penttilä A., Piersimoni A. M., Pineau F. X., Plachy E., Plum G., Poggio E., Poretti E., Poujoulet E., Prša A., Pulone L., Racero E., Ragaini S., Rainer M., Raiteri C. M., Rambaux N.,

Ramos P., Ramos-Lerate M., Re Fiorentin P., Regibo S., Reylé C., Ripepi V., Riva A., Rixon G., Robichon N., Robin C., Roelens M., Rohrbasser L., Romero-Gómez M., Rowell N., Royer F., Rybicki K. A., Sadowski G., Sagristà Sellés A., Sahlmann J., Salgado J., Salguero E., Samaras N., Sanchez Gimenez V., Sanna N., Santoveña R., Sarasso M., Schultheis M., Sciacca E., Segol M., Segovia J. C., Ségransan D., Semeux D., Shahaf S., Siddiqui H. I., Siebert A., Siltala L., Slezak E., Smart R. L., Solano E., Solitro F., Souami D., Souchay J., Spagna A., Spoto F., Steele I. A., Steidelmüller H., Stephenson C. A., Süveges M., Szabados L., Szegedi-Elek E., Taris F., Tauran G., Taylor M. B., Teixeira R., Thuillot W., Tonello N., Torra F., Torra J., Turon C., Unger N., Vaillant M., van Dillen E., Vanel O., Vecchiato A., Viala Y., Vicente D., Voutsinas S., Weiler M., Wevers T., Wyrzykowski Ł., Yoldas A., Yvard P., Zhao H., Zorec J., Zucker S., Zurbach C., Zwitter T. 2021, Gaia Early Data Release 3. Summary of the contents and survey properties, A&A, 649, A1, doi: 10.1051/0004-6361/202039657

García Pérez A. E., Allende Prieto C., Holtzman J. A., Shetrone M., Mészáros S., Bizyaev D., Carrera R., Cunha K., García-Hernández D. A., Johnson J. A., Majewski S. R., Nidever D. L., Schiavon R. P., Shane N., Smith V. V., Sobeck J., Troup N., Zamora O., Weinberg D. H., Bovy J., Eisenstein D. J., Feuillet D., Frinchaboy P. M., Hayden M. R., Hearty F. R., Nguyen D. C., O'Connell R. W., Pinsonneault M. H., Wilson J. C., Zasowski G. 2016, ASPCAP: The APOGEE Stellar Parameter and Chemical Abundances Pipeline, AJ, 151, 144, doi: 10.3847/0004-6256/151/6/144

Geballe T. R., Knapp G. R., Leggett S. K., Fan X., Golimowski D. A., Anderson S., Brinkmann J., Csabai I., Gunn J. E., Hawley S. L., Hennessy G., Henry T. J., Hill G. J., Hindsley R. B., Ivezić Ž., Lupton R. H., McDaniel A., Munn J. A., Narayanan V. K., Peng E., Pier J. R., Rockosi C. M., Schneider D. P., Smith J. A., Strauss M. A., Tsvetanov Z. I., Uomoto A., York D. G., Zheng W. 2002, Toward Spectral

Classification of L and T Dwarfs: Infrared and Optical Spectroscopy and Analysis, ApJ, 564, 466, doi: 10.1086/324078

Gelman A., Rubin D. B. 1992, Inference from Iterative Simulation Using Multiple Sequences, Statistical Science, 7, 457, doi: 10.1214/ss/1177011136

Gerasimov R., Burgasser A. J., Homeier D., Bedin L. R., Rees J. M., Scalco M., Anderson J., Salaris M. 2022, The HST Large Program on ω Centauri. V. Exploring the Ultracool Dwarf Population with Stellar Atmosphere and Evolutionary Modeling, ApJ, 930, 24, doi: 10.3847/1538-4357/ac61e5

Gilhool S. H., Blake C. H., Terrien R. C., Bender C., Mahadevan S., Deshpande R. 2018, The Rotation of M Dwarfs Observed by the Apache Point Galactic Evolution Experiment, AJ, 155, 38, doi: 10.3847/1538-3881/aa9c7c

Gillon M., Triaud A. H. M. J., Demory B.-O., Jehin E., Agol E., Deck K. M., Lederer S. M., de Wit J., Burdanov A., Ingalls J. G., Bolmont E., Leconte J., Raymond S. N., Selsis F., Turbet M., Barkaoui K., Burgasser A., Burleigh M. R., Carey S. J., Chaushev A., Copperwheat C. M., Delrez L., Fernandes C. S., Holdsworth D. L., Kotze E. J., Van Grootel V., Almleaky Y., Benkhaldoun Z., Magain P., Queloz D. 2017, Seven temperate terrestrial planets around the nearby ultracool dwarf star TRAPPIST-1, Nature, 542, 456, doi: 10.1038/nature21360

Gizis J. E. 2002, Brown Dwarfs and the TW Hydrae Association, ApJ, 575, 484, doi: 10.1086/341259

Gizis J. E., Monet D. G., Reid I. N., Kirkpatrick J. D., Liebert J., Williams R. J. 2000, New Neighbors from 2MASS: Activity and Kinematics at the Bottom of the Main Sequence, AJ, 120, 1085, doi: 10.1086/301456

Gizis J. E., Troup N. W., Burgasser A. J. 2011, A Very High Proper Motion Star and the First L Dwarf in the Kepler Field, ApJ, 736, L34, doi: 10.1088/2041-8205/736/2/L34

Golimowski D. A., Leggett S. K., Marley M. S., Fan X., Geballe T. R., Knapp G. R., Vrba F. J., Henden A. A., Luginbuhl C. B., Guetter H. H., Munn J. A., Canzian B., Zheng W., Tsvetanov Z. I., Chiu K., Glazebrook K., Hoversten E. A., Schneider D. P., Brinkmann J. 2004, L' and M' Photometry of Ultracool Dwarfs, AJ, 127, 3516, doi: 10.1086/420709

Goodman J., Weare J. 2010, Ensemble samplers with affine invariance, Communications in Applied Mathematics and Computational Science, Vol. 5, No. 1, p. 65-80, 2010, 5, 65, doi: 10.2140/camcos.2010.5.65

Goto M., Kobayashi N., Terada H., Gaessler W., Kanzawa T., Takami H., Takato N., Hayano Y., Kamata Y., Iye M., Saint-Jacques D. J., Tokunaga A. T., Potter D., Cushing M. 2002, Near-Infrared Adaptive Optics Spectroscopy of Binary Brown Dwarfs HD 130948B and HD 130948C, ApJ, 567, L59, doi: 10.1086/339800

Gray D. F. 1992, the Observation and Analysis of Stellar Photospheres, Journal of the British Astronomical Association, 102, 230

Gunn J. E., Siegmund W. A., Mannery E. J., Owen R. E., Hull C. L., Leger R. F., Carey L. N., Knapp G. R., York D. G., Boroski W. N., Kent S. M., Lupton R. H., Rockosi C. M., Evans M. L., Waddell P., Anderson J. E., Annis J., Barentine J. C., Bartoszek L. M., Bastian S., Bracker S. B., Brewington H. J., Briegel C. I., Brinkmann J., Brown Y. J., Carr M. A., Czarapata P. C., Drennan C. C., Dombeck T., Federwitz G. R., Gillespie B. A., Gonzales C., Hansen S. U., Harvanek M., Hayes J., Jordan W., Kinney E., Klaene M., Kleinman S. J., Kron R. G., Kresinski J., Lee G., Limmongkol S., Lindenmeyer C. W., Long D. C., Loomis C. L., McGehee P. M., Mantsch P. M.,

Neilsen Eric H. J., Neswold R. M., Newman P. R., Nitta A., Peoples John J., Pier J. R., Prieto P. S., Prosapio A., Rivetta C., Schneider D. P., Snedden S., Wang S.-i. 2006, The 2.5 m Telescope of the Sloan Digital Sky Survey, AJ, 131, 2332, doi: 10.1086/500975

Gwyn S. D. J. 2012, The Canada-France-Hawaii Telescope Legacy Survey: Stacked Images and Catalogs, AJ, 143, 38, doi: 10.1088/0004-6256/143/2/38

Hallinan G., Antonova A., Doyle J. G., Bourke S., Brisken W. F., Golden A. 2006, Rotational Modulation of the Radio Emission from the M9 Dwarf TVLM 513-46546: Broadband Coherent Emission at the Substellar Boundary?, ApJ, 653, 690, doi: 10.1086/508678

Hamuy M., Suntzeff N. B., Heathcote S. R., Walker A. R., Gigoux P., Phillips M. M. 1994, Southern Spectrophotometric Standards. II, PASP, 106, 566, doi: 10.1086/133417

Hamuy M., Walker A. R., Suntzeff N. B., Gigoux P., Heathcote S. R., Phillips M. M. 1992, Southern Spectrophotometric Standards. I., PASP, 104, 533, doi: 10.1086/133028

Hawley S. L., Covey K. R., Knapp G. R., Golimowski D. A., Fan X., Anderson S. F., Gunn J. E., Harris H. C., Ivezić Ž., Long G. M., Lupton R. H., McGehee P. M., Narayanan V., Peng E., Schlegel D., Schneider D. P., Spahn E. Y., Strauss M. A., Szkody P., Tsvetanov Z., Walkowicz L. M., Brinkmann J., Harvanek M., Hennessy G. S., Kleinman S. J., Krzesinski J., Long D., Neilsen E. H., Newman P. R., Nitta A., Snedden S. A., York D. G. 2002, Characterization of M, L, and T Dwarfs in the Sloan Digital Sky Survey, AJ, 123, 3409, doi: 10.1086/340697

Hayashi C., Nakano T. 1963, Evolution of Stars of Small Masses in the Pre-Main-Sequence Stages, Progress of Theoretical Physics, 30, 460, doi: 10.1143/PTP.30.460

Haywood M., Lehnert M. D., Di Matteo P., Snaith O., Schultheis M., Katz D., Gómez A. 2016, When the Milky Way turned off the lights: APOGEE provides evidence of

star formation quenching in our Galaxy, A&A, 589, A66, doi: 10.1051/0004-6361/201527567

Heinze A. N., Metchev S., Kellogg K. 2015, Weather on Other Worlds. III. A Survey for T Dwarfs with High-amplitude Optical Variability, ApJ, 801, 104, doi: 10.1088/0004-637X/801/2/104

Heinze A. N., Metchev S., Apai D., Flateau D., Kurtev R., Marley M., Radigan J., Burgasser A. J., Artigau É., Plavchan P. 2013, Weather on Other Worlds. I. Detection of Periodic Variability in the L3 Dwarf DENIS-P J1058.7-1548 with Precise Multi-wavelength Photometry, ApJ, 767, 173, doi: 10.1088/0004-637X/767/2/173

Henry T. J., Subasavage J. P., Brown M. A., Beaulieu T. D., Jao W.-C., Hambly N. C. 2004, The Solar Neighborhood. X. New Nearby Stars in the Southern Sky and Accurate Photometric Distance Estimates for Red Dwarfs, AJ, 128, 2460, doi: 10.1086/425052

Henry T. J., Walkowicz L. M., Barto T. C., Golimowski D. A. 2002, The Solar Neighborhood. VI. New Southern Nearby Stars Identified by Optical Spectroscopy, AJ, 123, 2002, doi: 10.1086/339315

Ho A. Y. Q., Rix H.-W., Ness M. K., Hogg D. W., Liu C., Ting Y.-S. 2017, Masses and Ages for 230,000 LAMOST Giants, via Their Carbon and Nitrogen Abundances, ApJ, 841, 40, doi: 10.3847/1538-4357/aa6db3

Holtzman J. A., Shetrone M., Johnson J. A., Allende Prieto C., Anders F., Andrews B., Beers T. C., Bizyaev D., Blanton M. R., Bovy J., Carrera R., Chojnowski S. D., Cunha K., Eisenstein D. J., Feuillet D., Frinchaboy P. M., Galbraith-Frew J., García Pérez A. E., García-Hernández D. A., Hasselquist S., Hayden M. R., Hearty F. R., Ivans I., Majewski S. R., Martell S., Meszaros S., Muna D., Nidever D., Nguyen D. C., O'Connell R. W., Pan K., Pinsonneault M., Robin A. C., Schiavon R. P., Shane N.,

Sobeck J., Smith V. V., Troup N., Weinberg D. H., Wilson J. C., Wood-Vasey W. M., Zamora O., Zasowski G. 2015, Abundances, Stellar Parameters, and Spectra from the SDSS-III/APOGEE Survey, AJ, 150, 148, doi: 10.1088/0004-6256/150/5/148

Holtzman J. A., Hasselquist S., Shetrone M., Cunha K., Allende Prieto C., Anguiano B., Bizyaev D., Bovy J., Casey A., Edvardsson B., Johnson J. A., Jönsson H., Meszaros S., Smith V. V., Sobeck J., Zamora O., Chojnowski S. D., Fernandez-Trincado J., Garcia-Hernandez D. A., Majewski S. R., Pinsonneault M., Souto D., Stringfellow G. S., Tayar J., Troup N., Zasowski G. 2018, APOGEE Data Releases 13 and 14: Data and Analysis, AJ, 156, 125, doi: 10.3847/1538-3881/aad4f9

Howell S. B., Sobeck C., Haas M., Still M., Barclay T., Mullally F., Troeltzsch J., Aigrain S., Bryson S. T., Caldwell D., Chaplin W. J., Cochran W. D., Huber D., Marcy G. W., Miglio A., Najita J. R., Smith M., Twicken J. D., Fortney J. J. 2014, The K2 Mission: Characterization and Early Results, PASP, 126, 398, doi: 10.1086/676406

Hsu C.-C., Theissen C., Burgasser A., Birky J. 2021, SMART: The Spectral Modeling Analysis and RV Tool, v1.0.0, Zenodo, doi: 10.5281/zenodo.4765258

Hsu C.-C., Burgasser A. J., Theissen C. A., Gelino C. R., Birky J. L., Diamant S. J. M., Bardalez Gagliuffi D. C., Aganze C., Blake C. H., Faherty J. K. 2021, The Brown Dwarf Kinematics Project (BDKP). V. Radial and Rotational Velocities of T Dwarfs from Keck/NIRSPEC High-resolution Spectroscopy, ApJS, 257, 45, doi: 10.3847/1538-4365/ac1c7d

Husser T.-O., Wende-von Berg S., Dreizler S., Homeier D., Reiners A., Barman T., Hauschildt P. H. 2013, A new extensive library of PHOENIX stellar atmospheres and synthetic spectra, A&A, 553, A6, doi: 10.1051/0004-6361/201219058

Irwin J., Berta Z. K., Burke C. J., Charbonneau D., Nutzman P., West A. A., Falco

E. E. 2011, On the Angular Momentum Evolution of Fully Convective Stars: Rotation Periods for Field M-dwarfs from the MEarth Transit Survey, ApJ, 727, 56, doi: 10.1088/0004-637X/727/1/56

Ivezić Ž., Smith J. A., Miknaitis G., Lin H., Tucker D., Lupton R. H., Gunn J. E., Knapp G. R., Strauss M. A., Sesar B., Doi M., Tanaka M., Fukugita M., Holtzman J., Kent S., Yanny B., Schlegel D., Finkbeiner D., Padmanabhan N., Rockosi C. M., Jurić M., Bond N., Lee B., Stoughton C., Jester S., Harris H., Harding P., Morrison H., Brinkmann J., Schneider D. P., York D. 2007, Sloan Digital Sky Survey Standard Star Catalog for Stripe 82: The Dawn of Industrial 1% Optical Photometry, AJ, 134, 973, doi: 10.1086/519976

Jackson R. J., Deliyannis C. P., Jeffries R. D. 2018, The inflated radii of M dwarfs in the Pleiades, MNRAS, 476, 3245, doi: 10.1093/mnras/sty374

Jackson R. J., Jeffries R. D. 2010, Are the spin axes of stars randomly aligned within a cluster?, MNRAS, 402, 1380, doi: 10.1111/j.1365-2966.2009.15983.x

Jahreiß H., Scholz R., Meusinger H., Lehmann I. 2001, Spectroscopic distance estimates for fourteen faint red LHS and NLTT stars, A&A, 370, 967, doi: 10.1051/0004-6361:20010248

Jameson R. F., Casewell S. L., Bannister N. P., Lodieu N., Keresztes K., Dobbie P. D., Hodgkin S. T. 2008a, Proper motions of field L and T dwarfs, MNRAS, 384, 1399, doi: 10.1111/j.1365-2966.2007.12637.x

Jameson R. F., Lodieu N., Casewell S. L., Bannister N. P., Dobbie P. D. 2008b, The ages of L dwarfs, MNRAS, 385, 1771, doi: 10.1111/j.1365-2966.2008.12973.x

Ji A. P., Li T. S., Hansen T. T., Casey A. R., Koposov S. E., Pace A. B., Mackey D., Lewis G. F., Simpson J. D., Bland-Hawthorn J., Cullinane L. R., Da Costa G. S., Hattori

K., Martell S. L., Kuehn K., Erkal D., Shipp N., Wan Z., Zucker D. B. 2020, The Southern Stellar Stream Spectroscopic Survey (S^5): Chemical Abundances of Seven Stellar Streams, AJ, 160, 181, doi: 10.3847/1538-3881/abacb6

Johnson D. R. H., Soderblom D. R. 1987, Calculating galactic space velocities and their uncertainties, with an application to the Ursa Major group, AJ, 93, 864, doi: 10.1086/114370

Jönsson H., Holtzman J. A., Allende Prieto C., Cunha K., García-Hernández D. A., Hasselquist S., Masseron T., Osorio Y., Shetrone M., Smith V., Stringfellow G. S., Bizyaev D., Edvardsson B., Majewski S. R., Mészáros S., Souto D., Zamora O., Beaton R. L., Bovy J., Donor J., Pinsonneault M. H., Poovelil V. J., Sobeck J. 2020, APOGEE Data and Spectral Analysis from SDSS Data Release 16: Seven Years of Observations Including First Results from APOGEE-South, AJ, 160, 120, doi: 10.3847/1538-3881/aba592

Jurić M., Ivezić Ž., Brooks A., Lupton R. H., Schlegel D., Finkbeiner D., Padmanabhan N., Bond N., Sesar B., Rockosi C. M., Knapp G. R., Gunn J. E., Sumi T., Schneider D. P., Barentine J. C., Brewington H. J., Brinkmann J., Fukugita M., Harvanek M., Kleinman S. J., Krzesinski J., Long D., Neilsen Eric H. J., Nitta A., Snedden S. A., York D. G. 2008, The Milky Way Tomography with SDSS. I. Stellar Number Density Distribution, ApJ, 673, 864, doi: 10.1086/523619

Kass R. E., Raftery A. E. 1995, Bayes Factors, Journal of the American Statistical Association, 90, 773, doi: 10.1080/01621459.1995.10476572

Kenyon S. J., Hartmann L. 1995, Pre-Main-Sequence Evolution in the Taurus-Auriga Molecular Cloud, ApJS, 101, 117, doi: 10.1086/192235

Kesseli A. Y., Muirhead P. S., Mann A. W., Mace G. 2018, Magnetic Inflation and Stellar

Mass. II. On the Radii of Single, Rapidly Rotating, Fully Convective M-Dwarf Stars, AJ, 155, 225, doi: 10.3847/1538-3881/aabccb

Kesseli A. Y., West A. A., Veyette M., Harrison B., Feldman D., Bochanski J. J. 2017, An Empirical Template Library of Stellar Spectra for a Wide Range of Spectral Classes, Luminosity Classes, and Metallicities Using SDSS BOSS Spectra, ApJS, 230, 16, doi: 10.3847/1538-4365/aa656d

Khata D., Mondal S., Das R., Ghosh S., Ghosh S. 2020, Understanding the physical properties of young M dwarfs: NIR spectroscopic studies, MNRAS, 493, 4533, doi: 10.1093/mnras/staa427

Kiman R., Schmidt S. J., Angus R., Cruz K. L., Faherty J. K., Rice E. 2019, Exploring the Age-dependent Properties of M and L Dwarfs Using Gaia and SDSS, AJ, 157, 231, doi: 10.3847/1538-3881/ab1753

Kipping D. 2018, The Orbital Period Prior for Single Transits, Research Notes of the American Astronomical Society, 2, 223, doi: 10.3847/2515-5172/aaf50c

Kipping D. M. 2013, Parametrizing the exoplanet eccentricity distribution with the beta distribution., MNRAS, 434, L51, doi: 10.1093/mnrasl/slt075

Kirkpatrick J. D. 2005, New Spectral Types L and T, ARA&A, 43, 195, doi: 10.1146/annurev.astro.42.053102.134017

Kirkpatrick J. D., Henry T. J., McCarthy Donald W. J. 1991, A Standard Stellar Spectral Sequence in the Red/Near-Infrared: Classes K5 to M9, ApJS, 77, 417, doi: 10.1086/191611

Kirkpatrick J. D., Henry T. J., Simons D. A. 1995, The solar neighborhood. 2: The first list of dwarfs with spectral types of M7 and cooler, AJ, 109, 797, doi: 10.1086/117323

Kirkpatrick J. D., Reid I. N., Liebert J., Cutri R. M., Nelson B., Beichman C. A., Dahn C. C., Monet D. G., Gizis J. E., Skrutskie M. F. 1999, Dwarfs Cooler than "M": The Definition of Spectral Type "L" Using Discoveries from the 2 Micron All-Sky Survey (2MASS), ApJ, 519, 802, doi: 10.1086/307414

Kirkpatrick J. D., Looper D. L., Burgasser A. J., Schurr S. D., Cutri R. M., Cushing M. C., Cruz K. L., Sweet A. C., Knapp G. R., Barman T. S., Bochanski J. J., Roellig T. L., McLean I. S., McGovern M. R., Rice E. L. 2010, Discoveries from a Near-infrared Proper Motion Survey Using Multi-epoch Two Micron All-Sky Survey Data, ApJS, 190, 100, doi: 10.1088/0067-0049/190/1/100

Kirkpatrick J. D., Cushing M. C., Gelino C. R., Griffith R. L., Skrutskie M. F., Marsh K. A., Wright E. L., Mainzer A., Eisenhardt P. R., McLean I. S., Thompson M. A., Bauer J. M., Benford D. J., Bridge C. R., Lake S. E., Petty S. M., Stanford S. A., Tsai C.-W., Bailey V., Beichman C. A., Bloom J. S., Bochanski J. J., Burgasser A. J., Capak P. L., Cruz K. L., Hinz P. M., Kartaltepe J. S., Knox R. P., Manohar S., Masters D., Morales-Calderón M., Prato L. A., Rodigas T. J., Salvato M., Schurr S. D., Scoville N. Z., Simcoe R. A., Stapelfeldt K. R., Stern D., Stock N. D., Vacca W. D. 2011, The First Hundred Brown Dwarfs Discovered by the Wide-field Infrared Survey Explorer (WISE), ApJS, 197, 19, doi: 10.1088/0067-0049/197/2/19

Kirkpatrick J. D., Kellogg K., Schneider A. C., Fajardo-Acosta S., Cushing M. C., Greco J., Mace G. N., Gelino C. R., Wright E. L., Eisenhardt P. R. M., Stern D., Faherty J. K., Sheppard S. S., Lansbury G. B., Logsdon S. E., Martin E. C., McLean I. S., Schurr S. D., Cutri R. M., Conrow T. 2016, The AllWISE Motion Survey, Part 2, ApJS, 224, 36, doi: 10.3847/0067-0049/224/2/36

Kirkpatrick J. D., Martin E. C., Smart R. L., Cayago A. J., Beichman C. A., Marocco F., Gelino C. R., Faherty J. K., Cushing M. C., Schneider A. C., Mace G. N., Tinney C. G.,

Wright E. L., Lowrance P. J., Ingalls J. G., Vrba F. J., Munn J. A., Dahm S. E., McLean I. S. 2019, Preliminary Trigonometric Parallaxes of 184 Late-T and Y Dwarfs and an Analysis of the Field Substellar Mass Function into the "Planetary" Mass Regime, ApJS, 240, 19, doi: 10.3847/1538-4365/aaf6af

Kirkpatrick J. D., Gelino C. R., Faherty J. K., Meisner A. M., Caselden D., Schneider A. C., Marocco F., Cayago A. J., Smart R. L., Eisenhardt P. R., Kuchner M. J., Wright E. L., Cushing M. C., Allers K. N., Bardalez Gagliuffi D. C., Burgasser A. J., Gagné J., Logsdon S. E., Martin E. C., Ingalls J. G., Lowrance P. J., Abrahams E. S., Aganze C., Gerasimov R., Gonzales E. C., Hsu C.-C., Kamraj N., Kiman R., Rees J., Theissen C., Ammar K., Andersen N. S., Beaulieu P., Colin G., Elachi C. A., Goodman S. J., Gramaize L., Hamlet L. K., Hong J., Jonkeren A., Khalil M., Martin D. W., Pendrill W., Pumphrey B., Rothermich A., Sainio A., Stenner A., Tanner C., Thévenot M., Voloshin N. V., Walla J., Wędracki Z., Backyard Worlds: Planet 9 Collaboration. 2021, The Field Substellar Mass Function Based on the Full-sky 20 pc Census of 525 L, T, and Y Dwarfs, ApJS, 253, 7, doi: 10.3847/1538-4365/abd107

Knapp G. R., Leggett S. K., Fan X., Marley M. S., Geballe T. R., Golimowski D. A., Finkbeiner D., Gunn J. E., Hennawi J., Ivezić Z., Lupton R. H., Schlegel D. J., Strauss M. A., Tsvetanov Z. I., Chiu K., Hoversten E. A., Glazebrook K., Zheng W., Hendrickson M., Williams C. C., Uomoto A., Vrba F. J., Henden A. A., Luginbuhl C. B., Guetter H. H., Munn J. A., Canzian B., Schneider D. P., Brinkmann J. 2004, Near-Infrared Photometry and Spectroscopy of L and T Dwarfs: The Effects of Temperature, Clouds, and Gravity, AJ, 127, 3553, doi: 10.1086/420707

Koch D. G., Borucki W. J., Basri G., Batalha N. M., Brown T. M., Caldwell D., Christensen-Dalsgaard J., Cochran W. D., DeVore E., Dunham E. W., Gautier Thomas N. I., Geary J. C., Gilliland R. L., Gould A., Jenkins J., Kondo Y., Latham

D. W., Lissauer J. J., Marcy G., Monet D., Sasselov D., Boss A., Brownlee D., Caldwell J., Dupree A. K., Howell S. B., Kjeldsen H., Meibom S., Morrison D., Owen T., Reitsema H., Tarter J., Bryson S. T., Dotson J. L., Gazis P., Haas M. R., Kolodziejczak J., Rowe J. F., Van Cleve J. E., Allen C., Chandrasekaran H., Clarke B. D., Li J., Quintana E. V., Tenenbaum P., Twicken J. D., Wu H. 2010, Kepler Mission Design, Realized Photometric Performance, and Early Science, ApJ, 713, L79, doi: 10.1088/2041-8205/713/2/L79

Koen C. 2013, An extensive search for rapid optical variability in ultracool dwarfs, MNRAS, 428, 2824, doi: 10.1093/mnras/sts208

Koen C., Matsunaga N., Menzies J. 2004, A search for short time-scale JHK variability in ultracool dwarfs, MNRAS, 354, 466, doi: 10.1111/j.1365-2966.2004.08208.x

Koen C., Miszalski B., Väisänen P., Koen T. 2017, Optical spectra of ultracool dwarfs with the Southern African Large Telescope, MNRAS, 465, 4723, doi: 10.1093/mnras/stw3106

Konopacky Q. M., Ghez A. M., Barman T. S., Rice E. L., Bailey J. I. I., White R. J., McLean I. S., Duchêne G. 2010, High-precision Dynamical Masses of Very Low Mass Binaries, ApJ, 711, 1087, doi: 10.1088/0004-637X/711/2/1087

Konopacky Q. M., Ghez A. M., Fabrycky D. C., Macintosh B. A., White R. J., Barman T. S., Rice E. L., Hallinan G., Duchêne G. 2012, Rotational Velocities of Individual Components in Very Low Mass Binaries, ApJ, 750, 79, doi: 10.1088/0004-637X/750/1/79

Kounkel M., Covey K., Moe M., Kratter K. M., Suárez G., Stassun K. G., Román-Zúñiga C., Hernandez J., Kim J. S., Peña Ramírez K., Roman-Lopes A., Stringfellow G. S., Jaehnig K. O., Borissova J., Tofflemire B., Krolikowski D., Rizzuto A., Kraus A.,

Badenes C., Longa-Peña P., Gómez Maqueo Chew Y., Barba R., Nidever D. L., Brown C., De Lee N., Pan K., Bizyaev D., Oravetz D., Oravetz A. 2019, Close Companions around Young Stars, AJ, 157, 196, doi: 10.3847/1538-3881/ab13b1

Kounkel M., Covey K. R., Stassun K. G., Price-Whelan A. M., Holtzman J., Chojnowski D., Longa-Peña P., Román-Zúñiga C. G., Hernandez J., Serna J., Badenes C., De Lee N., Majewski S., Stringfellow G. S., Kratter K. M., Moe M., Frinchaboy P. M., Beaton R. L., Fernández-Trincado J. G., Mahadevan S., Minniti D., Beers T. C., Schneider D. P., Barba R., Brownstein J. R., García-Hernández D. A., Pan K., Bizyaev D. 2021, Double-lined Spectroscopic Binaries in the APOGEE DR16 and DR17 Data, AJ, 162, 184, doi: 10.3847/1538-3881/ac1798

Kramida A., Yu. Ralchenko, Reader J., and NIST ASD Team. 2019, NIST Atomic Spectra Database (ver. 5.7.1), NIST Atomic Spectra Database (ver. 5.7.1), [Online]. Available: `https://physics.nist.gov/asd` [2019, September 12]. National Institute of Standards and Technology, Gaithersburg, MD.

Kraus A. L., Hillenbrand L. A. 2007, The Stellar Populations of Praesepe and Coma Berenices, AJ, 134, 2340, doi: 10.1086/522831

Kumar S. S. 1962, Study of Degeneracy in Very Light Stars., AJ, 67, 579, doi: 10.1086/108658

Kumar S. S. 1963, The Structure of Stars of Very Low Mass., ApJ, 137, 1121, doi: 10.1086/147589

Larkin J., Barczys M., Krabbe A., Adkins S., Aliado T., Amico P., Brims G., Campbell R., Canfield J., Gasaway T., Honey A., Iserlohe C., Johnson C., Kress E., LaFreniere D., Lyke J., Magnone K., Magnone N., McElwain M., Moon J., Quirrenbach A.,

Skulason G., Song I., Spencer M., Weiss J., Wright S. 2006, in Society of Photo-Optical Instrumentation Engineers (SPIE) Conference Series, Vol. 6269, Society of Photo-Optical Instrumentation Engineers (SPIE) Conference Series, ed. I. S. McLean, M. Iye, 62691A, doi: 10.1117/12.672061

Laughlin G., Bodenheimer P., Adams F. C. 1997, The End of the Main Sequence, ApJ, 482, 420, doi: 10.1086/304125

Law N. M., Hodgkin S. T., Mackay C. D. 2006, Discovery of five very low mass close binaries, resolved in the visible with lucky imaging*, MNRAS, 368, 1917, doi: 10.1111/j.1365-2966.2006.10265.x

Lawrence A., Warren S. J., Almaini O., Edge A. C., Hambly N. C., Jameson R. F., Lucas P., Casali M., Adamson A., Dye S., Emerson J. P., Foucaud S., Hewett P., Hirst P., Hodgkin S. T., Irwin M. J., Lodieu N., McMahon R. G., Simpson C., Smail I., Mortlock D., Folger M. 2007, The UKIRT Infrared Deep Sky Survey (UKIDSS), MNRAS, 379, 1599, doi: 10.1111/j.1365-2966.2007.12040.x

Lawrence A., Warren S. J., Almaini O., Edge A. C., Hambly N. C., Jameson R. F., Lucas P., Casali M., Adamson A., Dye S., Emerson J. P., Foucaud S., Hewett P., Hirst P., Hodgkin S. T., Irwin M. J., Lodieu N., McMahon R. G., Simpson C., Smail I., Mortlock D., Folger M. 2013, VizieR Online Data Catalog: UKIDSS-DR9 LAS, GCS and DXS Surveys (Lawrence+ 2012), VizieR Online Data Catalog, II/319

Leggett S. K., Geballe T. R., Fan X., Schneider D. P., Gunn J. E., Lupton R. H., Knapp G. R., Strauss M. A., McDaniel A., Golimowski D. A., Henry T. J., Peng E., Tsvetanov Z. I., Uomoto A., Zheng W., Hill G. J., Ramsey L. W., Anderson S. F., Annis J. A., Bahcall N. A., Brinkmann J., Chen B., Csabai I., Fukugita M., Hennessy G. S., Hindsley R. B., Ivezić Ž., Lamb D. Q., Munn J. A., Pier J. R., Schlegel D. J., Smith

J. A., Stoughton C., Thakar A. R., York D. G. 2000, The Missing Link: Early Methane ("T") Dwarfs in the Sloan Digital Sky Survey, ApJ, 536, L35, doi: 10.1086/312728

Leggett S. K., Saumon D., Albert L., Cushing M. C., Liu M. C., Luhman K. L., Marley M. S., Kirkpatrick J. D., Roellig T. L., Allers K. N. 2008, HN Peg B: A Test of Models of the L to T Dwarf Transition, ApJ, 682, 1256, doi: 10.1086/589146

Leggett S. K., Burningham B., Saumon D., Marley M. S., Warren S. J., Smart R. L., Jones H. R. A., Lucas P. W., Pinfield D. J., Tamura M. 2010, Mid-Infrared Photometry of Cold Brown Dwarfs: Diversity in Age, Mass, and Metallicity, ApJ, 710, 1627, doi: 10.1088/0004-637X/710/2/1627

Leinert C., Allard F., Richichi A., Hauschildt P. H. 2000, The multiple system LHS 1070: a case study for the onset of dust formation in the atmospheres of very low mass stars, A&A, 353, 691

Lépine S., Rich R. M., Shara M. M. 2003, Spectroscopy of New High Proper Motion Stars in the Northern Sky. I. New Nearby Stars, New High-Velocity Stars, and an Enhanced Classification Scheme for M Dwarfs, AJ, 125, 1598, doi: 10.1086/345972

Lépine S., Rich R. M., Shara M. M. 2007, Revised Metallicity Classes for Low-Mass Stars: Dwarfs (dM), Subdwarfs (sdM), Extreme Subdwarfs (esdM), and Ultrasubdwarfs (usdM), ApJ, 669, 1235, doi: 10.1086/521614

Lépine S., Shara M. M. 2005, A Catalog of Northern Stars with Annual Proper Motions Larger than 0.15" (LSPM-NORTH Catalog), AJ, 129, 1483, doi: 10.1086/427854

Line M. R., Marley M. S., Liu M. C., Burningham B., Morley C. V., Hinkel N. R., Teske J., Fortney J. J., Freedman R., Lupu R. 2017, Uniform Atmospheric Retrieval Analysis of Ultracool Dwarfs. II. Properties of 11 T dwarfs, ApJ, 848, 83, doi: 10.3847/1538-4357/aa7ff0

Line M. R., Brogi M., Bean J. L., Gandhi S., Zalesky J., Parmentier V., Smith P., Mace G. N., Mansfield M., Kempton E. M. R., Fortney J. J., Shkolnik E., Patience J., Rauscher E., Désert J.-M., Wardenier J. P. 2021, A solar C/O and sub-solar metallicity in a hot Jupiter atmosphere, Nature, 598, 580, doi: 10.1038/s41586-021-03912-6

Linsky J. L. 1969, On the Pressure-Induced Opacity of Molecular Hydrogen in Late-Type Stars, ApJ, 156, 989, doi: 10.1086/150030

Liu M. C., Dupuy T. J., Allers K. N. 2016, The Hawaii Infrared Parallax Program. II. Young Ultracool Field Dwarfs, ApJ, 833, 96, doi: 10.3847/1538-4357/833/1/96

Liu M. C., Leggett S. K., Golimowski D. A., Chiu K., Fan X., Geballe T. R., Schneider D. P., Brinkmann J. 2006, SDSS J1534+1615AB: A Novel T Dwarf Binary Found with Keck Laser Guide Star Adaptive Optics and the Potential Role of Binarity in the L/T Transition, ApJ, 647, 1393, doi: 10.1086/505561

Liu M. C., Delorme P., Dupuy T. J., Bowler B. P., Albert L., Artigau E., Reylé C., Forveille T., Delfosse X. 2011, CFBDSIR J1458+1013B: A Very Cold (>T10) Brown Dwarf in a Binary System, ApJ, 740, 108, doi: 10.1088/0004-637X/740/2/108

Lodieu N., Dobbie P. D., Hambly N. C. 2011, Multi-fibre optical spectroscopy of low-mass stars and brown dwarfs in Upper Scorpius, A&A, 527, A24, doi: 10.1051/0004-6361/201014992

Lodieu N., Scholz R.-D., McCaughrean M. J., Ibata R., Irwin M., Zinnecker H. 2005, Spectroscopic classification of red high proper motion objects in the Southern Sky, A&A, 440, 1061, doi: 10.1051/0004-6361:20042456

Logsdon S. E., Mace G. N., McLean I. S., Martin E. C. 2018, Probing Late-type T Dwarf J - H Color Outliers for Signs of Age, ApJ, 867, 96, doi: 10.3847/1538-4357/aade9b

Looper D. L., Gelino C. R., Burgasser A. J., Kirkpatrick J. D. 2008, Discovery of a T Dwarf Binary with the Largest Known J-Band Flux Reversal, ApJ, 685, 1183, doi: 10.1086/590382

Looper D. L., Kirkpatrick J. D., Burgasser A. J. 2007, Discovery of 11 New T Dwarfs in the Two Micron All Sky Survey, Including a Possible L/T Transition Binary, AJ, 134, 1162, doi: 10.1086/520645

Lu H.-p., Zhang L.-y., Shi J., Han X. L., Fan D., Long L., Pi Q. 2019, Magnetic Activities of M-type Stars Based on LAMOST DR5 and Kepler and K2 Missions, ApJS, 243, 28, doi: 10.3847/1538-4365/ab2f8f

Luhman K. L. 2004, New Brown Dwarfs and an Updated Initial Mass Function in Taurus, ApJ, 617, 1216, doi: 10.1086/425647

Luhman K. L. 2013, Discovery of a Binary Brown Dwarf at 2 pc from the Sun, ApJ, 767, L1, doi: 10.1088/2041-8205/767/1/L1

Luhman K. L., Herrmann K. A., Mamajek E. E., Esplin T. L., Pecaut M. J. 2018, New Young Stars and Brown Dwarfs in the Upper Scorpius Association, AJ, 156, 76, doi: 10.3847/1538-3881/aacc6d

Luhman K. L., Patten B. M., Marengo M., Schuster M. T., Hora J. L., Ellis R. G., Stauffer J. R., Sonnett S. M., Winston E., Gutermuth R. A., Megeath S. T., Backman D. E., Henry T. J., Werner M. W., Fazio G. G. 2007, Discovery of Two T Dwarf Companions with the Spitzer Space Telescope, ApJ, 654, 570, doi: 10.1086/509073

Lutz T. E., Upgren A. R. 1980, An analysis of parallaxes determined in two coordinates, AJ, 85, 1390, doi: 10.1086/112812

Mace G., Sokal K., Lee J.-J., Oh H., Park C., Lee H., Good J., MacQueen P., Oh J. S., Kaplan K., Kidder B., Chun M.-Y., Yuk I.-S., Jeong U., Pak S., Kim K.-M., Nah J., Lee S., Yu Y.-S., Hwang N., Park B.-G., Kim H., Chinn B., Peck A., Diaz R., Rutten R., Prato L., Jacoby G., Cornelius F., Hardesty B., DeGroff W., Dunham E., Levine S., Nofi L., Lopez-Valdivia R., Weinberger A. J., Jaffe D. T. 2018, in Society of Photo-Optical Instrumentation Engineers (SPIE) Conference Series, Vol. 10702, Ground-based and Airborne Instrumentation for Astronomy VII, ed. C. J. Evans, L. Simard, H. Takami, 107020Q, doi: 10.1117/12.2312345

Mace G. N. 2014, VizieR Online Data Catalog: Near-IR spectroscopy of low-mass binaries and brown dwarfs (Mace, 2014), VizieR Online Data Catalog, 5144

Mace G. N., Kirkpatrick J. D., Cushing M. C., Gelino C. R., Griffith R. L., Skrutskie M. F., Marsh K. A., Wright E. L., Eisenhardt P. R., McLean I. S., Thompson M. A., Mix K., Bailey V., Beichman C. A., Bloom J. S., Burgasser A. J., Fortney J. J., Hinz P. M., Knox R. P., Lowrance P. J., Marley M. S., Morley C. V., Rodigas T. J., Saumon D., Sheppard S. S., Stock N. D. 2013, A Study of the Diverse T Dwarf Population Revealed by WISE, ApJS, 205, 6, doi: 10.1088/0067-0049/205/1/6

Macintosh B., Graham J. R., Barman T., De Rosa R. J., Konopacky Q., Marley M. S., Marois C., Nielsen E. L., Pueyo L., Rajan A., Rameau J., Saumon D., Wang J. J., Patience J., Ammons M., Arriaga P., Artigau E., Beckwith S., Brewster J., Bruzzone S., Bulger J., Burningham B., Burrows A. S., Chen C., Chiang E., Chilcote J. K., Dawson R. I., Dong R., Doyon R., Draper Z. H., Duchêne G., Esposito T. M., Fabrycky D., Fitzgerald M. P., Follette K. B., Fortney J. J., Gerard B., Goodsell S., Greenbaum A. Z., Hibon P., Hinkley S., Cotten T. H., Hung L. W., Ingraham P., Johnson-Groh M., Kalas P., Lafreniere D., Larkin J. E., Lee J., Line M., Long D., Maire J., Marchis F., Matthews B. C., Max C. E., Metchev S., Millar-Blanchaer M. A., Mittal T., Morley

C. V., Morzinski K. M., Murray-Clay R., Oppenheimer R., Palmer D. W., Patel R., Perrin M. D., Poyneer L. A., Rafikov R. R., Rantakyrö F. T., Rice E. L., Rojo P., Rudy A. R., Ruffio J. B., Ruiz M. T., Sadakuni N., Saddlemyer L., Salama M., Savransky D., Schneider A. C., Sivaramakrishnan A., Song I., Soummer R., Thomas S., Vasisht G., Wallace J. K., Ward-Duong K., Wiktorowicz S. J., Wolff S. G., Zuckerman B. 2015, Discovery and spectroscopy of the young jovian planet 51 Eri b with the Gemini Planet Imager, Science, 350, 64, doi: 10.1126/science.aac5891

Madau P., Dickinson M. 2014, Cosmic Star-Formation History, ARA&A, 52, 415, doi: 10.1146/annurev-astro-081811-125615

Majewski S. R., Schiavon R. P., Frinchaboy P. M., Allende Prieto C., Barkhouser R., Bizyaev D., Blank B., Brunner S., Burton A., Carrera R., Chojnowski S. D., Cunha K., Epstein C., Fitzgerald G., García Pérez A. E., Hearty F. R., Henderson C., Holtzman J. A., Johnson J. A., Lam C. R., Lawler J. E., Maseman P., Mészáros S., Nelson M., Nguyen D. C., Nidever D. L., Pinsonneault M., Shetrone M., Smee S., Smith V. V., Stolberg T., Skrutskie M. F., Walker E., Wilson J. C., Zasowski G., Anders F., Basu S., Beland S., Blanton M. R., Bovy J., Brownstein J. R., Carlberg J., Chaplin W., Chiappini C., Eisenstein D. J., Elsworth Y., Feuillet D., Fleming S. W., Galbraith-Frew J., García R. A., García-Hernández D. A., Gillespie B. A., Girardi L., Gunn J. E., Hasselquist S., Hayden M. R., Hekker S., Ivans I., Kinemuchi K., Klaene M., Mahadevan S., Mathur S., Mosser B., Muna D., Munn J. A., Nichol R. C., O'Connell R. W., Parejko J. K., Robin A. C., Rocha-Pinto H., Schultheis M., Serenelli A. M., Shane N., Silva Aguirre V., Sobeck J. S., Thompson B., Troup N. W., Weinberg D. H., Zamora O. 2017, The Apache Point Observatory Galactic Evolution Experiment (APOGEE), AJ, 154, 94, doi: 10.3847/1538-3881/aa784d

Mamajek E. E., Bartlett J. L., Seifahrt A., Henry T. J., Dieterich S. B., Lurie J. C.,

Kenworthy M. A., Jao W.-C., Riedel A. R., Subasavage J. P., Winters J. G., Finch C. T., Ianna P. A., Bean J. 2013, The Solar Neighborhood. XXX. Fomalhaut C, AJ, 146, 154, doi: 10.1088/0004-6256/146/6/154

Manjavacas E., Goldman B., Reffert S., Henning T. 2013, Parallax measurements of cool brown dwarfs, A&A, 560, A52, doi: 10.1051/0004-6361/201321720

Manjavacas E., Apai D., Zhou Y., Lew B. W. P., Schneider G., Metchev S., Miles-Páez P. A., Radigan J., Marley M. S., Cowan N., Karalidi T., Burgasser A. J., Bedin L. R., Lowrance P. J., Kauffmann P. 2019, Cloud Atlas: Hubble Space Telescope Near-infrared Spectral Library of Brown Dwarfs, Planetary-mass Companions, and Hot Jupiters, AJ, 157, 101, doi: 10.3847/1538-3881/aaf88f

Mann A. W., Deacon N. R., Gaidos E., Ansdell M., Brewer J. M., Liu M. C., Magnier E. A., Aller K. M. 2014, Prospecting in Ultracool Dwarfs: Measuring the Metallicities of Mid- and Late-M Dwarfs, AJ, 147, 160, doi: 10.1088/0004-6256/147/6/160

Marley M., Saumon D., Morley C., Fortney J. 2018, Sonora 2018: Cloud-free, solar composition, solar C/O substellar evolution models, 1.0, Zenodo, doi: 10.5281/zenodo.2628068

Marley M. S., Saumon D., Visscher C., Lupu R., Freedman R., Morley C., Fortney J. J., Seay C., Smith A. J. R. W., Teal D. J., Wang R. 2021, The Sonora Brown Dwarf Atmosphere and Evolution Models. I. Model Description and Application to Cloudless Atmospheres in Rainout Chemical Equilibrium, ApJ, 920, 85, doi: 10.3847/1538-4357/ac141d

Marocco F., Andrei A. H., Smart R. L., Jones H. R. A., Pinfield D. J., Day-Jones A. C., Clarke J. R. A., Sozzetti A., Lucas P. W., Bucciarelli B., Penna J. L. 2013, Parallaxes

of Southern Extremely Cool Objects (PARSEC). II. Spectroscopic Follow-up and Parallaxes of 52 Targets, AJ, 146, 161, doi: 10.1088/0004-6256/146/6/161

Martin E. C., Mace G. N., McLean I. S., Logsdon S. E., Rice E. L., Kirkpatrick J. D., Burgasser A. J., McGovern M. R., Prato L. 2017, Surface Gravities for 228 M, L, and T Dwarfs in the NIRSPEC Brown Dwarf Spectroscopic Survey, ApJ, 838, 73, doi: 10.3847/1538-4357/aa6338

Martin E. C., Fitzgerald M. P., McLean I. S., Doppmann G., Kassis M., Aliado T., Canfield J., Johnson C., Kress E., Lanclos K., Magnone K., Sohn J. M., Wang E., Weiss J. 2018, in Society of Photo-Optical Instrumentation Engineers (SPIE) Conference Series, Vol. 10702, Ground-based and Airborne Instrumentation for Astronomy VII, ed. C. J. Evans, L. Simard, H. Takami, 107020A, doi: 10.1117/12.2312266

Martín E. L., Delfosse X., Guieu S. 2004, Spectroscopic Identification of DENIS-selected Brown Dwarf Candidates in the Upper Scorpius OB Association, AJ, 127, 449, doi: 10.1086/380226

Martín E. L., Lodieu N., Pavlenko Y., Béjar V. J. S. 2018, The Lithium Depletion Boundary and the Age of the Hyades Cluster, ApJ, 856, 40, doi: 10.3847/1538-4357/aaaeb8

Massey F. J. 1951, The Kolmogorov-Smirnov test for goodness of fit, Journal of the American Statistical Association, 46, 68

Mawet D., Fitzgerald M., Konopacky Q., Beichman C., Jovanovic N., Dekany R., Hover D., Chisholm E., Ciardi D., Artigau É., Banyal R., Beatty T., Benneke B., Blake G. A., Burgasser A., Canalizo G., Chen G., Do T., Doppmann G., Doyon R., Dressing C., Fang M., Greene T., Hillenbrand L., Howard A., Kane S., Kataria T., Kempton E., Knutson H., Kotani T., Lafrenière D., Liu C., Nishiyama S., Pandey G., Plavchan P., Prato L.,

Rajaguru S. P., Robertson P., Salyk C., Sato B., Schlawin E., Sengupta S., Sivarani T., Skidmore W., Tamura M., Terada H., Vasisht G., Wang J., Zhang H. 2019, in Bulletin of the American Astronomical Society, Vol. 51, 134. https://arxiv.org/abs/1908.03623

Mayor M., Queloz D. 1995, A Jupiter-mass companion to a solar-type star, Nature, 378, 355, doi: 10.1038/378355a0

McCaughrean M. J., Scholz R. D., Lodieu N. 2002, Search for nearby stars among proper motion stars selected by optical-to-infrared photometry. II. Two late M dwarfs within 10 pc, A&A, 390, L27, doi: 10.1051/0004-6361:20020928

McLean I. S., Graham J. R., Becklin E. E., Figer D. F., Larkin J. E., Levenson N. A., Teplitz H. I. 2000, in Society of Photo-Optical Instrumentation Engineers (SPIE) Conference Series, Vol. 4008, Optical and IR Telescope Instrumentation and Detectors, ed. M. Iye, A. F. Moorwood, 1048–1055, doi: 10.1117/12.395422

McLean I. S., McGovern M. R., Burgasser A. J., Kirkpatrick J. D., Prato L., Kim S. S. 2003, The NIRSPEC Brown Dwarf Spectroscopic Survey. I. Low-Resolution Near-Infrared Spectra, ApJ, 596, 561, doi: 10.1086/377636

McLean I. S., Prato L., McGovern M. R., Burgasser A. J., Kirkpatrick J. D., Rice E. L., Kim S. S. 2007, The NIRSPEC Brown Dwarf Spectroscopic Survey. II. High-Resolution J-Band Spectra of M, L, and T Dwarfs, ApJ, 658, 1217, doi: 10.1086/511740

McLean I. S., Becklin E. E., Bendiksen O., Brims G., Canfield J., Figer D. F., Graham J. R., Hare J., Lacayanga F., Larkin J. E., Larson S. B., Levenson N., Magnone N., Teplitz H., Wong W. 1998, Society of Photo-Optical Instrumentation Engineers (SPIE) Conference Series, Vol. 3354, Design and development of NIRSPEC: a near-

infrared echelle spectrograph for the Keck II telescope, ed. A. M. Fowler, 566–578, doi: 10.1117/12.317283

McMahon R. G., Banerji M., Gonzalez E., Koposov S. E., Bejar V. J., Lodieu N., Rebolo R., VHS Collaboration. 2013, First Scientific Results from the VISTA Hemisphere Survey (VHS), The Messenger, 154, 35

Meeus G., McCaughrean M. J. 2005, Using near-IR spectroscopy to classify substellar candidates in the Trapezium Cluster, Astronomische Nachrichten, 326, 977, doi: 10.1002/asna.200510448

Meisner A. M., Faherty J. K., Kirkpatrick J. D., Schneider A. C., Caselden D., Gagné J., Kuchner M. J., Burgasser A. J., Casewell S. L., Debes J. H., Artigau É., Bardalez Gagliuffi D. C., Logsdon S. E., Kiman R., Allers K., Hsu C.-c., Wisniewski J. P., Allen M. B., Beaulieu P., Colin G., Durantini Luca H. A., Goodman S., Gramaize L., Hamlet L. K., Hinckley K., Kiwy F., Martin D. W., Pendrill W., Rothermich A., Sainio A., Schümann J., Andersen N. S., Tanner C., Thakur V., Thévenot M., Walla J., Wędracki Z., Aganze C., Gerasimov R., Theissen C., The Backyard Worlds: Planet 9 Collaboration. 2020, Spitzer Follow-up of Extremely Cold Brown Dwarfs Discovered by the Backyard Worlds: Planet 9 Citizen Science Project, ApJ, 899, 123, doi: 10.3847/1538-4357/aba633

Melnikov S., Eislöffel J. 2012, The mass function of the Coma Berenices open cluster below 0.2 $M_{\odot}$: a search for low-mass stellar and substellar members, A&A, 544, A111, doi: 10.1051/0004-6361/201219314

Menten K. M., Reid M. J., Forbrich J., Brunthaler A. 2007, The distance to the Orion Nebula, A&A, 474, 515, doi: 10.1051/0004-6361:20078247

Mészáros S., Allende Prieto C., Edvardsson B., Castelli F., García Pérez A. E., Gustafsson

B., Majewski S. R., Plez B., Schiavon R., Shetrone M., de Vicente A. 2012, New ATLAS9 and MARCS Model Atmosphere Grids for the Apache Point Observatory Galactic Evolution Experiment (APOGEE), AJ, 144, 120, doi: 10.1088/0004-6256/144/4/120

Metchev S. A., Kirkpatrick J. D., Berriman G. B., Looper D. 2008, A Cross-Match of 2MASS and SDSS: Newly Found L and T Dwarfs and an Estimate of the Space Density of T Dwarfs, ApJ, 676, 1281, doi: 10.1086/524721

Metchev S. A., Heinze A., Apai D., Flateau D., Radigan J., Burgasser A., Marley M. S., Artigau É., Plavchan P., Goldman B. 2015, Weather on Other Worlds. II. Survey Results: Spots are Ubiquitous on L and T Dwarfs, ApJ, 799, 154, doi: 10.1088/0004-637X/799/2/154

Metodieva Y., Antonova A., Golev V., Dimitrov D., García-Álvarez D., Doyle J. G. 2015, Low-resolution optical spectra of ultracool dwarfs with OSIRIS/GTC, MNRAS, 446, 3878, doi: 10.1093/mnras/stu2370

Miles B. E., Skemer A. J. I., Morley C. V., Marley M. S., Fortney J. J., Allers K. N., Faherty J. K., Geballe T. R., Visscher C., Schneider A. C., Lupu R., Freedman R. S., Bjoraker G. L. 2020, Observations of Disequilibrium CO Chemistry in the Coldest Brown Dwarfs, AJ, 160, 63, doi: 10.3847/1538-3881/ab9114

Miller J. S., Stone R. P. S. 1994, The Kast Double Spectrograph, Tech. Rep. 66, University of California Lick Observatory Technical Reports

Miyamoto M., Nagai R. 1975, Three-dimensional models for the distribution of mass in galaxies, PASJ, 27, 533

Moe M., Kratter K. M., Badenes C. 2019, The Close Binary Fraction of Solar-type Stars

Is Strongly Anticorrelated with Metallicity, ApJ, 875, 61, doi: 10.3847/1538-4357/ab0d88

Moehler S., Modigliani A., Freudling W., Giammichele N., Gianninas A., Gonneau A., Kausch W., Lançon A., Noll S., Rauch T., Vinther J. 2014, Flux calibration of medium-resolution spectra from 300 nm to 2500 nm: Model reference spectra and telluric correction, A&A, 568, A9, doi: 10.1051/0004-6361/201423790

Mohanty S., Basri G. 2003, Rotation and Activity in Mid-M to L Field Dwarfs, ApJ, 583, 451, doi: 10.1086/345097

Mollière P., Snellen I. A. G. 2019, Detecting isotopologues in exoplanet atmospheres using ground-based high-dispersion spectroscopy, A&A, 622, A139, doi: 10.1051/0004-6361/201834169

Monet D. G., Levine S. E., Canzian B., Ables H. D., Bird A. R., Dahn C. C., Guetter H. H., Harris H. C., Henden A. A., Leggett S. K., Levison H. F., Luginbuhl C. B., Martini J., Monet A. K. B., Munn J. A., Pier J. R., Rhodes A. R., Riepe B., Sell S., Stone R. C., Vrba F. J., Walker R. L., Westerhout G., Brucato R. J., Reid I. N., Schoening W., Hartley M., Read M. A., Tritton S. B. 2003, The USNO-B Catalog, AJ, 125, 984, doi: 10.1086/345888

Morin J., Donati J. F., Petit P., Delfosse X., Forveille T., Jardine M. M. 2010, Large-scale magnetic topologies of late M dwarfs*, MNRAS, 407, 2269, doi: 10.1111/j.1365-2966.2010.17101.x

Nardiello D. 2020, A PSF-based Approach to TESS High quality data Of Stellar clusters (PATHOS) - III. Exploring the properties of young associations through their variables, dippers, and candidate exoplanets, MNRAS, 498, 5972, doi: 10.1093/mnras/staa2745

Naud M.-E., Artigau É., Malo L., Albert L., Doyon R., Lafrenière D., Gagné J., Saumon D., Morley C. V., Allard F., Homeier D., Beichman C. A., Gelino C. R., Boucher A. 2014, Discovery of a Wide Planetary-mass Companion to the Young M3 Star GU Psc, ApJ, 787, 5, doi: 10.1088/0004-637X/787/1/5

Ness M., Hogg D. W., Rix H. W., Ho A. Y. Q., Zasowski G. 2015, The Cannon: A data-driven approach to Stellar Label Determination, ApJ, 808, 16, doi: 10.1088/0004-637X/808/1/16

Newton E. R., Charbonneau D., Irwin J., Berta-Thompson Z. K., Rojas-Ayala B., Covey K., Lloyd J. P. 2014, Near-infrared Metallicities, Radial Velocities, and Spectral Types for 447 Nearby M Dwarfs, AJ, 147, 20, doi: 10.1088/0004-6256/147/1/20

Newton E. R., Irwin J., Charbonneau D., Berta-Thompson Z. K., Dittmann J. A., West A. A. 2016, The Rotation and Galactic Kinematics of Mid M Dwarfs in the Solar Neighborhood, ApJ, 821, 93, doi: 10.3847/0004-637X/821/2/93

Nidever D. 2021, dnidever/doppler: Cannon and Payne models, v1.1.0, Zenodo, Zenodo, doi: 10.5281/zenodo.4906681

Nidever D. L., Holtzman J. A., Allende Prieto C., Beland S., Bender C., Bizyaev D., Burton A., Desphande R., Fleming S. W., García Pérez A. E., Hearty F. R., Majewski S. R., Mészáros S., Muna D., Nguyen D., Schiavon R. P., Shetrone M., Skrutskie M. F., Sobeck J. S., Wilson J. C. 2015, The Data Reduction Pipeline for the Apache Point Observatory Galactic Evolution Experiment, AJ, 150, 173, doi: 10.1088/0004-6256/150/6/173

Nutzman P., Charbonneau D. 2008, Design Considerations for a Ground-Based Transit Search for Habitable Planets Orbiting M Dwarfs, PASP, 120, 317, doi: 10.1086/533420

Nuzzo R. 2014, Scientific method: Statistical errors, Nature, 506, 150, doi: 10.1038/506150a

Öpik E. 1924, Publications of the Tartu Astrofizica Observatory, 25, 6

Outred M. 1978in

Parsons S. G., Gänsicke B. T., Marsh T. R., Ashley R. P., Breedt E., Burleigh M. R., Copperwheat C. M., Dhillon V. S., Green M. J., Hermes J. J., Irawati P., Kerry P., Littlefair S. P., Rebassa-Mansergas A., Sahman D. I., Schreiber M. R., Zorotovic M. 2018, The scatter of the M dwarf mass-radius relationship, MNRAS, 481, 1083, doi: 10.1093/mnras/sty2345

Pecaut M. J., Mamajek E. E. 2013, Intrinsic Colors, Temperatures, and Bolometric Corrections of Pre-main-sequence Stars, ApJS, 208, 9, doi: 10.1088/0067-0049/208/1/9

Pecaut M. J., Mamajek E. E. 2016, The star formation history and accretion-disc fraction among the K-type members of the Scorpius-Centaurus OB association, MNRAS, 461, 794, doi: 10.1093/mnras/stw1300

Phan-Bao N., Bessell M. S., Martín E. L., Simon G., Borsenberger J., Tata R., Guibert J., Crifo F., Forveille T., Delfosse X., Lim J., de Batz B. 2008, Discovery of new nearby L and late-M dwarfs at low Galactic latitude from the DENIS data base, MNRAS, 383, 831, doi: 10.1111/j.1365-2966.2007.12564.x

Phillips M. W., Tremblin P., Baraffe I., Chabrier G., Allard N. F., Spiegelman F., Goyal J. M., Drummond B., Hebrard E. 2020, A new set of atmosphere and evolution models for cool T-Y brown dwarfs and giant exoplanets, arXiv e-prints, arXiv:2003.13717. https://arxiv.org/abs/2003.13717

Pineda J. S., Hallinan G., Kirkpatrick J. D., Cotter G., Kao M. M., Mooley K. 2016, A Survey for Hα Emission from Late L Dwarfs and T Dwarfs, ApJ, 826, 73, doi: 10.3847/0004-637X/826/1/73

Pinfield D. J., Gomes J., Day-Jones A. C., Leggett S. K., Gromadzki M., Burningham B., Ruiz M. T., Kurtev R., Cattermole T., Cardoso C., Lodieu N., Faherty J., Littlefair S., Smart R., Irwin M., Clarke J. R. A., Smith L., Lucas P. W., Gálvez-Ortiz M. C., Jenkins J. S., Jones H. R. A., Rebolo R., Béjar V. J. S., Gauza B. 2014, A deep WISE search for very late type objects and the discovery of two halo/thick-disc T dwarfs: WISE 0013+0634 and WISE 0833+0052, MNRAS, 437, 1009, doi: 10.1093/mnras/stt1437

Planck Collaboration, Ade P. A. R., Aghanim N., Arnaud M., Ashdown M., Aumont J., Baccigalupi C., Banday A. J., Barreiro R. B., Bartlett J. G., et al. 2016, Planck 2015 results. XIII. Cosmological parameters, A&A, 594, A13, doi: 10.1051/0004-6361/201525830

Prato L., Mace G. N., Rice E. L., McLean I. S., Kirkpatrick J. D., Burgasser A. J., Kim S. S. 2015, Radial Velocity Variability of Field Brown Dwarfs, ApJ, 808, 12, doi: 10.1088/0004-637X/808/1/12

Preibisch T., Brown A. G. A., Bridges T., Guenther E., Zinnecker H. 2002, Exploring the Full Stellar Population of the Upper Scorpius OB Association, AJ, 124, 404, doi: 10.1086/341174

Price-Whelan A. M., Hogg D. W., Foreman-Mackey D., Rix H.-W. 2017, The Joker: A Custom Monte Carlo Sampler for Binary-star and Exoplanet Radial Velocity Data, ApJ, 837, 20, doi: 10.3847/1538-4357/aa5e50

Price-Whelan A. M., Hogg D. W., Rix H.-W., De Lee N., Majewski S. R., Nidever D. L., Troup N., Fernández-Trincado J. G., García-Hernández D. A., Longa-Peña P.,

Nitschelm C., Sobeck J., Zamora O. 2018, Binary Companions of Evolved Stars in APOGEE DR14: Search Method and Catalog of ∼5000 Companions, AJ, 156, 18, doi: 10.3847/1538-3881/aac387

Price-Whelan A. M., Hogg D. W., Rix H.-W., Beaton R. L., Lewis H. M., Nidever D. L., Almeida A., Badenes C., Barba R., Beers T. C., Carlberg J. K., De Lee N., Fernández-Trincado J. G., Frinchaboy P. M., García-Hernández D. A., Green P. J., Hasselquist S., Longa-Peña P., Majewski S. R., Nitschelm C., Sobeck J., Stassun K. G., Stringfellow G. S., Troup N. W. 2020, Close Binary Companions to APOGEE DR16 Stars: 20,000 Binary-star Systems Across the Color-Magnitude Diagram, ApJ, 895, 2, doi: 10.3847/1538-4357/ab8acc

Radigan J., Jayawardhana R., Lafrenière D., Artigau É., Marley M., Saumon D. 2012, Large-amplitude Variations of an L/T Transition Brown Dwarf: Multi-wavelength Observations of Patchy, High-contrast Cloud Features, ApJ, 750, 105, doi: 10.1088/0004-637X/750/2/105

Raghavan D., McAlister H. A., Henry T. J., Latham D. W., Marcy G. W., Mason B. D., Gies D. R., White R. J., ten Brummelaar T. A. 2010, A Survey of Stellar Families: Multiplicity of Solar-type Stars, ApJS, 190, 1, doi: 10.1088/0067-0049/190/1/1

Rebull L. M., Stauffer J. R., Cody A. M., Hillenbrand L. A., Bouvier J., Roggero N., David T. J. 2020, Rotation of Low-mass Stars in Taurus with K2, AJ, 159, 273, doi: 10.3847/1538-3881/ab893c

Rebull L. M., Stauffer J. R., Cody A. M., Hillenbrand L. A., David T. J., Pinsonneault M. 2018, Rotation of Low-mass Stars in Upper Scorpius and ρ Ophiuchus with K2, AJ, 155, 196, doi: 10.3847/1538-3881/aab605

Reid I. N., Cruz K. L., Kirkpatrick J. D., Allen P. R., Mungall F., Liebert J., Lowrance P.,

Sweet A. 2008, Meeting the Cool Neighbors. X. Ultracool Dwarfs from the 2MASS All-Sky Data Release, AJ, 136, 1290, doi: 10.1088/0004-6256/136/3/1290

Reid I. N., Gizis J. E. 2005, Probing the LHS Catalog. II. Faint Proper-Motion Stars, PASP, 117, 676, doi: 10.1086/430462

Reid I. N., Kirkpatrick J. D., Gizis J. E., Dahn C. C., Monet D. G., Williams R. J., Liebert J., Burgasser A. J. 2000, Four Nearby L Dwarfs, AJ, 119, 369, doi: 10.1086/301177

Reid I. N., Kirkpatrick J. D., Liebert J., Gizis J. E., Dahn C. C., Monet D. G. 2002, High-Resolution Spectroscopy of Ultracool M Dwarfs, AJ, 124, 519, doi: 10.1086/340805

Reid I. N., Lewitus E., Allen P. R., Cruz K. L., Burgasser A. J. 2006, A Search for Binary Systems among the Nearest L Dwarfs, AJ, 132, 891, doi: 10.1086/505626

Reid I. N., Kirkpatrick J. D., Liebert J., Burrows A., Gizis J. E., Burgasser A., Dahn C. C., Monet D., Cutri R., Beichman C. A., Skrutskie M. 1999, L Dwarfs and the Substellar Mass Function, ApJ, 521, 613, doi: 10.1086/307589

Reid I. N., Cruz K. L., Allen P., Mungall F., Kilkenny D., Liebert J., Hawley S. L., Fraser O. J., Covey K. R., Lowrance P. 2003, Meeting the Cool Neighbors. VII. Spectroscopy of Faint Red NLTT Dwarfs, AJ, 126, 3007, doi: 10.1086/379173

Reid M. J., Menten K. M., Brunthaler A., Zheng X. W., Dame T. M., Xu Y., Wu Y., Zhang B., Sanna A., Sato M., Hachisuka K., Choi Y. K., Immer K., Moscadelli L., Rygl K. L. J., Bartkiewicz A. 2014, Trigonometric Parallaxes of High Mass Star Forming Regions: The Structure and Kinematics of the Milky Way, ApJ, 783, 130, doi: 10.1088/0004-637X/783/2/130

Reiners A., Basri G. 2006, Measuring Magnetic Fields in Ultracool Stars and Brown Dwarfs, ApJ, 644, 497, doi: 10.1086/503324

Reiners A., Basri G. 2007, The First Direct Measurements of Surface Magnetic Fields on Very Low Mass Stars, ApJ, 656, 1121, doi: 10.1086/510304

Reiners A., Basri G. 2008, Chromospheric Activity, Rotation, and Rotational Braking in M and L Dwarfs, ApJ, 684, 1390, doi: 10.1086/590073

Reiners A., Basri G. 2009a, A Volume-Limited Sample of 63 M7-M9.5 Dwarfs. I. Space Motion, Kinematic Age, and Lithium, ApJ, 705, 1416, doi: 10.1088/0004-637X/705/2/1416

Reiners A., Basri G. 2009b, On the magnetic topology of partially and fully convective stars, A&A, 496, 787, doi: 10.1051/0004-6361:200811450

Reiners A., Basri G. 2010, A Volume-Limited Sample of 63 M7-M9.5 Dwarfs. II. Activity, Magnetism, and the Fade of the Rotation-Dominated Dynamo, ApJ, 710, 924, doi: 10.1088/0004-637X/710/2/924

Reiners A., Zechmeister M., Caballero J. A., Ribas I., Morales J. C., Jeffers S. V., Schöfer P., Tal-Or L., Quirrenbach A., Amado P. J., Kaminski A., Seifert W., Abril M., Aceituno J., Alonso-Floriano F. J., Ammler-von Eiff M., Antona R., Anglada-Escudé G., Anwand-Heerwart H., Arroyo-Torres B., Azzaro M., Baroch D., Barrado D., Bauer F. F., Becerril S., Béjar V. J. S., Benítez D., Berdinas Z. M., Bergond G., Blümcke M., Brinkmöller M., del Burgo C., Cano J., Cárdenas Vázquez M. C., Casal E., Cifuentes C., Claret A., Colomé J., Cortés-Contreras M., Czesla S., Díez-Alonso E., Dreizler S., Feiz C., Fernández M., Ferro I. M., Fuhrmeister B., Galadí-Enríquez D., Garcia-Piquer A., García Vargas M. L., Gesa L., Gómez Galera V., González Hernández J. I., González-Peinado R., Grözinger U., Grohnert S., Guàrdia J., Guenther E. W., Guijarro A., de Guindos E., Gutiérrez-Soto J., Hagen H. J., Hatzes A. P., Hauschildt P. H., Hedrosa R. P., Helmling J., Henning T., Hermelo I., Hernández

Arabí R., Hernández Castaño L., Hernández Hernando F., Herrero E., Huber A., Huke P., Johnson E. N., de Juan E., Kim M., Klein R., Klüter J., Klutsch A., Kürster M., Lafarga M., Lamert A., Lampón M., Lara L. M., Laun W., Lemke U., Lenzen R., Launhardt R., López del Fresno M., López-González J., López-Puertas M., López Salas J. F., López-Santiago J., Luque R., Magán Madinabeitia H., Mall U., Mancini L., Mandel H., Marfil E., Marín Molina J. A., Maroto Fernández D., Martín E. L., Martín-Ruiz S., Marvin C. J., Mathar R. J., Mirabet E., Montes D., Moreno-Raya M. E., Moya A., Mundt R., Nagel E., Naranjo V., Nortmann L., Nowak G., Ofir A., Oreiro R., Pallé E., Panduro J., Pascual J., Passegger V. M., Pavlov A., Pedraz S., Pérez-Calpena A., Pérez Medialdea D., Perger M., Perryman M. A. C., Pluto M., Rabaza O., Ramón A., Rebolo R., Redondo P., Reffert S., Reinhart S., Rhode P., Rix H. W., Rodler F., Rodríguez E., Rodríguez-López C., Rodríguez Trinidad A., Rohloff R. R., Rosich A., Sadegi S., Sánchez-Blanco E., Sánchez Carrasco M. A., Sánchez-López A., Sanz-Forcada J., Sarkis P., Sarmiento L. F., Schäfer S., Schmitt J. H. M. M., Schiller J., Schweitzer A., Solano E., Stahl O., Strachan J. B. P., Stürmer J., Suárez J. C., Tabernero H. M., Tala M., Trifonov T., Tulloch S. M., Ulbrich R. G., Veredas G., Vico Linares J. I., Vilardell F., Wagner K., Winkler J., Wolthoff V., Xu W., Yan F., Zapatero Osorio M. R. 2018, The CARMENES search for exoplanets around M dwarfs. High-resolution optical and near-infrared spectroscopy of 324 survey stars, A&A, 612, A49, doi: 10.1051/0004-6361/201732054

Reylé C. 2018, New ultra-cool and brown dwarf candidates in Gaia DR2, A&A, 619, L8, doi: 10.1051/0004-6361/201834082

Reylé C., Jardine K., Fouqué P., Caballero J. A., Smart R. L., Sozzetti A. 2021, The 10 parsec sample in the Gaia era, A&A, 650, A201, doi: 10.1051/0004-6361/202140985

Ricker G. R., Winn J. N., Vanderspek R., Latham D. W., Bakos G. Á., Bean J. L.,

Berta-Thompson Z. K., Brown T. M., Buchhave L., Butler N. R., Butler R. P., Chaplin W. J., Charbonneau D., Christensen-Dalsgaard J., Clampin M., Deming D., Doty J., De Lee N., Dressing C., Dunham E. W., Endl M., Fressin F., Ge J., Henning T., Holman M. J., Howard A. W., Ida S., Jenkins J. M., Jernigan G., Johnson J. A., Kaltenegger L., Kawai N., Kjeldsen H., Laughlin G., Levine A. M., Lin D., Lissauer J. J., MacQueen P., Marcy G., McCullough P. R., Morton T. D., Narita N., Paegert M., Palle E., Pepe F., Pepper J., Quirrenbach A., Rinehart S. A., Sasselov D., Sato B., Seager S., Sozzetti A., Stassun K. G., Sullivan P., Szentgyorgyi A., Torres G., Udry S., Villasenor J. 2015, Transiting Exoplanet Survey Satellite (TESS), Journal of Astronomical Telescopes, Instruments, and Systems, 1, 014003, doi: 10.1117/1.JATIS.1.1.014003

Rojo P. M., Harrington J. 2006, A Method to Remove Fringes from Images Using Wavelets, ApJ, 649, 553, doi: 10.1086/506136

Rujopakarn W., Rieke G. H., Weiner B. J., Pérez-González P., Rex M., Walth G. L., Kartaltepe J. S. 2013, Mid-infrared Determination of Total Infrared Luminosity and Star Formation Rates of Local and High-redshift Galaxies, ApJ, 767, 73, doi: 10.1088/0004-637X/767/1/73

Rujopakarn W., Eisenstein D. J., Rieke G. H., Papovich C., Cool R. J., Moustakas J., Jannuzi B. T., Kochanek C. S., Rieke M. J., Dey A., Eisenhardt P., Murray S. S., Brown M. J. I., Le Floc'h E. 2010, The Evolution of the Star Formation Rate of Galaxies at 0.0 <= z <= 1.2, ApJ, 718, 1171, doi: 10.1088/0004-637X/718/2/1171

Ryan Jr. R. E., Thorman P. A., Schmidt S. J., Cohen S. H., Hathi N. P., Holwerda B. W., Lunine J. I., Pirzkal N., Windhorst R. A., Young E. 2017, The Effect of Atmospheric Cooling on Vertical Velocity Dispersion and Density Distribution of Brown Dwarfs, ApJ, 847, 53, doi: 10.3847/1538-4357/aa85ea

Sahlmann J., Lazorenko P. F., Ségransan D., Martín E. L., Mayor M., Queloz D., Udry S. 2015, Astrometric planet search around southern ultracool dwarfs. III. Discovery of a brown dwarf in a 3-year orbit around DE0630-18, A&A, 577, A15, doi: 10.1051/0004-6361/201525757

Sahlmann J., Burgasser A. J., Bardalez Gagliuffi D. C., Lazorenko P. F., Ségransan D., Zapatero Osorio M. R., Blake C. H., Gelino C. R., Martín E. L., Bouy H. 2020, Astrometric orbits of spectral binary brown dwarfs - I. Massive T dwarf companions to 2M1059-21 and 2M0805+48, MNRAS, 495, 1136, doi: 10.1093/mnras/staa1235

Sahlmann J., Dupuy T. J., Burgasser A. J., Filippazzo J. C., Martín E. L., Bardalez Gagliuffi D. C., Hsu C., Lazorenko P. F., Liu M. C. 2021, Individual dynamical masses of DENIS J063001.4-184014AB reveal a likely young brown dwarf triple, MNRAS, 500, 5453, doi: 10.1093/mnras/staa3577

Salim S., Lépine S., Rich R. M., Shara M. M. 2003, LSR 0602+3910: Discovery of a Bright Nearby L-Type Brown Dwarf, ApJ, 586, L149, doi: 10.1086/374794

Samland M., Mollière P., Bonnefoy M., Maire A. L., Cantalloube F., Cheetham A. C., Mesa D., Gratton R., Biller B. A., Wahhaj Z., Bouwman J., Brandner W., Melnick D., Carson J., Janson M., Henning T., Homeier D., Mordasini C., Langlois M., Quanz S. P., van Boekel R., Zurlo A., Schlieder J. E., Avenhaus H., Beuzit J. L., Boccaletti A., Bonavita M., Chauvin G., Claudi R., Cudel M., Desidera S., Feldt M., Fusco T., Galicher R., Kopytova T. G., Lagrange A. M., Le Coroller H., Martinez P., Moeller-Nilsson O., Mouillet D., Mugnier L. M., Perrot C., Sevin A., Sissa E., Vigan A., Weber L. 2017, Spectral and atmospheric characterization of 51 Eridani b using VLT/SPHERE, A&A, 603, A57, doi: 10.1051/0004-6361/201629767

Santana F. A., Beaton R. L., Covey K. R., O'Connell J. E., Longa-Peña P., Cohen R.,

Fernández-Trincado J. G., Hayes C. R., Zasowski G., Sobeck J. S., Majewski S. R., Chojnowski S. D., De Lee N., Oelkers R. J., Stringfellow G. S., Almeida A., Anguiano B., Donor J., Frinchaboy P. M., Hasselquist S., Johnson J. A., Kollmeier J. A., Nidever D. L., Price-Whelan A. M., Rojas-Arriagada A., Schultheis M., Shetrone M., Simon J. D., Aerts C., Borissova J., Drout M. R., Geisler D., Law C. Y., Medina N., Minniti D., Monachesi A., Muñoz R. R., Poleski R., Roman-Lopes A., Schlaufman K. C., Stutz A. M., Teske J., Tkachenko A., Van Saders J. L., Weinberger A. J., Zoccali M. 2021, Final Targeting Strategy for the SDSS-IV APOGEE-2S Survey, AJ, 162, 303, doi: 10.3847/1538-3881/ac2cbc

Saumon D., Marley M. S. 2008, The Evolution of L and T Dwarfs in Color-Magnitude Diagrams, ApJ, 689, 1327, doi: 10.1086/592734

Schmidt S. J., Cruz K. L., Bongiorno B. J., Liebert J., Reid I. N. 2007, Activity and Kinematics of Ultracool Dwarfs, Including an Amazing Flare Observation, AJ, 133, 2258, doi: 10.1086/512158

Schmidt S. J., West A. A., Bochanski J. J., Hawley S. L., Kielty C. 2014, Calibrating Ultracool Dwarfs: Optical Template Spectra, Bolometric Corrections, and χ Values, PASP, 126, 642, doi: 10.1086/677403

Schmidt S. J., West A. A., Hawley S. L., Pineda J. S. 2010, Colors and Kinematics of L Dwarfs from the Sloan Digital Sky Survey, AJ, 139, 1808, doi: 10.1088/0004-6256/139/5/1808

Schneider A. C., Cushing M. C., Kirkpatrick J. D., Mace G. N., Gelino C. R., Faherty J. K., Fajardo-Acosta S., Sheppard S. S. 2014, Discovery of the Young L Dwarf WISE J174102.78-464225.5, AJ, 147, 34, doi: 10.1088/0004-6256/147/2/34

Schneider A. C., Greco J., Cushing M. C., Kirkpatrick J. D., Mainzer A., Gelino C. R.,

Fajardo-Acosta S. B., Bauer J. 2016, A Proper Motion Survey Using the First Sky Pass of NEOWISE-reactivation Data, ApJ, 817, 112, doi: 10.3847/0004-637X/817/2/112

Scholz A., Muzic K., Geers V., Bonavita M., Jayawardhana R., Tamura M. 2012, Substellar Objects in Nearby Young Clusters (SONYC). IV. A Census of Very Low Mass Objects in NGC 1333, ApJ, 744, 6, doi: 10.1088/0004-637X/744/1/6

Scholz R. D. 2020, New ultracool dwarf neighbours within 20 pc from Gaia DR2, A&A, 637, A45, doi: 10.1051/0004-6361/201937373

Scholz R. D., Meusinger H. 2002, SSSPM J0829-1309: a new nearby L dwarf detected in SuperCOSMOS Sky Surveys, MNRAS, 336, L49, doi: 10.1046/j.1365-8711.2002.05998.x

Schönrich R., Binney J., Dehnen W. 2010, Local kinematics and the local standard of rest, MNRAS, 403, 1829, doi: 10.1111/j.1365-2966.2010.16253.x

Schwarz G. 1978, Estimating the Dimension of a Model, Ann. Statist., 6, 461, doi: 10.1214/aos/1176344136

Sebastian D., Gillon M., Ducrot E., Pozuelos F. J., Garcia L. J., Günther M. N., Delrez L., Queloz D., Demory B. O., Triaud A. H. M. J., Burgasser A., de Wit J., Burdanov A., Dransfield G., Jehin E., McCormac J., Murray C. A., Niraula P., Pedersen P. P., Rackham B. V., Sohy S., Thompson S., Van Grootel V. 2021, SPECULOOS: Ultracool dwarf transit survey. Target list and strategy, A&A, 645, A100, doi: 10.1051/0004-6361/202038827

Seifahrt A., Reiners A., Almaghrbi K. A. M., Basri G. 2010, On the kinematic age of brown dwarfs: radial velocities and space motions of 43 nearby L dwarfs, A&A, 512, A37, doi: 10.1051/0004-6361/200913368

Sharma S., Hayden M. R., Bland-Hawthorn J., Stello D., Buder S., Zinn J. C., Kallinger T., Asplund M., De Silva G. M., D'Orazi V., Freeman K., Kos J., Lewis G. F., Lin J., Lind K., Martell S., Simpson J. D., Wittenmyer R. A., Zucker D. B., Zwitter T., Chen B., Cotar K., Esdaile J., Hon M., Horner J., Huber D., Kafle P. R., Khanna S., Ting Y.-S., Nataf D. M., Nordlander T., Saadon M. H. M., Tepper-Garcia T., Tinney C. G., Traven G., Watson F., Wright D., Wyse R. F. G. 2021, Fundamental relations for the velocity dispersion of stars in the Milky Way, MNRAS, 506, 1761, doi: 10.1093/mnras/stab1086

Shkolnik E. L., Anglada-Escudé G., Liu M. C., Bowler B. P., Weinberger A. J., Boss A. P., Reid I. N., Tamura M. 2012, Identifying the Young Low-mass Stars within 25 pc. II. Distances, Kinematics, and Group Membership, ApJ, 758, 56, doi: 10.1088/0004-637X/758/1/56

Shulyak D., Reiners A., Wende S., Kochukhov O., Piskunov N., Seifahrt A. 2010, Modelling the molecular Zeeman-effect in M-dwarfs: methods and first results, A&A, 523, A37, doi: 10.1051/0004-6361/201015229

Sicilia-Aguilar A., Henning T., Kainulainen J., Roccatagliata V. 2011, Protostars and Stars in the Coronet Cluster: Age, Evolution, and Cluster Structure, ApJ, 736, 137, doi: 10.1088/0004-637X/736/2/137

Silaj J., Landstreet J. D. 2014, Accurate age determinations of several nearby open clusters containing magnetic Ap stars, A&A, 566, A132, doi: 10.1051/0004-6361/201321468

Skinner J., Covey K. R., Bender C. F., Rivera N., De Lee N., Souto D., Chojnowski D., Troup N., Badenes C., Bizyaev D., Blake C. H., Burgasser A., Cañas C., Carlberg J., Gómez Maqueo Chew Y., Deshpande R., Fleming S. W., Fernández-Trincado J. G., García-Hernández D. A., Hearty F., Kounkel M., Longa-Peñe P., Mahadevan S., Majew-

ski S. R., Minniti D., Nidever D., Oravetz A., Pan K., Stassun K., Terrien R., Zamora O. 2018, Forty-four New and Known M-dwarf Multiples in the SDSS-III/APOGEE M-dwarf Ancillary Science Sample, AJ, 156, 45, doi: 10.3847/1538-3881/aac9c2

Skrutskie M. F., Cutri R. M., Stiening R., Weinberg M. D., Schneider S., Carpenter J. M., Beichman C., Capps R., Chester T., Elias J., Huchra J., Liebert J., Lonsdale C., Monet D. G., Price S., Seitzer P., Jarrett T., Kirkpatrick J. D., Gizis J. E., Howard E., Evans T., Fowler J., Fullmer L., Hurt R., Light R., Kopan E. L., Marsh K. A., McCallon H. L., Tam R., Van Dyk S., Wheelock S. 2006, The Two Micron All Sky Survey (2MASS), AJ, 131, 1163, doi: 10.1086/498708

Skumanich A. 1972, Time Scales for Ca II Emission Decay, Rotational Braking, and Lithium Depletion, ApJ, 171, 565, doi: 10.1086/151310

Slesnick C. L., Carpenter J. M., Hillenbrand L. A. 2006, A Large-Area Search for Low-Mass Objects in Upper Scorpius. I. The Photometric Campaign and New Brown Dwarfs, AJ, 131, 3016, doi: 10.1086/503560

Slesnick C. L., Hillenbrand L. A., Carpenter J. M. 2008, A Large-Area Search for Low-Mass Objects in Upper Scorpius. II. Age and Mass Distributions, ApJ, 688, 377, doi: 10.1086/592265

Smart R. L., Marocco F., Sarro L. M., Barrado D., Beamín J. C., Caballero J. A., Jones H. R. A. 2019, The Gaia ultracool dwarf sample - II. Structure at the end of the main sequence, MNRAS, 485, 4423, doi: 10.1093/mnras/stz678

Smart R. L., Tinney C. G., Bucciarelli B., Marocco F., Abbas U., Andrei A., Bernardi G., Burningham B., Cardoso C., Costa E., Crosta M. T., Daprá M., Day-Jones A., Goldman B., Jones H. R. A., Lattanzi M. G., Leggett S. K., Lucas P., Mendez R., Penna J. L., Pinfield D., Smith L., Sozzetti A., Vecchiato A. 2013, NPARSEC: NTT

Parallaxes of Southern Extremely Cool objects. Goals, targets, procedures and first results, MNRAS, 433, 2054, doi: 10.1093/mnras/stt876

Smart R. L., Bucciarelli B., Jones H. R. A., Marocco F., Andrei A. H., Goldman B., Mendez R. A., d'Avila V. A., Burningham B., Camargo J. I. B., Crosta M. T., Daprà M., Jenkins J. S., Lachaume R., Lattanzi M. G., Penna J. L., Pinfield D. J., da Silva Neto D. N., Sozzetti A., Vecchiato A. 2018, Parallaxes of Southern Extremely Cool objects III: 118 L and T dwarfs, MNRAS, 481, 3548, doi: 10.1093/mnras/sty2520

Smith E. J., Davis L. J., Jones D. E., Coleman P. J. J., Colburn D. S., Dyal P., Sonett C. P., Frandsen A. M. A. 1974, The planetary magnetic field and magnetosphere of Jupiter: Pioneer 10, J. Geophys. Res., 79, 3501, doi: 10.1029/JA079i025p03501

Snellen I. A. G., Brandl B. R., de Kok R. J., Brogi M., Birkby J., Schwarz H. 2014, Fast spin of the young extrasolar planet β Pictoris b, Nature, 509, 63, doi: 10.1038/nature13253

Song I., Bessell M. S., Zuckerman B. 2002, Lithium Depletion Boundary in a Pre-Main-Sequence Binary System, ApJ, 581, L43, doi: 10.1086/345927

Sorahana S., Yamamura I. 2012, AKARI Observations of Brown Dwarfs. III. CO, CO_2, and CH_4 Fundamental Bands and Physical Parameters, ApJ, 760, 151, doi: 10.1088/0004-637X/760/2/151

Souto D., Cunha K., García-Hernández D. A., Zamora O., Allende Prieto C., Smith V. V., Mahadevan S., Blake C., Johnson J. A., Jönsson H., Pinsonneault M., Holtzman J., Majewski S. R., Shetrone M., Teske J., Nidever D., Schiavon R., Sobeck J., García Pérez A. E., Gómez Maqueo Chew Y., Stassun K. 2017, Chemical Abundances of M-dwarfs from the APOGEE Survey. I. The Exoplanet Hosting Stars Kepler-138 and Kepler-186, ApJ, 835, 239, doi: 10.3847/1538-4357/835/2/239

Souto D., Cunha K., Smith V. V., Prieto C. A., Covey K., García-Hernández D. A., Holtzman J. A., Jönsson H., Mahadevan S., Majewski S. R., Masseron T., Pinsonneault M., Schneider D. P., Shetrone M., Stassun K. G., Terrien R., Zamora O., Stringfellow G. S., Lane R. R., Nitschelm C., Rojas-Ayala B. 2022, Detailed Chemical Abundances for a Benchmark Sample of M Dwarfs from the APOGEE Survey, ApJ, 927, 123, doi: 10.3847/1538-4357/ac4891

Spitzer Lyman J., Schwarzschild M. 1953, The Possible Influence of Interstellar Clouds on Stellar Velocities. II., ApJ, 118, 106, doi: 10.1086/145730

Stassun K. G., Mathieu R. D., Valenti J. A. 2006, Discovery of two young brown dwarfs in an eclipsing binary system, Nature, 440, 311, doi: 10.1038/nature04570

Stauffer J. R., Schultz G., Kirkpatrick J. D. 1998, Keck Spectra of Pleiades Brown Dwarf Candidates and a Precise Determination of the Lithium Depletion Edge in the Pleiades, ApJ, 499, L199, doi: 10.1086/311379

Stephens D. C., Leggett S. K., Cushing M. C., Marley M. S., Saumon D., Geballe T. R., Golimowski D. A., Fan X., Noll K. S. 2009, The 0.8-14.5 μm Spectra of Mid-L to Mid-T Dwarfs: Diagnostics of Effective Temperature, Grain Sedimentation, Gas Transport, and Surface Gravity, ApJ, 702, 154, doi: 10.1088/0004-637X/702/1/154

Stephenson C. B. 1986, Dwarf K and M stars of high proper motion found in a hemispheric survey., AJ, 92, 139, doi: 10.1086/114146

Strauss M. A., Fan X., Gunn J. E., Leggett S. K., Geballe T. R., Pier J. R., Lupton R. H., Knapp G. R., Annis J., Brinkmann J., Crocker J. H., Csabai I., Fukugita M., Golimowski D. A., Harris F. H., Hennessy G. S., Hindsley R. B., Ivezić Ž., Kent S., Lamb D. Q., Munn J. A., Newberg H. J., Rechenmacher R., Schneider D. P., Smith J. A., Stoughton C., Tucker D. L., Waddell P., York D. G. 1999, The Discovery of a

Field Methane Dwarf from Sloan Digital Sky Survey Commissioning Data, ApJ, 522, L61, doi: 10.1086/312218

Strömberg G. 1924, The Asymmetry in Stellar Motions and the Existence of a Velocity-Restriction in Space, ApJ, 59, 228, doi: 10.1086/142813

Tamburo P., Muirhead P. S., McCarthy A. M., Hart M., Gracia D., Vos J. M., Bardalez Gagliuffi D. C., Faherty J., Theissen C., Agol E., Skinner J. N., Sagear S. 2022, The Perkins INfrared Exosatellite Survey (PINES) I. Survey Overview, Reduction Pipeline, and Early Results, AJ, 163, 253, doi: 10.3847/1538-3881/ac64aa

Tanner A., White R., Bailey J., Blake C., Blake G., Cruz K., Burgasser A. J., Kraus A. 2012, Keck NIRSPEC Radial Velocity Observations of Late-M Dwarfs, ApJS, 203, 10, doi: 10.1088/0067-0049/203/1/10

Tannock M. E., Metchev S., Hood C. E., Mace G. N., Fortney J. J., Morley C. V., Jaffe D. T., Lupu R. 2022, A 1.46-2.48 μm spectroscopic atlas of a T6 dwarf (1060 K) atmosphere with IGRINS: first detections of H_2S and H_2, and verification of H_2O, CH_4, and NH_3 line lists, MNRAS, 514, 3160, doi: 10.1093/mnras/stac1412

Tannock M. E., Metchev S., Heinze A., Miles-Páez P. A., Gagné J., Burgasser A., Marley M. S., Apai D., Suárez G., Plavchan P. 2021, Weather on Other Worlds. V. The Three Most Rapidly Rotating Ultra-cool Dwarfs, AJ, 161, 224, doi: 10.3847/1538-3881/abeb67

Terrien R. C., Mahadevan S., Deshpande R., Bender C. F. 2015, A Near-Infrared Spectroscopic Survey of 886 Nearby M Dwarfs, ApJS, 220, 16, doi: 10.1088/0067-0049/220/1/16

Theissen C. A. 2018, Parallaxes of Cool Objects with WISE: Filling in for Gaia, ApJ, 862, 173, doi: 10.3847/1538-4357/aaccfa

Theissen C. A., Konopacky Q. M., Lu J. R., Kim D., Zhang S. Y., Hsu C.-C., Chu L., Wei L. 2021, The 3-D Kinematics of the Orion Nebula Cluster: NIRSPEC-AO Radial Velocities of the Core Population, arXiv e-prints, arXiv:2105.05871. https://arxiv.org/abs/2105.05871

Theissen C. A., West A. A., Dhital S. 2016, Motion Verified Red Stars (MoVeRS): A Catalog of Proper Motion Selected Low-mass Stars from WISE, SDSS, and 2MASS, AJ, 151, 41, doi: 10.3847/0004-6256/151/2/41

Theissen C. A., West A. A., Shippee G., Burgasser A. J., Schmidt S. J. 2017, The Late-Type Extension to MoVeRS (LaTE-MoVeRS): Proper Motion Verified Low-mass Stars and Brown Dwarfs from SDSS, 2MASS, and WISE, AJ, 153, 92, doi: 10.3847/1538-3881/153/3/92

Thompson M. A., Kirkpatrick J. D., Mace G. N., Cushing M. C., Gelino C. R., Griffith R. L., Skrutskie M. F., Eisenhardt P. R. M., Wright E. L., Marsh K. A., Mix K. J., Beichman C. A., Faherty J. K., Toloza O., Ferrara J., Apodaca B., McLean I. S., Bloom J. S. 2013, Nearby M, L, and T Dwarfs Discovered by the Wide-field Infrared Survey Explorer (WISE), PASP, 125, 809, doi: 10.1086/671426

Tian H.-J., Xu Y., Liu C., Rix H.-W., Sesar B., Goldman B. 2020, The Extended Gaia-PS1-SDSS (GPS1+) Proper Motion Catalog, ApJS, 248, 28, doi: 10.3847/1538-4365/ab8d27

Ting Y.-S., Hawkins K., Rix H.-W. 2018, A Large and Pristine Sample of Standard Candles across the Milky Way:
100,000 Red Clump Stars with 3% Contamination, ApJ, 858, L7, doi: 10.3847/2041-8213/aabf8e

Ting Y.-S., Rix H.-W. 2019, The Vertical Motion History of Disk Stars throughout the Galaxy, ApJ, 878, 21, doi: 10.3847/1538-4357/ab1ea5

Torrence C., Compo G. P. 1998, A Practical Guide to Wavelet Analysis., Bulletin of the American Meteorological Society, 79, 61, doi: 10.1175/1520-0477(1998)079<0061:APGTWA>2.0.CO;2

Tran H. D., Cohen R., Colson A., Mader J. A., Swain M., Laity A. C., Kong M., Gelino C. R., Berriman G. B. 2016, in Proc. SPIE, Vol. 9910, Observatory Operations: Strategies, Processes, and Systems VI, 99102E, doi: 10.1117/12.2230963

Triaud A. H. M. J. 2018, in Handbook of Exoplanets, ed. H. J. Deeg, J. A. Belmonte, 2, doi: 10.1007/978-3-319-55333-7_2

Triaud A. H. M. J., Collier Cameron A., Queloz D., Anderson D. R., Gillon M., Hebb L., Hellier C., Loeillet B., Maxted P. F. L., Mayor M., Pepe F., Pollacco D., Ségransan D., Smalley B., Udry S., West R. G., Wheatley P. J. 2010, Spin-orbit angle measurements for six southern transiting planets. New insights into the dynamical origins of hot Jupiters, A&A, 524, A25, doi: 10.1051/0004-6361/201014525

Triaud A. H. M. J., Burgasser A. J., Burdanov A., Kunovac Hodžić V., Alonso R., Bardalez Gagliuffi D., Delrez L., Demory B.-O., de Wit J., Ducrot E., Hessman F. V., Husser T.-O., Jehin E., Pedersen P. P., Queloz D., McCormac J., Murray C., Sebastian D., Thompson S., Van Grootel V., Gillon M. 2020, An eclipsing substellar binary in a young triple system discovered by SPECULOOS, Nature Astronomy, 4, 650, doi: 10.1038/s41550-020-1018-2

Tsuji T. 2016, Near-infrared spectroscopy of M dwarfs. IV. A preliminary survey on the carbon isotopic ratio in M dwarfs*, PASJ, 68, 84, doi: 10.1093/pasj/psw076

Uehara S., Kawahara H., Masuda K., Yamada S., Aizawa M. 2016, Transiting Planet Candidates Beyond the Snow Line Detected by Visual Inspection of 7557 Kepler Objects of Interest, ApJ, 822, 2, doi: 10.3847/0004-637X/822/1/2

Van Hoof P. A. M. 2018, Recent Development of the Atomic Line List, Galaxies, 6, doi: 10.3390/galaxies6020063

Vogt S. S., Allen S. L., Bigelow B. C., Bresee L., Brown B., Cantrall T., Conrad A., Couture M., Delaney C., Epps H. W., Hilyard D., Hilyard D. F., Horn E., Jern N., Kanto D., Keane M. J., Kibrick R. I., Lewis J. W., Osborne J., Pardeilhan G. H., Pfister T., Ricketts T., Robinson L. B., Stover R. J., Tucker D., Ward J., Wei M. Z. 1994, in Proc. SPIE, Vol. 2198, Instrumentation in Astronomy VIII, ed. D. L. Crawford, E. R. Craine, 362, doi: 10.1117/12.176725

Vogt S. S., Radovan M., Kibrick R., Butler R. P., Alcott B., Allen S., Arriagada P., Bolte M., Burt J., Cabak J., Chloros K., Cowley D., Deich W., Dupraw B., Earthman W., Epps H., Faber S., Fischer D., Gates E., Hilyard D., Holden B., Johnston K., Keiser S., Kanto D., Katsuki M., Laiterman L., Lanclos K., Laughlin G., Lewis J., Lockwood C., Lynam P., Marcy G., McLean M., Miller J., Misch T., Peck M., Pfister T., Phillips A., Rivera E., Sand ford D., Saylor M., Stover R., Thompson M., Walp B., Ward J., Wareham J., Wei M., Wright C. 2014, APF—The Lick Observatory Automated Planet Finder, PASP, 126, 359, doi: 10.1086/676120

Vos J. M., Allers K. N., Biller B. A. 2017, The Viewing Geometry of Brown Dwarfs Influences Their Observed Colors and Variability Amplitudes, ApJ, 842, 78, doi: 10.3847/1538-4357/aa73cf

Vos J. M., Allers K. N., Biller B. A., Liu M. C., Dupuy T. J., Gallimore J. F., Adenuga

I. J., Best W. M. J. 2018, Variability of the lowest mass objects in the AB Doradus moving group, MNRAS, 474, 1041, doi: 10.1093/mnras/stx2752

Vos J. M., Faherty J. K., Gagné J., Marley M., Metchev S., Gizis J., Rice E. L., Cruz K. 2022, Let the Great World Spin: Revealing the Stormy, Turbulent Nature of Young Giant Exoplanet Analogs with the Spitzer Space Telescope, arXiv e-prints, arXiv:2201.04711. https://arxiv.org/abs/2201.04711

Vos J. M., Biller B. A., Bonavita M., Eriksson S., Liu M. C., Best W. M. J., Metchev S., Radigan J., Allers K. N., Janson M., Buenzli E., Dupuy T. J., Bonnefoy M., Manjavacas E., Brandner W., Crossfield I., Deacon N., Henning T., Homeier D., Kopytova T., Schlieder J. 2019, A search for variability in exoplanet analogues and low-gravity brown dwarfs, MNRAS, 483, 480, doi: 10.1093/mnras/sty3123

Vos J. M., Biller B. A., Allers K. N., Faherty J. K., Liu M. C., Metchev S., Eriksson S., Manjavacas E., Dupuy T. J., Janson M., Radigan-Hoffman J., Crossfield I., Bonnefoy M., Best W. M. J., Homeier D., Schlieder J. E., Brandner W., Henning T., Bonavita M., Buenzli E. 2020, Spitzer Variability Properties of Low-gravity L Dwarfs, AJ, 160, 38, doi: 10.3847/1538-3881/ab9642

Watson C. L., Henden A. A., Price A. 2006, The International Variable Star Index (VSX), Society for Astronomical Sciences Annual Symposium, 25, 47

Weinberger A. J., Boss A. P., Keiser S. A., Anglada-Escudé G., Thompson I. B., Burley G. 2016, Trigonometric Parallaxes and Proper Motions of 134 Southern Late M, L, and T Dwarfs from the Carnegie Astrometric Planet Search Program, AJ, 152, 24, doi: 10.3847/0004-6256/152/1/24

Wenger M., Ochsenbein F., Egret D., Dubois P., Bonnarel F., Borde S., Genova F., Jasniewicz G., Laloë S., Lesteven S., Monier R. 2000, The SIMBAD astronomical

database. The CDS reference database for astronomical objects, A&AS, 143, 9, doi: 10.1051/aas:2000332

Werner M. W., Roellig T. L., Low F. J., Rieke G. H., Rieke M., Hoffmann W. F., Young E., Houck J. R., Brandl B., Fazio G. G., Hora J. L., Gehrz R. D., Helou G., Soifer B. T., Stauffer J., Keene J., Eisenhardt P., Gallagher D., Gautier T. N., Irace W., Lawrence C. R., Simmons L., Van Cleve J. E., Jura M., Wright E. L., Cruikshank D. P. 2004, The Spitzer Space Telescope Mission, ApJS, 154, 1, doi: 10.1086/422992

West A. A., Hawley S. L., Bochanski J. J., Covey K. R., Reid I. N., Dhital S., Hilton E. J., Masuda M. 2008, Constraining the Age-Activity Relation for Cool Stars: The Sloan Digital Sky Survey Data Release 5 Low-Mass Star Spectroscopic Sample, AJ, 135, 785, doi: 10.1088/0004-6256/135/3/785

West A. A., Weisenburger K. L., Irwin J., Berta-Thompson Z. K., Charbonneau D., Dittmann J., Pineda J. S. 2015, An Activity-Rotation Relationship and Kinematic Analysis of Nearby Mid-to-Late-Type M Dwarfs, ApJ, 812, 3, doi: 10.1088/0004-637X/812/1/3

West A. A., Morgan D. P., Bochanski J. J., Andersen J. M., Bell K. J., Kowalski A. F., Davenport J. R. A., Hawley S. L., Schmidt S. J., Bernat D., Hilton E. J., Muirhead P., Covey K. R., Rojas-Ayala B., Schlawin E., Gooding M., Schluns K., Dhital S., Pineda J. S., Jones D. O. 2011, The Sloan Digital Sky Survey Data Release 7 Spectroscopic M Dwarf Catalog. I. Data, AJ, 141, 97, doi: 10.1088/0004-6256/141/3/97

Wielen R. 1977, The Diffusion of Stellar Orbits Derived from the Observed Age-Dependence of the Velocity Dispersion, A&A, 60, 263

Wilson J. C., Henderson C. P., Herter T. L., Matthews K., Skrutskie M. F., Adams J. D., Moon D.-S., Smith R., Gautier N., Ressler M., Soifer B. T., Lin S., Howard J., LaMarr

J., Stolberg T. M., Zink J. 2004, in Society of Photo-Optical Instrumentation Engineers (SPIE) Conference Series, Vol. 5492, Ground-based Instrumentation for Astronomy, ed. A. F. M. Moorwood, M. Iye, 1295–1305, doi: 10.1117/12.550925

Wilson J. C., Hearty F. R., Skrutskie M. F., Majewski S. R., Holtzman J. A., Eisenstein D., Gunn J., Blank B., Henderson C., Smee S., Nelson M., Nidever D., Arns J., Barkhouser R., Barr J., Beland S., Bershady M. A., Blanton M. R., Brunner S., Burton A., Carey L., Carr M., Colque J. P., Crane J., Damke G. J., Davidson J. W. J., Dean J., Di Mille F., Don K. W., Ebelke G., Evans M., Fitzgerald G., Gillespie B., Hall M., Harding A., Harding P., Hammond R., Hancock D., Harrison C., Hope S., Horne T., Karakla J., Lam C., Leger F., MacDonald N., Maseman P., Matsunari J., Melton S., Mitcheltree T., O'Brien T., O'Connell R. W., Patten A., Richardson W., Rieke G., Rieke M., Roman-Lopes A., Schiavon R. P., Sobeck J. S., Stolberg T., Stoll R., Tembe M., Trujillo J. D., Uomoto A., Vernieri M., Walker E., Weinberg D. H., Young E., Anthony-Brumfield B., Bizyaev D., Breslauer B., De Lee N., Downey J., Halverson S., Huehnerhoff J., Klaene M., Leon E., Long D., Mahadevan S., Malanushenko E., Nguyen D. C., Owen R., Sánchez-Gallego J. R., Sayres C., Shane N., Shectman S. A., Shetrone M., Skinner D., Stauffer F., Zhao B. 2019, The Apache Point Observatory Galactic Evolution Experiment (APOGEE) Spectrographs, PASP, 131, 055001, doi: 10.1088/1538-3873/ab0075

Wilson P. A., Rajan A., Patience J. 2014, The brown dwarf atmosphere monitoring (BAM) project. I. The largest near-IR monitoring survey of L and T dwarfs, A&A, 566, A111, doi: 10.1051/0004-6361/201322995

Yao Y., Meyer M. R., Covey K. R., Tan J. C., Da Rio N. 2018, IN-SYNC. VIII. Primordial Disk Frequencies in NGC 1333, IC 348, and the Orion A Molecular Cloud, ApJ, 869, 72, doi: 10.3847/1538-4357/aaec7a

York D. G., Adelman J., Anderson John E. J., Anderson S. F., Annis J., Bahcall N. A., Bakken J. A., Barkhouser R., Bastian S., Berman E., Boroski W. N., Bracker S., Briegel C., Briggs J. W., Brinkmann J., Brunner R., Burles S., Carey L., Carr M. A., Castander F. J., Chen B., Colestock P. L., Connolly A. J., Crocker J. H., Csabai I., Czarapata P. C., Davis J. E., Doi M., Dombeck T., Eisenstein D., Ellman N., Elms B. R., Evans M. L., Fan X., Federwitz G. R., Fiscelli L., Friedman S., Frieman J. A., Fukugita M., Gillespie B., Gunn J. E., Gurbani V. K., de Haas E., Haldeman M., Harris F. H., Hayes J., Heckman T. M., Hennessy G. S., Hindsley R. B., Holm S., Holmgren D. J., Huang C.-h., Hull C., Husby D., Ichikawa S.-I., Ichikawa T., Ivezić Ž., Kent S., Kim R. S. J., Kinney E., Klaene M., Kleinman A. N., Kleinman S., Knapp G. R., Korienek J., Kron R. G., Kunszt P. Z., Lamb D. Q., Lee B., Leger R. F., Limmongkol S., Lindenmeyer C., Long D. C., Loomis C., Loveday J., Lucinio R., Lupton R. H., MacKinnon B., Mannery E. J., Mantsch P. M., Margon B., McGehee P., McKay T. A., Meiksin A., Merelli A., Monet D. G., Munn J. A., Narayanan V. K., Nash T., Neilsen E., Neswold R., Newberg H. J., Nichol R. C., Nicinski T., Nonino M., Okada N., Okamura S., Ostriker J. P., Owen R., Pauls A. G., Peoples J., Peterson R. L., Petravick D., Pier J. R., Pope A., Pordes R., Prosapio A., Rechenmacher R., Quinn T. R., Richards G. T., Richmond M. W., Rivetta C. H., Rockosi C. M., Ruthmansdorfer K., Sandford D., Schlegel D. J., Schneider D. P., Sekiguchi M., Sergey G., Shimasaku K., Siegmund W. A., Smee S., Smith J. A., Snedden S., Stone R., Stoughton C., Strauss M. A., Stubbs C., SubbaRao M., Szalay A. S., Szapudi I., Szokoly G. P., Thakar A. R., Tremonti C., Tucker D. L., Uomoto A., Vanden Berk D., Vogeley M. S., Waddell P., Wang S.-i., Watanabe M., Weinberg D. H., Yanny B., Yasuda N., SDSS Collaboration. 2000, The Sloan Digital Sky Survey: Technical Summary, AJ, 120, 1579, doi: 10.1086/301513

Yu J., Liu C. 2018, The age-velocity dispersion relation of the Galactic discs from LAMOST-Gaia data, MNRAS, 475, 1093, doi: 10.1093/mnras/stx3204

Zacharias N., Finch C. T., Girard T. M., Henden A., Bartlett J. L., Monet D. G., Zacharias M. I. 2012, VizieR Online Data Catalog: UCAC4 Catalogue (Zacharias+, 2012), VizieR Online Data Catalog, I/322A

Zamora O., García-Hernández D. A., Allende Prieto C., Carrera R., Koesterke L., Edvardsson B., Castelli F., Plez B., Bizyaev D., Cunha K., García Pérez A. E., Gustafsson B., Holtzman J. A., Lawler J. E., Majewski S. R., Manchado A., Mészáros S., Shane N., Shetrone M., Smith V. V., Zasowski G. 2015, New H-band Stellar Spectral Libraries for the SDSS-III/APOGEE Survey, AJ, 149, 181, doi: 10.1088/0004-6256/149/6/181

Zapatero Osorio M. R., Martín E. L., Béjar V. J. S., Bouy H., Deshpande R., Wainscoat R. J. 2007, Space Velocities of L- and T-Type Dwarfs, ApJ, 666, 1205, doi: 10.1086/520673

Zapatero Osorio M. R., Martín E. L., Bouy H., Tata R., Deshpande R., Wainscoat R. J. 2006, Spectroscopic Rotational Velocities of Brown Dwarfs, ApJ, 647, 1405, doi: 10.1086/505484

Zasowski G., Johnson J. A., Frinchaboy P. M., Majewski S. R., Nidever D. L., Rocha Pinto H. J., Girardi L., Andrews B., Chojnowski S. D., Cudworth K. M., Jackson K., Munn J., Skrutskie M. F., Beaton R. L., Blake C. H., Covey K., Deshpande R., Epstein C., Fabbian D., Fleming S. W., Garcia Hernandez D. A., Herrero A., Mahadevan S., Mészáros S., Schultheis M., Sellgren K., Terrien R., van Saders J., Allende Prieto C., Bizyaev D., Burton A., Cunha K., da Costa L. N., Hasselquist S., Hearty F., Holtzman J., García Pérez A. E., Maia M. A. G., O'Connell R. W., O'Donnell C., Pinsonneault M., Santiago B. X., Schiavon R. P., Shetrone M., Smith V., Wilson J. C. 2013, Target Selection for the Apache Point Observatory Galactic Evolution Experiment (APOGEE), AJ, 146, 81, doi: 10.1088/0004-6256/146/4/81

Zasowski G., Cohen R. E., Chojnowski S. D., Santana F., Oelkers R. J., Andrews B., Beaton R. L., Bender C., Bird J. C., Bovy J., Carlberg J. K., Covey K., Cunha K., Dell'Agli F., Fleming S. W., Frinchaboy P. M., García-Hernández D. A., Harding P., Holtzman J., Johnson J. A., Kollmeier J. A., Majewski S. R., Mészáros S., Munn J., Muñoz R. R., Ness M. K., Nidever D. L., Poleski R., Román-Zúñiga C., Shetrone M., Simon J. D., Smith V. V., Sobeck J. S., Stringfellow G. S., Szigetiáros L., Tayar J., Troup N. 2017, Target Selection for the SDSS-IV APOGEE-2 Survey, AJ, 154, 198, doi: 10.3847/1538-3881/aa8df9

Zechmeister M., Dreizler S., Ribas I., Reiners A., Caballero J. A., Bauer F. F., Béjar V. J. S., González-Cuesta L., Herrero E., Lalitha S., López-González M. J., Luque R., Morales J. C., Pallé E., Rodríguez E., Rodríguez López C., Tal-Or L., Anglada-Escudé G., Quirrenbach A., Amado P. J., Abril M., Aceituno F. J., Aceituno J., Alonso-Floriano F. J., Ammler-von Eiff M., Antona Jiménez R., Anwand-Heerwart H., Arroyo-Torres B., Azzaro M., Baroch D., Barrado D., Becerril S., Benítez D., Berdiñas Z. M., Bergond G., Bluhm P., Brinkmöller M., del Burgo C., Calvo Ortega R., Cano J., Cardona Guillén C., Carro J., Cárdenas Vázquez M. C., Casal E., Casasayas-Barris N., Casanova V., Chaturvedi P., Cifuentes C., Claret A., Colomé J., Cortés-Contreras M., Czesla S., Díez-Alonso E., Dorda R., Fernández M., Fernández-Martín A., Fuhrmeister B., Fukui A., Galadí-Enríquez D., Gallardo Cava I., Garcia de la Fuente J., Garcia-Piquer A., García Vargas M. L., Gesa L., Góngora Rueda J., González-Álvarez E., González Hernández J. I., González-Peinado R., Grözinger U., Guàrdia J., Guijarro A., de Guindos E., Hatzes A. P., Hauschildt P. H., Hedrosa R. P., Helmling J., Henning T., Hermelo I., Hernández Arabi R., Hernández Castaño L., Hernández Otero F., Hintz D., Huke P., Huber A., Jeffers S. V., Johnson E. N., de Juan E., Kaminski A., Kemmer J., Kim M., Klahr H., Klein R., Klüter J., Klutsch A., Kossakowski D., Kürster M., Labarga F., Lafarga M., Llamas M., Lampón M., Lara L. M., Launhardt R., Lázaro

F. J., Lodieu N., López del Fresno M., López-Puertas M., López Salas J. F., López-Santiago J., Magán Madinabeitia H., Mall U., Mancini L., Mandel H., Marfil E., Marín Molina J. A., Maroto Fernández D., Martín E. L., Martín-Fernández P., Martín-Ruiz S., Marvin C. J., Mirabet E., Montañés-Rodríguez P., Montes D., Moreno-Raya M. E., Nagel E., Naranjo V., Narita N., Nortmann L., Nowak G., Ofir A., Oshagh M., Panduro J., Parviainen H., Pascual J., Passegger V. M., Pavlov A., Pedraz S., Pérez-Calpena A., Pérez Medialdea D., Perger M., Perryman M. A. C., Rabaza O., Ramón Ballesta A., Rebolo R., Redondo P., Reffert S., Reinhardt S., Rhode P., Rix H. W., Rodler F., Rodríguez Trinidad A., Rosich A., Sadegi S., Sánchez-Blanco E., Sánchez Carrasco M. A., Sánchez-López A., Sanz-Forcada J., Sarkis P., Sarmiento L. F., Schäfer S., Schmitt J. H. M. M., Schöfer P., Schweitzer A., Seifert W., Shulyak D., Solano E., Sota A., Stahl O., Stock S., Strachan J. B. P., Stuber T., Stürmer J., Suárez J. C., Tabernero H. M., Tala Pinto M., Trifonov T., Veredas G., Vico Linares J. I., Vilardell F., Wagner K., Wolthoff V., Xu W., Yan F., Zapatero Osorio M. R. 2019, The CARMENES search for exoplanets around M dwarfs. Two temperate Earth-mass planet candidates around Teegarden's Star, A&A, 627, A49, doi: 10.1051/0004-6361/201935460

Zeeman P. 1897, On the Influence of Magnetism on the Nature of the Light Emitted by a Substance., ApJ, 5, 332, doi: 10.1086/140355

Zhang Y., Snellen I. A. G., Mollière P. 2021a, The ^{12}CO/^{13}CO isotopologue ratio of a young, isolated brown dwarf. Possibly distinct formation pathways of super-Jupiters and brown dwarfs, A&A, 656, A76, doi: 10.1051/0004-6361/202141502

Zhang Z., Liu M. C., Best W. M. J., Dupuy T. J., Siverd R. J. 2021b, The Hawaii Infrared Parallax Program. V. New T-Dwarf Members and Candidate Members of Nearby Young Moving Groups, arXiv e-prints, arXiv:2102.05045. https://arxiv.org/abs/2102.05045

Zhang Z., Liu M. C., Best W. M. J., Magnier E. A., Aller K. M., Chambers K. C., Draper P. W., Flewelling H., Hodapp K. W., Kaiser N., Kudritzki R. P., Metcalfe N., Wainscoat R. J., Waters C. 2018, The Pan-STARRS1 Proper-motion Survey for Young Brown Dwarfs in Nearby Star-forming Regions. I. Taurus Discoveries and a Reddening-free Classification Method for Ultracool Dwarfs, ApJ, 858, 41, doi: 10.3847/1538-4357/aab269

Zhang Z. H., Burgasser A. J., Gálvez-Ortiz M. C., Lodieu N., Zapatero Osorio M. R., Pinfield D. J., Allard F. 2019, Primeval very low-mass stars and brown dwarfs - VI. Population properties of metal-poor degenerate brown dwarfs, MNRAS, 486, 1260, doi: 10.1093/mnras/stz777

Zhong J., Li J., Carlin J. L., Chen L., Mendez R. A., Hou J. 2019, Value-added Catalogs of M-type Stars in LAMOST DR5, ApJS, 244, 8, doi: 10.3847/1538-4365/ab3859

Zhou Y., Apai D., Metchev S., Lew B. W. P., Schneider G., Marley M. S., Karalidi T., Manjavacas E., Bedin L. R., Cowan N. B., Miles-Páez P. A., Lowrance P. J., Radigan J., Burgasser A. J. 2018, Cloud Atlas: Rotational Modulations in the L/T Transition Brown Dwarf Companion HN Peg B, AJ, 155, 132, doi: 10.3847/1538-3881/aaabbd

Zuckerman B. 2019, The Nearby, Young, Argus Association: Membership, Age, and Dusty Debris Disks, ApJ, 870, 27, doi: 10.3847/1538-4357/aaee66

Zuckerman B., Bessell M. S., Song I., Kim S. 2006, The Carina-Near Moving Group, ApJ, 649, L115, doi: 10.1086/508060

Zuckerman B., Song I. 2004, Young Stars Near the Sun, ARA&A, 42, 685, doi: 10.1146/annurev.astro.42.053102.134111

Zuckerman B., Vican L., Song I., Schneider A. 2013, Young Stars near Earth: The Octans-

Near Association and Castor Moving Group, ApJ, 778, 5, doi: 10.1088/0004-637X/778/1/5